2017

Nanoporous Calcium Carbonate-Based Substrates for the Controlled Delivery of Functional Materials

Levy, Charlotte Luanne Victoria

Signed: _____

Charlotte Levy

NANOPOROUS CALCIUM CARBONATE-BASED SUBSTRATES FOR THE CONTROLLED DELIVERY OF FUNCTIONAL MATERIALS

by

CHARLOTTE LUANNE VICTORIA LEVY

A thesis submitted to the University of Plymouth in partial fulfilment for the degree of

DOCTOR OF PHILOSOPHY

Environmental and Fluid Modelling Group

Centre for Research in Earth Sciences

School of Geography, Earth, and Environmental Sciences

Faculty of Science and Technology

University of Plymouth

This research has been kindly funded by Omya Development AG.

SEPTEMBER 2016

Supervisory team

Professor G. Peter Matthews
Environmental and Fluid Modelling Group
Room 601a Davy Building
School of Geography, Earth, and Environmental Sciences
University of Plymouth
Plymouth
Devon
PL4 8AA
Telephone: 01752 584798
Email: p.matthews@plymouth.ac.uk

Professor Patrick A. C. Gane
Vice President of Research and Development

Omya International AG
Baslerstrasse 42
CH-4665 Oftringen
Switzerland

School of Chemical Technology
Aalto University
FI-00076 Aalto
Helsinki, Finland

Telephone: +41 62 789 2422
Email: patrick.gane@omya.com

Dr Andrew Turner
B511 Portland Square
School of Geography, Earth, and Environmental Sciences
University of Plymouth
Plymouth
Devon
PL4 8AA
Telephone: 01752 584570
Email: a.turner@plymouth.ac.uk

Abstract

By Charlotte Levy

Nanoporous calcium carbonate-based substrates for the controlled delivery of functional materials.

THE overall aim of this project was to study 'functionalised' calcium carbonates (FCCs) for use as a carrier for the controlled release of 'actives,' by permeation and diffusion, and is being proposed as an environmentally friendly and non-toxic pharmaceutical excipient, nutraceutical, and flavour carrier. The delivery of a drug to its target site in the appropriate amount and time-frame in order for it to have a controlled release effect whilst achieving the maximum therapeutic effect remains a topic of design and development for novel drug delivery systems.

FCCs encompass a family of new pharmaceutical excipients in which the conditions of manufacture follow strict process regulations with respect to the grade of reagents that are employed and the microbiological environment under which they are produced, and include freedom from organic polymers.

Adjustments to the FCC production process can be used to produce a wide range of different morphologies, and raise the possibility of tailoring the void structures of the particles to provide controlled release delivery vehicles for actives across many fields, including drugs and flavours. However, such tailoring can only be fully optimised by a fundamental characterisation of the way in which a drug, loaded into an FCC, then flows and diffuses out over a period of time to provide the delayed release.

It was found that adsorption on the FCC surface is selective, for example, saccharin does not become adsorbed from 4-(2-hydroxyethyl)piperazine-1-ethanesulfonic acid (HEPES) buffer solution, and neither does anethole from ethanol. FCC also does not adsorb the cationic probe benzyltrimethylammonium bromide (BTMAB) or the anionic probe sodium 2-naphthalenesulphonate (Na2NS). However, it was found that vanillin adsorbs onto the FCC in an amount of 2.00 $\pm$ 0.59 mg g^{-1}. Aspirin and vanillin adsorption from ethanolic solutions with various additions of water onto FCC TP was investigated and fitted with the Tóth isotherm. It was estimated that vanillin adsorbed onto around 17 %, and aspirin onto around 39 %, of the overall FCC TP surface area without the addition of any water. An equation was formulated in order to approximate the adsorption as a function of the FCC's surface coverage by the water. This is discussed in Chapter 4 and has also been published in a peer-reviewed academic journal (Levy *et al.*, 2017).

Chapter 5 discusses the preliminary steps of the loading of vanillin and saccharin into FCC, and the results were inconclusive for a majority of samples, concluding that the loading and analysis methods need refining.

The modelling of the diffusion profiles of vanillin loaded FCC S07 and S10 was suc-

cessful, and resulted in diffusion coefficients of 231.9 $\times$ 10^{-16} m^2 s^{-1} and 248.44 $\times$ 10^{-16} m^2 s^{-1}, respectively. This is outlined in Chapter 6.

Chapter 7 describes the 'zero length column' (ZLC) technique, which was used as a way to characterise the diffusivity of the intraparticle pores of each FCC grade. However, it was established that there are many experimental artefacts present with such a method. This work outlines the development of the novel 'finite length column' (FLC), which was developed as a means to overcome the limitations of the ZLC (Levy *et al.*, 2015). Effective diffusivity coefficients in the long-term region of the diffusion curves of the FCC samples range from 1.06-106 $\times$ 10^{-16} m^2 s^{-1}.

The FLC was then used in preliminary trials to dilute FCC with an inert solid in order to further refine the ZLC technique, and is discussed in Chapter 8. Two mathematical methods were also developed to aid in the refinement. The reported effective diffusivity coefficient for FCC 03 in the long-term region of the diffusion curve is 49.5 $\times$ 10^{-16} m^2 s^{-1}.

In conclusion, this work confirms that FCC has potential for use as a carrier for the controlled release of 'actives' by diffusion. The utilisation of mathematical modelling in conjunction with experimental methods in the study of drug release and delivery is steadily increasing due to its enormous future potential; it will enable the optimisation of novel dosage forms and the elucidation of release mechanisms at a major reduction in cost and time compared with the number of experimental studies required to do so.

Contents

List of Figures

List of Tables

List of Equations

Acknowledgements

BENEATH the words written in this thesis lies 5 years worth of bewilderment, anxiety, enjoyment, and above all, growth. After 5 years I cannot believe that this project has come to an end. I chose to pursue a PhD because I believe the method of study suits my introverted and conscientious personality. I am a life long learner, and although I may not be the smartest, I am very persevering in my endeavours.

According to Napoleon Hill, the etymology of the word 'educate' is derived from the Latin word 'educo,' meaning to educe, to draw out, and to develop from within. This is the real meaning of the verb 'to educate.' His staunch words echo my own life's philosophy, and through my PhD study I have been able to further develop my own personal enlightenment and sagacity: "An educated man is not, necessarily, one who has an abundance of general or specialised knowledge. An educated man is one who has so developed the faculties of his mind that he may acquire anything he wants, or its equivalent, without violating the rights of others." Whatever outcome of this project I am pleased with where this journey has taken me and the destination at which I have arrived. I feel immense gratitude at the opportunities I've been so lucky to have received, and feel that I have become more educated not only in matters pertaining to academia, but in matters relating to the heart.

If I had to choose one word to summarise and describe all of the events in my life so far, that adjective would be 'serendipitous.' To a vast degree, we are all products of our environments, and I have been blessed with a wonderful support system. I'm extremely fortunate to have the people that are in my life as they believe and see potential in me during the dark times when I fail to do so myself. They are nothing but truthful and encouraging of my academic and personal endeavours.

Firstly, a huge thank you to my primary supervisor, Professor Graham Peter Matthews, for seeing my project through with me during its ups and downs. The reasons as to why I chose to stay in Plymouth to pursue a PhD were many, but one in particular was the quality of supervision I felt that I would receive. Having come to the end of my studies, I can only say that the relationship I have with my supervisor is one that I wouldn't change. Peter has been nothing but friendly and very supportive throughout, and for that, I am extremely thankful.

Secondly, a colossal thank you to Dr Giuliano Maurizio Laudone; although he is not officially a member of my supervisory team, he is an incredibly important member of the Environmental and Fluid Modelling Group in which I've been so privileged to have worked, and has made a significant contribution in my development as a researcher. His perpetual knowledge on a variety of disciplines and enthusiastic approach to tackling problems, as well as his love for Japanese food and culture, have made Maurizio a very inspiring person with whom I've been so lucky to have worked.

My deepest of thanks to Omya International AG. I recognise the financial aid provided and realise how wonderfully extraordinary and rare such funding is to come across. Thank you also, to Dr Patrick Gane, Dr Joachim Schoelkopf, Dr Daniel Gantenbein, Dr

Cathy Ridgway, Dr Daniel Gerard, and the rest of the researchers at the laboratories in Oftringen, for all of your advice, critique, discussions, and hospitality throughout my project and during my ventures in Switzerland.

Thank you, also, to Dr Andrew Turner and Dr Mike Foulkes at the University of Plymouth for all of their support throughout my project.

A resounding thank you to the wonderful people and friends I've been so lucky to have met throughout my research journey. I'll be hard pressed to find such wonderful colleagues in the future, who will listen to all of my gripes and woes about research, and will miss seeking out the best places in Plymouth to indulge in sushi. Thank you so much to all of my other friends who have been so very supportive, and their offers of chocolate, cake, and various other favourite foods of mine is great incentive to finish my studies.

And finally, my mother, my father, and my brother: my family and my best friends. I hate to think what I would be without these three most precious people in my life. There is nothing I can say that can convey the appreciation I feel for their existence. I dedicate this thesis to them.

Also, a quick note to acknowledge the contribution from the caffeine contained within the copious amounts of cups of tea and coffee that have fuelled late night and early morning thesis-writing sessions.

Thank you.

Author's declaration

THE work submitted for this research degree at the University of Plymouth has not formed part of any other university award. This study was in collaboration and financed with the aid of Omya International AG.

Relevant scientific seminars and conferences were regularly attended at which work was often presented. Two papers have been published in peer-reviewed academic journals.

Word count for the main body (Chapters 1-9) of this thesis, excluding headers and captions: **54 125**

Signed: _____

Date: _____

Conferences and presentations

7th International Conference on Porous Media & Annual Meeting. *Padova, Italy.* 18-21th May 2015. Oral presentation.

12th UK Particle Technology Forum 2014. *Manchester, England.* 16-17th September 2014. Poster presentation.

Particulate Systems Analysis 2014. *Manchester, England.* 15-17th September 2014. Oral presentation.

10th International Conference on Diffusion in Solids and Liquids DSL-2014. *Paris, France.* 23-27th June 2014. Oral presentation.

Unconventional Gas 2014. *Aberdeen, Scotland.* 25th March 2014. Attended.

Centre for Research in Earth Sciences (CRES) Research Conference. *Plymouth, England.* 20th November 2013. Oral presentation.

The Postgraduate Society Conference Series. *Plymouth, England.* 27th November 2012. Oral presentation.

CRES Research Conference. *Plymouth, England.* 21th November 2012. Oral presentation.

The Postgraduate Society Annual Conference. *Plymouth, England.* 26th June 2012. Poster presentation.

37th Iberian Adsorption Meeting (Reunión Ibérica de Adsorción, RIA). *Seville, Spain.* 12-14th September 2012. Attended.

Royal Society of Chemistry (RSC) Younger Member's Symposium. *Nottingham, England.* 13th June 2012. Attended.

Publications

Levy, C. L., Matthews, G. P., Laudone, G. M., Beckett, S., Turner, A., Schoelkopf, J. & Gane, P. A. C. *Mechanism of adsorption of actives onto microporous functionalised calcium carbonate (FCC).* Adsorption. 2017, 23 (4), pp 603–612.

Levy, C. L., Matthews, G. P., Laudone, G. M., Gribble, C. M., Turner, A., Ridgway, C. J., Gerard, D. E., Schoelkopf, J. & Gane, P. A. C. *Diffusion and tortuosity in porous functionalized calcium carbonate.* Industrial & Engineering Chemistry Research. 2015, 54 (41), pp 9938–9947.

List of symbols & abbreviations

β	A dimensionless infinite ZLC series parameter, defined by equation 7.2
ε	Permittivity of the material
$\varepsilon_{\mathrm{cl}}$	Critical field size
ε_{r}	Relative permittivity of the material
ε_{s}	Field size
η	Dynamic/absolute viscosity
$\frac{1}{n}$	The Freundlich exponent
Γ	Adsorption density
γ	A dimensionless ZLC parameter that characterises the ratio of external to internal holdup, defined by equation 7.5
Γ'_{max}	Maximum adsorption expressed in moles per gram of substrate
Γ_{max}	Adsorption at maximum equilibrium concentration in solution c_{eq}
λ_{d}	Debye length
λ_{max}	Wavelength of maximum absorbance of an analyte as measured by UV-visible spetroscopy
$\mathscr{N}$	Avogadro number
$\mathbb{E}^3$	Three-dimensional Euclidean space
ω_{D}	Drug to weight ratio
ω_{i}	i^{th} particle
$\bar{x}$	Sample mean
ϕ	Porosity
ϕ_{k}	Denotes a pair of touching particles
ϕ_{FCC}	The specific pore volume contributions from FCC of an MIP curve
ϕ_{GCC}	The specific pore volume contributions from GCC of an MIP curve
ρ	Density
ρ_{q}	Surface charge density

σ	Effective cross-sectional area of the adsorbing cation on the surface of the adsorbent
σ_{devn}	Standard deviation
τ	Tortuosity
c	Concentration
c_0	Initial value of the fluid phase sorbate/analyte concentration at time t = 0 during ZLC/FLC experiments, or the initial concentration of adsorbate in solution during adsorption experiments
C_ρ	Heat capacity of the calorimeter and its contents
C_{N}	Average coordination number of particles touching a randomly chosen particle
c_{p}	Particle concentration (i.e. amount of particulate adsorbent in solution when conducting an adsorption experiment)
c_s	The fluid phase sorbate/analyte concentration during ZLC/FLC experiments
c_{eq}	Equilibrium concentration of an adsorbate in dilute solution
D	Diffusion coefficient/diffusivity
d	Distance or diameter (context dependent)
D'	Effective diffusion coefficient
D'_{phase1}	D' calculated at corrected t = 1 200-1 400 s
D'_{phase2}	D' calculated at corrected t = 1 600-1 800 s
d^{**}	Diameters of particles above which are associated with coarse packing between agglomerates in MIP experiments
d^{*}	Diameters of particles above which, but below d^{**}, are associated with interparticle packing between agglomerates in MIP experiments; anything below this value is associated with the intraparticle porosity of the sample
D_{12}	Bulk diffusion coefficient
D_{FCC}	The calculated diffusion coefficient from Equation 6.2
$d_{\text{mode intrap}}$	The modal pore diameter representing the intraparticle pores in the specific pore volume distribution of an MIP curve
E	The expected (average) value of C_{N}
F	Force of interaction between the charges
F	Volumetric flow rate during ZLC/FLC experiments

f	Fraction of A particles in N
f'	Describes the effect of water on c_{eq}
f''	Describes the effect of water on Γ_{max}
G	Standard free energy
g	Gravitational force
H	Enthalpy
j	Rate of transfer per unit area of section (i.e. flux)
K	Dimensionless Henry constant
K_i	The centre of a particle
K_F	The Freundlich constant
K_L	The Langmuir constant
L	A dimensionless ZLC parameter representing the ratio of diffusional time to secondary transport time, defined by equation 7.3
L_c	Contour length
L_D	Diffusion length
l_k	Kuhn length
m	Heterogeneity index
m_D	Mass of drug
m_{FCC}	Mass of FCC
M_t	Amount of drug remaining in carrier at time t
$M_{v.t0}$	Mass of vanillin in the FCC when $t = 0$
M_v	Mass of vanillin in the FCC at time t
M_∞	Amount of drug in solution when t = infinity (i.e. equilibrium)
N	Total number of particles (N_1 + N_2)
n	Dummy variable or iteration number
N_1	Number of A particles
N_2	Number of B particles
n_{mol}	Number of moles of adsorbate
P	Pressure

P_N	Number of touching pairs of particles
Pr	Probability
q	Heat energy adsorbed or released
q_n	Electric charge of species n
R	Universal gas constant
r	Radius
R^2	Regression coefficient
S	Entropy
S_{ads}	Fraction of the total available surface area for adsorption
Sp	Speed of the centrifuge in rpm
T	Temperature
t	Time
$T_{adsorption}$	Measured temperature upon operating the solution calorimeter
V	Volume of sorbent in the ZLC/FLC bed
v	Velocity of the sphere/sedimentation rate
V_f	Volume of interstitial fluid in the ZLC/FLC bed
V_{total}	Volume of solution with concentration c_0 used in an adsorption experiment
W_{solid}	Weight of the adsorbent used during an adsorption experiment
x	Spatial coordinate
$X(\omega_i)$	A random variable that indicates the particle type for the i^{th} particle (ω_i) in the packed media
y	Spatial coordinate
z	Spatial coordinate
2D	Two-dimensional
3D	Three-dimensional
M	Molarity
A	A constant (only applies to Chapter 4)
A	Active, porous particles (only applies to Chapter 8)

ATC	Automatic Temperature Control
AU	Absorbance units
B	A constant (only applies to Chapter 4)
B	Inert, non-porous particles (only applies to Chapter 8)
BARGE	The Bioaccessibility Research Group of Europe
BTMAB	Benzyltrimethylammonium bromide
CAS	Chemical Abstracts Service
DAD	Diode array detector
DL	Drug load
EFMG	Environmental & Fluid Modelling Group
FAU	Formazin attenuation units
FCC	Functionalised calcium carbonate
FLC	Finite length column
GCC	Ground calcium carbonate
HAP	Hydroxy-(or hydroxyl-)appatite
HCl	Hydrochloric acid
HEPES	4-(2-Hydroxyethyl)piperazine-1-ethanesulfonic acid
HLS	Horizontally banded (large to small) structure
HLST	Horizontally banded (large surface throats) structure
HPLC	High performance liquid chromatograph(y)
HPMC	Hydroxypropyl methylcellulose
HSA	High surface area
HSL	Horizontally banded (small to large) structure
IPA	Isopropyl alcohol
IUPAC	International Union of Pure and Applied Chemistry
IWI	Incipient wetness impregnation
KPVS	Poly(vinyl sulphate) potassium salt
LCZ	Large centred structures
LF	Langmuir-Freundlich

MCC	Modified calcium carbonate
MEA	Metastable equilibrium adsorption
MIP	Mercury intrusion porosimetry
Na2NS	Sodium 2-naphthalene sulphonate
NaCl	Sodium chloride
PASCAL	Pressurization by Automatic Speedup and Continuous Adjustment Logic
PBET	Physiologically-based extraction test
PBS	Phosphate-buffered saline
PCC	Precipitated calcium carbonate
PCE	Particle concentration effect
PEEK	Polyether ether ketone
PET	Polyelectrolyte titration
PSD	Particle size distribution
PTFE	Polytetrafluoroethylene
RAM	Random access memory
rpm	Revolutions per minute
SCZ	Small centred structures
SDS	Sodium dodecyl sulphate
SEM	Scanning electron micrograph/microscopy
SLS	Sodium lauryl sulphate
SNEDDS	Self-nanoemulsifying drug delivery system
SP	Science Partner
spm	Strokes per minute
TG-DSC	Thermal gravimetry with differential scanning calorimetry
UBM	Unified BARGE method
UV	Ultraviolet
v/v	Volume/volume
VB	Vertically banded structure
w/w	Mass/mass
ZLC	Zero length column

Chapter 1

Introduction

1.1 Collaborative basis & aim of project

THIS research project was developed in collaboration between Omya International AG, a Swiss-based world-leading supplier of industrial minerals, and the Environmental & Fluid Modelling Group (EFMG) of the University of Plymouth.

The EFMG are the developers of PoreXpert®, which is a software that generates three-dimensional (3D) void structures from the inverse modelling of percolation characteristics, as measured by mercury intrusion in the case of this research. The software also enables pore-fluid behaviour to be modelled in the generated void structure, such as filtration and wetting (Price *et al.*, 2009). Knowledge in the fields of rheology and surface chemistry from the Research and Development department of Omya International AG, combined with the modelling and porous structure expertise of the EFMG, has given rise to many collaborative research endeavours.

The overall aim of this project is to study functionalised calcium carbonates (FCCs) as active substrates, e.g. as an excipient, for the controlled delivery of functional materials.

1.2 Structure of the thesis

The thesis is divided into nine chapters. Chapter 1 is an introductory chapter that provides the rationale behind this research. Chapter 2 is a review of the relevant literature underpinning this research project. Chapter 3 describes relevant experimental procedures and techniques.

The novel findings are described in Chapters 4-8; the end of each chapter comprises the key points to be taken from each. Chapter 4 describes the adsorption work conducted throughout this project, as well as the associated challenges, from which a publication was obtained. Chapter 5 describes the beginnings of procedures used for loading flavours and/or drugs into the mineral excipient used throughout this work and Chapter 6 describes a way to model the diffusion of the drug/flavour from the matrix using the Python programming language. Chapter 7 covers the interpretation of data gathered from a novel experimental technique with the aid of PoreXpert, which has given rise to a publication. Finally, Chapter 8 provides a suggestion for refinement of an existing experimental technique to study monolayer diffusivity.

Chapter 9 is an overview and summary in which conclusions are drawn that lead to an outlook for future work.

1.3 Rationale

FCC has potential for use as a carrier for the controlled release of 'actives', by permeation and diffusion, and is being proposed as an environmentally friendly and non-toxic pharmaceutical excipient, nutraceutical, and flavour carrier.

1.3.1 Hypotheses

The research outlined in this thesis aims to address the following hypotheses:

- **1:** FCC, because of its predominantly negatively charged surface, will adsorb small but significant amounts of cationic species.
- **2:** Sparingly soluble (dissolved) species will adsorb to a greater extent onto the FCC than strongly soluble (dissolved) species.
- **3:** The nature of the adsorbing surface of FCCs can be elucidated by studying different adsorption characteristics from a range of different adsorbates and solvents.
- **4:** The extent to which a flavour or drug compound can be physically loaded into the void volumes of FCC can be quantified by directly observing the loaded FCC by scanning electron microscopy (SEM).
- **5:** Computational methods can be used to calculate a diffusion coefficient from experimental data of flavour release from FCC.
- **6:** The diffusion characteristics of FCC can be studied by exposing a monolayer of FCC to a flow of solvent (i.e. a ZLC experiment).
- **7:** The diffusion characteristics of FCC can be studied by exposing a packed bed of FCC to a flow of solvent (i.e. an FLC experiment), and then subsequently deconvoluting the intra- from the interparticle processes using PoreXpert.
- **8:** The FLC can be used to approximate the ZLC by diluting sample particles (A particles) in a packed bed of an inert matrix (B particles).
- **9:** The efficacy of diluting a macroporous adsorber with an inert filler can be calculated mathematically.

Chapter 2

Theory & literature review

THIS chapter reviews the fundamental theory and literature that underpins this research work, in which the main thrust is that FCC is being proposed as an environmentally friendly and non-toxic pharmaceutical excipient, nutraceutical, and flavour carrier.

2.1 The delivery and controlled release of drugs & flavours

The delivery of a drug to its target site in the appropriate amount and time-frame in order for it to have a controlled release effect whilst achieving the maximum therapeutic effect remains a topic of design and development for novel drug delivery systems. Not only does controlled delivery decrease the administration frequency, but also minimises the risk-to-benefit ratio and any possible side-effects (Mishra *et al.*, 2010; Ukmar *et al.*, 2011; Berg, 2012). Additionally, the relief of chronic pain often requires frequent administration of drugs, and thus controlled-release and/or a sustained-release drug delivery methods would be beneficial in these circumstances (Berg, 2012; Jämstorp *et al.*, 2012).

Controlled-released systems must be very carefully designed and tested, because the amount of drug contained in these dosage forms is more than a single dose, and so any compromise or malfunction of the controlled-release delivery method may lead to dose dumping (i.e. the release of all the drug at once). There are some cases in which the current treatment method primarily relies on the use of conventional cytotoxic drugs, such as chemotherapy for cancer, in which the side effects are adverse and the effectiveness is limited, and this has been attributed to the lack of target specificity (Slowing *et al.*, 2008). Drugs, such as the synthetic opioid fentanyl, given to cancer patients to help alleviate chronic pain have a high potency and narrow therapeutic window (Jämstorp *et al.*, 2012). Therefore, the design of target-specific and controlled-release drug delivery systems is of significant interest. Figure 2.1 shows an illustration, taken from the work of Berg (2012), of an example scenario of different drug concentrations in the blood of a patient.

The drugs can be delivered through several routes (e.g. oral, buccal mucosal, transdermal, etc.) to various sites in the body (e.g. blood, brain, etc.) via various transport mechanisms (e.g. diffusion, absorption, etc.) (Berg, 2012). Oral drug delivery, however, is a preferred route because of good patient compliance (Shaji and Patole, 2008; Jain, 2008; Wen and Park, 2010; Patel *et al.*, 2011; Christophersen *et al.*, 2015).

Chewing gum should be considered as a potential delivery system for drugs intended to act locally in the oral cavity or as a flavour delivery system. For example, caries prevention and xerostomia are two conditions in which chewing gum has practical application in their local treatment (Rassing, 1994). The release is dependent on the

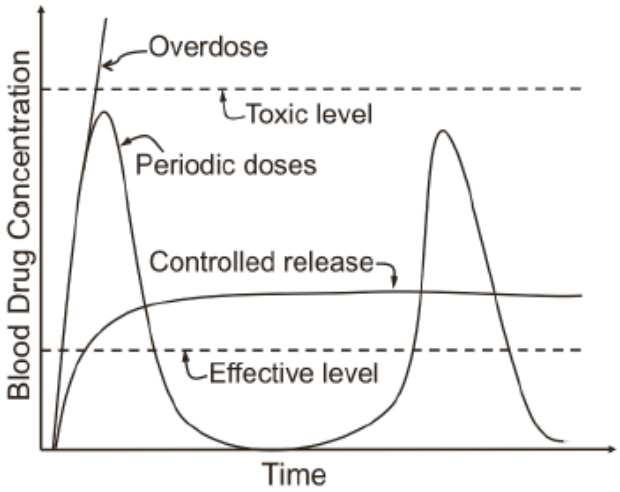

Figure 2.1: An illustration taken from the work of Berg (2012) of an example scenario of different drug concentrations in the blood of a patient. Permission to reproduce this image has been granted by the author.

water-solubility of the drug: water soluble substances are released rapidly and completely, whereas slightly water soluble drugs are released slowly and incompletely, and require special formulation to produce a satisfactory release profile (Rassing, 1994). It has also been found that the absorption rate of caffeine and aspirin increases, and its bioavailability is near comparable, when delivered from a chewing gum as opposed to a capsule (Kamimori *et al.*, 2002; Bousquet *et al.*, 1992). This was attributed to absorption through the buccal mucosa, which is characteristic of active ingredients from gum formulations. Any drug or flavour that is swallowed will enter the stomach in a dissolved or disperse form in the saliva, and will be available to the gastrointestinal tract (Rassing, 1994).

Aspergum®, which contains acetylsalicylic acid (i.e. aspirin), was the first medicated chewing gum to be marketed, and was retailed in 1924 in the USA (Woodford and Lesko, 1981; Rassing, 1994). Chewing gum consists of a neutral and tasteless masticatory gum base (15-40 %) and several non-masticatory ingredients including fillers, softeners, sweetening, and flavouring agents (Cherukuri *et al.*, 1982). It has been proposed that inorganic mineral filler, such as a natural calcium carbonate or a precipitated calcium carbonate carbonate (PCC), can be used as a chewing gum filler (Pedersen and Andersen, 2012).

Diffusion is one of the most common rate-controlling release mechanisms in inert monolithic systems (Jämstorp *et al.*, 2012; Berg, 2012). Therefore, the study of the diffusion of flavour and/or drugs from FCC will be the primary aim of this work.

2.2 Historical use and application of modified calcium carbonates (MCCs) and functionalised calcium carbonates (FCCs)

2.2.1 Modified calcium carbonates (MCCs)

Modified calcium carbonates (MCCs) have major application in the use of fillers and paper coatings. This is because the morphology of the mineral particles, combined with a desired particle size distribution, determine its functionality of use. MCCs are developed via a process by which the surface undergoes a progressive recrystallisation and spherical agglomeration, in which surface features, controlled to approximately 10-50 nm in thickness, are developed (Schoelkopf and Gane, 2008). They have hydrophilic surfaces and exhibit both calcium phosphate and carbonate crystalline structure (Gantenbein, 2012). The discrete bimodal porosity of a compaction of MCC allows for the parameters of absorption driving force and permeability to be separated; the understanding of which has enabled these MCCs to be designed as special rapid volume absorbing paper coatings (Ridgway *et al.*, 2004). The capillarity of a paper can be controlled by using such MCC pigments in a coating of filler application, because the discrete proportion of low aspect ratio nanopores within the MCC particles act up to the limit of the inertial absorbing optimum, which defines the fastest liquid imbibition at short times (Schoelkopf and Gane, 2008). This nano-scale surface functionality has been shown to have application in environmental clean-up technologies and purification purposes; e.g. in the adsorption of heavy metal ions, colloidal pitch droplets in pulp liquor and colloidal and dissolved material in industrial waste water. Further potential is seen as a flow modifier, for example in sealants and plastisols (Schoelkopf and Gane, 2008). Additionally, the high surface area of MCC provides the properties of calcium carbonate-based materials together with those of other highly porous materials, such as fumed or precipitated silica.

Surface functional groups and pH values are important characteristics for any adsorbent, as they indicate its acidity and basicity, and its net surface charge in solution (Al-Degs *et al.*, 2008). The surface properties of MCC have been studied with a variety of experimental techniques. Gane *et al.* (2000), for example, found that cationically charged dyes strongly adsorbed to the calcium carbonate surface via ionic forces. However, zeta potential analyses onto the surface of the MCCs have yielded complex results, suggesting that there must be both cationic and anionic surface adsorption sites (Gribble, 2010); the experimental results yielded from this technique should only be used as a blunt tool, especially in the case of amphoteric materials. Private communications with the Science Partner (SP) Technical Research Institute of Sweden regarding FCC S07 and S10 (Chapter 3) have revealed that they have zeta potential values of -10 mV and polyelectrolyte titration (PET) analysis values of -132.2 and -111.5 μVal g^{-1}, respectively, thus supporting the overall negative surface charge of MCCs, as found by Gane *et al.* (2000).

2.2.2 Functionalised calcium carbonates (FCCs)

Mesoporous silicates have been studied in the context of tunable drug delivery (Ukmar *et al.*, 2011; Angelos *et al.*, 2008; Di Pasqua *et al.*, 2008; Lin *et al.*, 2006) because their historically unique structure of large internal volumes, high surface areas, and straight narrow channels allow for the high adsorption of drugs and proteins (Hudson *et al.*,

2008; Slowing *et al.*, 2008). Their structure (e.g. pore size) or surface properties (e.g. surface polarity) can be modified in order to enhance or slow down release kinetics (Wang and Nancollas, 2008). Silica nanoparticles are also utilised in the realm of controlled drug delivery, and these particles are suggested to be useful in improving the oral bioavailability of poorly water soluble drugs (Zhang *et al.*, 2012). However, their synthesis is a complex process, which makes it a rather expensive material (Preisig *et al.*, 2014).

The biological response to such materials, however, has been much less well characterised regarding their biocompatibility and biodegradability (Di Pasqua *et al.*, 2008) and there have been various toxicological concerns (Hessler *et al.*, 2005; Tao *et al.*, 2008; Güngen *et al.*, 2016). For example, *in vitro* toxicity studies have shown dependence on particle size (Hudson *et al.*, 2008): microparticles are preferred to nanoparticles because the cellular uptake of the particles in the gastrointestinal tract is lower, thus making them toxicologically less problematic (Preisig *et al.*, 2014).

The term functionalised calcium carbonate (FCC) encompasses a family of new pharmaceutical excipients in which the conditions of manufacture is similar to those for MCC, but follows strict process regulations with respect to the grade of reagents that are employed, freedom from organic polymers, and the microbiological environment under which they are produced. Additionally, silica, for example, is retained as a foreign material in the body, whereas calcium carbonate and phosphorus salts are natural bodily ingredients, which can be positively assimilated or naturally removed. With respect to the work in this thesis, FCC and MCC properties are identical, and FCC nomenclature is used throughout.

FCCs are proving to have a wide range of novel applications (Gane *et al.*, 2004; Gane, Schölkopf, Gantenbein and Gerard, 2010; Gane, Schölkopf and Gantenbein, 2010). In particular, they are being proposed as an excipient and a pharmaceutical ingredient (Gane *et al.*, 2006; Pedersen and Andersen, 2012; Gane and Schölkopf, 2011; Machado *et al.*, 2013), because the inorganic nature of porous calcium carbonate offers a good stability of the ingredients, slow biodegradability, is easily produced, tasteless, stable, and biocompatible (Fujiwara *et al.*, 2008; Pedersen and Andersen, 2012; Ueno *et al.*, 2005; Lucas-Girot *et al.*, 2005; Arruebo, 2012; Haruta *et al.*, 2003; Sherry *et al.*, 2009; Biradar *et al.*, 2011).

Calcium carbonate is being used increasingly as an extender/excipient and as a pharmaceutical ingredient in medicinal and food supplement and nutraceutical formulations, and its application ranges from free addition to foodstuffs, dispersion constituents, as well as tablets of powdered precipitated and/or ground calcium carbonates (GCCs) (Gane *et al.*, 2006). FCCs can be utilised in various dosage forms, such as a chewing gum, a mouth spray, a nasal spray, an inhaling device, a tablet, a lozenge, a buccal sachet, a trans-dermal patch, and a powder (Pedersen and Andersen, 2012).

Natural calcium carbonates have been found to be a highly suitable carrier of various flavouring and active agents, such as vanillin and nicotine, and are also suitable for the controlled release of active ingredients in various formulations and products, such as in chewing gums, as an intranasal carrier of insulin, or with hydrophilic compounds, for example (Ueno *et al.*, 2005). The active ingredient may also be reversibly absorbed

and/or adsorbed onto the calcium carbonate, which is highly advantageous in order for a controlled release of the active ingredients (Pedersen and Andersen, 2012). However, it has also been shown that drugs or bioactive proteins do not adsorb strongly to the surface of porous calcium carbonate, and so may result in insufficient sustained release or targeting (Ueno *et al.*, 2005). Inorganic microparticles can be synthesised using mild aqueous conditions without involving any organic solvents and additives (e.g. emulsifiers) as opposed to the development of polymer-based microparticles (Peng *et al.*, 2010). Additionally, calcium carbonate is pH-sensitive, so while the structure is maintained in a neutral environment, an acidic environment in tumour tissues and lyosomes can trigger the drug release (Wei *et al.*, 2008). Sphere-shaped calcium carbonate particles, however, do not occur naturally (Qiu *et al.*, 2012), whereas FCC particles are generally spherical.

The use of hydroxyapatite/hydroxylapatite (HAP) as a drug carrier has also been discussed in the literature (Baradari *et al.*, 2012; Chevalier *et al.*, 2010; Cosijns *et al.*, 2007; Öner *et al.*, 2011; Sasikumar, 2013; Son *et al.*, 2011). FCC offers benefits over HAP because the current commercial methods used to produce HAP give a low yield mixed with several phases, so that the product is expensive and suitable only for small-scale and time-consuming production (Chen and Leng, 2015).

Adjustments to the FCC production process can be used to produce a wide range of different morphologies, and raise the possibility of tailoring the void structures of the particles to provide controlled release delivery vehicles for actives across many fields, including drugs and flavours. However, such tailoring can only be fully optimised by a fundamental characterisation of the way in which a drug, loaded into an FCC, then flows and diffuses out over a period of time to provide the delayed release.

2.2.2.1 Particulate filler

The bimodal pore-size distributions of FCCs will aid the controlled release of the active ingredient because the release times will be a function of the inter- and intraparticle pores (Ueno *et al.*, 2005), as these porosities can accommodate the drugs of interest. Individual FCC particles consist of denser cores (i.e. voids <500 nm) surrounded by a porous layer with larger pores and channels (i.e. voids >500 nm). The interparticle voids are also classified to be >500 nm, which makes the clear distinction between the outer intraparticle and interparticle voids difficult (Ridgway *et al.*, 2004). These distribution patterns are generally classified as intra- and interparticle voids, and are unique to each FCC as a result of specific changes to production parameters (Stirnimann *et al.*, 2014).

2.2.2.2 Granulation

FCC granules are agglomerates (i.e. coarse accumulations) of FCC and can be prepared by roller compaction or high shear granulation, which improves the flowability of the material and retains the significant mechanical strength of FCC tablets; a property unique to FCC (Stirnimann *et al.*, 2014). Due to the open system that wetted particles or agglomerates exhibit, the performance of such particles is limited as delivery systems themselves (Elabbadi *et al.*, 2000), and so the use of a protective barrier against the loss of active ingredient is required. FCC granules may, therefore, be encapsulated with a particular encapsulating agent or made into tablets (Stirnimann *et al.*, 2014)

before pharmacological application.

2.2.2.3 Encapsulation

Encapsulation is the base of controlled release methodology, in which a small unit consists of a biodegradable coating or shell material (mostly organic polymers) with an empty volume inside, where an active core can be incorporated (Gumí *et al.*, 2009; Berthod *et al.*, 1988). It is proposed that loaded FCC powder or granules can be the encapsulated core once the pores have been loaded. Camptothecin, an anticancer drug, has been successfully encapsulated into calcium carbonate microspheres via simple diffusion; subsequent studies showed pH dependent release and the desired effective cell growth inhibition (Qiu *et al.*, 2012).

Cellulose derivatives are often used to modify the release of drugs in tablet and capsule formations (Fahs *et al.*, 2010). Hydroxypropyl methylcellulose (HPMC) is used for the film coating of tablets and as a controlled-release tablet matrix (Burdock, 2007). The hydration of HPMC forms a gelatinous layer at the surface of the matrix through which the included drug diffuses. HPMC is the most extensively employed because of its ease of use, availability, water solubility, and non-toxicity (Fahs *et al.*, 2010).

2.2.2.4 Tablets

Chewable tablets dominate the market in Europe, whereas swallow-able type tablets are more common in the United States. For a breakdown of the structure into an acceptable texture in the mouth, the combination of packing structure and particle size range must allow for the uptake and permeation of liquids to assist in the tablet breakdown. Also, the volume of the tablet, which is strongly related to the particle size of the material used in its making (in this case, FCC), needs to promote the ease of swallowing. The presentation of surface area is also important in dissolution control (Gane *et al.*, 2006).

Recent studies have utilised this proposed excipient to form mechanically robust, orally dispersible tablets by direct compression and have loaded the material with drug via solvent-evaporation (Stirnimann *et al.*, 2013; Eberle *et al.*, 2014; Stirnimann *et al.*, 2014; Preisig *et al.*, 2014). The discrete bimodal nature of FCC can be destroyed by a simple gentle grinding so as to partially homogenise between the two intra- and interparticle network structures (Ridgway *et al.*, 2004). During compaction, however, the individual particles are forced so close together that more interparticle interactions are established and their structures consolidate with one another. When tablets are formed, it is necessary to measure the mercury porosimetry of each one as there is not a direct relationship between applied pressure and porosity (Schoelkopf, 2002). Compacted tablets exhibit high tensile strength and a higher final porosity, which are formed from much lower compressive pressures than those needed for the compaction of other excipients such as mannitol or cellulose, which also show a lower final porosity, and is attributed to the interlocking of surface lamellae between the FCC particles (Stirnimann *et al.*, 2014). Additionally, FCC particles are approximately 10 times smaller than those of plastically deforming microcrystalline cellulose; FCC therefore possesses a larger surface area in relation to the same volume, and thus could be another reason as to why FCC tablets exhibit this significant tensile strength (Stirnimann *et al.*, 2014). Figure 2.2 shows an example of a piece of apparatus that can be used to produce large

tablet samples (approximately 4 cm in diameter and 1 cm in thickness) from 60 g of homogenised powder; it is a hydraulic unit, taken from the work of Schoelkopf (2002), of which the cylinder can exert a force of up to 600 kN.

Figure 2.3 shows a schematic of two possible contact surface types: type I shows lamellar particles represented by the horizontal lines moving closer to one another, and type II shows more spherical edges. The upper schematic in Figure 2.3 shows a possible contact surface under low compressive pressures, whereas the lower schematic in the figure shows the same but under higher compressive pressures (Stirnimann *et al.*, 2014).

Under low compressive pressures the larger pores of FCC particles provide a larger contact surface for possible bonds (type Mark I) than an FCC which has a much smaller volume of larger pores (i.e. less interparticle than intraparticle pores), in which the contact surface for possible bonds was limited under low compressive pressures. The smaller the spherical particles, the smaller are the compaction pressures needed. Tablets formed from FCC grades with varying inter- and intraparticle porosities exhibited similar compact densities, which indicates the brittle deformation of the lamellae under pressure via fragmentation, providing new contact surfaces for potential bonds (type Mark II). Also, for FCCs with a high degree of intraparticle porosity, a possible reason for the stepwise increase in tensile strength of the FCC with increasing compressive pressure is because large intraparticle voids provide more new contact surfaces, thus resulting in a stronger grip than materials without such intraparticle porosity (Stirnimann *et al.*, 2014).

The mode of inclusion of an active pharmaceutical ingredient into a tablet of FCC would be influenced by the intra- and interparticle pores, where the former controls the diffusion spatially and the latter controls the permeability of the tablet (Gane *et al.*, 2006). Water penetrates the FCC rapidly by capillary forces due to the highly connected porosity of the FCC (Stirnimann *et al.*, 2014), thus making FCC ideal for the preparation of orally dispersible tablets (Stirnimann *et al.*, 2013). The study of intrusion into the tablet will provide insight into the capillary absorption in the outer layer of the pores, as this will allow a layered mechanism of the breakdown of the tablet to be proposed. If the pores are pre-filled with a liquid that has less affinity for the surface of the tablet (such as natural oils) a quasi “explosive” effect will be generated, which is pleasant in the mouth (Gane *et al.*, 2006).

2.3 Adsorption

The process in which a substance (sorbate) becomes associated with a solid phase (sorbent) is generally termed ‘sorption.’ Absorption is different from adsorption, whereby the former implies the penetration through a material while the latter is a surface phenomenon. Adsorption occurs whenever a solid surface is exposed to a gas or a liquid; the term ‘fluid’ is commonly used to describe such a gas or liquid (i.e. is in contact with the boundary of the surface of solids) (Dąbrowski, 2001). However, it is important to be aware of the fact that adsorption can occur in multiple systems, such as liquid-gas, liquid-liquid, solid-liquid, and solid-gas. Adsorption, therefore, is defined as the enrichment of material, or an increase in the density of the fluid, in the vicinity of an interface (Rouquerol *et al.*, 1999).

Figure 2.2: A custom-made hydraulic press for tablet compaction that is comprised of a hydraulic unit (on the bottom) with the electronic steering unit (on the top right) and the press-frame with the hydraulic cylinder exerting a force up to 600 kN. The tablets generated are large in size: approximately 4 cm in diameter and 1 cm in thickness. This image is taken from the work of Schoelkopf (2002).

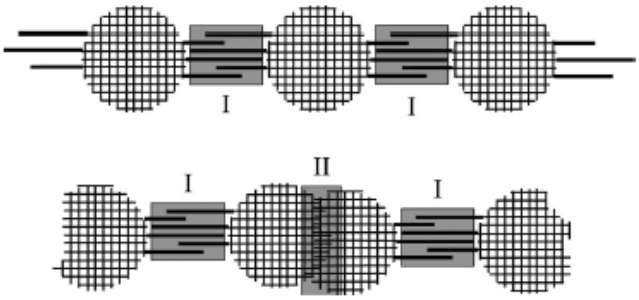

Figure 2.3: A schematic of two possible contact surface types of FCC particles, type I and type II, under compression (Stirnimann *et al.*, 2014). Permission to reproduce this image has been granted by the publisher.

Physical adsorption, or physisorption, is a non-specific and rapid process associated with acid-base interactions, weak van der Waals forces, or weak ionic forces (Mahato and Narang, 2012; Gantenbein, 2012); the reverse of which is termed 'desorption.' 'Ion exchange' is the term given to the desorption of one or more ionic species when accompanied by the simultaneous adsorption of an equivalent amount of ionic species (Dąbrowski, 2001). Chemical adsorption, or chemisorption, on the other hand, is irreversible and specific, in that the adsorbate is attached to the adsorbent via covalent chemical bonding (Gantenbein, 2012) and allows only a monomolecular layer (i.e. a monolayer) of adsorbed adsorbate. The specificity of chemisorption requires that an activation energy may be needed for it to take place, and therefore may be a slow process (Mahato and Narang, 2012).

Another important factor in the process of adsorption is the surface heterogeneity of the adsorbent, of which there are two types: geometric and energetic (Kalies *et al.*, 2009). Generally, geometric surface heterogeneity is caused by a deviation between the real structure of a material and its ideal crystal lattice. These disturbances may be caused by lattice defects or the presence of impurities embedded within the material. The main source of heterogeneity for microporous solids (please see section 2.4 for pore size classifications), however, is their complex structure of pores with different dimensions and shapes (Dąbrowski, 2001), which can be described by pore size distribution functions (Kalies *et al.*, 2009). This surface heterogeneity may cause the adsorbate to interact differently with the surface, and thus the adsorption that occurs on the whole heterogeneous surface can be considered in a first approximation.

The energetic heterogeneity of a surface, on the other hand, is described by the adsorption energy distribution function (Kalies *et al.*, 2009). When considering energetic heterogeneity, originally, the effects of geometric heterogeneity were ignored (Rudzinski *et al.*, 2001). In some cases, the geometric non-uniformity and the energetic heterogeneity of a material are considered separately; e.g. the former can be described by the fractal dimension of the surface, and the latter by an energy distribution function (Sokołowska, 1989). However, in other cases, the geometric non-uniformity of a surface can indeed influence the energetic distribution function (Seri-Levy and Avnir, 1993).

The adsorption isotherm is a fundamental concept in adsorption science and describes

the equilibrium relation between the amount of adsorbed material to the pressure or concentration in the bulk fluid phase at constant temperature and the energy distribution of adsorption sites (Hu and Do, 1993; Cascarini de Torre and Bottani, 1996; Dąbrowski, 2001). Freundlich (1906; 1909) developed his empirical adsorption equation which assumed that the adsorption occurred on heterogeneous sites with non-uniform energy level and is not restricted to a monolayer (Song *et al.*, 2013). Langmuir (1916; 1917) then proposed his adsorption model that is based on the assumption that adsorption occurs at homogeneous sites within the adsorbent surface at uniform energy levels, which suggests that adsorption is monolayer in nature.

An adsorption isotherm for liquid systems, at constant temperature (T), pressure (P), and medium composition (e.g. pH, ionic strength) (Pan and Liss, 1998*a*), is the adsorption density (Γ) plotted against the equilibrium concentration of the adsorbate/solute in dilute solution (c_{eq}). The isotherm should be independent of the reactant concentrations and the kinetics of the process (Pan and Liss, 1998*a*).

The International Union of Pure and Applied Chemistry (IUPAC) classified isotherms into six types, and are shown in Figure 2.4a. Type I shows the Langmuir isotherm, which is typical of many microporous adsorbents. Types II and III are typical of non-porous materials with strong or weak fluid-wall attractive forces, respectively. Mesoporous materials exhibit types IV and V isotherms and occur for strong and weak fluid-wall forces, respectively, in which the hysteresis loop is associated with the filling and emptying of the mesopores by capillary condensation. And finally, Type VI occurs for some materials with relatively strong fluid-wall forces, usually when the temperature is near the liquefaction point for the adsorbed gas (Balbuena and Gubbins, 1993; Horikawa and Nicholson, 2011).

Adsorption hysteresis is the deviation of the desorption curve from the adsorption curve, thus exhibiting a 'hysteresis loop.' The hysteresis loops exhibited by some materials vary in shape, and are most commonly associated with the capillary condensation phenomenon that occurs in mesoporous solids (Ruthven, 1984; Dąbrowski, 2001); they have also been classified into four types by the IUPAC, and these are shown in Figure 2.4b. The Type H1 loop is associated with adsorbent materials possessing a narrow and uniform pore distribution, and shows steep and parallel adsorption and desorption branches. The Type H2 loop is typically observed with adsorbents possessing networks of interconnected pores that vary in sizes and shapes; the hysteresis is broad with a gradual adsorption uptake and a steep desorption branch. Adsorbents with slit-shaped pores tend to exhibit H3 and H4 loops; because these loops do not terminate in a plateau at high relative pressures, the desorption boundary curve is difficult to define (Horikawa and Nicholson, 2011).

If there is hysteresis in the adsorption system, then it is implied that adsorption equilibrium has not been reached (Myers, 2004). This is because a perfect equilibrium state of the adsorbate would only be formed through an ideal thermodynamically reversible process, in which all molecules have equal opportunity and infinite time to occupy the most stable (i.e. lowest energy) value of chemical potential, which is represented by a unique c_{eq}; this is represented in Figure 2.5a (Pan and Liss, 1998*a*). In reality, the situation in Figure 2.5b may occur in which the adsorption process is irreversible, and the adsorbate molecules achieve meta-stable equilibrium states. This is demonstrated

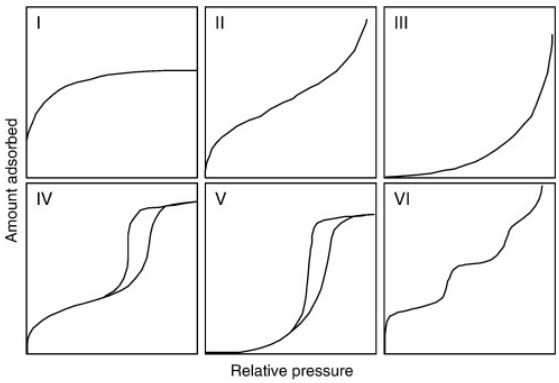

(a) The IUPAC classification of isotherms.

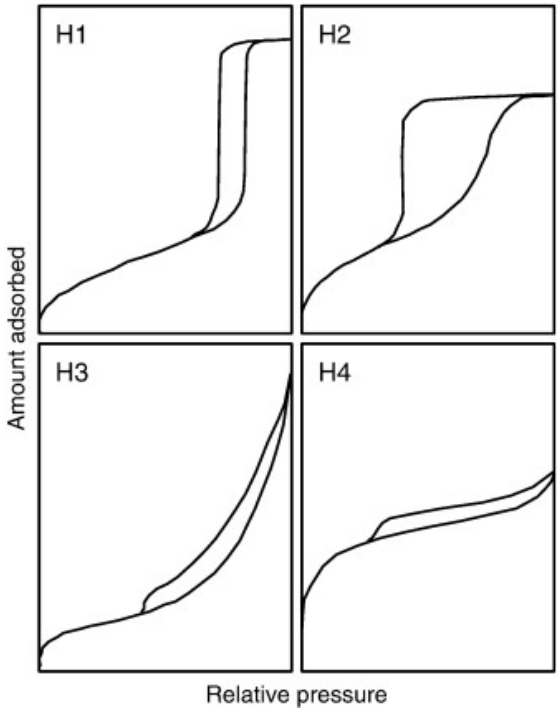

(b) The IUPAC classification of hysteresis loops.

Figure 2.4: The IUPAC classification of isotherms and hysteresis loops (Rouquerol *et al.*, 1999). Permission to reproduce this image has been granted by the author and publisher.

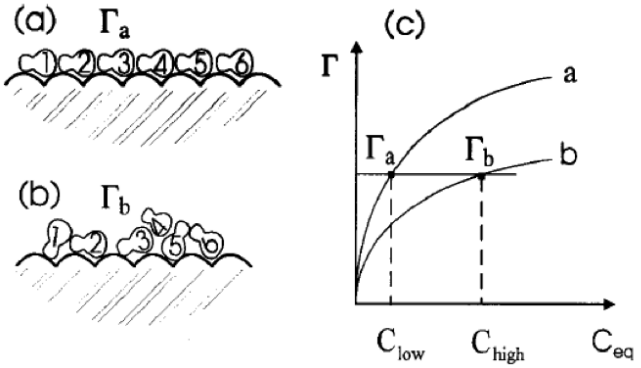

Figure 2.5: (a) An ideal equilibrium state of adsorbed molecules; (b) a meta-stable equilibrium state of adsorbed molecules; (c) isotherms a and b both represent the same value of adsorption density, however they possess different values of chemical potential and therefore correspond to different c_{eq} in solution (Pan and Liss, 1998*a*). Permission to reproduce this image has been granted by the publisher.

in Figure 2.5c, in which curve b has shifted to a lower position than curve a as a result of higher Gibbs free energy/chemical potential values (Pan and Liss, 1998*a*).

2.4 Porous media

Porous solids filled with a liquid or a gas play a pivotal role in engineering, e.g., in material science, the petroleum industry, chemical engineering, and soil mechanics as well as in biomechanics, and have recently attracted even more attention due to their potential as functional materials (Kaneko, 1994; de Boer, 1998; Kärger *et al.*, 2012). Within a majority of natural or artificial solids there are empty interstices, which are called pores (de Boer, 1998). This is the most common characteristic of porous media, which is known as its porosity or the volume fraction of the media relative to the total void space. A porous medium is a solid body containing many holes or voids, and narrow and/or tortuous connecting passages (Gribble, 2010). In some bodies, such as sponges or soils, these pores are immediately visible. However, other pores unrecognisable by the human eye are those such as the pores in human skin (de Boer, 1998).

The voids within porous media are characterised by their size; they may be large, small or intermediate in size, and connected or isolated from one another (Laudone *et al.*, 2005). The term 'diameter' is used when referring to the size of cylindrical pores, whereas 'width' is for those that are slit-shaped (Dąbrowski, 2001) 'Throat' is traditionally the term given to the smaller interconnecting pores (Laudone, 2005). Figure 2.6 shows this in diagrammatic form.

The total porosity of a material is usually classified into three groups: the IUPAC recommends that pores with diameters of less than 2 nm are called 'micropores,' and those in the range of 2 to 50 nm are called 'mesopores,' while those that posses a width greater than 50 nm are called 'macropores (Sing *et al.*, 1985; Rouquerol *et al.*, 1994; McCusker *et al.*, 2003). 'Nanopore' is now the expression used to encompass both micro- and

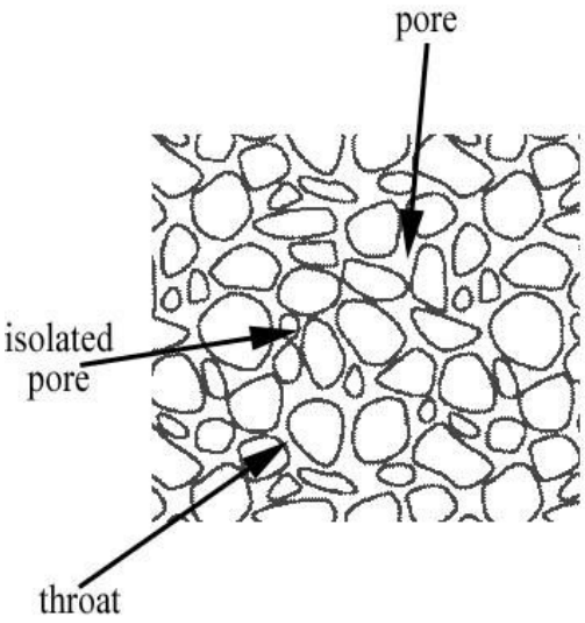

Figure 2.6: The pores, isolated pores, and smaller connected pores (throats) are clearly visible in this schematic of a porous medium. This image is taken from the work of Laudone (2005).

mesopores (Dąbrowski, 2001), although more commonly used to describe micropores (Horikawa and Nicholson, 2011). However, according to Mays (2007), 'nanopores' possess a size between 0.1-100 nm, 'micropores' is the term reserved for pores between 0.1-100 μm, and 'millipores' is for those between 0.1 and 100 mm. An overview of these different classification systems can be viewed in Table 2.1.

Table 2.1: Two different pore size classifications.

IUPAC classification (Sing *et al.*, 1985; Rouquerol *et al.*, 1994; McCusker *et al.*, 2003)				
Term	Pore size			
	nm	μm	mm	m
Micropore (Nanopore)	<2	<0.002	<0.000002	<0.000000002
Mesopore	2-50 nm	0.002-0.05	0.000002-0.00005	0.000000002-0.00000005
Macropore	>50	>0.05	>0.00005	>0.00000005

Mays' (2007) classification				
Term	Pore size			
	nm	μm	mm	m
Nanopore	0.1-100	0.0001-0.1	0.0000001-0.0001	0.0000000001-0.0000001
Micropore	100-100 000	0.1-100	0.0001-0.1	0.0000001-0.0001
Millipore	100 000-100 000 000	100-100 000	0.1-100	0.0001-0.1

The sizes of pores in an adsorbent plays a significant role in adsorption processes. The sizes of micropores may be comparable to the size of adsorbate molecules, which therefore suggests that the entirety of the adsorbate can indeed interact with adsorbent molecules (Dąbrowski, 2001). This means that the three size groups that comprise the total porosity of an adsorbent play a significant role in adsorption processes. Adsorption in micropores, for example, is essentially a pore-filling process in which their volume is the main controlling factor. In the case of mesopores, however, the boundary between adsorbent and adsorbate has a distinct physical meaning; the final filling of such pores proceeds according to the capillary condensation mechanism. In the case of macropores, however, adsorption does not occur throughout the pore volume of the adsorbent but merely at a close proximity to the surface (Dąbrowski, 2001).

Capillary condensation occurs in mesopores, not micro- or macropores, during gas adsorption. This phenomenon is preceded by the adsorption of a monomolecular layer on the pore walls, after which multilayer adsorption from the vapour phase proceeds to the point at which the pore space becomes filled with liquid that has condensed from the vapour phase. The adsorption and desorption isotherms of such a phenomenon always exhibits hysteresis (Horikawa and Nicholson, 2011).

2.5 Mineralogy

This section briefly introduces the minerals associated with this project. A brief description of silicates and zeolites is included because mesoporous silicates have been studied in the context of tunable drug delivery (Ukmar *et al.*, 2011; Angelos *et al.*, 2008; Di Pasqua *et al.*, 2008; Lin *et al.*, 2006), and zeolites were the first types of minerals to be investigated with the zero length cell (ZLC) (section 2.7) when it was first developed by Eic and Ruthven (1988). FCCs are generally composed of calcium carbonate and hydroxyapatite, and so descriptions of the latter two minerals are briefly included as well.

2.5.1 Silicates

Mesoporous silicas are solid materials comprised of a honeycomb-like porous structure with hundreds of empty channels (i.e. mesopores) that are capable of absorbing/encapsulating various molecules (Slowing *et al.*, 2008; Di Pasqua *et al.*, 2008).

2.5.1.1 Zeolites

Zeolites form the basis of many practical adsorbents and catalysts, and therefore have been studied in much greater detail than amorphous materials (Kärger *et al.*, 2012). They are crystalline aluminosilicates, which can be found in nature or may be produced synthetically. Zeolites are the most representative porous solids whose pores arise from the intrinsic crystalline structure (Kaneko, 1994). The basic structural units in zeolites are the SiO_4 or AlO_4 tetrahedra, which are joined together in regular structures through shared oxygen atoms, and because of their imperfect packing they create cavities within the structure. The structural regularity distinguishes the zeolites from other microporous materials such as activated carbon (an extremely porous form of carbon) (Kaneko, 1994; Brandani, 2002). The crystal structure of zeolites determines the regularity of its pore structure thus making the study of the effect of pore size on its transport properties possible in such systems (Kärger *et al.*, 2012).

2.5.2 Talc

Talc is a layered silicate mineral that consists of octahedral magnesium hydroxide (brucite) structures sandwiched between sheets of silicon-oxygen tetrahedra. Small amounts of titanium or aluminium can substitute for silicon in the tetrahedral layer, while calcium may substitute for magnesium in the octahedral brucite layer; the degree of silicon ion substitution depends upon the source of the talc (Burdukova *et al.*, 2007; Gantenbein, 2012).

The platelet-shaped lamellae particles are due to the layering of the talc sheets (Yildirim, 2001), which are held together by weak van der Waals forces thus making talc a readily delaminating and anisotropic material exhibiting distinct edge and basal planes (Gribble, 2010; Burdukova *et al.*, 2007). As a result, talc has unique surface properties: the basal silicate surfaces are hydrophobic, while the edge hydroxide surfaces are hydrophilic (Lobato, 2004). This is attributed to the tetrahedra being fully charge compensated, thus giving the basal surfaces its hydrophobic character, whereas the talc edge surfaces are considered to possess a negative charge resulting from the breaking of ionic covalent bonds in the brucite layer (Burdukova *et al.*, 2007). The idealised structure of talc is shown in Figure 2.7.

2.5.3 Calcium carbonate

Calcium carbonate is a naturally occurring compound found in many forms and is one of the world's most abundant minerals (Ni and Ratner, 2008); it is the most common mineral found in the Earth's crust, after quartz (Myers, 2007).

Calcium carbonate is found in organisms and many rocks, and is most commonly associated with chalk, limestone, and marble, which is metamorphic limestone (Myers, 2007). For example, as limestone it occurs as the calcareous exoskeleton of marine animals and as boiler scale (Ni and Ratner, 2008). Calcium carbonate has many applications: coating pigment for premium quality paper products in the paper industry, fillers in rubber, paints in polymer applications, and calcium-based antacid tablets in healthcare. It is one of the most abundant biological minerals formed by living organisms. Calcium carbonate is used as a biomaterial for bone reconstruction (Ni and Ratner, 2008).

It has three distinct polymorphs (de Leeuw and Parker, 1998). Calcite and aragonite are more thermodynamically stable structures, and they most commonly occur in nature (Dickinson and McGrath, 2004; Ni and Ratner, 2008; Plummer and Busenberg, 1982; Wang *et al.*, 2013); the former being the form primarily found in the Earth's crust (Myers, 2007). Vaterite seldom occurs in geological formations or during chemical processes (Brunson and Chaback, 1979).

The crystal structure of calcium carbonate can be thought of as a triangle, in which calcium is in the centre and a carbonate group is at each of the vertices (Myers, 2007) and is shown in Figure 2.8.

2.5.4 Hydroxyapatite

Calcium orthophosphate consists of three major chemical elements: calcium, phosphorus, and oxygen (Dorozhkin, 2007). Hydroxyapatite (HAP), the structure of which is

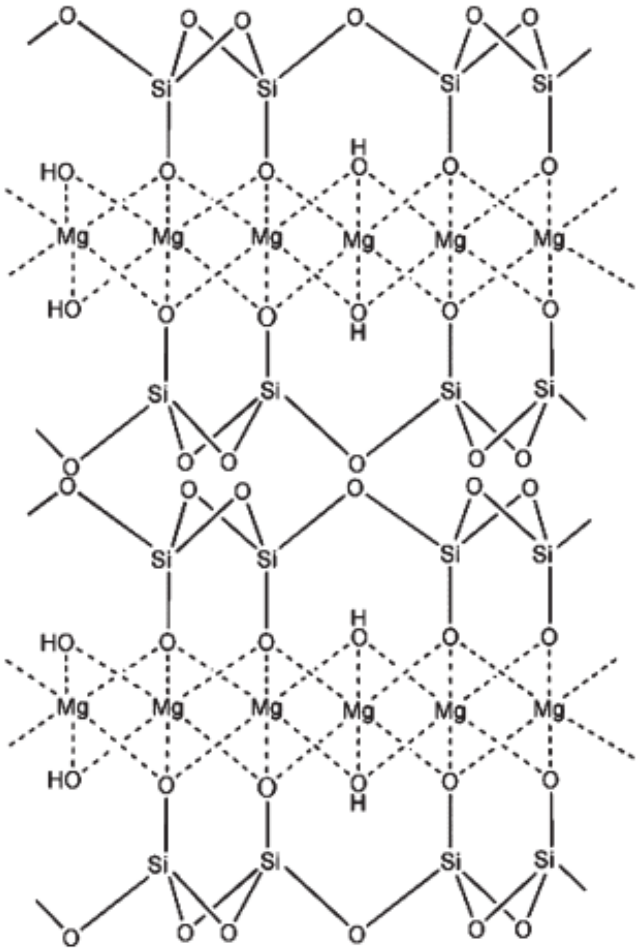

Figure 2.7: Idealised talc structure (Wallqvist *et al.*, 2009). Permission to reproduce this image has been granted by the publisher.

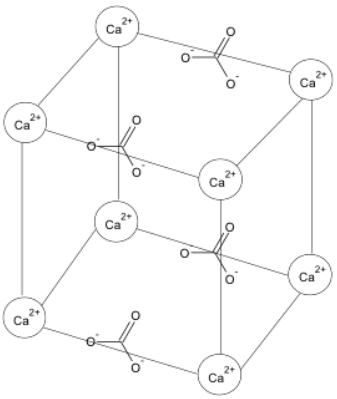

Figure 2.8: The crystal lattice structure of calcium carbonate.

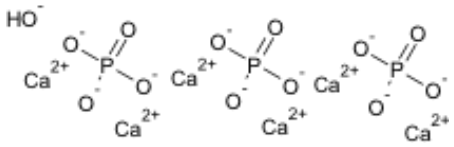

Figure 2.9: The structure of HAP.

displayed in Figure 2.9, possess Ca^{2+} sites surrounded by PO_4^{3-} tetrahedra. Calcium orthophosphates are the main mineral constituents of bones and teeth (Dorozhkin, 2007); synthetic HAP became commercially available in the 1980s for dental and orthopaedic applications as well as bone substitute materials (Kar, 2007).

2.5.5 Modified and functionalised calcium carbonates (MCCs & FCCs)

MCCs and FCCs are microporous particulate materials (5-15 mm in size) with highly developed surface and internal structures (Stirnimann *et al.*, 2014); the manufacturing of which shows some similarities to the production of PCC. The decomposition of calcium carbonate is the primary similarity, however, PCC is formed in near neutral solution whilst MCC/FCC is produced under acidic conditions (Stirnimann *et al.*, 2013).

MCCs and FCCs are produced by etching GCC with various concentrations of citric and phosphoric acid, which facilitates the *in situ* production of carbon dioxide. This *in situ* or externally supplied carbon dioxide, in the form of carbonic acid, leads to the formation of a modified lamellar surface structure via the progressive surface reprecipitation of inorganic mixed salts (Gane, 2001; Ridgway *et al.*, 2004; Schoelkopf and Gane, 2008; Gantenbein, 2012; Stirnimann *et al.*, 2014). Variations in the etching process produce a range of particle size distributions and morphologies with recrystallized surfaces (Gane *et al.*, 2004; Rowe *et al.*, 2009), and a discretely bimodal pore size is exhibited when the material is formed into a packed bed (Gantenbein, 2012). Some grades then undergo a second treatment with a different acid and/or are treated with additives (Gribble, 2010). Photographic examples of the structures of these minerals are displayed in Figure 3.1 of Chapter 3.

2.6 Diffusion

Diffusion can be defined as the migration of matter, as a result of random molecular thermal motions, down a concentration gradient (Crank, 1975; Atkins and de Paula, 2006; Mehrer, 2007; Gribble, 2010), and is a manifestation of the tendency towards maximum entropy or randomness (Kärger *et al.*, 2012). It is relatively fast in gases, slow in liquids, and very slow in solids (Mehrer, 2007). The diffusive transport of fluids through porous media has been studied extensively because of its important role in different fields of science and technology (Stockmeyer, 1993), and is essential for the development, design, and optimisation of the technological exploitation of porous materials in general (Kärger *et al.*, 2012).

Fick's laws of diffusion can be used in order to quantify diffusional mass transport. The first law correlates the molecular flux or rate of one-dimensional transfer per unit area of section (j) with the gradient of concentration of the diffusing species (c), yielding a factor of proportionality (i.e. the diffusion coefficient, or diffusivity, which is denoted

by D) (Tyrrell, 1964; Siepmann and Siepmann, 2008). Fick's first law is expressed by equation 2.1, and exhibits the notion that the number of molecules moving towards the lower concentration increases in direct proportion with the concentration gradient (Kärger and Ruthven, 2016). This is because in the presence of a gradient of molecular concentration, a molecular random walk gives rise to a concentration flux in the direction of decreasing concentration (Kärger and Ruthven, 2016).

The second law (equation 2.3) can be derived from the first law (equation 2.1) when taking into consideration equation 2.2 (Siepmann and Siepmann, 2008; Kärger and Ruthven, 2016). Equation 2.3 explicitly accounts for the fact that the diffusivity generally depends on concentration:

$$j = -D\frac{\partial c}{\partial x} \tag{2.1}$$

$$\frac{\partial c}{\partial t} = \frac{-\partial j}{\partial x} \tag{2.2}$$

$$\frac{\partial c}{\partial t} = D\left(\frac{\partial^2 c}{\partial x^2} + \frac{\partial^2 c}{\partial y^2} + \frac{\partial^2 c}{\partial z^2}\right) \tag{2.3}$$

where t denotes time and x, y, and z are spatial (Cartesian) coordinates.

Fick's laws adequately describe the mass transfer in nanoporous materials, providing that diffusion is the dominant mechanism and molecular exchange between different regions is sufficiently rapid (Kärger and Ruthven, 2016).

The mechanism of diffusive transport ranges from Knudsen to bulk diffusion when a material possess a wide range of pore diameters. Knudsen diffusion takes place in the micropores, whereas bulk diffusion occurs within the macropore regions.

Bulk and surface diffusion are the two main diffusion processes that can occur during a liquid ZLC experiment (Gribble, 2010). Bulk diffusion refers only to diffusion in the mobile phase, whereas surface diffusion contributes an additional transport path and involves molecules adsorbing and moving along pore walls. Concentration differences in bulk diffusion are caused by various factors, such as steric hindrances, whereas with surface diffusion the potential energy field imposed by the surface influences the motion of adsorbed species (Zalc *et al.*, 2003). Knudsen diffusion is believed to be the dominant transport mechanism of gases in mesoporous materials (Malek and Coppens, 2003), but is not relevant in the present case, since the mean free path in a liquid phase is significantly smaller than the pore size (Ukmar *et al.*, 2011).

2.6.1 Modelling of processes

When mathematical modelling, it is necessary to simplify these complex processes, hence a mathematical model mainly focuses on one or two dominant driving forces (Fu and Kao, 2010).

Generally, it it suggested that solute diffusion, polymeric matrix swelling, and material

degradation are the main driving forces for solute transport from drug containing polymeric matrices (Arifin *et al.*, 2006). Models that use equations to describe real phenomena, such as diffusion and dissolution, are known as mechanistic realistic mathematical theories (Siepmann and Siepmann, 2008). The design of a drug delivery system's rate-controlling release mechanism or type of mass transport process (i.e. diffusion, erosion, swelling) often determines their classification (Frenning, 2011), thus simplifying the mathematical description of the drug release rate (Siepmann and Siepmann, 2012). This work focuses on diffusion-controlled release systems.

Fickian diffusion is often adequate enough to describe the solute transport processes in a polymeric matrix when the polymer relaxation time is much greater than the characteristic solvent diffusion time. However, when these times are similar, the macroscopic drug release becomes anomalous or non-Fickian (Grassi and Grassi, 2005; Fu and Kao, 2010).

2.6.2 Modelling of structures

Various approaches can be taken when modelling porous materials and their characteristics. The schematic in Figure 2.10 is a representation of different categories of porous media from the work of Schoelkopf (2002). One approach with which to model porous structures is the continuum model, in which the porous structure and its physical characteristics are described using bulk parameters such as diffusion coefficients and permeabilities. However, the mathematical theory underpinning the assumptions and approximations used to calculate the bulk parameters limit the application of such continuum models to materials other than those with similar physical and chemical characteristics to those modelled (Laudone, 2005).

Pan *et al.* (1995) describes a different approach, which utilises a three-dimensional network model of the porous structure. However, it has severe limitations: the connectivity of the structure is fixed with a value of 6, which means that each cubical pore is connected to another by six throats, and the pore size distribution is completely arbitrary.

A basic approach derived from direct porosimetric measurement is that of the capillary bundle approximation, in which the porous material is treated as a series of separate capillaries all parallel to one another within the solid medium. Structures (3) and (4) in Figure 2.10 present two capillary bundle structures, each having different average pore diameters but similar porosity. The mercury intrusion and porometry data for a material can be used to obtain a capillary cross-sectional size distribution from an idealised capillary bundle model; the first derivative of the mercury intrusion and liquid expulsion curves are assumed to be directly related to the pore size distribution of the void space. The mercury or gas pressure is converted to a 'pore' size (i.e. the size of the entry throat) using the Washburn equation (Washburn, 1921). However, the resulting capillary sizes are skewed to an unrealistically small range of diameters (Matthews *et al.*, 2006), when in reality the pore voids are much larger due to well-known shielding effects in real porous media (i.e. large pores being shielded by smaller throats during mercury intrusion and liquid expulsion) (Webb and Orr, 1997).

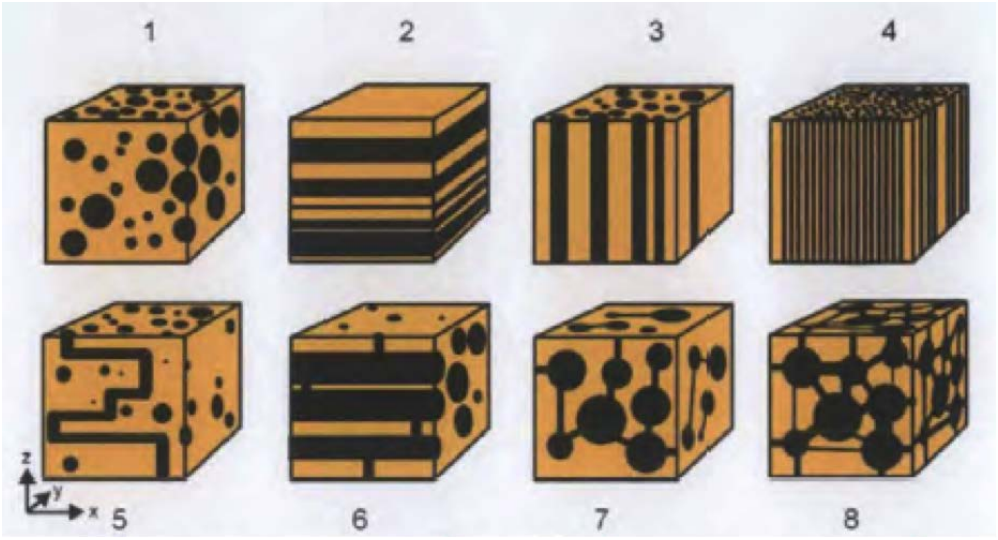

Figure 2.10: Schematic of some different morphological properties: (1) closed pores, no permeability, and zero connectivity; (2) strongly anisotropic structure, permeable only in the x,y plane; (3) unidirectional capillaries, connectivity $\approx$ 2, but no tortuosity; (4) same as (3) but different number median d_{50} pore diameter despite similar porosity; (5) no connectivity but high tortuosity; (6) small connectivity with high tortuosity, permeability is strongly non isotropic; (7) showing features of distinct pores and throats, multimodal pore size distribution, monomodal throat size distribution, low connectivity, high tortuosity, and reduced permeability; (8) distinct pores and throats, multi-modal pore and throat size distributions, high connectivity, medium tortuosity, and high permeability. This image is taken from the work of Schoelkopf (2002).

2.6.2.1 PoreXpert®

PoreXpert is the more powerful successor of Pore-Cor Research Suite, developed by the EFMG of the University of Plymouth, and is a computer software that generates a three-dimensional void structure from the inverse modelling of percolation characteristics, as measured by mercury intrusion in the case of this research. It does this by generating a void size distribution using an Euler beta function (Gribble, 2010), creating a three-dimensional network, simulating mercury intrusion through the created network, and converging the simulated onto the experimental mercury intrusion using an iterative fitting of pore and throat sizes until a closest fit is found. The fitting process is undertaken using a Boltzmann-annealed simplex algorithm, which works to find the global minima for a five-dimensional surface; the network structures generated by the software hold the same percolation characteristics as those derived from the experimental data. It then allows the modelling of pore-fluid behaviour, such as wetting (Gribble *et al.*, 2011; Laudone *et al.*, 2008, 2005) , and pore-level processes such as depth filtration (Price *et al.*, 2009). Although the basis of the model generation is the same, PoreXpert allows larger structures than Pore-Cor, permits manipulation of the structures, and features a newly developed tortuosity algorithm (Laudone *et al.*, 2015).

To simulate the mercury intrusion and expulsion, a computational representation of a fluid is applied to the top face of the unit cell only, and percolates downwards in the $-z$ direction (i.e. as in Figure 2.11). The throat skew, throat spread, pore skew, connectivity, and correlation level (Price *et al.*, 2009) are adjusted by the eight-dimensional Boltzmann-annealed amoeboid simplex (Press and Teukolsky, 1991; Johnson *et al.*, 2003) to give a close fit to the entire mercury intrusion curve or liquid expulsion curve. There are three additional Boolean constraints on the simplex: it rejects structures in which the network is fragmented, in which voids overlap, or which cannot be adjusted to give the experimental porosity without contradicting the experimental percolation characteristics.

Throat spread and throat skew define the variance and the asymmetry of the logarithmic throat size distribution. The distribution follows an Euler beta function, which encompasses Gaussian-like and Poisson-like types, as well as bimodal distributions with most void sizes at close to $d_{\min}$ and $d_{\max}$. The pore skew parameter bulks up the volume of pores, and compensates for the difficulty of achieving, in a regularly spaced and hence inefficiently packed matrix of void features, a value of porosity matching the value obtained experimentally. The representation of this effect in the resulting unit cells is that there are large numbers of pores at the maximum size of the distributions. These could be individual pores, but are more likely to be clusters of pores which are undifferentiated by the mercury porosimetry, because they comprise a single narrow throat allowing entry into a cluster of pores and throats all with dimensions greater than the single narrow throat.

Connectivity is defined as the average of the local connectivities between neighbouring voids averaged over the entire sample, or in this case over the entire representation of the sample, i.e. over a single unit cell. The average is typically found to be around 3.5, although it is recognised that in natural samples, much higher local connectivities can be observed. The short-range size auto-correlation is quantified by a correlation level parameter, which can vary between 0 for a random structure, to 1 in which

throats, and hence adjoining pores, are grouped into pre-determined loci according to their size. The six predetermined loci or 'structure types' are: completely random, vertically banded (i.e. in the $\hat{\mathbf{y}}\hat{\mathbf{z}}$ plane) (VB), horizontally banded (in the $\hat{\mathbf{x}}\hat{\mathbf{y}}$ plane) with large surface features at $z = h$ leading into smaller internal features (large to small) (HLS), horizontally banded with small surface features leading into larger internal features (small to large) (HSL), horizontally banded with large surface throats (HLST), and structures with a central spherical zone of small voids (SCZ) or large voids (LCZ).

The void network resulting from this optimisation procedure is not unique, so a set of several stochastic realisations may be generated which match the experimental intrusion characteristics. The most representative simulated structure for each sample is then found by choosing realisations for which none of the fitting parameters has a deviation from the mean of the set larger than the standard deviation of the set. If more than one sample meets that criterion, then the sample with all parameters closest to the mean is chosen.

PoreXpert simulations represent the void structure of a porous medium as a series of identical unit cells with periodic boundary conditions. Each unit cell of side length h comprises an array of $n \times n \times n$ pores $\{n \in \mathbb{Z} \mid 5 \leq n \leq 30\}$, equally spaced in a Cartesian cubic-close-packed array. Cubic pores are positioned with their centres at each node, and are connected by other, smaller cylindrical pores in each Cartesian direction (which are referred to as throats). Void shapes are simplified to cubic pores, positioned with their centres at each node, connected by up to six cylindrical throats in each Cartesian direction. The simplification of the void shapes does not greatly affect the percolation or diffusion properties, which depend mainly on those other properties which are quantitatively matched to the experiment, namely the volume, cross-sectional size, and connectivity of the voids. Although a simplified geometry is utilised for the description of the pores and throats (i.e. Figure 2.11), this model has the advantage of being free from an arbitrary choice of values for the typical parameters describing porous materials (Laudone, 2005), such as in the work of Pan *et al.* (1995).

The void network model can generate different types of structures, which together represent different arrangements of pores and throats found in natural and man-made porous materials. For example, if a structure is known to contain distinct layers of different sizes of pores and throats, then a vertically banded or horizontally banded structure would be more suitable than the capillary bundle model.

Fickian diffusion within the porous network is quantitatively simulated with diffusion coefficients based on Einstein-Stokes coefficients that have been corrected for steric hindrance (Laudone *et al.*, 2008). Surface diffusion, which occurs as adsorbed molecules move along the surface of the porous sample, is not taken into consideration although it can contribute significantly to the overall diffusion flux, especially at low values of porosity (Gribble, 2010; Laudone *et al.*, 2008; Zalc *et al.*, 2003).

A virtual reality representation from Pore-Cor Research Suite of the diffusion process of benzene in cyclohexane after 1.34 seconds in a structure with 25 % porosity is given in Figure 2.11 (Laudone *et al.*, 2008).

The structures used for diffusion modelling are those that match the percolation properties and porosities of real materials as measured by mercury intrusion or water reten-

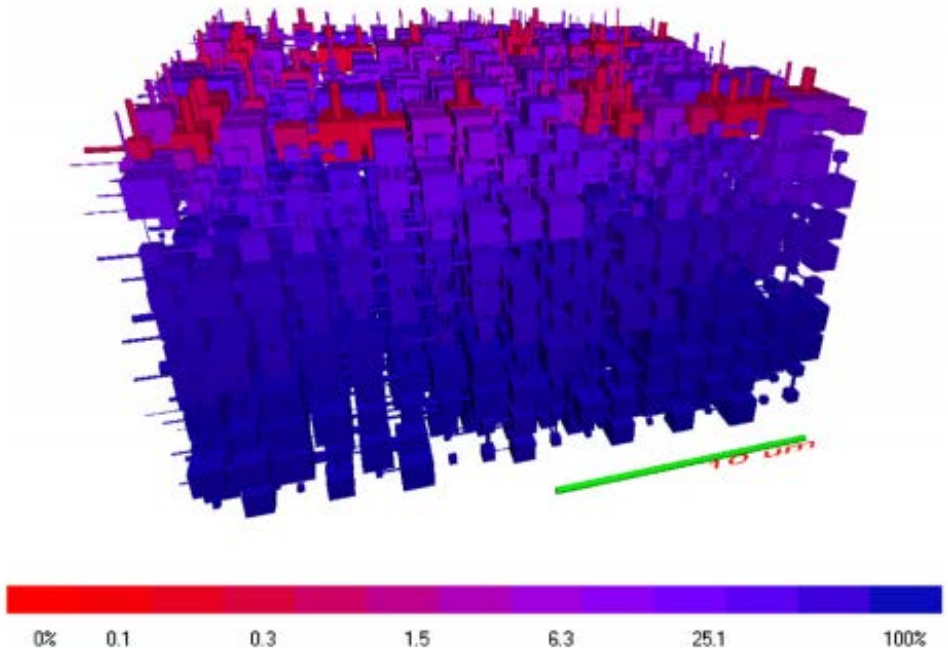

Figure 2.11: A virtual reality representation from Pore-Cor Research Suite of the diffusion process of benzene in cyclohexane after 1.34 seconds in a structure with 25 % porosity; the blue/darkest features have 100 % of the initial benzene concentration, and 0 % at the red/lightest features (Laudone *et al.*, 2008). Permission to reproduce this image has been granted by the publisher.

tion. The approach therefore provides a tool for the study of diffusion process in a wide range of materials used in various applications, such as chromatography, catalysis, and even printing (Laudone *et al.*, 2008).

The solution of Fick's diffusion equation gives the profile of concentrations (c) and can be seen in equation 2.3. In diffusion problems, the diffusion length (L_D) is the characteristic length scale used to define the extent of the effective concentration (Gribble, 2010):

$$L_D = \sqrt{4Dt} \tag{2.4}$$

The diffusion length is important in dictating the concentration profiles. A diffusion length longer than the system means that the profile is linear; a shorter diffusion length implies a gradient that is non-linear. The diffusion calculation occurs in three concurrent (but sequentially calculated) time steps. The first step is diffusion in the z direction, followed by the x and y directions, respectively. After each time step the concentration of the species in each pore is calculated and used for each subsequent time steps (Laudone *et al.*, 2008; Gribble, 2010).

The effective diffusion coefficients can only be used for optimisation of the FCC void structure if they are related to quantitative void structure parameters of the samples. As such characteristics are not measurable by direct microscopy, since that gives only two-dimensional views of the interparticle space and the particle surfaces, nor directly from any other single experimental technique, then it is necessary to gain the information with the help of a void structure model. PoreXpert is software that generates three-dimensional void structures from the inverse modeling of percolation characteristics, in this case mercury intrusion. It then allows the modelling of pore-fluid behaviour, such as wetting (Gribble *et al.*, 2011; Laudone *et al.*, 2008, 2005), and pore-level processes such as depth filtration (Price *et al.*, 2009). In this work, we have employed a newly developed algorithm (Laudone *et al.*, 2015) to measure the intraparticle tortuosity of the simulated structures for comparison with the measured diffusion coefficients (Levy *et al.*, 2015). This work is described in Chapter 7.

2.7 The zero length column (ZLC)

The 'zero length' column or cell (ZLC), developed by Eic and Ruthven (1988), permits the near-real-time study (Kärger and Ruthven, 2016) of the intraparticle diffusivity of a sample, and has been extensively applied to microporous materials. This method has been developed for both one-dimensional (slab) and three-dimensional (spherical) pore network geometries (Cavalcante Jr *et al.*, 1997). The technique involves decoupling the intraparticle diffusivity from the interparticle flow by allowing only a monolayer or zero length of sample, which is typically ~1-6 mg (Ruthven and Brandani, 2000; Teixeira *et al.*, 2013), to be equilibrated in a gas stream of the adsorbate in an inert carrier at known partial pressure, after which the desorption and/or diffusion is monitored when being purged by the pure carrier (Eic and Ruthven, 1988; Micke *et al.*, 1993; Duncan and Möller, 2000*a*; Loos *et al.*, 2000; Brandani, 2002; Brandani *et al.*, 2003; Ruthven and Vidoni, 2012). Figure 2.12 shows a schematic of this experimental arrangement.

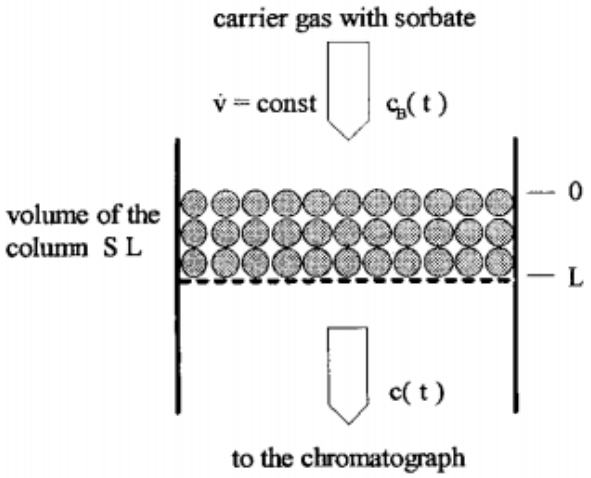

Figure 2.12: The experimental arrangement of a zero length column or cell (ZLC); here, S is the cross-section of the tube, L is the length of the sorbent, $c(t)$ is the outlet concentration, $C_{\mathrm{B}}(t)$ is the outlet concentration in a blank experiment, and $\bar{v}$ is the volumetric flow rate (Micke *et al.*, 1993; Eić *et al.*, 2002). Permission to reproduce this image has been granted by the publisher.

This technique has also been extended to study liquid-phase adsorption systems (Brandani and Ruthven, 1995; Cherntongchai and Brandani, 2003; Zabka and Rodrigues, 2007), the application of which is experimentally less convenient than for gas-phase systems, largely because of the greater importance of the fluid-phase holdup (Brandani and Ruthven, 1995). The fluid phase holdup of a gaseous system can be neglected because of the low molecular density within such a system, as it is generally negligible to a very good approximation, thus simplifying the ZLC model (Brandani and Ruthven, 1995).

The basic assumption of the ZLC is that mass transport is controlled entirely by bulk diffusion. For liquid systems the flow is assumed to be laminar and the equilibrium between fluid and adsorbed phases is maintained at all times at the outer surface of the sample, i.e. there is zero holdup of the active passing into the mobile interparticle liquid phase. It is also assumed that the fluid phase is well mixed and its concentration is constant throughout the sample, i.e. mathematically identical to a differential plug flow reactor or an infinitesimally small continuous stirred tank reactor. The model examined here assumes spherical geometries (Cavalcante Jr *et al.*, 1997; Duncan and Möller, 2000*b*; Teixeira *et al.*, 2013).

Chapter 3

Materials & techniques

THIS chapter outlines the compounds and minerals, and reviews the fundamental theory that underpins the experimental techniques, utilised throughout this project.

3.1 Materials

This section provides information as to where the materials, compounds, and solvents utilised throughout experimentation outlined in this project were sourced. The Chemical Abstracts Service (CAS) numbers for each compound has also been provided where applicable. If a material has been used in only a small portion of experimental work, then its information will be available in the specific chapter in which it is mentioned.

3.1.1 Minerals

The various minerals utilised regularly throughout this project are detailed here. They were all provided and stored as dry powders. Calcium carbonate (>99 %, CAS no. 471-34-1) was purchased from Fisher Scientific. HAP (CAS no. 1306-06-5) was purchased from Acros Organics. GCC and FCC grades were provided by Omya International AG; their properties can be viewed in Table 3.1, and various SEM images can also be seen in Figures 3.1 and 3.2.

Table 3.1: Properties of the mineral particles; the porosity reported is the total pore space of a compacted sample, since GCC has no intrinsic porosity of its own.

Sample	Particle size d_{50} (μm)	Surface area ($m^2\ g^{-1}$)	Porosity (%)	Intraparticle porosity (%)	Pore size (μm)	Morphology descriptor
GCC	7.7	1.5	22.2	-	-	-
HAP	7.1	63.2	61.8	34.2	0.05	Heterogeneous, blocky
FCC TP	7.0	55.4	61.6	25.9	2.38	Roses
FCC 02	4.9	54.1	61.2	24.4	1.22	Roses
FCC 03	3.1	33.5	49.3	10.4	0.51	Caviar
FCC 06	5.5	141.5	67.3	25.2	1.86	Brain
FCC 07	6.3	48.5	57.9	12.3	1.22	Caviar
FCC 12	10.0	81.0	70.1	29.6	3.59	Flaky eggs
FCC 13	23.5	66.0	53.4	37.0	0.11	Golf balls

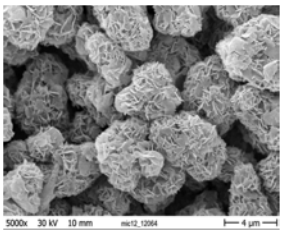

(a) FCC 02; scale bar = 4 μm.

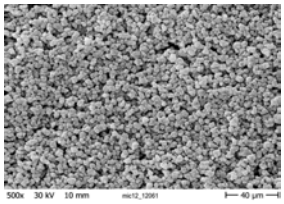

(b) FCC 02; scale bar = 40 μm.

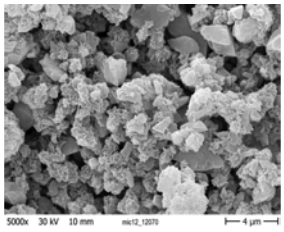

(c) FCC 03; scale bar = 4 μm.

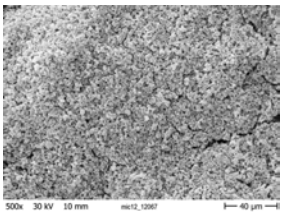

(d) FCC 03; scale bar = 40 μm.

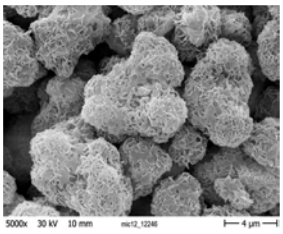

(e) FCC 06; scale bar = 4 μm.

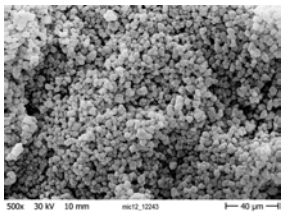

(f) FCC 06; scale bar = 40 μm.

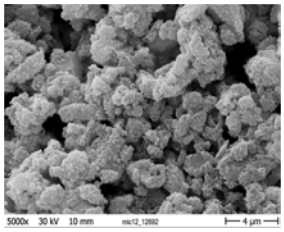

(g) FCC 07; scale bar = 4 μm.

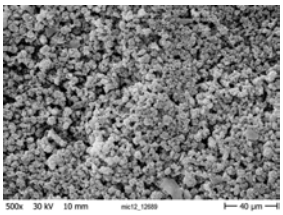

(h) FCC 07; scale bar = 40 μm.

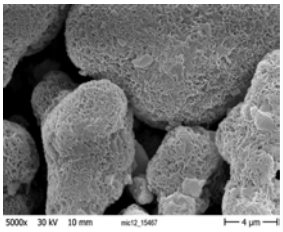

(i) FCC 12; scale bar = 4 μm.

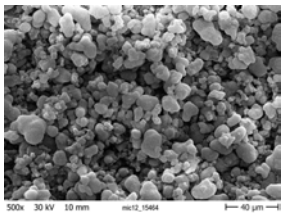

(j) FCC 12; scale bar = 40 μm.

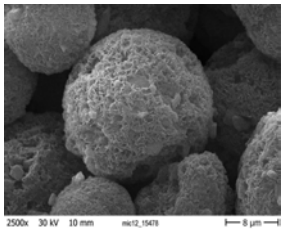

(k) FCC 13; scale bar = 8 μm.

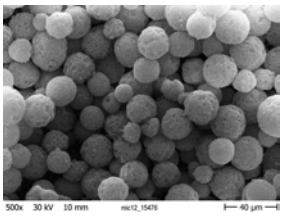

(l) FCC 13; scale bar = 40 μm.

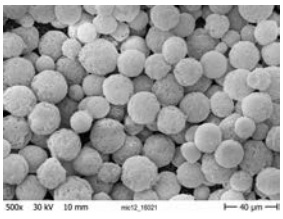

(m) FCC 13; scale bar = 40 μm.

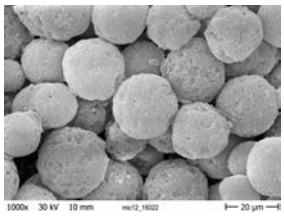

(n) FCC 12; scale bar = 20 μm.

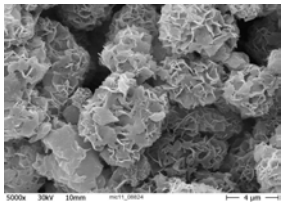

(o) FCC TP; scale bar = 4 μm.

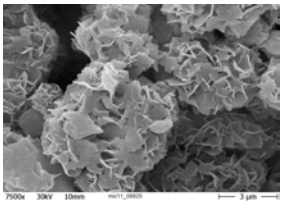

(p) FCC TP; scale bar = 3 μm.

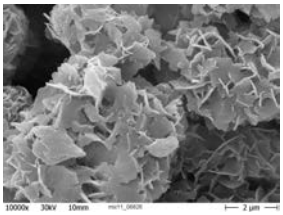

(q) FCC TP; scale bar = 2 μm.

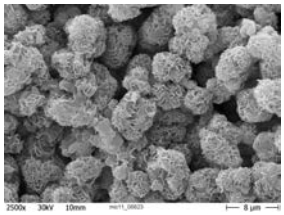

(r) FCC TP; scale bar = 8 μm.

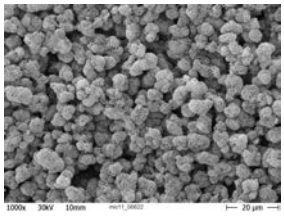

(s) FCC TP; scale bar = 20 μm.

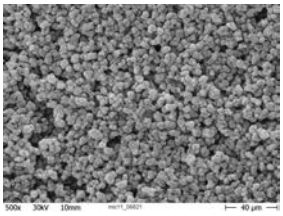

(t) FCC TP; scale bar = 40 μm.

Figure 3.1: SEMs of a varity of FCCs provided by Omya International AG.

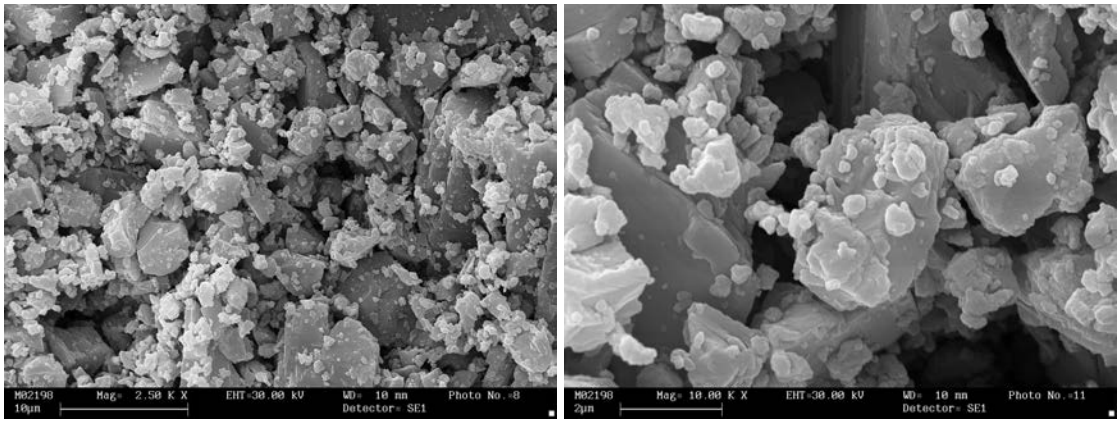

(a) GCC; scale bar = 10 μm. *(b)* GCC; scale bar = 2 μm.

Figure 3.2: SEMs of the GCC grade utilised throughout experimentation outlined in this thesis provided by Omya International AG.

Figure 3.1 shows the morphologies of the FCC particles, which can be matched up with the subjective morphological categorisation descriptors, based on their appearance in the micrographs, in Table 3.1. The micrographs were obtained with a JEOL 7001F field emission and a LEO 435 VPi scanning electron microscope. All the particles were approximately spherical, including the non-porous GCC, and so for modelling purposes were assumed to be the same. All the FCC samples have clearly identifiable lamellar platelet structures protruding from their surfaces, creating the intraparticle porosity, except FCC 07 which is more akin to GCC. The particles are shown spread out in order to take the micrographs, but the interparticle porosity when they are more densely packed can be readily inferred.

FCC SFC06.2 has been utilised sparingly in some of the work outlined in this thesis and has a particle size d_{50} value of 5.1 μm, a surface area of 72 $m^2\ g^{-1}$, and a porosity of 80 %.

Particle sizes were measured with a Malvern Master Sizer 2000, which measured the static light scattering of particles dispersed in water, interpreted using the Mie approximation (Gustav, 1908). They are expressed in Table 3.1 as d_{50} values, namely the median particle diameters at which 50 % by volume of the sample is finer than the stated value. Values of d_{98}, and the full distributions, can be seen in the 'Supporting Information' of the work published by Levy *et al.* (2015). The value of 7.7 μm for GCC is somewhat higher than its stated d_{50} of 5 μm based on Stokes' Law sedimentation in aqueous suspension.

Surface areas were measured with a Micromeritics Gemini V surface area analyser.

Mercury intrusion porosimetry (MIP) was carried out on the HAP sample using Thermo Fisher Pascal instruments. Each intrusion pressure was automatically held for long enough so that the intrusion volume to become constant by means of the instruments' PASCAL (Pressurization by Automatic Speedup and Continuous Adjustment Logic) algorithms. The low pressure intrusion of HAP was carried out twice and the porosity was calculated from the second run; this was to exclude the agglomeration of the pow-

der from the porosity calculations. The remaining samples in Table 3.1 were measured using Micromeritics Autopore mercury porosimeters, with a long (60 second) equilibration time at each pressure. The resulting intrusion curves were truncated so that no low pressure intrusion was taken into account corresponding to void sizes greater than 10 μm (Gane *et al.*, 2006). This removed any variation in measured porosity due simply to changes in the initial agglomeration of the particles by the mercury. Pore and throat size distributions of each sample, generated by PoreXpert, can be viewed in the 'Supporting Information' of the work published by Levy *et al.* (2015).

The pore sizes were obtained by visual inspection of the pore-size distribution graphs, provided by Omya International AG (except for the HAP sample, which was obtained from mercury porosimetry measurements); the peaks of these graphs corresponded to the pore sizes of the samples. Therefore, based on the definition provided by Sing *et al.* (1985), Rouquerol *et al.* (1994), and McCusker *et al.* (2003), the FCCs are macroporous. However, according to Mays (2007), they are microporous. The contents of this thesis follow Mays' (2007) scientific definition of pore size, whereas the title of the thesis follows a legislative definition.

The mercury intrusion curves are shown in Figure 3.3. After compensation for particle agglomeration effects, as described previously, the resulting portions of the mercury intrusion curves were all bimodal to some degree, as shown by an intermediate reduction in gradient. These points, shown as small vertical lines in Figure 3.3, were taken to mark the change-overs from intrusion of the interparticle space to intrusion of the intraparticle space. The intrusion volume at which this change-over occurred was used to calculate the intraparticle porosity.

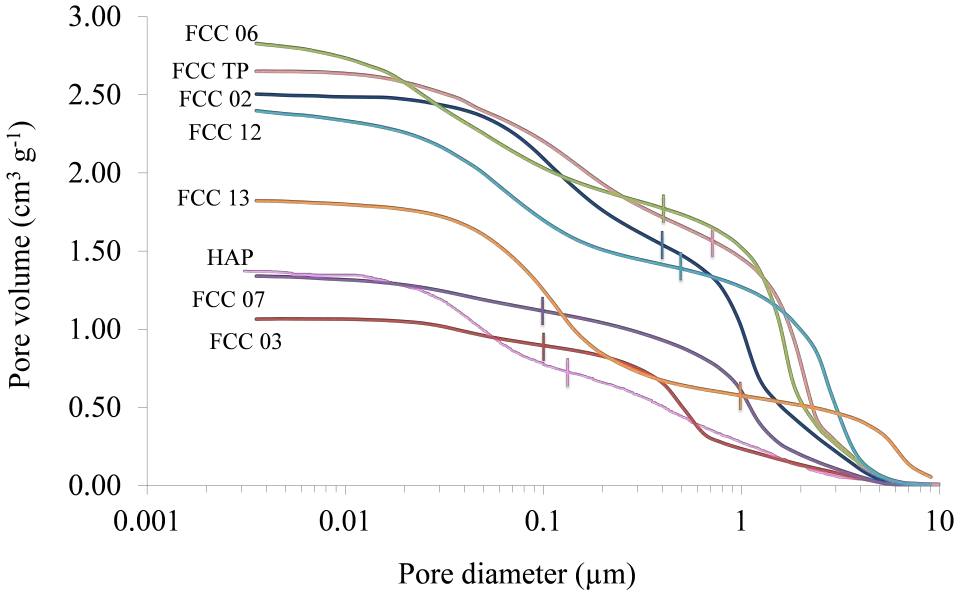

Figure 3.3: Mercury intrusion porosimetry curves for HAP and all FCC samples in Table 3.1, the latter were all provided by Omya International AG; a vertical line indicates the point at which the data were cut to model the intraparticle structure with PoreXpert.

The GCC was manufactured from marble, as was the FCC TP. The remaining FCCs in Table 3.1 were manufactured from limestone.

3.1.2 Flavours, solvents, & other compounds

Various flavour compounds were used throughout the experimentation outlined in this work and were chosen not only for their role in flavours and fragrance, but also for their role in pharmaceutics. Anethole was originally chosen because of its high solubility in ethanol. However, when work with FCC loading began (Chapter 5) it became apparent that there would be issues with anethole due to its volatility. Vanillin, a common and popular flavour compound readily soluble in ethanol, was then chosen as the flavour species to work with because it is solid at room temperature, thereby having potential to be loaded into the pores of an FCC in future work (Preisig *et al.*, 2014). Saccharin was also selected for use at a later stage during this research project in aqueous solutions.

Trans-anethole (99 %, CAS no. 4180-23-8), vanillin (99 %, CAS no. 121-33-5), saccharin (sodium salt, hydrate, 99+ %, CAS no. 82385-42-0), 4-(2-Hydroxyethyl)piperazine-1-ethanesulfonic acid sodium salt (CAS no. 75277-39-3 99 %), and 4-(2-Hydroxyethyl)piperazine-1-ethanesulfonic acid (CAS no. 7365-45-9 99 %) were all purchased from Acros Organics. Absolute ethanol, both laboratory reagent and high performance liquid chromatography (HPLC) grade (99.8+ %, CAS no. 64-17-5), analytical grade hydochloric acid (HCl; CAS no. 7647-01-0; 36 %), and isopropyl alcohol (IPA; CAS no. 67-63-0), were purchased from Fisher Scientific. HPLC grade solvents were used in all instances except where otherwise specified.

The ultrapure water (18 MΩ-Cm) used throughout experimentation, unless otherwise mentioned, was produced by a Milli-Q Reagent Grade Water System by Millipore.

3.1.2.1 Anethole

Anethole (1-methoxy-4-(1-propenyl)benzene; Figure 3.4) has a unique liquorice odour and taste, and is largely used as a flavour agent in the food industry, in cakes, ice-creams, and alcoholic beverages (Freire Rosemayre *et al.*, 2005). Studies have shown that anethole possesses several pharmacological activities, such as anti-inflammatory (Chainy *et al.*, 2000), anti-oxidant, and gastroprotective (Freire Rosemayre *et al.*, 2005) properties. It is the principal aromatic molecule of Pastis and other anise-flavoured alcoholic beverages and is commonly known as *trans*-anethole. Both isomers occur in nature, with *trans*-anethole being the most abundant, and is a major constituent of several essential oils, including anise seed oil (80-90 %), star anise oil (>90 %) and sweet fennel oil (80 %) (Kishore and Kannan, 2006). *Cis*-anethole has been reported as toxic and possessing an unpleasant scent and flavour (Castro *et al.*, 2010).

Trans-anethole has important use as a flavouring substance in baked goods, candy, ice cream, chewing gum and alcoholic beverages. It is the major volatile component in sweet and bitter fennel and anise (Newberne *et al.*, 1999). *Trans*-anethole is reportedly used in baked goods at 494.9 ppm, frozen dairy at 53.45 ppm, meat products at 10.01 ppm, soft candy at 530.6 ppm, sweet sauce at 86 ppm, gelatine pudding at 52.8 ppm, non-alcoholic beverages at 42.54 ppm, alcoholic beverages at 722.5 ppm, gravies at 5.01 ppm, hard candy at 491.7 ppm, and chewing gum at 2 564 ppm (Burdock, 2004). However, its application is food products is limited because of its volatility and very low

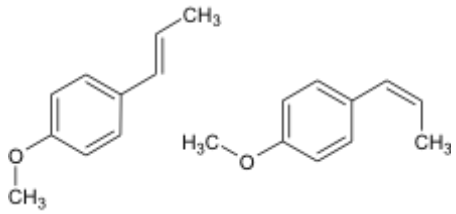

Figure 3.4: The structure of 1-methoxy-4-(1-propenyl)benzene. *Trans*-anethole is on the left and *cis*-anethole is on the right.

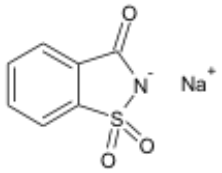

Figure 3.5: The structure of sodium saccharin.

aqueous solubility (Kfoury *et al.*, 2014).

3.1.2.2 Saccharin

Saccharin (1,2-benzisothiazole-3-one-1,1-dioxide) can be found in a variety of beverages and foods in the form of its sodium salt since 1885 (Gençer *et al.*, 2012), with its primary function being to add sweetness with minimal caloric damage. It can be found in soft drinks, tabletop sweeteners, chewing gums, confectioneries, jams, juices, and sauces (Calorie Control Council, 2001). It is reported as being 300-500 times sweeter than sucrose (Wang *et al.*, 2011), and was first synthesised in 1879 (Whysner and Williams, 1996). Unfortunately, saccharin compounds have been intensively investigated due to their suspected carcinogenic nature (Gençer *et al.*, 2012). Additionally, the use of saccharin in a variety non-food applications over the last century has been realised.

Not only was sodium saccharin (Figure 3.5) selected because of its high water solubility (Whysner and Williams, 1996) and relevance in the final application of this work, but also because of its non-food use. The heterocycle has pharmaceutical importance in that it is a key structural element of certain central nervous system-active drugs, thus it can be viewed as a scaffold in the field of medicinal chemistry and can play the role as a pharmacophore in bioactive molecules (Gençer *et al.*, 2012). Previous experiments that have investigated the diffusion of various model drugs included sodium saccharin as a model drug (Jämstorp *et al.*, 2012).

3.1.2.3 Vanillin

Vanillin (4-hydroxy-3-methoxybenzaldehyde; Figure 3.6) is the major component of natural vanilla, and although more than 12,000 tonnes of vanillin are produced each year, less than 1 % of this is natural vanillin (Walton *et al.*, 2003).

Approximately 50 % of the worldwide production of synthetic vanillin is used as an intermediate in chemical and pharmaceutical industries for the production of herbicides, antifoaming agents, or drugs, and also has a biogenetic relationship to molecules of

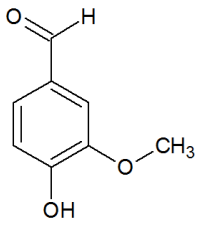

Figure 3.6: The structure of vanillin.

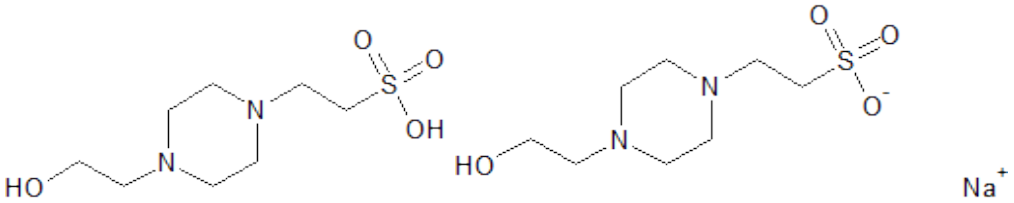

(a) Structure of HEPES free acid.

(b) Structure of HEPES sodium salt.

Figure 3.7: Structures of HEPES free acid and sodium salt.

physiological significance, such as salicylate (Walton *et al.*, 2003).

3.1.2.4 HEPES

4-(2-Hydroxyethyl)piperazine-1-ethanesulfonic acid (HEPES) is a widely used buffer for the neutral pH range, and was introduced by Good and Izawa (1972) when developing a series of zwitterionic molecules suitable for biochemical and physiological studies. Its biocompatibility arises because HEPES was introduced as a compound that would not form complexes with metal ions in aqueous solution (Bettelheim *et al.*, 2010), and is very close to the physiological pH of 7.4 (Sokołowska and Bal, 2005). Its pH is between the ranges of 6.8-8.2, and it has been described as one of the best all-purpose buffers for biological research (Good *et al.*, 1966).

This zwitterionic buffer was used to provide a neutral pH only minimally affected by CO_2 concentration and temperature. However, although the use of aqueous-based solutions in these experiments would be more applicable to biological situations, ethanol-soluble compounds offers an advantage in ease of loading (i.e. ethanol has a lower evaporation temperature than water) and in designing simpler experiments (i.e. a buffer may complicate adsorption and diffusion processes in our systems).

The HEPES buffer is made by combining an accurate and calculated amount of HEPES free acid (Figure 3.7a) with its sodium salt (Figure 3.7b) in a known volume of ultrapure water. To make the buffer solution in 2 dm^3 of ultrapure water, 3.62 g of HEPES free acid and 1.25 g of HEPES sodium salt was required.

3.2 Techniques & technique development

This section describes techniques that were developed within this project except adsorption measurements, which are described in Chapter 4. Other techniques, specif-

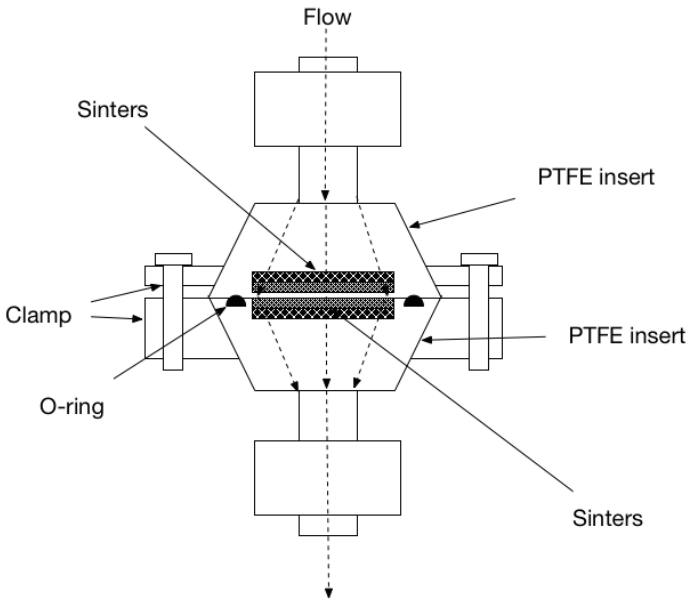

Figure 3.8: A schematic (side view) of the ZLC designed for liquid systems.

ically MIP, envelope pycnometry, and helium pycnometry, among others, were used according to standard practices, and may only be briefly described further in an appropriate chapter.

3.2.1 The zero length column (ZLC)

The 'zero length' cell (ZLC) was developed by Eic and Ruthven (1988) and is a specialised chromatographic column that can be used with various detectors. It was originally designed for use with gas chromatography systems, but for this work it has been adapted to liquid systems for use with an HPLC. One of the original liquid ZLC systems used a packing material to hold the monolayer of sample in place (Ruthven and Stapleton, 1993). A disadvantage of this is that the mobile phase could interact with the packing material, and it was difficult to change the material once embedded (Gribble, 2010). For these investigations, the design of the ZLC is a development of that described by Zabka and Rodrigues (2007), in which an effective monolayer of porous material, which is approximately 3-5 mg of FCC (Gribble, 2010), can be sandwiched between two fine stainless steel sinters. Originally, Mark I of the ZLC involved a resin-embedded stainless steel sinter within an empty chromatography column tube. However, the mobile phase flowed around the edges of the sinter and did not provide a laminar flow. The sinter was then changed to a cylindrical shape and was silver-soldered into the chromatography column tube (Mark II), changing the sinter properties from a uniform pore size to a dual-layer, bimodal pore size of approximately 1 μm on the top sinter and 15 μm on the bottom (Gribble, 2010). An O-ring was added in order to ensure a good seal between the two ZLC halves. A schematic of the ZLC system can be seen in Figure 3.8, and Figures 3.9a and 3.9b show a schematic and a photograph, respectively, of the Mark II sinters used in this work.

The entry and exit channels in the ZLC has been shaped in order to optimise its design,

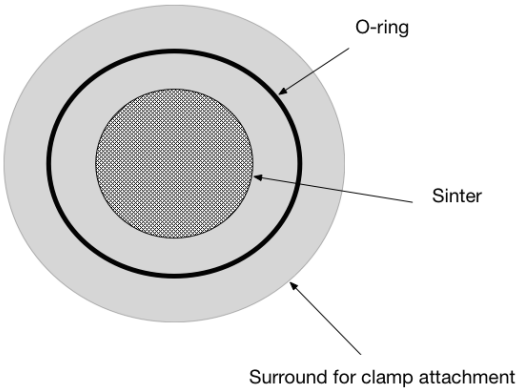

(a) A cross-sectional schematic perpendicular to the axis of flow of the ZLC designed for liquid systems (top view).

(b) A photograph of the Mark II ZLC sinters utilised throughout experiments outlined in this work.

Figure 3.9: Top view schematic of the ZLC designed for liquid systems and a photograph of the Mark II sinters.

and this was done so using inserts in order to minimise dead-space. The Mark I and II ZLCs use brass inserts, while a Mark III ZLC uses polytetrafluoroethylene (PTFE) inserts combined with the Mark II sinters, which can be viewed in Figure 3.10. The experimental work outlined in this thesis used the Mark III version throughout. The volume through which the mobile phase flows is 1.3 cm^3, and the internal diameter of the entry and exit tubes is 0.12 mm. (Gribble, 2010).

Previously, work conducted with the ZLC involved using up to 20 g dm^{-3} of benzene in cyclohexane as the mobile phase in order to measure the desorption and diffusion coefficients of several grades of FCC to determine how the coefficients vary as a result of differing porosities, surface area, etc. The aromatic nature of benzene results in a high sensitivity with an ultraviolet-visible (UV) detector (Gribble, 2010), and thus benzene in cyclohexane was selected as the sorbate-solvent system in previous projects. However, it is difficult to obtain a stable baseline with non-aqueous solvents, and the effects of a monolayer of FCC on the diffusion of the analyte were very small, especially as only very low concentrations of analyte can be used in the ZLC.

The dead space within the HPLC flow line, detector chamber, and ZLC entry and exit ports have caused the mobile phase liquids to mix in a manner similar to a chromatographic line broadening effect. Since the effects being studied are so subtle as to be masked in a ZLC by this line broadening, it was necessary to lengthen the ZLC in the flow direction, converting it to what we refer to as a finite length cell (FLC). The lengtheners of 2.7, 5, and 10 mm in length can be viewed in Figure 3.11. A schematic of the FLC can be seen in Figure 3.12 and a photograph of all of the FLC equipment is shown in Figure 3.13. Additional drawbacks of the ZLC are discussed further in Chapter 7.

3.2.1.1 The finite length column (FLC)

The use of an FLC has the advantage of making the diffusional effects observable. Also, the use of a larger sample volume in the FLC is closer to that which would be found in a controlled release tablet, relative to the monolayer in a ZLC. However, the

Figure 3.10: A photograph of the brass and PTFE inserts used in ZLC liquid designs.

Figure 3.11: ZLC lengthening columns constructed at the University of Plymouth. From left to right, the lengths of the sinters are 10, 5, and 2.7 mm, respectively.

disadvantage is that the measured release rates then become dependent on diffusion and permeation effects within both the intra- and interparticle porosity, and that the system is less well described by the original ZLC mathematical assumptions (Chapter 2). Rather than precise diffusion coefficients D, the measurements are therefore of effective diffusion coefficients D'.

It is always assumed that the flow is laminar through the column. The design of the zero length column allows one to assume that the concentration at the surface of each particle is the same as in the bulk mobile phase (Brandani and Ruthven, 1995).

In between experiments, the ZLC and lengtheners had to be cleaned. This was done using a HCl solution with a concentration of approximately 2M. Once the ZLC/FLC was disconnected from the HPLC and dismantled, the two sinters were scrubbed with a wire brush in the HCl solution before being immersed in ultrapure water for approximately 5 minutes. The sinters were then dried with paper towels prior to being left to air dry completely before the subsequent experiment. The lengthening columns were simply rinsed and wiped clean with IPA and ultrapure water, respectively.

In order to load the ZLC with powdered sample, an aluminium weighing boat was tared on an analytical balance (in all cases a Mettler Toledo Excellence Plus XP504 analytical balance was used), in which a monolayer of sample, approximately 3-5 mg

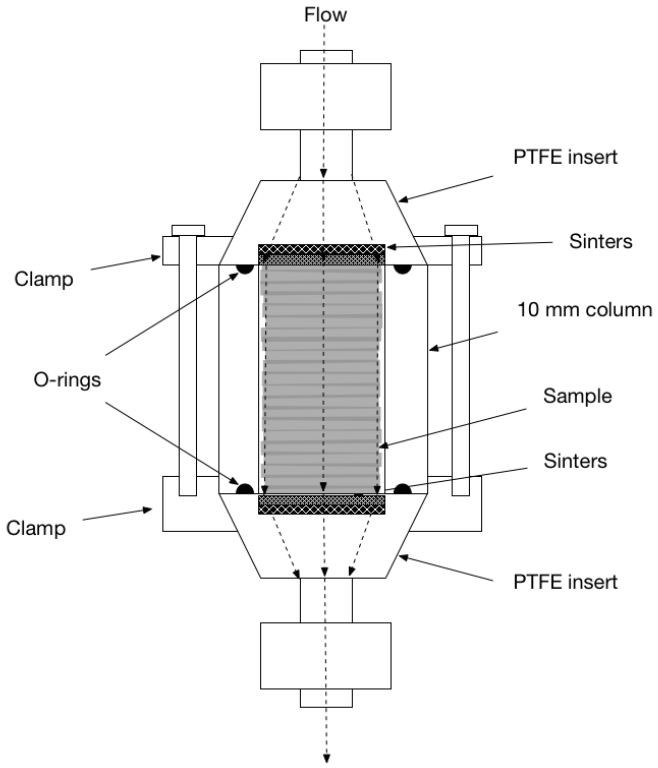

Figure 3.12: A cross-sectional schematic of the FLC.

Figure 3.13: A photograph of all FLC components.

(Gribble, 2010), was weighed. The micro spatula was then used to push the sample onto the 'top' half of the ZLC (i.e. the 'flat' side with no O-ring) and was spread out as much as possible using a fine tip at the opposite end of the spatula. The weighing boat was reweighed in order to calculate how much sample had theoretically been transferred/loaded into the ZLC. The ZLC was then assembled and attached to the HPLC.

The FLC, on the other hand, is loaded by using the envelope density of the sample to calculate how much sample should be packed into it; the bottom sinter (with the O-ring) and the lengthening column of choice is tared on an analytical balance (in all cases a Mettler Toledo Excellence Plus XP504 analytical balance was used), and the sample is weighed directly into the FLC, whilst using the spatula to press the FCC down lightly if required. Figure 3.14a demonstrates this. Once the FLC is loaded, it is attached to the HPLC, as in Figure 3.14b, with the O-ring on the bottom.

The envelope densities of the samples were measured using a Micromeritics GeoPyc 1360 Envelope Density Analyzer equipped with a chamber of an internal diameter of 12.7 mm. The chamber is filled with a volume of a displacement medium, and the instrument agitates and compresses it in the chamber with a consolidation force of 28 *N*. The sample is then immersed in the displacement medium before the instrument agitates and compresses it yet again and collects the displacement data, which is equivalent to the envelope volume of the sample. The displacement medium used was DryFlo, also manufactured by Micromeritics, and is a powder designed to flow like a liquid composed of small, rigid silica beads lubricated by fine graphite particles (Wade *et al.*, 2015). The measurements were approximate, because they involved the use of a powder to investigate the packing of a powder. They were therefore used simply as a cross-check to ensure that there was efficient packing into the FLC.

3.2.1.2 High performance liquid chromatography (HPLC)

High performance liquid chromatography (HPLC; also used to refer to the high performance liquid chromatograph) is a widely used separation technique, and can be used with a number of different analytical detection methods depending upon the nature of the analyte. HPLC was utilised in this work given the liquid nature of the experimental systems and the high pressures required to obtain a consistent flow rate through the fine sinters of the ZLC (Gribble, 2010).

The detection method utilised within the HPLC was UV-visible spectroscopy using a diode array detector (DAD). The first ZLC experiments conducted on the HPLC system within the EFMG utilised a mobile phase of benzene in cyclohexane (Gribble, 2010), and are similar compounds to those used in previous ZLC experiments published in the literature. Although, benzene yields a high UV response (Gribble, 2010), which makes UV-visible spectroscopy suitable as a detection method, the DAD provides a simple and straightforward way to detect a variety of different compounds.

The HPLC system used was a Hewlett Packard (now Agilent) HP 1050 series, a photograph of which can be seen in Figure 3.15. The bottom module is the autosampler and vial tray, the module above is the DAD, the module above that is the quaternary pump, and the topmost module is the solvent conditioning unit. Each unit was connected to one another and then to a computer (an RM Education Innovator tower with

(a) A photograph in the midst of loading the FLC with an FCC sample.

(b) A photograph of the FLC assembled and attached to the HPLC.

Figure 3.14: Photographs of loading the FLC and once it is assembled and attached to the HPLC.

a CTX Technology monitor) running Windows 2000 Professional as the operating system. Agilent ChemStation for LC Systems (Rev. A.09.03, copyright Agilent Technologies 1990-2002) was the software employed to set up experiments and to programme the HPLC.

The solvent conditioning unit on top of the HPLC is to provide a constant stream of helium into each solvent reservoir. Unfortunately, the unit was broken. Therefore, in order to degas solvents prior to use, the helium line was directed into each solvent reservoir for 10-15 minutes; helium was bubbled through the solvent as vigorously as possible without any spilling out. This was done for each solvent at the beginning of each day before use.

Once the solvents were degassed, the HPLC was purged at 5 cm^3 min^{-1} with equal amounts of all solvents that were to be used in subsequent experiments for approximately 10 minutes. The flow was then changed to 100 % of the solvent that was to be used first in the subsequent experiment for approximately 5 minutes. The pump was stopped and the ZLC or FLC was attached to the HPLC before switching the pump back on for another 5-10 minutes. The flow was changed to the desired rate for a few minutes before the experiment was started.

3.2.1.3 Issues

Through the experimentation outlined in this thesis, many issues have arisen regarding the ZLC, FLC, and HPLC systems. This section outlines the major issues faced including various blockages and leaks in the systems.

Issue 1 One issue that was rather frequent was the stainless steel capillary of the HPLC becoming stuck in the ZLC. The case shown in Figure 3.16a was rather a serious one, because in instances like these the capillary can be eased out over a period of time with gentle rotation. However, in this particular case, two adjustable spanners were sourced in order to take apart the ZLC and to replace the top nut, as in Figure 3.16b, from the Mark II ZLC. As a result of this particular incident, the stainless steel capillaries in contact with the ZLC were replaced with polyether ether ketone (PEEK) tubing and finger-tight PEEK fittings.

Another issue arose when the FLC was first tested: it kept leaking from the top of the lengthening column, as in Figure 3.17a. Upon further inspection of the O-rings, it became apparent that the O-ring in the lengtheners did not protrude from the column as far as the O-ring in sinter, as in Figure 3.17b.

Seals and O-rings from other companies did not provide the dimensions required for this particular application, and so other options were considered to resolve this issue. Figure 3.18a shows an attempt at raising the O-ring in the lengthening column by padding out the bottom with plastic paraffin film, and Figure 3.18b shows a similar attempt but using a thick filter paper. As suspected, neither of the two fixes created the desired outcome. Ultimately, the lengtheners were taken back to the workshop to have approximately 0.12 mm shaved off. Table 3.2 shows the lengths of the newly shaved FLC columns measured in three different spots on each lengthener using a Mitutoyo Digital Caliper 600-880 (Absolute Digimatic, model no. CD-6" CP).

Figure 3.15: A photograph of the Hewlett Packard (now Agilent) HP 1050 series HPLC used throughout this project. The bottom component is the autosampler, the part above is the DAD, the module above that is the pump, and the topmost section is the solvent conditioning module.

Table 3.2: Lengths of the FLC columns, measured in three different spots on each lengthener.

FLC lengthener identifier	Lengthener length (mm) 1	2	3	Average length (mm)
2.7 mm	2.63	2.62	2.63	2.62 ± 0.00
5 mm	4.72	4.72	4.71	4.72 ± 0.01
10 mm	9.85	9.87	9.87	9.86 ± 0.01

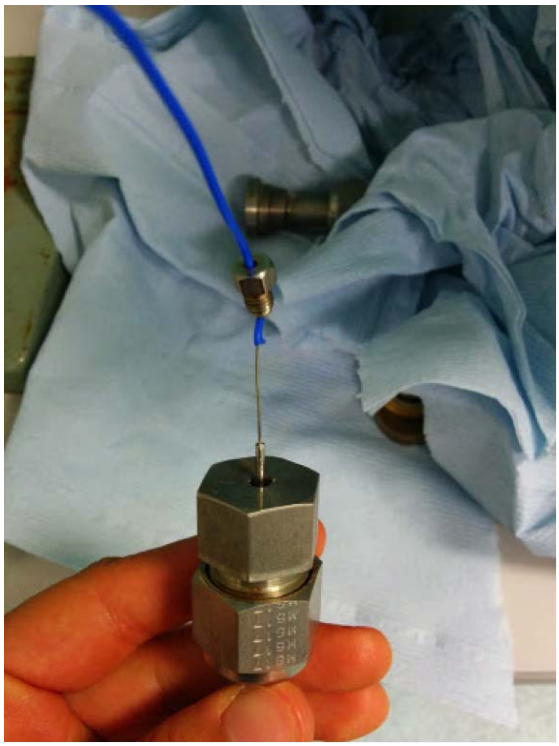

(a) A photograph of the stainless steel capillary stuck in the ZLC.

(b) A photograph of the nut that is used to form one half of the ZLC.

Figure 3.16: Photographs of ZLC issues and resolutions.

(a) A photograph of the FLC leaking during an experiment.

(b) A photograph of O-rings on the bottom ZLC sinter and the 2.7 mm lengthening column.

Figure 3.17: Photographs of the FLC leak issue. Note that the O-ring of the lengthening column does not protrude as far out as the O-ring in the sinter in Figure 3.17b.

(a) A photograph of the O-ring in a lengthening column being padded out with parafilm.

(b) A photograph of the O-ring in a lengthening column being padded out with thick filter paper.

Figure 3.18: Photographs of the FLC leak issue resolution attempts.

Issue 2 Another issue arose when the FLC leaked from the bottom nut during experiments in which saccharin was the diffusing species and HEPES buffer was the mobile phase. The leak was present regardless of the flow rate or sample; even during blank experiments, the column continued to leak. The FLC was cleaned multiple times. However, it appeared that if the FLC was clamped together particularly tightly and/or oriented in a certain way, the leak stopped, although the pressure was extremely high. The sinters were cleaned by placing them into a beaker and immersing them into 2 M HCl. The beaker was then placed in a sonic bath for an hour. The sinters were then submerged in ultrapure water for 15 minutes before being reattached to the HPLC, yet the issue of an apparent blockage still persisted.

Upon further testing of the system without the FLC, it became apparent that the blockage must be somewhere in the HPLC system. Further tests revealed that the blockage was in the PEEK capillary tubing after the FLC flow; upon further inspection it could be seen that it was visibly blocked. The capillary was replaced.

Despite the FLC being disconnected from the system, and a PEEK capillary having been changed, the HPLC still seemed to be operating at too high a pressure. The capillaries were altered so that the flow bypassed the autosampler component of the HPLC, after which the HPLC functioned normally. The problem was narrowed down to a PEEK capillary connector used on one of the capillaries that leads into the autosampler. This was tested by allowing the HPLC flow to simply flow through the capillary and the connector into a waste beaker; when the pump was switched on, the solvent seemed to be forced through at such a high pressure and out of the connector before settling down to a drip as normal. It appeared as though there was some sort of blockage, but disconnecting the connector somehow gave enough space for the pressure to push out whatever was blocking it. The HPLC and FLC system from then on functioned as normal.

Issue 3 A long-standing issue with the HPLC arose when the detection sensitivity, i.e. the absorbance as measured in absorbance units (AU), of the analyte changed drastically almost overnight, as in Figure 3.19. Unfortunately, because the instrument is >20 years old and is an obsolete model, it was not possible to call out an Agilent engineer without incurring great expense. Additionally, it was received second-hand from AstraZeneca, and so any modifications that may have been made to it and its prior usage history is unknown. It was possible to call out a private engineer, however, that would have incurred steep costs.

In instances like this, a multitude of problems could potentially be the cause of the issue. For example, it may have been a dirty HPLC system in which a build up of various materials had accumulated. Or, the issue could have been related to the hardware or electronics of the instrument itself. The HPLC was flushed through with IPA and ultrapure water for several hours each, but to no avail. Various sections or modules of the HPLC were bypassed (e.g. the autosampler) in order to try and pinpoint the location of any blockage or issue. Initially, it was thought that something had happened to the saccharin in HEPES solution; a fresh solution of the same concentration, 1 g dm^{-3}, was made and analysed via UV-visible spectroscopy. There were no detectable differences between the freshly made solution and the older solution.

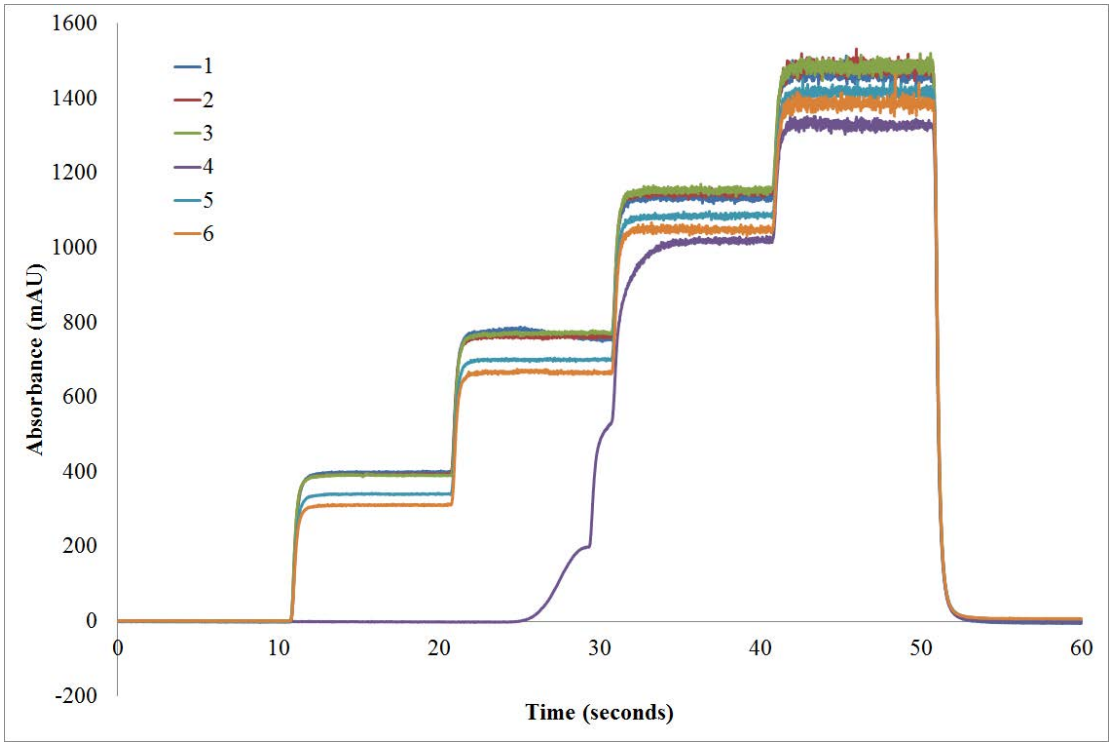

Figure 3.19: Saccharin in HEPES 10 mm FLC calibration runs; note the inconsistent detection sensitivity. The absorbance was measured at 269 nm.

It was thought that the deuterium lamp may have needed replacing, but upon inspection of the lamp it appeared very clean. Intensity tests were performed on the deuterium lamp, which was run from the ChemStation computer software. Ultrapure water was run through the HPLC when the tests were conducted, and it showed that the intensity of the lamp had decreased over the past several months. Therefore, a new lamp was purchased and tested. It was then suggested that the flow cell may be dirty, or a similar component, however, the box in which the flow cell assembly was located was bolted shut and unable to be opened by hand. An Agilent 1100 HPLC was located and obtained from another department within the university and was to be used for the experimental work instead. Unfortunately, it had its own issues that were attributed to it having been out of action for some time. Figure 3.20 shows the calibration runs on the original HPLC, the newly acquired HPLC, and a calibration curve of saccharin in HEPES run on the original HPLC when it was operating normally (labelled as 'previous calibration'), the latter being the desired level of maximal noise along the y-axis.

In Figure 3.20 the 'previous calibration' is an example of an ideal HPLC calibration, and rises in increments of 100 mg of saccharin per cubic decimetre of HEPES solution, (starting from 0 and ending in 400 mg dm^{-3}) every 10 minutes, and is an average of three runs; the y-axis error bars are the standard deviations of the three runs. The 'new(er) HPLC' runs are calibration trials using the newly acquired Agilent 1100 HPLC. The remaining runs were performed on the original HPLC using saccharin in ultrapure water when bypassing the autosampler and/or using the new deuterium lamp. However, it can be seen that the issue of too much noise still persists.

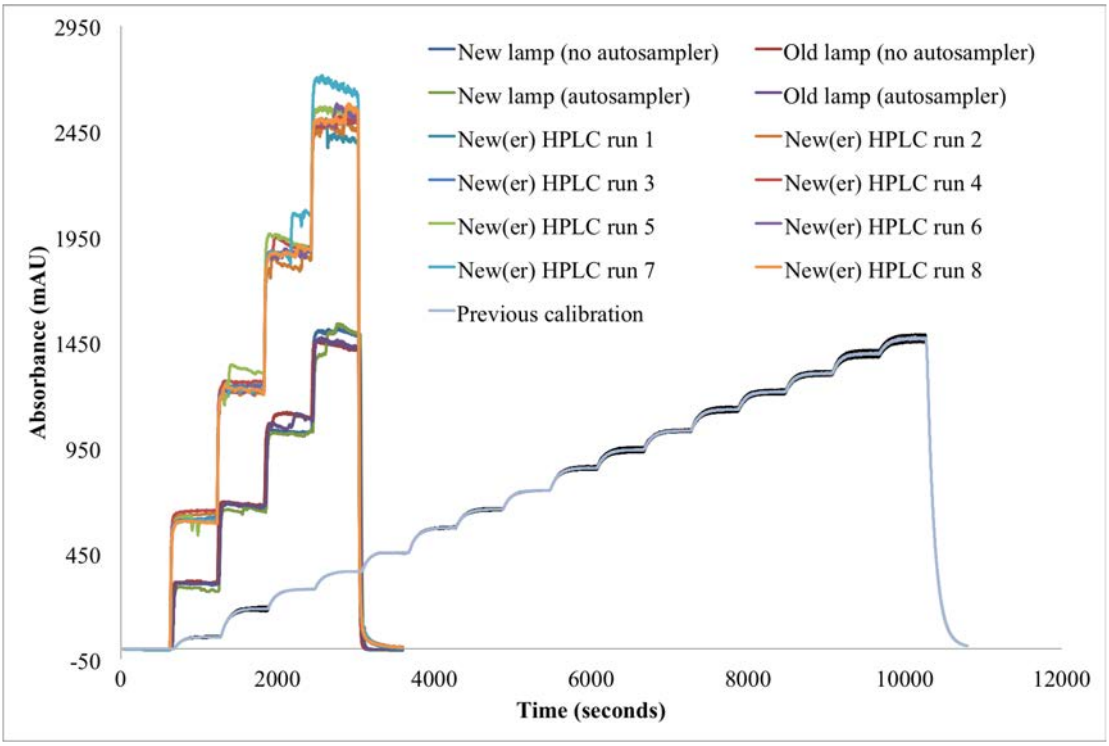

Figure 3.20: Saccharin in HEPES 10 mm FLC calibration runs; note the noisy detection sensitivities. The 'previous calibration' represents the average of 3 previous calibration runs when the HPLC was functioning normally, and the y-axis error bars are the standard deviations of the 3. The other runs demonstrate the difficulties faced regarding the detection sensitivity of the HPLC changing; the runs labelled 'New(er) HPLC' refer to the Agilent 1100 HPLC acquired frmo elsewhere within the university. The absorbance was measured at 269 nm.

It was then suggested to remove the flow cell when conducting lamp intensity tests, because if the flow cell is dirty then this will give the impression that the lamp is the issue. However, getting to the flow cell proved very difficult, because the flow cell was located in a black box inside the DAD module of the HPLC (as in Figures 3.21a and 3.21b), which was bolted shut by its previous users. This required having to take the HPLC apart and dismantle the actual DAD module, as in Figure 3.21c, in order to gain an appropriate angle to drill through the bolt with an electric saw.

(a) A photograph of the bolt sealing the flow cell assembly inside the black box.

(b) A photograph of the bolt from a bird's eye view.

(c) A photograph of the DAD module of the HPLC when dismantled in order to gain an appropriate angle to drill through the bolt.

Figure 3.21: Photographs of the HPLC and the bolt locking the flow cell assembly in the DAD module.

Once the flow cell assembly could be accessed, lamp intensity tests were conducted without the assembly, and a screenshot of these test results are displayed in Figure 3.22. The blue spectrum in the figure was taken in February 2014 with the flow cell in, and the red spectrum was taken in September 2014 with the flow cell in, also; this demonstrates that there has been a considerable decrease in the lamp's intensity, and is attributed to causing the noise issue in Figures 3.19 and 3.20. However, on the same day in September 2014, when the flow cell assembly was removed and the lamp intensity test was conducted again, a considerable increase in the lamp's intensity was observed (i.e. the green spectrum in Figure 3.22). The flow cell was placed back into the HPLC and the test ran again, which yielded the pink spectrum. The results certainly suggested that the flow cell is the issue.

A flow cell cleaning kit was purchased from a private consultant because the particular kit required was an obsolete item that was no longer sold by Agilent. The quartz window cartridges were unscrewed and removed (Figure 3.23a shows the removal of the front window) and the front and back gaskets were disposed. The inside of the flow cell assembly was rinsed with IPA, wiped clean with paper towel, and left to air dry. New gaskets were then inserted (Figure 3.23b shows the front gasket being replaced). Figure 3.23c is a photograph of flow cell window cartridges; the leftmost cartridge is new and clean while the middle and rightmost cartridges were the ones being replaced in the HPLC. It is apparent that the cartridges taken from the HPLC are visibly dirty when compared to the new cartridge. The new quartz window cartridges were screwed into the flow cell assembly. Other additional cleaning and maintenance procedures were undertaken, for example, the changing of various frits in the HPLC. Figure 3.24 shows the changing of a pump frit, and the visual differences between the new and old frits show the extent of how dirty the older frit was. Figure 3.25 shows calibration experiments performed once the flow cell windows were changed, thus rendering the issue as resolved.

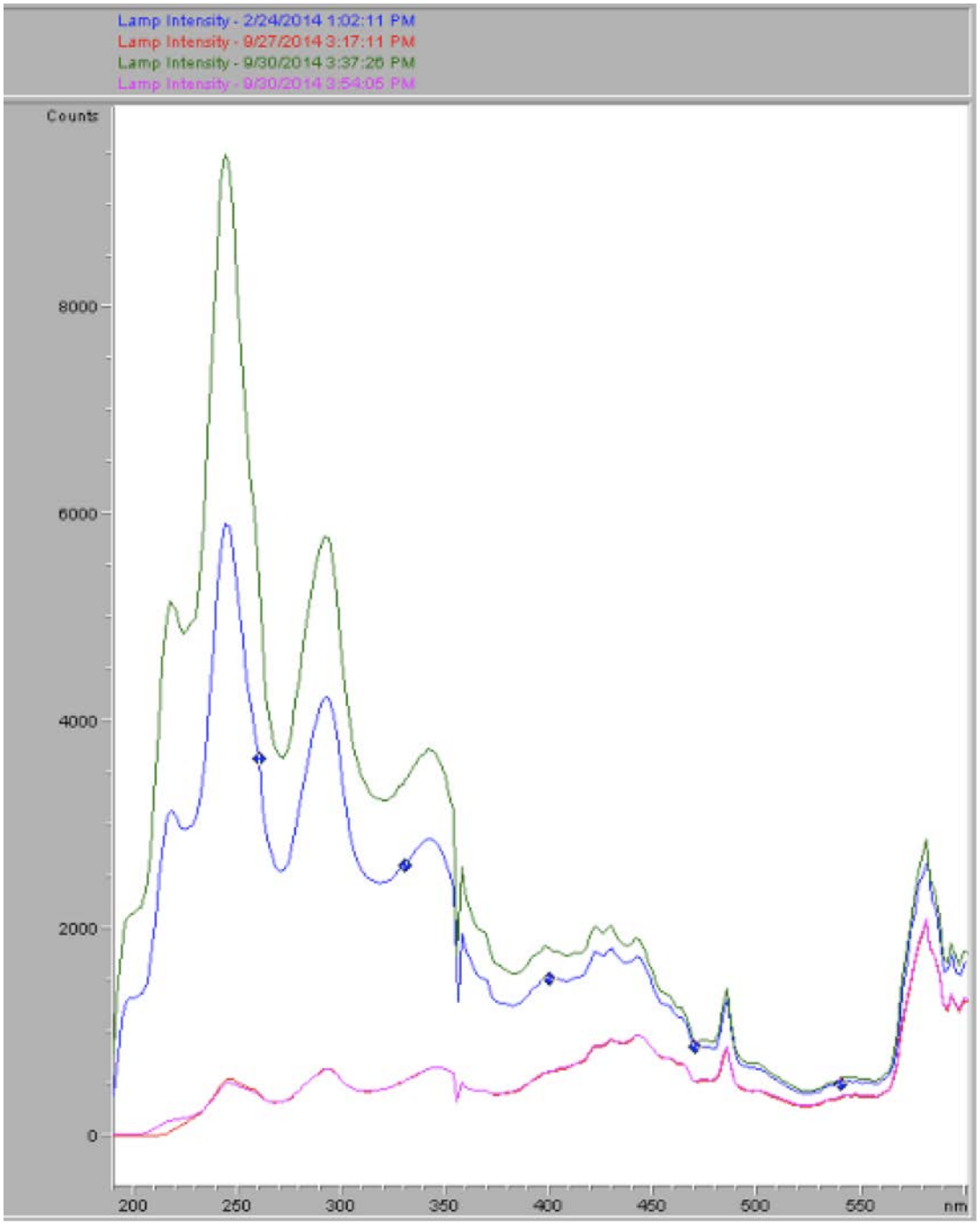

Figure 3.22: Deuterium lamp intensity test spectra. The x-axis is the wavelength in nm, and the y-axis is the lamp intensity in counts. The blue spectrum was taken in February 2014 with the flow cell in; the red and pink spectra were taken in September 2014 with the flow cell in (note how they overlap one another very closely); and the green spectrum was taken in September 2014 with the flow cell out.

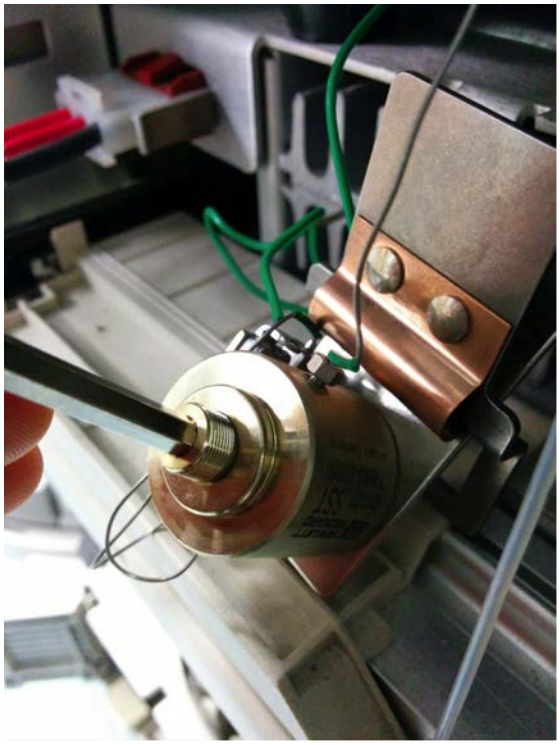

(a) A photograph of the front quartz window cartridge in the flow cell assembly being removed.

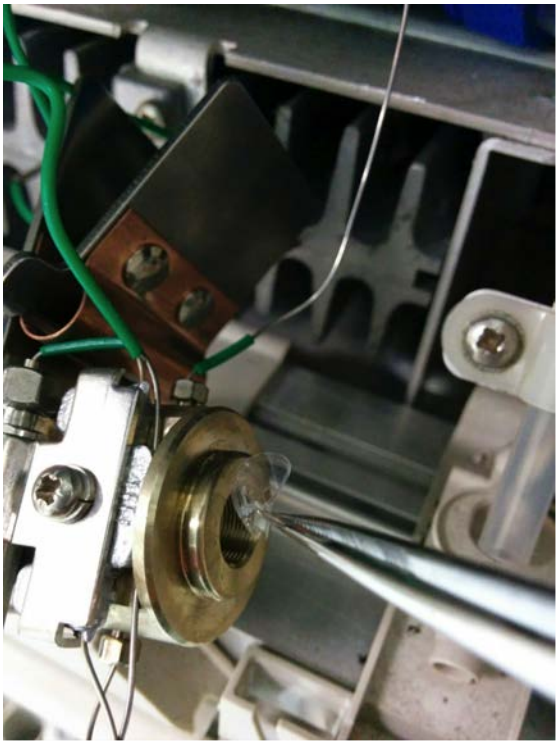

(b) A photograph of the front gasket in the flow cell assembly being removed.

(c) A photograph of flow cell window cartridges; the leftmost cartridge is new and cleanwhile the middle and rightmost cartridges were the ones being replaced in the HPLC. It is apparent that the cartridges taken from the HPLC are visibly dirty when compared to the new cartridge.

Figure 3.23: Photographs of the flow cell assembly components inside the HPLC.

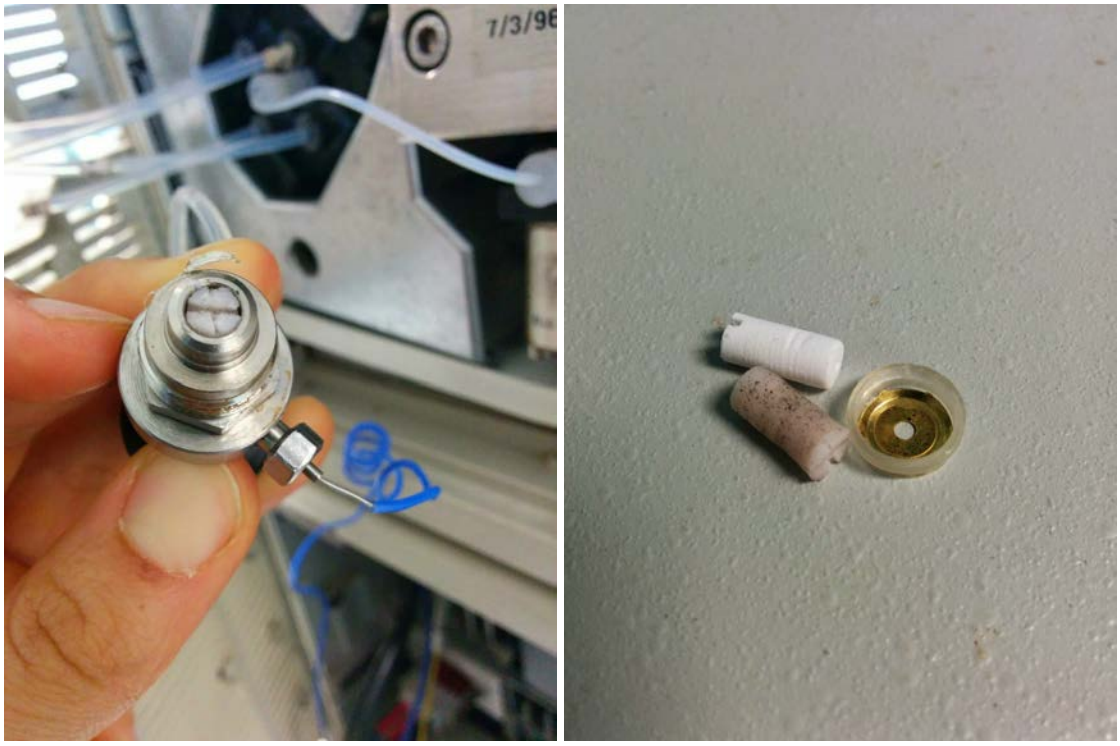

(a) A photograph of the removal of an HPLC pump frit.

(b) A photograph of the new and old HPLC pump frit; the old one is visibly a lot dirtier than the new one.

Figure 3.24: Photographs of the changing of an HPLC pump frit.

Issue 4 And the final issue outlined here is that of the computer that operates the HPLC software: this involved the computer display not working/turning off while it was on. A restart was attempted, however, it made a prolonged beeping sound and would not load. A simple solution would be to obtain a new computer, however, that was not possible because the ChemStation software used to control this particular HPLC runs on only obsolete versions of the Windows operating system. Additionally, because the HPLC is over 20 years old, it only connects to computers using general purpose interface bus cables, so it would not have been possible to connect it to a more modern computer using a local area network connection, for example. According to an email from the Agilent Sales and Service Centre, 'this is the risk of running obsolete instrumentation.'

Cables that connected the screen to the hard drive were changed and ruled out as an issue, as was the battery in the hard drive. Other issues that may have been the problem involved the failure of more serious components, such as the random access memory (RAM), the motherboard, or the hard drive itself. A new RAM was purchased through a second-hand selling website, which solved the issue.

Conclusion In retrospect, these issues could have been avoided or resolved more quickly if a current HPLC model had been used. However, the HP 1050 model had

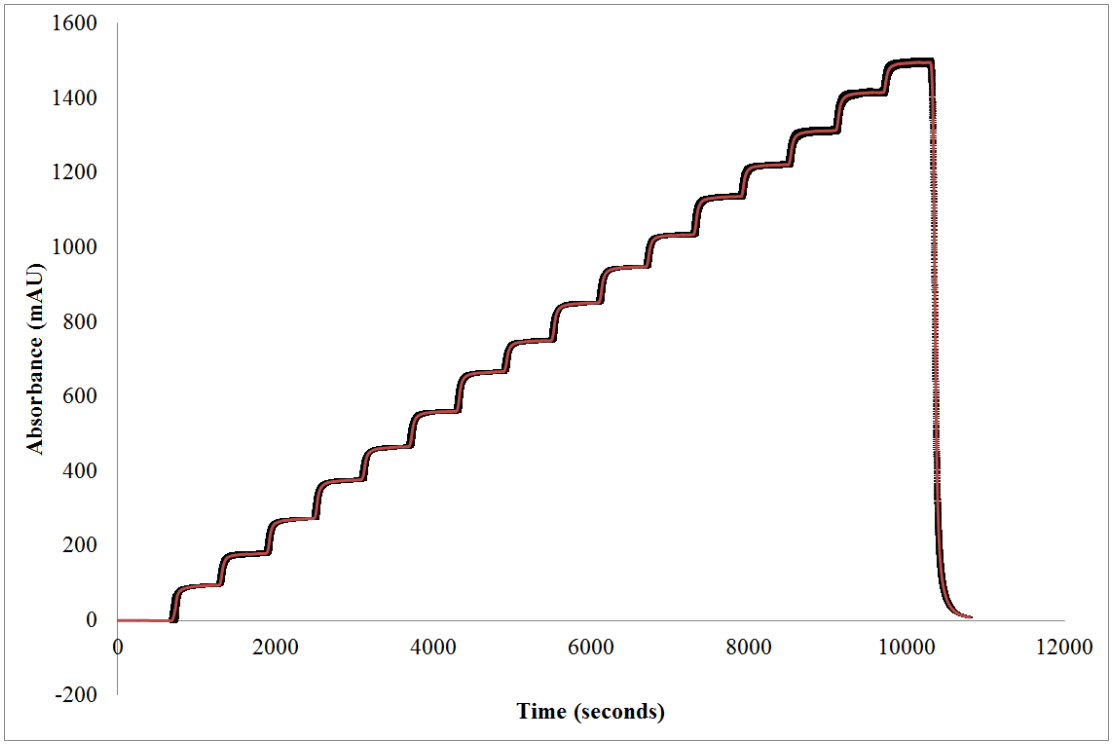

Figure 3.25: Saccharin in HEPES 10 mm FLC calibration runs after the flow cell windows were changed. The absorbance was measured at 269 nm, and the y-axis error bars are the standard deviations of the 3 runs.

proven successful in previous ZLC experiments conducted within the EFMG, and it was known that the required analysis was very simple in chromatographic terms. Hence the decision to continue using the HP 1050 model.

3.2.2 Python

Python is an interpreted, interactive, object-oriented programming language, and is used in various instances throughout this work (chapters 4, 6, and 8). Python provides a powerful open source tool for numerical computations and scripting. Various open source software is available to edit the code; PyCharm, developed by JetBrains, was utilised for the work outlined in Chapter 8. The work in chapters 4 and 6 used IPython as a kernel for writing Python code in the Jupyter Notebook, which is an open source web-based application that enables the editing of Python code in a computer's internet browser.

Chapter 4

Function of FCCs in adsorption

THIS chapter outlines exploratory work in adsorption, including all of the struggles faced. The idea behind the adsorption work was to find a model system that could be utilised in future release work.

The early stages of loading the FCC with flavour (Chapter 5) involved using adsorption processes to do so. If anethole were to adsorb and experimental parameters were established in which the adsorption could be characterised, for example, the system could be used to load the FCC with anethole and continue with subsequent release experiments. Adsorption work can also be used to characterise the surface of the proposed mineral excipients through the use of adsorption isotherms.

Some of the work and results reported here have also been published in a peer-reviewed academic journal (Levy *et al.*, 2017).

4.1 Introduction

The adsorption processes of drugs onto their delivery surfaces are very important to consider, since adsorption is the basic mechanism most commonly used for the loading of drugs onto surfaces such as nanodiamonds (Mochalin *et al.*, 2013), and unwanted adsorption onto a surface may compromise the intended therapeutic benefit, driving up dosage levels, thus increasing treatment costs (Tzannis *et al.*, 1997). A study by Mochalin *et al.* (2013) has also shown that the adsorption of poorly soluble drugs onto the surface of their nanodiamond particles may be suitable in overcoming the poor bioavailability of the drugs. They also state that the monolayer capacity for a particular drug on their surface must be determined in order to gain full advantage of the mechanism while avoiding excessive loading in order to minimise potential leakage of dangerous drugs. Pinholt *et al.* (2011) found that it is important to study the adsorption of peptide and protein drug products, as proteins are known to interact with interfaces of the particulate delivery system in which the effects are often irreversible adsorption and structural changes of the proteins. Kojima and Watanabe (2012) have studied HAP as a biomaterial and the adsorption and desorption of two bioactive proteins (cytochrom c and insulin) onto its surface; they concluded that HAP is a potential protein carrier with controlled release. A study by Neuvonen *et al.* (1984) has shown that the bioavailability of both aspirin and quinidine sulphate was significantly reduced when ingested with activated charcoal, and that a significant desorption of aspirin, but not that of quinidine, was subsequently detected. Tsuchiya and Levy's 1972 paper suggests that it may be possible to make reasonable predictions concerning the relative antidotal effectiveness of activated charcoal in humans on the basis of appropriate *in vitro* adsorption studies. Sellers *et al.* (1977) conducted comparative *in vitro* studies to determine the adsorption characteristics of 12 drugs onto activated charcoal in or-

der to remediate any poorly absorbed drugs. They concluded that activated charcoal would not be helpful. Therefore, when a new drug delivery vehicle is being proposed, investigation into the adsorptive properties of the surface is of paramount importance.

FCCs have a wide range of applications, particularly for the controlled release of actives such as drugs, plant protection chemicals, and food additives such as flavours. It has been proposed that the particles be utilised in various dosage forms, such as in chewing gum, a mouth or nasal spray, an inhaling device, a tablet, a lozenge, a transdermal patch, and a powder (Pedersen and Andersen, 2012). FCCs can be tailored to suit a particular need; for example, plastically compressible FCC grades are available in the case where flavour release may require a compressive destruction of the inert carrier in the mouth combined with controlled release in order to excite the recipient's senses with flavour (Gane *et al.*, 2006).

Gane *et al.* (2000) have shown that dyes with a cationic charge show a strong adsorption onto anionically pre-dispersed natural ground calcium carbonate surfaces. This indicates that coulombic forces contribute the strongest part of the adhesion force and is in agreement with the adsorbing mechanisms of ink jet dyes. Acidic dye molecules have a significantly weaker adhesion mechanism in which it is assumed that the COOH groups probably interact with the free surface of the calcium carbonate. Dyes with an anionic colorant revealed no adsorption onto slightly anionically dispersed MCC surfaces, suggesting the possible existence of shielded cationic sites (Lamminmäki *et al.*, 2011). In practice, ink jet dyes are usually anionic, and ink jet paper coatings must therefore be cationised, at high cost. Therefore, it was expected that FCC would adsorb positively charged adsorbates.

It has also been suggested in previous work (Norris *et al.*, 1993), however, that cationic sites on a mineral may be shielded by the sphere of hydration of the surface water molecules; this concept may be applied to the FCC in that a negatively charged adsorbate would have to pass the anionically charged outer surfaces if the intraparticle pore space of the FCC is cationically charged. Alternatively, the cationically charged sites may be distributed together with neighbouring anionic sites, which would act to repel the adsorbate thus making an approach to sorption sites limited. This idea is supported by the work of Gribble (2010) and Gantenbein *et al.* (2012), who have previously shown that MCC has an affinity for anionic polyelectrolytes and reduced the anionic charge of their system substantially. Lamminmäki *et al.* (2012) have shown that the cationic dispersing of MCC produces a slightly higher porosity than subsequent anionic redispersing, which may suggest that the increased porosity increases the access to the cationically charged sites of the MCC. Various findings suggest that MCC has a mix of both positively and negatively charged surface sites, each of which can be accessed depending on the properties of the MCC itself and the system in which it is studied.

Kallio *et al.* (2006) studied the adsorption of Food Black 2 (a diazo dye) onto coating pigments from polar liquids, such as water and ethanol, and from non-polar cyclohexane. They similarly concluded that electrostatic interactions (hydrophobic interactions in the case of talc) are the predominating driving force for adsorption onto a variety of minerals, such as kaolin, calcium carbonate, and talc.

With respect to drugs, Mahato and Narang (2012) have found that adsorption generally

increases as the ionisation of the drug is suppressed, so that the extent of adsorption reaches a maximum when the drug is completely un-ionised. For amphoteric compounds, adsorption is at a maximum at the isoelectric point. pH and solubility effects act in concert since the un-ionized form of most drugs in aqueous solution has a low solubility. The physicochemical nature of the adsorbent affects the rate and extent of adsorption through changes in the molecular forces of attraction between the adsorbate and the adsorbent. Other work on the effect of changing the solvent showed that adsorption of actives onto calcium carbonate was irreversible from chloroform, but not from ethanol (Misra, 1991).

Benzyltrimethylammonium bromide (BTMAB) and sodium 2-napthalene sulphonate (Na2NS) are charged, water soluble species. BTMAB has been successfully adsorbed onto talc by Charnay *et al.* (2001) along with a similar water soluble anionic probe (benzene sulphonate) in order to infer information about the surface of the talc, and hence we use similar charged species to adsorb onto talc as a starting point for this work before attempting to infer surface information about the FCCs. Charnay *et al.* (2001) have reported adsorption of BTMAB onto talc, with 33 % chlorite of surface area of 6 $m^2\ g^{-1}$, with a maximum adsorption capacity Γ_{max} of 2.14 mg g^{-1}.

This chapter has tested the following hypothesis to varying degrees:

- **1:** FCC, because of its predominantly negatively charged surface, will adsorb small but significant amounts of cationic species.
- **2:** Sparingly soluble (dissolved) species will adsorb to a greater extent onto the FCC than strongly soluble (dissolved) species.
- **3:** The nature of the adsorbing surface of FCCs can be elucidated by studying different adsorption characteristics from a range of different adsorbates and solvents.

4.1.1 Adsorption isotherms

Adsorption density (Γ) was calculated according to the standard definition provided by Pan and Liss (1998*a*):

$$\Gamma = \frac{(c_0 - c_{eq})\, V_{total}}{W_{solid}} \tag{4.1}$$

where c_0 is the initial concentration of adsorbate in solution, c_{eq} is the supernatant concentration after adsorption has taken place, V_{total} is the volume of solution of concentration c_0 used in an adsorption experiment, and W_{solid} is the weight of the adsorbent used during the adsorption experiment.

Freundlich (1906; 1909) showed that adsorption can be described by equation 4.2, which is called the 'Freundlich isotherm,' and described many of the adsorption processes at that time (Rudzinski *et al.*, 2001). This isotherm type is considered to be a multi-layer process in which the amount of adsorbed solute per unit adsorbent mass

increases gradually (Chung *et al.*, 2015).

$$\Gamma = K_F c_{eq}^{\frac{1}{n}} \tag{4.2}$$

where K_F is the Freundlich constant, and $\frac{1}{n}$ is the Freundlich exponent. The linear form of an adsorption isotherm equation can be used to evaluate whether the adsorption process satisfies the isotherm.

In 1916, Langmuir (1916; 1917) published the first theoretical isotherm, displayed in equation 4.3, which assumed adsorption on a flat surface with energetically equivalent adsorption sites onto which only one molecule may adsorb, and was able to explain the plateaus commonly found in experimental adsorption isotherms (Rudzinski *et al.*, 2001). The maximum adsorption capacity per unit adsorbent mass is determined along with the Langmuir constant showing the solute affinity to the adsorbent (Chung *et al.*, 2015).

$$\Gamma = \frac{K_L c_{eq} \Gamma_{max}}{1 + K_L c_{eq}} \tag{4.3}$$

where K_L is the Langmuir constant, and Γ_{max} is the adsorption at maximum equilibrium concentration in solution c_{eq}.

The Freundlich model, although semi-empirical, is nevertheless not applicable to many heterogeneous materials, is only valid within certain concentration limits, and is unable to model saturation behaviour (Umpleby *et al.*, 2001). Consequently, some results followed neither Langmuir nor Freundlich characteristics. They showed a somewhat better fit to a hybrid Langmuir-Freundlich (LF) adsorption isotherm, also known as the Sips equation (Sips, 1948), which has previously been applied to systems such as the adsorption behaviour onto molecularly imprinted polymers (Umpleby *et al.*, 2001), and is displayed in equation 4.4.

$$\Gamma = \frac{(K c_{eq})^m \Gamma_{max}}{1 + (K c_{eq})^m} \tag{4.4}$$

here K is an adsorption equilibrium constant, and m is the heterogeneity index that varies from 0 to 1. For a homogeneous material m = 1, and the LF isotherm reduces to the Langmuir isotherm; when m <1 the material is heterogeneous.

The Tóth isotherm has the correct functionality at both limits as $c_{eq} \to 0$ and $c_{eq} \to \infty$, and has previously proved useful for fitting isotherms of porous adsorbents (Rudzinski and Everett, 1992). It has the form:

$$\Gamma = \Gamma_{max} \left(\frac{(K_L c_{eq})^m}{1 + (K_L c_{eq})^m} \right)^{1/m} \tag{4.5}$$

In the present work, the Tóth isotherm is used to describe the adsorption of aspirin and vanillin from ethanol onto FCC, and in the presence of up to 20 % by volume of added water it becomes (Levy *et al.*, 2017):

$$\Gamma = f''(\Gamma_{\max}) \left(\frac{[K_{\mathrm{L}} f'(c_{\mathrm{eq}})]^m}{1 + [K_{\mathrm{L}} f'(c_{\mathrm{eq}})]^m} \right)^{1/m} \tag{4.6}$$

where the functions f' and f'' describe the effect of water on c_{eq} and $\Gamma_{\max}$, respectively.

4.1.2 The particle concentration effect (PCE)

The particle concentration effect (PCE) was also very briefly investigated to ensure that the amount of adsorbent utilised in the experimental matrix had no effect on the equilibrium concentration of the adsorbate in solution post-experiment.

The PCE describes the decline in the extent of adsorption of an adsorbate per unit mass of adsorbent (i.e. the adsorption density) as the particle concentration (c_{p}) increases (i.e. amount of particulate adsorbent in solution) (Utomo and Hunter, 2010). Two theories that describe the PCE are the metastable equilibrium adsorption (MEA) (Pan and Liss, 1998*a*) and flocculation theory (Helmy *et al.*, 2000).

In MEA theory, it is proposed that adsorption isotherms can be affected by adsorption reversibility and other kinetic factors (Pan and Liss, 1998*a*), whereas flocculation theory hypothesises that the adsorption changes with adsorbate concentration, because particles stick together through flocculation as a result of van der Waals attraction forces and interparticle bridging with increasing c_{p}, thus decreasing the available surface area for adsorption (Helmy *et al.*, 2000).

4.2 Materials & methods

Other minerals, adsorbates, solvents, and compounds used throughout this project have been described in Chapter 3; those that have only been utilised in adsorption work outlined in this chapter are described here.

In some cases adsorption isotherms were fitted using .ipynb IPython Notebook files, in which code was edited using Jupyter Notebook in Google Chrome (Version 50.0.2661.102, 64-bit). The Anaconda distribution was used to install Python (version 3.5) and Jupyter.

4.2.1 Minerals

The GCC and various grades of FCC samples were provided by Omya International AG (Oftringen, Switzerland); their properties are listed in Table 3.1 (Chapter 3).

FCC 01, which is not reported in Table 3.1, has been utilised sparingly in some of the work outlined in this chapter. It has a particle size d_{50} value of 5.1 μm, a d_{90} value of 0.9 μm, and a surface area of 69 $m^2\ g^{-1}$.

Analytical reagent grade calcium carbonate (99.98 %, CAS no. 471-34-1) was purchased from Fisher Chemical.

Some adsorption experiments utilised a high surface area (HSA) talc with low chlorite content, specially produced by Omya International AG. Talc is a trioctahedral 2:1 phyl-

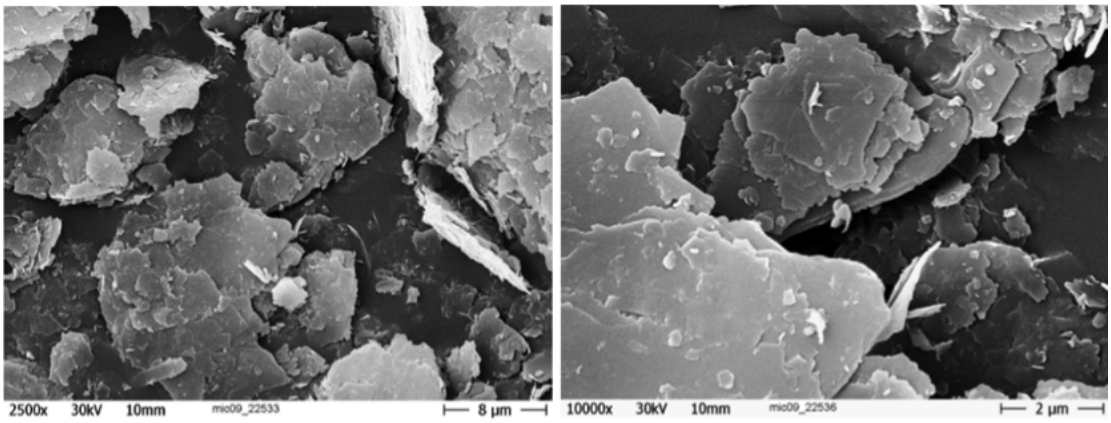

Figure 4.1: SEM images of HSA talc; the scale bars are 8 and 2 μm on the left and right images, respectively. These images were taken from the work of Gantenbein (2012).

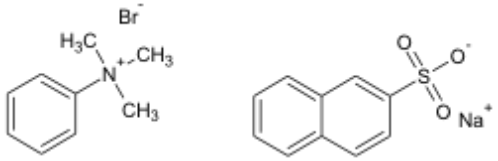

Figure 4.2: The structures of benzyltrimethylammonium bromide (BTMAB; left) and sodium 2-naphthalene sulphonate (Na2NS; right).

losilicate (Lv *et al.*, 2014) with unique surface properties. It is in the form of platelets due to the layered structure of the mineral, with hydrophobic basal surfaces containing siloxane bonds. Grinding causes the breaking of sheets to expose OH (silanol) groups, which cause their edge surfaces to be hydrophilic (Lobato, 2004; Charnay *et al.*, 2001). In this work, to ensure good adsorption, the talc had been processed to have a high surface area of 45.3 $m^2\ g^{-1}$. It also has a particle size d_{50} value of 5.02 μm (Gribble, 2010) and a high aspect ratio and plate-like morphology. Figure 4.1 displays some SEMs of this material. The overall porosity of HSA talc varies according to how closely the platey particles are packed.

4.2.2 Adsorbates, solvents, & other compounds

Chloroform (CAS no. 67-66-3), for HPLC, stabilised with amylene (CAS no. 513-35-9) and HPLC grade hexane (~95 %, CAS no. 110-54-3) were both purchased from Acros Organics.

Benzyltrimethylammonium bromide (BTMAB; 99 %, CAS no. 5350-41-4) was purchased from Sigma-Aldrich, and sodium 2-naphthalene sulphonate (Na2NS; for ion pair chromatography, >99 %, HPLC, CAS no. 532-02-5) was purchased from Fluka Analytical, whose structures can be seen in Figure 4.2. Sodium chloride (NaCl) was purchased from Fisher Scientific (CAS no. 7647-14-5).

Poly(vinyl sulphate) potassium salt (KPVS; average molecular weight ~170 000, CAS no. 26182-60-5) was purchased from Sigma-Aldrich. KPVS is a linear polyelectrolyte

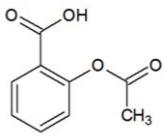

Figure 4.3: The structure of aspirin.

of high molar mass and high charge density (Mocchiutti and Zanuttini, 2007), and is often used as the anionic polyelectrolyte in colloidal titrations. Terayama (1952) first proposed one of the most frequently employed methods know as a polyelectrolyte titration (PET), in which the concentration of a cationic polyelectrolyte is titrated against an anionic polyelectrolyte in the presence of a cationic indicator in order to determine the cationic demand of a pulp suspension (Mocchiutti and Zanuttini, 2007).

Acetylsalicylic acid (99+ %; CAS no. 50-78-2), or aspirin, was purchased from Sigma-Aldrich, the structure of which can be seen in Figure 4.3. Salicylates, in the form of willow bark, were used as an analgesic (painkiller) during the time of Hippocrates, and their antipyretic (fever-quelling) effects have been recognised for more than 200 years (Awtry and Loscalzo, 2000). Pure acetylsalicylic acid was first synthesised in 1897 and marketed in 1899 under the registered trademark of aspirin (Sneader, 2000). After almost 90 years of clinical use, aspirin remains one of the world's most extensively used over-the-counter drugs, and it is still recognised as the standard analgesic, antipyretic, anti-inflammatory, and agent against which newer drugs are assessed (Clissold, 1986).

4.2.3 General adsorption experimental procedure

Firstly, before any adsorption experiments were commenced the λ_{max} for each adsorbate/analyte was determined using a Hewlett Packard (now Agilent) 8452 UV-visible spectroscopy system. A calibration graph was made of each of compound in its respective solvent. The adsorbate was prepared by making a stock solution from which subsequent stock solutions were made by serial dilution using graduated and bulb glass pipettes.

The procedure for a general adsorption experiment, unless stated otherwise, was to weigh (using a Mettler Toledo XP504 Analytical Balance) an accurately known amount of FCC into a 50 cm^3 polypropylene centrifuge tube (Fisherbrand), after which 25 cm^3 of the desired concentration of adsorbate in its respective solvent was pipetted, using a glass bulb pipette, into the tube and shaken briefly by hand. The tube was then placed on a reciprocal shaker at 205 strokes per minute (spm) for 1 hour. The tube was then centrifuged at 3 000 revolutions per minute (rpm; 1507 g) for 30 minutes using a Centaur 2 (Sanyo, MSE) centrifuge. The supernatant was decanted into a clean borosilicate glass beaker, which was then covered with plastic paraffin film to avoid contamination and loss of solvent, transported to the UV-visible spectroscopy instrument and then analysed for adsorbate concentration. In most cases, the results of three experimental replicates were obtained for a variety of different adsorbate concentrations.

Control experiments were also conducted for most isotherms, in which an adsorption experiment was conducted without the adsorbent sample (i.e. the FCC). The control

experiments and experiments with the sample were often conducted at different times to each other. The interpretation of the raw experimental data required subtracting the absorbance of the supernatant from the control experiment, as measured by the UV-visible spectrometer, from the absorbance of the supernatant from the experiment with the FCC sample, in order to account for any adsorption onto the sides of the container.

Not all adsorption experiments conducted have been reported.

4.2.4 Initial flavour adsorption

This section describes some of the initial adsorption experiments of anethole from ethanol and saccharin from HEPES solution onto FCC.

4.2.4.1 Anethole in ethanol

The λ_{max} for anethole in ethanol was determined as 259 nm. A calibration graph of anethole in ethanol was made with the concentrations 0, 2, 4, 6, 8, and 10 mg dm^{-3}, with an R^2 value of 0.11.

Adsorption experiments utilised c_0 solutions of 1 200, 900, 600, and 300 mg dm^{-3}, and an accurately known amount of approximately 0.01 g FCC SFC 06.2. The supernatants were diluted by a factor of 240 before being analysed by UV-visible spectroscopy.

A quick adsorption experiment was also conducted in which no dilutions of the supernatants were required, and this involved utilising c_0 solutions of 5, 7.5, and 10 mg dm^{-3}.

And finally, FCC SFC 06.2 from three experimental replicates of adsorption experiments of anethole in ethanol, utilising an accurately known amount of approximately 0.01 g FCC, were dried in an oven overnight at approximately 40°C. 2-3 mg of the resulting dried FCC from each adsorption experiment were analysed in a EA1110 CHN elemental analyser (CE Instruments).

4.2.4.2 Saccharin in HEPES

Saccharin was analysed for the intensity of its absorption at 269 nm, with a calibration linearity of R^2 of 0.99 in 10 mmol HEPES up to a concentration of 400 mg dm^{-3}. The concentrations used in the construction of the calibration graph were 0, 10, 20, 30, 40, 50, 100, 200, 300, and 400 mg dm^{-3}. The pH of the HEPES was tested using a Meterlab PHM201 Portable pH Meter (Radiometer Copenhagen).

0.2 g of FCC TP was used in each adsorption experiment. Once the supernatant was analysed via UV-visible spectroscopy, it was filtered using a 0.2 μm syringe filter (Whatman Puradisc 25 PP Disposable Filter Device with a BD Plastipak 100ml Luer lock syringe) before being analysed again in order to determine if ultrafine particulates were affecting the UV-visible spectroscopy reading.

Further adsorption experiments were conducted on different minerals with differing values of W_{solid}.

4.2.5 Adsorption of charged molecules

BTMAB was analysed for the intensity of its absorption at 262 nm, and Na2NS at 274 nm. The λ_{max} of each adsorbate was determined using a Perkin Elmer Lambda 2 UV-visible spectrometer. A calibration graph was made of BTMAB between the con-

centrations of 0.001-1 g dm^{-3} and of Na2NS between the concentrations of 0.001-0.1 g dm^{-3} both in 0.1 M NaCl. Both graphs exhibited linearity, with R^2 values of 0.9978 and 0.9937, respectively.

Electrolyte solutions were used to decrease the thickness of the electrical double layer and increase the probability of interactions between any surface charge on the mineral and the adsorbate. The adsorption experiments were carried out in 0.1 M NaCl, unless otherwise stated.

The two grades of FCC utilised regularly throughout these experiments were FCC 12 and FCC 13. Occasionally, FCC TP was also used. As a validation of the experimental procedures, HSA talc was also used as a substrate, since it is known to be a strong adsorbent.

The methodology for the experiments utilising BTMAB and Na2NS outlined in this section differ slightly from the general procedure outlined in section 4.2.3. In this instance, the procedure was to weigh an accurate amount of approximately 2 g of adsorbent into a 50 cm^3 graduated polypropylene conical test tube (Kartell S.p.A.) using a Mettler Toledo Classic AB304-5 balance. A borosilicate glass bulb pipette was then used to add 25 cm^3 of the adsorbate solution; each solution contained a concentration of adsorbate ranging from 0-10 g dm^{-3}, which were each made up in 100 cm^3 volumetric flasks from a 20 g dm^{-3} stock solution that had been made up in a 1 L volumetric flask. Once the adsorbate solution was added to the plastic tube containing 2 g of adsorbent, the tube was sealed and placed in a large ceramic cylinder (Alpine Augsburg 1/25 LK; Figure 4.4) and rolled for 1 hour. The tubes were then centrifuged for 6 minutes at 4 500 revolutions per minute (4 166 g) using a Rotina 420 (Hettich Zentrifugen).

The supernatants were then decanted into a 20 cm^3 plastic syringe (Henke Sass Wolf, non-pyrogenic/non-toxic, latex free, sterile), and pushed through a 0.20 μm regenerated-cellulose syringe filter (Sartorius RC25) into a clean 50 cm^3 polyethylene bottle with a screw cap (Assistant, made in Germany). The pH of each supernatant was recorded (Mettler Toledo SevenMulti pH meter); the pH meter was calibrated on each day of use with buffer solutions of pH 4.0, 7.0, and 10.0 (Hannah Instruments).

Once the samples were filtered, they were ready for analysis. However, they had to be diluted in order for the intensity of the λ_{max} to be within the calibration range. In order to dilute the samples, an aliquot of the supernatant was pipetted into a quartz cuvette along with an aliquot of the solvent. The pipettes utilised were an Eppendorf Research 500-5 000 cm^3, an Eppendorf Research 100-1000 cm^3, a Rainin MR-250 Pos-D 50-250 cm^3, and a Rainin MR-50 Pos-D 20-50 cm^3. In between analyses, the solvent was shaken out of the cuvette, rinsed with the solvent, and shaken out again until no visible drops remained. The diluted supernatants were then analysed with a Perkin Elmer Lambda 2 UV-visible spectrometer.

A control sample for each concentration of adsorbate was also made. For example, a 10 g dm^{-3} solution of BTMAB with 2 g of FCC in a plastic centrifuge tube also had another tube of that concentration of adsorbate, but no adsorbent (i.e. FCC) running in parallel to the centrifuge tube with the FCC; it went through the exact same procedure at the same time. This was so that the absorbance of the control, as analysed by the UV-visible spectrometer, was subtracted from the absorbance of the actual sample in

Figure 4.4: A ceramic cylinder, inside of which contains the sample centrifuge tubes, was placed on two rollers powered by a motor (Alpine Augsburg 1/25 LK) in order to continuously agitate the samples.

order to account for adsorption onto the walls of the tube.

Adsorption experiments were also carried out on FCC in ultrapure water, 0.005 M phosphoric acid, 2 M sodium chloride solution.

Dried FCC (i.e. all water removed) and FCC in its slurry form (i.e. after production but before drying at high temperatures to produce a fine powder) were also put through an adsorption experiment in 0.1 M sodium chloride solution. This was to establish that the removal of water during drying does not somehow change the crystal structure at the surface of the mineral.

The procedure in the case of slurry FCC was as previously described, except the amount of mineral weighed out was pipetted (using a Pasteur pipette) into the plastic centrifuge tube on a tared balance. The amount pipetted was calculated from the mineral content of the slurry in order to ensure that 2 g of mineral were in each test tube. The mineral content of each slurry was determined using a Mettler Toledo HB43-S Halogen. The control samples involved pipetting tap water into the centrifuge tubes, and was always equivalent to the amount of tap water in the FCC slurry.

4.2.5.1 Polyelectrolyte adsorption

This section outlines the adsorption of KPVS onto FCC TP in ultra-pure water.

A calibration graph of KPVS was made at 256 nm in ultrapure water between 0-0.1 g dm^{-3} (0, 0.01, 0.02, 0.04, 0.06, 0.08, and 0.1 g dm^{-3}). The graph proved to be linear with an R^2 of 0.99. A large stock solution of 1 g dm^{-3} of KPVS in ultrapure water was made up in a volumetric flask. From this solution the other stock solutions were made.

The procedure outlined in section 4.2.3 was adhered, although the following differences include the use of a difference balance (an Oxford A2204 analytical balance), which was utilised to accurately weigh an approximate amount of FCC into centrifuge tubes. And, a glass bulb pipette was used to add 25 or 50 cm^3 of the adsorbate solution; each solution contained a concentration of adsorbate ranging from 0-100 mg dm^{-3}.

Viscometry experiments were also performed using an Ostwald viscometer (type BS/U, Rheotek; Figure 4.5) to analyse the supernatants from the KPVS adsorption experiments that utilised 2 g of FCC TP. The viscometer was rinsed with ultra-pure water and the appropriate supernatant before being filled through the opening at point (g) with the supernatant to be analysed until the meniscus was in line with point (f) in Figure 4.5. The viscometer and its liquid contents were left to equilibrate for 5 minutes in a water bath (SUB Aqua 5 Plus, Grant Instruments) set to a temperature of 21°C. The temperature of the water bath was continuously monitored using a mercury thermometer.

A pipette filler was then used over opening (g) to push the meniscus of the supernatant past line (c) in Figure 4.5; the meniscus was kept in this position by keeping a finger over the capillary entry at (d). The pipette filler was then removed and the supernatant released; a stopwatch was used to record the length of time it took for the meniscus of the supernatant to fall from line (c) to line (b) under the pressure caused by its own weight (Matthews, 1985). This procedure was completed three times for each supernatant.

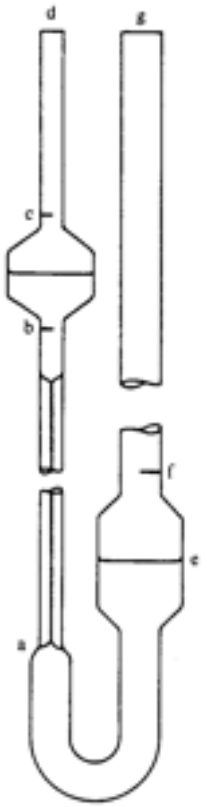

Figure 4.5: A schematic of an Ostwald viscometer (Matthews, 1985). Permission to reproduce this image has been granted by the publisher.

4.2.6 Experimental artefact investigation

Eight centrifuge tubes with 25 cm^3 ethanol and 1 % FCC 01 were studied using the adsorption isotherm protocol, as outlined in section 4.2.3. The supernatant, however, was filtered through a 1.6 μm filter and analysed via UV-visible spectroscopy. The remaining solid was dried in an oven at 40°C. An additional 25 cm^3 of ethanol was added to the dried FCC and the process was repeated. This was repeated 4 times in total. The final analysis of the supernatants used a 0.2 μm syringe filter for filtration.

A stock solution of vanillin in ethanol with a concentration of 25 mg dm^{-3} was made with an absorbance of 1.77 AU at 279 nm. This solution was used in adsorption experiments with 0.01 g of FCC 06 and 1.5 g FCC 06.

Two more stock solutions of vanillin in ethanol were made with the concentrations of 0.17 and 37.5 mg dm^{-3} with absorptions of 0.12 and 2.48 AU, respectively, at 279 nm. These solutions were used in adsorption experiments with 1.5 g of FCC 06.

UV-visible spectroscopy absorption spectra were also obtained of FCC TP in ethanol, which involved analysing the supernatant of an adsorption experiment using 0.2 g of FCC TP, but with no adsorbate at all.

An adsorption experiment was performed with varying W_{solid} on FCC TP and FCC 02 but with no adsorbate. The solvents used were ethanol and ultrapure water for the two types of adsorption experiments. The supernatant was analysed using a HACH DR/890 Colorimeter (Camlab). The ethanol and water supernatants were then filtered using a 0.1 μm (Puradisc 25 TF, Whatman) and a 0.2 μm (Puradisc 25 PP, Whatman) syringe filter, respectively.

Finally, FCC TP, FCC 02, and HAP were used in adsorption experiments with a BTMAB concentration of 1 g dm^{-3} and another set of experiments with 0.1 g dm^{-3}. The supernatants were analysed at 262 nm, filtered using a 0.2 μm syringe filter, and analysed again. Some supernatants were diluted and analysed again.

4.2.7 Vanillin adsorption

The λ_{max} for vanillin in ethanol was found to be 279 nm, and 275 nm for vanillin in chloroform. The upper limit of quantification concentration was 40 mg dm^{-3} for both solvents using the UV-visible spectrometer. A vanillin in ethanol calibration curve was constructed at 279 nm up to 100 mg dm^{-3}. 0, 5, 10, 20, 30, 40, 50, 100 mg dm^{-3} (the 50 and 100 mg dm^{-3} solutions were diluted to bring them below the upper limit of the instrument's quantification) with an R^2 value of 0.99. The vanillin in chloroform calibration also had an R^2 of 0.99 and was made from the following concentration solutions: 0, 10, 40, 100, and 300 mg dm^{-3} (the 100 and 300 mg dm^{-3} solutions were diluted).

The vanillin stock solutions were prepared via serial dilution of a 1 g dm^{-3} stock solution using borosilicate glass bulb pipettes. The c_0 solutions used of vanillin in ethanol were of the following concentrations: 0, 5, 10, 20, 30, 40, 50, 70, 100, 120, 200, and 300 mg dm^{-3}. And for vanillin in chloroform, the following concentrations were used to conduct adsorption experiments: 0, 10, 40, 100, and 300 mg dm^{-3}.

The adsorption experimental procedure outlined in section 4.2.3 was followed. The amount of FCC TP added into the centrifuge tube was 0.2 g, and supernatants with

initial concentrations (c_0) above 40 mg dm^{-3} were diluted by a factor of 10 in 100 cm^3 volumetric flasks. The supernatants were not filtered.

As an additional control experiment, adsorption onto FCC TP from ethanol was measured with constant c_0 (30 mg dm^{-3}) but varying W_{solid} (0, 0.03, 0.07, 0.10, 0.13, 0.17, and 0.20 g). This investigates the extent of PCE, if any, within the vanillin in ethanol system by varying only the c_p. The results of three experimental replicates were obtained.

Some adsorption experiments were performed that involved a portion of the overall 25 cm^3 volume of vanillin in ethanol being replaced by water. For example, 20 cm^3 of the desired concentration of vanillin in ethanol was pipetted using a borosilicate glass bulb pipette, and the remaining 5 cm^3 volume of water was pipetted using a Thermo Scientific Finnpipette (100-1 000 mm^3).

The volumetric proportions of water in ethanol ranged from 1 % to 20 %, and Table 4.1 shows the volumes of water and vanillin in ethanol solution used in each experiment. For the 1 % water experiment, the following c_0 concentrations of vanillin in ethanol were used: 0, 10, 40, 100, and 300 mg dm^{-3}. The other % water experiments utilised a smaller range of c_0 solutions.

Table 4.1: The proportions of vanillin in ethanol solution and water used in each adsorption experiment.

Water (%)	Vanillin in ethanol (%)	Volume of water (cm^3)	Volume of vanillin in ethanol (cm^3)
1	99	0.25	24.75
3	97	0.75	24.25
5	95	1.25	23.75
6	94	1.50	23.50
7	93	1.75	23.25
10	90	2.50	22.50
20	80	5.00	20.00

For each concentration of adsorbate used in these adsorption experiments, another control experiment was carried out without any adsorbent sample but with the same concentration of adsorbate and proportion of water.

4.2.8 Aspirin adsorption

The aspirin adsorption experiments were performed mostly by an undergraduate final year applied chemistry student in the same manner as the vanillin adsorption experiments outlined in section 4.2.7, and were conducted under my supervision.

The λ_{max} was established to be 225 nm. Each set of experiments were self-calibrated; this means that the absorbance of the c_0 solutions were used to make a calibration graph, of which the linear trendline equation was used to interpret the results from that set of experiments. However, a calibration graph with aspirin in ethanol concentrations ranging from 0-40 mg dm^{-3} (0, 1, 5, 10, 20, and 40 mg dm^{-3}) had an R^2 of 0.99. The c_0 concentrations were as follows: 0, 5, 10, 20, 40, 50, 100, 150, and 250 mg dm^{-3}. Other

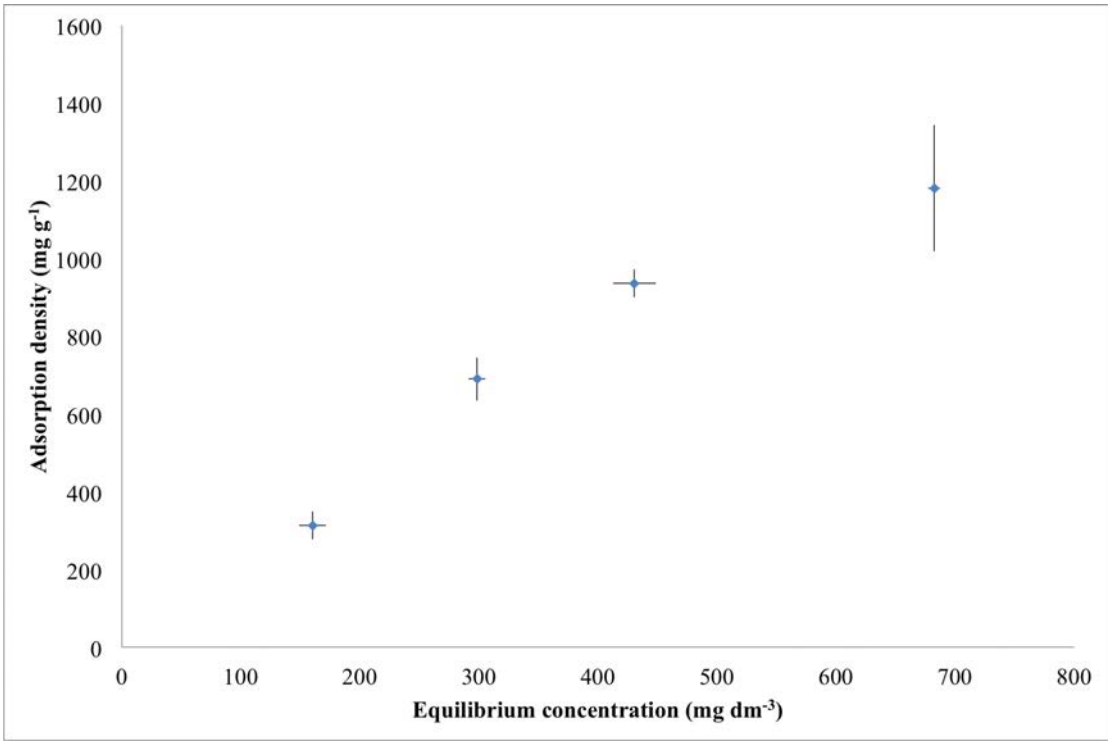

Figure 4.6: Adsorption isotherm obtained from initial anethole in ethanol adsorption experiments onto FCC SFC 06.2. Each data point represents three experimental replicates; the error bars are standard deviations of the three.

aspirin in ethanol adsorption experiments were also conducted with various different percentages of water, as with vanillin in section 4.2.7, but with fewer c_0 solutions.

4.3 Results & discussion

4.3.1 Initial flavour adsorption

This section discusses the results obtained from anethole in ethanol and saccharin in HEPES buffer solution adsorption experiments.

4.3.1.1 Anethole in ethanol

The adsorption isotherm obtained from initial anethole in ethanol adsorption experiments are shown in Figure 4.6.

However, when the absorbance of the stock solutions themselves were analysed, it became apparent that they were approximately half of the concentration that was originally thought. When this was corrected for, the isotherm in Figure 4.6 became that of Figure 4.7. This was because it was assumed that the initial concentration c_0 were the concentrations intended.

Figure 4.7 suggests that no adsorption is taking place. It was hypothesised that the reason for the concentration of the stock solutions being much lower than the intended concentration was that the plastic centrifuge tubes ma have been degrading in the ethanol solvent and masking the anethole peaks in some way, or that the anethole was

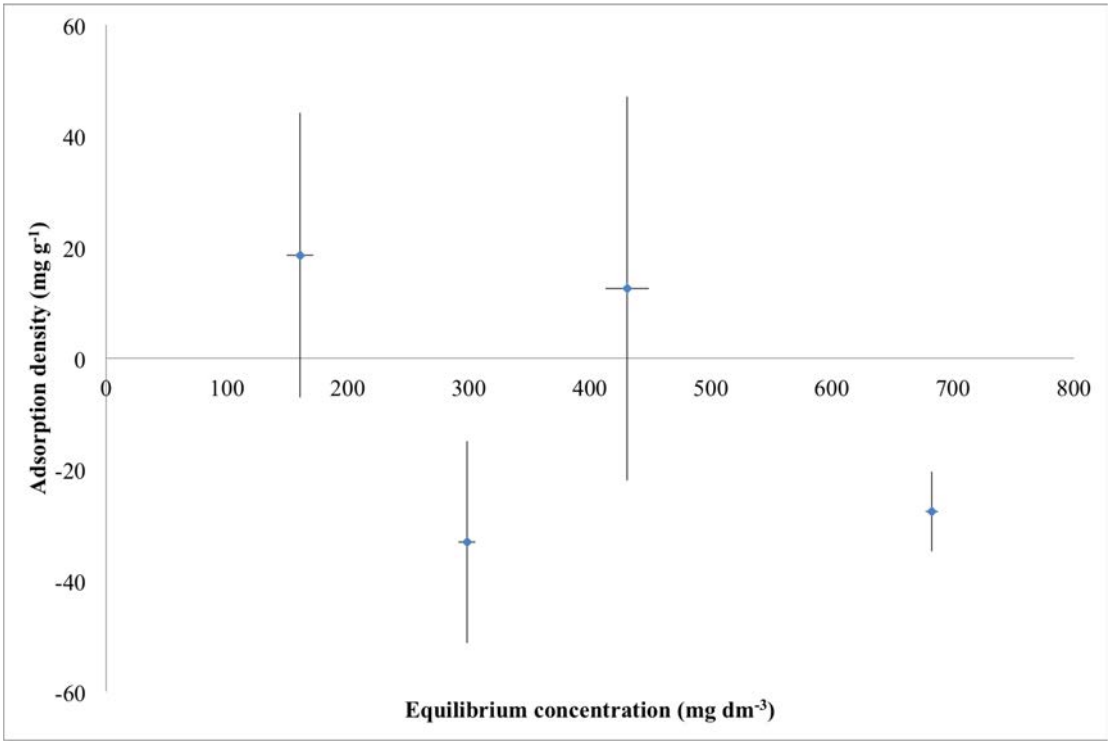

Figure 4.7: Adsorption isotherm from Figure 4.6 corrected for stock solution concentration.

sticking to the sides of the container. However, this was proven not to be the case by comparing the absorbancies of the same concentration of anethole in ethanol after an adsorption experiment that had been conducted in all glassware to one conducted in the plastic centrifuge tubes (Figure 4.8). The procedure was exactly the same other than the container (which was a borosilicate glass beaker) and the way of diluting the supernatants (both comparisons utilised glass pipettes and serial dilutions as opposed to using ThermoFisher Finnpipettes and one large dilution).

Figure 4.8 shows that after an adsorption experiment there is a slight increase in concentration as analysed by UV-visible spectroscopy, however, it was concluded that the dilution procedure of the supernatants caused the loss in anethole when analysing via UV-visible spectroscopy, thus giving the 'false' isotherm in Figure 4.6.

Adsorption experiments were then conducted that did not involve any dilution of the supernatants, with c_0 concentration of 5, 7.5, and 10 mg dm^{-3}. The calculated adsorption densities of three experimental replicates for c_0 concentration of 5, 7.5, and 10 mg dm^{-3} were -0.55 $\pm$ 0.66, -0.93 $\pm$ 1.24, and 0.22 $\pm$ 0.36 respectively. This suggests no adsorption.

In order to determine that UV-visible spectroscopy is an adequate method for constructing adsorption isotherms, another method was utilised: elemental analysis. Figure 4.9 shows the results of elemental analysis on the remaining solid after an adsorption experiment, and represents the mass of anethole adsorbed onto the surface of the FCC, which was calculated from the C content of the FCC post-adsorption. Samples of pure

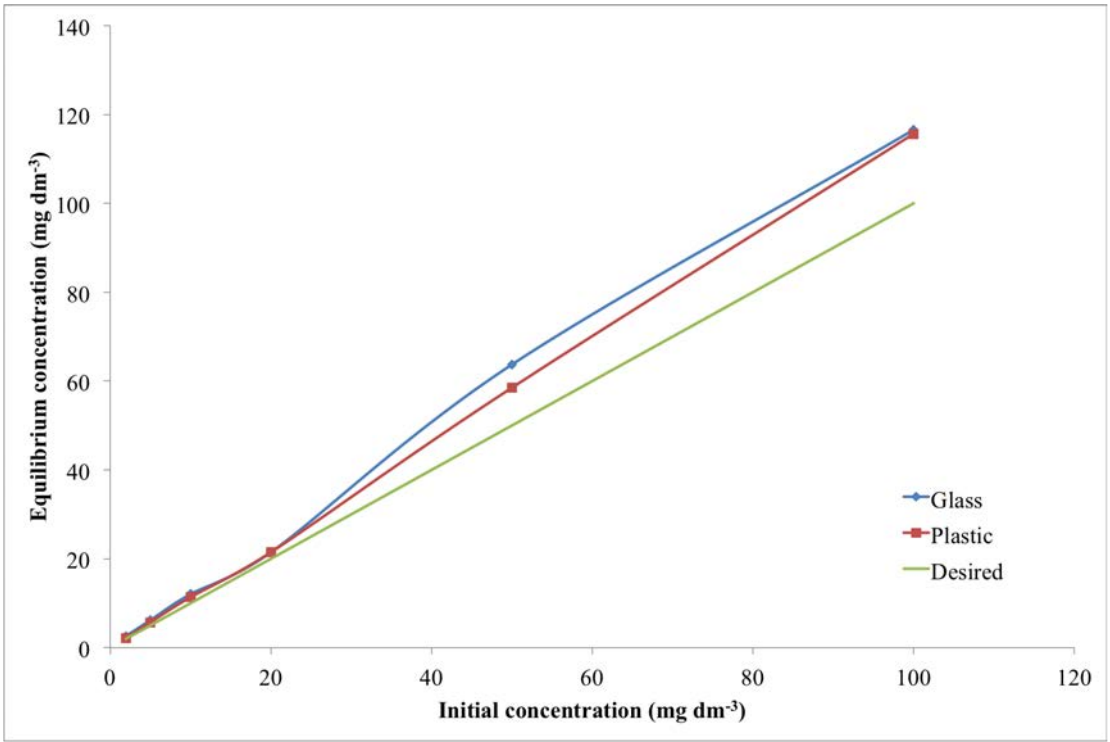

Figure 4.8: The comparison between glass and plastic laboratory equipment when conducting an anethole in ethanol adsorption experiment.

anethole were analysed prior to the FCC samples and were too large in mass, thus saturating the detector. As a result, the subsequent FCC samples gave anethole readings that appeared to be higher in concentration than in actuality. It is unknown how long the detector took to return to normal after saturation; however only the error bars of the first set of results encompass a higher adsorption density than the rest of the results. The error bars are the standard deviations of three analytical replicates per data point. There are three data points per average c_{eq} (along the x-axis) that represent three experimental replicates.

It was expected that as the concentration of anethole in ethanol increased, so would the amount of anethole adsorbed to the FCC. The results, however, show that this is not the case and actually suggests that anethole is not adsorbing.

It is interesting to note that analytical reagent grade calcium carbonate was analysed alongside the rest of the samples, and was expected to have a 12 % C content, which it did. The FCC used in the experimentation discussed throughout this report was also analysed and was shown to have 7-8 % C content. It was thought that this was due to the phosphate content of the FCC.

Although the CHN analysis should be conducted again for conclusive evidence with the use of more blanks and standards, these results combined with the adsorption data suggest that anethole is not adsorbing. It was hypothesised that the high solubility of the anethole in ethanol (i.e. miscible in all proportions) dictated that the anethole would not adsorb to the FCC.

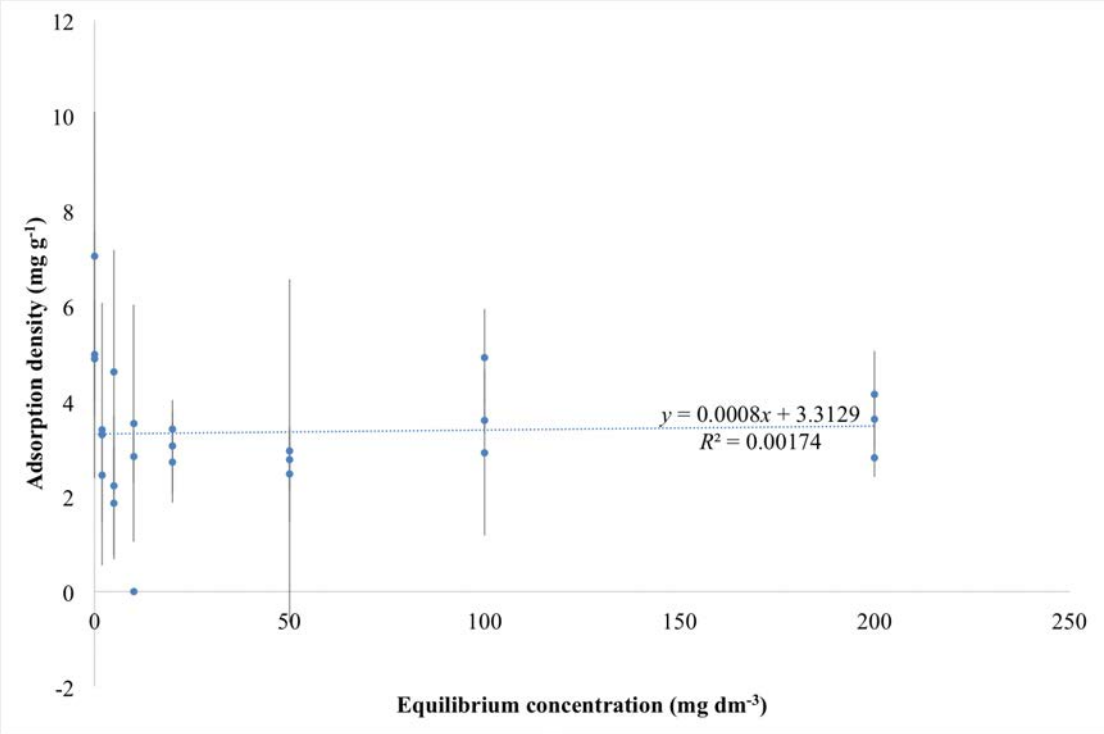

Figure 4.9: CHN elemental analyser results for an adsorption experiment of anethole on FCC SFC 06 in ethanol.

4.3.1.2 Saccharin in HEPES

Figure 4.10 displays the adsorption isotherms of saccharin in HEPES on FCC TP, and the results of the same supernatants once filtered.

It can be inferred from the results that there is no adsorption occurring, because many points show a negative adsorption density, which is not possible. Generally, however, as the concentration of the starting stock solution increases, the degree of negative adsorption density decreases. This supports an idea that 'fines' (i.e. ultrafine particles) from the mineral are interfering with the absorption reading of the UV-visible spectrometer.

Table 4.2 displays other experiments that tested adsorption onto other minerals, and whether filtering led to a positive adsorption density.

It has been reported that the tendency for a molecule to adsorb is a function of its affinity for the solvent as compared to its affinity for the adsorbent, and adsorption onto the adsorbent generally increases as the solubility of the adsorbate in the solvent decreases (Snoeyink and Summers, 1999). As saccharin is very water soluble, it may be possible that the saccharin is not adsorbing to the FCC.

Investigating the effect of the HEPES buffer is also required, because the HEPES may inhibit the adsorption of saccharin, although HEPES is extremely hygroscopic and as mentioned above may well not adsorb to the FCC.

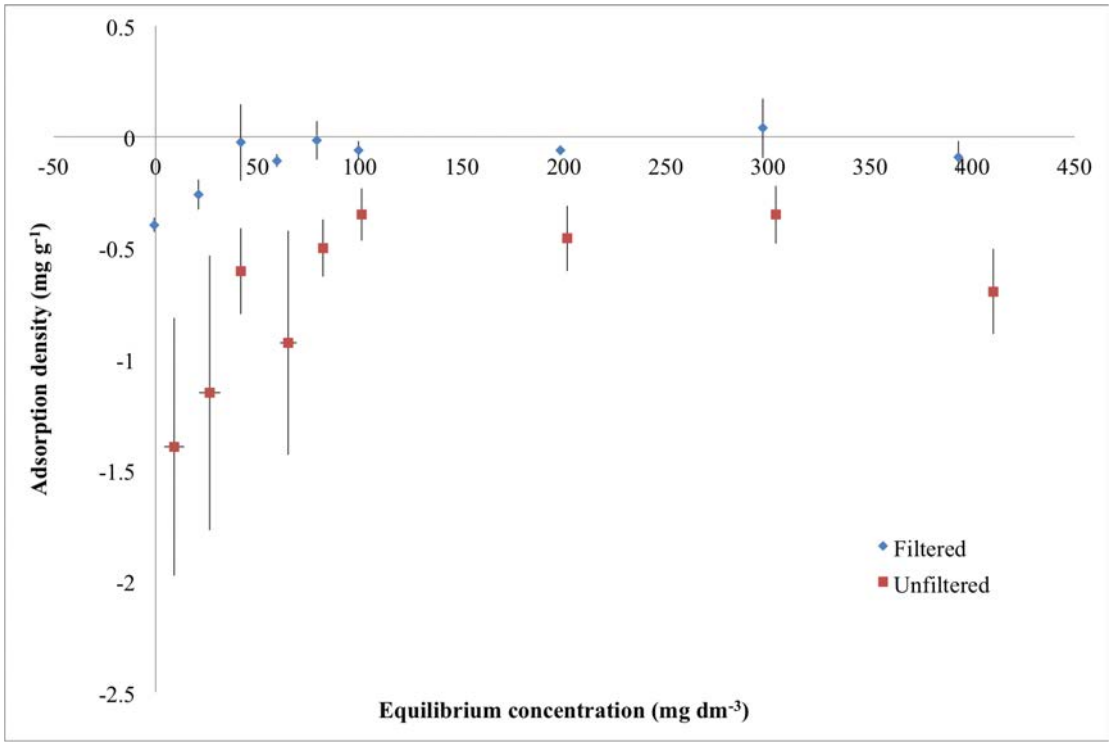

Figure 4.10: Adsorption isotherm of saccharin in HEPES on FCC TP, one in which the supernatants had been filtered, and one in which they remained unfiltered. The error bars are the standard deviations of three experimental replicates.

Table 4.2: Adsorption experiments of saccharin from HEPES that tested adsorption onto various minerals; the filtered samples were filtered through a 0.2 μm syringe filter, and the absorbance of saccharin was measured at 269 nm.

Sample	Adsorption density (mg g^{-1})			
	W_{solid} = 0.1 g		W_{solid} = 0.02 g	
	Unfiltered	Filtered	Unfiltered	Filtered
FCC TP	-0.82 $\pm$ 0.56	-	-11.48 $\pm$ 2.47	3.05 $\pm$ 1.03
GCC	-3.44 $\pm$ 0.68	-1.62 $\pm$ 1.27	-9.91 $\pm$ 0.75	-4.65 $\pm$ 1.78
HAP	-3.86 $\pm$ 0.19	-3.26 $\pm$ 0.43	-10.96 $\pm$ 7.95	-0.99 $\pm$ 0.70
HSA talc	-11.41 $\pm$ 4.08	-4.23 $\pm$ 0.15	-	-

4.3.1.3 Overview of initial flavour adsorption

The results suggest that anethole and saccharin do not adsorb to FCC, which is contrary to what was initially expected. As the isotherms presented thus far have demonstrated that no adsorption occurs within these systems, ZLC/FLC experiments conducted will be diffusion-based only, rendering no need to worry about any sorption processes.

However, it is still suggested at this point that fine particulate material originating from the mineral during adsorption experiments may hinder the detection of a low concentration of adsorbate, thus giving the impression that adsorption has not taken place. There will always be some fine material in real systems. Therefore, within the limits of detection, adsorption is not observable.

In order to characterise the extent to which ultrafine particles may be present in the supernatant, the use of various other experimental methods may be conducted. These are briefly discussed below:

High-speed centrifugation The Stokes equation (equation 4.7) calculates the velocity of sedimentation and describes the movement of a sphere in a gravitational field. The particle size and density is what determines the rate of separation of particles in a suspension by way of gravitational force.

$$v = \frac{d^2(\rho_{\text{particle}} - \rho_{\text{medium}})g}{18\eta} \tag{4.7}$$

where v is the sedimentation rate/velocity of the sphere, d is the diameter of the sphere, ρ_{particle} is the density of the particle, ρ_{medium} is the density of the medium/solvent, η is the viscosity of the medium/solvent, and g is the gravitational force.

The Stokes equation can be used to calculate the sedimentation rate of FCC particles less than 0.2 μm in diameter to try and remove ultrafine particles from the supernatant. The g force produced by the centrifuge used can be calculated from equation 4.8:

$$g = (1.118 \times 10^{-5}) r Sp^{-2} \tag{4.8}$$

where r is the radius of the centrifuge rotor in cm and Sp is the speed of the centrifuge in rpm.

As the distance that the FCC particles are needed to move through the solvent is known, equation 4.7 can be rearranged to calculate the g force required to do so. The appropriate centrifuge can then be found to meet the required g value.

Phosphate tests A HACH colorimeter can be utilised, using their PhosVer 3 (Ascorbic Acid) Method, to test the supernatant for orthophosphate (PO_4^{3-}). However, the instrument is designed for use with water samples. In order to determine whether the HACH method will work with ethanol, a series of standards of orthophosphate in

ethanol will have to be made and tested. Potassium orthophosphate (K_2HPO_4) is very soluble in alcohol, and this can be used to make the standards (CRC Press, 1983).

Calorimetry Calorimetric techniques are designed to measure the amount of heat that may be generated (exothermic) or consumed (endothermic) by a chemical reaction, and can be used as an alternative way to establish adsorption.

For example, one particular paper studied the adsorption of *n*-hexane on pillared clays using thermal gravimetry with differential scanning calorimetry (TG-DSC) (Pires *et al.*, 2000). A similar experiment may be conducted by passing a stream of vapour of *trans*-anethole, for example, in an inert gas over an FCC sample. This would enable the measurement of adsorption from a gravimetric point of view. The measured heats of adsorption can then be compared to those of a vapour of ethanol passing over the FCC, which can be measured using a solution calorimeter in the absence of TG-DSC.

The enthalpy of a reaction in solution is measured by allowing a known amount of substance to react inside a solution calorimeter and measuring the consequential rise in temperature. Two reactant solutions inside the calorimeter are initially are kept separate by having one solution contained in a mixing device that is immersed in the other solution (Matthews, 1985). Solution calorimetry can be used to measure the enthalpy change of the addition of FCC to anethole in anethole in ethanol.

The two substances are then mixed by operating the mixing device from outside the calorimeter. The temperature rise is measured and then used to calculate the enthalpy of reaction (or in this case, adsorption) using equation 4.9, where ΔH is the enthalpy of adsorption of one mole of anethole, $\Delta T_{\text{adsorption}}$ is the measured temperature rise upon operating the mixing device, C_ρ is the heat capacity of the calorimeter and its contents, and n_{mol} is the number of moles of anethole present (Matthews, 1985).

$$-\Delta H = \frac{\Delta T_{\text{adsorption}} C_\rho}{n_{\text{mol}}} \tag{4.9}$$

The standard free energy of a change of a mole of anethole adsorbed may be calculated using equation 4.10:

$$\Delta G = \Delta H - T\Delta S \tag{4.10}$$

where ΔG is the standard free energy change, ΔS is the entropy change, and T is the temperature. However, as the entropy change (ΔS) is unknown, the Van't Hoff equation (equation 4.11) can be used to calculate the standard free energy (ΔG) (He *et al.*, 2010; Matthews, 1985),

$$\Delta G = -RT\ln K_{\text{L}} \tag{4.11}$$

where R is the universal gas constant. This requires an adsorption isotherm, as the

various parameters can be entered into the linear form of the Langmuir equation and solved for K_L (Ho, 2006).

After ΔG has been calculated from equation 4.10, the value can be inserted into equation 4.11, which can be solved for ΔS. From a thermodynamic viewpoint, the free energy change (ΔG) can be used as indicative of the affinity of the sorbent (i.e. the FCC) for anethole, and further provide a criterion as to whether water sorption is a spontaneous ($-\Delta G$) or non-spontaneous ($+\Delta G$) process, depending on the sign on the value (McMinn *et al.*, 2005).

ΔS can be calculated for the anethole in ethanol system in the same manner by keeping the two solutions separate, and upon mixing, measuring the temperature change. The entropy can be calculated from equation 4.12:

$$\Delta S = \frac{q}{T} \tag{4.12}$$

where q is the heat energy absorbed or released and T is the absolute temperature at which the reaction and mixing took place. Therefore when a spontaneous process occurs, there is an increase in entropy. For a spontaneous reaction occurring at constant temperature and pressure, ΔG must be negative. Referring to equation 4.10, a negative enthalpy change is the most important factor governing the spontaneity of a reaction at low temperatures. At high values of T, $-T\Delta S$ becomes large and an increase in entropy of the system is essential for a spontaneous process.

4.3.2 Adsorption of charged molecules

The aim of this work was to attempt to better characterise the surface of the FCC, in which BTMAB and Na2NS are charged, water soluble species used as cationic and anionic probes, respectively. HSA talc was also used as an adsorbent in a bid to mimic the work of Charnay *et al.* (2001). Table 4.3 gives an overview of the experiments conducted, and Figure 4.11 displays the adsorption isotherms of BTMAB and Na2NS onto FCC TP, FCC 12, and FCC 13 in various aqueous solutions, as detailed in Table 4.3.

There was a lack of adsorption of BTMAB and Na2NS onto FCC 13 in the presence of 0.1 M NaCl. Furthermore, there was no adsorption of either probe in the presence of 2 M NaCl, or in 0.005 M H_3PO_4 electrolyte solutions, or in ultrapure water. The lack of adsorption at increased concentration of electrolytes showed that adsorption did not occur even when the electric double layer at the surface of the FCC was suppressed. The null results in ultrapure water showed that the electrolyte was not itself interfering with adsorption. The use of the H_3PO_4 solution provided a check of whether the FCC surface could be re-activated, again showing a null result.

The pH of the BTMAB and Na2NS stock solutions was in the range of 5.7-6.2. The pH of the supernatants involving FCC as the adsorbent was in the range of 7.9-8.3, and the pH of the supernatants involving talc as the adsorbent was in the range of 8.6-8.9. These measurements showed that, as expected, the supernatant pH rose after an adsorption experiment because of the release of cations from the minerals in aqueous solution to form counter ions.

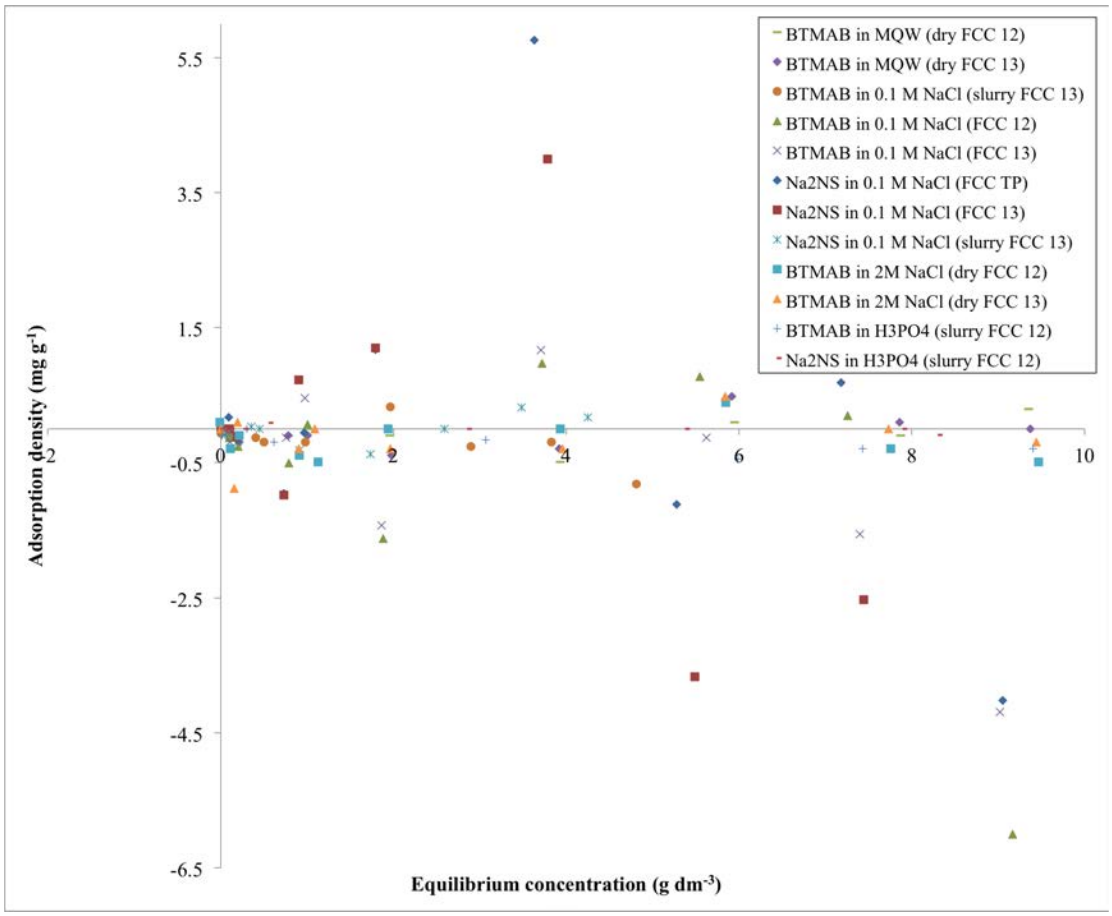

Figure 4.11: The adsorption isotherms of BTMAB and Na2NS onto FCC TP, FCC 12, and FCC 13 in various aqueous solutions.

Table 4.3: The adsorption experiment parameters; the isotherms of which can be seen in Figure 4.11.

Adsorbate	Solvent	Adsorbent
BTMAB	0.1 M Na Cl	FCC 12
		FCC 13
		Slurry FCC 13
	2 M Na Cl	Dry FCC 12
		Dry FCC 13
	Ultrapure water	Dry FCC 12
		Dry FCC 13
	H_3PO_4	Slurry FCC 12
Na2NS	0.1 M NaCl	FCC TP
		FCC 13
		Slurry FCC 13
	H_3PO_4	Slurry FCC 12

The isotherms in the case of the FCC also display some negative adsorption densities (Table 4.4), whereas the talc isotherms did not. This can be explained in terms of the extent of adsorption. As talc adsorbed, the equilibrium adsorbate concentration was always lower than the initial adsorbate concentration, and so when calculating the adsorption density (from equation 4.1), the value would always be positive. However, as the FCC adsorbed less, if at all, the absorbance of the supernatant (as analysed by UV-visible spectroscopy) would have to be exactly the same as the control sample, which is realistically impossible to achieve. And therefore, negative adsorption densities sometimes occur.

Figures 4.12 and 4.13 show the adsorption isotherms of BTMAB and Na2NS onto HSA talc, respectively, each with only one experimental replicate per point. Table 4.5 shows various parameters obtained from applying different isotherms to the curves. Further parameters are displayed in Table 4.12 and discussed in a later section.

The maximum observed adsorption of 9.2 mg g^{-1}, slowly asymptoting to a Γ_{max} of 25.8 mg g^{-1} (Tóth isotherm; Table 4.12), is in accord with the maximum adsorbance of 2.14 mg g^{-1} onto talc with 33 % chlorite as observed by Charnay *et al.* (2001) and described earlier.

Regarding the null results of the FCCs: it was necessary to confirm that such results were not due to an error in experimental procedure. Error bars were calculated, based on an estimated accuracy of 1 % in determining the BTMAB concentration. Figure 4.14 displays the experimental equilibrium concentrations obtained, for both the control and the sample, plotted against the theoretical concentration of the stock solution. It can be seen that for the null results, the error bars overlap, thus maintaining the idea that there

Table 4.4: The adsorption experiment parameters and maximum and minimum calculated values of adsorption density; the isotherms of which can be seen in Figure 4.11.

Adsorbate	Solvent	Adsorbent	Adsorption density (mg g^{-1})		
			Upper limit	Lower limit	Std devn
BTMAB	0.1 M Na Cl	FCC 12	0.97	-6.00	2.01
		FCC 13	1.17	-4.19	1.48
		Slurry FCC 13	0.32	-0.81	0.28
	2 M Na Cl	Dry FCC 12	0.39	-0.49	0.28
		Dry FCC 13	0.48	-0.87	0.35
	Ultrapure water	Dry FCC 12	0.29	-0.49	0.20
		Dry FCC 13	0.48	-0.39	0.24
	H_3PO_4	Slurry FCC 12	0.00	-0.45	0.15
Na2NS	0.1 M NaCl	FCC TP	5.77	-4.02	3.26
		FCC 13	6.07	-3.66	2.86
		Slurry FCC 13	0.32	-0.38	0.20
	H_3PO_4	Slurry FCC 12	0.09	-0.09	0.04

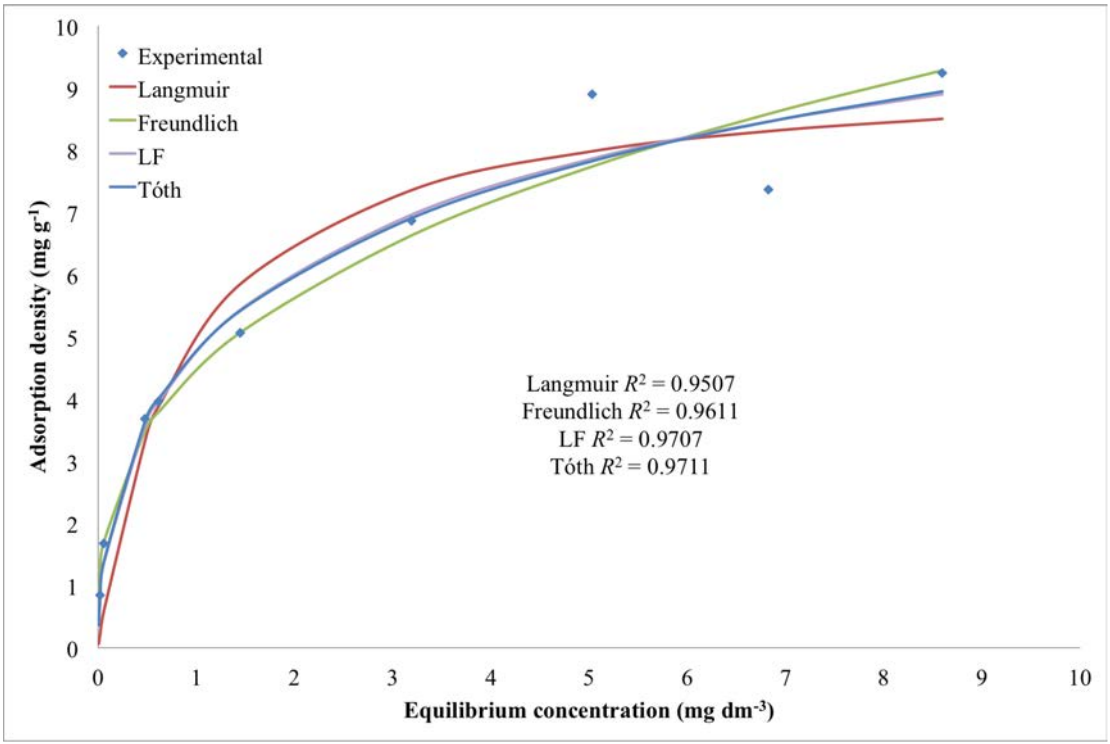

Figure 4.12: Adsorption isotherm of BTMAB onto HSA talc in 0.1 M NaCl.

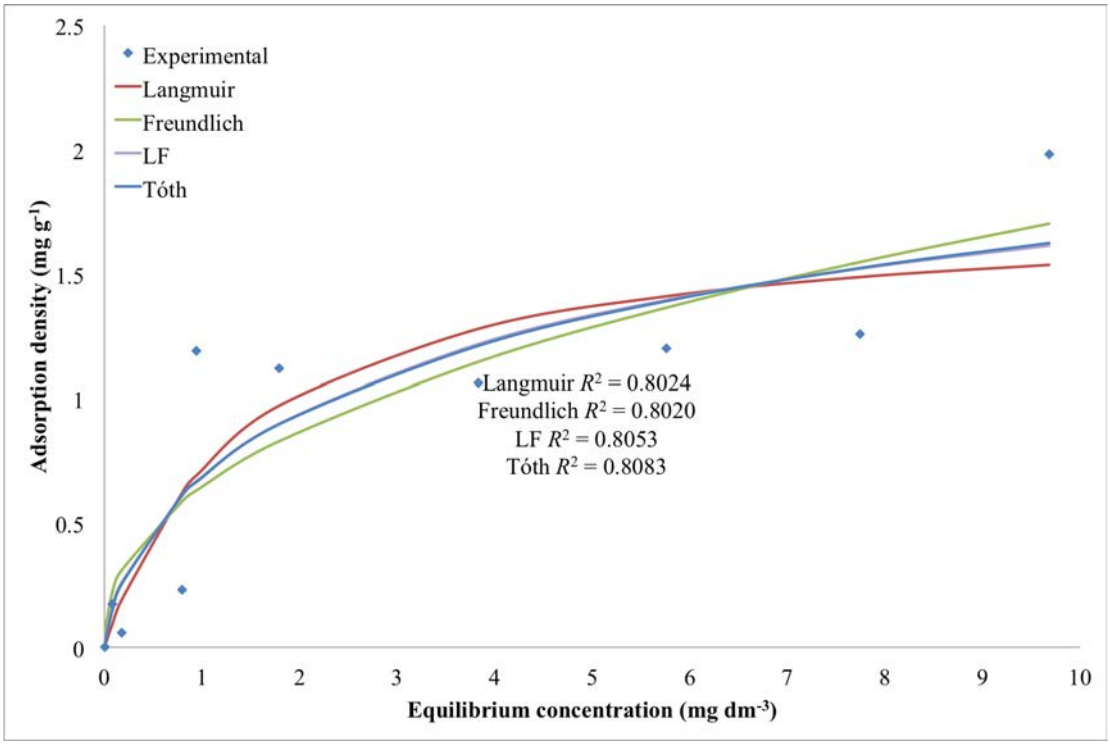

Figure 4.13: Adsorption isotherm of Na2NS onto HSA talc in 0.1 M NaCl.

Table 4.5: Parameters fitted using Python for the isotherms describing the adsorption of BTMAB and Na2NS onto HSA talc from 0.1 M NaCl.

Parameter	BTMAB	Na2NS
Langmuir isotherm		
Γ_{max} (mg g^{-1})	9.36	1.77
K_L (dm^3 mg^{-1})	1.15	0.68
R^2	0.95	0.80
Freundlich isotherm		
K_F (dm^3 $^{\frac{1}{n}}$ mg$^{1-\frac{1}{n}}$ g^{-1})	4.47	0.65
$\frac{1}{n}$	0.34	0.43
R^2	0.96	0.80
LF isotherm		
Γ_{max} (mg g^{-1})	14.56	2.57
K (dm^3 mg^{-1})	0.49	0.36
m	0.55	0.68
R^2	0.97	0.81
Tóth isotherm		
Γ_{max} (mg g^{-1})	25.84	3.65
K_L (dm^3 mg^{-1})	11.35	1.12
m	0.26	0.40
R^2	0.97	0.81

is no significant adsorption taking place. This is evident for all experiments except for the adsorption of BTMAB onto HSA talc.

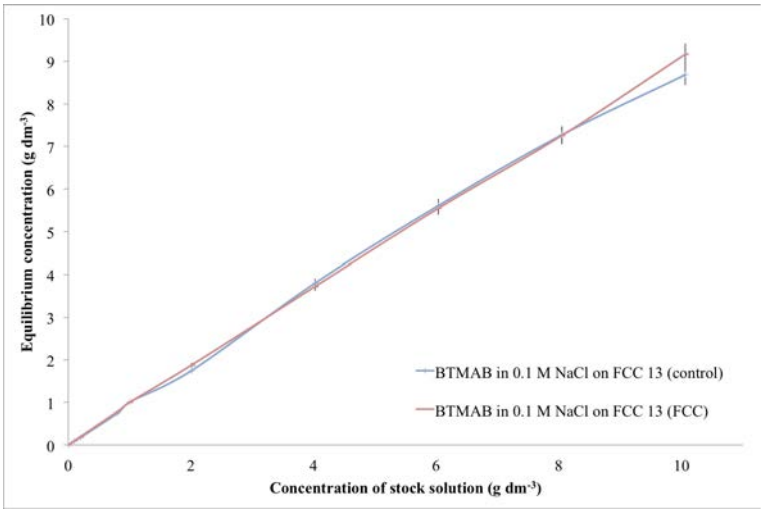

(a) BTMAB in 0.1 M NaCl on FCC 13 control and adsorption experiments.

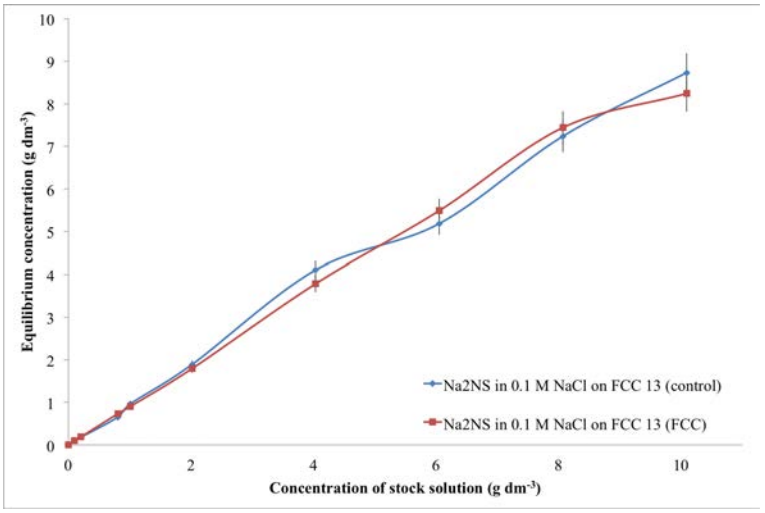

(b) Na2NS in 0.1 M NaCl on FCC 13 control and adsorption experiments.

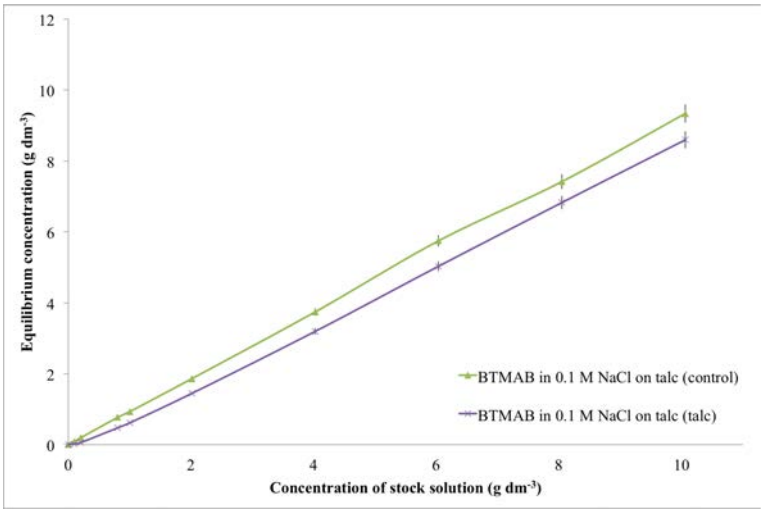

(c) BTMAB in 0.1 M NaCl on talc control and adsorption experiments.

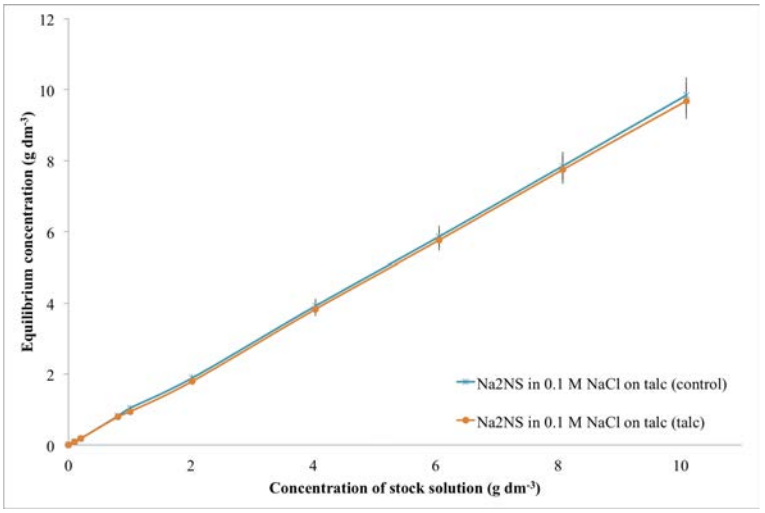

(d) Na2NS in 0.1 M NaCl on talc control and adsorption experiments.

Figure 4.14: The equilibrium concentration of the supernatants from adsorption experiments of BTMAB and Na2NS onto talc and FCC are plotted with the supernatants of their respective control experiments for comparison.

Therefore, Figure 4.14 shows the lack of adsorption of BTMAB and Na2NS onto FCC 13 in the presence of 0.1 M NaCl. There was also no adsorption in 2 M NaCl, or in 0.005 M H_3PO_4 electrolyte solutions, or in ultrapure water. The lack of adsorption at increased concentration of electrolytes showed that adsorption did not occur even when the electric double layer at the surface of the FCC was suppressed. The null results in ultrapure water showed that the electrolyte was not itself interfering with adsorption. Finally, the use of an H_3PO_4 solution provided a check as to whether the FCC surface could be re-activated, again showing a null result. And, in light of Figure 4.14, it was found that there was no adsorption of Na2NS onto talc, whereas for the adsorption of BTMAB onto HSA talc, an isotherm was produced (Figure 4.12).

4.3.2.1 Discussion of charged species adsorption

Charnay *et al.* (2001) state that BTMAB has a lack of hydrophobic moiety and so adsorbs onto talc via hydrophilic interactions only, although the planar surfaces of talc do in fact behave hydrophobically. They monitored the presence of divalent cations (Mg^{2+} and Ca^{2+}) present in the supernatant and the amount of ions exchanged was nearly an ideal stoichiometric ratio of 2:1 (BTMAB to divalent cations). They also state that the maximum amount adsorbed was 2.14 mg g^{-1} (9.3 μmol g^{-1}), whereas the isotherm in Figure 4.12 suggests a maximum adsorption of 9.2 mg g^{-1} onto talc. However, this must be attributed to the difference in the purities of talc and the surface area. Charnay *et al.* (2001) used a talc-chlorite sample (33 % chlorite) with a surface area of 6 m^2 g^{-1}, whereas the HSA talc utilised in this experiment exhibits a surface area of 51 m^2 g^{-1}, and is most probably why this work claims higher adsorption densities.

Charnay *et al.* (2001) used a surfactant, sodium dodecyl sulphate (SDS) to characterise the hydrophobic cationic sites of talc, and stated that 3.11 mg g^{-1} (10.8 μmol g^{-1}) of SDS was adsorbed. They also used benzene sulphonate, similar in some ways to Na2NS, to characterise the hydrophilic surface area of their talc samples via electrostatic interactions and stated that a 'very low density of positive surface sites was evidenced and therefore neglected' as it is consistent with a very low density of positive charged surface sites on their studied talcs. Although Na2NS has more hydrophobic character than benzene sulphonate, and so may adsorb hydrophobically, the adsorption isotherm (Figure 4.13) appears to plateau, and so supports the idea that there is not much cationic character to the talc sample.

In this work, no adsorption of BTMAB or Na2NS was observed from aqueous solution onto any grade of FCC used, thus this work suggests the contradiction of hypotheses 1 and 2. More experimental replicates would need to be carried out to make certain that the results are accurate and precise. However, the overall trend does suggest that there are not as many surface cationic sites as there are anionic sites.

It was expected that the FCC would adsorb mostly cationic species because of its mostly negatively charged surface (i.e. phosphate groups). This was also the reason as to why the adsorption of Na2NS in ultrapure water and a high concentration of NaCl was not tried. However, the isotherms in Figure 4.11 support that the FCC grades used do not adsorb cationic or anionic species.

The FCCs are made in tap water, since the low concentrations of Ca^{2+} and Mg^{2+} ions prevent dissolution of the solid phase. The surface of the FCC was attempted to be

reactivated by the addition of phosphoric acid. This did not aid adsorption. However, this may be due to phosphoric acid being in too low a concentration.

Lamminmäki *et al.* (2011) postulate that water adsorbs strongly to the surface of FCC via hydrogen bonding. Such a postulate is supported by the fact that the FCC is highly hydrophilic. The contact angle for water reported for 98 % pure calcium carbonate is 10° (Ren *et al.*, 2003), and for HAP is 31° (Toriyama *et al.*, 1995). As FCC is a composite of both of these materials, the FCC will also be hydrophilic. Direct observation of the contact angle of water onto FCC is not possible because water adsorbs onto the microporous surface too quickly (Tåg *et al.*, 2010). Other studies also support the idea of an adsorbed water layer: "it seems that the adsorption was prevented by the competitive adsoption of polar liquid molecules" (Lamminmäki *et al.*, 2011). FCC is likely to have at least a monolayer of physically adsorbed water when exposed in ambient air (Misra, 1988).

It would be extremely beneficial if several grades of FCC were made that were a) only treated with phosphoric acid and no other additives, b) had no added dispersant, and c) were made in ultrapure water (as opposed to tap water).

The fundamental law of electrostatics, Coulomb's law, expresses the inverse square law of force between two electric charges q_1 and q_2 separated by a distance d in a medium surrounding both charges:

$$F = \frac{q_1 q_2}{4\pi\varepsilon d^2} \tag{4.13}$$

where ε is the permittivity of the material. If q_1 and q_2 have the same sign, the force is repulsion; if they have the opposite sign, the force is attraction (Everett, 1988). By increasing the concentration of the electrolyte the charge on the surface of the mineral has decreased, which has been investigated by increasing the concentration of NaCl. However, future work can investigate the adsorption of polyelectrolytes, as their heavier molecular weight (i.e. the length of the molecule) is a lot larger than smaller ionised molecules, and FCC is claimed to be an amphoteric material showing anionic and cationic electrochemical charge values (Gantenbein, 2012). It is also suggested to try a different electrolyte solution, as the Schulze-Hardy rule states that as the valence of the ions having a charge opposite to that of the colloid increases, so does the coagulation of the colloid (Hiemenz and Rajagopalan, 1997) and hence the thickness of the double layer.

4.3.2.2 Polyelectrolyte adsorption

This section describes the results of the polyelectrolyte KPVS adsorption and viscometry experiments.

Figures 4.15 and 4.16 shows the adsorption density plotted against the amount of FCC TP used during experiments that utilised a solution with an initial concentration (c_0) of 0.1 and 1 g dm^{-3} KPVS, respectively; the blank (0 g of FCC TP used) was not included in these graphs to demonstrate how the data conforms well to a power law trend line. The regression coefficients of 0.99 indicate good reliability and so the experiments were not run in triplicate. However, a second experiment that utilised 0.2 g of mineral

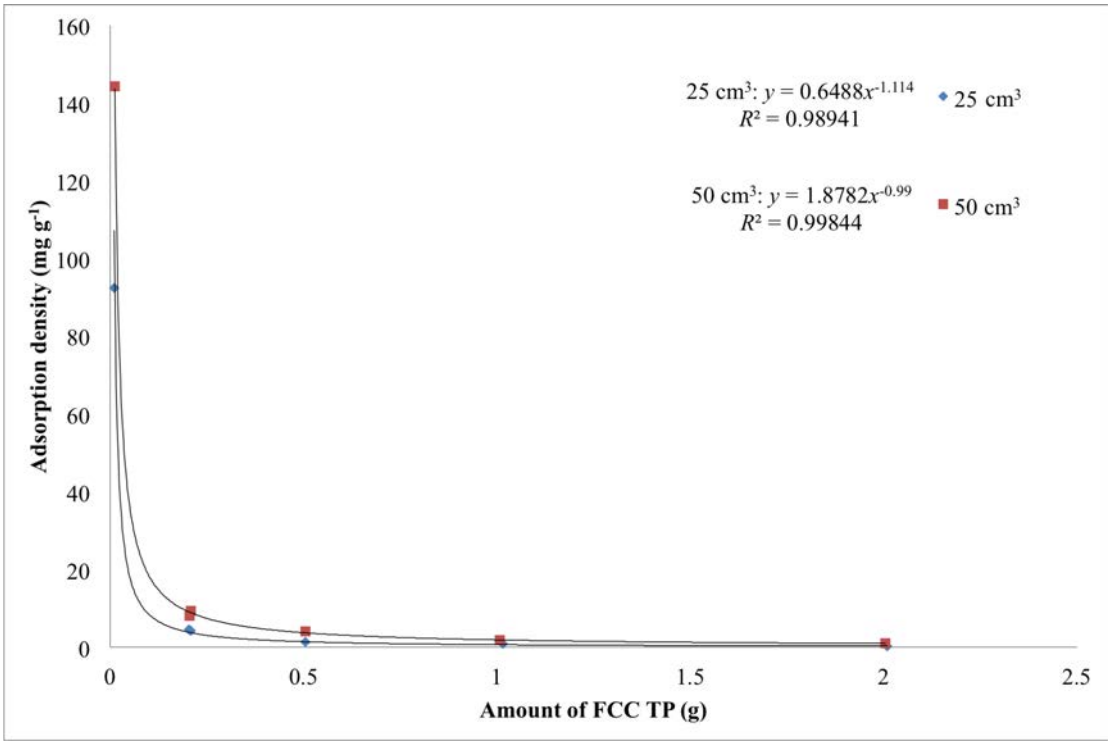

Figure 4.15: Adsorption density plotted against the amount of FCC used in the KPVS adsorption experiments when c_0 = 0.1 g dm^{-3} .

was conducted to ensure that the results were similar.

It was expected that the more adsorbent there was present in the experimental matrix, the more adsorbate it would have adsorbed in a direct linear fashion. However, in this instance, the more mineral adsorbent present in the experimental matrix saw a decline in the extent of adsorption. The power law trend observed in Figures 4.15 and 4.16 is not observed in results obtained from the vanillin in ethanol adsorption experiments specifically designed to briefly investigate the PCE in that system outlined in section 4.2.7. Figure 4.17 demonstrates this, and is a plot of the results in Table 4.9 from a later section. Although these results span a smaller range of c_{p} or W_{solid}, the power law trend, or PCE, is not evident in this system. All of the data when combined has an average adsorption density of 2.31 $\pm$ 0.25 mg g^{-1}.

It was also expected that despite the amount of adsorbent, the adsorption density would have remained the same, however, the dependence of the adsorption density on c_{p} violates the assumptions of the Langmuir and Freundlich theories in that c_{eq} and Γ are state variables and represent a unique value of chemical potential (Pan and Liss, 1998*a*,*b*). It was theorised that the PCE, in this instance, may have been caused by aggregating of the mineral, as described by the flocculation theory (Helmy *et al.*, 2000).

It is evident from Figures 4.15 and 4.16 that when utilising twice as much volume of stock solution during an adsorption experiment the FCC adsorbs twice as much as when using half the volume of stock solution; this supports the idea that the FCC may have been aggregating, and so with more volume, the FCC was able to disperse better,

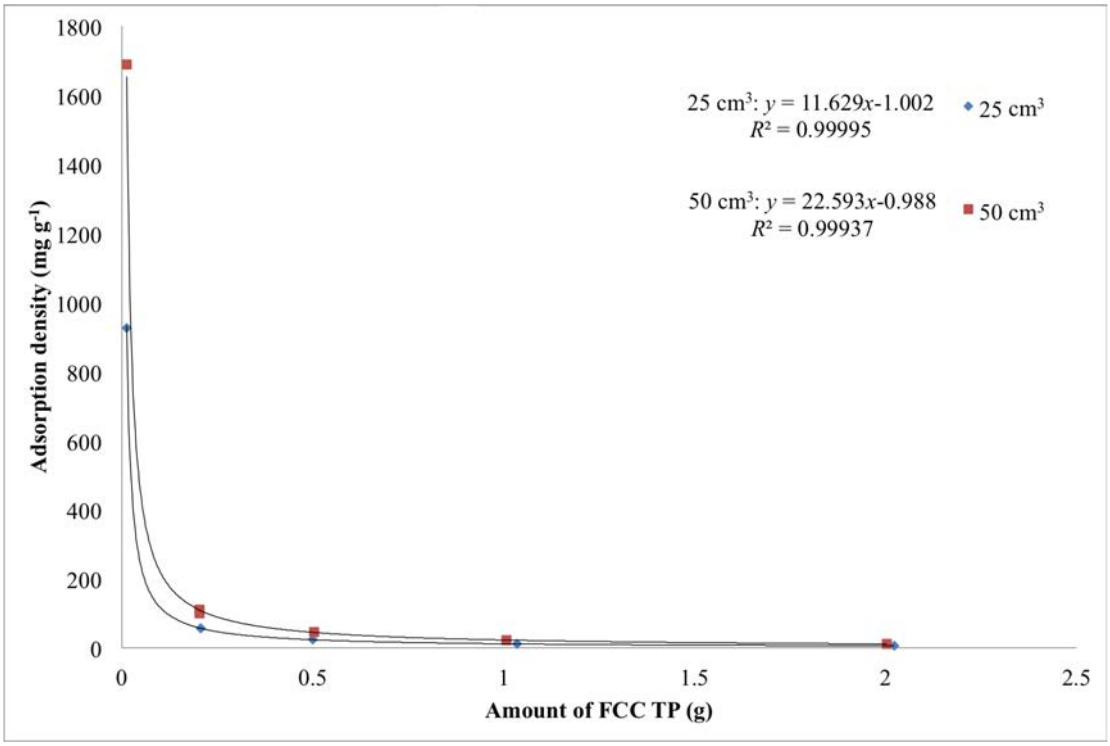

Figure 4.16: Adsorption density plotted against the amount of FCC used in the KPVS adsorption experiments when c_0 = 1 g dm^{-3} .

meaning that there was more surface area for the KPVS on which to adsorb. Yet, Γ is still showing the PCE with a power law trend. Also, when using 0.01 g of FCC, it seems to have adsorbed just under twice as much when using 50 cm^3 of KPVS stock solution compared with when using 25 cm^3. This may indicate a limit as to when the PCE no longer follows the power law trend.

It is unclear as to what is happening during these adsorption experiments to yield the PCE. However, as it is observed that c_{eq} is reduced by approximately half during adsorption experiments, it could be concluded that the FCC may not have an influence in the PCE being exhibited. Still, the PCE is only evident when there is FCC present, and so the mineral must somehow be playing a role in the PCE.

A possible explanation for the PCE in this system is that the adsorption of a highly charged polyelectrolyte onto a charged surface may strongly depend on the lateral organisation of the surface charges (Clausen-Schaumann and Gaub, 1999). KPVS has a molecular weight of ~170 000 g mol^{-1} and is a medium molecular weight polymer (Oliveira *et al.*, 2010), and thus may not be considered 'highly charged.' However, the idea that the adsorption of polymers may depend on the lateral organisation is relevant for low, medium, and high molecular weight polymers, and can be illustrated by the following thought experiment: consider a chessboard-like surface with an attractive and a repulsive interaction between the polymer and the black and white fields, respectively, as in Figure 4.18. Even if the contour length (L_{c}), the Kuhn length (l_{k}), the Debye length (λ_{d}), and the average surface charge density (ρ_{q}) are kept constant, the amount

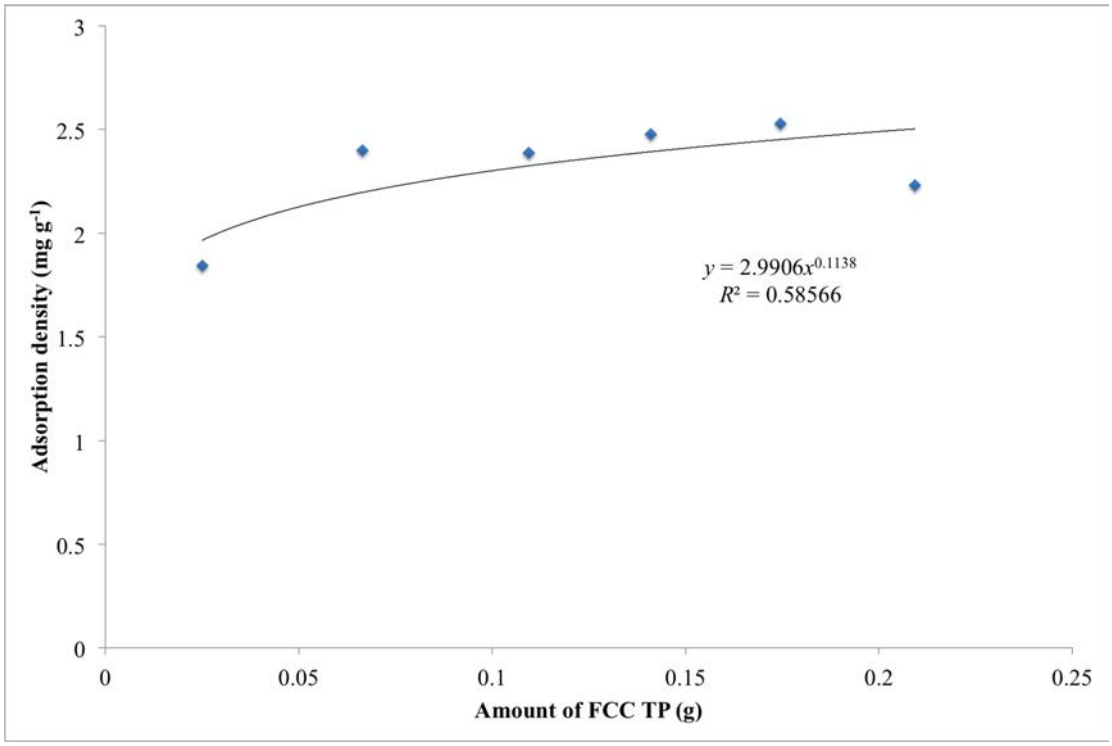

Figure 4.17: Adsorption density plotted against the amount of FCC used in vanillin experiments specifically designed to briefly investigate the PCE in the system outlined in section 4.2.7, the results of which can be seen in Table 4.9 in a later section.

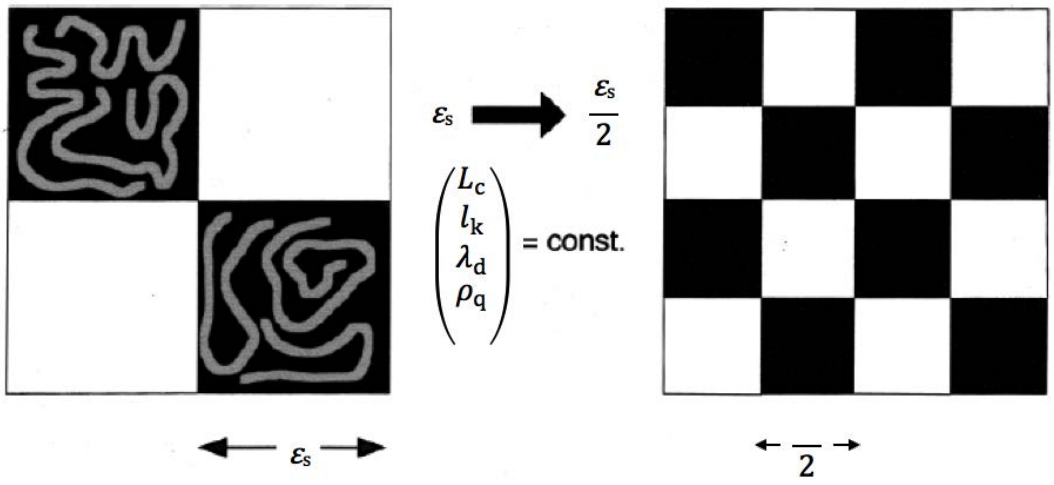

Figure 4.18: Schematics of the adsorption of charged polymers onto a chessboard-like surface with attractive electrostatic interaction between the polymer and the black fields and repulsive electrostatic interaction between the polymer and white fields (Clausen-Schaumann and Gaub, 1999) Permission to reproduce this image has been granted by the publisher.

of adsorbed polymers should decrease as the size (ε_s) of the individual fields reaches either the Kuhn length (l_k) of the polymer or the Debye screening length (λ_d) of the surrounding electrolyte solution (Clausen-Schaumann and Gaub, 1999). Therefore, as the size of the individual fields (ε_s) decreases beyond a critical length (ε_{cl}), even if the average charge density of the surface (ρ_q) is kept constant, the amount of adsorbed polymer should decrease (Clausen-Schaumann and Gaub, 1999).

This relates to the adsorption of KPVS onto FCC TP in that as the FCC is thought to have cationic and anionic surface sites (Lamminmäki *et al.*, 2011), the more FCC that is in the experimental matrix of an adsorption experiment will result in less adsorbed KPVS due to shielded cationic sites by the sites of opposite charge, which is hypothesised to have a similar effect as decreasing the size of the individual fields, and is a possible explanation as to why the PCE is evident in these adsorption experiments.

The results of the viscometry experiments are displayed in Table 4.6; the experiment ID denotes the adsorption matrix used to obtain the supernatant, and the letter 'a,' 'b,' or 'c' differentiates between experimental replicates. An asterisk indicates that the sample was not a supernatant from an adsorption experiment, but simply a solvent or solution used for the viscometry experiments. The average time is the average of three analytical replicates, and the shading is to aid in the discussion of the results later in the document. The results in Table 4.6 are displayed pictorially in Figure 4.19.

The ultrapure water*, ultrapure water a, and ultrapure water c viscometry results in Table 4.6 show that these samples all took 1 minute and 48 seconds to move from line (c) to line (b) in the Ostwald viscometer (Figure 4.5), whereas the ultrapure water b took approximately 2 seconds longer. All of these results in Table 4.6 are adjacent to one another and shaded the same colour to highlight that, theoretically, they should all have the same retention time as each other. This demonstrates that the adsorption

Table 4.6: Results from viscometry experiments; the asterisk next to the experiment ID signifies that it was not a supernatant from an adsorption experiment, but a solvent or solution.

Experiment ID	Weight of FCC TP used during adsorption experiment (g)	Average time for meniscus to fall (mins:secs:msecs)	Standard deviation (mins:secs:msecs)
Ultrapure water*	n/a	01:48:03	00:00:18
Ultrapure water a	0.00	01:48:22	00:00:14
Ultrapure water b	0.00	01:51:57	00:00:28
Ultrapure water c	0.00	01:48:06	00:00:04
FCC in Ultrapure water a	2.02	01:48:07	00:00:45
FCC in Ultrapure waterb	2.01	01:47:28	00:00:15
FCC in Ultrapure water c	2.00	01:47:56	00:00:36
0.1 g dm^{-3} KPVS*	n/a	01:50:35	00:00:15
0.5 g dm^{-3} KPVS*	n/a	01:56:47	00:00:16
1 g dm^{-3} KPVS*	n/a	02:02:12	00:00:51
1 g dm^{-3} KPVS a	0.00	01:59:47	00:00:34
1 g dm^{-3} KPVS	0.00	01:57:07	00:00:16
1 g dm^{-3} KPVS c	0.00	01:56:58	00:00:18
FCC in 1 g dm^{-3} KPVS a	2.01	01:46:57	00:00:14
FCC in 1 g dm^{-3} KPVS b	2.00	01:46:28	00:00:26
FCC in 1 g dm^{-3} KPVS c	2.00	01:46:20	00:00:10

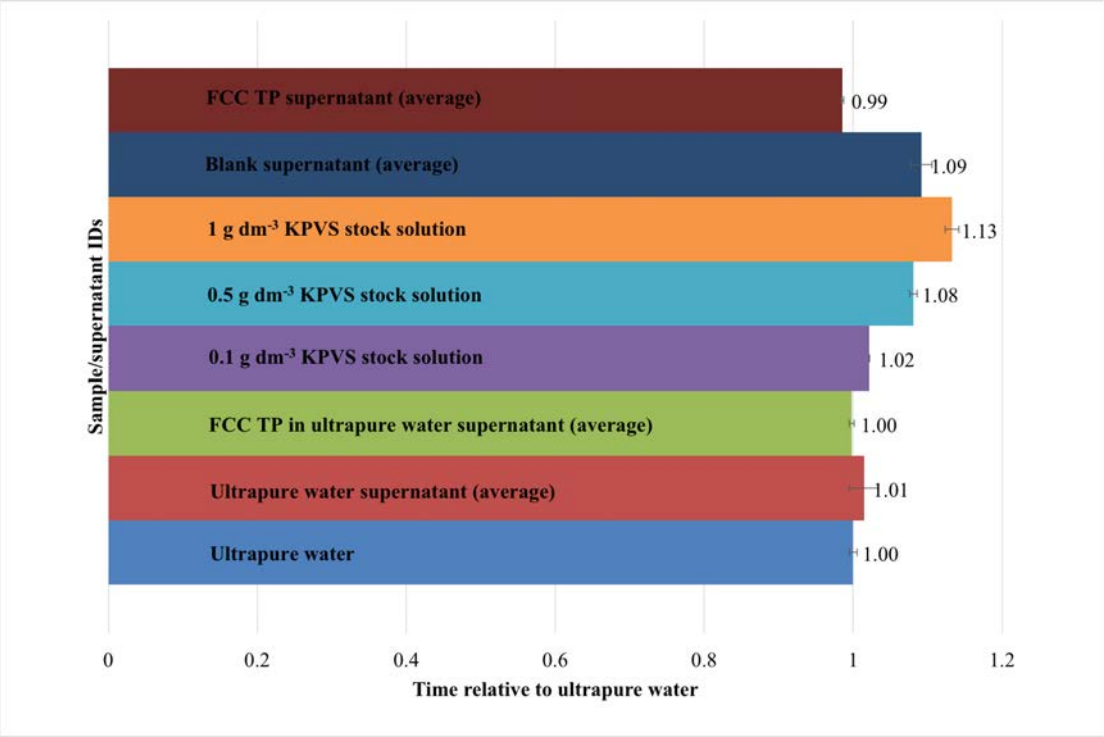

Figure 4.19: The viscometry results from Table 4.6 displayed pictorially relative to Ultrapure water*.

experiment, without any FCC TP, did not alter the ultrapure water in any way.

The FCC in ultrapure water a, FCC in ultrapure water b, and FCC in ultrapure water c are all within 1 second of one another, and therefore highlighted the same colour. These values are very similar to those of the ultrapure water *, ultrapure water a, ultrapure water b, and ultrapure water c samples in Table 4.6, and suggests that the FCC TP does not alter the solvent in any way during an adsorption experiment. The average retention time of samples ultrapure water *, ultrapure water a, ultrapure water b, ultrapure water c, FCC in ultrapure water a, FCC in ultrapure water b, and FCC in ultrapure water c is 01:48:34 $\pm$ 00:01:31 (mins:secs:msecs).

The stock solutions of KPVS with the concentrations 0.1, 0.5, and 1 g dm^{-3} were also studied with the viscometer, and it can be seen in Table 4.6 that as the concentration of the solution increases, as does the retention time due to the solution becoming more viscous as more polyelectrolyte is introduced. These columns have been highlighted the same colour in Table 4.6 in order to group them together for better readability.

The 1 g dm^{-3} KPVS a, 1 g dm^{-3} KPVS b, and 1 g dm^{-3} KPVS c samples have been grouped together in Table 4.6, and so have been shaded and placed adjacent to one another, to demonstrate that they should all have the same retention time as 1 g dm^{-3} KPVS *. However, this is not the case. 1 g dm^{-3} KPVS b and 1 g dm^{-3} KPVS c have a similar time to 0.5 g dm^{-3} KPVS *. The adsorption experiment results in Figures 4.15 and 4.16 show that the concentration of KPVS decreases by approximately half only when FCC TP is present, whereas the viscometry experiments suggest that this may be happening without FCC TP being present. The average retention time of these three experiments is 01:57:57 $\pm$ 00:01:35 (mins:secs:msecs).

However, the three experimental replicates FCC in 1 g dm^{-3} KPVS a, FCC in 1 g dm^{-3} KPVS b, and FCC in 1 g dm^{-3} KPVS c have an average retention time of 01:46:35 $\pm$ 00:00:20 (mins:secs:msecs), which is 00:01:59 $\pm$ 00:01:11 (mins:secs:msecs) faster than the average retention times of samples ultrapure water *, ultrapure water a, ultrapure water b, ultrapure water c, FCC in ultrapure water a, FCC in ultrapure water b, and FCC in ultrapure water c, which is 01:48:34 $\pm$ 00:01:31 (mins:secs:msecs). These experiments have been grouped together, and hence placed adjacent to one another and shaded the same colour in Table 4.6 to demonstrate that these should have the same retention times as one another.

Viscometry experiments on the supernatants suggest that after an adsorption experiment, the supernatant concentration (c_{eq}) of KPVS is 0 g dm^{-3}, whereas UV-visible spectroscopy indicates that the concentration in the supernatant (c_{eq}) falls to approximately half of its initial concentration. It is theorised that the larger KPVS polymeric chains are flocculating or aggregating at the bottom of the centrifuge tube during centrifugation when conducting an adsorption experiment, leaving mostly monomers behind in the supernatant; the monomers are then analysed by UV-visible spectroscopy, as the polymeric chains remain in the sediment with the FCC TP, and the supernatant concentration (c_{eq}) always relates to approximately half of the initial concentration, because the same amount of KPVS polymeric chains have aggregated at the bottom of the centrifuge tube during each adsorption experiment. This then translates into appearing as though the FCC TP has adsorbed more KPVS when there is a lower c_p than

when there is a higher c_p, and so seems to exhibit the PCE. Viscometry experiments, on the other hand, suggest that the c_{eq} is 0 g dm^{-3} KPVS, however, if there are simply monomers remaining in the supernatant, the supernatant retention times may be the same as the ultrapure water retention times, which is what was shown in Table 4.6 and Figure 4.19.

More viscometry experiments using supernatants from adsorption experiments with differing c_p could be conducted to see if the viscosity of the supernatant changes in the same way each time, which would further support the idea that only monomers of KPVS are being left behind in the supernatant. Other types of FCC mineral pigment may be used, or other minerals altogether, to see if the PCE is still evident with different types of adsorbate. However, it is deduced that the PCE will be evident with other minerals in the adsorption of KPVS in ultrapure water, because the adsorption of vanillin onto FCC TP in ethanol does not exhibit the PCE (Figure 4.17).

Adsorbing KPVS onto FCC TP showed what appeared to be the particle concentration effect (PCE). Viscometry suggests that there may be nucleation and flocculation of the larger KPVS molecules. It is concluded that the FCC does not adsorb uncharged species, whereas with charged species it is an unclear process.

4.3.3 Experimental artefact investigation

Blank experiments were incorporated into the adsorption experiment methodology, which accounted for the potential of adsorption of the analyte onto the sides of the containers. This section describes results obtained from various other experiments that attempted to identify any other weaknesses in the adsorption methodology, as it was expected that the FCC would adsorb.

Figure 4.20 shows the absorption spectrum of a supernatant from FCC in ethanol that had been through the adsorption protocol outlined in section 4.2.3. It was expected that the spectrum of the supernatant would have the same characteristics as that of pure ethanol, however, the supernatant's spectrum was noisier.

The same volume of ethanol was added back to the FCC after it was left to dry overnight, and the process was repeated 4 times in total. After the second washing of the FCC samples, the peaks were generally more intense than the previous washings. However, after the third washing the spectra appeared slightly cleaner. The last washing was filtered through a 0.2 μm filter and the spectra can be seen in Figure 4.21; the peaks are also a lot smaller and more consistent than those in Figure 4.20, supporting the idea that fine particles originating from the mineral adsorbent may be interfering with the UV-visible spectrum when measuring levels of adsorbate.

The results imply FCC particulates are still dispersed in the supernatant that are finer than 0.2 μm. This baseline shift is not unique to FCC; it is also exhibited by the analytical reagent grade calcium carbonate, a calcium phosphate, and a potassium phosphate in ethanol.

Further tests utilising 25 mg dm^{-3} vanillin in ethanol solution were conducted, which involved using 0.01 g of FCC 06 in an adsorption experiment. The resultant AU from the analysis of the supernatant via UV-visible spectroscopy of three experimental replicates was 1.72 $\pm$ 0.00 AU. The result of three blank experiment replicates was 1.74 $\pm$ 0.00

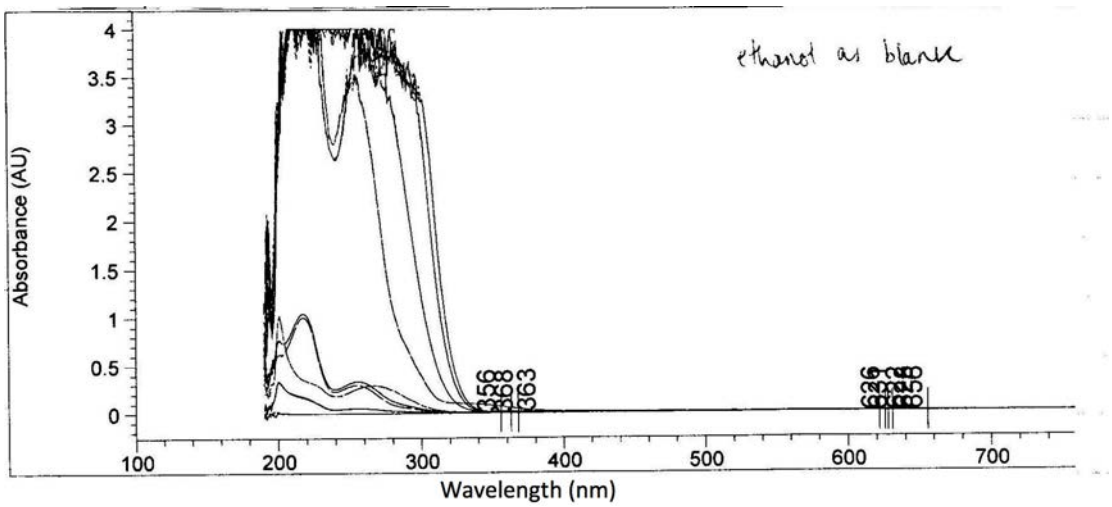

Figure 4.20: The resulting spectra from UV-visible spectroscopy analysis of supernatants after the first washing of FCC, filtered through 1.6 μm membrane.

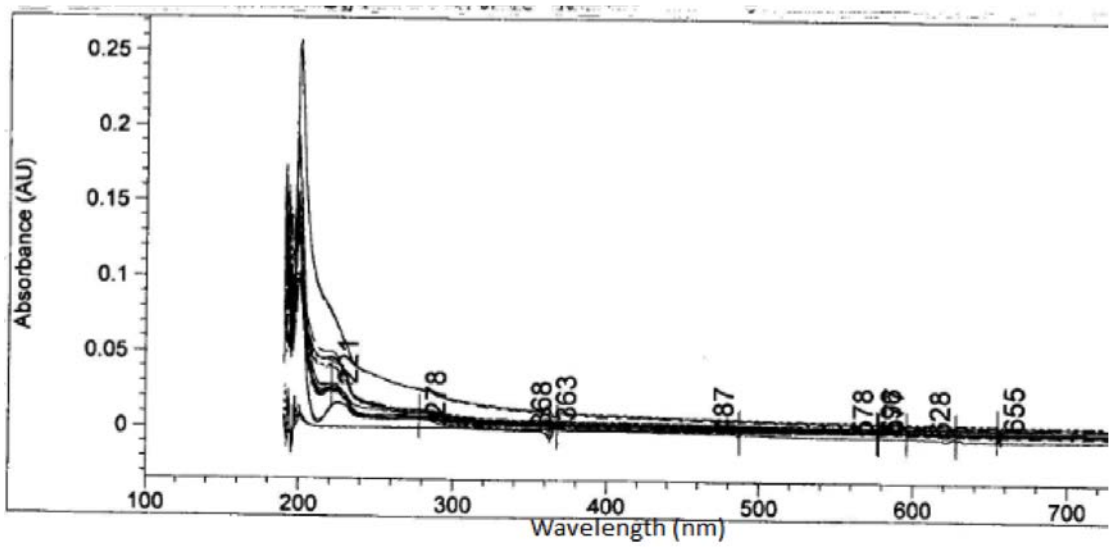

Figure 4.21: The resulting spectra from UV-visible spectroscopy analysis of supernatants after the fourth washing of FCC, filtered through 0.2 μm membrane.

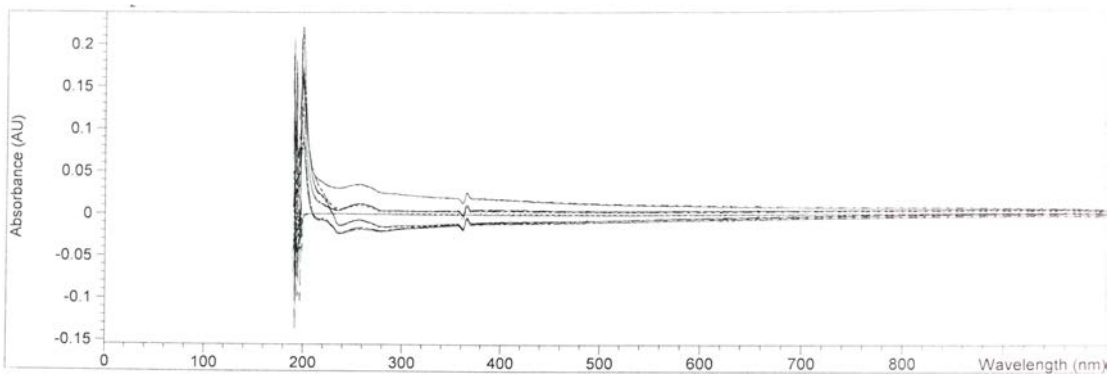

Figure 4.22: The resulting spectra from UV-visible spectroscopy analysis of supernatants utilising FCC TP in ethanol.

AU. When using 1.5 g FCC, the resulting AU was 0.04 $\pm$ 0.00. It is hypothesised that the fine particles were covering the vanillin absorption peak on the UV-visible spectrum.

Another similar test was made but using a vanillin in ethanol concentration of 0.17 mg dm^{-3}, which had an AU of 0.12. This solution was used with 1.5 g of FCC 06 in an adsorption experiment, and the supernatant had an AU of 0.17, whereas the blank was 0.12. The supernatant of the sample was then filtered with a 0.1 μm syringe filter and the AU was 0.07. This suggests that adsorption may have taken place.

The same was performed but using a 37.5 mg dm^{-3} stock solution, which had an AU of 2.48. The blank, however, had an AU of 3.06. This may have been some sort of contamination. However, the supernatant of an adsorption experiment that utilised 1.5 g FCC had an AU of 0.07, and after filtering it was 0.08. This may also indicate adsorption.

These experiments support the idea that if vanillin is high enough in intensity, or if perhaps the removal of fines is efficient, then the detection of the analyte may be unobscured.

To demonstrate the way in which the spectra are shifted, 0.2 g of FCC TP in 25 cm^3 of ethanol was put through an adsorption experiment, and the resulting spectra are shown in Figure 4.22.

Further examples of how the spectra are shifted with the addition of FCC can be found in Figures 4.23 and 4.24. The former are ethanol supernatant spectra with and without FCC TP (i.e. a blank), and the latter is a series of aspirin in ethanol spectra.

Figures 4.23 and 4.24 suggest that aspirin will not be covered or obscured by any fines. However, the fines prove extremely difficult to quantify, and is dependent at least to some extent upon the efficiency of centrifugation.

Turbidity experiments were conducted that involved putting 0.5 g of FCC 02 in ethanol and putting that through an adsorption experiment. The same was done also with water as the solvent. The colorimeter measured the ethanol supernatant to have a turbidity of 183 formazin attenuation units (FAU), and after filtering with a 0.1 μm filter it reduced to 0. The water supernatant had an FAU of 36, but when filtered with a 0.2 μm filter it was

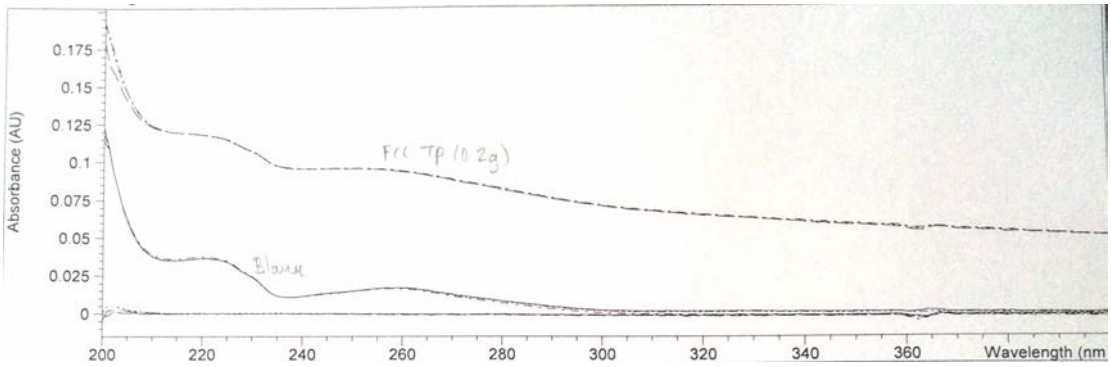

Figure 4.23: The resulting spectrum from UV-visible spectroscopy analysis of supernatants utilising FCC TP in ethanol, and a spectrum without any FCC present during the experiment.

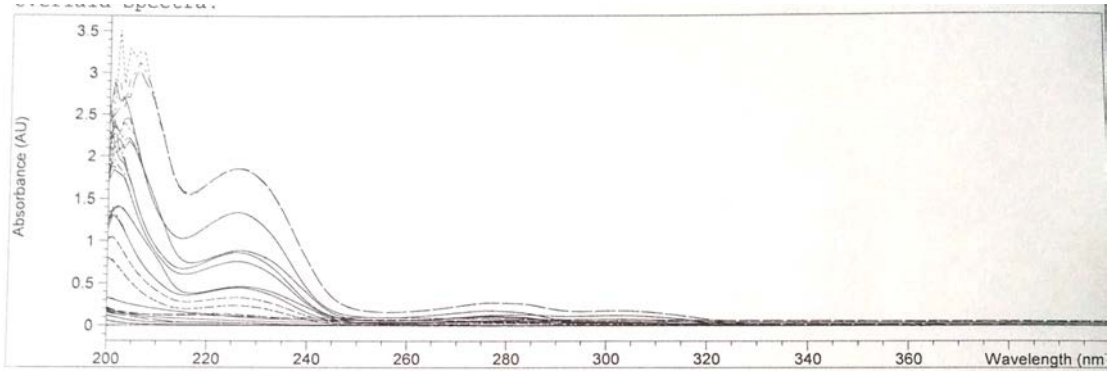

Figure 4.24: The resulting spectrum from UV-visible spectroscopy analysis of aspirin in ethanol.

39. The same experiments were conducted again, but with 2 g of FCC. The ethanol had an FAU of 3, and when filtered is reduced to 0. Water had an FAU of 56, and when filtered it became 65. This suggests that the UV-visible spectrometer baseline is worsened by the filtering of the supernatant, however, the baseline shift may be small enough to still detect analyte. Diluting the supernatants also reduces this measured baseline shift.

Therefore, if a concentration of analyte is chosen that absorbs less intensely than the fines, it is expected that the c_{eq} of a sample will be lower than that of the blank, even if the supernatant is diluted (as the ratio of fines to analyte will remain the same). It is expected, however, that after filtering the supernatant, the concentration of analyte will increase to be the same as the blank (providing that no adsorption has taken place).

BTMAB, according to the calibrations, absorbs at 262 nm with the following intensities at the following concentrations (calibration performed between 0.01-1g dm^3):
0.01 g dm^{-3} BTMAB = 0.01 AU
0.1 g dm^{-3} BTMAB = 0.18 AU
1.0 g dm^{-3} BTMAB = 1.65 AU

According to turbidity experiments, 2 g of FCC TP will cover the 262 nm peak with the following intensities:
Supernatant = ~0.3 AU
Supernatant diluted x10 = ~0.03 AU
Supernatant diluted x 100 = ~-0.02 AU

Previous experiments have shown that 10 g dm^{-3} BTMAB with 2 g of mineral and a x10 dilution of the supernatant yields the same absorbance intensity of BTMAB as the blank, thus indicating no adsorption. However, according to the previously quoted absorbance values, if 2 g of FCC were used in an adsorption experiment with 1 g dm^{-3} BTMAB the supernatant should theoretically be able to be analysed accurately via UV-visible spectroscopy without the need for dilution of filtration.

If a 0.1 g dm^{-3} BTMAB solution was used, however, it is expected that the peak would be covered with by the fine particles from 2 g of the mineral. Resultantly, this may give the impression that adsorption is taking place, even if the supernatant was to be diluted. However, if the supernatant was filtered (as opposed to diluted), then it is expected that the BTMAB concentration/absorbance intensity will be the same as the blank sample.

The result of experiments that investigate these theories are displayed in Table 4.7. Note that the turbidity of the supernatants decreased as the supernatant was diluted.

In both cases (i.e. when c_0 was either 0.1 or 1 g dm^{-3} BTMAB) the blank experiments had the same AU as the stock solutions, which rules out the possibility of BTMAB adsorbing to the sides of the centrifuge tube as an experimental caveat. However, in each case, the FCC TP AU deviated the most from the blank experiments, then followed by FCC 02, then followed by HAP. The turbidity data (not reported) also showed that the turbidity of the supernatants also declined in the same order.

Table 4.7: The absorbance intensities of BTMAB in adsorption experiments designed to investigate the effects of filtering and diluting the supernatant of various samples.

Sample	Weight of mineral (g)	AU (262 nm) Supernatants	Filtered	Diluted	Diluted then filtered
		1 g dm^{-3} BTMAB			
1 g dm^{-3} stock	n/a	1.67	-	-	-
Blank	2.0	1.66	1.66	-	-
FCC TP		2.32	1.75	0.20	0.19
FCC 02		1.88	1.68	0.19	0.19
HAP		1.77	1.67	-	-
		0.1 g dm^{-3} BTMAB			
0.1 g dm^{-3} stock	n/a	0.19	-	-	-
Blank	2.0	0.18	0.19	-	-
FCC TP		0.46	0.26	-	-
FCC 02		0.264	0.21	-	-
HAP		0.22	0.20	-	-
Blank	0.5	0.18	0.18	0.02	-
FCC TP		0.30	0.21	0.02	0.03
FCC 02		0.281	0.20	-	-
HAP		0.21	0.20	-	-

Table 4.8: The average adsorption density of three experimental replicates of vanillin in ethanol on different grades of FCC and HSA talc. The average adsorption density of the minerals (excluding GCC and HSA Talc) is 2.00 $\pm$ 0.59 mg g^{-1}.

Mineral	Adsorption density (mg g^{-1})
HAP	2.28 $\pm$ 0.02
HSA Talc	0.15 $\pm$ 0.01
GCC	-0.04 $\pm$ 0.00
FCC 02	1.90 $\pm$ 0.04
FCC 03	0.78 $\pm$ 0.07
FCC 06	2.01 $\pm$ 0.05
FCC 07	1.73 $\pm$ 0.04
FCC 12	2.45 $\pm$ 0.02
FCC 13	2.25 $\pm$ 0.02
FCC TP	2.67 $\pm$ 0.01

In each case, filtering the supernatant improved the AU (i.e. became closer to that of the blank), although the same pattern was still followed (i.e. FCC TP had the highest discrepancy of all the samples).

To conclude, the extent to which fine particles from the sample covers the absorbance intensity of the analyte is most likely dependent on the analyte and the extent to which the fines are effectively removed from the supernatant. Regarding systems in which this is an issue, the question arises of how to remove, or at least get around the issue of, the ultrafine particles.

4.3.4 Vanillin adsorption

In the context of the frustrations of studying adsorption from aqueous systems, it was decided to study the adsorption of vanillin from fully or partially non-aqueous systems. Although the use of aqueous solutions in these experiments would be more applicable to biological situations, in this work adsorption from chloroform and ethanol/water solutions was studied in order to facilitate the loading of the vanillin onto the FCC, and to avoid the need for aqueous buffering which could interfere with the adsorption processes.

Table 4.8 displays the average adsorption density of three experimental replicates of vanillin in ethanol on different grades of FCC and some other minerals, each with an initial starting concentration of 30 mg dm^{-3} of vanillin in ethanol. The average adsorption density of the minerals (excluding GCC and HSA Talc) is 2.00 $\pm$ 0.59 mg g^{-1}. It was found that there was a minimal difference in the adsorption characteristics of vanillin from ethanol between different grades of FCC. Table 4.9 shows the average adsorption density of vanillin in ethanol on different amounts of FCC TP to demonstrate that the PCE is not present in this system. The results of three experimental replicates were obtained, and showed no non-proportionate effect of substrate weight between 0.025 and 0.21 g.

Therefore, this system supports the notion that vanillin is adsorbing to the FCC, also

Table 4.9: The average adsorption density of vanillin in ethanol on different amounts of FCC TP, all averaging an adsorption density of 2.31 $\pm$ 0.25 mg g^{-1}.

Weight of FCC TP (g)	Adsorption density (mg g^{-1})
0.0250	1.84
0.0664	2.40
0.1094	2.39
0.1410	2.48
0.1745	2.53
0.2093	2.23

supporting the notion of hypothesis 2.

Figure 4.25 shows three adsorption isotherms: Langmuir, Freundlich, and LF, fitted to the vanillin adsorption data, and Table 4.10 shows the parameters obtained from these fits. Figure 4.26 shows the LF fits only, and Table 4.10 shows the parameters arising from these fits. As expected, the adsorption density of vanillin decreased with the addition of water, and even further when chloroform was the solvent.

Figure 4.30 shows the effect on adsorption of adding water to an ethanolic solution of vanillin, based on interpolated results from experiments with c_0 = 40 and 100 mg dm^{-3}. The error bars are the standard deviations of three experimental replicates. As expected, the adsorption density of vanillin decreased with an increasing % of water.

GCC was used as a control substrate. No adsorption was observed of any of the species studied, from any of the solvents used. The reason GCC was used as a comparison for adsorption was to see if the adsorption would follow a different trend and so we could infer something about the FCC TP's mesoporous structure being the reason as to why the adsorption is a mix between Freundlich and Langmuir. However, the GCC does not adsorb vanillin from neither ethanol nor chloroform.

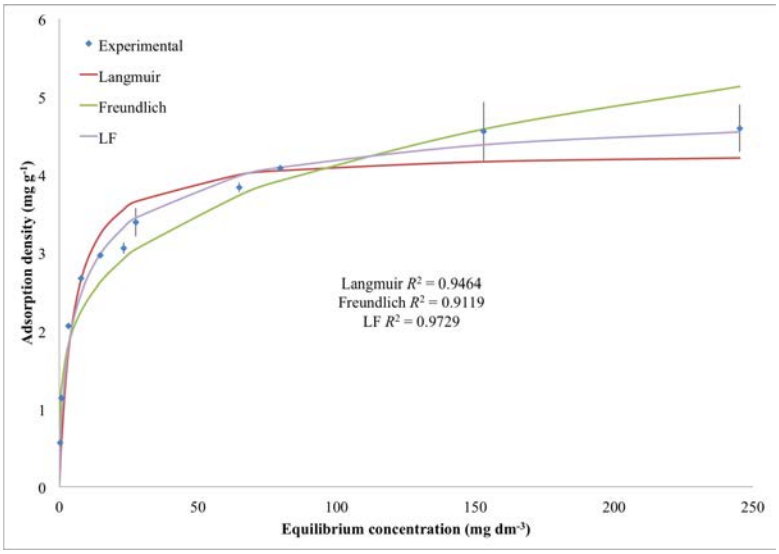

(a) Ethanol.

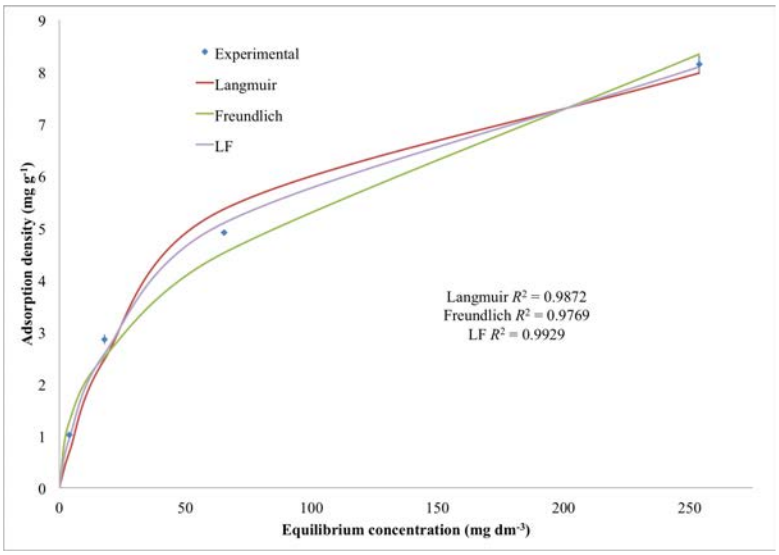

(b) Chloroform.

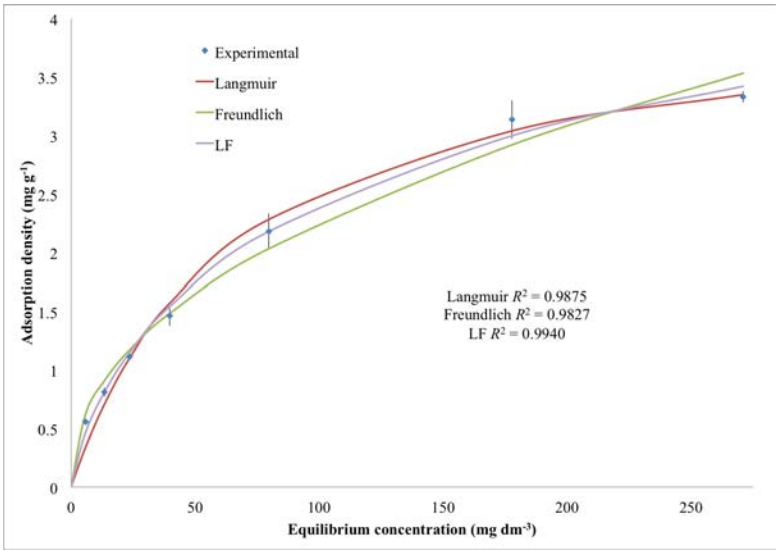

(c) Ethanol (1 % water).

Figure 4.25: Vanillin adsorption isotherms from a) ethanol, b) chloroform, and c) ethanol (with 1 % water by volume). The error bars are the standard deviations of three experimental replicates.

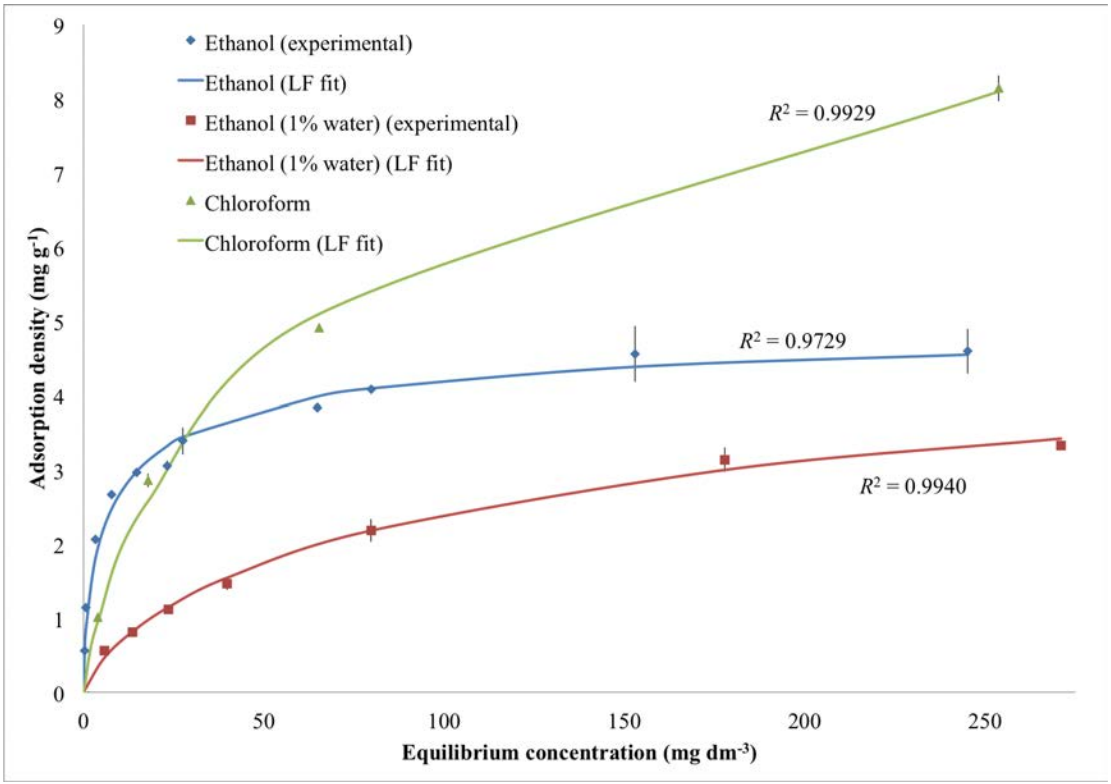

Figure 4.26: Vanillin adsorption isotherms from a) ethanol, b) chloroform, and c) ethanol (1 % water by volume), each fitted with the LF equation (resulting parameters can be seen in Table 4.10). The error bars are the standard deviations of three experimental replicates.

4.3.5 Aspirin adsorption

Aspirin was also used by a final year applied chemistry undergraduate student, under my supervision, alongside the work of vanillin adsorption. Its adsorption from aqueous ethanolic solutions is reported. Aspirin is a widely studied non-steroidal anti-inflammatory, antipyretic, and analgesic drug (Vane and Botting, 2003).

Figure 4.27 shows the results of aspirin in ethanol adsorption isotherms personally conducted plotted alongside those of the undergraduate student to show concordance between our results.

The adsorption of aspirin onto FCC from ethanolic solutions with various relative concentrations of water, relative permittivity ε_r = 78.5, (CRC Press, 2006), and their LF fits as fitted with Python, are shown in Figure 4.28, and the resulting parameters in Table 4.11.

Figure 4.29 shows the aspirin isotherms from Figure 4.28 and the vanillin isotherms from Figure 4.26 for visual comparison.

4.3.5.1 Vanillin and aspirin adsorption described with the Tóth isotherm

The adsorption of vanillin from chloroform, ε_r = 4.8 (CRC Press, 2006), was higher than from the more polar ethanol, ε_r = 24.6 (CRC Press, 2006), and can be seen in Figure

Table 4.10: Parameters for the isotherms describing the adsorption of vanillin onto FCC from ethanol, chloroform, and ethanol with 1% water by volume (Figure 4.26).

Parameter	Ethanol	Chloroform	Ethanol (1% water)
Langmuir isotherm			
Γ_{max} (mg g^{-1})	4.30	9.60	4.16
K_L (dm^3 mg^{-1})	0.21	0.02	0.02
R^2	0.96	0.99	0.99
Freundlich isotherm			
K_F (dm^3 $\frac{1}{n}$ mg$^{1-\frac{1}{n}}$ g^{-1})	1.38	0.68	0.28
$\frac{1}{n}$	4.18	2.21	2.21
R^2	0.91	0.98	0.98
LF isotherm			
Γ_{max} (mg g^{-1})	5.10	11.9	5.52
K (dm^3 mg^{-1})	0.30	0.03	0.03
m	0.63	0.77	0.75
R^2	0.97	0.99	0.99

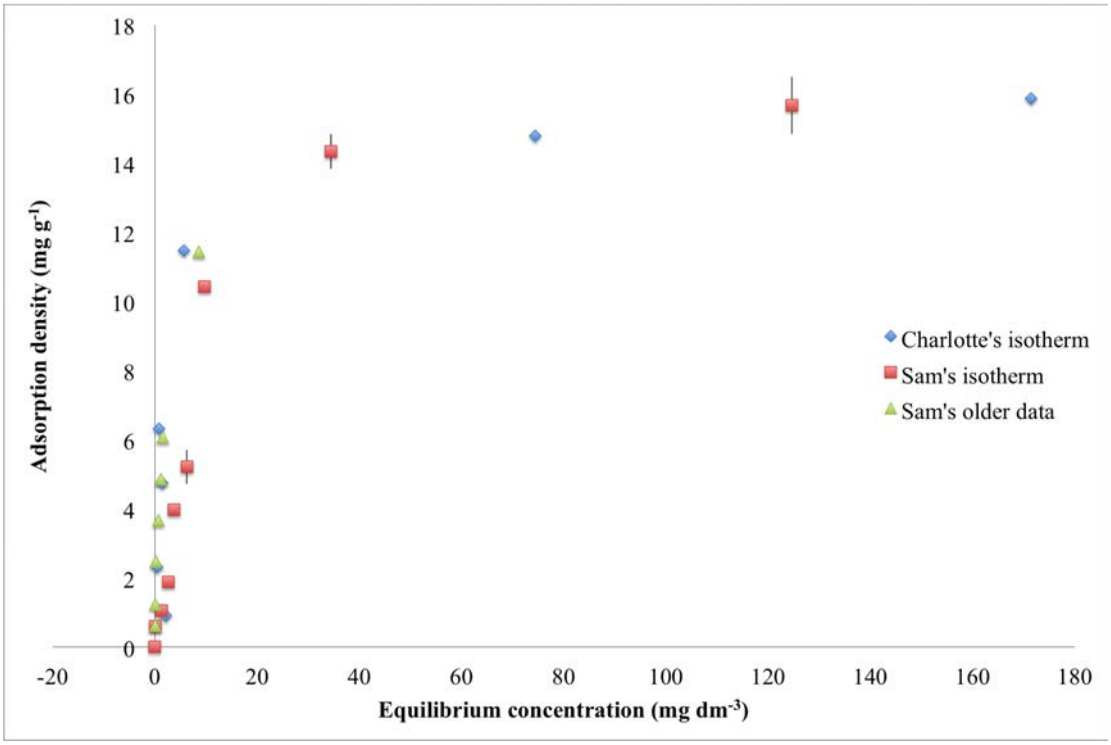

Figure 4.27: Aspirin adsorption from ethanol onto FCC compared with those of an undergraduate final year applied chemistry student. The student's y-error bars are of three experimental replicates.

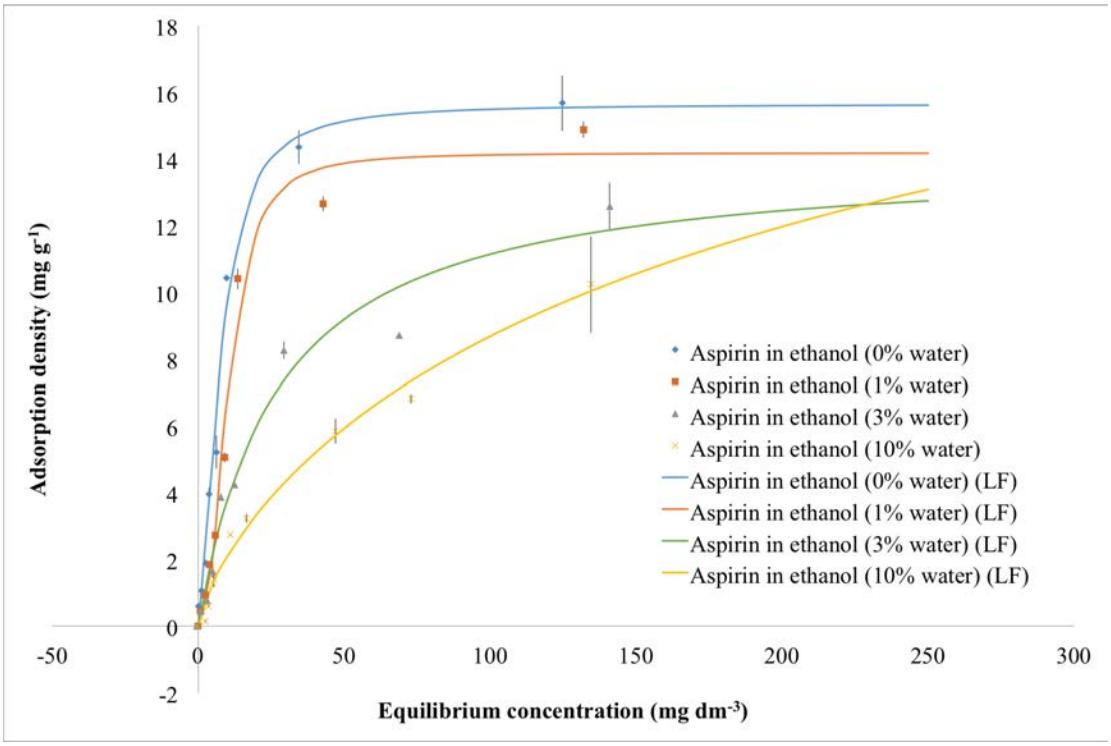

Figure 4.28: Aspirin in ethanol adsorption isotherms, conducted by an undergraduate final year applied chemistry student. The y-error bars are the standard deviations of three experimental replicates.

Table 4.11: Parameters for the isotherms describing the adsorption of aspirin onto FCC from ethanol and ethanol with 1%, 3%, and 10% water by volume.

Parameter	Ethanol	1 % water	3 % water	10 % water
Langmuir isotherm				
Γ_{max} (mg g^{-1})	18.00	17.69	14.22	14.52
K_L (dm^3 mg^{-1})	0.088	0.054	0.036	0.015
R^2	0.96	0.94	0.97	0.98
Freundlich isotherm				
K_F (dm^3 $\frac{1}{n}$ mg$^{1-\frac{1}{n}}$ g^{-1})	3.07	2.06	1.24	0.54
$\frac{1}{n}$	0.36	0.43	0.47	0.60
R^2	0.86	0.86	0.95	0.99
LF isotherm				
Γ_{max} (mg g^{-1})	15.64	14.18	14.06	26.73
K (dm^3 mg^{-1})	0.03	0.00	0.04	0.02
m	1.79	2.40	1.02	0.75
R^2	0.99	0.98	0.97	0.99

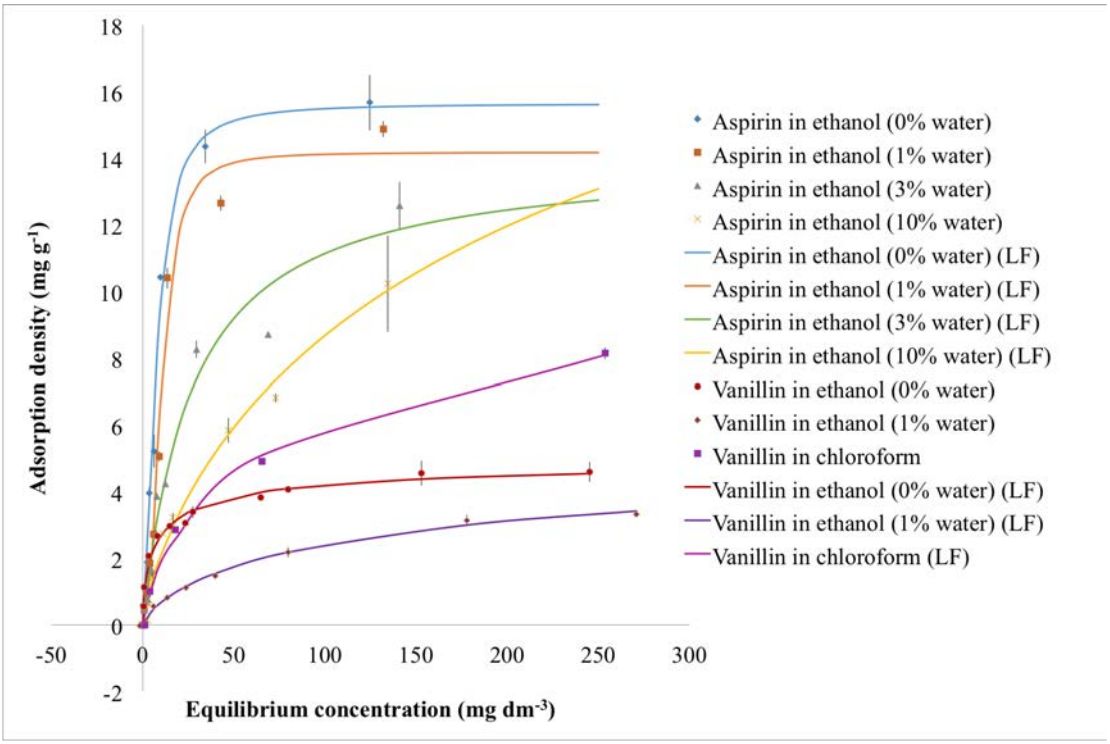

Figure 4.29: Aspirin in ethanol adsorption isotherms, conducted by an undergraduate final year applied chemistry student (Figure 4.28) plotted with the vanillin in ethanol and chloroform adsorption isotherms for visual comparison (Figure 4.26). The y-error bars are the standard deviations of three experimental replicates.

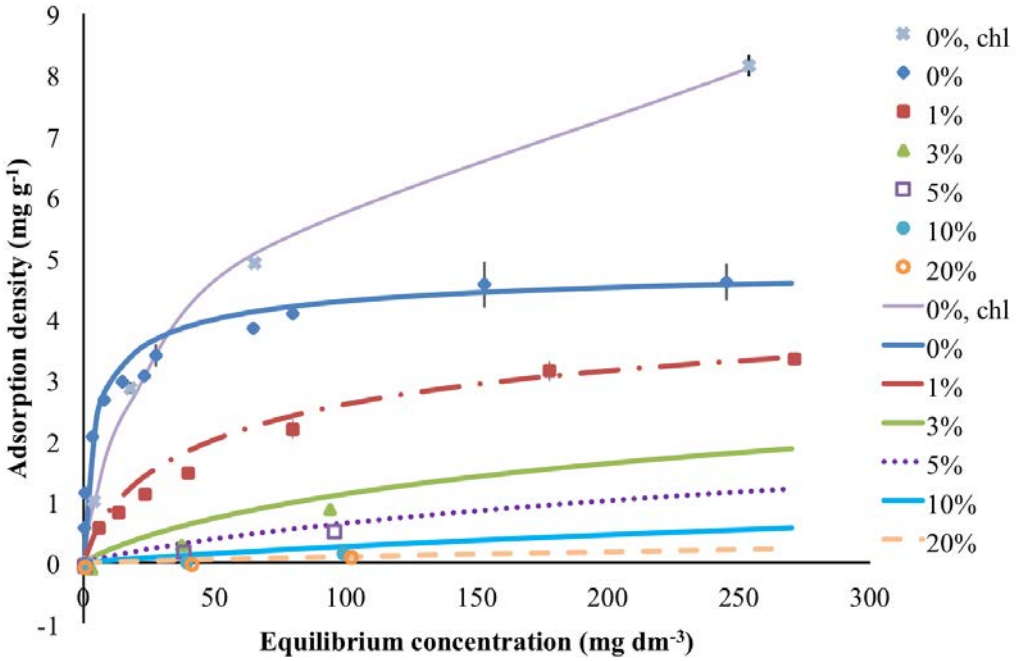

Figure 4.30: Vanillin adsorption from aqueous ethanolic solutions onto FCC with relative volumetric percentage of water as shown, adsorption from chloroform (chl), and corresponding Tóth isotherms.

4.26.

Figure 4.30 includes Tóth isotherm fits for the % of water with fewer points. The adsorption of vanillin onto FCC from aqueous ethanolic solutions is shown in Figure 4.30, for three replicates with error bars as shown. Also shown are the corresponding modified Tóth isotherms in Table 4.12.

The adsorption of aspirin onto FCC from ethanolic solutions with various relative concentrations of water is shown in Figure 4.31. Three different stock solutions were used, and up to seven replicates were measured for each c_{eq}, with error bars as shown, which correspond to one standard deviation (σ_{devn}). Also shown are the corresponding modified Tóth isotherms, (equation 4.6) which are discussed below. In this case, $m = 1$, i.e. the adsorption from pure ethanol follows a Langmuir isotherm.

The hydrophobic moieties associated with aspirin and vanillin may well play a role in the way they adsorb. Misra (1988) stated that 'a coupling agent possessing a hydrogen-bonding moiety could effectively interact with the adsorbed water on the apatite substrate.'

The agent will be easily displaced from the surface by water or any other hydrogen-bonding solvent if it does not possess hydrophobic moieties concomitantly with its hydrogen-bonding groups.

In ethanolic solutions, it is possible that the -OH functional group on the ethanol orders itself around the HAP surface, leaving the -CH_3 pointing away from the surface, thus creating effectively hydrophobic sites. As the aspirin or vanillin approaches the FCC

surface it can orientate itself so that hydrophobic interactions take place. Such speculation is supported by the observation that the use of relatively apolar chloroform (ε_r = 4.8) as a solvent increases the amount of vanillin adsorbed (Figure 4.30 and Table 4.12).

Greater insights into the adsorption process can be made by taking a more quantitative approach, firstly in terms of fractional surface coverage using the relation below, and then expressing it as a fraction of the total available surface area:

$$S_{ads} = \Gamma'_{max} \mathscr{N} \sigma \tag{4.14}$$

here Γ'_{max} is the maximum adsorption (Table 4.12) expressed in moles per gram of substrate, $\mathscr{N}$ is the Avogadro number, and σ is the effective cross-sectional area of the adsorbing cation on the surface of the substrate. Γ'_{max} is the asymptote of an imprecise extrapolation of the observed experimental data to infinite c_{eq}, and σ is also an estimate, so the equation can only give a very approximate estimate of surface coverage. Nevertheless, it can shed some light on the process occurring. Charnay *et al.* (2001) assumed $\sigma = 0.6$ nm^2.

Using equation 4.14, the surface area coverage of the vanillin molecule on FCC TP for each solvent used was calculated. The adsorption cross-sectional area was estimated by first measuring the volume of a known quantity of vanillin by helium pycnometry (Thermo Scientific Pycnomatic ATC). From this, the volume of one vanillin molecule was calculated, and the cross-sectional area of a vanillin molecule was inferred, assuming that each molecule is spherical in shape. The cross-sectional area of a vanillin molecule calculated in this way was 4.36 $\times$ 10^{-19} m^2. It follows that the calculated surface covered of FCC TP by vanillin adsorption from ethanol was 9.53 m^2 g^{-1}, which is around 17 % of the overall FCC TP surface area (Table 3.1). For adsorption from chloroform the surface coverage was calculated to be 26.33 m^2 g^{-1}, which is 48 % of the FCC's surface area.

Using equation 4.14, the surface area coverage of the aspirin molecule on FCC TP for each solvent used was calculated. The adsorption cross-sectional area was estimated by first using the density of aspirin as reported by Sun (2004), and using that to calculate the volume of an aspirin molecule, assuming that each molecule is spherical in shape. The cross-sectional area of an aspirin molecule calculated in this way was 4.31 $\times$ 10^{-19} m^2. It follows that the calculated surface covered of FCC TP by aspirin adsorption from ethanol was 21.64 m^2 g^{-1}, which is 39 % of the overall FCC TP surface area (Table 3.1).

According to Schatzberg (1967), the molecular diameter of water is approximately 0.25 nm; treating each water molecule as a sphere, the cross-sectional area of a water molecule is 4.91 x 10^{-20} m^2. The lowest percentage of water used in an adsorption experiment was 1 %. This occupied 0.25 cm^3 of the total solvent volume of 25 cm^3 used in the adsorption experiment, which equates to 8.36 $\times$ 10^{21} molecules of water. Multiplying this by the cross-sectional area of a water molecule, the total cross-sectional surface area of the water molecules in the system was approximately 410 m^2. The surface area of 0.2 g of FCC TP, calculated from the value in Table 3.1, used in each

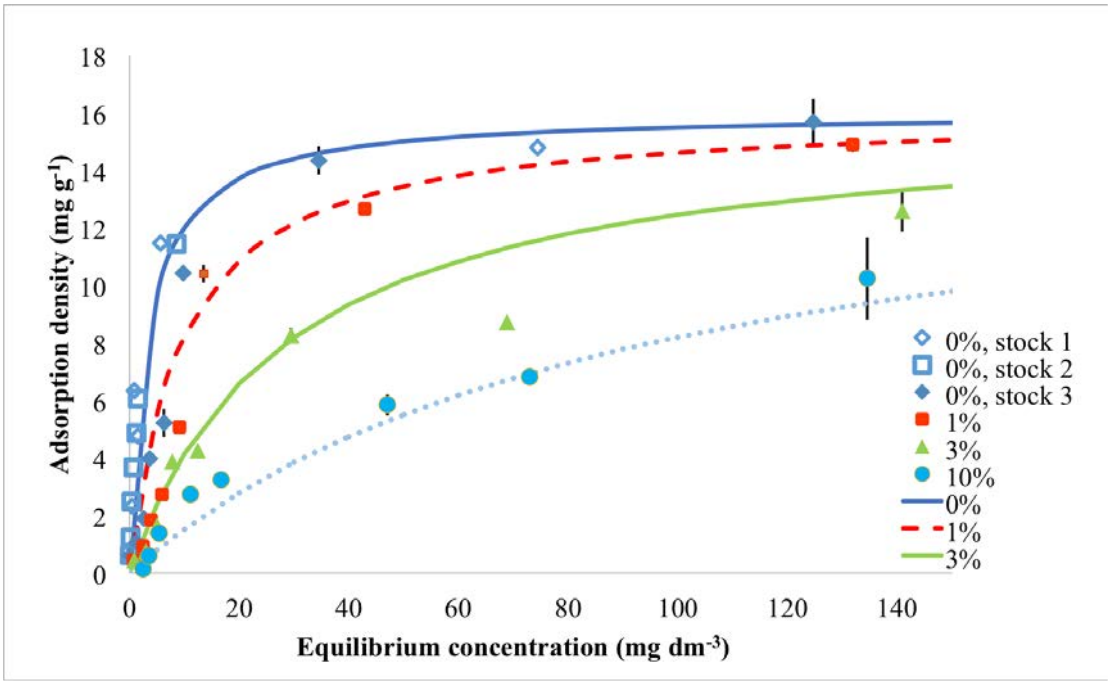

Figure 4.31: Aspirin adsorption from aqueous ethanol solutions onto FCC with relative volumetric percentage of water as shown, from three different stock solutions, and corresponding Tóth isotherms.

adsorption experiment had a surface area of only 11 m^2. It is apparent from these calculations that there is more than enough water in the experiments to cover the entire surface of the FCC. Therefore, the water does not simply competitively inhibit the vanillin adsorption.

It is assumed that the adsorption process must be analogous for both aspirin and vanillin when quantitatively explaining the effect of water on the Tóth adsorption isotherms. In the presence of water, the second derivative of the adsorption with respect to c_{eq} (i.e. curvature of the isotherm) reduces, and in the case of vanillin becomes negative as the relative water content is increased (Figures 4.30 and 4.31). As shown in these figures, it is found that to a realistic level of approximation:

$$f'(c_{eq}) = c_{eq}\left(\frac{A}{[H_2O]}\right)^B \tag{4.15}$$

with the parameters shown in Table 4.12. Furthermore, it is found that there is no effect of water on Γ_{max}, i.e. $f'' = 1$. Therefore it is confirmed that the added water is not reducing the number of adsorption sites, in agreement with the calculation above. Instead, the results can be satisfactorily explained by assuming that there is a reduction in the effective flux of adsorbate reaching the FCC surface, caused by a stagnant layer of water trapped within the FCC microporosity (Figure 4.32). The orientation of the ethanol, described above, creates sites or zones which are effectively hydrophobic, shown as x in Figure 4.32.

Table 4.12: Tóth isotherm parameters derived from equations 4.5, 4.6, and 4.15.

Adsorbate	Aspirin	Vanillin	Vanillin	BTMAB
Substrate	FCC	FCC	FCC	talc
Solvent	Aqueous ethanol	Aqueous ethanol	Chloroform	Water
Γ_{max} (mg g^{-1})	16.0	5.0	15.3	25.8
K_L (dm^3 mg^{-1})	0.3	0.57	0.028	11.35
m	1.0	0.58	0.50	0.25
A	0.0035	0.0020	-	-
B	0.7	1.7	-	-

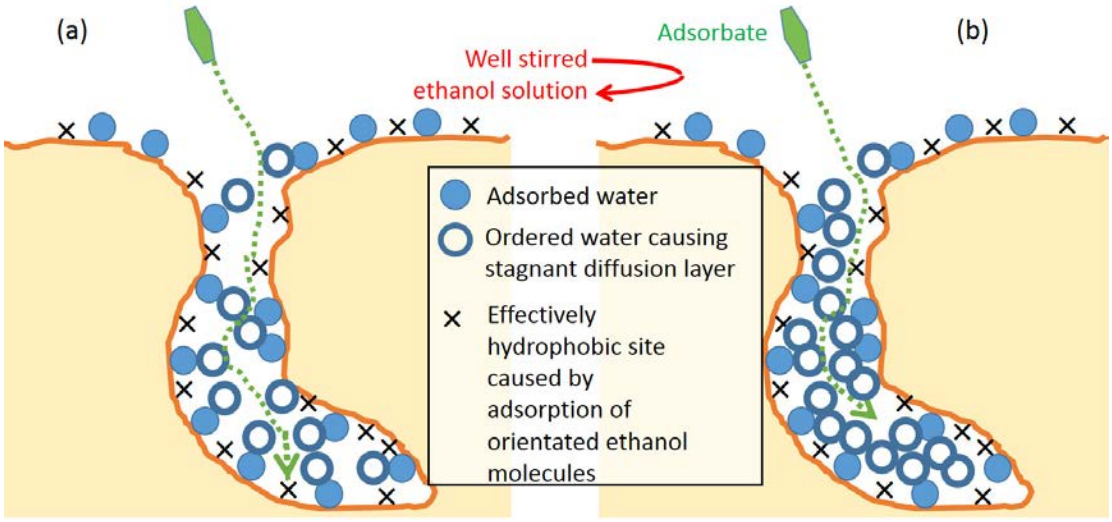

Figure 4.32: Schematic diagram, not to scale, of the postulated mechanism for the adsorption of aspirin and vanillin onto FCC in the presence of (a) lower and (b) higher relative concentrations of water.

Crank (1975) in his Figure 4.2 shows that as time increases, then for the flux Q_t at time t through a stagnant diffusion layer of thickness l, Q_t/lc_1 becomes linearly proportional to Dt/l^2, and therefore at constant diffusion coefficient D and bulk solution concentration c_1, $Q_t \propto l^{-1}$ as $t \to \infty$. If the thickness of this diffusion layer was directly proportional to the water concentration, then $Q_t \propto [H_2O]^{-1}$. In practice, it is found that Q_t reduces approximately as $[H_2O]^{-0.7}$ for aspirin and $[H_2O]^{-1.7}$ for vanillin (Table 4.12). Inspection of Figure 4.31 shows that at higher c_{eq}, the adsorption density Γ does not follow the perturbed Tóth isotherm exactly (equation 4.6). These discrepancies, and the fact that the exponents are not in unity, are to be expected because the aqueous diffusion layer exists within a random tortuous mesoporosity (Levy *et al.*, 2015), rather than being in the form of a stable planar layer.

4.4 Conclusions & future work

The hypotheses postulated in this chapter are as follows:

- **1:** FCC, because of its predominantly negatively charged surface, will adsorb small but significant amounts of cationic species.
- **2:** Sparingly soluble (dissolved) species will adsorb to a greater extent onto the FCC than strongly soluble (dissolved) species.
- **3:** The nature of the adsorbing surface of FCCs can be elucidated by studying different adsorption characteristics from a range of different adsorbates and solvents.

FCC does not adsorb from the aqueous systems utilised in this project, but it does adsorb from the ethanolic solutions. Hypothesis 2 is proven to a degree in that saccharin in HEPES and anethole in ethanol, both of which are extremely soluble and miscible, respectively, in their selected solvents, did not adsorb to the FCC. On the other hand, vanillin and aspirin, which have a limited solubility in their selected solvents, did adsorb.

The mechanism of adsorption of two typical actives were investigated in order to deduce information about the nature of the FCC surface. The adsorbates were the flavour compound vanillin and the anti-inflammatory drug aspirin from chloroform and aqueous ethanolic solutions, and a mechanism for the adsorption can be deduced which is quantitatively supported both by calculations of surface coverage and by the effect of water on the shapes of the adsorption isotherms. There is indirect evidence from the quantitative perturbation of Tóth isotherms that their adsorption is hindered by a stagnant diffusion layer of water trapped in the microporosity of the FCC. This proves hypothesis 3 to some extent.

Similarly sized particles of GCC were used as a (null) control adsorbent. Finnish talc with a high surface area was used as a control to check the methodology of measuring the (null) adsorption of BTMAB onto FCC.

To complement previous studies of the surface of FCC, it was also tested with the cationic probe BTMAB and the anionic probe Na2NS. FCC does not adsorb these species from aqueous solution, this disproving hypothesis 1. Unlike talc, which has a surface that can be characterised by the adsorption of BTMAB, the surface of FCC is amphoteric and characterisation of adsorption sites is much more elusive.

The understanding of the mechanism of adsorption opens the way for innovative, tailored loading of actives onto FCC. It suggests that during controlled release (Levy *et al.*, 2015), adsorption effects need not be taken into account. Additionally it is shown that there will be no interference with functional groups of the active, and the flavour or drug will be delivered without alteration of its efficacy or activity.

Chapter 5

The loading of functionalised calcium carbonate (FCC)

THIS chapter describes the process by which anethole, saccharin, and vanillin were attempted to be loaded into the pores of FCC.

5.1 Introduction

The aims of the work outlined in this chapter were to investigate the loading of flavour into the pores of the FCC, which can then be used in subsequent diffusion experiments. Various loading techniques were trialled. Eventually, the FLC can then be used to quantify the amount of flavour loaded into the pores of the sample, thus creating a novel use for the FLC (see Chapter 7 for more information), and would be used in conjunction with other characterisation techniques for the quantification.

Several candidates were considered when it came to flavour selection, such as artificial sweeteners like aspartame, flavours such as cinnamic acid, oils like geraniol, and drugs or drug analogues such as theobromine, salicylic acid, benzocaine, acetyl salicylic acid, and L-ascorbic acid.

Much of the experimental work in this project started with anethole as the primary flavour compound, simply because it has very interesting properties and generates the Ouzo effect, which were kept in mind for future experimental work (see Chapter 9). However, the low melting point of anethole meant that it would be difficult to keep in the pores of the FCC at room temperature, and so a sample that is solid at room temperature needed to be considered. Vanillin and saccharin were decided to be used because they are both compounds that have been involved in other work throughout this project; the former is very soluble in ethanol and the latter in water.

This leads to the formation of the first hypothesis of this chapter (hypothesis 4): the extent to which a flavour or drug compound can be physically loaded into the void volumes of FCC can be quantified by directly observing the loaded FCC by scanning electron microscopy (SEM).

5.2 Materials & methods

5.2.1 Flavours & sweeteners

The *trans*-anethole, sodium saccharin, and vanillin were the flavour compounds utilised throughout the work outlined in this chapter. The information for each compound and solvent can be found in Chapter 3.

5.2.2 FCCs and minerals

FCC 02, 03, 06, 07, 12, 13, TP, and SFC 06.2 were used in the loading experiments, along with GCC and HAP. Their properties and other information are listed in Chapter 3.

5.2.3 Anethole loading

This section describes three attempts made, using two procedures, in loading anethole into FCC SFC 06.2. Three experimental replicates from each batch were analysed in the ZLC (please see Chapter 7 for the results and method). FCC SFC 06.2 was received from Omya International AG in 2011 along with four other FCC samples, and of these samples FCC SFC 06.2 had the mid-range particle size.

Batch 1 To prepare batch 1 of anethole loaded FCC, an accurately known amount of approximately 5 g of FCC was weighed into a glass beaker with a screw cap. Approximately 100 cm^3 of a solution with a concentration of 2.9 mg dm^{-3} of anethole in ethanol were added into the beaker. The contents of the beaker were left to equilibrate for approximately 5 hours (340 minutes). The FCC was then filtered using a Büchner filtration kit with a glass microfibre filter paper (Whatman, grade GF/F), and the remaining wet FCC was transferred to a plastic bottle, freeze-dried, and re-weighed. There was a small loss of sample during the filtering process.

Batch 2 The preparation of batch 2 involved weighing an accurately known amount of approximately 5 g of FCC into a 50 cm^3 plastic centrifuge tube, into which 40 cm^3 of a 2.9 mg of anethole per dm^3 of ethanol solution was pipetted into each. The tubes were left to equilibrate for approximately 5 hours (330 minutes) before being centrifuged at 3,000 rpm, after which the supernatant was decanted and disposed, and the remaining FCC was freeze-dried and weighed.

Batch 3 The preparation of batch 3 was exactly the same as batch 2, however, the lids of the centrifuge tubes of batch 3 were blown off during the freeze-drying process, and there was a small loss of sample.

The freeze-drier used throughout was an Edwards Freeze Dryer Modulyo.

5.2.4 Vanillin loading

This section describes two methods used to load vanillin into a variety of FCCs.

Vanillin loading via solvent evaporation Drug loading trials into FCC conducted at the University of Basel used drug loads of 25, 30, 35, 40, 45, and 50 %, of which 35-40 % was the maximum drug load (DL) that could be used without any agglomerates forming (Preisig *et al.*, 2014). They concluded that above this level, the intraparticle pores cannot be filled any further because the interparticle voids also begin to fill, thus causing the formation of agglomerates. Agglomerates are undesirable because they may have a negative effect on drug-release properties, thus making it necessary to determine the drug-loading capacity by a qualitative and systematic method, such as SEM image analysis (Preisig *et al.*, 2014). Equations 5.1 and 5.2 can be used to

calculate the drug load based on mass/mass (w/w) percent ratios of drug to FCC:

$$\mathrm{DL} = \omega_\mathrm{D} \times 100 \tag{5.1}$$

$$\omega_\mathrm{D} = \frac{m_\mathrm{D}}{m_\mathrm{D} + m_\mathrm{FCC}} \tag{5.2}$$

where ω_D is the flavour to weight ratio, m_D is the mass of drug used, and m_FCC is the mass of FCC used.

According to equations 5.1 and 5.2, 0.8 g of vanillin loaded into 1.2 g of FCC will yield a 40 % load. A 50 cm^3 round-bottomed flask (Glassco, Boro 3.3, with a 14/23 opening for glass stoppers) was tared on a Mettler Toledo XP504 Analytical Balance, into which 1.2 g of FCC were weighed. A 25 cm^3 volumetric flask was tared on the balance, into which 0.8 g of vanillin were weighed, before being topped up to the mark with ethanol. The more precise weights of the different grades of FCC and vanillin used are displayed in Table 5.1. The contents of the volumetric flask were poured into the round-bottomed flask, which was then placed in a 150 cm^3 beaker filled with water, which was subsequently suspended and immersed in the water of a sonic bath. The flask and its contents were sonicated for approximately 5-10 minutes. After sonication, the flask underwent rotary evaporation using a Büchi Vacuum Controller V-855 (171-173 mbar), Büchi Rotavapor R-215 (105 rpm), and a Büchi Heating Bath B-491 (set to 45°C) until the solvent had evaporated. The contents of the round-bottomed flasks were left to air dry overnight to evaporate the remaining ethanol. The product (i.e. loaded FCC) was scraped out using a glass rod into a ceramic mortar (Royal Worcester), and the FCC was loosely milled with a pestle, made of the same material as the mortar, before being transferred to a 180 μm stainless steel mesh filter assembly (BS410-1:2000, aperture: 180 MIC, serial no: 0307283, Fisherbrand). Once the FCC was sieved, it was transferred to a small glass sample pot and weighed. The loaded FCC was stored in a desiccator.

Table 5.1: The weights of vanillin and FCC used for loading experiments via rotary evaporation to make a 40 % vanillin load in each mineral.

FCC	Weight of FCC (g)	Weight of vanillin (g)
FCC 02	1.2073	0.8070
FCC 03	1.2001	0.8061
FCC 06	1.2055	0.8142
FCC 07	1.2075	0.8091
FCC 12	1.2090	0.8083
FCC 13	1.2060	0.8025

Vanillin loading quantification attempt Upon visual inspection of the loaded FCC micrographs, it was concluded that FCC 02, 03, and 06 may have successfully been

loaded with vanillin (Figure 5.5). Therefore, these three samples were analysed via UV-visible spectroscopy in an attempt to quantify the amount loaded.

The vanillin loaded into the pores of FCC 02, 03, and 06 was attempted to be quantified using UV-visible spectroscopy. 0.01 g of FCC was weighed into a plastic centrifuge tube and 25 cm^3 of ethanol, measured with a glass measuring cylinder, was added. The centrifuge tube was placed on a Stuart SSL2 reciprocating shaker for 1 hour at 205 strokes per minute (20 mm orbit amplitude), and one experimental replicate was performed per grade of FCC whose pores were established as filled. A bulb pipette was used to pipette 5 cm^3 of the supernatant in a 50 cm^3 volumetric flask to dilute the supernatant ten-fold. The supernatant was then analysed via UV-visible spectroscopy with a Hewlett Packard (now Agilent) 8452 UV-visible spectroscopy system.

Vanillin loading using the incipient wetness impregnation (IWI) technique The incipient wetness impregnation (IWI) technique was used to load vanillin into FCC 13 in preparation for the basic release experiments outlined in Chapter 6. IWI involves mixing or agitating the powder to be loaded with flavour or drug while pipetting or spraying the liquid onto it. The amount of liquid must be equal to the volume of the pores of the sample, and therefore capillary action, rather than diffusion, will draw the liquid into the pores. The calculations for the IWI technique are based on volume/volume (v/v) equations.

The first step in the loading of vanillin into the FCC pores was to calculate the intraparticle voidage of FCC 13. The volume of 100 g of FCC 13 including its pores was determined to be 260 cm^3, and was calculated using the envelope density value of 0.3843 g cm^{-3}. The intraparticle porosity value of the FCC (Chapter 3) was then used to then determine the volume of intraparticle pore space of FCC 13; this was determined to be 96 cm^3 per 100 g.

The next step was to calculate the amount of vanillin that can fit inside the intraparticle pore space, and this was achieved by multiplying the skeletal density of vanillin with the previously calculated intraparticle pore space; it was calculated that 112 g of vanillin can fit into the pores of 100 g of FCC 13. This value was then multiplied by the solubility of vanillin in ethanol to obtain the amount of vanillin dissolved in ethanol that will fit into the pores of FCC 13, which was 4.8 g. This equates to a 4.3 % load.

Therefore, when 95 cm^3 of a 50 g dm^{-3} vanillin in ethanol solution is introduced to 100 g of FCC 13, the pores will be loaded with a load of approximately 4 % vanillin by volume. And so, for every 100 g of FCC there will be 203 mg of vanillin.

These experiments loaded 10 g of FCC 13 at a time, and so 10 cm^3 of a 50 g dm^{-3} vanillin in ethanol solution was used to load vanillin into its pores.

The first attempt at using the IWI technique to load vanillin into the pores of FCC 13 involved taring a 50 cm^3 glass volumetric flask on a Mettler Toledo Analytical Balance, and weighing in 2.5 g (2.3791 g) of vanillin. Ethanol was added to half of the volume of the flask, the vanillin was dissolved, and ethanol was then used to top the rest of the flask up until the mark on it was reached. A 250 cm^3 glass beaker was tared on the same balance, and 10 g (10.0513 g) of FCC 13 was weighed into it. A Humbrol airbrush powered by a GoSystem 2175 Butance Propane Mix Gas cartidge fitted with Standard

Type EN 417 Threaded Self-Sealing Safety Valve was used to spray the FCC powder with 10 cm^3 (measured out using a glass measuring cylinder of the same volume) of the vanillin in ethanol solution in a fume cupboard. Unfortunately, the airbrush caused the FCC to blow out of the beaker, as expected, because it was a powerful spray and had no sensitivity setting. Also, the airbrush is too awkward to use with the small volumes of vanillin in ethanol solution utilised because it has to be angled so that the reservoir of the airbrush is perpendicular to the floor, thus making it impossible to angle the spray so that it is sprayed directly onto the FCC.

The second attempt involved weighing 10 g (9.6955 g) of FCC 13 into a 1 dm^3 glass conical flask that was tared on an Mettler Toledo XP504 Analytical Balance. The same measuring cylinder as from the previous IWI technique attempt was used to measure out 10 cm^3 of the vanillin in ethanol solution into a 60 cm^3 plastic spray bottle (Superdrug). Approximately 5 cm^3 of the solution was sprayed onto the FCC before stopping; this was because the solution sprayed the sides of the flask rather than all of it being sprayed directly onto the FCC. Therefore, the rest of the solution inside the spray bottle was simply poured onto the FCC. The flask was then stoppered and everything was shaken by hand in order to attempt to cover the FCC with the vanillin in ethanol solution. The stopper was removed and the ethanol was left to evaporate for 5 hours and 45 minutes. As much loaded FCC as possible was transferred to a clean glass beaker. The total weight of the loaded FCC was 16.9911 g, of which 7.2956 g was vanillin; therefore, per 100 g of loaded FCC 13 there was 75.25 g of vanillin. This vanillin loaded FCC 13 was used for subsequent release experimental trials outlined in Chapter 6.

5.2.5 Saccharin loading

This section describes two methods used to load saccharin into a variety of FCCs; one method was then subsequently altered very slightly.

Saccharin loading via solvent evaporation Upon further reflection, it was decided that no more than 30 or 35 % of saccharin was to be loaded into the FCC in order to lower the chance of agglomerate formation, however, that was then reduced to no more than 25 % in order to err on the side of certainty. To yield a 25 % load, according to equations 5.1 and 5.2, 1.7 g of saccharin will need to be loaded into 5 g of FCC.

A 50 cm^3 round-bottomed flask (Glassco, Boro 3.3, with a 14/23 opening for glass stoppers) was tared on a Mettler Toledo XP504 Analytical Balance, in which 5 g of FCC and 1.7 g of saccharin were weighed. Figure 5.1 shows an image during the weighing of these components. A 25 cm^3 glass bulb pipette ($\pm$ 0.06 cm^3, Fisherbrand FB50179, Class C, Ex 20°C, ISO648 – BS1583, DIN 12690, 2005) was used to pipette 25 cm^3 of ultrapure water into the flask. The flask was then placed in a 150 cm^3 beaker filled with water, which was subsequently suspended and immersed in the water of a sonic bath (Fisher Scientific FC15050). The saccharin, ultrapure water, and FCC were sonicated for approximately 5-10 minutes.

After sonication, the flask underwent rotary evaporation for 3-4 hours, using a Büchi Vacuum Controller V-855 (171-173 mbar), Büchi Rotavapor R-215 (105 rpm), and a Büchi Heating Bath B-491 (set to 75°C); Figure 5.2 shows this set up. Unfortunately,

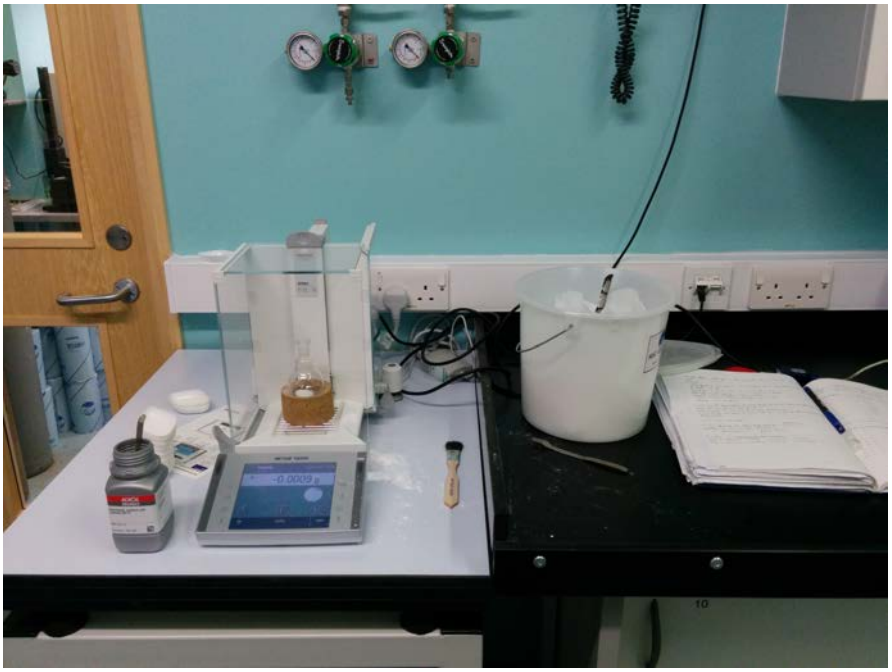

Figure 5.1: Weighing FCC and saccharin into a round-bottomed flask; ready to load saccharin into the pores of the FCC.

this method of evaporating the water did not work, as the water was condensing before reaching the trap in the rotary evaporator and falling back into the flask. Some samples dried when the temperature was turned up, such as the GCC and HAP, but this caused a loss of sample as a lot of it ended up in the trap.

Saccharin loading via an oven method After trial and error, an oven loading method was developed. This involved weighing in 1.7 g saccharin into a beaker, whose weight is known, along with 5 g of FCC. The beaker and its contents were put in an oven (Thermo Scientific Heraeus) set to 105°C for 24 hours to remove any moisture. The beaker and its contents were left to cool and then reweighed. A 25 cm^3 glass bulb pipette was used to pipette 25 cm^3 of ultrapure water into the beaker, which was then covered with a plastic paraffin film. The beaker and its contents were sonicated in a water bath (Branson B3510 Ultrasonic Cleaner) for approximately 5 minutes, before being placed back in the oven, uncovered, for another 24 hours. The beaker and its contents were then left to cool and reweighed. The product (i.e. loaded FCC) was scraped out using a glass rod into a ceramic mortar, and the FCC was loosely milled with a pestle, made of the same material as the mortar, before being transferred to a 180 μm stainless steel mesh filter assembly (BS410-1:2000, aperture: 180 MIC, serial no: 0307283, Fisherbrand). Once the FCC was sieved, it was transferred to small glass sample pot and weighed. The loaded FCC was stored in a desiccator.

While the saccharin in water solution was evaporating in the oven, the beakers were swirled by hand every 15 minutes until the water level had decreased enough so that it was in line with the FCC level to ensure that the solution and FCC were homogenised. The beakers that were not swirled are labelled as 'no mix,' and can be seen in various

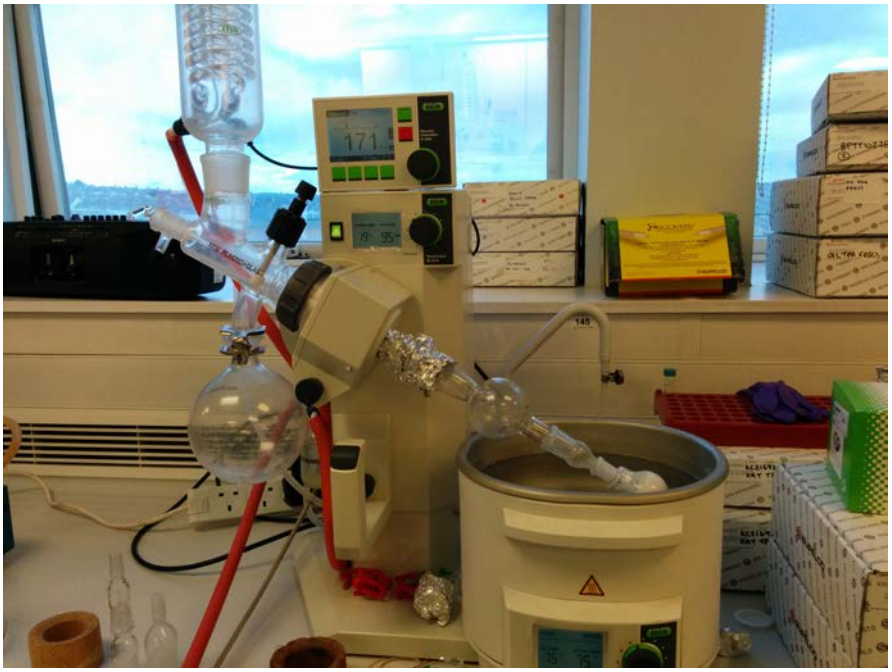

Figure 5.2: A round-bottomed flask with saccharin, FCC, and ultrapure water undergoing rotary evaporation.

SEM images in Figures 5.6 and 5.7; this was to investigate whether swirling the beakers had any apparent effects on loading.

Saccharin loading via an oven method (no sieving) It was later decided not to sieve the loaded FCC for two reasons: 1) as a time-saving step, and 2) for fear of breaking up any agglomerates rendering them undetectable during SEM analysis, thus making it difficult to determine whether the FCC had been successfully loaded or not. The beakers, whilst drying in the oven, were not swirled at all.

5.2.6 Scanning electron microscopy (SEM) analysis

The loaded FCC was analysed via SEM in order to visually determine if the saccharin and vanillin had been loaded successfully. The qualitative estimation of flavour loading efficiency in this work will loosely follow that of Preisig *et al.* (2014), in that “excellent" or successful loading is assumed if no separate flavour crystals or agglomerates can be detected.“Poor" or unnsuccessul loading is when numerous agglomerates and separate flavour crystals are detected. Figure 5.3 gives example SEM images of the successful and unsuccessful loading criteria.

The FCC loaded with vanillin via rotary evaporation was covered with a gold coating using a Quorum EMITECH K550X Sputter Coater before images were taken of the surface using a JEOL JSM-6610LV Scanning Electron Microscope. The FCC loaded with saccharin using the oven method (both sieved and non-sieved samples) were twice covered with gold using a Q150T Turbo-Pumped Sputter Coater/Carbon Coater, and images of the surface were taken using a JEOL JSM-7001F Field Emission Scanning Electron Microscope.

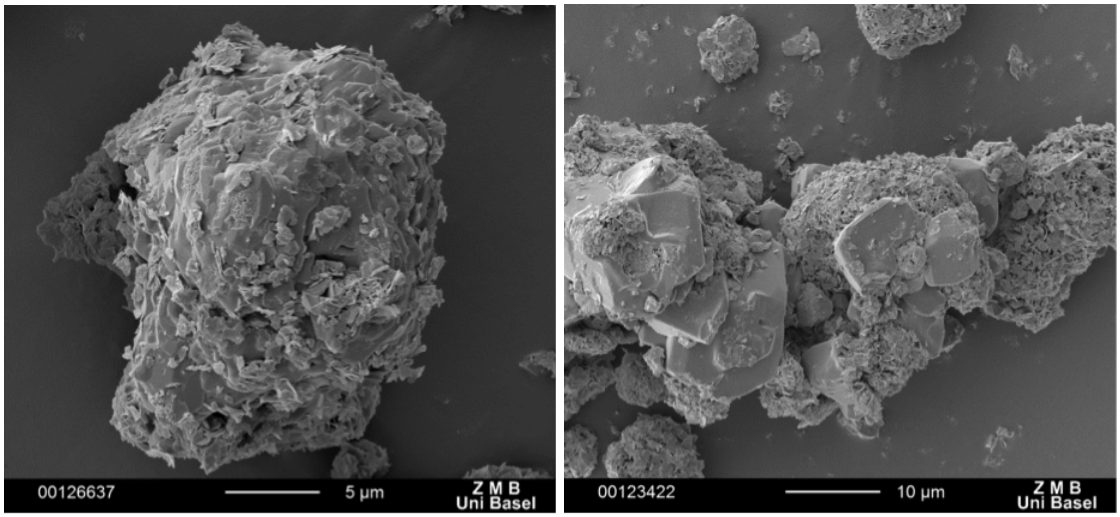

(a) Successfully loaded FCC particle; scale bar = 5 μm.

(b) Unsuccessfully loaded FCC particle; scale bar = 10 μm.

Figure 5.3: SEMs of a succesfully and an unsuccessfully loaded FCC particle. The images were provided via personal communications with the Pharmaceutical Technology research group at the University of Basel, Switzerland, and were part of a research project commissioned by Omya International AG.

5.2.7 Scanning electron microscopy (SEM) elemental analysis

The JEOL JSM-7001F Field Emission Scanning Electron Microscope was used to perform elemental analysis on saccharin-loaded FCC 13 and FCC 02 (using the oven method, not sieved) after they were twice coated with carbon using a Q150T Turbo-Pumped Sputter Coater/Carbon Coater. This enabled the qualitative detection of certain elements that are only present in the saccharin molecule on the inside or outside of the visible FCC pores.

5.2.8 Density measurements

A Thermo Scientific Pycnomatic Automatic Temperature Control (ATC) helium pycnometer was used to measure the skeletal density of various loaded and unloaded FCC samples. The final reported density measurement is an average of at least 5 analytical replicates in the instance where each measurement is within 0.05 % of each other. A maximum of 20 analytical replicates were taken.

A Micromeritics GeoPyc 1360 Envelope Density Analyzer was used to measure the envelope density of various loaded and unloaded FCC samples. The sample chamber diameter was 12.7 mm and a consolidation force of 28 N was used. The final reported density measurement is an average of 10 analytical replicates. Please see section 3.2.1.1 of Chapter 3 for more details about this technique.

5.2.9 Particle size distribution (PSD) measurement of DryFlo

A Malvern Mastersizer 2000 G was used to measure the particle size distribution (PSD) of the DryFlo powder, which is used for density measurements in the Micromeritics GeoPyc 1360 Envelope Density Analyzer (please see Chapter 3 for a description of the experimental technique). This was done by taring a 250 cm^3 plastic Nalgene bottle on a Mettler Toledo XP504 Analytical Balance and weighing in approximately 40 g of DryFlo. A 100 cm^3 glass bulb pipette was used to pipette 200 cm^3 of ultrapure water into the beaker to make a solution with approximately 20 % DryFlo content. The bottle was placed sideways on a Stuart SSL2 reciprocating shaker at 205 spm for 30 minutes. Just before analysis in the particle size analyser, a Fisherbrand MiniMax Magnetic Stirrer was used to keep the DryFlo in suspension in the plastic bottle. The instrument measured the static light scattering of the DryFlo particles dispersed in water, interpreted using the Mie approximation, using a refractive index of 2.42 and the absorption index was estimated and set to 0.1.

5.2.10 MIP analysis

MIP was conducted on saccharin loaded (using the oven-drying method without sieving) and unloaded FCC 13, and was used as another tool to indirectly indicate whether the pores are filled or if the saccharin has recrystallised outside of the FCC. The experiments were carried out with a PASCAL 140 and a PASCAL 440 mercury porosimeter (Thermo Fisher Scientific, Italy), allowing intrusion to be measured from just above vacuum to 400 MPa applied pressure.

5.3 Results & discussion

5.3.1 Anethole loading

The characterisation of the anethole loaded FCC was made using the ZLC, and is discussed in Chapter 7.

An alternative way of loading liquids and oils into the FCC is by using the oil absorption method. The technique was demonstrated at Omya International AG (Oftringen, Switzerland), and it was advised that 1 cm^3 of oil is added to 10 g of GCC or only 1-5 g of FCC (due to its porous nature). A palette knife is then used to combine and mix the two; drops of oil are then added and mixed in each time until the mineral, when flattened on the non-porous surface on which it is being homogenised, curls at the edges when the palette knife is dragged through it. If the mineral flakes, rather than curls, then it is not deemed as fully saturated. Equation 5.3 shows how to calculate the oil number of a mineral.

$$\text{oil number} = \frac{\text{amount of oil} \times \text{density of solid}}{\text{weight of solid}} \times 100 \tag{5.3}$$

5.3.2 Vanillin loading

Vanillin loading via solvent evaporation Figure 5.5 in section 5.3.4 shows the SEMs of the vanillin loaded samples as well as their interpretation.

Vanillin loading quantification attempt FCC 02, 03, and 06 were loaded with 40 % vanillin and analysed via UV-visible spectroscopy to determine the actual % loading. The results vary significantly and suggest that in most cases, a loading of 40 % of vanillin inside of the FCC pores has not been achieved: it was determined that FCC 02 was filled with 0.3 % vanillin, FCC 03 was 58 % loaded, and FCC 06 was 29 % loaded. It is plausible that FCC 06 may have been loaded with 20 % vanillin, and that may be the maximum vanillin capacity for that particular grade. However, the very small amount of vanillin present from FCC 02 suggests that the vanillin did not enter the pores during loading. And the 58 % load of FCC 03 is not possible, because no more than 40 % worth of vanillin to be loaded was added to the experimental matrix. The reason for a high amount of vanillin may be attributed to UV-visible spectroscopy discrepancies in the detection of such small concentrations. To be certain, more experiments have to be conducted.

Vanillin loading using the incipient wetness impregnation (IWI) technique Please see Chapter 6 for the experimental release trial results.

5.3.3 Saccharin loading

Saccharin loading via solvent evaporation Loading saccharin using the solvent evaporation method had its difficulties. These are attributed to having to use water as the solvent, which required a high water bath temperature when using the rotary evaporator therefore increasing the likelihood of bumping. Regardless of how long the flasks were rotary evaporating, the water appeared to be condensing before reaching the trap, thus falling back into the flask.

Saccharin loading via an oven method The first attempt at loading using the oven method resulted in unaccountable discrepancies in the pre- and post-loading and drying FCC weights because the FCC was not dried beforehand. The whole procedure was repeated again, however, the FCC was dried beforehand, and the results are displayed in Table 5.2.

Table 5.2: The weights of FCC being loaded with saccharin, using the oven drying method, throughout the loading procedure.

Round-bottomed flask ID	Weight of beaker (g)	Weight of saccharin (g)	Weight of FCC (g)	Weighed total weight (g)	Weight after 24h in oven (g)	Weight discrepancy (g)	Weight of beaker after H2O addition (g)	Weight of beaker after evaporation (g)	Amount of loaded sample (g)	Yield (%)
Control 1	65.15	1.70	n/a	66.85	66.61	0.24	91.66	66.66	1.51	88.74
Control 2	72.26	1.70	n/a	73.96	73.71	0.25	98.78	73.72	1.46	85.95
Control 3	82.25	1.70	n/a	83.96	83.71	0.24	108.75	83.71	1.46	85.98
Blank 1 (GCC)	84.73	n/a	5.04	89.77	89.76	0.01	114.78	89.77	5.04	99.90
Blank 2 (GCC)	78.09	n/a	5.02	83.11	83.10	0.01	108.15	83.11	5.02	99.90
Blank 3 (GCC)	76.27	n/a	5.07	81.34	81.33	0.01	106.33	81.33	5.06	99.88
HAP 1	63.53	1.71	5.10	70.34	69.98	0.35	95.043	69.95	6.42	94.27
HAP 2	76.30	1.70	5.02	83.023	82.68	0.35	107.76	82.64	6.34	94.23
HAP 3	83.65	1.70	5.04	90.39	90.03	0.36	115.10	90.00	6.35	94.24
GCC 1	76.51	1.71	5.02	83.245	83.00	0.24	108.11	83.00	6.49	96.35
GCC 2	73.79	1.70	5.02	80.53	80.28	0.24	105.32	80.28	6.49	96.40
GCC 3	69.76	1.70	5.03	76.46	76.22	0.25	101.27	76.22	6.46	95.94
FCC TP 1	77.83	1.70	5.08	84.62	84.28	0.34	109.28	84.24	6.41	94.46
FCC TP 2	77.38	1.71	5.06	84.15	83.81	0.34	108.85	83.78	6.39	94.46
FCC TP 3	83.61	1.70	5.05	90.36	90.04	0.33	115.05	89.99	6.38	94.48
FCC 02 1	75.69	1.70	5.02	82.42	82.08	0.34	107.10	82.04	6.35	94.46
FCC 02 2	76.76	1.70	5.03	83.50	83.16	0.34	108.19	83.16	6.35	94.37
FCC 02 3	85.00	1.71	5.07	91.78	91.44	0.34	116.49	91.40	6.40	94.38
FCC 03 1	82.95	1.70	5.05	89.70	89.42	0.28	114.40	89.41	6.46	95.72
FCC 03 2	77.60	1.70	5.06	84.36	84.08	0.28	109.10	84.07	6.48	95.73
FCC 03 3	86.81	1.70	5.10	93.62	93.33	0.29	118.32	93.33	6.51	95.75
FCC 06 1	78.69	1.71	5.02	85.41	84.90	0.51	109.93	84.85	6.17	91.72
FCC 06 2	64.10	1.70	5.07	70.86	70.38	0.49	95.40	70.31	6.22	91.87
FCC 06 3	83.44	1.71	5.02	90.17	89.67	0.50	114.67	89.62	6.18	91.87
FCC 07 1	63.53	1.71	5.05	70.29	70.00	0.30	95.01	69.97	6.44	95.30
FCC 07 2	75.65	1.70	5.03	82.38	82.08	0.30	107.13	82.06	6.42	95.26
FCC 07 3	83.09	1.70	5.06	89.85	89.55	0.30	114.56	89.56	6.50	96.11
FCC 12 1	78.94	1.71	5.05	85.70	85.31	0.38	110.35	85.27	6.33	93.81
FCC 12 2	89.78	1.70	5.02	96.50	96.13	0.38	121.16	96.08	6.31	93.80
FCC 12 3	74.31	1.71	5.03	81.05	80.67	0.38	105.73	80.63	6.32	93.75
FCC 13 1	76.80	1.71	5.06	83.56	83.20	0.36	108.21	83.15	6.35	93.86
FCC 13 2	53.75	1.71	5.05	60.50	60.14	0.36	85.13	60.08	6.34	93.79
FCC 13 3	79.38	1.70	5.04	86.12	85.75	0.37	110.02	85.71	6.33	93.90

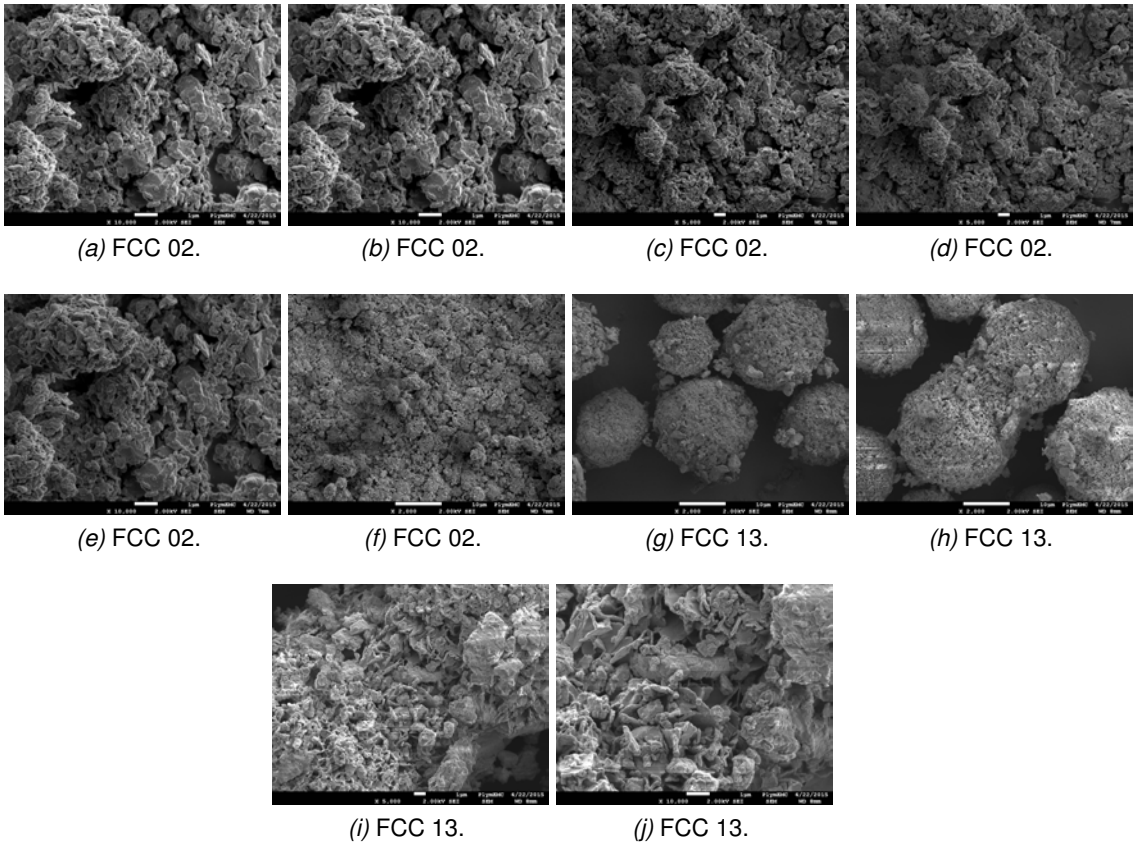

(a) FCC 02. *(b)* FCC 02. *(c)* FCC 02. *(d)* FCC 02.

(e) FCC 02. *(f)* FCC 02. *(g)* FCC 13. *(h)* FCC 13.

(i) FCC 13. *(j)* FCC 13.

Figure 5.4: SEMs of unloaded FCC 02 and FCC 13.

Saccharin loading via an oven method (no sieving) Table 5.3 shows the weights of the FCC during the saccharin loading procedure with no sieving. Figures 5.6 and 5.7 in section 5.3.4 show various SEM images of saccharin loaded FCCs.

The values in Tables 5.2 and 5.3 suggest that there is no significant unaccounted weight loss or gain whilst loading.

5.3.4 SEM analysis

This section shows the SEMs of the various loaded and unloaded FCCs. The clogging of pores and smooth outer pore surfaces, as in Figure 5.3, are indicators of pore filling and provides qualitative evidence for successful flavour loading.

Figure 5.4 shows images of unloaded FCC 02 and FCC 13. The SEMs of loaded FCC were compared to the unloaded SEMs provided by Omya International AG (Figure 3.1 in Chapter 3). Unfortunately, due to the higher quality of the SEMs provided by Omya, it was easy to possibly misinterpret a loaded FCC as having been successfully loaded when it may simply be differences in image quality rather than flavour in the FCC pores. When the loaded SEMs are compared to the unloaded SEMs in Figure 5.4, it becomes difficult to determine any differences between the images.

Table 5.3: The weights of FCC being loaded with saccharin, using the oven drying method (no sieving post-loading), throughout the loading procedure.

Round-bottomed flask ID	Weight of beaker (g)	Weight of mineral (g)	Weight of saccharin (g)	Calculated total weight (g)	Weight after drying (g)	Weight discrepancy (g)	Weight after evaporation (g)	Amount of loaded sample (g)	Yield (%)
Control	88.33	n/a	1.71	90.03	89.80	0.24	89.80	1.47	86
Control (NS)	65.53	n/a	n/a	65.53	65.53	0.00	65.53	0.00	n/a
HSA talc (NS)	75.80	5.08	n/a	80.88	80.86	0.02	80.86	5.05	99
HSA talc	72.65	5.05	1.72	79.42	79.15	0.26	79.15	6.50	96
AR-CaCO3	88.29	5.05	1.73	95.00	94.84	0.24	94.84	6.54	96
AR-CaCO3 (NS)	72.94	5.02	n/a	78.00	77.96	0.00	77.96	5.02	99
HAP	63.36	5.05	1.71	70.13	75.79	-5.67	75.74	12.37	183
HAP (NS)	85.38	5.01	n/a	90.40	90.31	0.09	90.32	4.94	99
GCC	79.39	5.01	1.73	86.13	85.88	0.24	85.88	6.49	96
GCC (NS)	75.82	5.09	n/a	80.90	80.90	0.00	80.90	5.08	99
FCC TP	77.41	5.09	1.71	84.20	83.90	0.31	83.84	6.43	95
FCC TP (NS)	65.13	5.01	n/a	70.13	70.07	0.07	70.06	4.93	99
FCC 02	85.00	5.08	1.72	91.79	91.48	0.32	91.42	6.43	95
FCC 02 (NS)	86.69	5.01	n/a	91.69	91.61	0.08	91.61	4.93	98
FCC 03	84.34	5.05	1.70	91.10	90.83	0.26	90.81	6.47	96
FCC 03 (NS)	69.47	5.00	n/a	74.47	77.45	-2.98	74.44	4.98	99
FCC 06	84.95	5.01	1.71	91.66	91.21	0.46	91.12	6.17	92
FCC 06 (NS)	75.30	5.03	n/a	80.33	80.12	0.21	80.11	4.81	96
FCC 07	86.55	5.02	1.73	93.29	93.00	0.29	92.97	6.42	95
FCC 07 (NS)	95.82	5.05	n/a	100.86	100.82	0.04	100.82	5.00	99
FCC 12	74.27	5.06	1.72	81.06	80.70	0.35	80.63	6.36	94
FCC 12 (NS)	76.30	5.10	n/a	81.40	81.28	0.11	81.29	4.99	98
FCC 13	77.14	5.10	1.70	83.93	83.60	0.33	83.52	6.38	94
FCC 13 (NS)	74.81	5.09	n/a	79.89	79.80	0.09	79.80	4.99	98

Vanillin loading via solvent evaporation Figure 5.5 shows the FCCs loaded with vanillin using the rotary evaporation method. The micrographs are of poor quality because of the difficulty of coating loaded, porous samples with gold.

Table 5.4 gives an overview as to whether the FCC has been established as succesfully loaded or unsuccessfully loaded.

Saccharin loading via an oven method Figures 5.6 and 5.7 show SEM images of the initial loading of saccharin into FCC using the oven method. The samples whose SEMs are captioned 'no mix' went through the same procedure as the other samples, however, their beakers were not swirled or shaken during oven drying. As expected, this appeared to make no noticeable difference on loading.

It is difficult to infer information from the SEM images shown in this chapter because the samples were charging too much in the instrument. The samples in Figures 5.6 and 5.7 were coated with gold a second time in order to try and reduce this effect, but to no avail. Although, FCC 02 and FCC 13 appear to be the easiest grades to determine whether they are loaded nor not when comparing with the unloaded SEMs in Figure 5.4. The only way to determine if the FCCs are successfully loaded, however, would be to use a variety of different techniques to suggest that loading has taken place. Table 5.4 gives an overview as to whether the FCC has been established as succesfully loaded or unsuccessfully loaded.

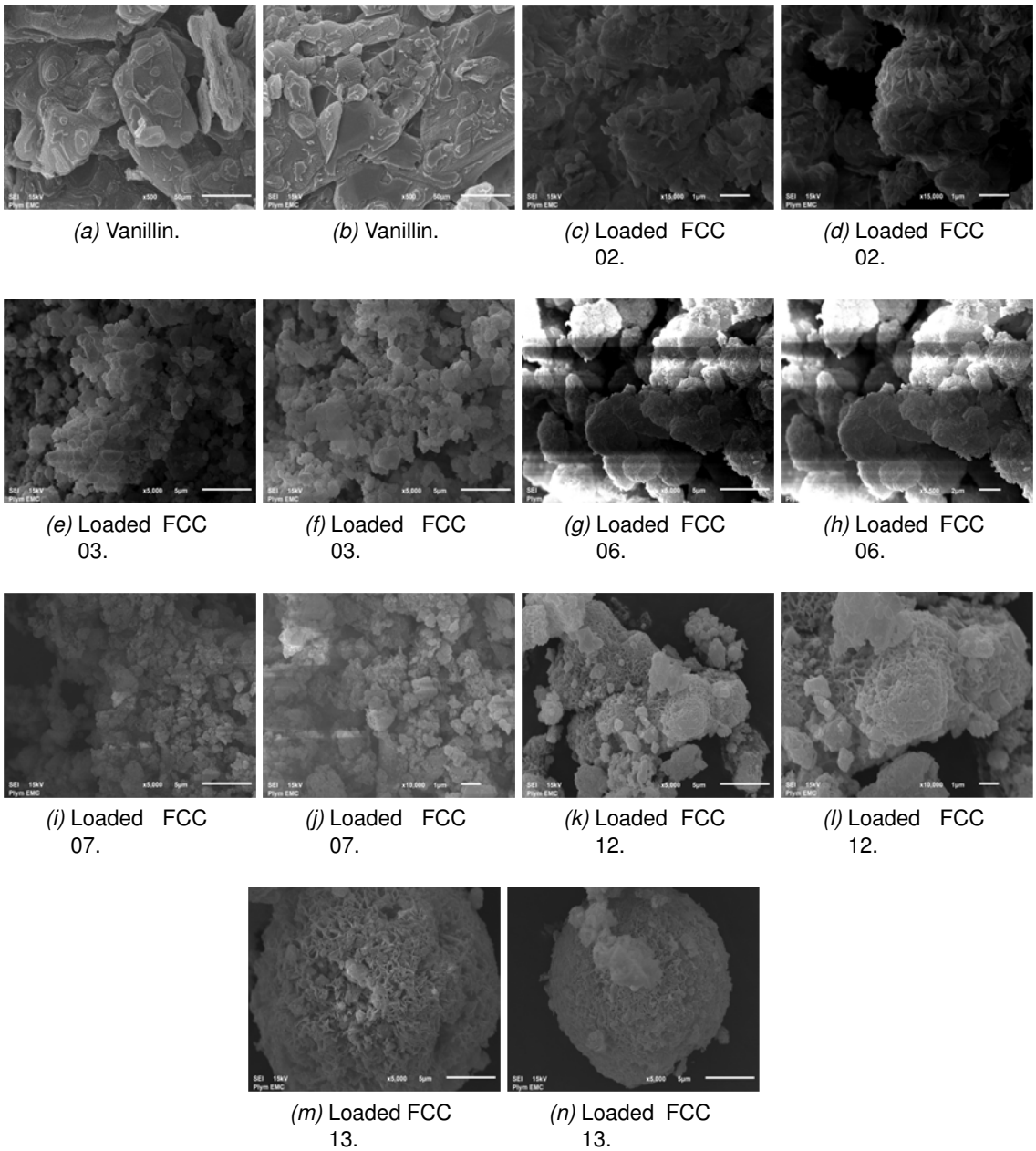

(a) Vanillin. *(b)* Vanillin. *(c)* Loaded FCC 02. *(d)* Loaded FCC 02.

(e) Loaded FCC 03. *(f)* Loaded FCC 03. *(g)* Loaded FCC 06. *(h)* Loaded FCC 06.

(i) Loaded FCC 07. *(j)* Loaded FCC 07. *(k)* Loaded FCC 12. *(l)* Loaded FCC 12.

(m) Loaded FCC 13. *(n)* Loaded FCC 13.

Figure 5.5: SEMs of various FCC grades loaded with vanillin via the solvent evaporation method.

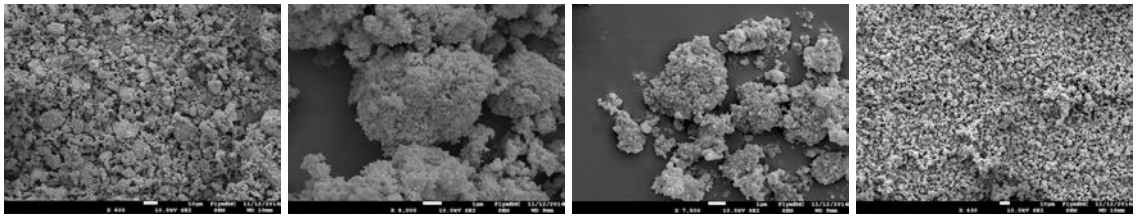

(a) Loaded GCC. *(b)* Loaded HAP. *(c)* Loaded HAP. *(d)* Loaded FCC02.

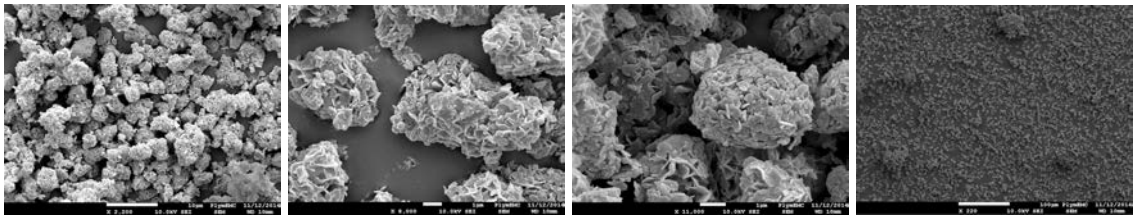

(e) Loaded FCC02. *(f)* Loaded FCC02. *(g)* Loaded FCC02. *(h)* Loaded FCC 02 (not mixed).

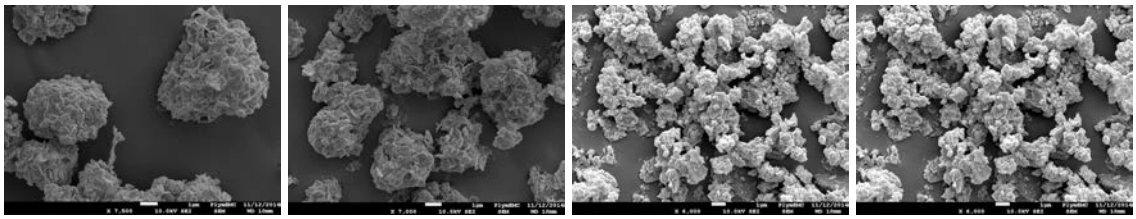

(i) Loaded FCC 02 (not mixed). *(j)* Loaded FCC 02 (not mixed). *(k)* Loaded FCC03. *(l)* Loaded FCC03.

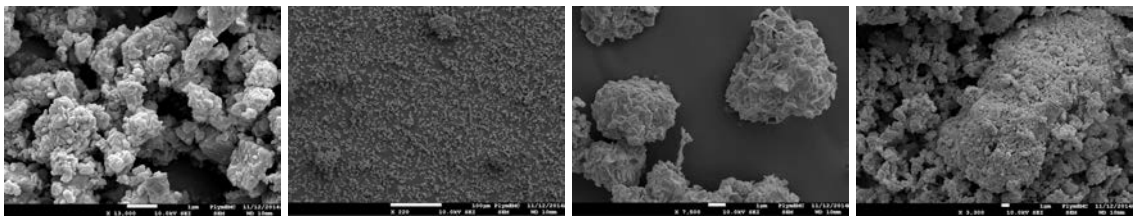

(m) Loaded FCC03. *(n)* Loaded FCC 03 (not mixed). *(o)* Loaded FCC 03 (not mixed). *(p)* Loaded FCC 03 (not mixed).

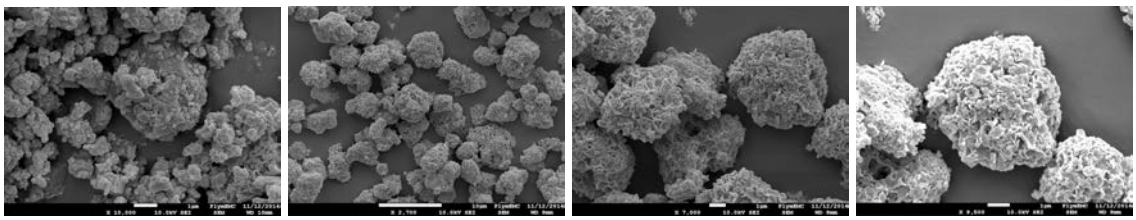

(q) Loaded FCC03 (not mixed). *(r)* Loaded FCC 06. *(s)* Loaded FCC 06. *(t)* Loaded FCC 06.

Figure 5.6: SEMs of saccharin loaded FCCs using the oven method.

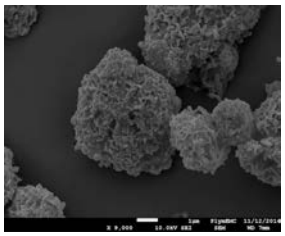

(a) Loaded FCC 06.

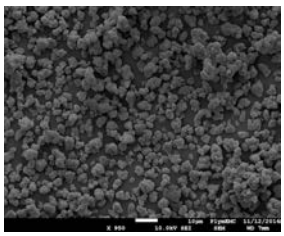

(b) Loaded FCC 06 (not mixed).

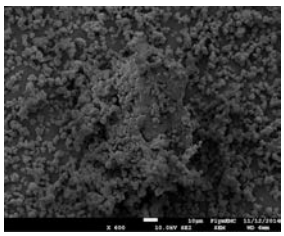

(c) Loaded FCC 06 (not mixed).

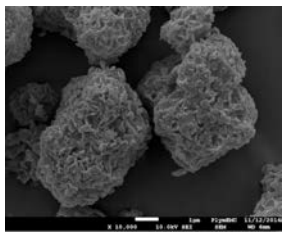

(d) Loaded FCC06 (not mixed).

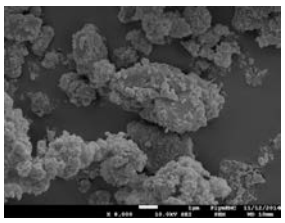

(e) Loaded FCC 07.

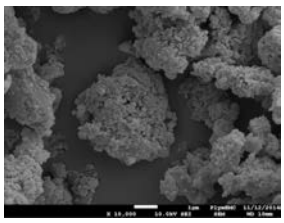

(f) Loaded FCC 07.

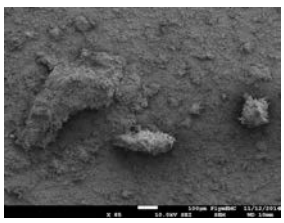

(g) Loaded FCC 07.

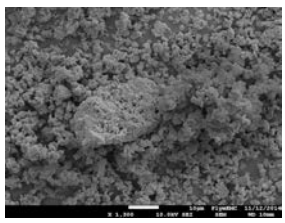

(h) Loaded FCC 07.

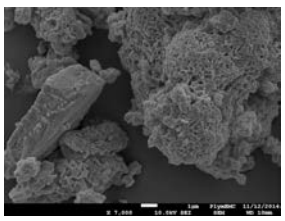

(i) Loaded FCC 12.

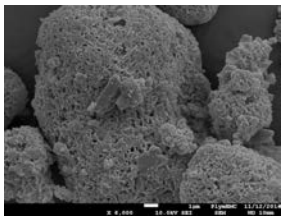

(j) Loaded FCC 12.

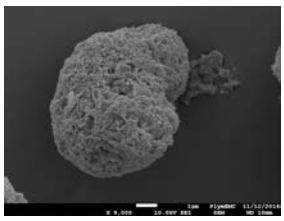

(k) Loaded FCC 12.

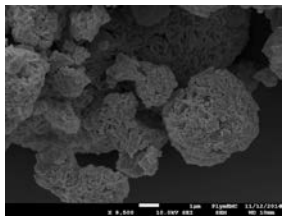

(l) Loaded FCC 12.

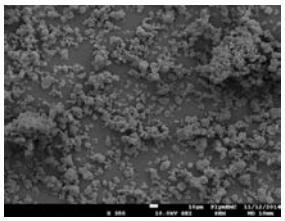

(m) Loaded FCC 12.

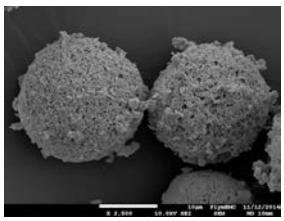

(n) Loaded FCC 13.

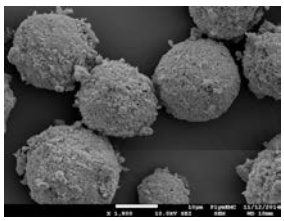

(o) Loaded FCC 13.

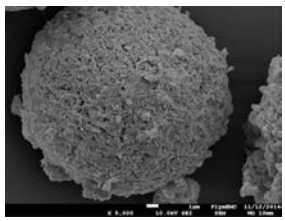

(p) Loaded FCC 13.

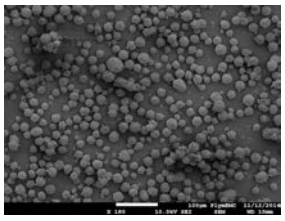

(q) Loaded FCC 13.

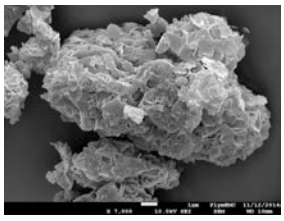

(r) Loaded FCC 13.

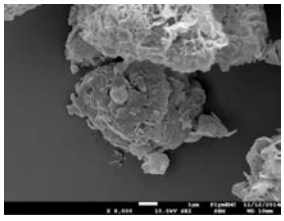

(s) Loaded FCC 13.

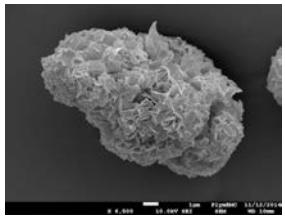

(t) Loaded FCC 13.

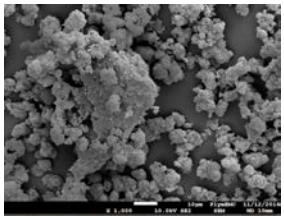

(u) Loaded FCC 13.

Figure 5.7: SEMs of saccharin loaded FCCs using the oven method.

Saccharin loading via an oven method (no sieving) Figures 5.8 and 5.9 show SEM images of the initial loading of saccharin into FCC using the oven method with no sieving, and Table 5.4 gives an overview as to whether the FCC has been established as successfully loaded or unsuccessfully loaded.

5.3.5 SEM elemental analysis

Figures 5.10 and 5.11 show the SEM images of saccharin, unloaded FCC 13, saccharin loaded FCC 13, unloaded FCC 02, and saccharin loaded FCC 02. These two FCC grades were chosen to undergo the elemental analysis because they appeared to have been successfully loaded according to the SEM images. This elemental analysis allows the instrument to pinpoint inside and outside of the pores on an SEM image to determine the presence of certain elements at that point. Although the measurement is not quantitative, it can give a qualitative perspective.

Figures 5.10a and 5.10b are the SEM and the spectrum of the control sample, respectively, and it can be seen that Na and S are in abundance, but Ca and P are not, as expected.

Figures 5.10c and 5.10d show the SEM and spectrum of unloaded FCC 13, respectively, which unfortunately appears almost identical to those of the loaded FCC 13 (Figures 5.10e and 5.10f), other than the S peak, which appears to have slightly shrunk. Therefore, it can be inferred that no saccharin is present in that sample. Figures 5.11a and 5.11b show the SEM and related spectrum of a specific point on the Figure 5.10c, and the absence of Na and S peaks supports that no saccharin in present in the unloaded FCC sample. However, Figures 5.11c and 5.11d show the SEM and related spectrum of a specific point from Figure 5.10e, and the absence of the Na and S peaks also supports that there is no saccharin, when in fact it would be expected to see saccharin present.

Additionally, Figures 5.11e and 5.11f, which show the SEM and related spectrum of a particular point on a loaded FCC 02 sample, respectively, also suggests that no saccharin is present. This is the opposite of what was expected.

Reasons for the lack of saccharin being detected may be because the saccharin has not recrystallised inside the pores of the FCC, and the places that happened to undergo SEM elemental analysis did not have any saccharin present. Another reason is because of the poor quality highly charged SEMs, which prevented the detection of saccharin present.

Table 5.4 gives an overview as to whether the FCC has been established as having been successfully loaded or unsuccessfully loaded based on all SEMs.

This section shows the SEMs of the various loaded and unloaded FCCs. The clogging of and smooth outer pore surfaces, as in Figure 5.3, were used as indicators of pore filling thus providing qualitative evidence for successful flavour loading. Generally, it is extremely difficult to infer information from the SEM images. Additionally, the loaded SEMs in this chapter were all compared to the unloaded FCC SEMs provided by Omya International AG (Figure 3.1 in Chapter 3), however, when compared to the unloaded FCC SEMs taken at Plymouth University (Figure 5.4) it became evident that it was even more difficult to infer information from the SEMs. Due to the higher quality of

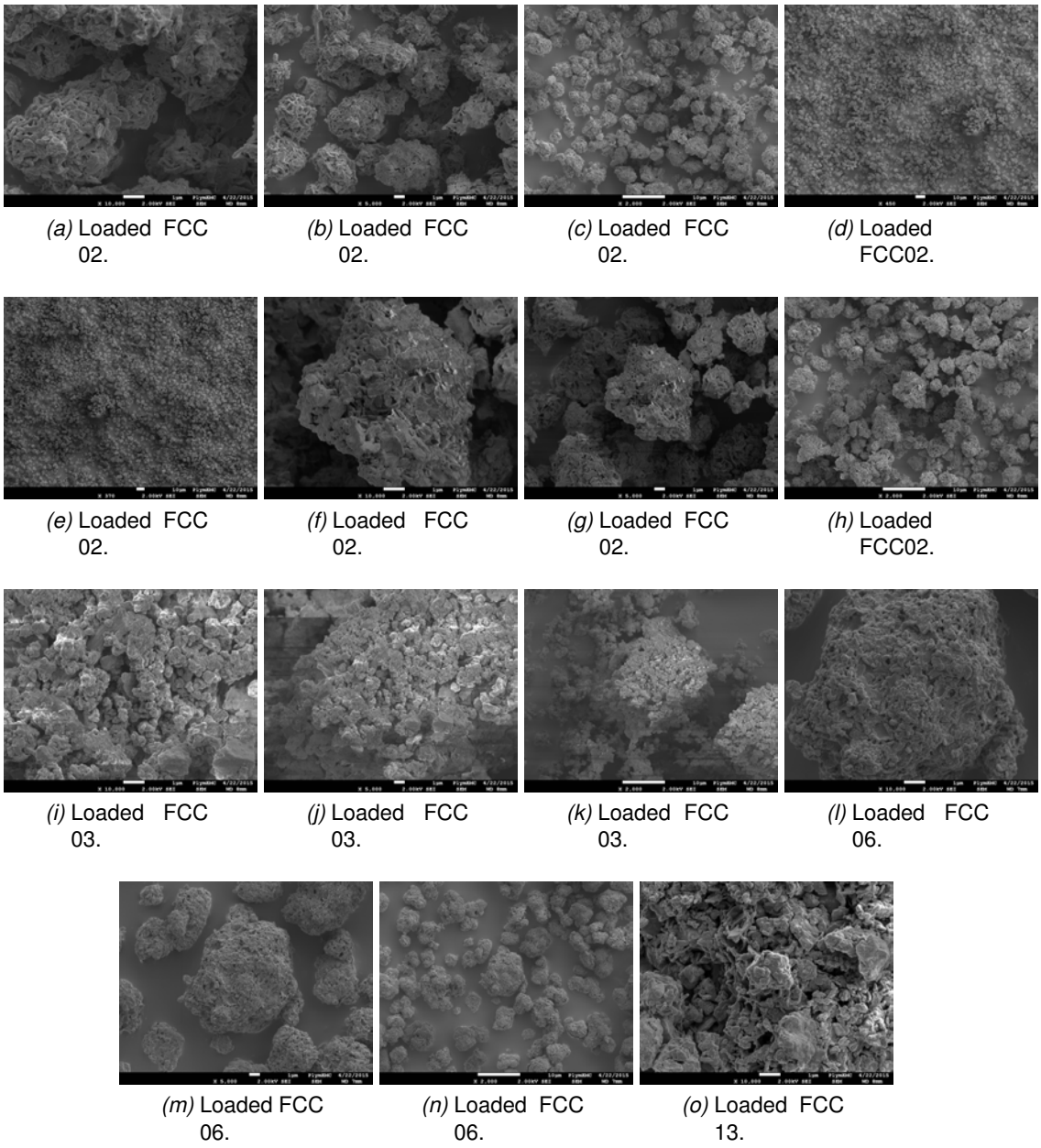

(a) Loaded FCC 02. *(b)* Loaded FCC 02. *(c)* Loaded FCC 02. *(d)* Loaded FCC02.

(e) Loaded FCC 02. *(f)* Loaded FCC 02. *(g)* Loaded FCC 02. *(h)* Loaded FCC02.

(i) Loaded FCC 03. *(j)* Loaded FCC 03. *(k)* Loaded FCC 03. *(l)* Loaded FCC 06.

(m) Loaded FCC 06. *(n)* Loaded FCC 06. *(o)* Loaded FCC 13.

Figure 5.8: SEMs of saccharin loaded FCCs using the oven method (no sieving).

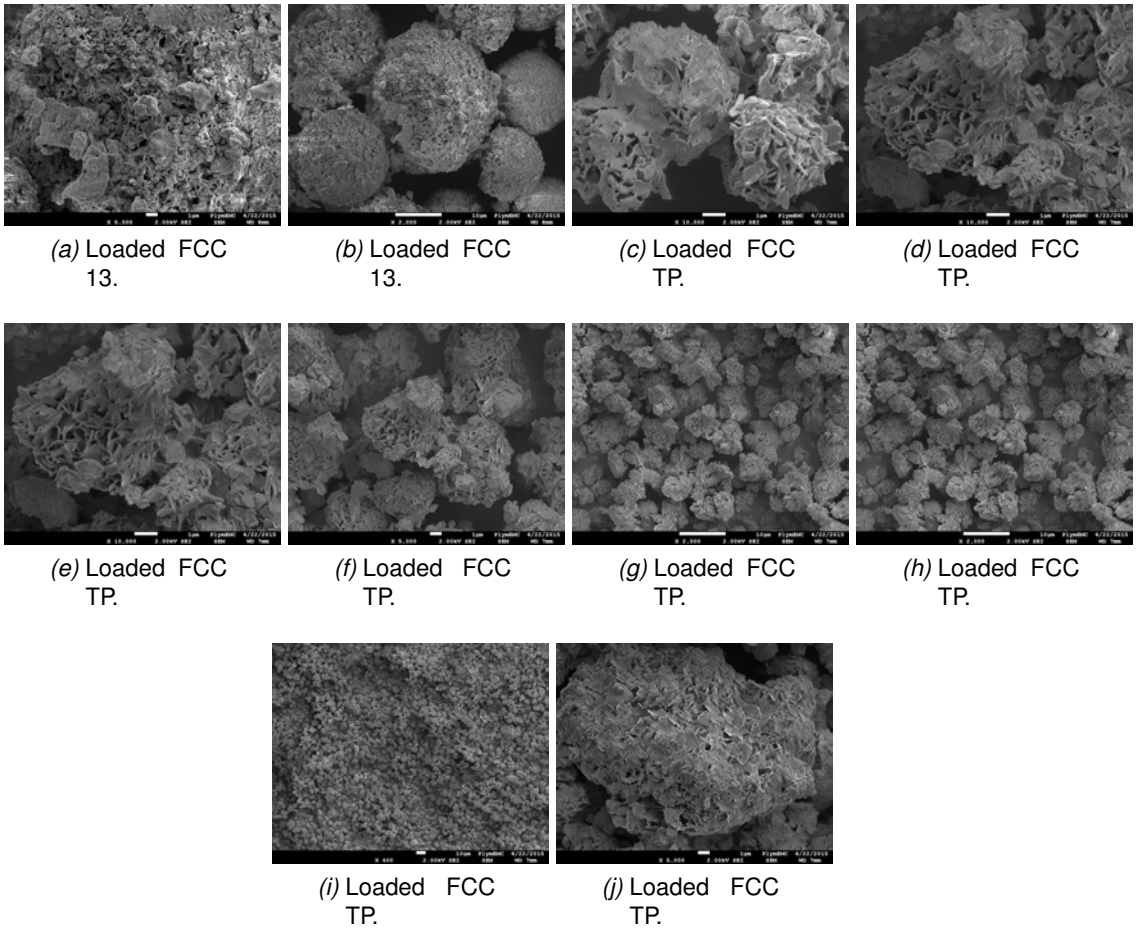

(a) Loaded FCC 13. *(b)* Loaded FCC 13. *(c)* Loaded FCC TP. *(d)* Loaded FCC TP.

(e) Loaded FCC TP. *(f)* Loaded FCC TP. *(g)* Loaded FCC TP. *(h)* Loaded FCC TP.

(i) Loaded FCC TP. *(j)* Loaded FCC TP.

Figure 5.9: SEMs of saccharin loaded FCCs using the oven method (no sieving).

Table 5.4: A qualitative summary of successful or unsuccessful FCC flavour loading.

Sample	Vanillin loading via solvent evaporation	Saccharin loading via oven method	Saccharin loading via oven method (no sieving)
GCC	n/a	Not filled	n/a
HAP	n/a	Not filled	n/a
FCC TP	n/a	Not filled	Not filled
FCC 02	Filled	Filled	Filled
FCC 03	Filled	Not filled	Not filled
FCC 06	Filled	Filled	Filled
FCC 07	Not filled	Not filled	n/a
FCC 12	Not filled	Filled	n/a
FCC 13	Not filled	Filled	Filled

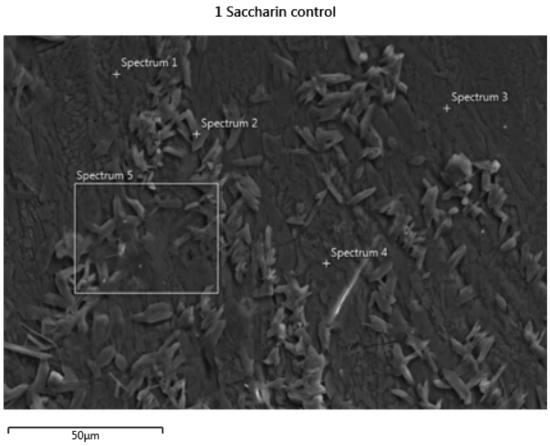

(a) Saccharin SEM.

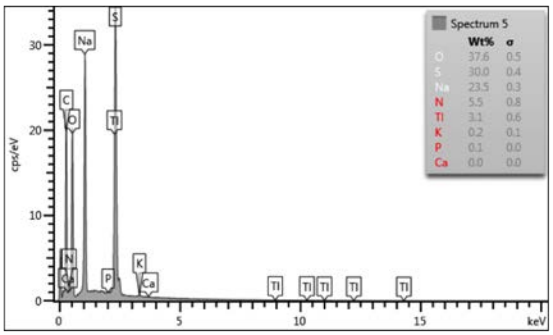

(b) Saccharin spectrum.

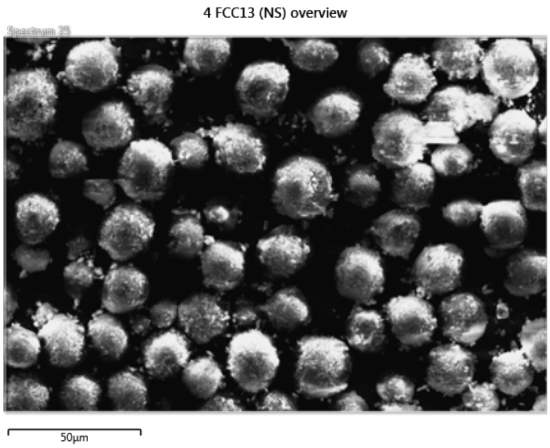

(c) Unloaded FCC 13 SEM.

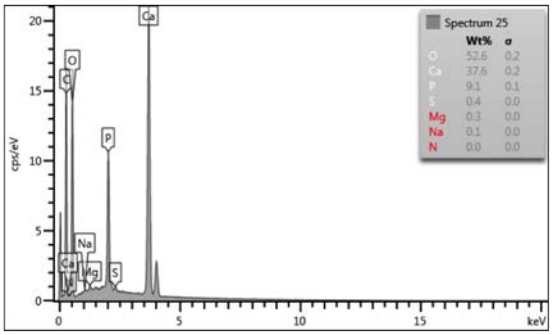

(d) Unloaded FCC 13 spectrum.

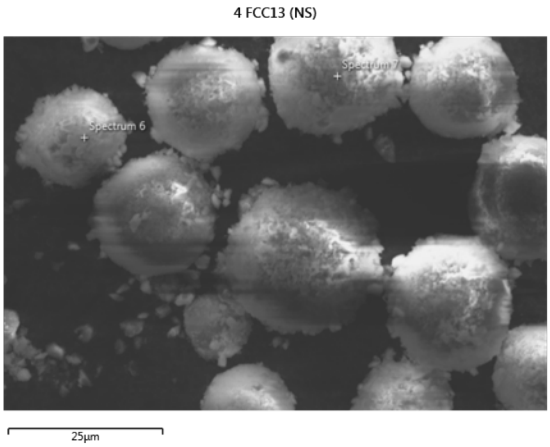

(e) Unloaded FCC 13 SEM of point 6.

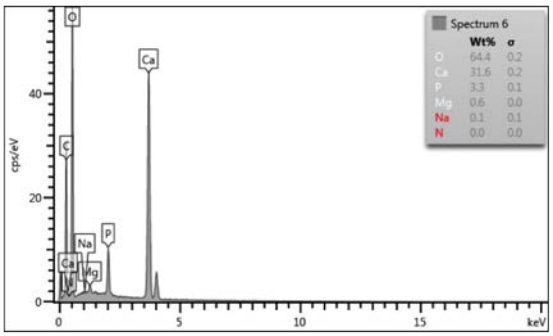

(f) Unloaded FCC 13 spectrum of point 6.

Figure 5.10: SEM elemental analysis of saccharin loaded FCCs using the oven method (no sieving).

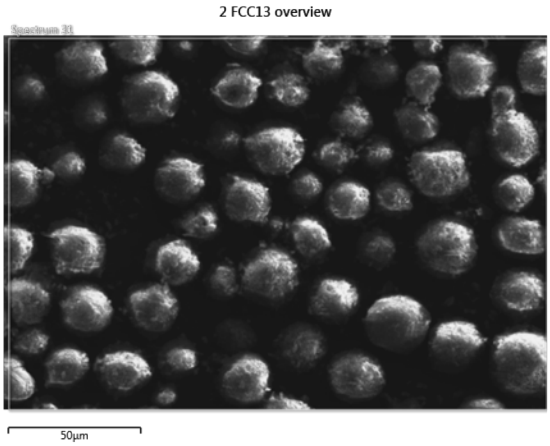

(a) Loaded FCC 13 SEM.

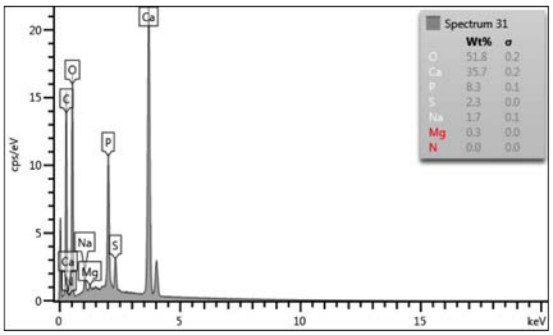

(b) Loaded FCC 13 spectrum.

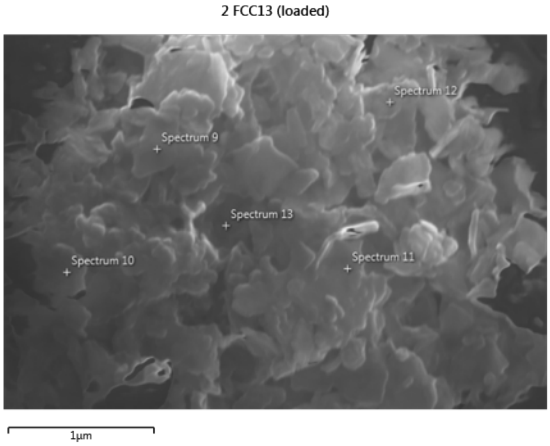

(c) Loaded FCC 13 SEM of point 6.

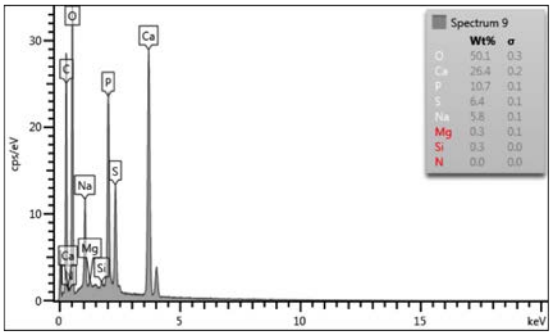

(d) Loaded FCC 13 spectrum of point 9.

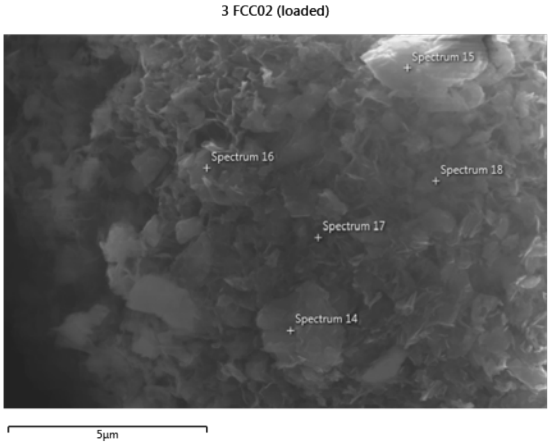

(e) Loaded FCC 02 SEM of point 14.

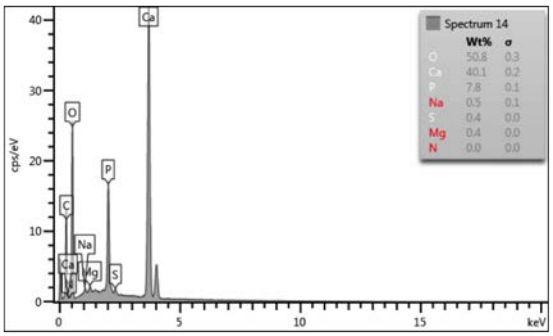

(f) Loaded FCC 02 spectrum of point 14.

Figure 5.11: SEM elemental analysis of saccharin loaded FCCs using the oven method (no sieving).

Table 5.5: The measured skeletal and envelope densities of unloaded and saccharin loaded FCCs using the oven method.

Sample	Density pre-loading (g cm^{-3})			Density post-loading (g cm^{-3})		
	Absolute	Envelope	Porosity (%)	Absolute	Envelope	Porosity (%)
Control (saccharin)	1.69	1.12	33.54	1.86	1.07	42.61
Blank (GCC)	-	-	-	3.35	2.11	39.76
GCC	2.99	1.29	56.97	2.91	1.56	32.62
HAP	3.74	0.61	83.78	3.90	0.59	84.91
FCC TP	3.25	0.40	87.57	3.49	0.75	78.73
FCC 02	4.10	0.38	90.66	4.51	0.45	90.07
FCC 03	4.00	0.88	78.12	3.34	0.63	81.26
FCC 06	3.41	0.29	90.43	4.34	0.38	91.24
FCC 07	3.81	1.04	72.71	4.88	1.11	77.39
FCC 12	3.62	0.42	88.30	3.01	0.73	75.91
FCC 13	3.12	0.38	87.68	3.03	0.57	81.16
Maximum	4.10	1.29	90.66	4.88	1.56	91.24
Minimum	2.99	0.29	56.97	2.91	0.38	32.62
Average	3.56	0.63	81.80	3.71	0.75	77.03
Standard deviation	0.39	0.35	11.07	0.73	0.37	17.49

the SEMs provided by Omya, it was easy possibly to misinterpret a loaded FCC as having been successfully loaded when it may simply be differences in image quality rather than flavour in the FCC pores. When the loaded SEMs are compared to the unloaded SEMs in Figure 5.4, it becomes difficult to determine any differences between the images. Therefore, it would be useful if more images could be taken of unloaded FCCs using the same instrument and settings as for the taking of the loaded FCC SEMs. The quality of the SEM images are poor, and that is attributed mainly to the surface charging on the samples. The porous nature of the sample made it difficult to obtain a continuous gold coating.

However, despite being unable to differentiate between saccharin and FCC in the images, it is speculated that the saccharin may be inside the FCC anyway. In Figure 5.6a it may be possible to see recrystallised saccharin dotted around the GCC. The weights taken of the materials during the loading procedure (Tables 5.3 and 5.2) show no loss of saccharin throughout.

5.3.6 Density measurements

Saccharin loading via an oven method Table 5.5 shows the results of the density measurements on unloaded and saccharin loaded FCCs.

Saccharin loading via an oven method (no sieving) Table 5.6 shows the results of the density measurements on unloaded and saccharin loaded FCCs using the oven method (no sieving).

As expected, the samples become less porous once loaded with saccharin in Table 5.5, however, FCC 12 and 13 are more porous after loading than before. It was at this point that it was speculated that envelope pycnometry may not be measuring anything,

Table 5.6: The measured skeletal densities of unloaded and saccharin loaded FCCs using the oven method (no sieving).

Sample	Volume (cm^3)		Absolute density ($g\ cm^{-3}$)	
	Not loaded	Loaded	Not loaded	Loaded
Control (saccharin)	0.89	0.76	1.78	1.73
Talc	0.48	0.58	2.93	2.57
Ar-CaCO3	0.23	0.73	3.36	2.61
GCC	0.96	0.89	2.85	2.48
HAP	0.33	0.51	3.54	2.89
FCC TP	0.12	0.27	4.35	3.07
FCC 02	0.17	0.28	3.55	3.07
FCC 03	0.49	0.49	3.06	2.77
FCC 06	0.14	0.21	4.20	3.17
FCC 07	0.50	0.29	3.17	2.80
FCC 12	0.32	0.19	3.57	2.98
FCC 13	0.25	0.18	3.86	3.21

because if the FCC is finer than the DryFlo, the FCC will sit in between the DryFlo particles as opposed to any real density measurements being made. This is what prompted the measurement of the particle size distribution of the DryFlo power, and is discussed in the subsequent section.

It is also interesting to note that the skeletal density of loaded FCC should be lower than unloaded FCC, however, this is not the case with HAP, FCC TP, FCC 02, FCC 06, and FCC 07 based on the figures in Table 5.5. Reasons for this may be because the samples were not dried in an oven before analysis, thus slightly altering the final measurement due to the presence of additional water.

Regarding the results in Table 5.6, as expected, the samples have an increase in volume and a decrease in skeletal density when loaded with saccharin.

Unfortunately, however, although density measurements can be used to infer as to whether the FCC has been successfully loaded or not, the expected changes in density do not prove that the saccharin has recrystallised inside the pores of the FCC as is desired. Envelope density measurements would provide most useful in this instance, however, due to the discussion regarding whether the DryFlo powder is too coarse for the FCC samples, the measurements may not show anything, anyway.

5.3.7 PSD measurement of DryFlo

The particle size distribution results of the DryFlo powder are displayed in Table 5.7, alongside available data for various FCC grades provided by Omya International AG.

The d_{99} value for the DryFlo is 321 μm, signifying that 99 % of the volume of the sample has particles finer than this diameter. FCC 02, for example, has 98 % by volume of its particles finer than 9.4 μm; it is evident that the DryFlo's particles are generally larger than the FCC's. However, these values do not necessarily mean that most of the DryFlo's particles are less than 9.4 μm despite the much higher d_{99} value that DryFlo has compared to FCC 02.

Table 5.7: The particle size distribution data of the DryFlo powder, and any available data for various minerals used in this project; they are displayed as d_N values, namely the median particle diameters at which N % by volume of the sample is finer than the stated value.

Sample	Particle size (μm)								
	$d_{0.01}$	$d_{0.05}$	$d_{0.25}$	$d_{0.50}$	$d_{0.75}$	$d_{0.90}$	$d_{0.95}$	$d_{0.98}$	$d_{0.99}$
DryFlo	47.50	61.02	94.83	131.43	180.03		264.91		321.10
GCC	1.51	-	-	7.70	-	2.027	-	-	-
HAP	1.15	2.05	3.39	7.08	16.77		29.93		55.27
FCC S01	1.02	3.24	6.22	12.46	96.15		173.69		396.86
FCC 02	-	-	-	4.9	-	-	-	9.4	-
FCC 03	-	-	-	3.1	-	-	-	6.9	-
FCC 06	-	-	-	5.5	-	-	-	10.6	-
FCC 07	-	-	-	6.3	-	-	-	18.5	-
FCC 12	-	-	-	10	-	-	- -	25	-
FCC 13	-	-	-	23.5	-	-	-	40.1	-
FCC TP	-	-	-	7	-	-	-	16.1	-

The next size distribution that can be compared will be the d_{50} values: DryFlo's is 131 μm, whereas for FCC 02 it is 4.9 μm. The difference in % between DryFlo's d_{99} and d_{50} is 49 %, which means that 99 % of the particles are less than 321 μm, and 50 % are less than 131 μm. Therefore, 49 % are more than 131 μm in size, but less than 321 μm. Thus, it can be concluded that a bulk of the DryFlo's particles are much larger in size than those of FCC 02.

The significance of these findings is that powder pycnometry cannot be used to measure the envelope density of powdered FCC samples, as the FCC particles will simply fall in between the coarser DryFlo particles during the consolidation process.

5.3.8 MIP analysis

Figure 5.12 shows the mercury intrusion graphs for the unloaded and saccharin loaded FCC 13, and Table 5.8 shows the porosities and densities obtained from the MIP measurements.

Table 5.8: The porosities and envelope densities of unloaded and saccharin loaded FCC 13.

	Unloaded	Loaded	Difference
Accessible porosity (%)	77.93	69.28	8.65
Intraparticle porosity (%)	38.46	10.38	28.08
Envelope density (g cm^{-3})	0.3506	0.4461	0.0955

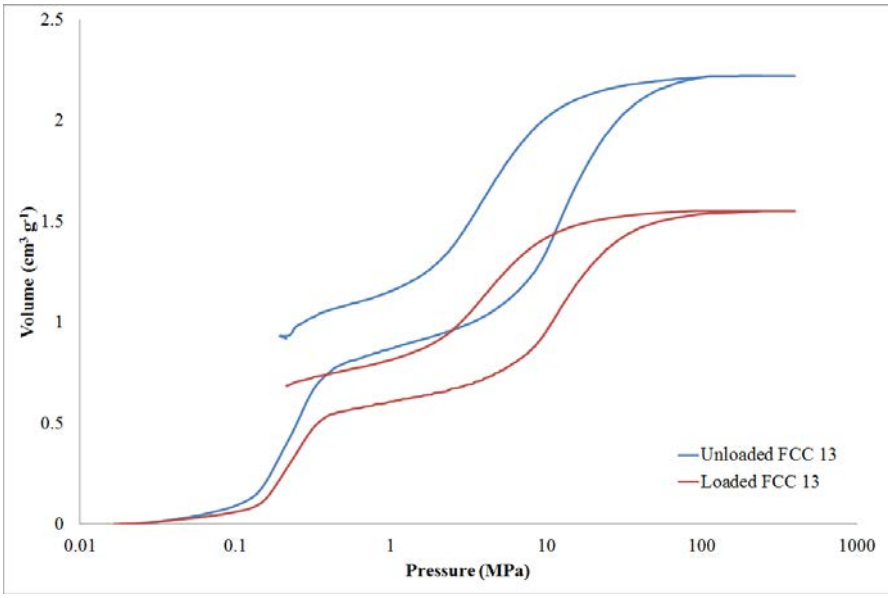

Figure 5.12: The mercury intrusion curves for the unloaded and saccharin loaded FCC 13.

The values in Table 5.8 are as expected; the porosity of the loaded sample reduces and the envelope density increases. Figure 5.12 shows that the loaded FCC has been intruded with a lower volume of mercury than the unloaded sample, which suggests the pores have indeed been filled with saccharin.

Despite the MIP measurements showing that the loading of FCC 13 with saccharin has indeed been successful, there still remains the issue of not knowing with certainty that the actual pores of the FCC are filled with saccharin. The porosity of a saccharin and FCC mix would decrease when inferred from MIP measurements even if the saccharin is not loaded into the FCC's pores. Therefore, MIP measurements would have to be made on such a mix in order to rule out this artefact.

5.3.9 General discussion comments

The work of Preisig *et al.* (2014) shows that FCC can be loaded with drugs using a solvent evaporation method, and the results reported in this chapter support this notion although it is not explicitly proven. In order to generate more conclusive results a larger experimental matrix would be needed, more time to analyse all samples via MIP, and better SEM images would need to be obtained. However, the primary aim of these loading experiments was not to establish the best and most efficient way of loading, but merely to infer that some sort of loading has taken place for use of the loaded FCC in subsequent release experiments. Unfortunately, that proved more difficult than initially expected from the results of Preisig *et al.* (2014). As a result, obtaining the diffusion profile of a loaded FCC is perhaps the only option to determine that the FCC has been successfully loaded.

5.4 Conclusions & future work

The hypothesis postulated in this chapter is as follows:

- **4:** The extent to which a flavour or drug compound can be physically loaded into the void volumes of FCC can be quantified by directly observing the loaded FCC by scanning electron microscopy (SEM).

The techniques employed in an attempt to load the FCC with anethole, vanillin, and saccharin are discussed in this chapter. Previous work, e.g. Stirnimann *et al.* (2013) and Preisig *et al.* (2014), has suggested that the FCC can be successfully loaded with drugs and drug analogues. Therefore, the aim of this work was not to establish the best method of loading or maximal and efficient loading, but merely as a first step in the characterisation of the diffusion profile characterisation for each grade of FCC. The idea was to load the FCC with flavours utilised in this work in order to study the diffusion profiles of each FCC; this means that the amount of flavour loaded is not necessarily important, but simply being able to characterise qualitatively whether each FCC has actually been loaded or not is.

Initially, attempts to load anethole into the FCC were made. However, complexities arose with the possibility of drying the anethole loaded FCC as a result of the anethole being liquid at room temperature. Using the oil loading method outlined in section 5.3.1 was an alternative because this avoided the need for drying; the paste can then be directly applied to the ZLC/FLC, however, it would pose difficulties in that anethole will be lost and the need to work quickly would be emphasised. Also, it would be difficult to quantify the amount loaded and lost. However, it can also be argued that when studying the diffusion of anethole in the ZLC/FLC, it is the diffusion at longer-times that is the real characterising property of each individual FCC; this is further discussed in Chapter 7 (Levy *et al.*, 2015).

At the time of using anethole, it was suggested to use aqueous systems; anethole is very insoluble in water, and so experiments utilising other flavours with the potential to dissolve in water (i.e. vanillin and saccharin) were pursued instead. Although work outlined in this thesis uses both aqueous and non-aqueous solvents, the benefit of these compounds over anethole is that they are solid at room temperature, and so can crystallise more easily post-loading.

As this work, and the work of others, has developed, it has become apparent that diffusion-based loading is simple but will not yield the most efficient and optimal loading, because the dilute flavour is too low in concentration to be able to utilise the full potential of the FCC pores. The IWI technique theoretically should yield maximal and more efficient loading. Therefore, future work as part of this project would involve using this technique to load the FCC with vanillin or saccharin (in the case of saccharin, the oven method would be used to drive water off of the FCC before and after loading) and be characterised afterwards. SEMs are useful to characterise each grade qualitatively, however, adjustments are needed with the microscopy technique in order to yield clearer and higher quality images. MIP can also be utilised to infer whether the pores have been filled or not. Preisig *et al.* (2014) used qualitative SEM analysis and HPLC quantification and deemed those techniques as sufficient to estimate both loading efficiency and loading capacity. However, the authors did state that additional analysis of porosity, surface area, and crystallinity was necessary to elucidate the loading mechanism.

In conclusion, the loading work outlined in this chapter used procedures in which it was difficult to determine the loading efficiency, as it was hindered by poor quality SEM images and some experimental artefacts of the other characterisation techniques employed. However, this work can be considered as a good preliminary step in the loading of vanillin and saccharin into FCC. Although loading was not explicitly established, it was suggested that the FCC may be loaded, thus partially fulfilling hypothesis 4.

Once a loading technique has been established and the FCC well characterised, the loaded FCC can then be used in release experiments similar to those described in Chapter 6.

Chapter 6

The modelling of diffusion from a spherical particle

THIS chapter outlines the initial experimental work designed to measure the diffusion from vanillin loaded FCC (as described in Chapter 5). These tests involved identifying the limitations of such experiments in order to help find an experimental matrix to use in subsequent experimental work, which consider particles individually as opposed to in a packed bed (like the experiments described in Chapter 7). However, experimental design difficulties and time constraints resulted in using another source of data for the diffusion modelling.

The SP Technical Research Institute of Sweden measured the release of vanillin from FCC, and did so under a project commissioned by Omya International AG; their results were used in the modelling outlined in this chapter. A numerical approach based on Fick's second law of diffusion was used to investigate flavour release kinetics from porous FCCs. This lead to the postulation of the following hypothesis (hypothesis 5): that computational methods can be used to calculate a diffusion coefficient from experimental data of flavour release from FCC.

6.1 Introduction

6.1.1 Release & diffusion experiments

The idea underpinning these release experiments is that the diffusion was being studied from multiple individual particles, as opposed to the idea underpinning FLC studies (Chapters 7 and 8), in which diffusion from a packed bed of particles was considered. The experiments are loosely based on those performed by Fries and Zarfl (2012), Öner *et al.* (2011), and Eberle *et al.* (2014), in which the particles of interest are immersed into a vessel containing a release medium, and the release medium is analysed for concentrations of a specific compound over a period of time.

6.1.2 Modelling

The design of rate-controlling release mechanisms, i.e. diffusion or swelling, of a drug delivery system often determines its classification. A water soluble drug incorporated into a matrix is mainly released by diffusion, whereas self-erosion of the inert matrix that contains a low water soluble drug will be the principal release mechanism in this instance (Costa and José, 2001). This work focuses on modelling diffusion-controlled release mechanisms, which are usually split into two types: a reservoir system and a matrix or monolithic system, the latter also being known as a 'one-block' system (Siepmann and Siepmann, 2008; Frenning, 2011).

The reservoir system utilises a release rate controlling membrane that serves as the

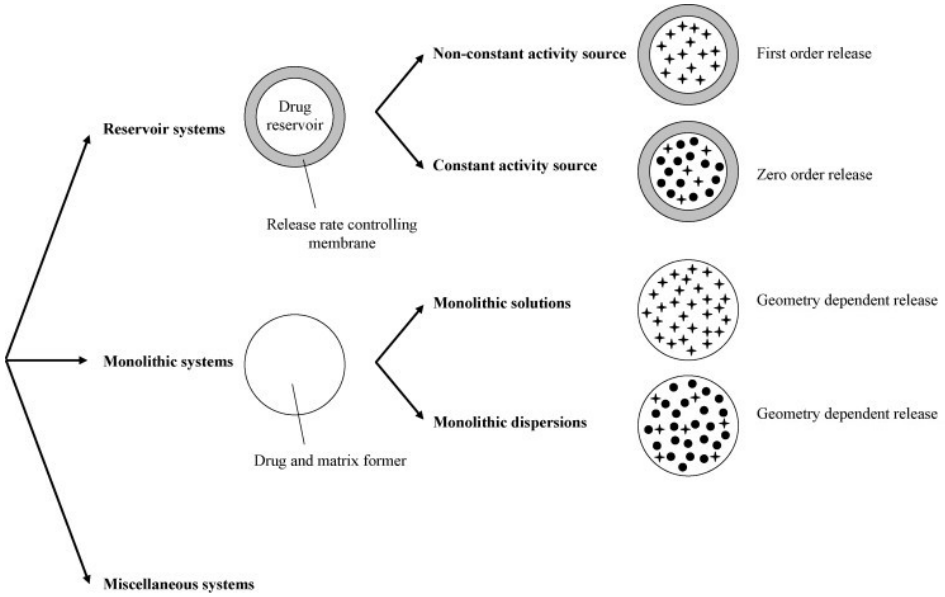

Figure 6.1: Classification system for primarily diffusion controlled drug delivery systems. Plus symbols represent individual drug molecules, while black circles represent drug crystals and/or amorphous aggregates. Only spherical dosage forms are illustrated, but the classification system is applicable to any type of geometry (Siepmann and Siepmann, 2008). Permission to reproduce this image has been granted by the publisher.

main diffusion barrier. Inside the membrane is a concentration of drug; if the amount of drug within is below the drug solubility (e.g. a polymer-coated tablet or pellet with a low drug loading) then the released drug molecules will continuously decrease with time, thus making it a non-constant activity source. If the initial drug concentration within the membrane exceeds the solubility in solution, the released molecules will be replaced by the partial dissolution of drug crystals or amorphous aggregates, thus resulting in a constant activity source (Siepmann and Siepmann, 2008; Frenning, 2011).

System geometry, however, significantly affects the drug release kinetics of monolithic devices. If the initial drug concentration is below the drug solubility, then the molecules are dissolved within the carrier material making a monolithic solution. Otherwise, dissolved drug crystals also co-exist with crystals or amorphous aggregates, thus making monolithic dispersions, of which the resulting mathematical descriptions becomes even more complex. Higuchi (1960; 1961) developed an equation in which the relationship between the amount of drug released from a thin ointment film, with negligible edge effects, and the square root of time was established. However, this equation holds true only if there is a large excess of drug, of which the initial concentration far outweighs its solubility. Unfortunately, Higuchi's equation is often misused and is applied to drug delivery systems that do not fulfil essential criteria (Siepmann and Siepmann, 2008).

Figure 6.1 shows the classification system for primarily diffusion controlled drug delivery systems (Siepmann and Siepmann, 2008).

For monolithic solutions whose drug release is primarily diffusion controlled, providing

constant properties of the inert carrier matrix (i.e. no swelling or dissolution of the structure) and the maintenance of perfect sink conditions, the release of the drug from a spherical dosage form can be described based on Fick's second law of diffusion as follows (Vergnaud, 1993; Siepmann and Siepmann, 2008; Crank, 1975; Grathwohl, 1998; Gaonkar *et al.*, 2014):

$$\frac{M_t}{M_\infty} = \frac{6}{\pi^2}\sum_{n=1}^{\infty}\frac{1}{n^2}\exp\left(-\frac{Dn^2\pi^2 t}{r^2}\right) \tag{6.1}$$

where M_t is the amount of drug remaining in carrier at time t, M_∞ is the amount of drug in solution when t is infinity (i.e. equilibrium), n is a dummy variable, D the diffusion coefficient of the drug within the matrix, and r is the radius of the sphere. The application of equation 6.1 has been used successfully to quantify drug release from non-degradable controlled release microparticles (Hombreiro-Pérez *et al.*, 2003).

6.2 Materials & methods

6.2.1 FCCs

The FCC grades utilised by the SP Technical Institute in their diffusion studies were FCC S07 and FCC S10. Their properties and SEM images of their structures can be viewed in Table 6.1 and Figure 6.2, respectively. The two grades have approximately the same particle size (~ 7.5 μm) but different pore sizes, and is demonstrated by a screenshot of the pore size differential of the mercury intrusion porosimetry data in Figure 6.3, in which it can be seen that the critical pore diameter, for both the inter- and intraparticle pores, (Aligizaki, 2005) of FCC S07 is smaller than those of FCC S10.

6.2.2 Release & diffusion experiments

A vanillin in ethanol calibration graph was made for the Hewlett Packard (now Agilent) 8452 UV-visible spectrometer utilised in these experiments. A Mettler Toledo XP504 Analytical Balance was used to tare a 250 cm^3 volumetric flask, into which 0.2501 g of vanillin was weighed. Ethanol was added up to the mark of the volumetric flask to make a stock solution of 1 000 mg dm^{-3}. From that stock solution a range of serial dilutions were made in 100 cm^3 volumetric flasks using glass bulb and graduated pipettes to obtain concentrations ranging from 0.01-40 mg dm^{-3}. The wavelength at which measurements of these solutions were taken was 279 nm, and the cuvette used was a QC High Precision Cell made of synthetic quartz glass (Hellma Analytics, Art. No: 100-600-10-41, light path: 10 mm, QC: 855).

The FCC 13 loaded with vanillin via the IWI technique, described in section 5.2.4, was utilised for the release experiments. The first step in designing the release experiments was to decide how much loaded FCC 13 was to be used. Previously, there have been issues with speculated FCC 'fines' covering up the UV-visible absorbance signal from vanillin and other compounds. However, adsorption experiments using UV-visible spectroscopy in a similar fashion showed that there appeared to be no 'fines' interfering with vanillin readings when utilising 0.2 g of FCC in 25 cm^3 of ethanol (Chapter 4).

A Mettler Toledo XP504 Analytical Balance was used to weigh 0.35 g of loaded FCC (weight also included that of vanillin) into a tared weighing boat, which was then trans-

Table 6.1: Properties of the FCC samples used in diffusion experiments by the SP Research Institute of Sweden; data provided by Omya International AG, including values from polyelectrolyte titration (PET) analyses.

Property	FCC sample	
	S07	S10
Specific surface area ($m^2\ g^{-1}$)	154.1	77.0
d_{50} (μm)[1]	7.7	7.6
d_{98} (μm)[1]	15.7	14.6
Total pore volume ($cm^3\ g^{-1}$)[2]	3.68	4.97
Intraparticle pore volume ($cm^3\ g^{-1}$)[2]	1.12	1.62
Interparticle pore volume ($cm^3\ g^{-1}$)[2]	1.80	2.30
Pore volume ($cm^3\ g^{-1}$)[3]	3.5	0.5
Pore size (nm)[3]	90.1	26.3
PET analysis (μeq g^{-1})	-132.2	-111.5

[1] Laser Diffraction, Malvern Mastersizer 2000 (volume based).
[2] Mercury Porosimetry, Micromeretics Autopore IV.
[3] BET determination, Micromeretics Gemini V.

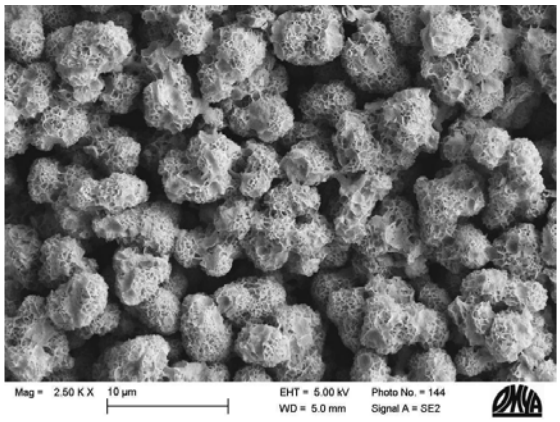

(a) FCC S07; scale bar = 10 μm.

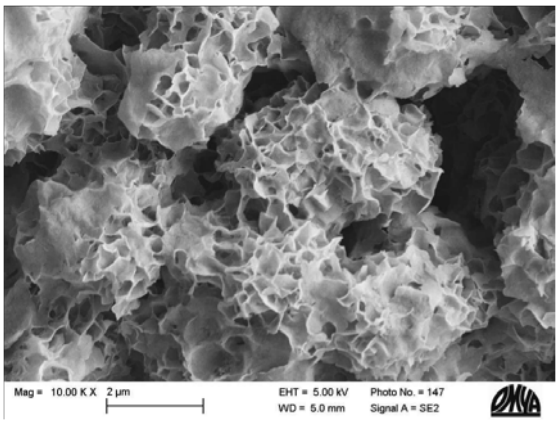

(b) FCC S07; scale bar = 2 μm.

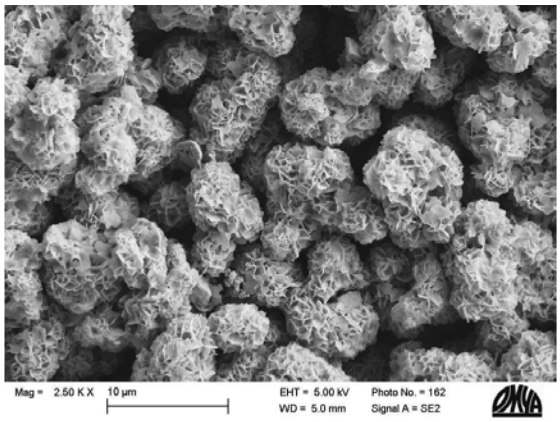

(c) FCC S10; scale bar = 10 μm.

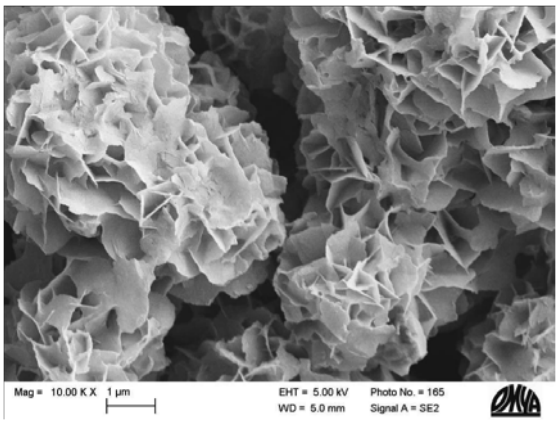

(d) FCC S10; scale bar = 1 μm.

Figure 6.2: SEMs of FCC S07 and S10 provided by Omya International AG.

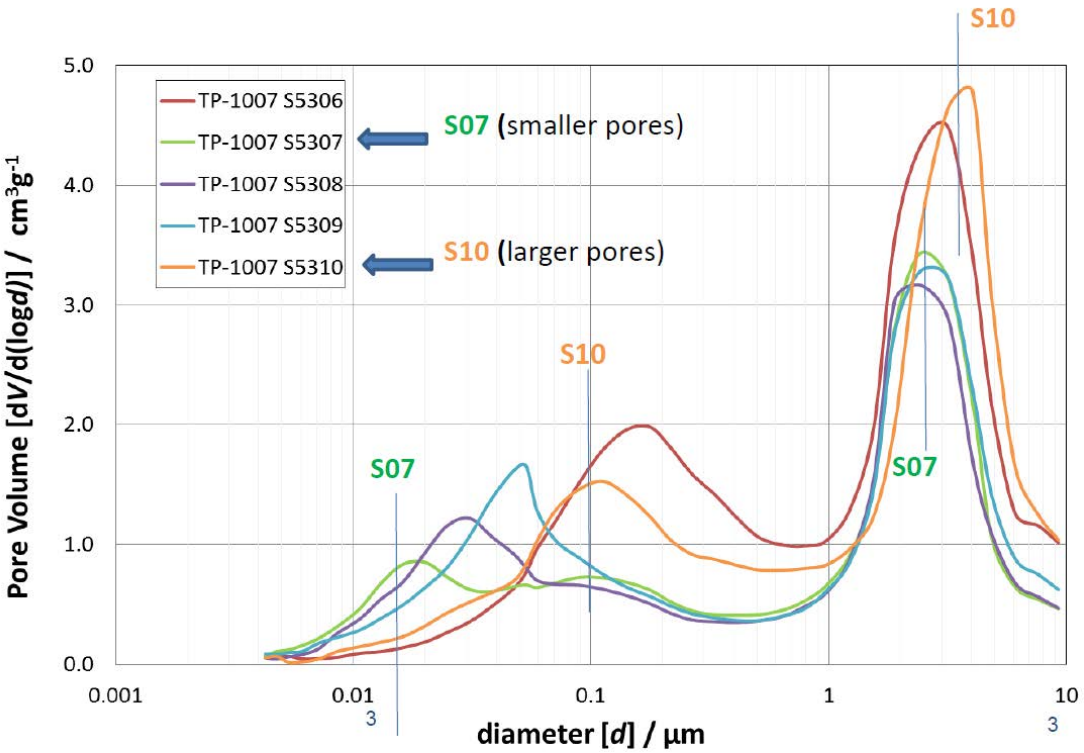

Figure 6.3: Screenshot of the mercury intrusion porosimetry pore size differential of the FCC samples provided by Omya International AG and studied by the SP Technical Research Institute of Sweden. The samples of interest in this chapter are FCC S07 and S10. The two vertical lines for FCC S07 and S10 cross the steepest part of the slope of the pore size differential of the intraparticle pores (i.e. the leftmost peak) and the interparticle pores (i.e. the rightmost peak); the point at which the vertical line crosses the x-axis is the critical pore diameter.

ferred to the ethanol in the beaker for the release experiments. The release medium was ethanol poured up to the mark of a 250 cm^3 glass beaker in which a magnet was placed, as a Stuart Scientific Magnetic Stirrer was used to mix the release medium throughout the experiment. It was established from the UV-visible spectroscopy calibration that the maximum concentration of vanillin in ethanol that can be detected is 40 mg dm^{-3}. If 0.2 g of loaded FCC (excluding the weight of the vanillin) is used, however, there will be 0.406 g (406 mg) of vanillin released; this would make a 1.624 g dm^{-3} (1 620 mg dm^{-3}) vanillin in ethanol concentration in a 250 cm^3 volume, which far exceeds the upper detection limit of the UV-visible instrument. Therefore, it was decided that 1 000 mm^3 aliquots of the release medium were to be taken using a Thermo Scientific Finnpipette (100-1,000 mm^3 in range) at certain time intervals and diluted in 50 cm^3 volumetric flasks with ethanol before being analysed via UV-visible spectroscopy. The time intervals were 5 seconds, 30 seconds, 1 minute, 5 minutes, 10 minutes, 15 minutes, 20 minutes, and 25 minutes after addition of the loaded FCC.

6.2.3 Modelling

Omya International AG provided a range of raw data generated by the SP Technical Institute under a commissioned project, in which the diffusion of L-carvone, vanillin, and curcumin from loaded FCC was studied. The data is as yet unpublished and was obtained through personal communications. The diffusion data of theirs utilised in this chapter for modelling purposes only was that of vanillin release from FCC S07 and FCC S10 each loaded with 15 % vanillin. The loading method involved dissolving the vanillin in acetone (loading is based on the solubility of vanillin in acetone, which, according to the SP Institute, is 350 g dm^{-3}) and dropping the solution directly onto the power whilst agitating. The loading criteria was that the loaded particles should flow as nicely as the unloaded powder. This is effectively the IWI technique as described in Chapter 5.

The diffusion experiment involved 100 cm^3 of release medium being continuously stirred (115 rpm); the release medium was a degassed 1 % surfactant sodium lauryl sulphate (SLS) in a phosphate-buffered saline (PBS) solution (Sigma, P5368). The SLS was used to aid in the dissolution of water-insoluble substances. UV-visible spectroscopy measurements (Lambda 650, Perkin-Elmer, USA) were obtained every second through an automated pumping system in which a flow of the solution (2.5 cm^3 min^{-1} flow rate, through a 0.2 μm syringe filter with a polyethersulfone membrane from VWR, 5140072) reached the spectrometer in approximately 20 seconds where a reading was then taken (cuvette volume was 0.5 cm^3). The wavelength used for detection was 265 nm. The solution was then returned to the bulk solution. Five minutes after the experiment was started, the loaded FCC was added to the release media, and the concentration of the diffusing species was monitored. Two diffusion experiments per FCC grade were performed: 9.2 and 9.5 mg of loaded FCC S07 were used, and 9.2 mg of loaded FCC S10 were used for both experiments.

The system considered in these modelling simulations is that of a monolithic solution, according to Figure 6.1, in which the diffusion of the drug out of the FCC will be geometry dependent. In this case, a flavour is being used as the drug analogue. Equation 6.2 (Vergnaud, 1993), which is slightly adapted from equation 6.1, was used to calculate

the diffusion coefficients for the vanillin diffusion data from FCC S07 and FCC S10:

$$M_{\mathrm{v}} = M_{\mathrm{v.t0}} \frac{6}{\pi^2} \sum_{n=1}^{n=1000} \frac{1}{n^2} \exp\left(-\frac{D_{\mathrm{FCC}} n^2 \pi^2 t}{r^2}\right) \tag{6.2}$$

where M_{v} and $M_{\mathrm{v.t0}}$ are the masses of vanillin in the FCC at time t and at $t = 0$ (or the theoretical mass of vanillin in solution at equilibrium), respectively, and D_{FCC} is the calculated diffusion coefficient.

The diffusion coefficients were calculated using .ipynb IPython Notebook files, in which code was edited using Jupyter Notebook in Google Chrome (Version 50.0.2661.102, 64-bit). The Anaconda distribution was used to install Python (version 3.5) and Jupyter. The code was written with the aid of Dr G. Maurizio Laudone's Python expertise, in which a quasi-infinite series (in this case, n = 1 000) of exponential functions were utilised to solve the partial differential equation 6.2 considering the respective initial and boundary conditions: 1) perfect sink conditions are maintained throughout, 2) the particles are spherical in diameter, all of the same size (7.5 μm), 3) the vanillin distribution in the FCC is homogeneous before exposure to the release medium (t = 0), 4) the vanillin is highly soluble, and 5) the diffusion coefficient of the vanillin is constant (Öner *et al.*, 2011; Cosijns *et al.*, 2007; Grathwohl, 1998). The skeletal density of the FCC needed to be included in the code to calculate the volume of an FCC particle within the code. However, the densities of FCC S07 and S10 are unknown, so the skeletal density of FCC TP (3.25 g cm^{-3}) was used for both grades.

6.3 Results & discussion

6.3.1 Release & diffusion experiments

A calibration graph of vanillin in ethanol was made with the UV-visible spectrometer, and the resultant graph is shown in Figure 6.4. The results of a trial vanillin release experiment are shown in Figure 6.5.

It was expected that as soon as the loaded powder was placed into the ethanol that there would be an initial rapid vanillin release; this is known as the 'burst' effect (Eberle *et al.*, 2014; Berthod *et al.*, 1988). However this did not appear to be evident in Figure 6.5. Although burst release is not uncommon in matrix systems, they do run less risk of dose dumping than reservoir systems (Huang and Brazel, 2001; Frenning, 2011), which may contribute to the lack of the burst effect in Figure 6.5.

Figure 6.5 suggests that all vanillin is released from the FCC by the 5-minute mark. It is suggested for future experimentation that the frequency with which the aliquots are taken is increased, especially immediately after the loaded FCC is introduced to the release medium, and perhaps the volume of release medium should be reduced.

6.3.2 Modelling

Figure 6.6 displays the diffusion curves and simulated fits of the entire diffusion experiment (excluding approximately 200 seconds at the end of the experiment, and the first 5 minutes at the beginning). As soon as the loaded powder was placed in the solvent there was an initial rapid vanillin release (i.e. the 'burst' effect), which was attributed to

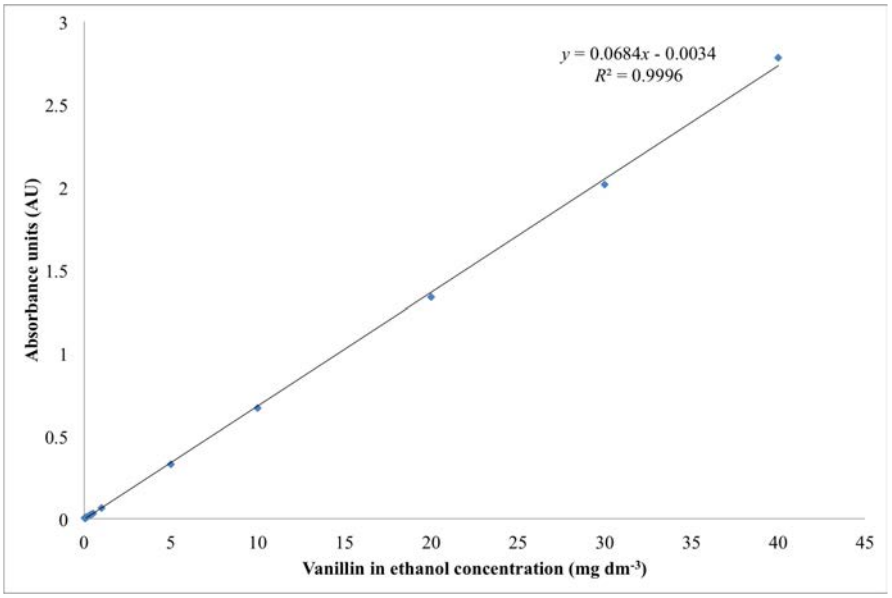

Figure 6.4: Vanillin in ethanol UV-visible calibration graph for vanillin release trial experiments.

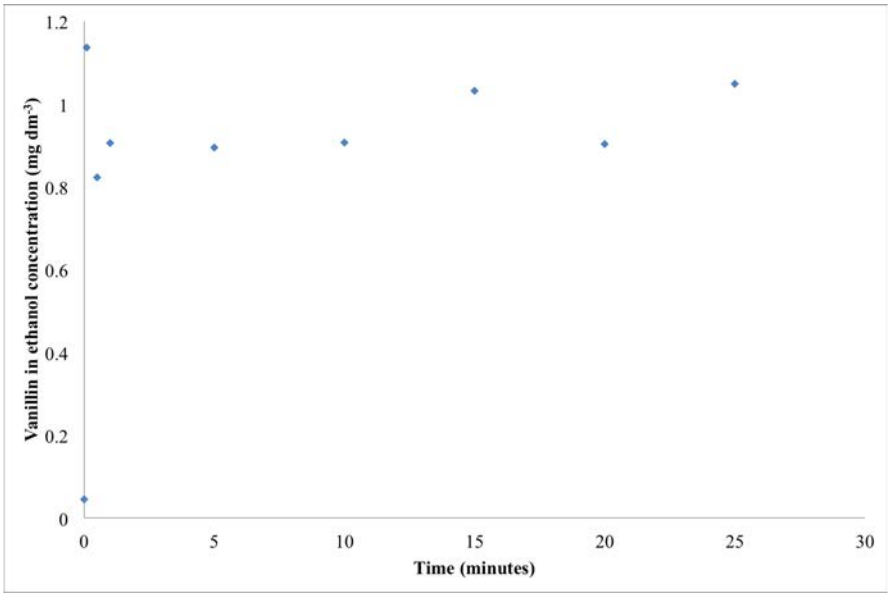

Figure 6.5: Experimental data of vanillin release trial from FCC loaded using the IWI technique in section 5.2.4.

the solid vanillin dissolving in the solvent before diffusing out from the pores. Additionally, there was also most probably a layer of vanillin solidified on the surface of the FCC that needed to dissolve before pore diffusion took place. Figure 6.7 displays the diffusion curves from Figure 6.6, but with the initial 'burst' of vanillin chopped off, and their simulated fits. Figure 6.8 shows the long term diffusion data from Figure 6.6 and the simulated fits. Effectively it is being postulated that there are three distinct parts to the diffusion curve: 1) the entire diffusion curve as in Figure 6.6, which encompasses any initial 'bursts' of vanillin, 2) the short-term diffusion, in which Figure 6.7 encompasses the short-term and long term diffusion but no 'burst,' and 3) the long term diffusion in Figure 6.8.

The burst of flavour exhibited in Figure 6.6 is attributed to the dissolution of vanillin before its diffusion, and because dissolution kinetics can sometimes affect the release profile in its early stages, and monolithic systems are typically diffusion-controlled (Frenning *et al.*, 2005; Frenning, 2011), it was decided that cutting off the initial portion of the curve was warranted. As the FCC was saturated with solvent it became uniform in concentration and so was able to generate a simulated fit with a higher R^2 value than with the initial portion of the curve considered (Table 6.2). The point at which the curve in Figure 6.7 begins is when the FCC is assumed to be fully saturated.

Table 6.2 displays the diffusion coefficients obtained from Figures 6.6, 6.7, and 6.8, along with their calculated R^2 values, in which it can be seen that the R^2 fit is generally better for FCC S10 than S07. However, for both FCC samples, the best R^2 fit is of the diffusion portion of the curve (i.e. no dissolution/initial 'burst).

Table 6.2: The diffusion coefficients obtained of the simulated fits from Figures 6.6, 6.7, and 6.8 using equation 6.2. The values in parenthesis are the R^2 values.

FCC	D_{FCC} (10^{-14} m^2 s^{-1})		
	Diffusion following dissolution	Diffusion	Long term diffusion
S07	2.32 (0.89)	1.76 (0.94)	0.05 (0.90)
S10	2.48 (0.90)	2.22 (0.98)	0.35 (0.91)

Table 6.3 shows the critical pore diameter of the intraparticle pores of FCC S07, S10, and the FCC grades from Chapter 7 (Levy *et al.*, 2015). The values were obtained visually from the steepest part of the slope of the leftmost peak on the pore size differential of the mercury intrusion porosimetry data for each sample (see Figure 6.3 for an example). Table 6.3 also shows the D'_{phase2} calculated from Chapter 7 (Levy *et al.*, 2015) and the D_{FCC} calculated from the computational methods outlined in this chapter. Please see section 7.1.2 of Chapter 7 for details regarding D' and section 7.2.2 for details regarding D'_{phase2}.

FCC S07 has smaller pores (Table 6.3) and a smaller pore volume (Table 6.1), and so it would appear that this is what gives it a slightly slower diffusion coefficient than FCC S10. This initial quantitative result merits further investigation.

Regarding comparing the FLC values (D'_{phase2}) to the modelled values from this chapter

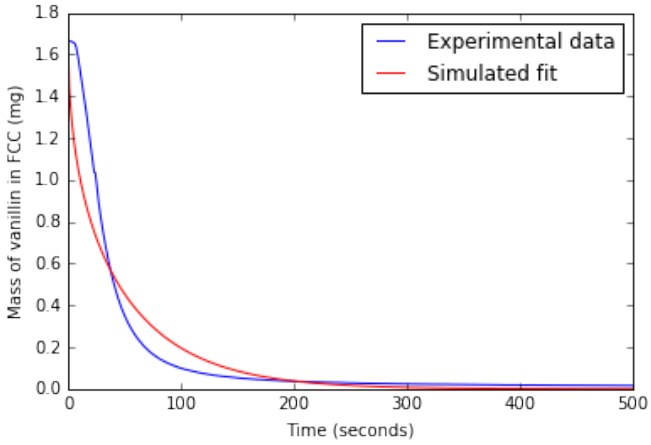

(a) The entire experimental and simulated diffusion curves of vanillin from FCC S07.

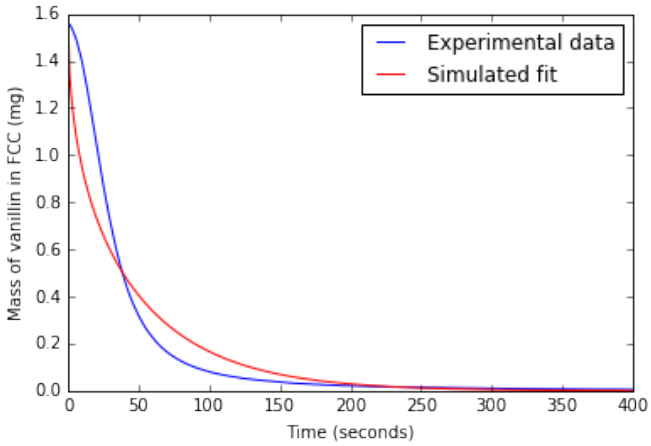

(b) The entire experimental and simulated diffusion curves of vanillin from FCC S10.

Figure 6.6: The blue line represents the experimental diffusion data provided by Omya International AG, generated by the SP Technical Research Institute of Sweden under a commissioned project. The red line represents the simulated fit to the experimental data using equation 6.2. The y-axis is the time in seconds, and the x-axis is the mass of vanillin in the FCC in mg.

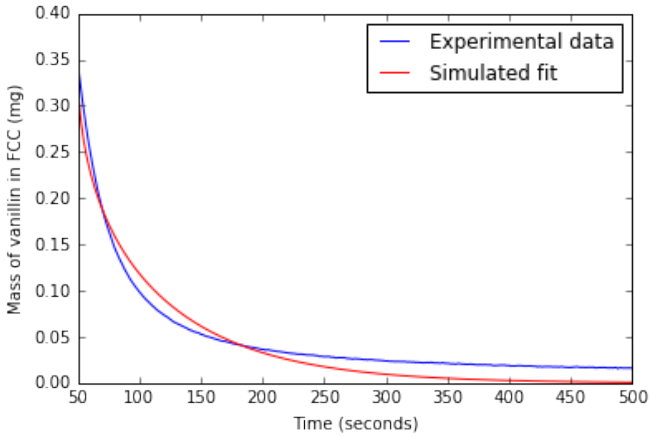

(a) Experimental and simulated diffusion curves of vanillin from FCC S07.

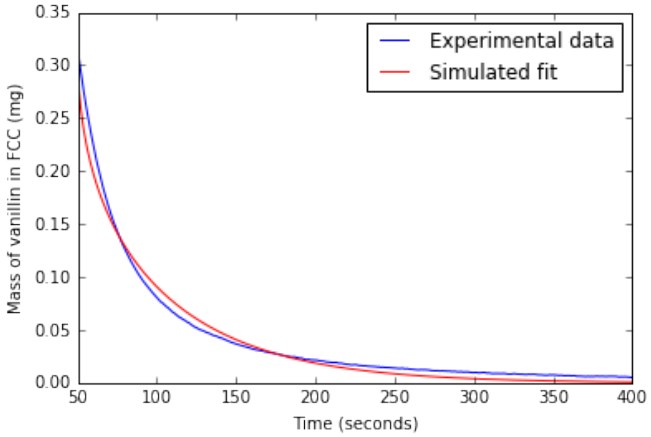

(b) Experimental and simulated diffusion curves of vanillin from FCC S10.

Figure 6.7: The blue line represents the experimental diffusion data provided by Omya International AG, generated by the SP Technical Research Institute of Sweden under a commissioned project, in which the first 50 seconds of data from Figure 6.6 were cut off. The red line shows the simulated fit to the experimental data using equation 6.2. The y-axis is the time in seconds, and the x-axis is the mass of vanillin in the FCC in mg.

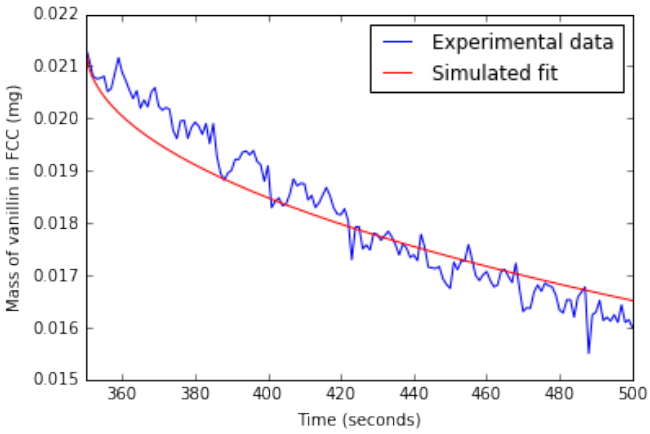

(a) Experimental and simulated long term diffusion curves of vanillin from FCC S07.

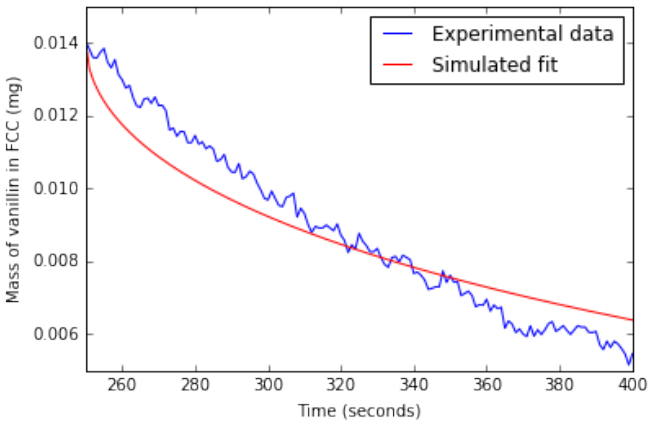

(b) Experimental and simulated long term diffusion curves of vanillin from FCC S10.

Figure 6.8: The blue line shows the experimental diffusion data provided by Omya International AG, generated by the SP Technical Research Institute of Sweden under a commissioned project, in which only the last 150 seconds of the experimental curve from Figure 6.6 were considered. The red line shows the simulated fit to the experimental data using equation 6.2. The y-axis is the time in seconds, and the x-axis is the mass of vanillin in the FCC in mg.

Table 6.3: The critical intrapore diameter of various FCCs, along with the D'_{phase2} calculated from the work of Levy *et al.* (2015), also outlined in Chapter 7, and the D_{FCC} calculated from the computational methods outlined in this chapter.

FCC	D'_{phase2} (10^{-16} m^2 s^{-1})[1]	Critical intrapore diameter (μm)
FCC 02	4.05	0.11
FCC 03	1.06	0.51
FCC 06	3.97	0.03
FCC 07	6.55	1.22
FCC 12	19.7	0.07
FCC 13	106	0.11
FCC TP	6.85	0.18
HAP	6.17	0.06

FCC	D_{FCC} (10^{-16} m^2 s^{-1})	Intrapore diameter (μm)
S07	232	0.02
S10	248	0.10

[1] Values obtained from Levy *et al.* (2015).

(D_{FCC}): a comparison is not possible. Both systems are effectively measuring intraparticle diffusivity in that the FLC values have been calculated from the long term portion of the diffusion curve (Levy *et al.*, 2015), and the simulated values are of individual particles in a solution (and so no interparticle tortuosity influences the diffusion). However, both systems are inherently different from one another: one is a packed bed of particles through which a stream of solvent flows, and the other is a series of individual particles in a beaker of solvent.

The D' calculated from FLC packed bed experiments was dependent on the particle size of the mineral (Levy *et al.*, 2015); this is because the particle size influences the interparticle tortuosity of the packed column. Additionally, the diffusing species also has the potential to diffuse into the adjacent particle. The experiments conducted in a beaker, however, have no interparticle effects that need to be considered, or worries that the diffusing species would diffuse into another particle, and this explains why the diffusion coefficients calculated from section 6.2.3 are much larger than those from the work of Levy *et al.* (2015) (Chapter 7).

Ultimately, the best way to draw comparisons between FCC samples would be to compare the diffusion coefficients calculated from not only the same methodology, but the same instrumentation; a proposed future work idea would be to measure and calculate D' of FCC S07 and S10 using the method and apparatus outlined in the work of Levy *et al.* (2015). The SP Technical Research Institute of Sweden can then load vanillin and measure its diffusivity from the FCC samples used in the work of Levy *et al.* (2015) in the same way as done for FCC S07 and S10; the D_{FCC} can then be calculated for each of them computationally as outlined in section 6.2.3. Ideally, the same trends in diffusion coefficient exhibited by FLC experiments and computational modelling from beaker diffusion experiments would be observed, which would be substantive confirmation that intraparticle diffusivity is the rate-determining factor of the diffusion of vanillin from FCC.

Although the dissolution of vanillin has been identified in the diffusion curves obtained from the SP Institute (Figure 6.6), the high R^2 values of the fit to the experimental data (Table 6.2) indicate that diffusion is the dominant physical process occurring in the release of vanillin. Therefore, because the dominant physical process occurring has been identified, the accuracy of the mathematical model can be increased by introducing more model parameters to take into account the dissolution and potential adsorption of vanillin (Siepmann and Siepmann, 2008).

The dissolution rate can be thought of as the rate of decrease of the mass of the active as being proportional to the surface area taking part in the dissolution process (Frenning, 2011; Costa and José, 2001), and can be described by the well-known Noyes-Whitney equation.

Additionally, the adsorption of vanillin onto the FCC from the dissolution medium should be investigated (Frenning and Strømme, 2003).

Finally, a comment regarding the increase in the solubilisation of vanillin: the SP Institute state that vanillin from loaded FCC is solubilised in a 1 % SLS water solution within a few minutes, as opposed to after approximately 20 minutes if the powder is added directly to the 1 % SLS in water solution. This is similar to reports of drug dissolution

from FCC in other work (Preisig *et al.*, 2014). This could be advantageous in the realm of drug delivery. For example, the absorption of an active from a gum formulation occurs primarily through the buccal mucosa and is a well accepted method to increase the rate of drug absorption. It has also been demonstrated that the incorporation of an active into a chewing gum increases its absorption as compared to a standard tablet formulation (Kamimori *et al.*, 2002). Another example is that of mesoporous silica nanoparticles, which are suggested to be useful in improving the oral bioavailability of poorly water soluble drugs (Zhang *et al.*, 2012).

6.4 Conclusions & future work

The hypothesis postulated in this chapter is as follows:

- **5:** Computational methods can be used to calculate a diffusion coefficient from experimental data of flavour release from FCC.

The release experiments outlined in this chapter require a lot of refinement, but the primary objective before release experiments are designed and tested would be to establish that the FCCs are filled as described in Chapter 5. Once the release experiments have been designed and tested, the solvent used can progress onto synthesised saliva of gastric phases, for example. For a fuller description of this, please refer to Chapter 9. Eventually these experiments can be conducted on loaded FCC tablets and granules. The release profiles can be modelled in a similar fashion to that outlined in this chapter in order to gain a better understanding of the release so that the FCC can be adapted to suit consumer requirements.

If the particle-size distribution data of FCC S07 and S10 can be obtained, then the Python code can be altered in such a way so that the diffusion coefficient of the FCC is calculated based on the relative abundance of the different sized particles, rather than assuming a uniform particle size for each FCC sample. This should increase the accuracy of the diffusion coefficient calculations.

The successful modelling of the diffusion profile of the vanillin loaded FCCs provided by the SP Institute and Omya International AG fulfills hypothesis 5, however, improvements to the modelling code can be made. For example, if the particle-size distribution data of FCC S07 and S10 can be obtained, then the Python code can be altered as described in the previous paragraph, rather than assuming a uniform particle size for each FCC sample. Also, the code can be modified to contain mathematical descriptions to take into account the dissolution of vanillin at the beginning of the experiment (i.e. the burst effect) and any adsorption that may also be taking place.

Chapter 7

Diffusion and tortuosity in porous functionalised calcium carbonate (FCC) for controlled drug and flavour release

7.1 Introduction

The overarching aim of this chapter is to report the exploratory work involving the novel zero length cell (ZLC), as well as the struggles and limits of such a technique that prompted the development of the finite length cell (FLC). Issues faced with the HPLC instrument are described in Chapter 3. Experimental work conducted with the FLC is also reported here, much of which has been published in a peer-reviewed journal (Levy *et al.*, 2015).

7.1.1 The zero length column (ZLC)

For gaseous systems the time dependent diffusion curve obeys equation 7.1 (Duncan and Möller, 2000*b*):

$$\frac{c_s}{c_0} = 2L \sum_{n=1}^{\infty} \frac{\exp(-\beta_n^2 (D/r^2)t)}{\beta_n^2 + L(L-1)} \tag{7.1}$$

where c_s is the fluid phase sorbate/analyte concentration, c_0 is the initial value of the fluid phase sorbate/analyte concentration at time t = 0, r is the radius of the sample particles (i.e. the diffusional length scale in spherical coordinates), D is the diffusion coefficient, β is a dimensionless infinite series parameter defined by equation 7.2, and L is a dimensionless parameter defined by equation 7.3.

L may be interpreted as the ratio of a characteristic diffusion and bulk washout time constant (r^2/D) to a convection/adsorption time (VK/F) (Duncan and Möller, 2000*b*; Ruthven *et al.*, 2005; Teixeira *et al.*, 2013). This parameter is also equal to the dimensionless adsorbed phase concentration gradient at the surface of the solid at time zero.

$$\beta_n \cot \beta_n + L - 1 - \gamma \beta_n^2 = 0 \tag{7.2}$$

$$L = \frac{Fr^2}{3VKD} \tag{7.3}$$

where F is the volumetric flow rate, V is the volume of sorbent in the ZLC bed, and K is the dimensionless Henry constant. At low adsorbate concentrations an adsorption

isotherm should approach a simple linear form, known as Henry's law region, of which the slope is known as Henry's constant; it is a proportionality constant between the adsorbed phase and the bulk phase concentrations (Brandani, 2002).

However, for liquid systems, it has been shown that the time-dependent diffusion curve obeys equation 7.4 (Ruthven and Stapleton, 1993; Brandani and Ruthven, 1995; Brandani, 1996; Duncan and Möller, 2000*b*; Ruthven and Brandani, 2000), in which the holdup in the sample chamber cannot be neglected. Thus, equation 7.1 becomes equation 7.4.

$$\frac{c_s}{c_0} = \sum_{n=1}^{\infty} \frac{2L\exp(-\beta_n^2(D/r^2)t)}{\beta_n^2 + (1-L+\gamma\beta_n^2)^2 + L - 1 + \gamma\beta_n^2} \tag{7.4}$$

where γ is a dimensionless parameter defined by equation 7.5.

$$\gamma = \frac{V_f}{3VK} \tag{7.5}$$

where V_f is the volume of interstitial fluid in the ZLC bed. For gaseous systems (equation 7.1), holdup in the sample chamber is often neglected (Teixeira *et al.*, 2013). In the case of negligible interparticle fluid holdup, i.e. γ = 0, equation 7.4 simplifies to equation 7.1 (Duncan and Möller, 2000*b*).

In the long time region only the first term of the summation is significant, so equation 7.6 applies, which defines the logarithmic time asymptote, and β is now given by equation 7.7.

$$\ln\frac{c_s}{c_0} \approx \ln\left[\frac{2L}{\beta_1^2 + L(L-1)}\right] - \beta_1^2\frac{Dt}{r^2} \tag{7.6}$$

$$\beta_n \cot\beta_n + L - 1 = 0 \tag{7.7}$$

For large values of L there is a further simplification since $\beta_1 \to \pi$ (Brandani, 1996; Ruthven and Stapleton, 1993; Ruthven and Vidoni, 2012).

L gives an indication of how far removed the system is from equilibrium control, and is proportional to the flow rate. The flow rate of the mobile phase is large enough when L >1 to ensure that transport processes, rather than equilibrium control, are occurring. Equilibrium control occurs when the flow rate is too low, which results in the diffusing species being investigated to slow because the concentration gradient is not maximised at all times (Brandani, 1996; Zabka and Rodrigues, 2007; Gribble, 2010). To extract a reliable time constant, it is necessary to run the experiment with at least two different flow rates (Ruthven *et al.*, 2005), as it is not possible to obtain such a time constant because the two parameters, β and γ, are unknown (Silva and Rodrigues, 1996).

However, the value of L is disregarded for the purpose of the experiments within this project, because the effective diffusion coefficients (D') were calculated towards the

end of the experiment, when diffusion was expected to be occurring, and the initial washout of the sorbate in the interparticle space would have already been achieved.

The ZLC has been used to study lots of materials, especially zeolites, in an attempt to study their microporosity. For example, the diffusivity of cyclohexane gas through synthesised silicalite particles with length scales varying across 3 orders of magnitude was studied by Teixeira *et al.* (2013); they concluded that transport control was likely due to either pore narrowing at the surface or an extension of the diffusional length scale near the surface due to total pore blockages. Other work has suggested, as with other systems, that the interparticle diffusion of cyclohexane from between small zeolite crystals is slower than that between larger particles (Cavalcante and Ruthven, 1995; Duncan and Möller, 2000*a*). Also, Ruthven and Stapleton (1993) measured the diffusion of mesitylene in cyclohexane through zeolites, and reported coefficients in the range of 2.8 x 10^{-19} to 6.0 x 10^{-15} m^2 s^{-1}; they also attributed the low values to the small crystal size of the zeolites, which was around 1-2 μm, with diffusion likely to be controlled by interparticle rate processes. The characterisation of diffusion in microporous materials, however, remains a significant technical challenge (Teixeira *et al.*, 2013).

The ZLC technique was employed as part of the research undertaken for this project in order to study the intraparticle diffusion of FCCs, thus allowing the proposition of the first hypothesis of this chapter (hypothesis 6): that the diffusion characteristics of FCC can be studied by exposing a monolayer of FCC to a flow of solvent (i.e. a ZLC experiment). The analytes of interest for these diffusion studies were anethole and vanillin, each dissolved in ethanol, and the study of saccharin in HEPES buffer solution. More information about these compounds, solvents, and solutions can be found in Chapter 3.

However, despite its utility and relevance it became apparent that there were many limitations with the ZLC method. For example, although the monolayer concept is theoretically sound, the practical application of measuring out and spreading a monolayer of sample between the sinters of the ZLC in a reproducible manner is impossible. Previous studies have concluded that interparticle rate processes were the dominant factor in the diffusion characteristics measured experimentally (Ruthven and Stapleton, 1993; Cavalcante and Ruthven, 1995; Duncan and Möller, 2000*a*). Additionally, the dead space within the HPLC flow line, detector chamber, and ZLC entry and exit ports caused the liquids to mix in a manner similar to a chromatographic line broadening effect. The asymptote at long times and low concentrations may be adversely affected by an erroneous baseline coupled with any inaccuracy of the measuring device. To counter this, other short time and intermediate time solution methods have been proposed (Brandani and Ruthven, 1995, 1996), whereas Duncan and Möller (2000*a*) have suggested that these issues may be overcome by careful experimental design and operation. Additionally, the deviation from the model shown by the desorption curves in the literature occurs in the initial part of the experiment (Hufton and Ruthven, 1993; Brandani and Ruthven, 1995; Duncan and Möller, 2000*a*).

Since the effects being studied are so subtle as to be masked in a ZLC by this line broadening, and seeing that in some cases the ZLC is not suited for its purpose of deconvoluting the intra- from the interparticle diffusional effects, it was necessary to

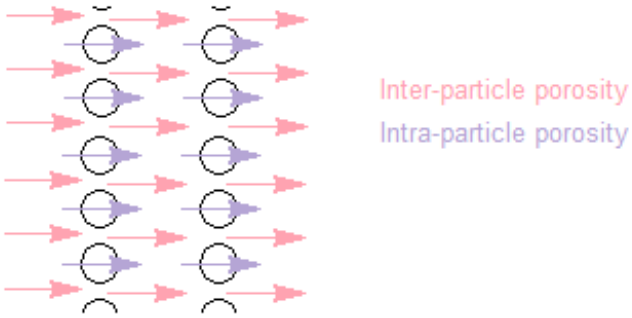

Figure 7.1: Demonstration of inter- and intraparticle porosity.

lengthen the ZLC in the flow direction, converting it to what is referred to as a finite length column or cell (FLC). An alternative approach was therefore to pack more sample into the FLC to avoid erroneous baselines by amplifying the magnitude of the diffusional effects from the samples thus making them observable, and to calculate diffusion coefficients from the long time region of the curve. Additionally, the use of a sample volume of around 1 cm^3 in the FLC is closer to that which would be found in a controlled release tablet, relative to the monolayer in a ZLC. However, the disadvantage is that the measured release rates are now dependent on diffusion and permeation effects within both the intra- and interparticle porosity, and that the system is less well described by the mathematical assumptions outlined in this section.

7.1.2 The finite length column (FLC)

Many of the principles of the ZLC, i.e. the assumption of laminar flow, apply to the FLC. However, the assumption of a monolayer of sample can no longer be made.

The porosity of a packed bed of porous particles has two distinct length scales: the channels between the particles, which is typically in the order of millimetres, and the channels within the particles, which typically have a length scale in the order of tens of microns and smaller (Kaneko, 1994; Ilankoon and Neethling, 2013). The former is referred to as the 'interparticle posority' of a system, and the latter as its 'intraparticle porosity,' based on the location of the pores (i.e. outside or inside of the sample particles, respectively). Although, some literature sources refer to these length scales as 'macro-' and 'microporosity,' respectively (Cunningham and Geankoplis, 1968; Whitaker, 1983; Verma *et al.*, 2007; Dong *et al.*, 2016). This dual-porosity of an aggregation of particles is shown schematically in Figure 7.1, of which the interparticle pores are flexible in nature (Kaneko, 1994). The dominant flow mechanisms within and around the particles are quite different (Ilankoon and Neethling, 2013).

Although equation 7.4 should therefore be used to interpret FLC diffusion curves, Brandani and Ruthven (1995) have shown that the interstitial fluid holdup in a well-mixed sorbent bed may be neglected if the adsorption constant of the system is large enough so that $\gamma < 0.1$. Negligible fluid holdup leads to the standard relation for ZLC diffusion curves, which is displayed in equation 7.1. The definition of the parameter γ is displayed in equation 7.5, and may be interpreted as the ratio of the volume of fluid in the

adsorbent bed (V_f) to an equivalent volume of the sorbent itself (VK); V_f and V can usually be related through bed voidage, and thus γ is not a function of bed length, but rather of the adsorption constant (K) (Duncan and Möller, 2000*b*).

As it has been shown that the adsorption of vanillin is similar in extent for a majority of the FCC samples used in this project (Chapter 4), the value of K will be similar regardless of the FLC bed length. Therefore, the calculation of the diffusion coefficients from the FLC experimental data is the same as for a ZLC experiment.

However, the disadvantage is that the measured release rates are now dependent on diffusion and permeation effects within both the intra- and interparticle porosity, and that the system is less well described by the mathematical assumptions described earlier. Rather than precise diffusion coefficients D, the measurements are therefore of effective diffusion coefficients D'.

7.1.3 PoreXpert®

The effective diffusion coefficients calculated from FLC experimental data can only be used for optimisation of the FCC void structure if they are related to quantitative void structure parameters of the samples. As such characteristics are not measurable by direct microscopy, since that gives only two-dimensional views of the interparticle space and the particle surfaces, nor directly from any other single experimental technique, then it is necessary to gain the information with the help of a void structure model.

Each unit cell generated of side length h comprises an array of $n \times n \times n$ pores; in this work, $n = 15$. The characteristics of the unit cell are adjusted using an eight-dimensional Boltzmann-annealed amoeboid simplex, which moves around parameter space searching for an optimum void network that matches closely the experimentally measured porosity and percolation characteristics of the porous media. The five parameters defining the parameter space are throat skew, throat spread, pore skew, connectivity, and correlation level (Price *et al.*, 2009).

The tracking of weighted routes through the structure allows an estimation of tortuosity, defined as the ratio of the median of actual path lengths through a sample to the straight path across the unit cell (Laudone *et al.*, 2015). The tortuous path length through a cluster is assumed to be the same as if the cluster was in fact a large pore of the same volume. Since all the pores and throats in the cluster are larger than the access throats to the cluster, and the access throats therefore control the overall tortuosity of the cluster, this is a reasonable approximation, which has been validated in other work (Laudone *et al.*, 2015).

Van Brakel and Heertjes (1974) formulated an equation that relates the diffusion coefficient (D) with the tortuosity of the sample (τ), porosity of the sample (ϕ), and the bulk diffusion coefficient (D_{12}):

$$\frac{D}{D_{12}} = \frac{\phi}{\tau^2} \tag{7.8}$$

Equation 7.8 is used in this work to aid in the interpretation of the calculated effective diffusion coefficients.

Therefore, the second hypothesis addressed by the work outlined in this chapter (hypothesis 7) asks whether the diffusion characteristics of FCC can be studied by exposing a packed bed of FCC to a flow of solvent (i.e. an FLC experiment), and then subsequently deconvoluting the intra- from the interparticle processes using PoreXpert.

The validation of the predecessor to PoreXpert, known as Pore-Cor, has included a comparison of the void sizes when the model was mathematically microtomed, compared to image analysis of actual microtomed samples. Although the model voids were one or two orders of magnitude too small compared to experiment, use of the fallacious capillary bundle model produced voids which were some 8 orders of magnitude too small (Matthews *et al.*, 2006). The calculation of tortuosity with the current PoreXpert model has recently been validated against experimental measurements on sandstone and limestone (Laudone *et al.*, 2015).

7.2 Materials & methods

The analytes used in ZLC and FLC experimental work outlined here were anethole, saccharin, and vanillin. Ethanol and the HEPES buffer solution were utilised throughout. Chapter 3 provides more information about these compounds, solvents, and solutions. The HPLC instrument used with the ZLC/FLC is also discussed in Chapter 3, and utilises a DAD as the detection method.

The general procedure for a ZLC or an FLC experiment is essentially the same. The methodology followed was that developed by Ruthven and Stapleton (1993) for the ZLC, namely to saturate the sample with a solution, then change to solvent and measure the lag caused by diffusion of the dissolved species out of the sample.

Firstly, the wavelength of maximum absorbance ($\lambda_{\max}$) for each analyte was determined from absorption spectra obtained using a Hewlett Packard (now Agilent) 8452 UV-visible spectroscopy system. Then a calibration graph for each analyte was created at this characteristic wavelength in order to convert the HPLC signal to a concentration value.

The HPLC calibration data for each analyte was obtained by flowing known concentrations of the analyte in an appropriate solvent through an empty ZLC or FLC column in increasing stepwise increments; the concentration was increased when the signal from the HPLC appeared to have equilibrated. An example of this is shown in Figure 7.2 in a later section. The calibration curve is then made from this data by averaging the absorbance/signal for the equilibrated portion of each 'step' (i.e. the portion of the curve parallel to the x-axis) and plotting this on a separate graph against the concentration of analyte that it represents. A linear regression line is plotted, and the equation of this line is the formula used to convert the absorbance/signal (x) from an experiment to a concentration (y). An example of this is shown in Figure 7.3 in a later section. Once the calibration curve was made, experimental work began.

For the vanillin in ethanol FLC experiments (sections 7.2.2.1 and 7.3.2.1) the initial conditioning of the sample was carried out by flowing solvent at 0.5 cm^3 min^{-1} through it for 30 minutes. Then 50 % by volume of a solution of 100 mg dm^{-3} vanillin in ethanol was added to the flow stream, and the overall flow rate increased to up to 4 cm^3 min^{-1}

for 30 minutes. Finally, flow was switched back to pure solvent for 45 minutes at a flow rate of 1 cm^3 min^{-1} in most cases and the lag in the concentration profile of the solution emerging from the sample was measured. The time at which the flow was switched back to pure solvent is shown as the time axis origin $(t=0)$ in the data graphs reported in this chapter. This procedure was generally the same for ZLC or FLC experiments with their respective solutions.

The Reynolds number (Eckhardt, 2009) of the fluid flow was of the order of 0.01 in the HPLC capillary tubes and packed FLC, indicating laminar flow. Since the relative thickness of the hydrodynamic and mass transfer boundary layers within the current system were unknown, the Schmidt number cannot be calculated exactly. However, it is assumed that the Péclet number, which is the product of the Reynolds and Schmidt numbers, is made small by the smallness of the Reynolds number, and that diffusive transport is therefore significant with respect to advective transport in the system.

It is also assumed that the fluid phase is well mixed and its concentration constant throughout the sample, i.e. mathematically identical to a differential plug flow reactor or an infinitesimally small continuous stirred tank reactor.

If there was fully efficient flushing, then it can be readily shown that the whole volume of the particle pack was flushed in less than a minute, in an experiment lasting around 2 000 seconds overall. Therefore the assumption is appropriate but not perfect.

7.2.1 Zero length cell (ZLC) experiments

The general procedure for a ZLC experiment is described section 7.2, and was followed unless stated otherwise.

7.2.1.1 Anethole in ethanol

When initial adsorption isotherms were obtained of anethole adsorbing onto FCC from ethanol, they incorrectly showed that adsorption took place (Chapter 4). Under this assumption, these ZLC experiments were conducted, and involved 'adsorbing' the flavour to the FCC, drying the product, and analysing the desorption of the flavour with the ZLC. Therefore, the aim behind these experiments was to adsorb a monolayer of anethole onto a known mass of FCC and to use the ZLC to measure 1) the rate at which it desorbs and 2) the amount that had been adsorbed.

Solutions of varying concentrations of anethole in ethanol were analysed with a Hewlett Packard (now Agilent) 8453 UV-visible spectroscopy system and anethole was found to absorb at 258 nm. Collaborative work with an undergraduate project student determined that the upper detection threshold of anethole in ethanol using this particular UV-visible spectroscopy system was 2.9 mg dm^{-3}; however, individual work later re-established it to be 10 mg dm^{-3}.

Calibration curves of anethole in ethanol at 258 nm were made on the HPLC, operating under the assumption that 2.9 mg dm^{-3} was the maximum concentration able to be detected on the UV-visible spectrometer, and thus further (and incorrectly) assumed that the maximum concentration that could be detected by the HPLC would be the same. Therefore, a second calibration was made, in which increasing concentrations of anethole in ethanol were flowed through an empty ZLC, and the concentration of

anethole increased by 5 mg dm^{-3} every 7 minutes. A concentration of 100 mg dm^{-3} of anethole in ethanol was kept in one of the solvent reservoirs of the HPLC, and in another reservoir was only ethanol. Different ratios of these two solutions gave desired concentrations of anethole in ethanol. The flow rate of the solvent (i.e. a mixture of the two solutions in the solvent reservoirs to make the desired concentration) was 2 cm^3 min^{-1}.

Calibrations of a second type were also made. These involved using the autosampler module of the HPLC to inject a known volume of a known concentration of anethole in ethanol into a stream of ethanol, and the area under the resulting DAD peak was plotted against the amount (i.e. mass) of anethole in that injection. This was to enable a peak area, as detected by the HPLC, to be converted to an amount of anethole.

Two calibrations of this type were made. The first involved injecting 1, 5, 10, 15, and 20 mm^3 of a 2.9 mg dm^{-3} anethole in ethanol solution, and the second involved injecting 1, 3, 5, 10, 15, 20, 40, and 60 mm^3 of a 14.5 mg dm^{-3} anethole in ethanol solution.

Then the experiments were conducted. The experiments utilised the three batches of anethole loaded FCC SFC 06.2 from section 5.2.3 of Chapter 5, which were analysed in the ZLC. This involved flowing a stream of ethanol being pumped through the ZLC at a rate of 2 cm^3 min^{-1}. When the absorbance baseline and pressure stabilised, the flow was stopped and the ZLC quickly opened, and a pre-weighed amount of dosed FCC was sandwiched between the sinters (approximately 3-4 mg), before being quickly reassembled and restarting the ethanol flow. The release profile of anethole was then recorded. This was carried out three times per batch of loaded FCC. The following amounts of loaded FCC per experiment were spread across the sinters: 4.4 mg $\pm$ 0.5 of batch 1, 4.3 mg $\pm$ 0.3 of batch 2, and 4.3 mg $\pm$ 0.1 of batch 3.

7.2.1.2 Vanillin in ethanol

Several experiments were conducted on GCC and FCC 06 with the ZLC using vanillin in ethanol as the diffusing species. A blank analysis was performed a total of three times. GCC was loaded into the ZLC on three separate occasions (i.e. experimental replicates), and on each loading the experiment was performed three times (i.e. analytical replicates). Runs 1-3 used 3.6 mg of GCC, runs 4-6 used 3.7 mg, and runs 7-9 used 3.8 mg. This format used for the analysis of GCC, as well as the weights of mineral loaded into the ZLC, was also used for the analysis of FCC 06.

The ZLC calibration used had an R^2 value of 0.99 to a maximum concentration of 50 mg dm^{-3}, which was used as the concentration of analyte during the equilibration phase of the FLC experiment. The analyte was analysed at a wavelength of 279 nm.

7.2.2 Finite length cell (FLC) experiments

The general procedure for an FLC experiment is described in section 7.2, and followed the same outline as a ZLC experiment, although an alternative method to load the column is required, both of which are described in section 3.2.1 of Chapter 3.

Other experiments were designed in order to investigate the way in which the packing affects the area of the curve from which D' is calculated. Data gathered from FLC experiments on each separate packing of the same FCC represent experimental repli-

cates, whereas data gathered from the three experiments performed on one packing arrangement of FCC represent analytical replicates. The FCC grades used for these types of packing experiments were FCC 02 and FCC 07, because the highest and lowest % packing into the FLC were achieved with these grades during vanillin in ethanol FLC experiments (Table 7.2 in section 7.3.2.1). Table 7.1 shows the weights used in these packing experiments as well as the calculated % FLC loading based on the two envelope density measurements available of the FCC grades.

Table 7.1: The weights of FCC 02 and FCC 07 used for the vanillin in ethanol FLC experiments; each experiment involved packing an FCC sample into the column on three separate occasions (i.e. experimental replicates), and three experiments were run on each different FLC packing of the FCC (i.e. analytical replicates). The % packing efficiency is also displayed in the table, as well as well as back-calculations utilising the envelope density obtained from MIP measurements, as opposed to the method that utilises the DryFlo powder (for reasons that are discussed in Chapter 5).

Sample	Amount of sample used per experimental replicate (g)					Packing efficiency achieved (%)	
	1	2	3	Average	Standard deviation	DryFlo	MIP
FCC 02	0.4694	0.4641	0.4640	0.4658	0.0031	98	154
FCC 07	0.7682	0.7799	0.7765	0.7749	0.0060	60	144

Additionally, published experimental work (Levy *et al.*, 2015) calculated effective diffusion coefficients (D') in regions where the minimum absorbance was 1.18 mAU, which, according to the calibration used to interpret such data, corresponds to a concentration of 1.2 mg dm^{-3}. The calibration, however, had a minimum vanillin in ethanol concentration of 10 mg dm^{-3}, which had an absorbance in the region of 300 mAU. Therefore, in order to address this issue, a subsequent calibration was made in a the same manner as before but with vanillin in ethanol concentrations between 0.1 and 10 mg dm^{-3}.

7.2.2.1 Vanillin in ethanol

A series of experiments were conducted with the FLC using vanillin in ethanol as the diffusing species. The ZLC calibration used had an R^2 value of 0.99 to a maximum concentration of 50 mg dm^{-3}, which was used as the concentration of analyte during the equilibration phase of the FLC experiment. The analyte was analysed at a wavelength of 279 nm.

Table 7.2 shows the envelope densities of the FCC samples calculated from both DryFlo and MIP measurements. Additionally, the table shows the theoretical weight that would constitute a 100 % efficient packing based on the density measurements, along with the amount of weight of each FCC used for the FLC experimental replicates.

Table 7.2: The weight of FCC loaded into the FLC for vanillin in ethanol diffusion experiments, along with the calculated expected weight and % packing efficiency based on calculations that utilised two envelope density measurements: one obtained from DryFlo measurements, and one obtained from MIP measurements.

Sample	Amount used (g)	DryFlo method			MIP method		
		Envelope density (g cm^{-3})	Amount to use (g)	% loading	Envelope density (g cm^{-3})	Amount to use (g)	% loading
GCC	1.5763	1.2878	1.6073	98	1.3000	1.6230	97
HAP	0.7233	0.6064	0.7569	96	0.4502	0.5619	129
FCC TP	0.3576	0.4037	0.5039	71	0.2322	0.2898	123
FCC 02	0.4507	0.3829	0.4779	94	0.2422	0.3023	149
FCC 03	0.8804	0.8756	1.0928	81	0.4633	0.5782	152
FCC 06	0.3131	0.2855	0.3563	88	0.2379	0.2969	105
FCC 07	0.7963	1.0386	1.2963	61	0.4317	0.5388	148
FCC 12	0.4821	0.4239	0.5291	91	0.2921	0.3646	132
FCC 13	0.4263	0.3848	0.4796	89	0.2928	0.3654	117

7.2.2.2 PoreXpert® modelling

PoreXpert® was used to model the void network of the FCC samples, and its recently developed tortuosity algorithm feature (Laudone *et al.*, 2015) was applied to the simulated void network structures. The algorithm was employed on the resulting computational structures in order to further attempt to deconvolute the intraparticle diffusivity of the vanillin in ethanol FLC experiments outlined in section 7.2.2.1 from the interparticle processes.

The void network resulting from this optimisation procedure is not unique, so a set of several stochastic realisations may be generated that match the experimental intrusion characteristics. The most representative simulated structure for each sample is then found by choosing realisations for which none of the fitting parameters has a deviation from the mean of the set larger than the standard deviation (σ_{devn}) of the set. If more than one sample meets that criterion, then the sample with all parameters closest to the mean was chosen. This approach is exemplified in Table 7.6 in section 7.3.2.1.

7.2.2.3 Saccharin in HEPES

A series of experiments were conducted with the FLC using saccharin in HEPES as the diffusing species. The FLC calibration used had an R^2 value of 0.99 to a maximum concentration of 400 mg dm^{-3}, which was used as the concentration of analyte during the equilibration phase of the FLC experiment.

Table 7.3 shows the weights of FCC loaded into the FLC for each experiment, along with the calculated expected weight and % packing efficiency based on calculations that utilised two envelope density measurements: one obtained from DryFlo measurements, and one obtained from MIP measurements. The implications on the packing of the FCC in the FLC, in light of the DryFlo caveat (as discussed in Chapter 5), are the same as those discussed in section 7.3.2.1.

Table 7.3: The weight of FCC loaded into the FLC for saccharin in HEPES diffusion experiments, along with the calculated expected weight and % packing efficiency based on calculations that utilised two envelope density measurements: one obtained from DryFlo measurements, and one obtained from MIP measurements.

Sample	Amount used (g)	DryFlo method			MIP method		
		Envelope density (g cm^{-3})	Amount to use (g)	% loading	Envelope density (g cm^{-3})	Amount to use (g)	% loading
GCC	1.5780	1.2878	1.5794	99	1.3000	1.5944	99
HAP	0.7432	0.6064	0.7437	99	0.4502	0.5522	135
FCC TP	0.4914	0.4037	0.4951	99	0.2322	0.2848	173
FCC 02	0.4675	0.3829	0.4696	99	0.2422	0.2971	157
FCC 03	0.9783	0.8756	1.0739	91	0.4633	0.5682	172
FCC 06	0.3473	0.2855	0.3502	99	0.2379	0.2918	119
FCC 07	0.9476	1.0386	1.2738	74	0.4317	0.5295	179
FCC 12	0.5052	0.4239	0.5199	97	0.2921	0.3582	141
FCC 13	0.4696	0.3848	0.4713	99	0.2928	0.3591	131

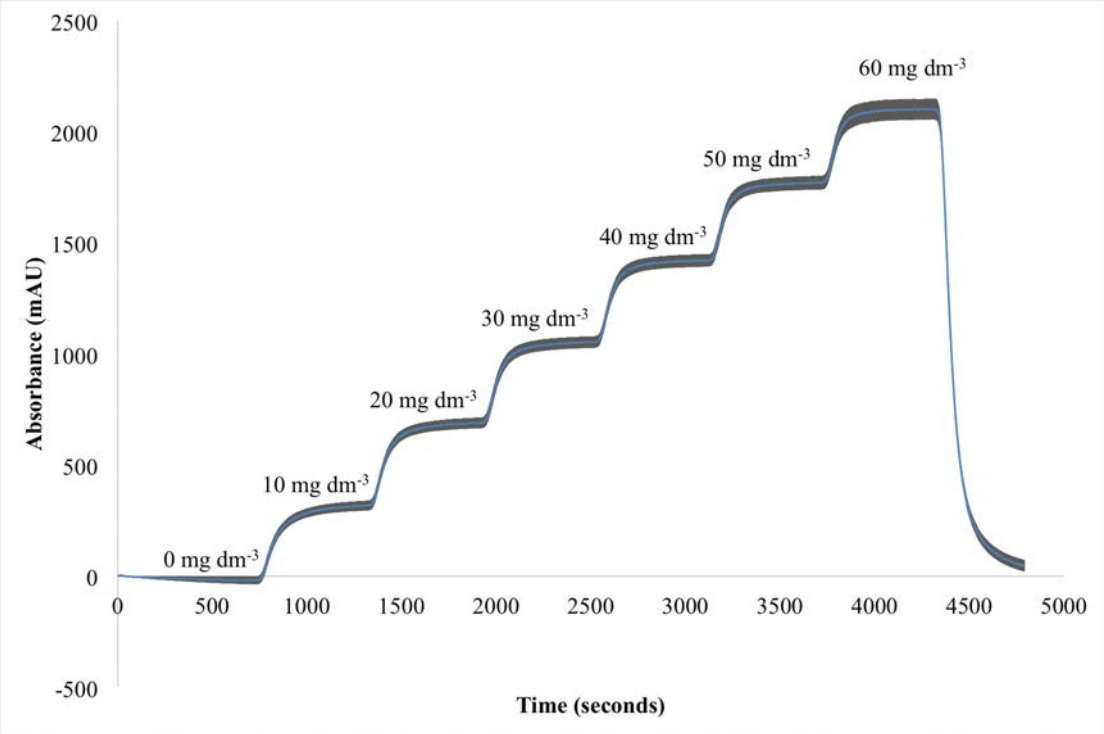

Figure 7.2: Vanillin in ethanol flowing through an empty ZLC column in stepwise increments of 10 mg dm^{-3}, from 0 to 60 mg dm^{-3}, at a wavelength of 279 nm. The graph represents an average of three experimental replicates, of which the y-error bars are the standard deviations of the three.

7.3 Results & discussion

Figure 7.2 shows calibration data obtained from the HPLC of vanillin in ethanol flowing through an empty ZLC. Figure 7.3 shows the calibration graph constructed from the aforementioned calibration data in Figure 7.2.

The processing of the experimental data obtained from ZLC and FLC experiments will now be discussed using the vanillin in ethanol FLC experiments from section 7.3.2.1 as examples. Firstly, the data is plotted in a graph of absorbance/signal against corrected time, an example of which can be seen in Figure 7.4. The abscissa labelled as 'corrected time' is simply the time shifted so that the point of the curve at which the HPLC pump switches from vanillin in ethanol to pure ethanol (i.e. the last 30 minute portion of the experiment) starts at 0. The experiment start times are adjusted to allow the direct comparison of the curves, in the knowledge that the absolute start time of the experiment does not affect the measured slopes. The thickness of the plots represents $\pm\sigma_{\text{devn}}$, where σ_{devn} is the standard deviation of a series of at least two, and sometimes three, analytical replicates. Secondly, the y-axis of the plots are then converted to concentration using the calibration curve, and the resulting curves are displayed in Figure 7.5. Thirdly, the y-axis is then divided by the data at the point corresponding to corrected time = 0, and this can be seen in Figure 7.6. And finally, the natural logarithm of the y-axis is taken, yielding the semi-logarithmic plot Figure 7.7. The slopes of these plots yield (D'/r^2).

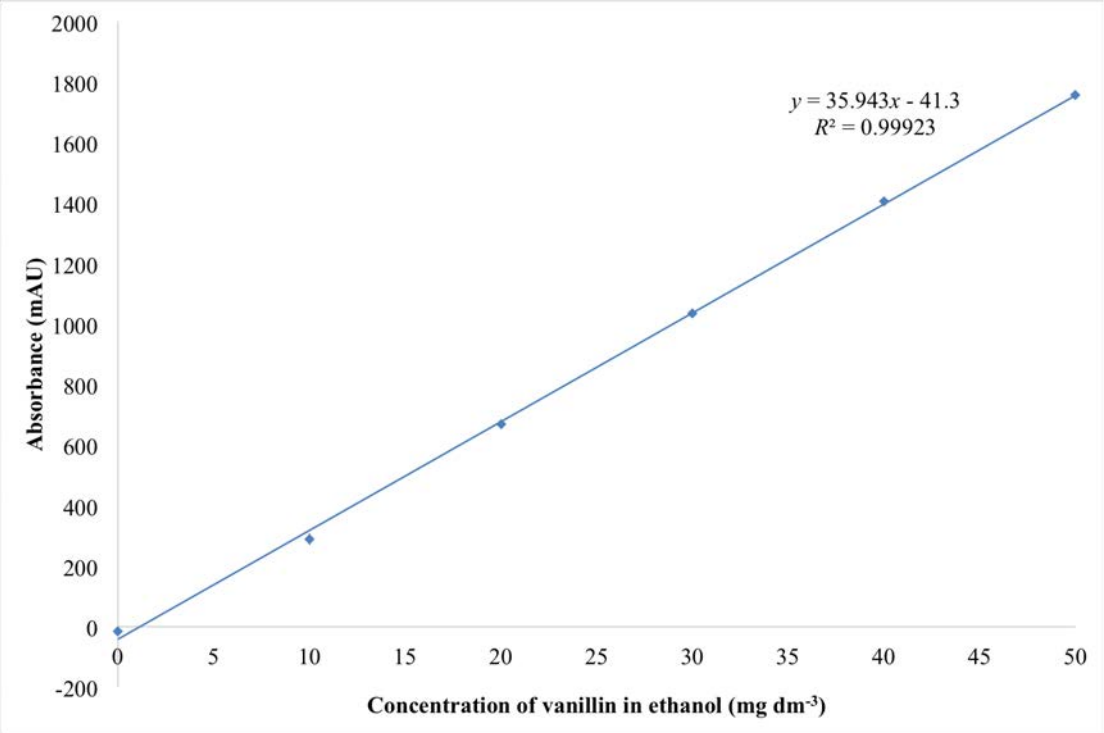

Figure 7.3: The calibration curve constructed, at 279 nm and up to 50 mg dm^{-3}, from the data in Figure 7.2. The y-error bars are the standard deviations of the average data used to create each data point from Figure 7.2.

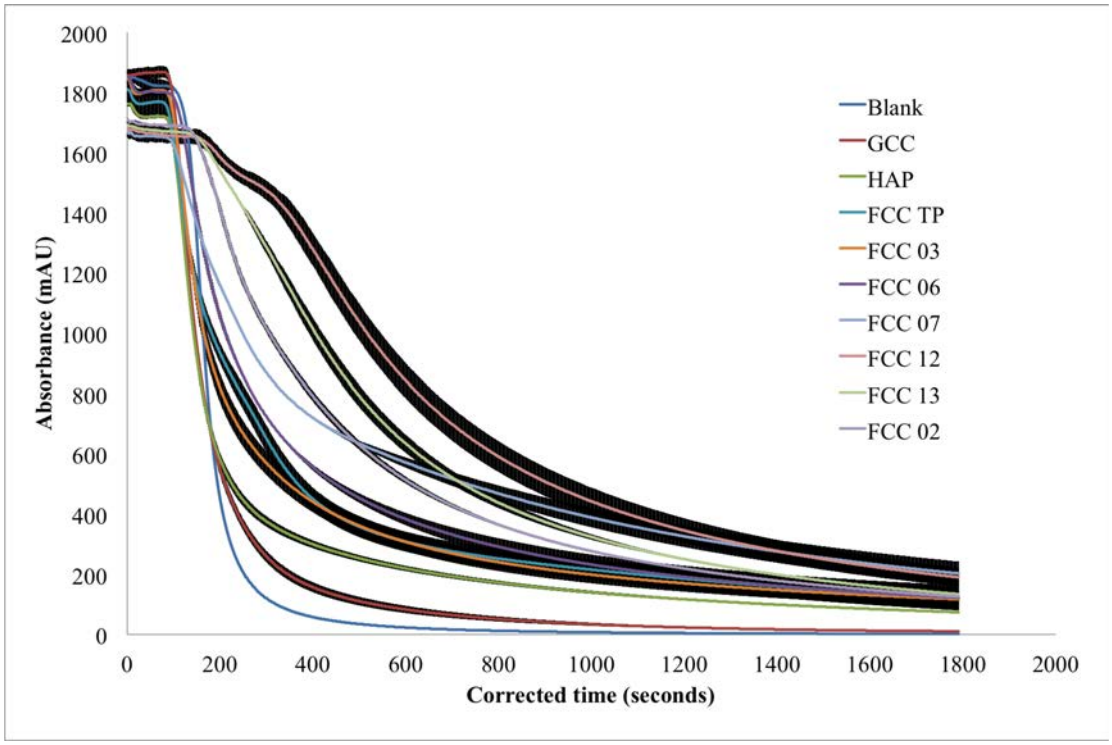

Figure 7.4: Data from vanillin in ethanol FLC experiments. The absorbance of vanillin was measured at 279 nm. The y-error bars, which are the standard deviations of the average data from three analytical replicates, give each curve a black 'cloud.'

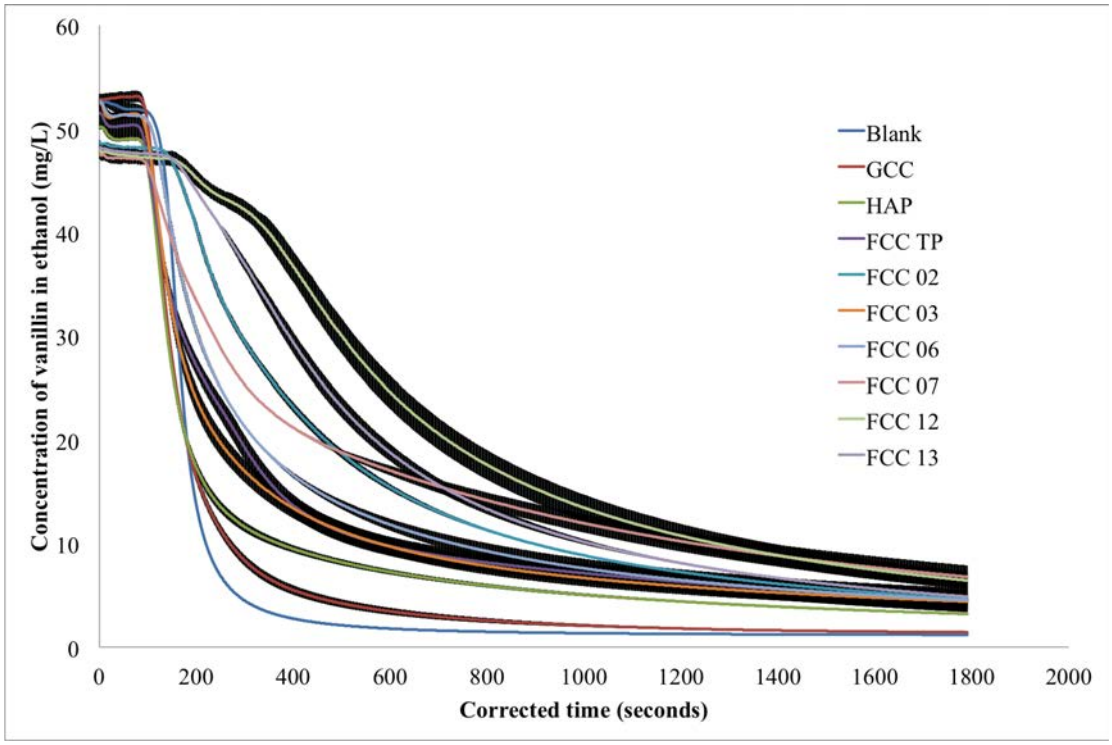

Figure 7.5: Data from vanillin in ethanol FLC experiments from Figure 7.4 whose y-axis has been converted to concentration using the calibration in Figure 7.3. The y-error bars, which are the standard deviations of the average data from three analytical replicates, give each curve a black 'cloud.'

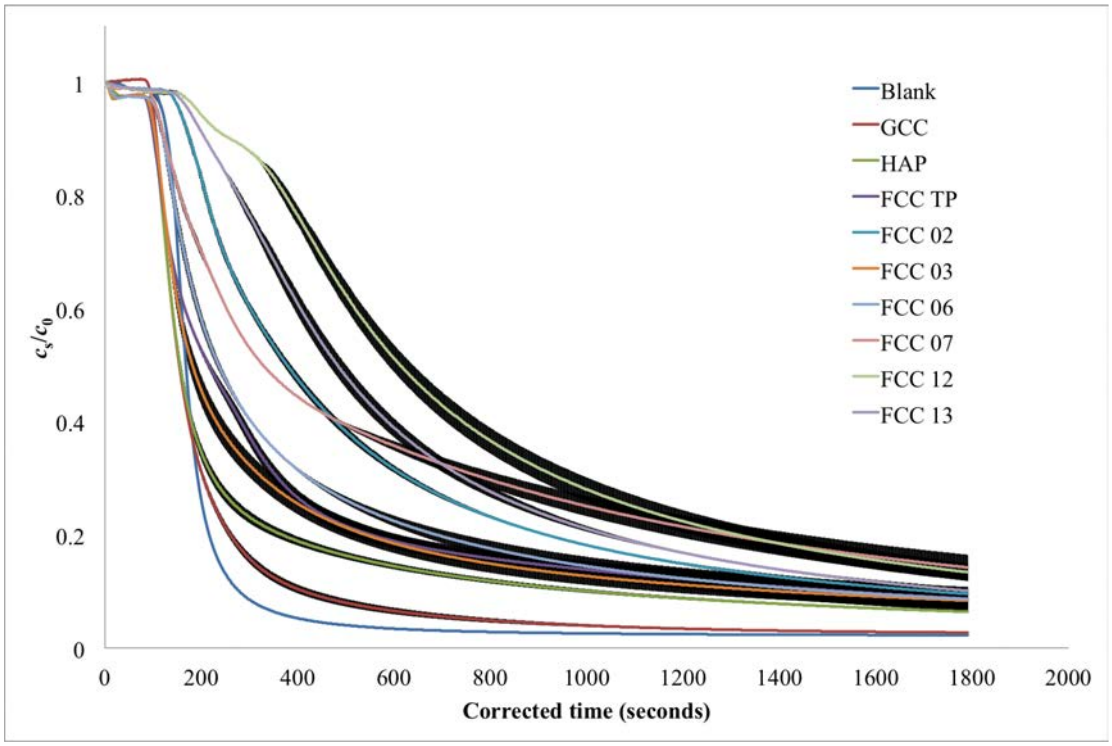

Figure 7.6: Data from vanillin in ethanol FLC experiments from Figure 7.5 whose y-axis has been divided by c_0. The y-error bars, which are the standard deviations of the average data from three analytical replicates, give each curve a black 'cloud.'

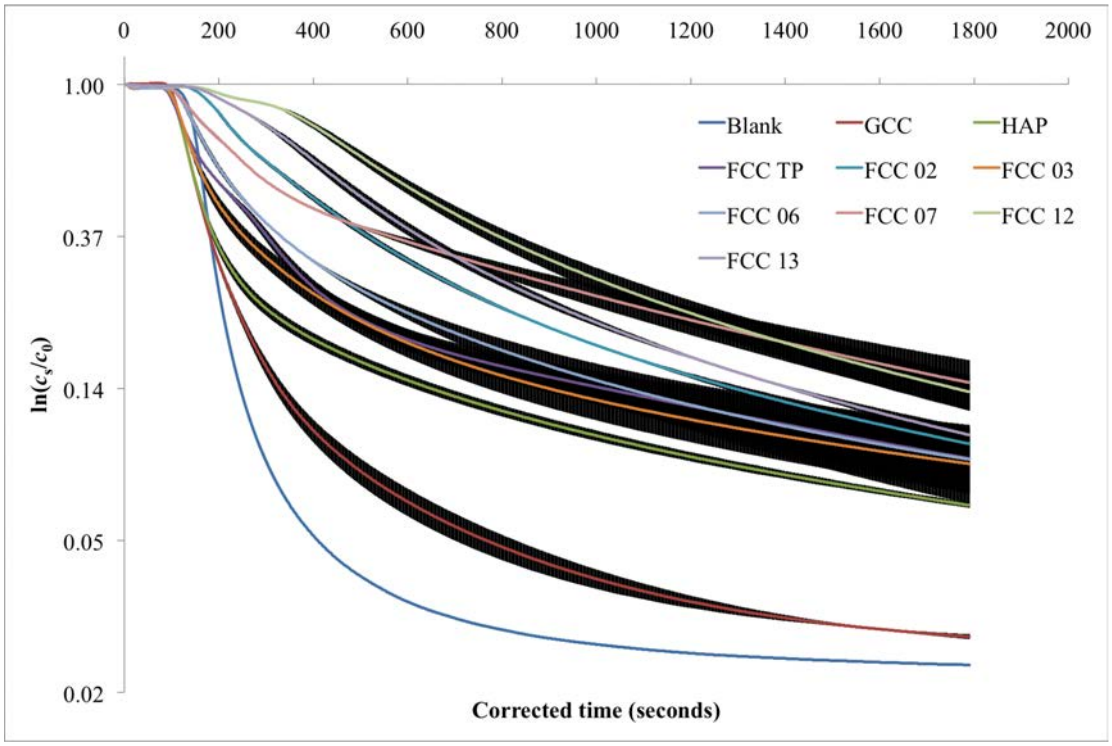

Figure 7.7: Data from vanillin in ethanol FLC experiments from Figure 7.6 of which the natural log of the y-axis has been taken. The y-error bars, which are the standard deviations of the average data from three analytical replicates, give each curve a black 'cloud.'

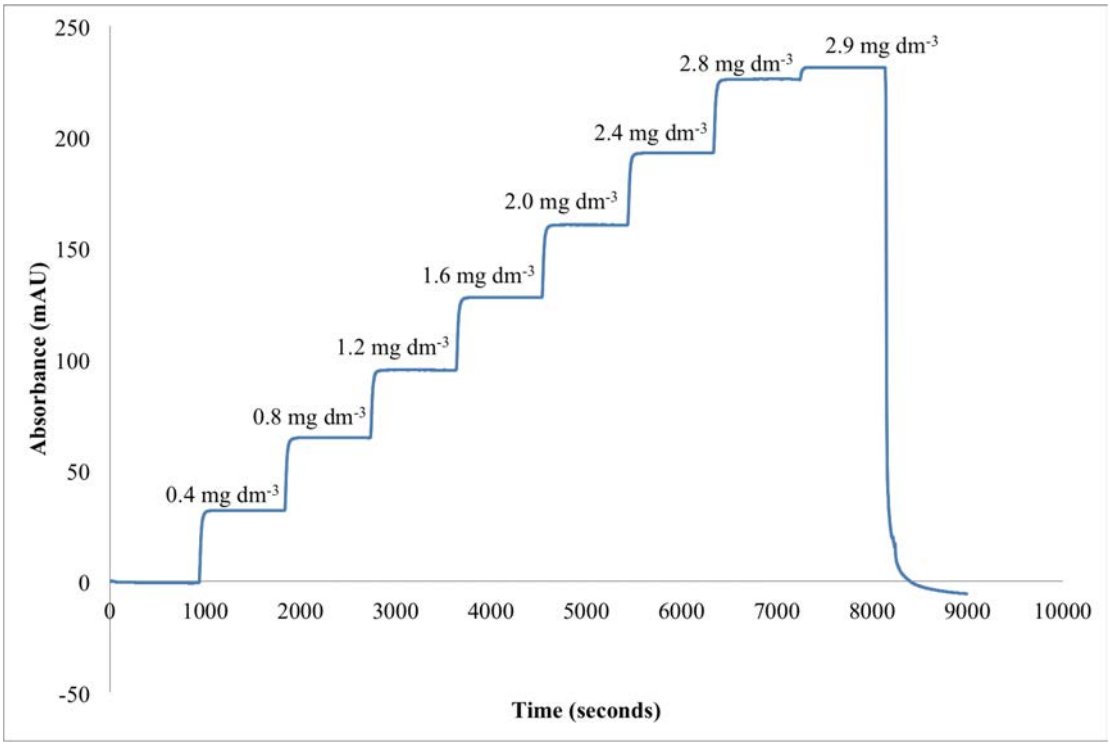

Figure 7.8: Anethole in ethanol flowing through an empty ZLC column in stepwise increments of 5 mg dm^{-3}, from 0 to 2.9 mg dm^{-3}, at a wavelength of 258 nm.

The calculation of D' from the semi-logarithmic plots (i.e. Figure 7.7) was taken from the long time region of the curve. It has been shown that the long time, low concentration region of the desorption curve in a ZLC experiment is controlled by an effectively linear adsorption isotherm (Brandani, 1998; Duncan and Möller, 2000*a*; Brandani *et al.*, 2000). Therefore the diffusivity as loading tends to zero may still be measured, even if the system under study does not strictly conform to the assumptions of the standard ZLC model. Hufton and Ruthven (1993; 2000*a*) have shown that a long-time solution method is very robust for obtaining intraparticle diffusivities. Regarding FLC experiments, the long time region of the curves are also used because the effects of packing and the line-broadening type of effects had become small.

7.3.1 Zero length cell (ZLC) experiments

7.3.1.1 Anethole in ethanol

Figure 7.8 shows the initial calibration data of anethole in ethanol for the HPLC under the assumption that the maximum concentration it could detect was 2.9 mg dm^{-3}. Figure 7.9 shows the actual calibration.

Figure 7.10 shows the second set of calibration data of anethole in ethanol for the HPLC up to 30 mg dm^{-3}. The noise becomes significantly apparent at a concentration of 35 mg dm^{-3}. The resulting calibration graph is displayed in Figure 7.11. The response was found to be linear (R^2 = 0.99), and the correlation equation was used to

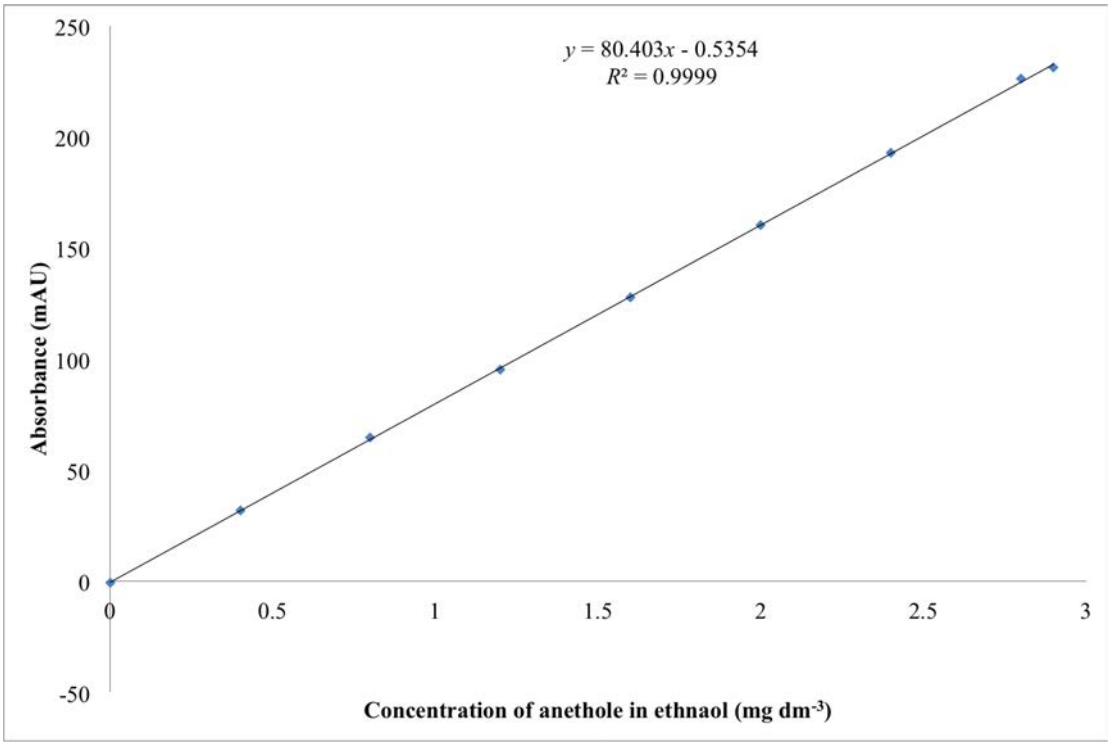

Figure 7.9: The calibration curve constructed, at 258 nm and up to 2.9 mg dm^{-3}, from the data in Figure 7.8. The y-error bars are the standard deviations of the average data used to create each data point from Figure 7.8.

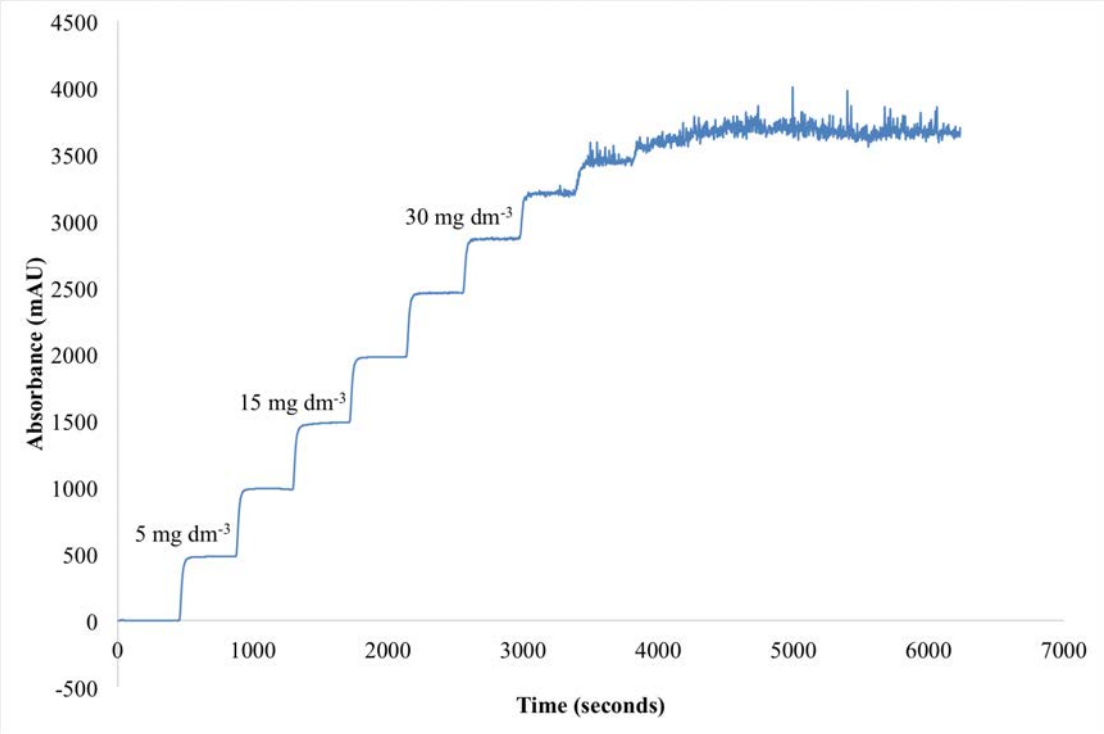

Figure 7.10: Anethole in ethanol flowing through an empty ZLC column in stepwise increments of 5 mg dm^{-3}, from 0 to 50 mg dm^{-3}, at a wavelength of 258 nm.

convert the absorbance signal from the DAD to concentration.

Figure 7.12 shows the injection calibration made by injecting volumes of 1, 5, 10, 15, and 20 mm^3 of a 2.9 mg dm^{-3} solution of anethole in ethanol, and Figure 7.13 shows the injection calibration made by injecting volumes of 1, 3, 5, 10, 15, 20, 40, and 60 mm^3 of a 14.5 mg dm^{-3} solution of anethole in ethanol.

The reason for the curved shapes, as opposed to a straight line, in Figures 7.12 and 7.13 may be due to a non-linear limit of detection when the concentration of anethole is too low for the DAD to detect accurately, or that as such a small amount of a low concentration is being injected, it is possible that not all of the aliquot was injected into the ethanol stream by the HPLC system.

The absorbance data resulting from the ZLC analysis of the anethole loaded FCC (section 5.2.3, Chapter 5) was shifted so that there were no negative absorbance values. An example of this data is shown in Figure 7.14. The area under the entire curve was calculated and was converted using one of the two calibration curves above (Figures 7.12 and 7.13).

The calibration curve in Figure 7.13 was used to convert the area under the curve of batch 1's loaded FCC data to an amount of anethole, and the calibration in Figure 7.12 was used to interpret the results of batches 2 and 3. The resulting calculations can be seen in Table 7.4.

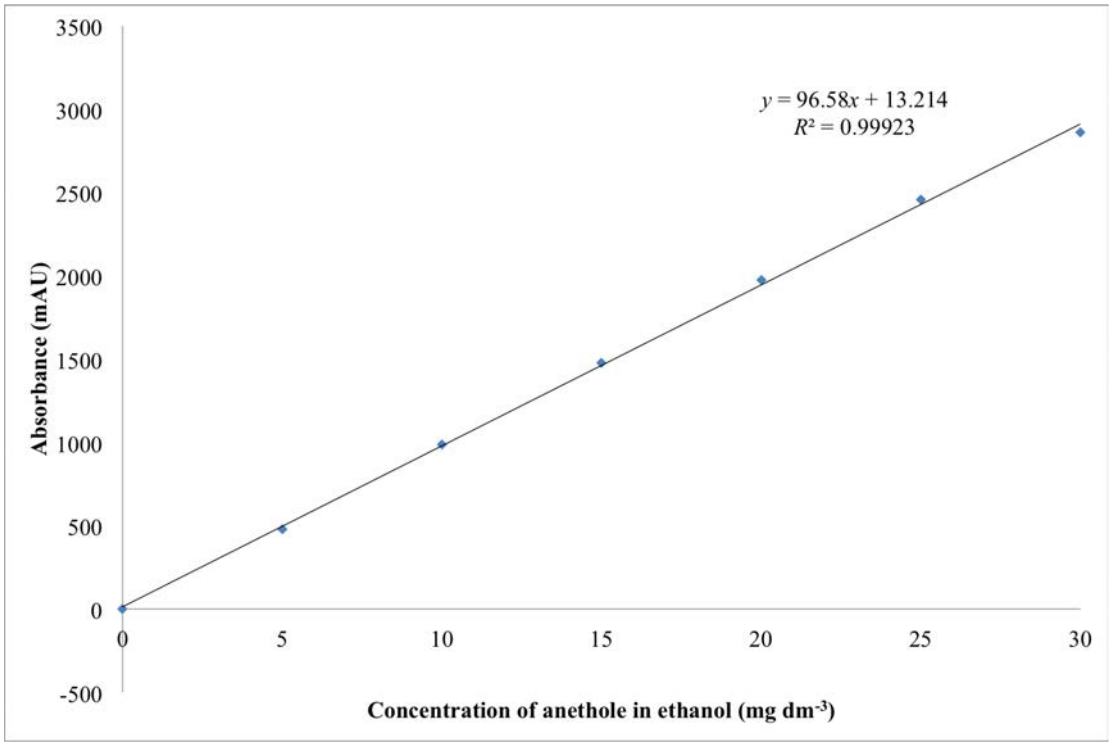

Figure 7.11: The calibration curve constructed, at 258 nm and up to 30 mg dm^{-3}, from the data in Figure 7.10. The y-error bars are the standard deviations of the average data used to create each data point from Figure 7.10.

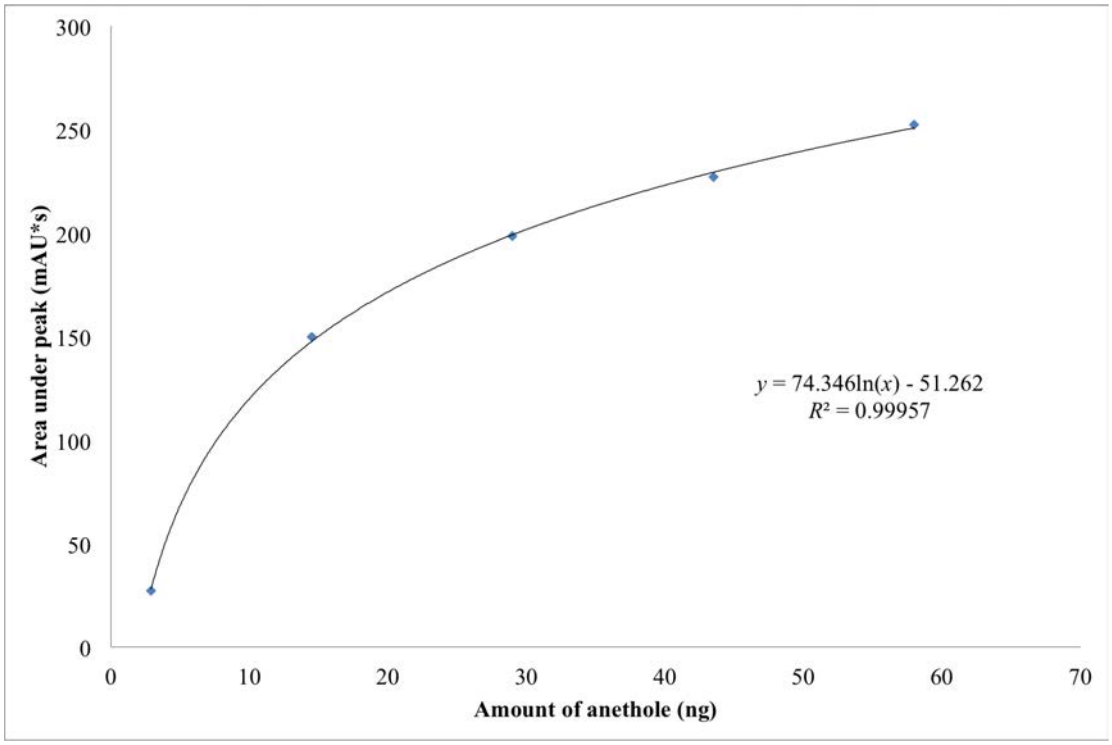

Figure 7.12: Calibration made by injecting volumes of 1, 5, 10, 15, and 20 mm^3 of a 2.9 mg dm^{-3} solution of anethole in ethanol. The anethole was detected at a wavelength of 258 nm. Each point represents the average of three data sets, and the y-error bars are the standard deviations of the three. The asterisk in the units of the y-axis (mAU*s) denotes a multiplication symbol (mAU $\times$ s).

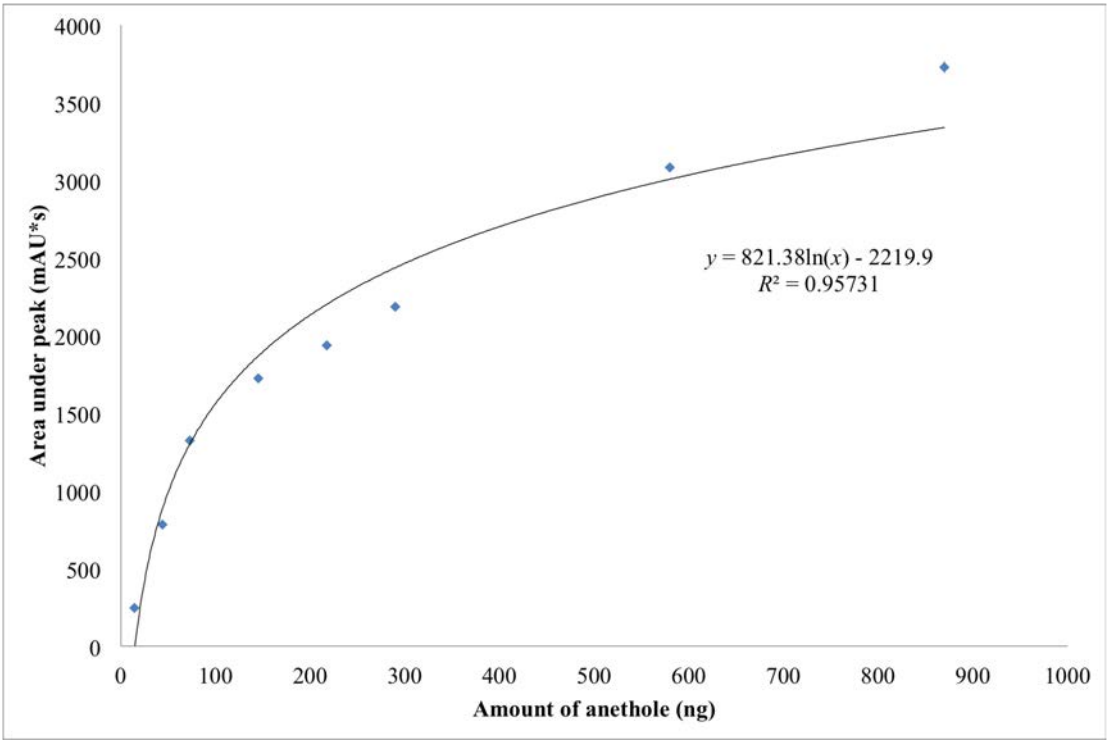

Figure 7.13: Calibration made by injecting volumes of 1, 3, 5, 10, 15, 20, 40, and 60 mm^3 of a 14.5 mg dm^{-3} solution of anethole in ethanol. The anethole was detected at a wavelength of 258 nm. Each point represents the average of three data sets, and the y-error bars are the standard deviations of the three. The asterisk in the units of the y-axis (mAU*s) denotes a multiplication symbol (mAU $\times$ s).

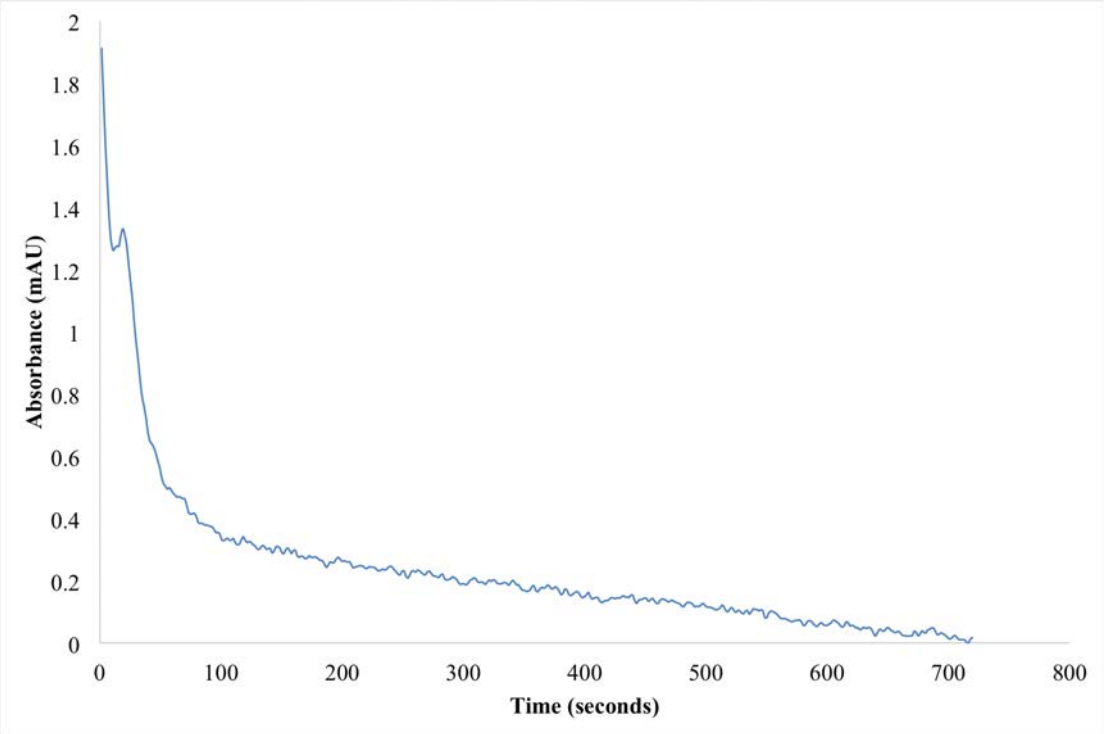

Figure 7.14: The results of an experiment in which anethole loaded FCC was sandwiched in the ZLC through which a steady flow of ethanol was pumped. The resultant anethole release was detected.

It can be seen in Table 7.4 that the results are varied and with large deviations, especially for batch 2. Therefore, in an effort to estimate the amount of anethole expected, some calculations were performed. The radius of an anethole molecule was taken to be 0.28 nm, thus making the surface area 1.21 x 10^{-9} m^2 per molcule of anethole when applying the relation that surface area is equal to πr^2. From this it was calculated that 0.146 g of anethole can adsorb as a monolayer onto this grade of FCC. However, it is apparent that none of the values calculated in Table 7.4 are around this value, although batches 1 and 3 are less than this value, which is possible.

The results show that more anethole was released from the sample than the actual weight of the sample. Providing that the sample weight encompassed the weight of the FCC and the anethole loaded, the anethole released as measured by the ZLC/HPLC system could not have been more than the sample weight. One possible explanation may have been the introduction of air bubbles into the ZLC upon interrupting the ethanol flow to apply the sample may have altered the baseline, thus giving false readings. As the amount of anethole to be detected was always very small, any baseline fluctuations would have caused relatively high inaccuracies. Another explanation may be that the samples weighed were in fact comprised mostly of solidified anethole, rather than FCC, and thus contributed to the large amount of anethole desorbed from the sample. Additionally, the anethole may not have actually adsorbed to the FCC.

This method of using the ZLC to quantify the amount of anethole desorbing from the

Table 7.4: Effective diffusion coefficients D' calculated of vanillin in ethanol at corrected t = 1 200-1 400 s (phase 1) and 1 600-1 800 s (phase 2).

Batch	Area under curve (mAU*s)				
	1	2	3	Average	Stdev
1	171	308	259	246	69
2	1670	1455	872	1332	413
3	860	951	883	898	47

Batch	Amount of loaded FCC used in ZLC experiment (g)				
	1	2	3	Average	Stdev
1	0.0042	0.0050	0.0040	0.0044	0.0005
2	0.0040	0.0043	0.0045	0.0043	0.0003
3	0.0043	0.0042	0.0044	0.0043	0.0001

Batch	Amount of loaded FCC used in ZLC experiment (g)					
	1	2	3	Average	Stdev	Units
1	4.38	4.34	5.11	4.61	0.44	μg
2	28389	146	0.06	995	1599	g
3	49	171	65	95	66	mg

FCC has many pitfalls and further investigation and experimentation is required. One large drawback to this method is that it does not provide any information on adsorption, and is assumed that the anethole has in fact been adsorbed, when it may simply be mixed with the FCC. It may also prove useful to not dry the sample to avoid the difficulties and complexities related with sample loss. The sample may be applied as a paste or slurry to the ZLC. Chapter 5 discusses this as an alternative for loading the FCC.

7.3.1.2 Vanillin in ethanol

Figure 7.15 shows the data gathered from the vanillin in ethanol ZLC experiments. For these experiments, the calibration from Figure 7.3 was to be used to convert the data from Figure 7.15 to a concentration. However, it can be seen that the differences between the blank, GCC, and FCC 06 in all regions of the diffusion profile are almost indistinguishable from one another, especially when compared with the results from the FLC experiments in Figure 7.4.

It became evident that the diffusional effects exhibited by the ZLC are not large enough to distinguish diffusion from an FCC from the baseline fluctuations exhibited by the instrument. The ZLC method is based on a lot of assumptions and uncertainties. For example, it is realistically impossible to achieve a monolayer of sample that is perfectly spread across the ZLC sinter in the same arrangement each time an experiment is

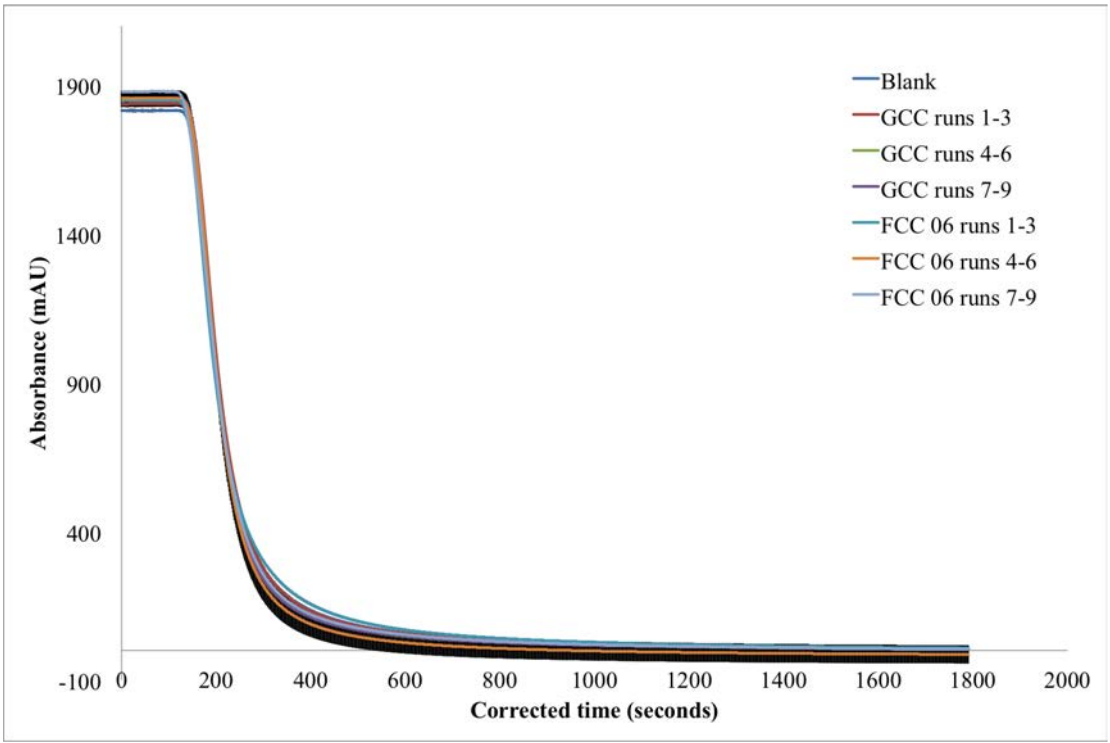

Figure 7.15: Data from vanillin in ethanol ZLC experiments. The absorbance of vanillin was measured at 279 nm. The y-error bars, which are the standard deviations of the average data from three analytical replicates, give each curve a black 'cloud.'

run. This is because the error margin to achieve such a feat is very narrow: too much sample and there is no monolayer, while too little sample creates a dead space on the sinter. When such a small amount of sample is being used, the impact of having too much or too little sample is magnified.

These experimental problems are what lead to the development of the FLC. It could be argued that because D' is calculated in the long time region of the curve, there should be no need for the development of such a column and its novel application. However, the asymptote at long times and low concentrations may be adversely affected by an erroneous baseline coupled with any inaccuracy of the measuring device. To counter this, other short time and intermediate time solution methods have been proposed (Brandani and Ruthven, 1995, 1996), whereas Duncan and Möller (2000*a*) have suggested that these issues may be overcome by careful experimental design and operation. This is where the FLC comes into its own, especially when used in conjunction with PoreXpert. The deviation from the model shown by the desorption curves in the literature occurs in the initial part of the experiment (Hufton and Ruthven, 1993; Brandani and Ruthven, 1995; Duncan and Möller, 2000*a*). Therefore, this approach involved packing more sample into the FLC than would be used in a ZLC, to avoid erroneous baselining by amplifying the magnitude of the diffusional effects from the samples, and to calculate diffusion coefficients from the long-time region of the curve.

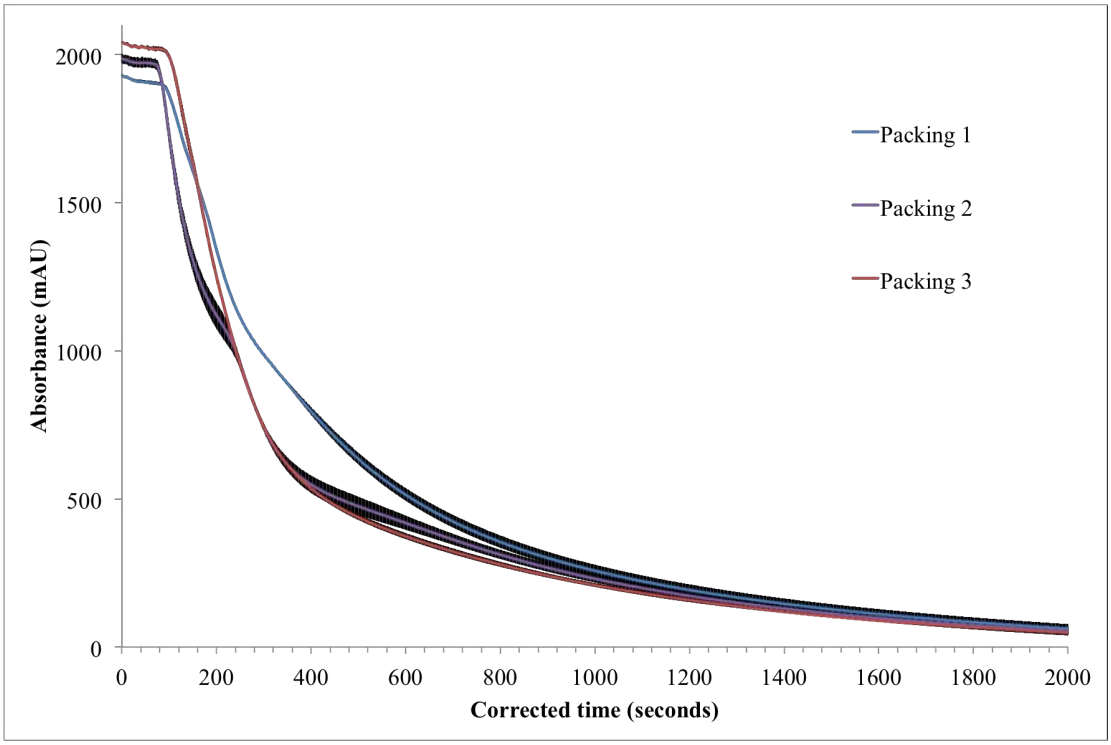

Figure 7.16: The results (absorbance measured at a wavelength of 279 nm) of the FLC experiments conducted on three experimental replicates of different packings of FCC 02. The y-error bars, which are the standard deviations of the average data from three analytical replicates, give each curve a black 'cloud.'

7.3.2 Finite length cell (FLC) experiments

The results of the FLC experiments conducted on three experimental replicates of different packings of FCC 02 and FCC 07 are shown in Figures 7.16 and 7.17, respectively. The vertical axes show the absolute signal from the detector (Figure 7.6 demonstrates that the normalisation of the absolute signal does not degrade the experimental results). It confirms that different packing affects the first section of the concentration versus time curve, where interparticle effects dominate, but not the later part of the curve where the decline in concentration is rate-limited by intraparticle diffusion effects.

Figure 7.18 shows the calibration data between the vanillin in ethanol concentrations of 0.1 and 10 mg dm^{-3}. The calibration from this data is displayed in Figure 7.19, which confirms that the detection of vanillin in ethanol using the HPLC is linear down to 0.9 mg dm^{-3}. Therefore, D' is calculated from a region of the diffusion curves that falls within the calibration of the HPLC instrument.

Additionally, it can be seen in Figure 7.16 that although the signal for packing 2 decreases monotonically, it has variations in its rate of decrease, such that its second derivative is not monotonic. However, replicate experiments with the same packing closely track along the same curve. This supports the theoretical derivation cited earlier (Brandani and Ruthven, 1995), which shows that at shorter times the rate of con-

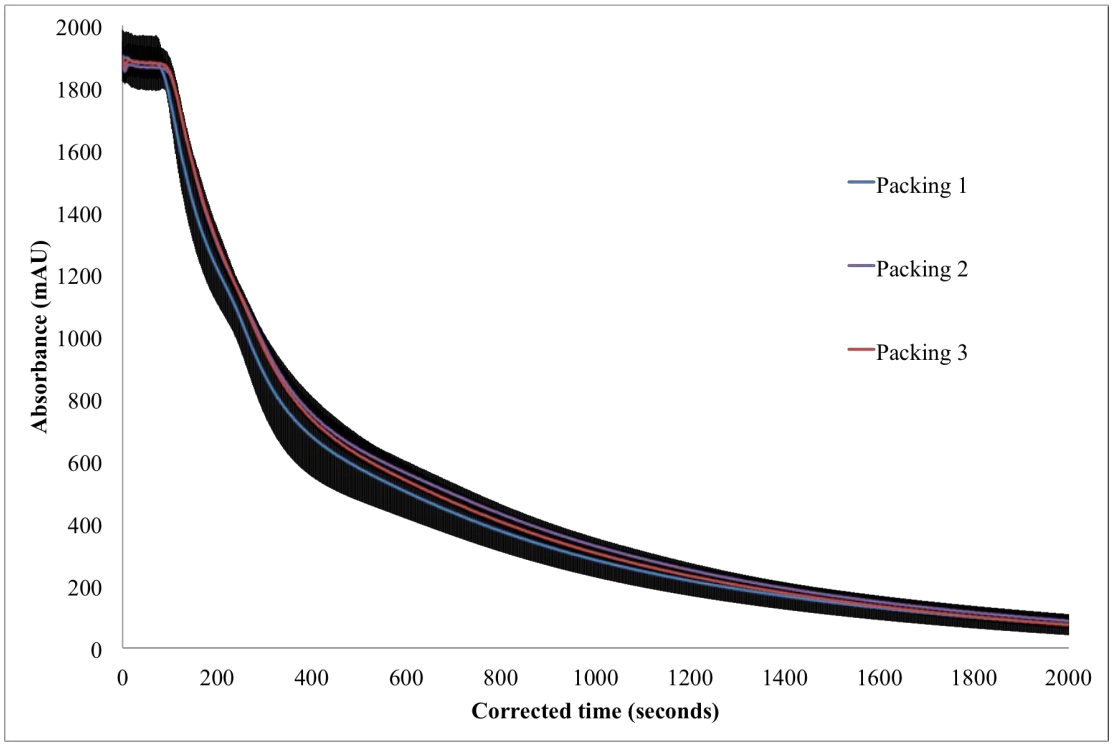

Figure 7.17: The results (absorbance measured at a wavelength of 279 nm) of the FLC experiments conducted on three experimental replicates of different packings of FCC 07. The y-error bars, which are the standard deviations of the average data from three analytical replicates, give each curve a black 'cloud.'

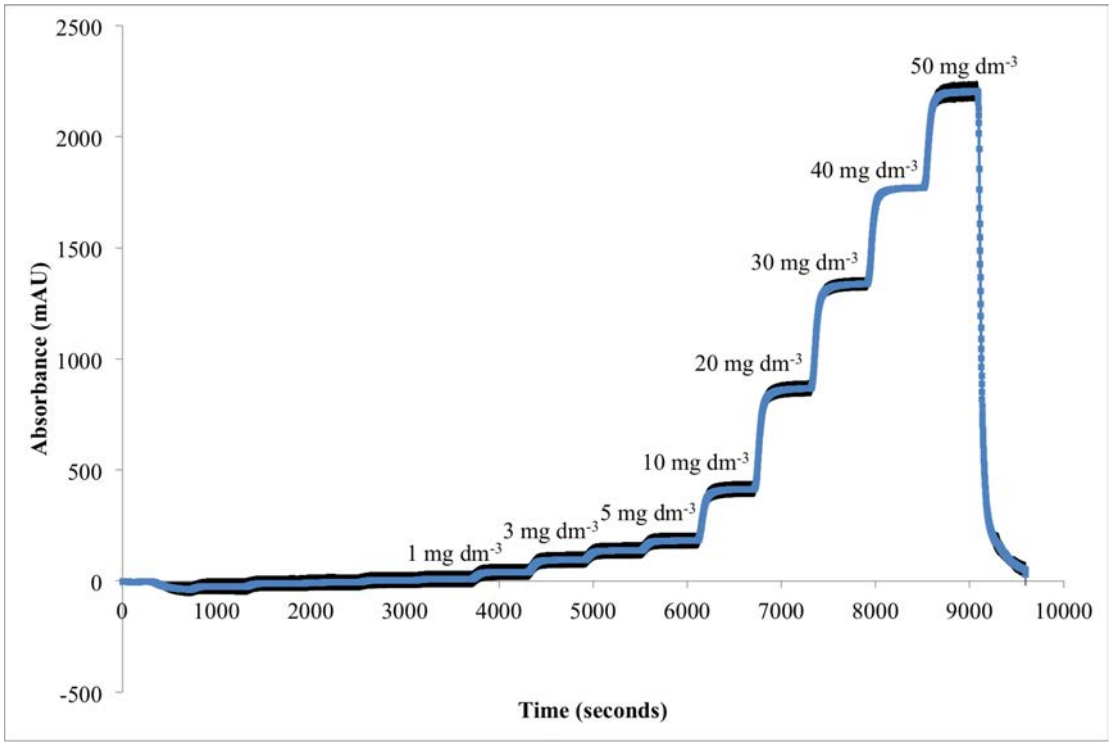

Figure 7.18: Vanillin in ethanol flowing through an empty FLC column in stepwise increments between 0.1 to 10 mg dm^{-3}, at a wavelength of 279 nm. The y-error bars, which are the standard deviations of the average data from three analytical replicates, give each curve a black 'cloud.'

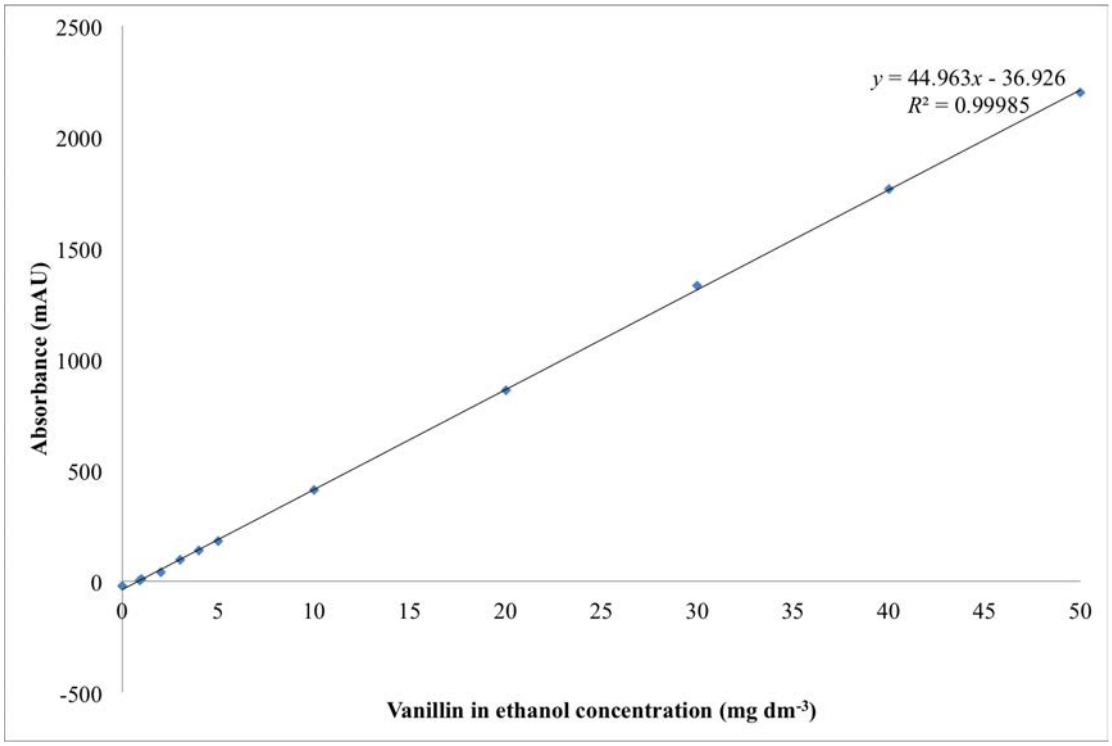

Figure 7.19: The calibration curve constructed of vanillin in ethanol from the data in Figure 7.18. The absorbance of vanillin was measured at 279 nm. The y-error bars are the standard deviations of the average data used to create each data point.

centration decrease is dependent on the time constant for the washout process. It can be seen that this washout process is highly reproducible, and that therefore the flow regime is behaving reproducibly under conditions of entirely stable packing and low Reynolds and Péclet numbers.

7.3.2.1 Vanillin in ethanol

The calibration in Figure 7.3 was used to convert the data from Figure 7.4 to that displayed in Figure 7.5. The data is divided by c_0 and displayed in Figure 7.6, and Figure 7.7 shows graphs of the natural logarithm of relative concentration plotted against corrected time. It can be seen that σ_{devn} does not increase with time for the blank, GCC, and HAP control experiments, but does increase for most of the porous samples. In this instance, σ_{devn} represents the spread of 2 and sometimes 3 analytical replicates. For comparison, slopes D' of the semi-logarithmic curves were measured over two different sections of the curve, one between corrected t = 1 200-1 400 s, and the other between 1 600-1 800 s; the subsequent calculated D' values are labelled as D'_{phase1} and D'_{phase2}, respectively. These time ranges were chosen through visual inspection of the curves; the earlier time range was initially chosen when interpreting ZLC data, however, the FLC experiments may still have bulk washout occurring through the packed column at this time, hence the calculation of D' also at a later time. All these 200 second sections were themselves linear ($R^2 > 0.997$), even though it can be seen that over the entire time of the experiments, the curves were non-linear when plotted semi-logarithmically, because of the mixed inter- and intraparticle effects.

To calculate D' the median size, $r = d_{50}$, which can be seen in Table 3.1 in Chapter 3, is used. Then applying the relation $r = d_{50}/2$ values of D' may be obtained, and can be seen in Table 7.5. It can be seen that the phase 1 diffusion coefficients are always greater than those of phase 2, demonstrating that during phase 1, and possibly phase 2, the diffusion effects have not yet converged onto a single process with a constant diffusion coefficient, as discussed earlier (i.e. Figures 7.16 and 7.17).

Figure 7.20 shows the dependence of the effective diffusion coefficients on particle size. It can be seen that there is some degree of dependence, as shown by a correlation coefficient of R^2 = 0.99 for both phase 1 and phase 2 for a second order polynomial fit to logarithmic values of D'. Figures 7.21 and 7.22 show a possible weak dependency on porosity if FCC 13 is regarded as an outlier, and no dependence on surface area.

The average adsorption of vanillin from ethanol onto all the FCC samples and HAP is small: 2.01 $\pm$ 0.58 mg g^{-1} when the sample is immersed in a 30 mg dm^{-3} solution (Chapter 4). The desorption process, once the surrounding liquid in the experiments is switched back to pure solvent, will contribute to D' to an extent unquantified in this work.

Table 7.2 shows the envelope densities of the FCC samples calculated from both DryFlo and MIP measurements. Additionally, the table shows the theoretical weight that would constitute a 100 % efficient packing based on the density measurements, along with the amount of weight of each FCC used for the experimental replicate for the FLC experiments.

The amount of FCC that was weighed and packed into the FLC was calculated based

Table 7.5: Effective diffusion coefficients D' calculated of vanillin in ethanol at corrected t = 1 200-1 400 s (phase 1) and 1 600-1 800 s (phase 2).

Sample	Intraparticle porosity	D'_{phase1} (10^{-16} m^2 s^{-1})	D'_{phase2} (10^{-16} m^2 s^{-1})
GCC	-	7.96	3.93
HAP	34.2	7.58	6.17
FCC TP	25.9	7.53	6.85
FCC 02	24.4	5.17	4.05
FCC 03	10.4	1.33	1.06
FCC 06	25.2	5.30	3.97
FCC 07	12.3	7.37	6.55
FCC 12	29.6	24.5	19.7
FCC 13	37.0	135	106

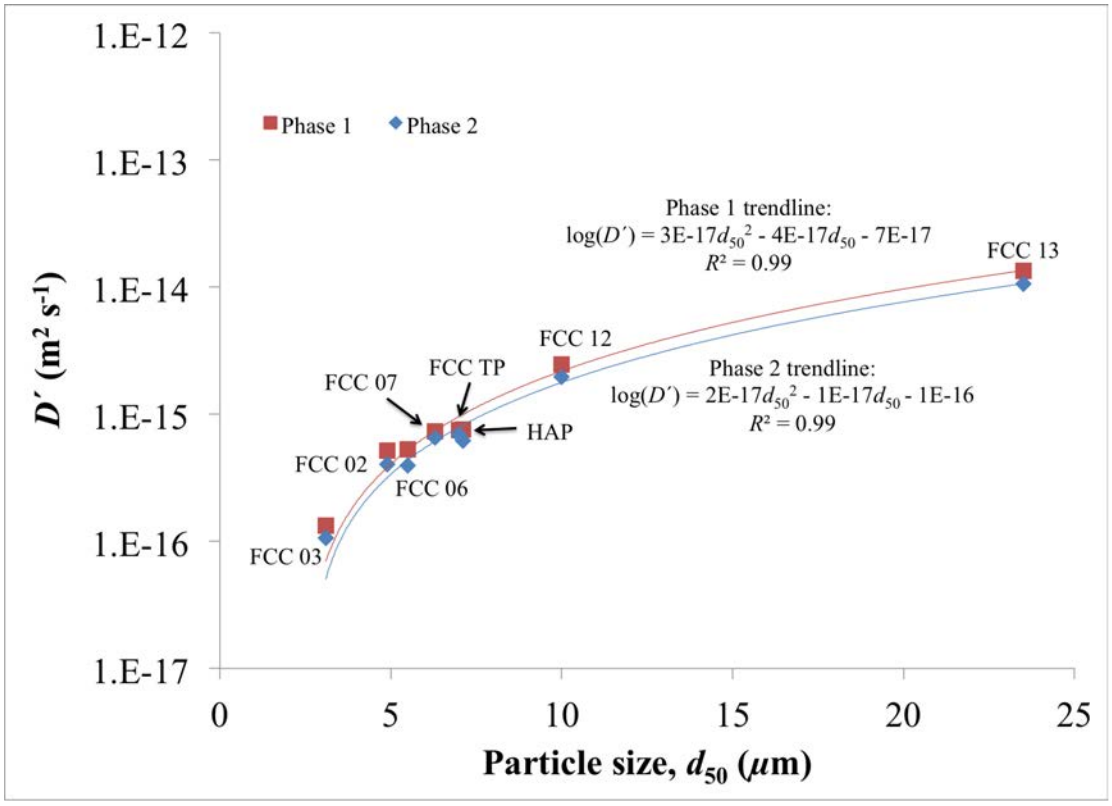

Figure 7.20: Dependence of D' on particle size.

on envelope pycnometry measurements. However, Chapter 5 has shown that the powder used to conduct such experiments is too large in particle size to accurately measure

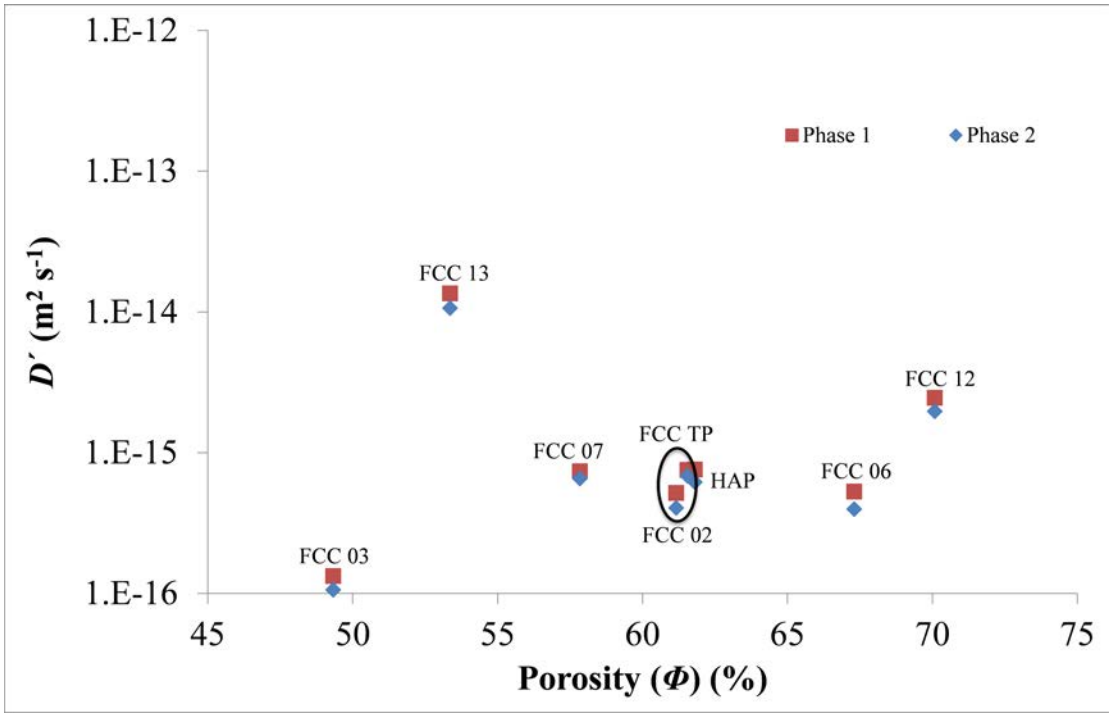

Figure 7.21: Dependence of D' on porosity.

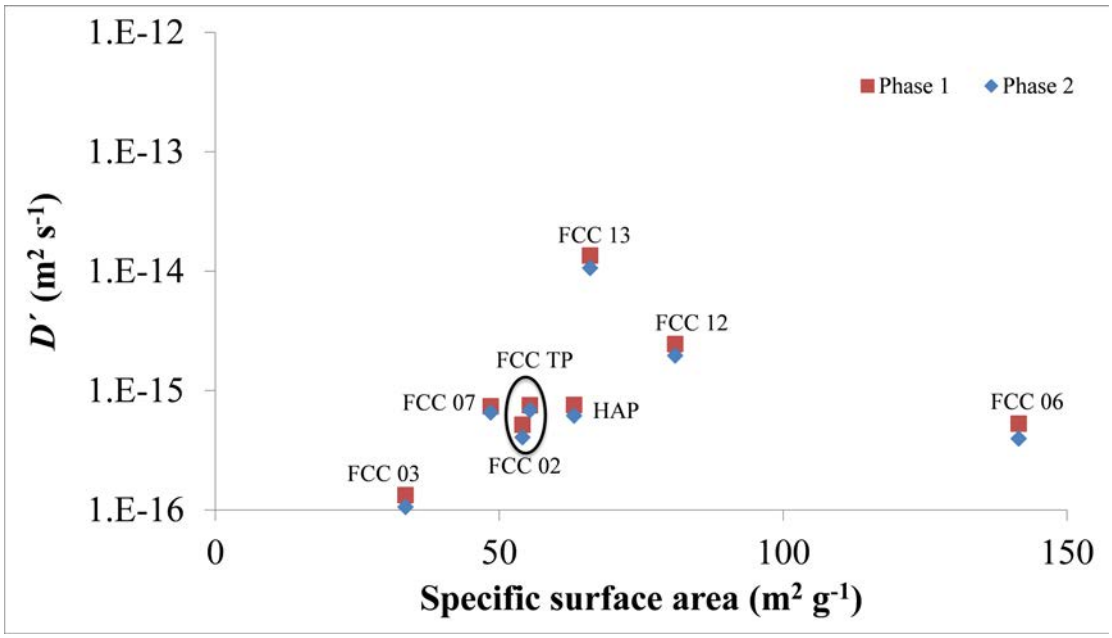

Figure 7.22: Dependence of D' on surface area.

the FCC powder, thus rending any measurement efforts futile. It can be seen in Table 7.2 that the amount of FCC packed into the FLC, when back-calculated using the envelope densities obtained from MIP measurements, far exceeds the weight required for a 100 % packing.

Table 7.6: Fitting parameters for FCC 03 when fitting with five different stochastic realisations. Values greater than $\pm\sigma_{devn}$ from the mean are underlined.

Parameter	Stochastic realisation number				
	1	2	3	4	5
Pore skew	6.80	9.68	5.12	1.37	1.48
Throat skew	-15.16	-32.48	-27.31	46.12	0.46
Throat spread	0.99	0.96	0.89	0.91	0.92
Connectivity	4.35	4.26	4.03	3.99	4.12
Correlation level	0.06	0.07	0.09	0.01	0.04
Distance (%)	1.35	1.65	1.36	1.30	1.37
Tortuosity	1.20	1.20	1.13	1.40	1.33

The implications this has on the calculation of D' may be minimal; the results in Figures 7.16 and 7.17 represent stochastic generations regarding the way in which the FCC is packed, and it has already been discussed that the packing arrangement does not affect the convergence of experimental replicates during the times at which the D' is calculated. Therefore, regarding the comparison of D' between analytical and experimental replicates, the calculation of D' is still valid providing that the same % of FCC has been packed into the FLC column each time.

However, regarding the comparison of D' between FCC grades, the fact that different packing efficiencies have been achieved for each grade perhaps poses certain implications. Ideally, the packing efficiency needs to be as close to 100 % as possible. It can be seen from Table 7.2 that the efficiency was less than 100 % for each sample, despite attempts to try and pack the FLC column with as much as possible in an attempt to achieve a 100 % packing efficieny. However, upon inspection of the actual packing efficiency when using the envelope density of the FCCs obtained from MIP measurements for the calculations, each FCC grade is well above 100 % packing efficiency. As a result, the measurements were approximate because they involved the use of a powder to investigate the packing of a powder. They were therefore used simply as a cross-check to ensure that there was efficient packing into the FLC.

7.3.2.2 PoreXpert® modelling

This section discusses the results of the PoreXpert void modelling and tortuosity simulations performed on the generated structures, and how they can be applied to the interpretation of D' from vanillin in ethanol FLC experiments (sections 7.2.2.1 and 7.3.2.1).

The entire mercury intrusion curves shown in Figure 3.3 (Chapter 3) were modelled using PoreXpert. Also modelled were the separate higher pressure (smaller diameter) and lower pressure sections. Figure 7.23 gives an example of an entire mercury intrusion curve for sample FCC 03, used as input for the network simulation software, PoreXpert, with the simulated curve overlaid to show the closeness of fit. The structure type was HLST, with fitting parameters shown in Table 7.6, and the closeness of fit was 1.4% (Table 7.7). Stochastic realisation 5 was chosen as the representative structure, because all of the parameter values were within $\pm\sigma_{devn}$ of the mean. Values outside this range are underlined in Table 7.6.

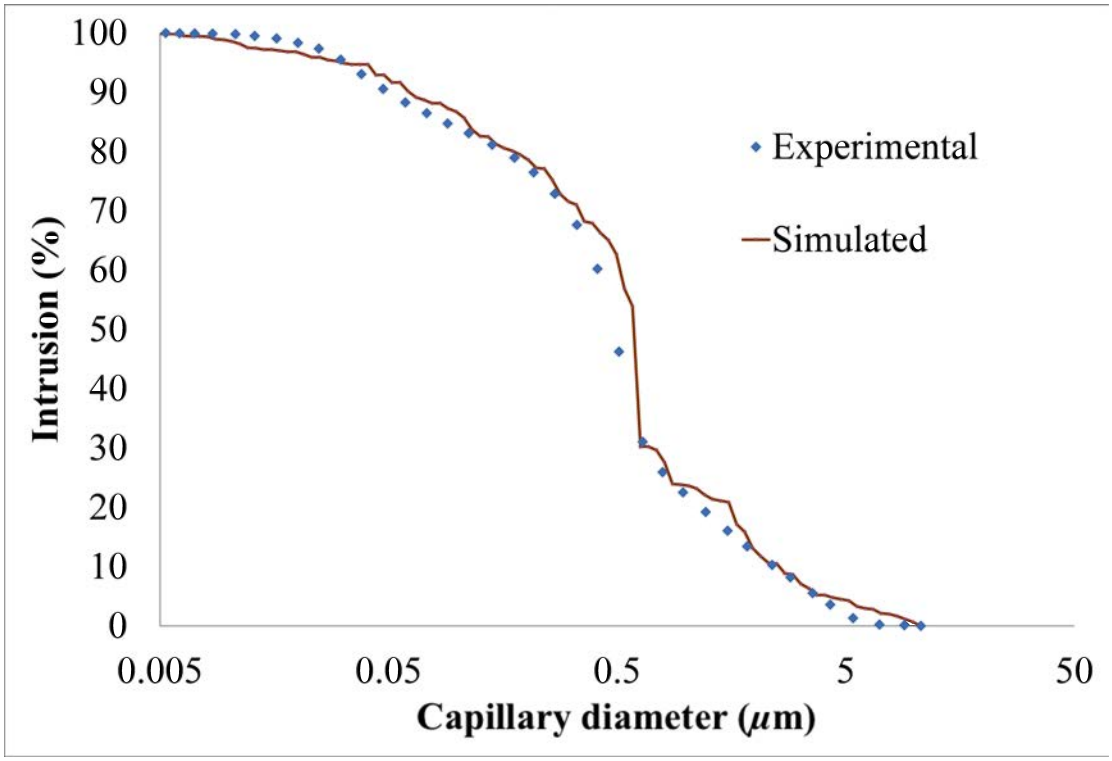

Figure 7.23: Experimental and simulated mercury intrusion characteristics for sample FCC 03.

Figure 7.24 shows the PoreXpert unit cell of the interparticle void space of the simulated porous structure of FCC 03 corresponding to Figure 7.23 and Table 7.6. Figure 7.24 also shows the unit cell of the intraparticle void space simulation. Figure 7.25 displays the corresponding throat and pore-size distributions; both unit cells contain large numbers of pores of maximum size which are labelled in (c) and (d) as undifferentiated - they could be either single pores or clusters. For the interparticle void space, with pore skew of 1.6, they are likely to be single pores. For the intraparticle space, with a pore skew of 6.1, they are more likely to be clusters, and so are shown with textured surfaces in Figure 7.24, just visible in the enlargement shown in Figure 7.26.

To reveal more of the structural characteristics of the void networks, the properties of which are governed by the sizes of the throats often obscured by pores in the figures, both unit cells are shown injected by mercury (dark grey) to 50 % of their void space from the top faces in the figures. It can be seen that percolation in the intrapore structure shown on the right of Figure 7.24 forms an almost planar percolation front, whereas percolation through the interpore structure is much more heterogeneous. Percolation is governed by throats, rather than pores, and this difference is in accord with the throat size distributions shown in Figure 7.25 (a) and (b), which are bimodal and Poisson-like respectively.

Table 7.7 provides a summary of the fits to all of the overall and intraparticle sections of the mercury intrusion curves, in terms of structure type and fit discrepancies. It also lists the corresponding simulated tortuosities.

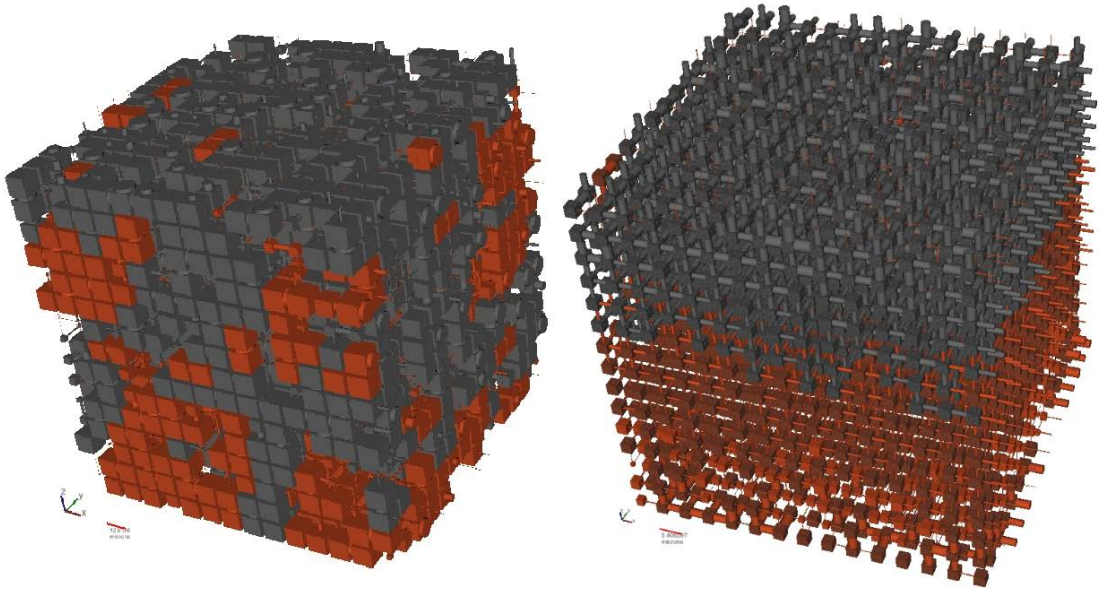

Figure 7.24: Simulation of the void space of the sample FCC 03 filled with 50 % of mercury from the top face. For clarity, the void space is shown solid, the solid phase is transparent, and the mercury is dark grey. The left structure is the simulated interparticle space, and the small scale bar bottom left is of length 12.6 μm. The right structure is the intraparticle space, and the small scale bar bottom left is of length 0.41 μm, i.e. 28 times smaller than the left-hand structure.

There is no discernible trend when the quantity $(\phi/\tau^2_{\text{overall}})$ is plotted against D'. However, a trend does emerge for $(\phi/\tau^2_{\text{intraparticle}})$ against D' (Figure 7.27). In terms of exponential relationships, which appear linear on the log-linear plots, R^2 = 0.63 and 0.62 for phase 1 and phase 2, respectively.

7.3.2.3 Model validation

Unlike many investigations of porous materials that use highly ordered or model systems, this investigation is of real systems destined for a specific purpose - that of controlled drug or flavor release. Rather than a single sample, a range of samples with different properties and morphologies have been studied. The flushing and diffusion processes are complex, and difficult to resolve. There are uncertainties introduced by the experimental approach; the HPLC system causes line broadening, and the packing of samples into the FLC (rather than ZLC) sample chamber can never be entirely reproducible. The modeling involves a simplification of void shapes and positions, and a sometimes imperfect fit to the experimental intrusion characteristics, particularly for the highly bimodal sample FCC 13 (Table 7.7).

Therefore, one needs to ask to what extent the investigation is valid. Validation comes from several sources. The first is the difference between rate of concentration reduction for the porous samples and those of the blank and GCC (Figure 7.7), the latter with a similar particle size to the porous samples. The rate of reduction for all of the porous samples is much slower than either the blank or GCC. Secondly, the replicates showing

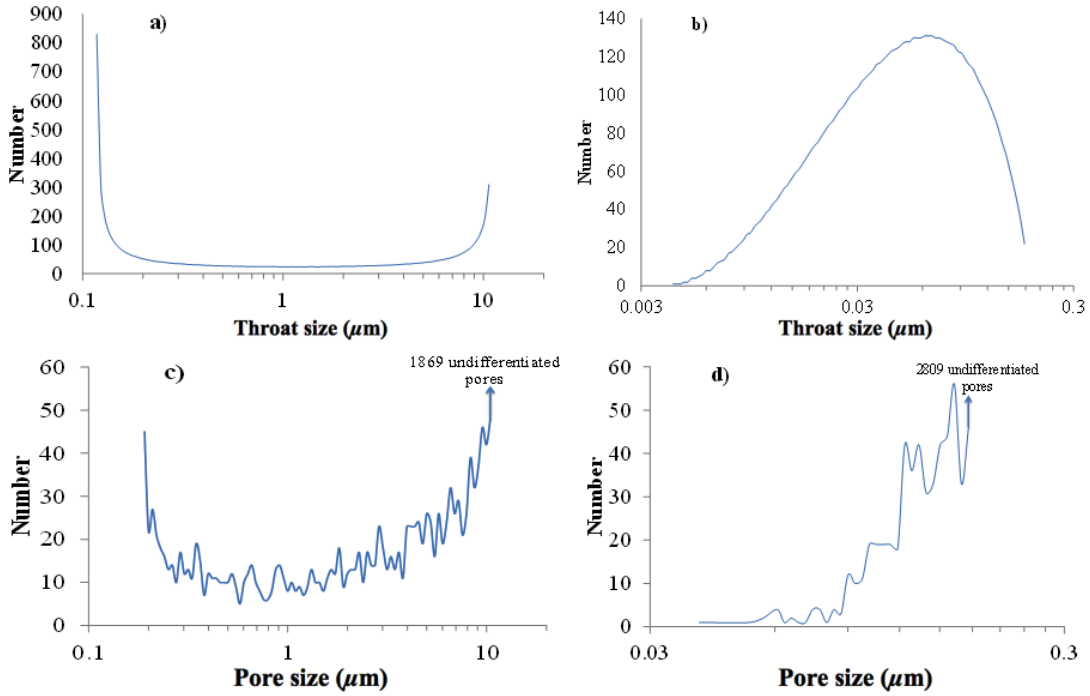

Figure 7.25: The numbers of pore-throats and pores within the single unit cells of sample FCC 03. Figures (a) and (c) display those of interparticle void space; Figures (b) and (d) display those of the intraparticle void space.

the effect of packing of the same sample (Figure 7.16), confirm that the measured diffusion coefficients in this work, taken from the sections of the curve above 1 200 seconds, are unaffected by packing and hence interparticle effects, but are rate-limited by the intraparticle effects. Thirdly, it can be seen in Figure 7.16 that although the signal for packing 2 decreases monotonically, it has variations in its rate of decrease, such that its second derivative is not monotonic. However, replicate experiments with the same packing closely track along the same curve. This supports the theoretical derivation cited earlier (Brandani and Ruthven, 1995), which shows that at shorter times the rate of concentration decrease is dependant on the time constant for the washout process. It can be seen that this washout process is highly reproducible, and that therefore the flow regime is behaving reproducibly under conditions of entirely stable packing and low Reynolds and Péclet numbers.

The validation of the predecessor to PoreXpert, known as Pore-Cor, has included a comparison of the void sizes when the model was mathematically microtomed, compared to image analysis of actual microtomed samples. Although the model voids were one or two orders of magnitude too small compared to experiment, use of the fallacious capillary bundle model produced voids which were some 8 orders of magnitude too small (Matthews *et al.*, 2006). The calculation of tortuosity with the current PoreXpert model has recently been validated against experimental measurements on sandstone and limestone (Laudone *et al.*, 2015).

An overall validation is the trend shown in Figure 7.27. Equation 7.8 shows that this is

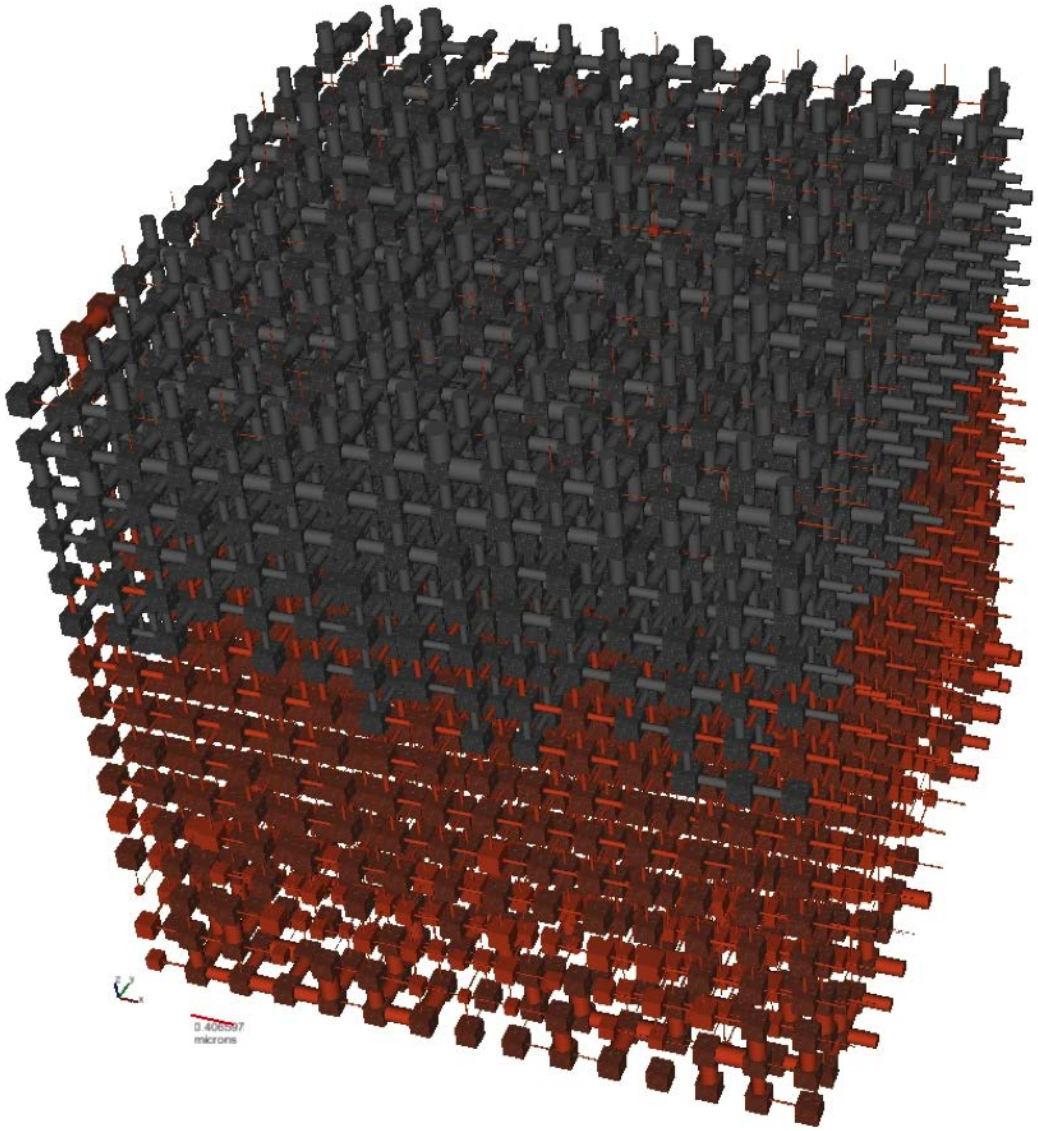

Figure 7.26: Simulation of the intraparticle void space of the sample FCC 03 filled 50 % by volume of mercury from the top face; the small scale bar bottom left is of length 0.41 μm. For clarity, the void space is shown solid, the solid phase is transparent, and the mercury is dark grey. Pores with textured surfaces may be pore clusters.

effectively a graph of D_{model}/D_{12} against D'. Since D_{12} is constant, then if only intraparticle effects were present, there would be a linear relationship between the two. In practice, there is an approximate logarithmic relationship as shown, due to the change-over from mixed inter- and intraparticle processes to only intraparticle processes. However, it is believed that the relationships shown, with R^2 of 0.63 and 0.62, are strong enough to provide validation.

Figure 7.20 shows a strong dependence of D' on particle size. However, Figures 7.21, 7.22, 7.28, and 7.29 show no trends of D' with porosity, surface area, intraparticle

Table 7.7: PoreXpert structure types, fit discrepancies, and calculated tortuosities.

Sample	Overall			Intraparticle		
	Structure type	Discrepancy of fit (%)	Overall tortuosity	Structure type	Discrepancy of fit (%)	Overall tortuosity
HAP	HLS	1.7	1.73	HLS	1.1	1.27
FCC TP	VB	1.3	1.40	SCZ	1.4	1.13
FCC 02	VB	1.3	1.33	VB	1.2	1.20
FCC 03	HLST	1.4	1.33	HLS	1.2	1.27
FCC 06	VB	1.4	1.27	HLS	1.7	1.27
FCC 07	VB	1.2	1.27	VB	1.9	1.20
FCC 12	VB	2.3	1.27	HSL	1.8	1.13
FCC 13	HLS	3.8	1.33	HSL	1.2	1.20

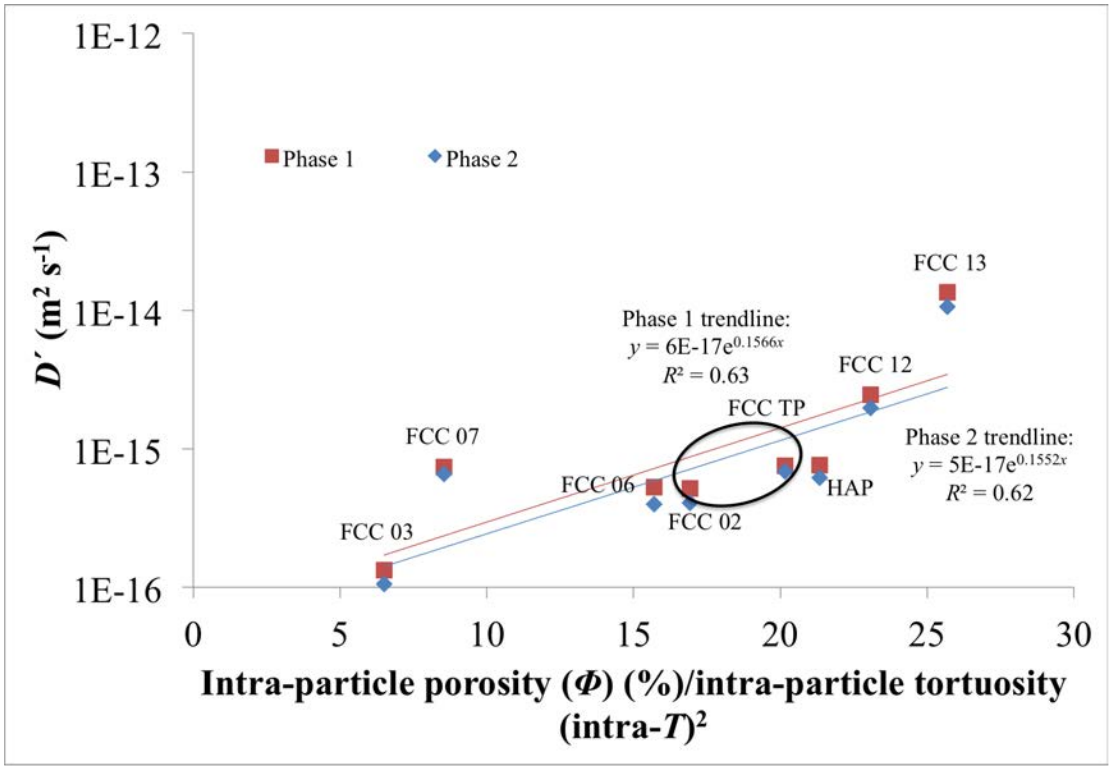

Figure 7.27: A plot of intraparticle tortuosity scaled with respect to intraparticle porosity versus D'. The black oval serves to represent two samples , namely FCC 02 and FCC TP, whose relationships on the graph cluster closely with each other due to their similar morphologies (as summarised in Table 3.1).

porosity, and intraparticle tortuosity.

It therefore follows that these three relationships must be dominated by morphological differences within the intraparticle voidage. A closer examination of the graphs can reveal something of the nature of this domination. Take the case of samples FCC 02

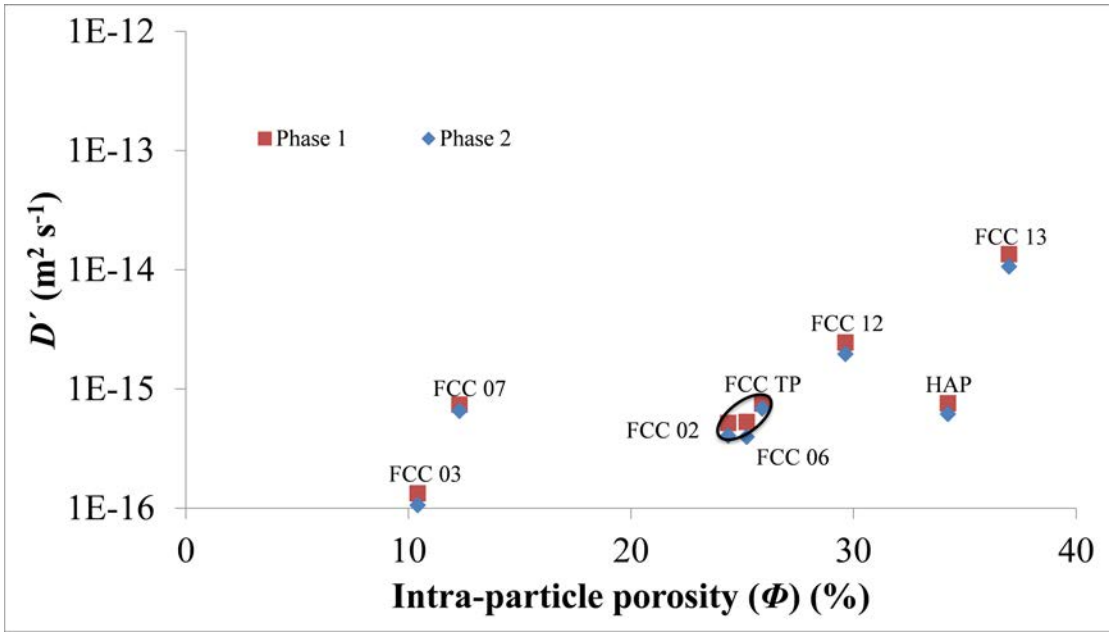

Figure 7.28: A plot of intraparticle porosity versus D'. The black oval serves to represent two samples , namely FCC 02 and FCC TP, whose relationships on the graph cluster closely with each other due to their similar morphologies (as summarised in Table 3.1).

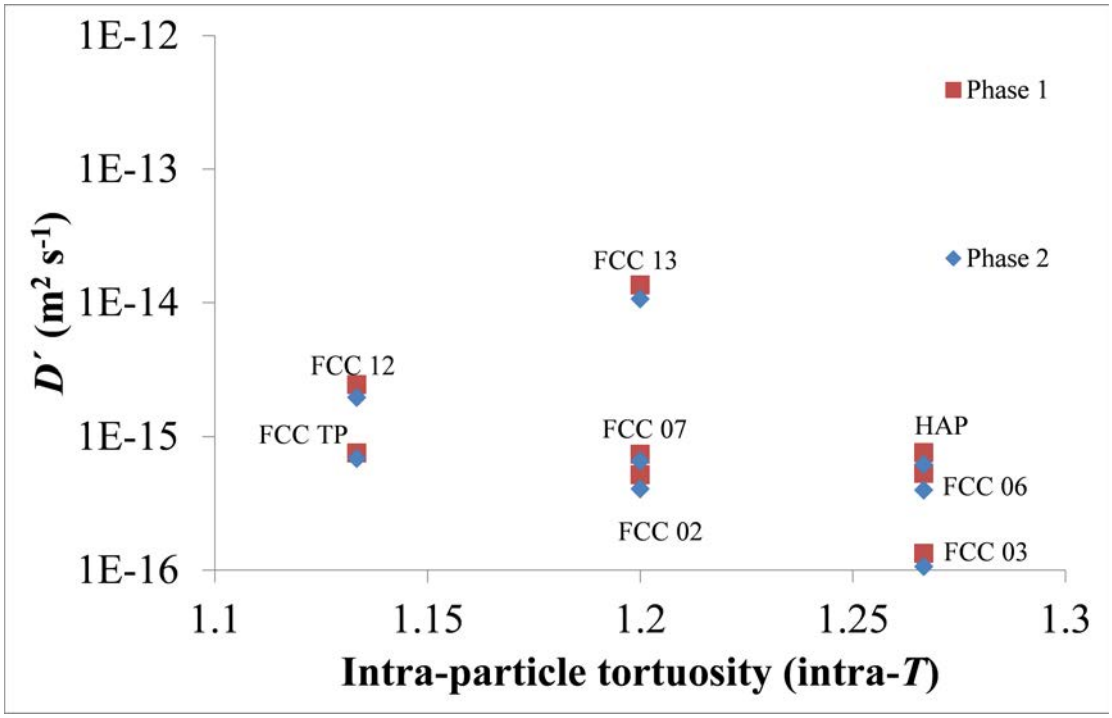

Figure 7.29: A plot of intraparticle tortuosity versus D'.

and FCC TP, as summarised in Table 3.1, to have morphologies very similar to each

other. Inspection of Figures 7.21 and 7.22 show that these two samples cluster closely with respect to porosity and surface area, as highlighted by oval lines on the figures. However, they vary with respect to intraparticle tortuosity (Figure 7.29), which implies sub-surface differences in the void space morphology of these particles not visible in electron micrographs of their surfaces (Figure 3.1).

7.3.2.4 Saccharin in HEPES

The calibration data can been seen in Figure 7.30 and the actual calibration curve in Figure 7.31. The analyte was analysed at a wavelength of 269 nm. Figure 7.32 shows graphs of the data divided by c_0 against corrected time, from which the D' values in Table 7.8 were calculated.

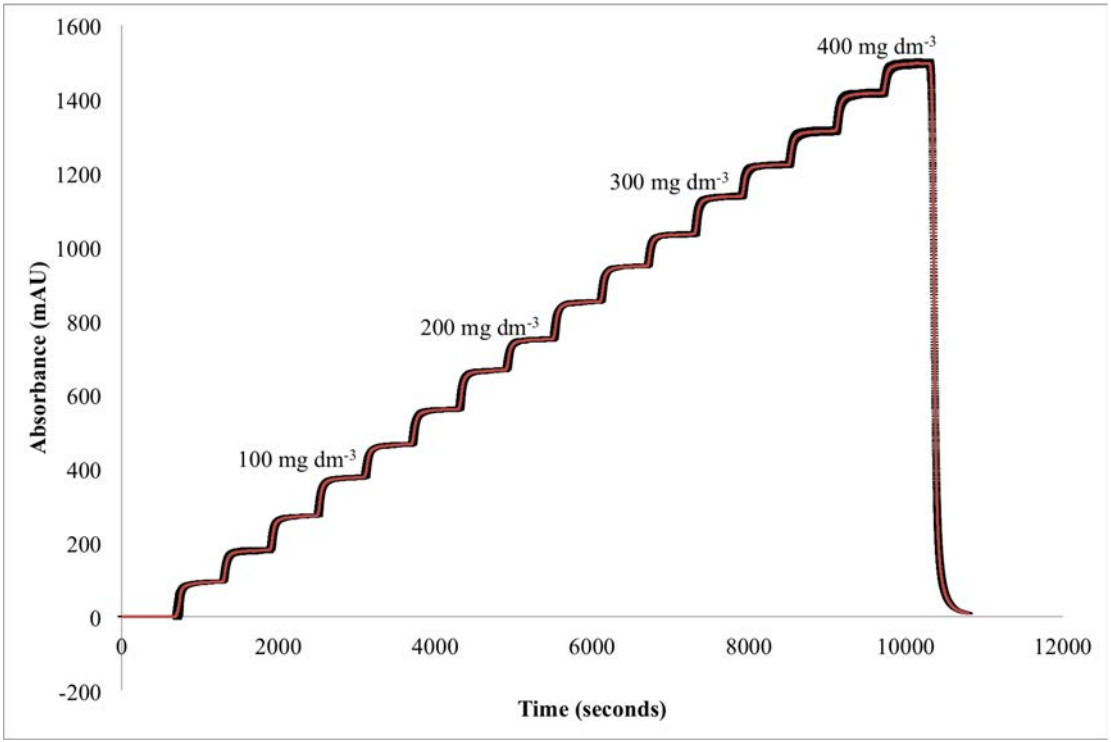

Figure 7.30: Saccharin in HEPES flowing through an empty FLC column in stepwise increments of 25 mg dm^{-3}, from 0 to 400 mg dm^{-3}, at a wavelength of 269 nm. The y-error bars, which are the standard deviations of the average data from three analytical replicates, give each curve a black 'cloud.'

It is immediately noticeable that the blank and FCC 13 in Figure 7.32 'diffuse' slower than the other samples. Regarding the blank, it may be explained in terms of the FLC volume (i.e. there is more empty space in an empty FLC for more saccharin solution, thus taking longer to empty out). Regarding FCC 13, it may simply be a characteristic of its large particle size (Table 3.1 in Chapter 3). The other FCC samples are diffusing much faster than it would appear from visual comparison of Figure 7.32 to the samples from the vanillin in ethanol FLC work (Figure 7.6). This suggests that saccharin is not coming out of the other FCC samples, or perhaps never went into its pores in the first instance. This issue, however, is not evident with any of the samples from the vanillin

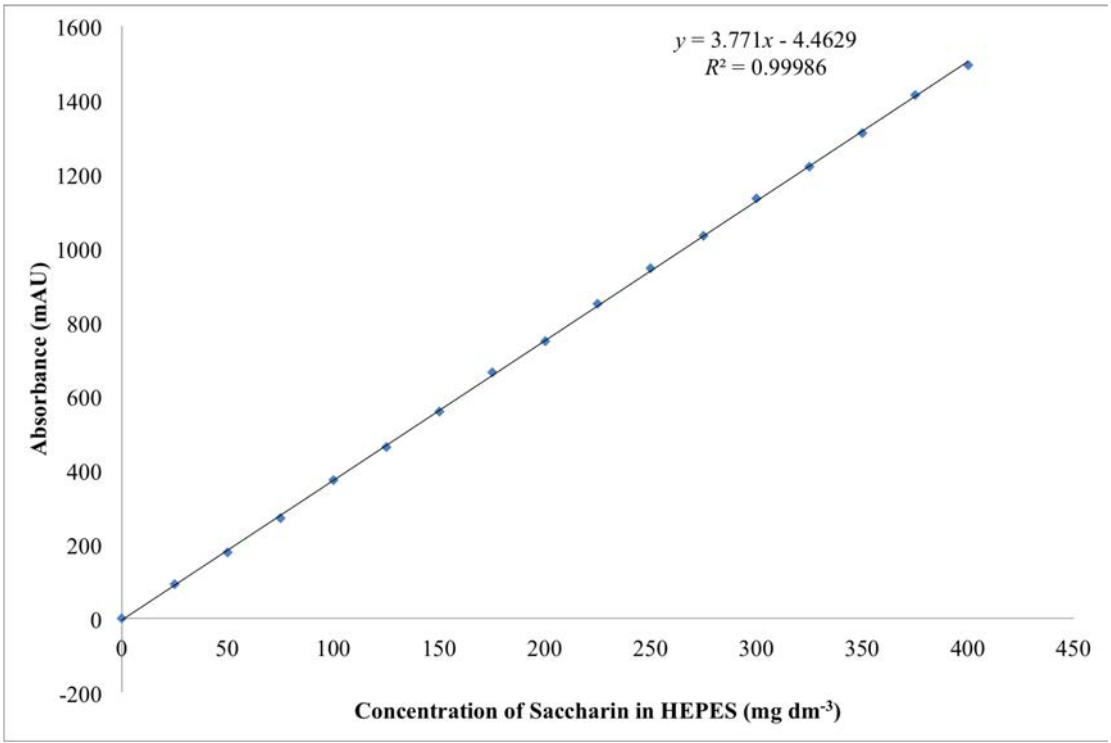

Figure 7.31: The calibration curve constructed, at 269 nm and up to 400 mg dm^{-3}, from the data in Figure 7.30. The y-error bars are the standard deviations of the average data used to create each data point from Figure 7.30.

Table 7.8: Effective diffusion coefficients D' calculated of saccharin in HEPES at corrected t = 1 200-1 400 s (phase 1) and 1 600-1 800 s (phase 2).

Sample	Intraparticle porosity (%)	D'_{phase1} (10^{-16} m^2 s^{-1})	D'_{phase2} (10^{-16} m^2 s^{-1})
GCC	-	1.07	8.55
HAP	34.2	9.08	5.70
FCC TP	25.9	6.31	5.34
FCC 02	24.4	2.85	4.25
FCC 03	10.4	2.30	1.60
FCC 06	25.2	6.97	7.95
FCC 07	12.3	3.22	2.87
FCC 12	29.6	18.32	21.51
FCC 13	37.0	53.91	26.40

in ethanol FLC work (Figure 7.6).

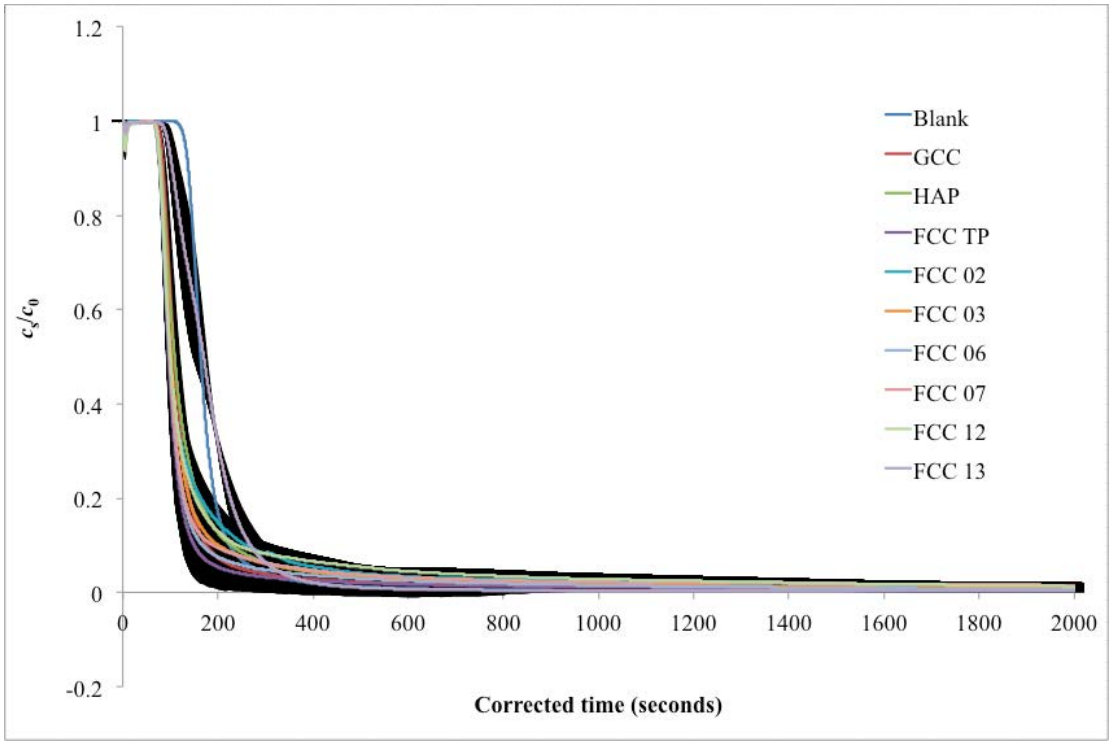

Figure 7.32: Data from saccharin in HEPES FLC experiments whose y-axis has been divided by c_0. The data was gathered at 269 nm. The y-error bars, which are the standard deviations of the average data from three analytical replicates, give each curve a black 'cloud.'

The calculated D' in Table 7.8 were not analysed with PoreXpert or taken any further, as they were in section 7.3.2.1, because it was during this period where a lot of the HPLC issues occurred, particularly the drastic change in detection sensitivity, as outlined in Chapter 3. When these issues were resolved, vanillin in ethanol was system chosen to be used in other experimental work and became the main focus, because of its simpler and gives the FCCs easier potential to be loaded with vanillin via rotary evaporation (Chapter 5).

7.4 Conclusions & future work

The two hypotheses postulated in this chapter are as follows:

- **6:** The diffusion characteristics of FCC can be studied by exposing a monolayer of FCC to a flow of solvent (i.e. a ZLC experiment).
- **7:** The diffusion characteristics of FCC can be studied by exposing a packed bed of FCC to a flow of solvent (i.e. an FLC experiment), and then subsequently deconvoluting the intra- from the interparticle processes using PoreXpert.

The work described in this chapter utilised the following systems with the ZLC: anethole in ethanol, saccharin in HEPES, and vanillin in ethanol; the latter two systems were also utilised in the FLC, which was created in order to make the diffusional effects from

the FCC larger than with the ZLC method. Anethole loaded FCC was studied in the ZLC, but the many drawbacks and limitations to the experimental methods requires that these caveats are addressed before this work can be continued, thus disproving hypothesis 6. The same applies to the saccharin in HEPES FLC experiments.

Regarding the vanillin in ethanol FLC experiments, we have described a method of measuring combined diffusional effects of a dissolved liquid species loaded into the void space of a pack of interporous particles. The results are validated by comparison with blank experiments and experiments with non-porous particles of a similar size. The results show that diffusion is dependent on particle size, and that the intraparticle tortuosity, modelled by the inversion of mercury intrusion characteristics using PoreXpert, trends with diffusion when scaled by porosity, thus at least partially fulfilling hypothesis 7. The approach offers an important new indirect method of measuring intraparticle tortuosity, which cannot be measured directly. The validation of the experimental method and the modelling, and the demonstration of the dependence on morphology from the close tracking of two samples, opens the way for the tailoring of morphology and other properties to optimise diffusion characteristics for the optimisation of functionalised calcium carbonate and other porous materials for applications such as controlled drug and flavour release. Further experiments may be carried out with aqueous solutions and simulated digestive fluids, and with samples in which the active has been directly loaded onto the porous substrate.

Other future work regarding the FLC method can be found in Chapter 9.

Chapter 8

Zero length cell (ZLC) approximation using the finite length cell (FLC)

THE aim of this chapter is to describe a novel method in which a ZLC approximation is derived from experimental data using the FLC.

8.1 Introduction

The ZLC is designed to measure only the intraparticle diffusivity of a sample by sandwiching a monolayer of the sample between stainless steel sinters, however the ZLC technique has some major drawbacks. For example, a monolayer of sample is far too small to weigh and transfer accurately to the sinter, and it is impossible for a monolayer of particles to be spread across the surface of the sinter in such a way that there is a perfectly even layer of particles that can also be reproduced. Additionally, the diffusional effects exhibited by a monolayer of sample are often far too small to be detected adequately (Chapter 6). Thus, in an effort to enhance and exaggerate the diffusional effects of the sample, the FLC was born (Levy *et al.*, 2015), in which the inter- and intraparticle processes of a sample are measured.

It is proposed that the FLC can be used to approximate the ZLC by diluting the sample particles (A particles) in an inert matrix of non-porous particles (B particles), similar to catalyst dilution studies in packed beds, in order to enhance the diffusional effects of the sample by using more than a monolayer. This approximates a ZLC but only to a limit: the sample particles A are separated from one another, thus minimising radial diffusion and diffusion into another type A particle. However, in a true monolayer the A particles are next to each other, in an xy plane for example, but there is no interference between each A particle because the flow is going past in the z-direction. Therefore, the fluid is prevented from moving in an xy plane and radial diffusion or dispersion is completely minimised. Diluted in the FLC with particles of type B, however, means that fluid issued from one A particle could not only encounter another A particle at a similar x or y position, but also a different z. Additionally, by packing the particles in a bed, there is a still a need to deconvolute the interparticle effects from the intraparticle diffusivity.

Many activity measurements of heterogeneous catalysts (particles of type A) are carried out in fixed-bed reactors, in which the catalysts are diluted with inert particles (particles of type B). Improper mixing of the catalyst and diluent, however, may result in the mobile phase bypassing the catalyst-rich zones (Berger *et al.*, 2002).

Trickle-bed reactors are examples in which catalyst particles are diluted by small inert particles (i.e. fines), through which a concurrent flow of gas and liquid flows. The use of fines increases solid-solid contact points and areas over which the liquid flows,

particularly near the reactor wall, because there is better spreading of the liquid film over the external surface of catalyst, thus increasing catalyst wetting and liquid holdup (Al-Dahhan *et al.*, 1995; Al-Dahhan and Dudukovi, 1996).

Catalyst particles keep their intrinsic activity, but they are dispersed in an inert surrounding, giving rise to a discrete particle problem, i.e. whether the reaction locally in the bed takes place or not. Hence, catalyst-diluent particle distribution and radial bed transport seem to be important parameters (Berger *et al.*, 2002).

Four variables control the packing of materials in reactor tubes: 1) the particle itself (e.g. size and shape), 2) the reactor vessel (e.g. shape, size, and surface properties), 3) deposition (i.e. the loading of the packing materials into the vessel), and 4) treatment after deposition (e.g. process vibration) (Afandizadeh and Foumeny, 2001).

The concepts underpinning these types of catalyst dilution experiments can be attributed to those proposed in this chapter, thus proposing the first hypothesis of this chapter (hypothesis 8): that the FLC can be used to approximate the ZLC by diluting sample particles (A particles) in a packed bed of an inert matrix (B particles).

It is suggested that an ideal B particle be inert, non-porous, and of the same size as the A particles, because any differences detected between diffusion curves of different A particles would then be due to the intrinsic porosity of that sample. It was proposed that the diluent be silica, glass, polystyrene, or polymer particles, on which adsorption experiments be conducted to determine the effects the diluent material may have on the analyte/flavour/adsorbate prior to diffusion experiments. Unfortunately, purchasing dry beads of the same particle size proves difficult, because most of them are sold dispersed in liquid, and thus raises questions regarding how to clean the beads in between runs, which increases the amount of time the experiments need to be completed. Glass spheres seemed to be the simplest option, however there were concerns over the beads unknowingly cracking or breaking during homogenisation of the diluent and sample.

Additionally, ideal situations can never be achieved, because a variety of glass beads of different sizes would need to be purchased in order to match the particle sizes of the different samples, and this would prove very costly. Even if funds were available to do so, it would be an impossible task to match the particle sizes of the beads (B particles) to those of the sample (A particles). This would involve purchasing a variety of molecular sieves, which would further increase the costs involved.

Therefore, in order to study the activity of FCCs, it was decided that the diluent material simply be a GCC, as it has already been shown that it is non-porous (Chapter 3) and does not adsorb vanillin (Chapter 4), and would be adequate enough for initial proof of concept experiments; if the experiments yield the desired outcome then it may be worth investing more time and resources into controlling the particle size of the sample and diluent to exert more control over the experiments, and thus reproducibility.

The question is how to pack the diluent and sample into the FLC in such a way so that the sample particles are as far away from one another as possible at a specified concentration. In industrial practice, particles of desired size and shape are dumped randomly into a container to form a packed bed (Afandizadeh and Foumeny, 2001),

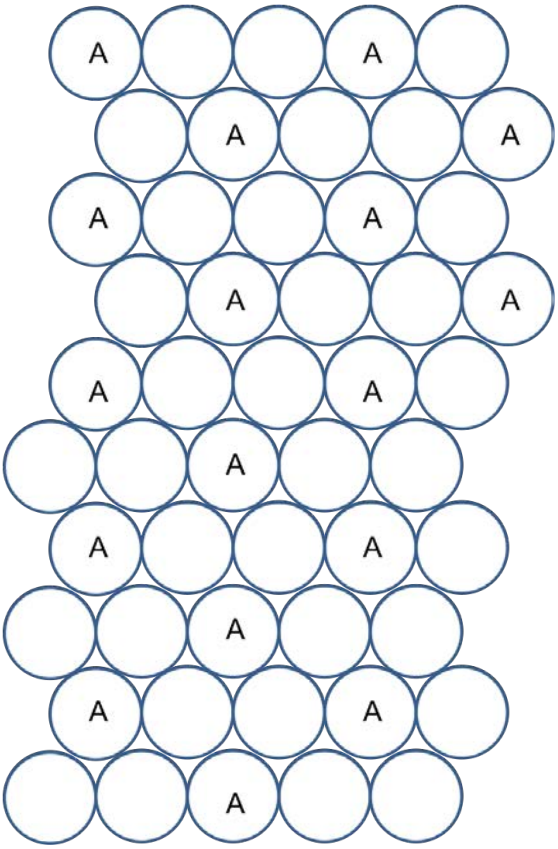

Figure 8.1: A thought experiment in which one visualises a 2D cylinder packed with perfectly ordered particles. In this instance, the cylinder is 5 particles in width and 10 particles in length, and all particles are of the same diameter; some are type A and the unlabelled particles in the diagram are type B. In the diagram there are as many A particles as possible without them touching one another.

and so a way of mixing the materials together can be standardised (i.e. by using a reciprocating shaker for a certain period of time) in hopes that the bed structure would be entirely random. However, in order to minimise the number of sample particles touching one another, the question of what is an appropriate fraction of the sample particles (f) to diluent becomes apparent.

In order to design the experimental matrix a simple thought experiment was made, in which one visualises a two-dimensional (2D) cylinder packed with perfectly ordered particles, 5 particles in width and 10 particles in length, of the same diameter. Some of these particles are type A and others are B; ideally there needs to be as many A particles as possible in the experimental matrix without them touching one another. If this is the case in the thought experiment, as in Figure 8.1, then 17 particles would be type A and 33 particles would be type B. Extending this to the 3D experiment, the FLC would need to be packed with 34 % of A particles and 66 % of B particles.

The major drawback of this is that because the loading of the material into the FLC will rely on the random placement of the particles; there is no guarantee that there will be

no A particles touching. Therefore, it needs to be decided what an acceptable number of A particles touching can be for these experiments. However, one must first be able to calculate the number of A particles touching other A particles there are in the system.

8.1.1 Particle pairs model

A mathematical model was created with the aid of an applied mathematician and professional engineer at an environmental consulting firm via personal communications, and further refined with the aid of Dr Malgorzata Wojtys, a lecturer in statistics from the University of Plymouth, in order to calculate the number of A particle pairs there would be in a packed bed, assuming a mixture of two particle types: A and B. The model was then applied to the FLC system.

The assumptions of the model are that the packed media is homogeneous and infinite in extent and that the A particles and B particles are spherical in shape with the same diameter. The model is based on a theorem derived from Bezdek and Reid (2013), which states that the number of touching pairs of particles in the packed bed (P_{N}) out of the total number of particles (N) in three-dimensional Euclidean space ($\mathbb{E}^3$) when $N \geq 2$ can be bound in the following way:

$$P_{\mathrm{N}} < 6N - 0.926N^{\frac{2}{3}} \tag{8.1}$$

where 0.926 is the highest possible particle packing density. The derivations of this model state that $X(\omega_{\mathrm{i}})$ is a binary random variable that indicates the particle type for the i^{th} particle (ω_{i}) in the packed media:

$$X(\omega_{\mathrm{i}}) = \begin{cases} 1 \text{ if } \omega_{\mathrm{i}} = \mathrm{A} \\ 0 \text{ if } \omega_{\mathrm{i}} = \mathrm{B} \end{cases} \tag{8.2}$$

The assumption of homogeneity implies that $X(\omega_{\mathrm{i}})$ are independent of one another and $Pr(X(\omega_{\mathrm{i}}) = 1) = f$, where f is the fraction of A particles in N. Therefore, $Pr(X(\omega_{\mathrm{i}}) = 1 \bigcap X(\omega_{\mathrm{j}}) = 1) = f^2, \forall \mathrm{i} \neq \mathrm{j}$, where $\bigcap$ is based on set theory and refers to the intersection or coexistence of elements of the two sets or conditions. The notation of Pr stands for 'probability.'

Let $\phi_{\mathrm{k}} = \omega_{\mathrm{i}}, \omega_{\mathrm{j}}$ denote a pair of touching particles. ϕ_{k} is denoted using indexed sets, where the ordering of the particles in the pair is irrelevant, and designates the same pairing. The probability that any two particles will be type A is of no concern, however, the probability that any two touching particles are both type A is.

The assumption of homogeneity implies that the composition of the pairs is independent of one another, but the risk of double-counting the number of particles involved in the pairs arises, because some pairs may share a common particle. To address this, the average coordination number (C_{N}) will be calculated and used to calculate the number of unique particles among the pairings:

$$C_{\mathrm{N}} = 2\frac{P_{\mathrm{N}}}{N} \tag{8.3}$$

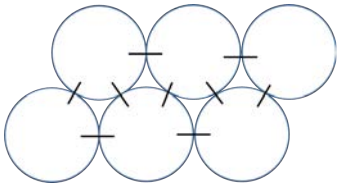

Figure 8.2: A diagrammatic example of the coordination number of a particle, where a black line indicates a coordination; in this case C_N = 3.

To demonstrate, consider Figure 8.2, in which 6 particles (N = 6) are shown along with black lines to indicate the pairing of the particles. The value of P_N that can be counted in Figure 8.2 will now be used to calculate C_N:

$$\begin{aligned} C_N &= 2\frac{P_N}{N} \\ C_N &= 2\frac{9}{6} \\ C_N &= 3 \end{aligned} \tag{8.4}$$

The average coordination number is 3.

However, it can also be seen in Figure 8.2 that N = 6, and so in this instance, equation 8.1 can then be used to find an upper bound on C_N:

$$\begin{aligned} P_N &< 6N - 0.926N^{\frac{2}{3}} \\ P_N &< 32.942 \end{aligned} \tag{8.5}$$

P_N = 33 will now be used to calculate C_N:

$$\begin{aligned} C_N &= 2\frac{P_N}{N} \\ C_N &< 11 \end{aligned} \tag{8.6}$$

Therefore, the derivations of this model are saying that each particle coordinates to no more than 11 other particles on average, whereas the more accurate value of 3 was calculated using the more accurate P_N that was counted from Figure 8.2.

So it appears as though the equations are correct, but the boundaries used to calculate P_N are very broad. It can be seen, however, that when using an accurate P_N, C_N becomes less than 12. This is because the derivations of equation 8.1 are based on the fact that the kissing number of a central particle in 3D $\mathbb{E}^3$ is 12 (Hales, 2005), and the equation also is based on the assumption that the packed bed is infinite in extent and does not take into account any wall boundaries. When calculating C_N with an accurate P_N, it seems as though the wall boundaries are taken into account and C_N becomes more accurate. The value of P_N calculated above, however, will be used to continue with the model derivations (P_N = 33).

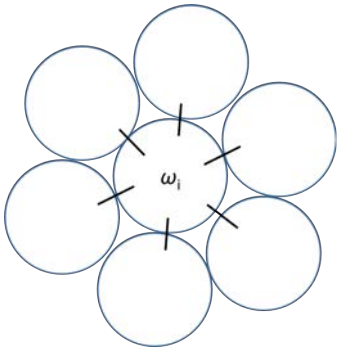

Figure 8.3: A diagrammatic example of the number of touching pairs of particles in a system, where a black line indicates a pair of particles; in this case P_N = 6.

Each particle can be thought of as being the centre of a cluster with C_N branches, rounding C_N to the nearest integer. The number of (A,A) pairings in the cluster is given by K_i, with the centre of the particle being ω_i. Figure 8.3 shows this in diagrammatic form.

The expected (average) value (E) is obtained based on the conditions that how many A particle pairings are with the central particle ω_i is calculated, but not any pairings that concern ω_j (hence the 0 value from equation 8.8):

$$E\left[K_i|\omega_i = \mathrm{A}\right] = C_N f \tag{8.7}$$

$$E\left[K_i|\omega_i = \mathrm{B}\right] = 0 \tag{8.8}$$

and so averaging out for a randomly chosen particle, which is the mean number of (A,A) pairings:

$$E\left[K_i\right] = C_N f.f + 0\frac{N_2}{N} \tag{8.9}$$

$$E\left[K_i\right] = C_N f.f \tag{8.10}$$

Then all of the particles are multiplied out by the pairings:

$$NC_N f.f = NC_N f^2 = \text{all A particles} \tag{8.11}$$

$$0\frac{N_2}{N} = \text{all B particles} \tag{8.12}$$

In conclusion, to calculate the average number of (A,A) pairings in the packed bed, equation 8.11 should be utilised.

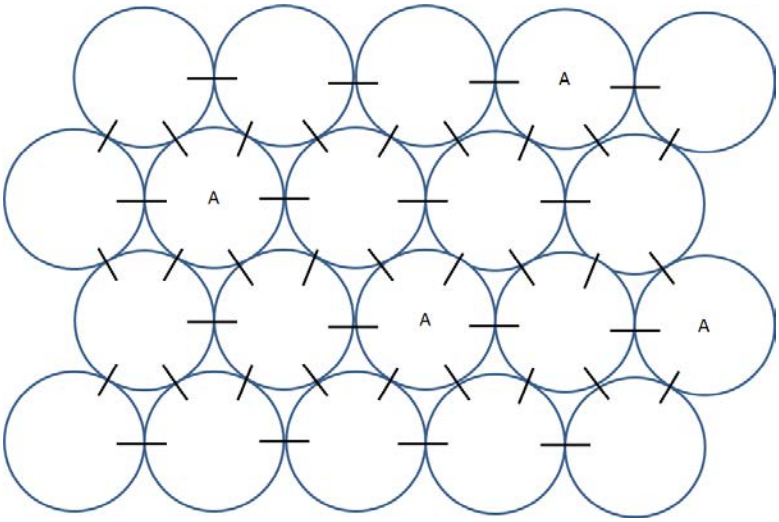

Figure 8.4: A diagrammatic example of a system in which N = 20 and f = 0.2.

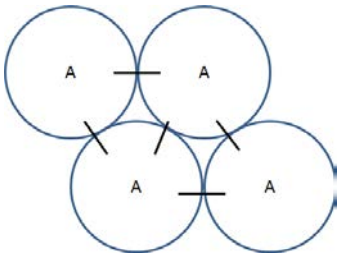

Figure 8.5: A diagrammatic example of a cluster of A particles in a packed bed arranged in such a way that they have been randomly packed next to one another to exhibit the maximum number of (A,A) pairings possible.

8.1.1.1 Worked example

Consider a system of N = 20 with f = 0.2, as in Figure 8.4, in which P_N is calculated to be 113.18, and results in a C_N of 11.32. However, it can be counted in Figure 8.4 that P_N is actually 43, thus resulting in a C_N of 4.3. Using equations 8.7, 8.9, and 8.11, $C_N f$ is 0.86, $C_N f^2$ is 0.172, and $NC_N f^2$ is 3.44.

The derivation of the number of (A,A) pairings calculated implies that this is the maximum number of possible (A,A) pairings for the given system. For example, Figure 8.5 shows a scenario in which the four A particles from Figure 8.4 happen to fall randomly next to one another in such a way that they exhibit the maximum possible (A,A) pairings, which is 5. These two values are close to one another, however, without more worked examples it is difficult to determine whether it is mere coincidence or a model that generates significant values.

If the calculated P_N from equation 8.1 is used to calculate C_N (rather than the more accurate visually observed P_N number from Figure 8.4), $NC_N f^2$ becomes 9.05. Therefore, the model is saying that the average number of (A,A) pairs is less than 9.05.

It is evident, however, that the method used to calculate P_N does not generate incor-

rect values, but the boundaries used are too broad so that the values generated are imprecise. It has been discussed that to calculate the number of pairs of A particles would simply be to divide the fraction of A in the packed bed by the number of nearest neighbours of a particle (i.e. 12). However, this viewpoint makes the whole idea of creating a model redundant, because it assumes an even distribution of all particles, rather than a random generation, as it does not take into account the type of particle that the centre of a randomly chosen particle in the system may be (i.e. either a type A particle or a type B). If, for example, one considers a B particle that has 9 A particles surrounding it, then the fraction of A particles surrounding it is 0.75 (i.e. $\frac{9}{12}$). However, because that particle is a B particle it need not be considered in the model, which is simply concerned with how many (A,A) pairings there are.

In conclusion, the aims of this model were to attempt to calculate the number of (A,A) pairs that may randomly arise in a packed bed of a mixture of A and B particles. However, there are drawbacks in that the boundaries lead to a very imprecise estimate. The work outlined in this section may be seen as a lemma in generating a more robust and accurate model or theorem. For the purpose of the work outlined in this chapter, however, Monte-Carlo simulations may provide the answers.

8.1.2 Monte-Carlo simulations

In order to overcome the issues posed by being unable to derive a mathematical model to calculate the number of pairs of A particles there would be in a randomly mixed system of A and B particles, a series of Monte-Carlo simulations were conducted. In catalyst dilution studies, stochastic models have been developed to attempt to describe the influence that catalyst dilution has quantitatively on the conversion due to different distributions of catalyst and inert particles at different dilutions (Van Den Bleek *et al.*, 1969).

The Monte-Carlo simulation code was created with the aid of Dr G. Maurizio Laudone's Python expertise. The simulations were run using Python source code files, which were opened and edited using the PyCharm Community Edition Version 4.5.2 software. The simulations generated a network of a finite number of particles, all spherical and of the same diameter, of which a fraction of that network were designated as type A particles. The simulation randomly assigned each particle either as A or B before placing the particles in a 2D grid (Figure 8.6). A hexagonal packing arrangement was utilised because it is the densest of all possible circle packings (Chang and Wang, 2010; Fukshansky, 2011; Sloane, 1998). The number of pairs of A particles there were in the generated network were then counted. The aim of this model, therefore, was to use it to determine what percentage of A particle pairs there will be in the real FLC experimental packed bed. This tests the second hypothesis of this chapter (hypothesis 9), namely that the efficacy of diluting a macroporous adsorber with an inert filler can be calculated mathematically.

8.1.2.1 Conversion from 2D to 3D

The code was then converted to a 3D system; this changed the way in which the particles packed, because in 2D the coordination number of a central circle is 6, whereas in 3D it is a centred sphere with a coordination number of 12 (Hales, 2005). This involved having to add an additional Euclidean plane on which to place the particles. In

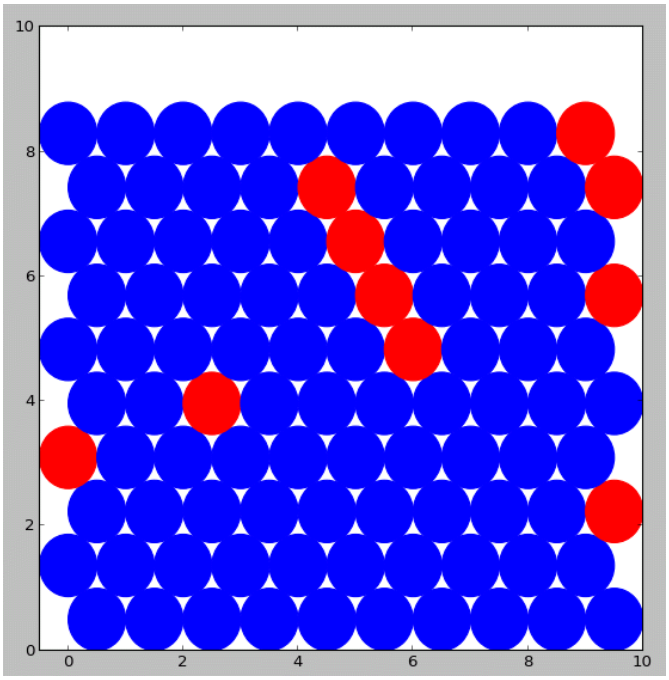

Figure 8.6: A visual representation of a Monte-Carlo simulation. This grid is 10^2 (100 particles) in size with a fraction of 0.1 type A particles. The A particles are red circles, whereas the B particles are blue.

3D there are two simple regular lattices that can achieve the highest average packing density: 1) face-centred cubic or cubic close packed, and 2) hexagonal close packed. This model uses hexagonal close packed, however, the 3D visual representation has not been coded.

Once the simulations have been completed they can be compared to the values obtained from the model outlined in section 8.1.1 to test hypothesis 9.

8.1.2.2 Results & discussion

The 2D and 3D models were both used to generate results using different fractions of A particles and different simulated grid sizes, the results of which can be seen in Table 8.1. The results reported in Table 8.1 are the averages $\pm$ the standard deviations of 10 stochastic generations, and it is evident that as the grid size increases, the results between the 2D and 3D models converge and the standard deviations decrease. When averaging out the % A particle pairs for all experimental matrix sizes, Table 8.1 shows that for a 0.1 A particle fraction the 3D simulation has an average of 1.02 % A particle pairs $\pm$ 0.06 %, and for 2D the value is 1.02 $\pm$ 0.16 %. For the 0.5 A particle fraction, the 3D value is 24.91 $\pm$ 0.08 %, and for 2D it is 25.08 $\pm$ 0.19 %.

The law of large numbers is one of the foundational results of probability theory, and describes the result of performing the same experiment many times (Terán, 2008, 2014). The larger the experimental matrix the better, because the sample mean ($\bar{x}$) tends to get closer to the theoretical mean as the sample size is increased (Chatfield, 1978). Therefore, when generating results using this Monte-Carlo method, it is best to use

Table 8.1: Monte-Carlo simulation results using a 2D and 3D grid, different A particle fractions, and different grid sizes. The A particle pairs reported are the averages of 10 stochastic generations, along with their standard deviations.

FCC fraction	Matrix/grid size		% A particle pairs	
	2D	3D	2D	3D
0.1	5^2 (25)	5^3 (125)	1.25 $\pm$ 1.21	1.11 $\pm$ 0.48
	10^2 (100)	10^3 (1 000)	0.88 $\pm$ 0.48	0.96 $\pm$ 0.11
	100^2 (10 000)	25^3 (12 625)	0.96 $\pm$ 0.04	1.02 $\pm$ 0.03
	150^2 (22 500)	50^3 (125 000)	1.00 $\pm$ 0.03	1.00 $\pm$ 0.01
0.5	5^2 (25)	5^3 (125)	25.36 $\pm$ 4.19	24.91 $\pm$ 1.32
	10^2 (100)	10^3 (1 000)	24.90 $\pm$ 1.59	25.11 $\pm$ 0.56
	100^2 (10 000)	25^3 (12 625)	25.05 $\pm$ 0.16	25.00 $\pm$ 0.07
	150^2 (22 500)	50^3 (125 000)	25.02 $\pm$ 0.10	25.01 $\pm$ 0.04

as large a grid size as possible; in this instance, the largest grid size that could be used without compromising simulation speed was 25^3 (15 625 particles). Figure 8.7 shows the simulated results of 10 stochastic realisations using the aforementioned grid size; it simply shows that as the fraction of FCC increases, the % number of FCC pairs within the simulated matrix also increases, and this can be described by a polynomial equation.

8.1.3 Comparison of the two models

This section aims to confirm or nullify hypothesis 9 postulated in section 8.1.2, by comparing the result given by the two different models outlined in sections 8.1.1 and 8.1.2.

Using the model outlined in section 8.1.2, the average number and standard deviation of A particle pairs generated from 10 stochastic realisations is 898.10 $\pm$ 21.78, which equates to 1.022 $\pm$ 0.025 % of A particle pairs (relative to the total number of pairs), using a grid size of 25^3 (15 625 particles) and an A particle fraction of 0.10.

The model outlined in section 8.1.1 states that the number of touching pairs of particles in the packed bed (P_N) out of the total number of particles (N) in 3D $\mathbb{E}^3$ when $N \geq 2$ is:

$P_N < 6N - 0.926N^{\frac{2}{3}}$
$P_{15\ 625} < 93\ 171.25$

$C_N = 2 \times \frac{P_N}{N}$
$C_N = 11.93$

Using equations 8.7, 8.9, and 8.11, $C_N f$ is 1.19, $C_N f^2$ is 0.119, and $NC_N f^2$ (i.e. the average number of (A,A) pairings in the packed bed) is less than 1 864, which is significantly higher than the value generated from the Monte-Carlo simulations.

To conclude, the two models do agree with one another. However, the congruency

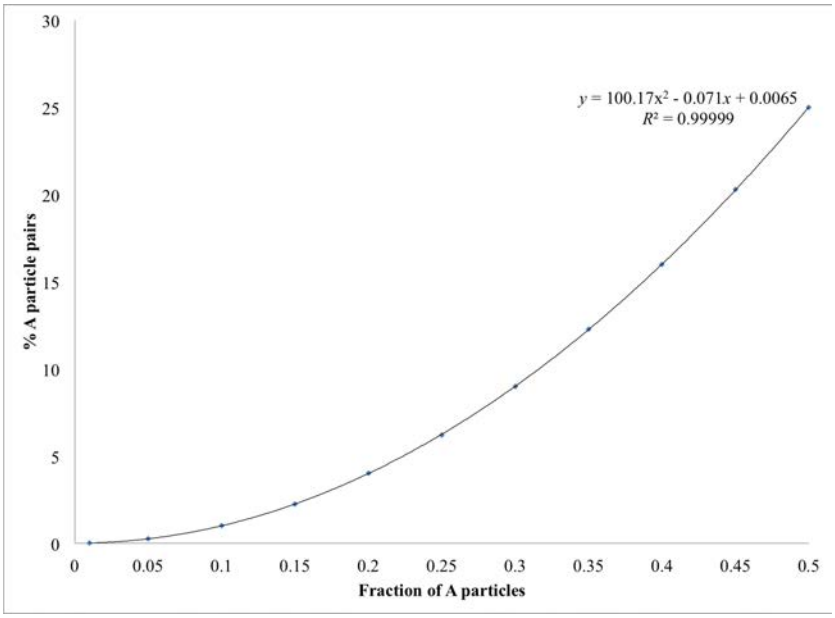

Figure 8.7: The simulated results of 10 stochastic realisations using a 25^3 grid size (15 625 particles) with a polynomial fit. The y-axis error bars are so small that it appears as though there are none.

between the two needs to be improved. Thus partially fulfilling hypothesis 9.

Although there is now a way to calculate the number of A particle pairs there would be in a packed bed of finite size, the issue of deciding which is the best fraction of A particles to use in FLC experiments is still at hand. The question that needs to be answered is: what is an acceptable % of A particles that can touch one another without significantly affecting the diffusivity profiles of the sample beyond a monolayer of A particles?

The idea behind diluting the A particles is to retain as high a concentration of A particles in the packed bed as possible, without there being too many A particles touching other A particles. The only way to guarantee that an A particle will not touch another is if there were only 1 particle in the packed bed, however, the diffusional profile of this particle will be too small to detect using the current experimental apparatus. Therefore, as small a fraction of A particles as possible is wanted, but just enough so that the diffusional profile of the sample can be detected so that the differences in diffusional profiles between samples can be seen. A way to do this experimentally is to generate diffusivity profiles and values for different fractions of A particles to assess which one would give the most desirable result. Although the model, in this instance, has not driven the design of the experimental arrangement, it can be used in the instances where the number of pairs of active particles (e.g. catalyst) is required to be known. However, it can be predicted from Figure 8.7 that there will be a polynomial rise in diffusion coefficient with increasing FCC fraction.

8.1.4 FLC experiments

In order to approximate the ZLC, it has been decided to dilute FCC particles (i.e. A particles) in a packed bed of GCC (i.e. B particles) within the FLC. This was done by creating a set of five random mixes of the same fraction of FCC in GCC, then measuring the diffusion of vanillin three times per mix using the FLC method outlined in Levy *et al.* (2015). The effective diffusion coefficient (D') was then plotted against the fraction of FCC in the packed bed (f), which enables one to normalise for an unknown f. This curve can then be extrapolated to a level of mix fraction that equates a monolayer in order to find the D' of a monolayer of sample, which is provided by the gradient at $\lim_{f \to 0}$ of the slope of the aforementioned curve.

8.2 Materials & methods

The FCC sample chosen to be used for the initial preliminary investigations was FCC 03 because its D' calculated by Levy *et al.* (2015) was the slowest out of the FCC samples tested in that work.

The envelope densities of FCC 03 and GCC were used to calculate the weight of each sample required per FLC experiment, depending on the fraction of FCC in the packed bed. The appropriate weight of FCC and GCC for 10 experimental replicates per FCC fraction was weighed into a 200 cm^3 tared plastic bottle using a Mettler Toledo XP 504 analytical balance. The bottle was then laid sideways on a Stuart orbital shaker SSL1 for at least 2 hours at 300 strokes per minute.

The FLC was then tared on the analytical balance in which the FCC mix was weighed, in exactly the same way as described in section 3.2.1 of Chapter 3. The FLC was loaded with no less than 99.4 % of the calculated amount for any given experiment, and the loaded FLC can be seen in Figure 8.8, before it was assembled and connected to the HPLC.

The FLC experimental format was the same as outlined in Levy *et al.* (2015): the maximum vanillin concentration used was be 50 mg dm^{-3}, from a solution of 100 mg dm^{-3} mixed in a 1:1 ratio with ethanol, and was detected at 279 nm. The experiment involved 30 minutes of ethanol flowing through the sample at a rate of 0.5 cm^3 min^{-1}, then 30 minutes of 50 mg dm^{-3} vanillin in ethanol at a rate of 4 cm^3 min^{-1}, and finally 30 minutes of pure ethanol at a rate of 1 cm^3 min^{-1}. It was this last 30 minute period during which the concentration of vanillin was recorded.

The empty FLC was run through the experimental process 3 times, and this was the blank. The blank was run periodically to ensure that there were no changes in detection sensitivity (i.e. as in section 3.2.1.3 of Chapter 3). Each FCC fraction was packed in the FLC five times, and the FLC experiment was run three times for each packing.

8.3 Results & discussion

Figure 8.9a shows the diffusion curves of each fraction of FCC used. Each line represents the average of at least five experimental replicates, within which are the averages of their three analytical replicates. The y-error bars are the standard deviations of the aforementioned experimental replicates. The use of the FLC stipulates that the measured release rates are now dependent on diffusion and permeation effects within both

Figure 8.8: A photograph of the loaded FLC before being assembled and attached to the HPLC.

the intra- and interparticle porosity, and that the system is less well described by the mathematical assumptions described in Chapter 7 for the ZLC. Rather than precise diffusion coefficients D, the measurements are therefore of effective diffusion coefficients D'. The D' was calculated in the same way as in Chapter 7 (Levy *et al.*, 2015): D' is the D'_{phase1} calculated from the diffusion curve between 1 200-1 400 corrected seconds, and D'_{phase2} was from 1 600-1 800 corrected seconds, of which these regions can be seen in Figure 8.9b. The D' were then plotted against f; the results of which are in Figure 8.10a. The GCC values were removed, thus yielding Figure 8.10b, in which a polynomial trendline was fitted. The GCC values were removed because they represent advection rather than diffusion processes, and are therefore nominal. Table 8.2 displays the individual D' calculated for each replicate. The equations of the regression lines in Figure 8.10b were then used to extrapolate to D' for when f is equal to a monolayer.

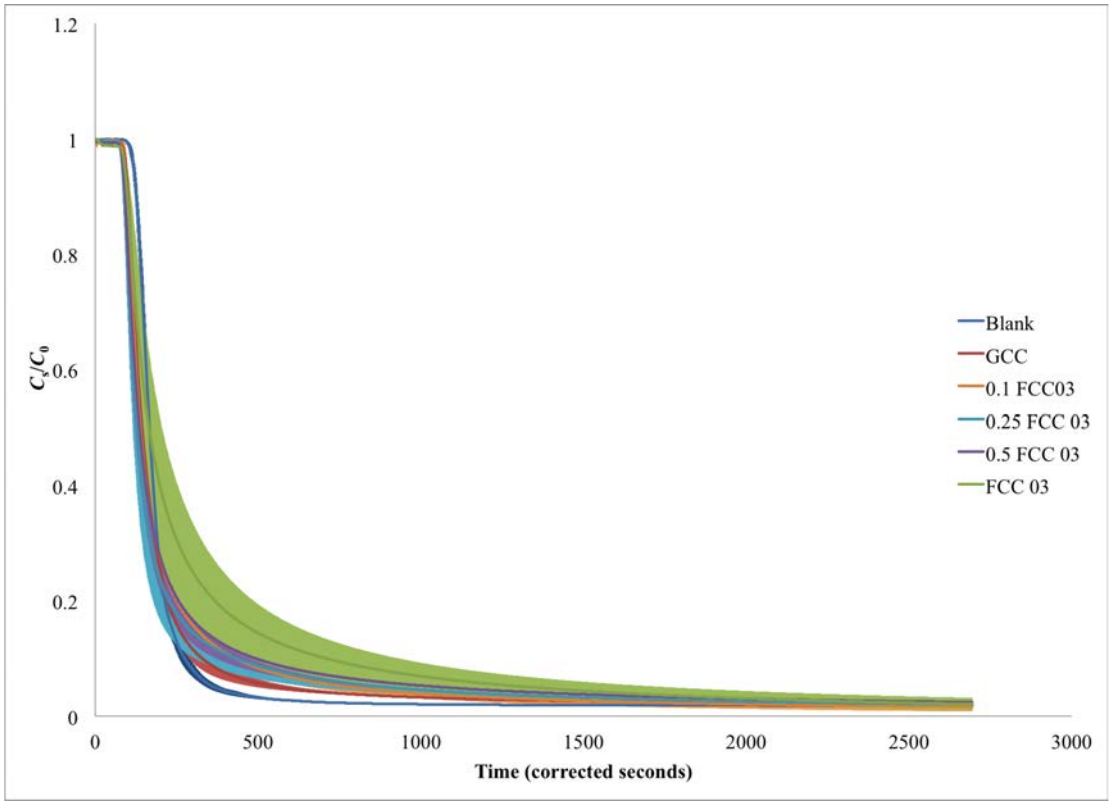

(a) FLC diffusion curves of different FCC fractions.

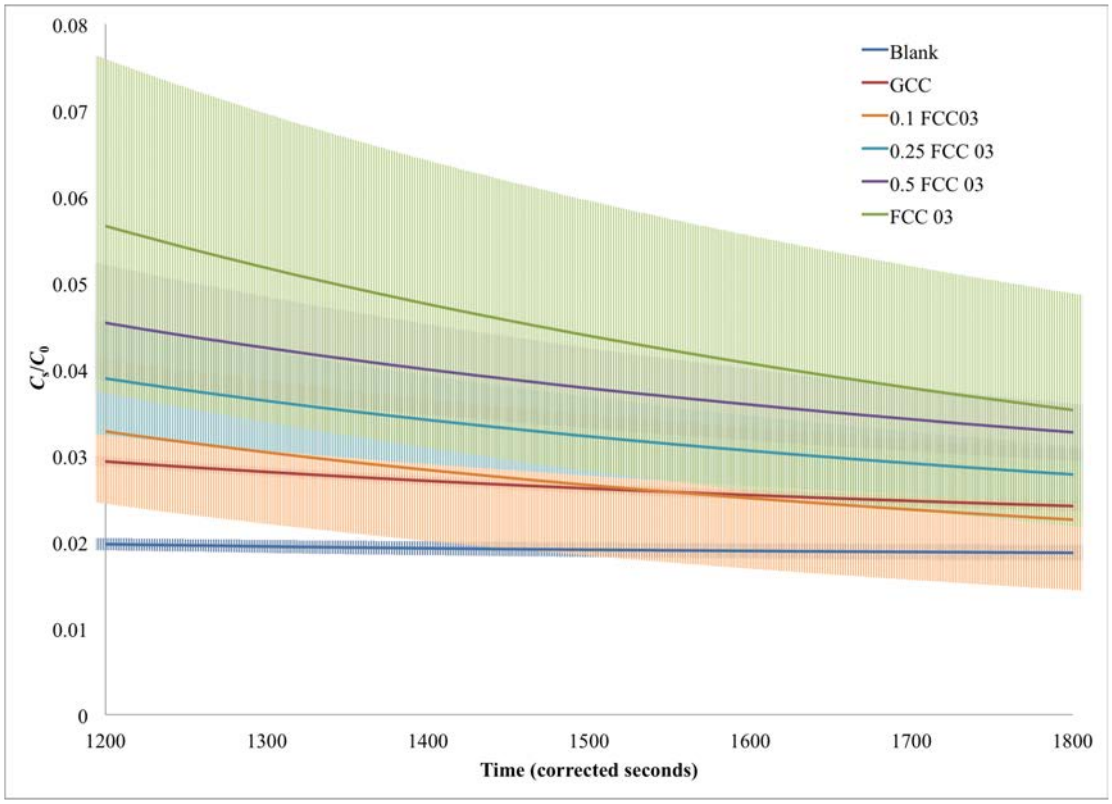

(b) Close up of the FLC diffusion curves of different FCC fractions in Figure 8.9a.

Figure 8.9: Each line in Figure 8.9a/8.9b represents the average of at least five experimental replicates, of which are the averages of their three analytical replicates. The y-error bars, which are the standard deviations of the average data from three analytical replicates, give each curve a 'cloud' that is coloured in accordance with the colour of its curve.

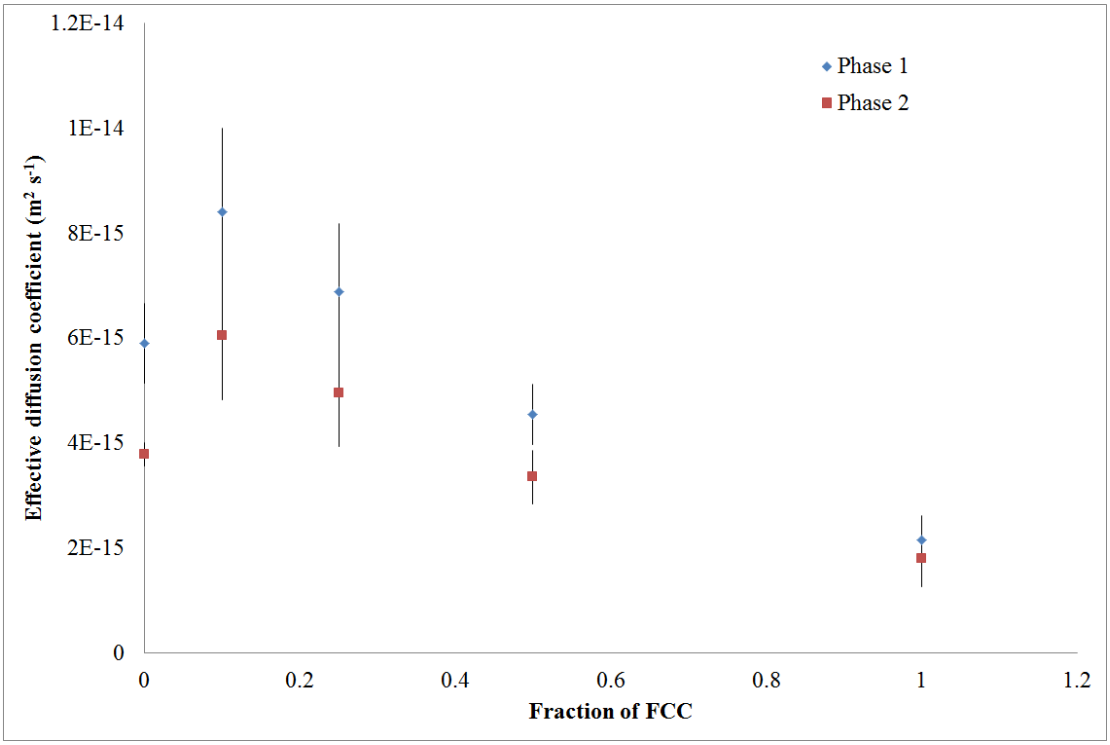

(a) D' against f.

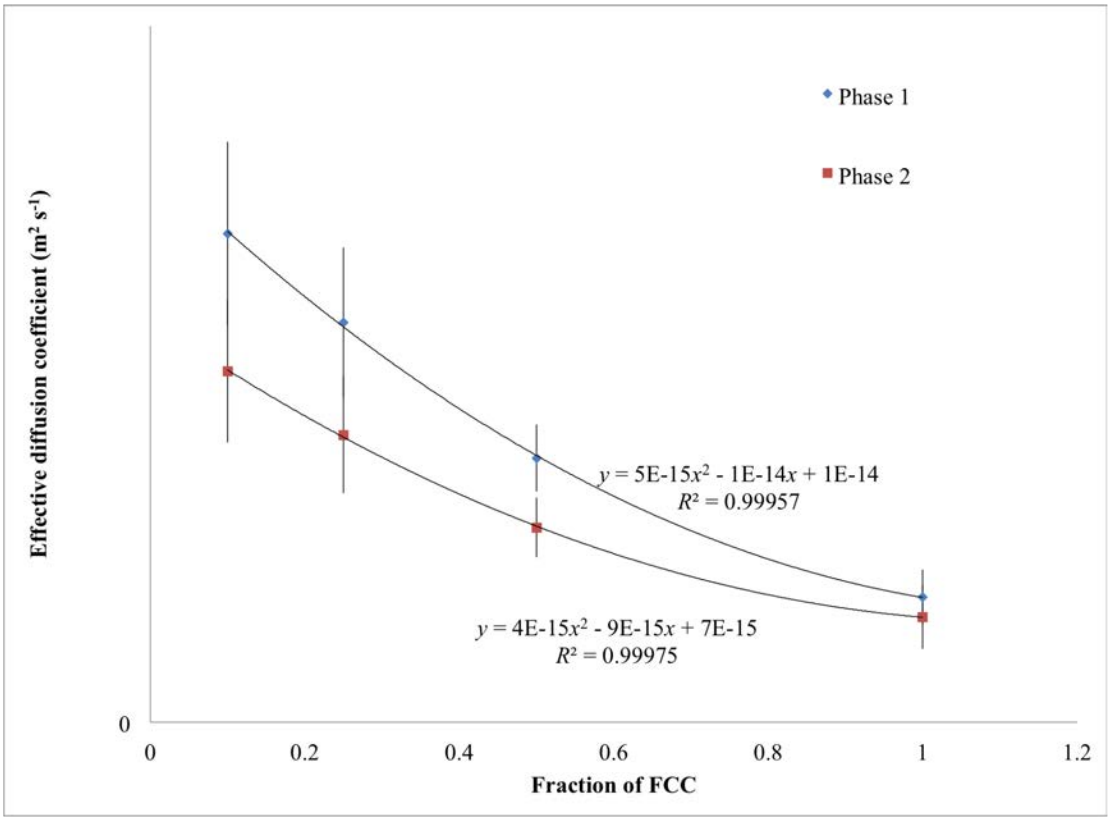

(b) D' against f from Figure 8.10a with nominal values removed.

Figure 8.10: Figure 8.10b is the same as Figure 8.10a, except with the nominal GCC D' removed, and a polynomial regression line fitted. The points on the two aforementioned figures are the averages of the calculated D' for each line in Figure 8.9a.

Table 8.2: Individual D' calculated for each FLC replicate.

D'_{phase1} (1 200-1 400 corrected seconds) (10^{-15} m^2 g^{-1})								
f	Experimental replicate						Average	Standard deviation
	1	2	3	4	5	6		
1.00	2.26	2.54	1.87	1.92	1.53	2.82	2.16	47.38
0.50	4.86	4.10	4.21	4.17	5.42	-	4.55	57.54
0.25	7.46	7.88	4.83	6.43	7.86	-	6.89	1.29
0.10	9.11	9.63	5.90	7.85	9.60	-	8.42	1.58
0.00	4.72	5.97	6.75	6.30	5.79	-	5.90	75.81
D'_{phase2} (1 600-1 800 corrected seconds) (10^{-15} m^2 g^{-1})								
f	Experimental replicate						Average	Standard deviation
	1	2	3	4	5	6		
1.00	1.85	2.24	1.48	1.51	1.15	2.64	1.81	54.75
0.50	3.74	2.86	3.08	3.03	4.06	-	3.36	51.56
0.25	5.37	5.64	3.31	4.70	5.75	-	4.95	1.01
0.10	6.56	6.89	4.04	5.74	7.03	-	6.05	1.23
0.00	3.47	3.75	4.09	3.75	3.87	-	3.79	22.45

In prior ZLC work (Gribble, 2010) 4-5 mg of GCC was used in ZLC experiments. Via private communications it was revealed that a similar amount of FCC would also comprise a monolayer in ZLC experiments. A monolayer of FCC is different for each grade, depending upon its characteristics. The way in which a monolayer of FCC was calculated was by using the particle size distribution data of the sample to calculate how many particles of each reported diameter can cover the ZLC sinter, which was then multiplied by the fraction of the particles of that diameter in the sample. These data were used to calculate the volume of the particles that can cover the sinter, which was then converted to a weight by multiplying by the envelope density of the sample. Table 8.3 displays the results of these calculations, which are significantly smaller than the aforementioned 4-5 mg.

Table 8.3: Calculated weights of FCC samples that constitute a monolayer to cover the ZLC sinter.

Sample	Weight (mg)
GCC	0.5981
FCC TP	0.1002
FCC 03	1.2048
FCC 13	0.3836

The fraction of FCC (f) for when a monolayer of FCC 03 (see Table 8.3) is diluted in the FLC is 0.0021. This value was substituted as x in the trendline equations from

Figure 8.10b in order to find y, which is D'. Using this method, D'_{phase1} is 9.98 $\times$ 10^{-15} m^2 s^{-1}, and D'_{phase2} is 6.98 $\times$ 10^{-15} m^2 s^{-1}. It was predicted, based on the polynomial relationship between the simulated % of FCC pairs and the fraction of FCC in the bed (Figure 8.7), that there may be a polynomial relationship between the calculated D' and the fraction of FCC. The high R^2 values in Figure 8.10b support this prediction.

The D' values from the FLC experiments reported in Chapter 7 (Levy *et al.*, 2015) for phase 1 are: 1.33 $\times$ 10^{-16} m^2 s^{-1} (0.13 $\times$ 10^{-15} m^2 s^{-1}), and for phase 2 is: 1.06 $\times$ 10^{-16} m^2 s^{-1} (0.11 $\times$ 10^{-15} m^2 s^{-1}). The D'_{phase2} is smaller (i.e. slower) than the D'_{phase1} calculated from both prior work (Levy *et al.*, 2015) and the work outlined here, which is expected because the values are calculated using a portion of the diffusion curve later in time (i.e. when there was less vanillin diffusing). However, both the D'_{phase1} and D'_{phase2} values are smaller from Levy *et al.* (2015) than for the work outlined here; although care was taken to correct for the effects that the intraparticle porosity and tortuosity had the play on the diffusion curves in the work outlined by Levy *et al.* (2015), the smaller diffusion coefficients may be due to the vanillin diffusing back into the another vanillin particle, which is minimised during the FLC dilution experiments outlined here.

Regarding the packing of the particles in the FLC: a perfectly homogeneous mixing of the FCC and GCC is not possible due to their finite dimensions, and also results in a distribution of local activities, such as changes in residence time occurring (Van Den Bleek *et al.*, 1969). Additionally, it is impossible to be certain that the FCC is evenly distributed in the packed bed and not touching one another; one way, however, to ensure that the FCC will not be touching other FCC particles would be to use an FCC grade that has a particle size smaller than that of the GCC, so that it sits in-between the interparticle voids of the GCC particles. According to Al-Dahhan *et al.* (1995) and Al-Dahhan and Dudukovi (1996), this method ensures a more uniform catalyst (i.e. FCC) and fines (i.e. GCC) distribution and reproducibility of such distribution, which are not obtainable by other packing methods. However, according to Al-Dahhan *et al.* (1995); Al-Dahhan and Dudukovi (1996) also, the use of fines in this way would minimise axial dispersion and increase radial mixing (Van Den Bleek *et al.*, 1969), when in actual fact we want to limit only the radial diffusion. Because the design of the FLC means that all particles are saturated during an experiment, the use of inert fines to promote radial dispersion, and therefore diffusivity, is unnecessary.

In reality, the distribution of the particles within the FLC that is obtained may be less homogeneous than expected due to a non-ideal behaviour of the particles (e.g. non-equal size distributions and different particle shapes) (Berger *et al.*, 2002). Additionally, when using a high inert bed dilution, the assumption of plug flow behaviour is often not allowed (Berger *et al.*, 2002). Therefore, to overcome this issue a coarse diluent would be used ideally.

8.3.1 MIP analysis on diluted FCC

Figures 8.11 and 8.12 shows various MIP experimental data curves provided by Omya International AG, who conducted MIP on a series of packed FCC (FCC OP, which has not been used in experimental work outlined elsewhere in this thesis) in GCC dilutions, the results of which are displayed in Figure 8.11a. The samples were first

passed through a 1 mm mesh sieve in order to remove any agglomerates that may have formed before the packed FCC in GCC dilutions, based on mass, were mixed via random shaking for 15 minutes.

The aim of these experiments was twofold: 1) to experimentally investigate whether the intraparticle pore space of the FCC is modified in any way depending upon increasing FCC particle pairs, and 2) to determine if the intraparticle pores of the FCC maintain their discreteness with increasing ratios of GCC present, or whether they are buried in similarly sized interparticle GCC pores; if the former is shown, then the data supports the use of FLC dilutions using type B particles and the assumptions of eluent flow in respect to the permeability of the diluent packing. An extrapolation to the limit of zero FCC content was performed and permitted the study of the progression of the intraparticle peak position as a function of GCC dilution.

The specific pore volume cumulative distribution curves of the series of FCC and GCC mixes in Figure 8.11a have been truncated from diameter d^{**} (Table 8.4), as anything above this diameter is associated with the coarse packing between any agglomerates. At diameters below this initial intrusion volume there was a rise there in a bimodal portion of the curve showing the fine packing of the particles themselves (between diameters d^{*} and d^{**} in Table 8.4) and the intraparticle pores (between diameters 0.004 μm and d^{*} in Table 8.4).

Table 8.4: d^{*} and d^{**} are various diameters that represent various pore types applied to the MIP data in Figure 8.11a. Diameters above d^{**} are attributed to the coarse packing of the sample. The intraparticle porosity of the sample is attributed to diameters below d^{*}, while diameters between d^{*} and d^{**} are representative of the interparticle pore space of the sample.

FCC / GCC ratio	d^{*}	d^{**}
100 OmyaPharm / 0 Omyacarb 5	0.41	0.35
90 OmyaPharm / 10 Omyacarb 5	0.38	3.1
80 OmyaPharm / 20 Omyacarb 5	0.38	3.1
70 OmyaPharm / 30 Omyacarb 5	0.38	3.1
60 Omyapharm / 40 Omyacarb 5	0.38	3.1
50 OmyaPharm / 50 Omyacarb 5	0.34	3.1
40 OmyaPharm / 60 Omyacarb 5	0.31	3.1
30 OmyaPharm / 70 Omyacarb 5	0.31	3.1
20 OmyaPharm / 80 Omyacarb 5	0.25	3.1
10 OmyaPharm / 90 Omyacarb 5	0.25	3.1
0 OmyaPharm / 100 Omyacarb 5	-	3.1

The first derivative of the cumulative intrusion curves, as shown in Figure 8.11b, reveals the pore size distributions based on equivalent Laplace diameters, which includes pore-shielding. The rightmost peak of the figure represents the interparticle pore volume of the samples, which lies at approximately 1.8 μm for all dilutions, thus confirming the

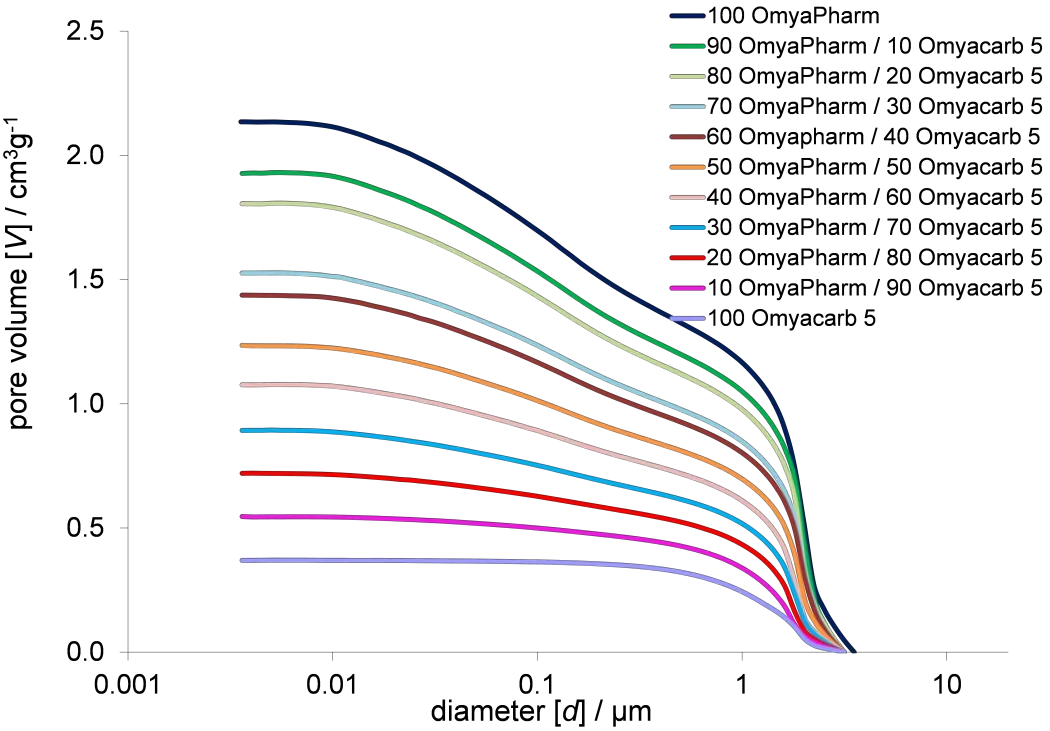

(a) Truncated specific pore volume cumulative distribution curves.

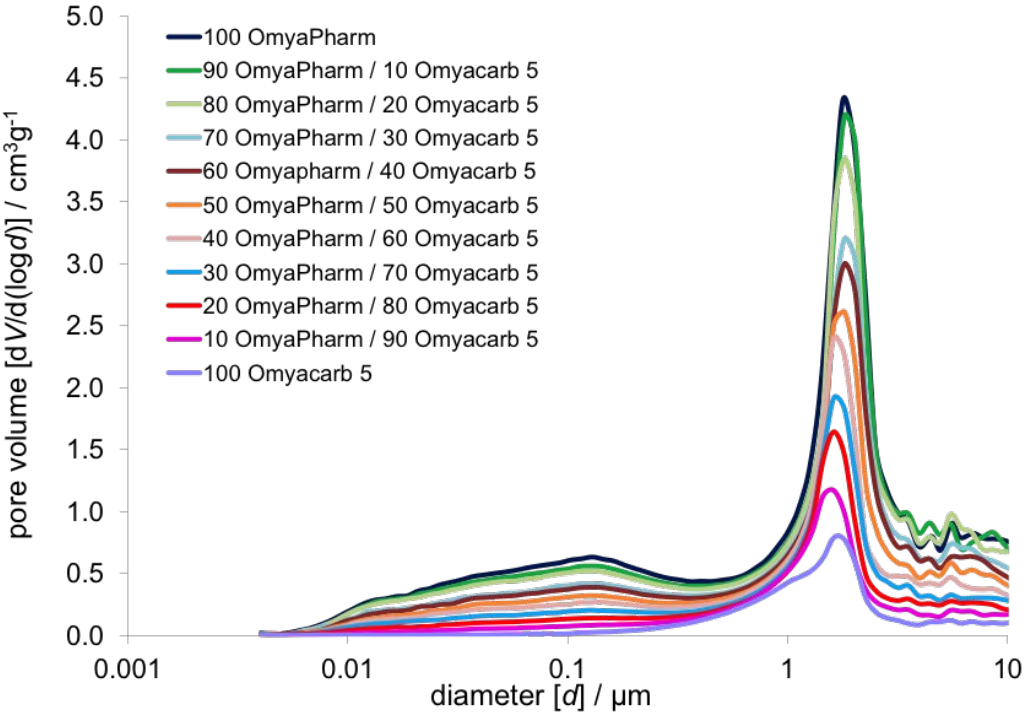

(b) The first deivative of the cumulative intrusion curves.

Figure 8.11: Various MIP experimental data curves provided by Omya International AG, who conducted MIP on a series of packed FCC (FCC OP) in GCC dilutions.

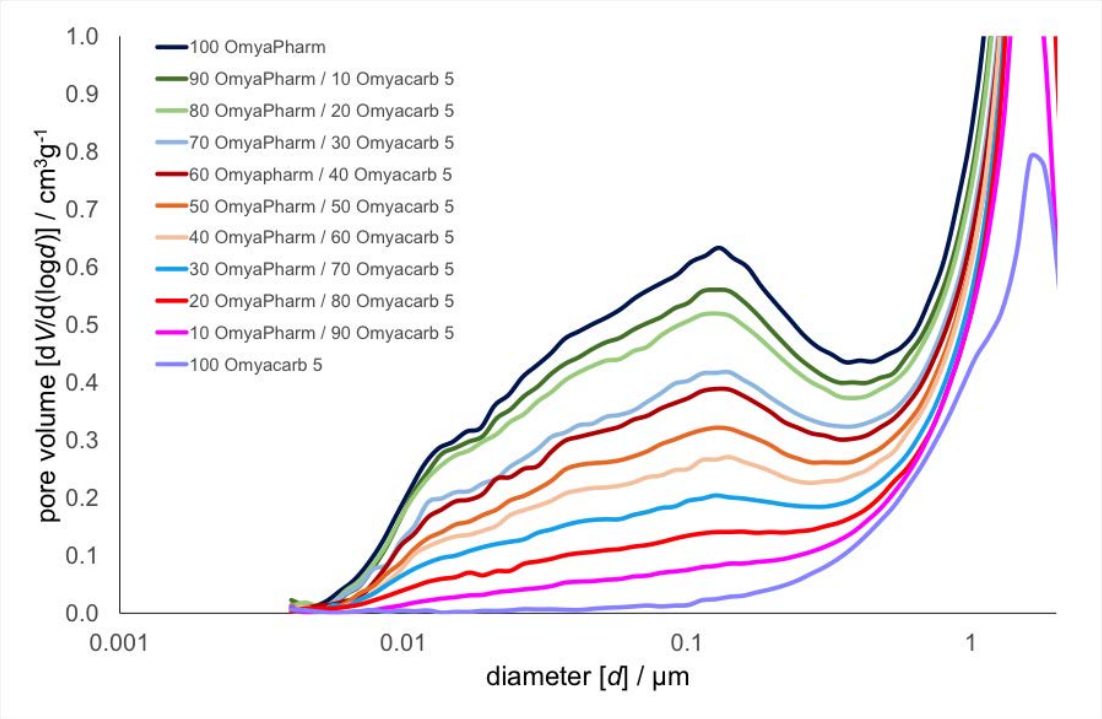

(a) A close up of the intraparticle pore region of the first deivative of the cumulative intrusion curves in Figure 8.11b.

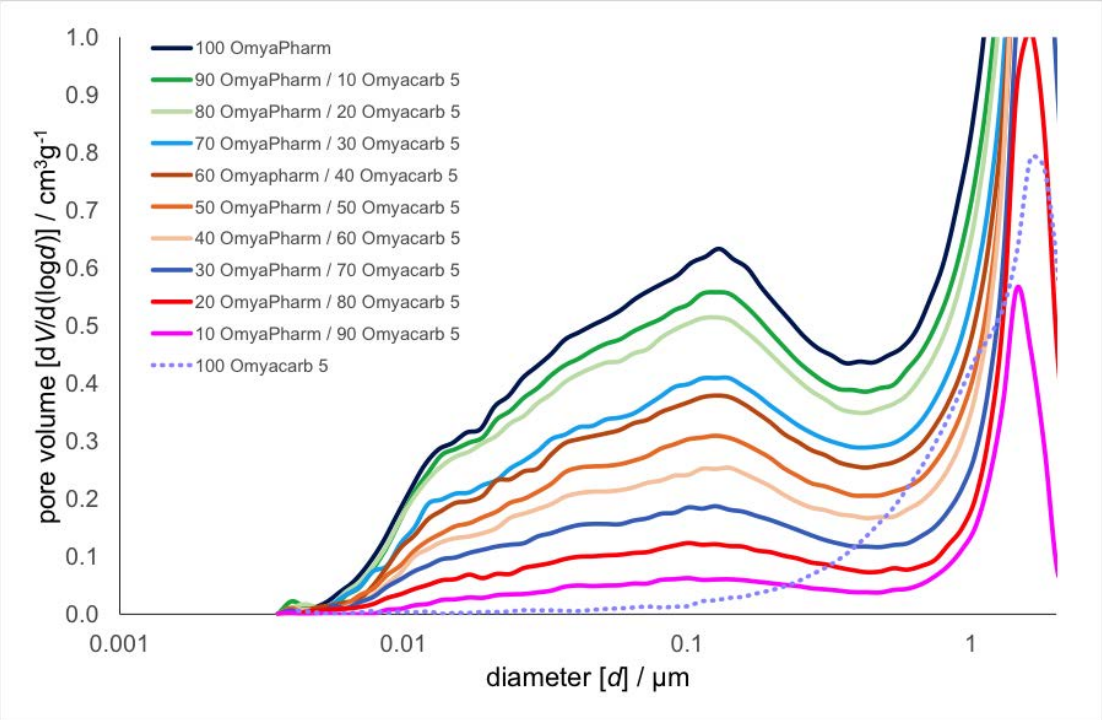

(b) A close up of the intraparticle pore region of the first deivative of the cumulative intrusion curves in Figure 8.11b that has been corrected by removing the GCC contribution.

Figure 8.12: Various MIP experimental data curves provided by Omya International AG, who conducted MIP on a series of packed FCC (FCC OP) in GCC dilutions.

similar weight median particle size between the FCC and GCC, although the 100 % FCC has a more monosized distribution than the 100 % GCC, which is somewhat broader. The interparticle peak is the highest for 100 % FCC and reduces in height as the amount of GCC present increases, which corresponds with the total specific pore volume in Figure 8.11a.

The smaller peaks to the left of the interparticle peaks in Figure 8.11b represent the intraparticle pore volume, which lie at 0.13 μm, and reduce in height as the ratio of FCC decreases. A close up of this region is shown in Figure 8.12a, the data of which is corrected by subtracting the proportion of pore volume contributed by the GCC in order to show the pore volume of the FCC ratio only, and the resulting curves are shown in Figure 8.12b. The resulting curves in Figure 8.12b show that the peak lies consistently at approximately 0.13 μm, with a very slight drift toward finer pore size as the zero length condition (i.e. FCC - GCC contribution, which tends to zero, as simultaneously the FCC tends to zero), and is expressed in equation 8.13:

$$d_{\text{mode intrap}} \lim_{\phi_{\text{FCC}} \to 0} (\phi_{\text{GCC}} - \phi_{\text{FCC}}) = \text{constant} \tag{8.13}$$

where $d_{\text{mode intrap}}$ is the modal pore diameter representing the intraparticle pores in the specific pore volume distribution, and ϕ_{FCC} and ϕ_{GCC} represent the specific pore volume contributions from FCC and GCC, respectively.

The MIP analysis suggests that the intraparticle pore volume size distribution of the FCC is constant in the presence of varying ratios of GCC, at least to a first approximation. This suggests that the bulk permeability from a packed FLC bed of 100 % FCC can be deconvoluted from the intraparticle porosity, providing that the FCC is closely monosized, thus achieving the same effect as intended by the ZLC. The data and subsequent extrapolation also suggests that the number of FCC pairs is not an issue in FLC experiments providing that the size of the particles is sufficiently large compared with the intraparticle pore size, i.e. as was previously proposed for absorption: the bimodality of the FCC pore size distribution is effectively discretely separable (Ridgway *et al.*, 2006). Therefore, this data suggests that FCC in GCC dilution may be unnecessary but only providing that the aforementioned conditions are met. However, the data strongly supports the validity of the work carried out previously (Levy *et al.*, 2015).

8.4 Conclusions & future work

The two hypotheses postulated in this chapter are as follows:

- **8:** The FLC can be used to approximate the ZLC by diluting sample particles (A particles) in a packed bed of an inert matrix (B particles).
- **9:** The efficacy of diluting a macroporous adsorber with an inert filler can be calculated mathematically.

The results from this preliminary work show the expected trend, and thus fulfils hypothesis 8, despite the many assumptions of the experimental design being made (i.e. all

particles are spherical in shape and of the same size, and that the packing of the sample and diluent is random and homogeneous). The accurate design of such systems have to be subjected to rigorous laboratory and pilot tests, as it is necessary to quantify the transport phenomena and reaction kinetics that govern the performance of the sample (Afandizadeh and Foumeny, 2001). Future work involves using a coarse GCC grade (i.e. diluent) in the packed bed, which will hopefully yield more accurate results. The D' of other FCC grades can also be measured and calculated, and compared to those from prior work Levy *et al.* (2015). Additionally, the FCC dilution fraction (f) can also be increased to see if the polynomial fit in Figure 8.7 matches experimental results.

The two models outlined in sections 8.1.1 and 8.1.2 both agree with one another, however their congruency can be improved, specifically the accuracy of the FCC pairs model outlined in section 8.1.1, thus only partially fulfilling hypothesis 9. The FCC pairs model needs to be further refined, because the boundaries associated with the initial derivation equations are too broad.

In light of the MIP data provided by Omya International AG in Figures 8.11 and 8.12, the pore structure and connectivity of the intraparticle pores of the FCC could be simulated as a function of GCC dilution using PoreXpert. The pore structure of a single FCC particle can then be approximated from the PoreXpert simulations and compared to the intraparticle pore fraction of the distribution of a 100 % FCC packed FLC bed. This may enable the diffusion modelling of a single particle, which would also be applicable to other vector carrier particles of interest. Additionally, the FCC in GCC system would be a homogenised matrix thus making the extraction of any single particle information extremely difficult: if all of the MIP curves in Figure 8.11a are modelled using PoreXpert, then one would expect to see an increasing number of intraparticle pores with an increasing FCC fraction, which would simply be a verification of the software. The work outlined in Chapter 6 is similar to the proposed single particle diffusion modelling in that the diffusion of many single particles in bulk solution is simulated.

Table 8.5 shows all D' values of vanillin diffusing in ethanol from FCC calculated using the various methods as outlined in Chapters 6, 7, and 8. The D' values taken from Chapter 7 are published in a peer-reviewed academic journal (Levy *et al.*, 2015), and the values shown from this chapter are the average values quoted from Table 8.2 for a 0.25 fraction of FCC diluted with GCC in the FLC, because this fraction of FCC had the lowest standard deviations for both phase 1 and phase 2.

The intraparticle porosities of FCC S07 and FCC S10 displayed in Table 8.5 were calculated based on the pore volume values in Table 6.1 from Chapter 6.

It is interesting to view the variety of calculated D' values in Table 8.5, as they vary in magnitude. Although it would be very interesting to cross-compare the D' calculated via different methods, ultimately, this cannot be done because different methods represent different systems, in which the FCC behaves differently each time. It would be interesting to study the same group of FCC grades using these different methods to establish a relationship between the FCC grades, and whether that relationship is apparent regardless of the system in which D' is measured and calculated.

Table 8.5: Effective diffusion coefficients D' of vanillin in ethanol calculated at corrected t = 1 200-1 400 s (phase 1) and 1 600-1 800 s (phase 2) from Chapters 6, 7 (Levy *et al.*, 2015), and 8.

Sample	Intraparticle porosity (%)	D'_{phase1} (10^{-16} m^2 s^{-1})	D'_{phase2} (10^{-16} m^2 s^{-1})
		Chapter 6	
FCC S07	38.36	-	232
FCC S10	41.33	-	248
		Chapter 7	
GCC	-	7.96	3.93
HAP	34.2	7.58	6.17
FCC TP	25.9	7.53	6.85
FCC 02	24.4	5.17	4.05
FCC 03	10.4	1.33	1.06
FCC 06	25.2	5.30	3.97
FCC 07	12.3	7.37	6.55
FCC 12	29.6	24.5	19.7
FCC 13	37.0	135	106
		Chapter 8	
FCC 03	10.4	68.9 $\pm$ 1.29	49.5 $\pm$ 1.01

Chapter 9

Overview

THE main thrust of the work outlined in this thesis is that functionalised calcium carbonate (FCC) is being proposed as an environmentally friendly and non-toxic pharmaceutical excipient, nutraceutical, and flavour carrier.

9.1 Findings & conclusions

This work outlined in this thesis postulated and addressed the following hypotheses:

- **1:** FCC, because of its predominantly negatively charged surface, will adsorb small but significant amounts of cationic species. ✗
- **2:** Sparingly soluble (dissolved) species will adsorb to a greater extent onto the FCC than strongly soluble (dissolved) species. (✓)
- **3:** The nature of the adsorbing surface of FCCs can be elucidated by studying different adsorption characteristics from a range of different adsorbates and solvents. (✓)
- **4:** The extent to which a flavour or drug compound can be physically loaded into the void volumes of FCC can be quantified by directly observing the loaded FCC by scanning electron microscopy (SEM). (✓)
- **5:** Computational methods can be used to calculate a diffusion coefficient from experimental data of flavour release from FCC. ✓
- **6:** The diffusion characteristics of FCC can be studied by exposing a monolayer of FCC to a flow of solvent (i.e. a ZLC experiment). ✗
- **7:** The diffusion characteristics of FCC can be studied by exposing a packed bed of FCC to a flow of solvent (i.e. an FLC experiment), and then subsequently deconvoluting the intra- from the interparticle processes using PoreXpert. (✓)
- **8:** The FLC can be used to approximate the ZLC by diluting sample particles (A particles) in a packed bed of an inert matrix (B particles). ✓
- **9:** The efficacy of diluting a macroporous adsorber with an inert filler can be calculated mathematically. (✓)

where ✗denotes a disproved hypothesis, ✓a proved hypothesis, and (✓) a partially proved hypothesis.

Chapter 4 addressed hypotheses 1-3; hypothesis 1 was disproved, and hypotheses 2 and 3 were partially proven. Chapter 5 partially validated hypothesis 4, and Chapter 6

proved hypothesis 5. Chapter 7 nullified hypothesis 6 and partially proved hypothesis 7. Finally, Chapter 8 validated hypothesis 8, and partially validated hypothesis 9.

In conclusion, this work suggests that 'functionalised' calcium carbonate (FCC) has potential for use as a carrier for the controlled release of 'actives,' by permeation and diffusion. The novel FLC method enabled the study of the diffusion of vanillin in ethanol through various FCC grades, which led to the arrival at this conclusion. These results (Chapter 7) show that diffusion is dependent on particle size, and that the intraparticle tortuosity trends with diffusion when scaled by porosity. Chapter 8 discusses ways in which the FLC can be used to dilute the powdered sample in an inert matrix in order to approximate a ZLC measurement; this is preliminary work attempting to overcome the limitations of the current ZLC method. Additionally, the utilisation of mathematical modelling in conjunction with experimental methods is discussed: Chapter 6 discusses the successful modelling of diffusion profiles of the vanillin loaded FCCs, and Chapter 8 displays two ways in which particle pairs of FCCs can be calculated in a packed bed of finite volume. Chapter 5 discusses the potential for loading the FCC with flavour and/or drug, which may then be used in subsequent experimentation, which is further discussed in this chapter.

Adjustments to the FCC production process can be used to produce a wide range of different morphologies, and raise the possibility of tailoring the void structures of the particles to provide controlled release delivery vehicles for actives across many fields, including drugs and flavours. However, such tailoring can only be fully optimised by a fundamental characterisation of the way in which a drug, loaded into an FCC, then flows and diffuses out over a period of time to provide the delayed release.

A way in which the diffusivity of the intraparticle pores of each FCC grade can be characterised is through the ZLC technique, however, it was been established that there are many experimental artefacts present with such a method. The FLC has been developed as a means to overcome the limitations of the ZLC.

The utilisation of mathematical modelling in conjunction with experimental methods in the study of drug release and delivery is steadily increasing due to its enormous future potential; it will enable the optimisation of novel dosage forms and the elucidation of release mechanisms at a major reduction in cost and time compared with the number of experimental studies required to do so.

9.2 Future work

There are many ideas for future work littered throughout this thesis. This section, however, summarises some of the more significant and general future work suggestions and ideas.

9.2.1 FLC studies and further development

The experimental work with the FLC (Chapter 7) has so far proved successful. This section outlines future work that could potentially be undertaken as the next steps in this project. The main adaptations to the FLC would be to 1) use simulated saliva, gastric, intestinal, and duodenal phases as solvents, 2) quantify the release of loaded FCC using the FLC, and 3) study the diffusion of loaded FCC powders and tablets.

9.2.1.1 Simulated body fluids

Previously, benzene in cyclohexane was used as the sorbate-solvent system for use with the FLC technique developed within the EFMG. The research outlined in this thesis has progressed to using non-toxic systems; the use of ethanol has been extensively used throughout this work in the FLC as a solvent, as has the brief use of ultrapure water (Chapter 7), as well as the exploration of the usage of a potential neutral buffer, HEPES (Chapter 4). However, more realistic model solvents regarding future application of the experimental work, such as water and saline, which are considered valid by the scientific community, are proposed.

A simulated *in vitro* gastro-intestinal extraction procedure, commonly described in the scientific literature under the specific name of the 'physiologically-based extraction test' (PBET), has been previously used to measure the bioavailability of compounds that may be harmful to humans and/or the environment, such as evaluating the bioaccessibility of metals, e.g. from soil, dust, or food (Intawongse and Dean, 2011). *In vitro* extraction procedures make use of simulated gastric and intestinal fluids which are applied to samples to try to predict the availability of metals for human absorption (Juhasz *et al.*, 2011). These simulated gastric and intestinal fluids may be used as future solvents for use with the FLC. The Bioaccessibility Research Group of Europe (BARGE) have models of these various intestinal and gastric fluids that can be accessed depending upon the nature of the research (Wragg *et al.*, 2011).

The unified BARGE method (UBM) provides models with regards to preparing saliva, gastric, duodenal, and bile phases (Juhasz *et al.*, 2011), which can then be altered according to differing research needs. Tables A.1, A.2, A.3, and A.4 in section A.1 of the appendix outline the reagents required for preparing saliva, gastric, duodenal, and bile phases, respectively, which can be used as a starting point.

Gastric pH in humans, with its accompanying buffering capacity, ranges from a basal level of 1-2 to 4-6 after the ingestion of food (Ruby *et al.*, 1993, 1996). It is one of the most important physiological factors in predicting the bioavailability of various elements, such as Pb and As (Ruby *et al.*, 1993, 1996). Another critical factor is the residence time in the stomach. The gastric contents are completely emptied into the small intestine within approximately 2 hours in humans (Ruby *et al.*, 1993, 1996). When making up solutions to represent various gastric fluids, the selection of appropriate concentrations of digestive enzymes is problematic because concentrations are highly variable in the human system (Ruby *et al.*, 1993). Gastric mixing rate (the rate at which ingested material is mixed with fluid in the stomach due to peristalsis) will also affect mineral dissolution kinetics and influence the concentrations of metals and other elements in the stomach (Ruby *et al.*, 1993). These are important factors to consider when determining the bioavailability of any element of a compound.

Although it is apparent that simulating a body fluid phase is incredibly difficult due to the complexities of the human system, it is important to move onto more realistic solvents in order to gain a better understanding of the release mechanism in a more applicable environment. This is because the release rates of different compounds varies drastically depending on the release medium. For example, the release of drug from chewing gum is dependent on the water solubility of the drug; water soluble substances

are released rapidly and completely, whereas slightly water soluble drugs are released slowly and incompletely, and therefore require special formulation to produce a satisfactory release profile (Rassing, 1994).

9.2.1.2 Diluting the HPLC flow

It was discussed in Chapter 5 that a way to load oils and liquid compounds into the FCC may be via the oil absorption method, and the resultant paste can be applied to the ZLC sinters for subsequent experiments. It was rationalised that the burst effect would have no effect on the diffusional characteristics of each FCC grade because the diffusion is studied from the long term region of the curve.

However, a pure compound loaded directly into the pores may saturate the DAD and inhibit the determination of the true quantity of compound. Therefore, a way to avoid this saturation of the detector would be to use a method similar to column chromatography, in which fractions of the post-column flow is captured in a beaker and diluted by hand (i.e. in volumetric flasks) before being transferred to a UV-visible spectrometer for analysis. A major drawback, however, is that very small volumes would be needed to capture the desorption and diffusion characteristics of each grade of FCC, especially if the differences are particularly subtle. Moreover, diffusion in dilute solutions is easier to understand in physical terms than a pure liquid. A diffusion flux is the rate per unit area at which mass moves. A concentration profile is simply the variation of the concentration versus time and position. These ideas are much more easily grasped than concepts like momentum flux, which is the momentum per area per unit of time (Cussler, 1997).

A way in which the FLC experiments can run while using higher concentrations of analyte is by introducing more solvent flow in the HPLC post-ZLC/FLC in order to dilute the analyte before it reaches the detector. Figure 9.1 displays this set-up, in which two T-pieces are used; the first is to dispose of one section of flow post-ZLC/FLC (ideally this will have an adjustable split flow ratio), and the second T-piece is used to introduce more solvent to the flow. A Dionex GP40 Gradient Pump was found in the department within the university and can be used to pump the additional solvent required to dilute the flow through the second T-piece.

9.2.2 Tablets

Once (loaded) tablets have been made not only can they be studied via simple diffusion experiments (as in Chapter 6), but also in FLC experiments (as in Chapter 7). The first issue, however, would be making tablets that suit the experimental requirements.

Unfortunately, when tablets are immersed in liquid they do not saturate due to the trapped air in the internal pores; therefore, to achieve full saturation slow imbibition or forced percolation is required from one face only. Resultantly, the release of analyte is unlikely to reach a steady state until saturation is guaranteed. Furthermore, the liquid forced in by whatever force (imbibition or external) will already alter the loading distribution, as diffusion and 'internal washing' will have taken place. This is where the FLC can provide the forced percolation required for a tablet to achieve full saturation.

An alternative would be, as opposed to submerging saturated tablets into solvent, is to submerge a loaded tablet into simulated gastric fluids, i.e. as in the work of Cosijns

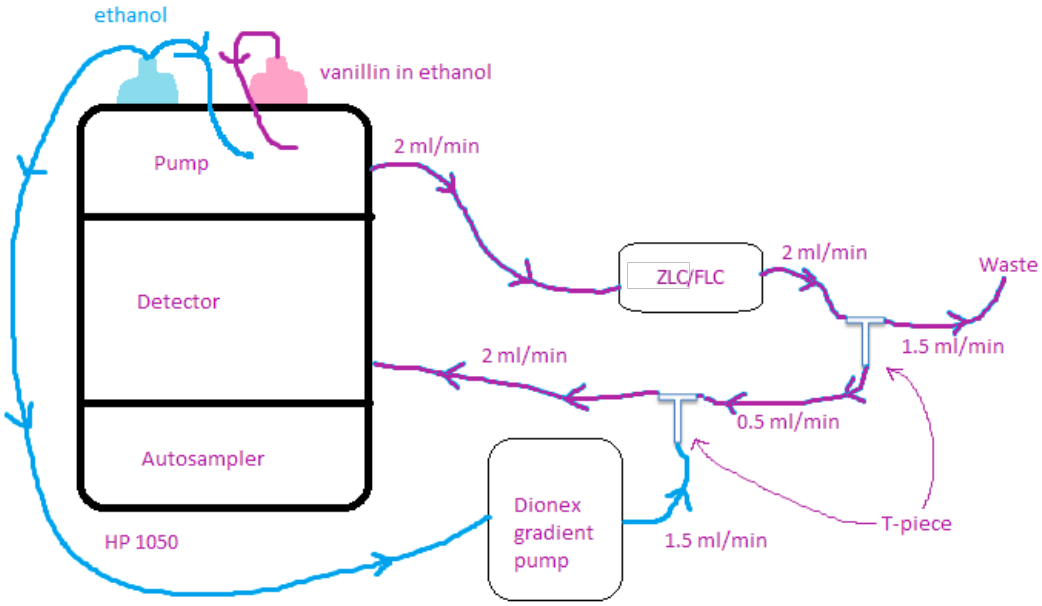

Figure 9.1: The ideal set-up for the way in which FLC experiments can run while using higher concentrations of analyte, which involves diluting the post-ZLC/FLC flow. The arrows represent the direction of the flow through the capillaries, of which vanillin in ethanol is the representative system in this instance.

et al. (2007), and to measure the release of the drug as the tablet dissolves. A proposed compound to use in this work would be peppermint oil, as that has been reported to be good for one's digestion and for irritable bowel syndrome (Riachi and De Maria, 2015). If this is performed in a beaker, as opposed to the FLC, there may be a way of stopping the dissolution of the tablet at particular time intervals, performing MIP analysis on the remaining tablet structure, and using PoreXpert to model the structure.

According to personal communications with Omya International AG approximately 60 g of GCC is required to make a tablet using the hydraulic press in Figure 2.2 of Chapter 2. Initially, it was proposed that a solution of the analyte of interest is used to saturate the tablet using a method similar to that of Laudone *et al.* (2015), and the saturated tablet will be stored in the same concentration solution used to percolate through the tablet. However after discussion, it became apparent that there is concern that the tablet would fall apart.

Alternatively, it was suggested that the FCC powder could be loaded using the IWI technique (Chapter 5) and this loaded powder could then be used to make tablets. However, after more experiments were conducted at Omya International AG using their tablets, it was confirmed that they fall apart within the first minute after being submerged into solution, and are extremely delicate. It was suggested that each side of the tablet may be embedded with resin (Gane *et al.*, 2000; Schoelkopf *et al.*, 2003*a*,*b*), however, as soon as the tablet is saturated it will start to crack, and this will give a constant change in contact area. In essence, although many designs were drawn up for tablet experiments, the complexities behind these designs are not to be encompassed

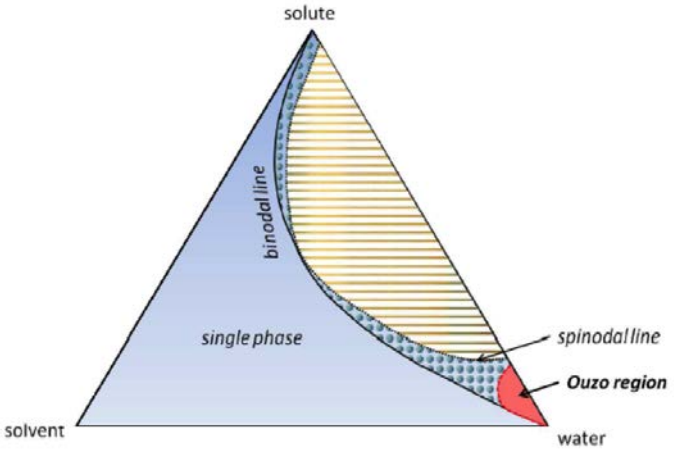

Figure 9.2: Generic phase diagram for solute-solvent-water ternary mixture, when the solute is not soluble in water (Botet, 2012). Permission to reproduce this has been granted by the publisher.

in this work.

9.2.3 Emulsions

Trans-anethole was used throughout experimental work outlined in this thesis because of its importance as a flavouring substance and its pharmacological activities (Chapter 3). Another interesting property of *trans*-anethole is its ability to form what is known as the 'ouzo effect.'

The ouzo effect is the spontaneous emulsification between the ternary system comprised of *trans*-anethole, water, and ethanol (Sitnikova *et al.*, 2005), and occurs in the metastable spinodal decomposition region of the phase diagram in Figure 9.2. Anise-flavoured alcoholic beverages, such as Pastis, Ricard, Ouzo, and Sambuca, all appear transparent when bottled with an ethanol content of around 40 % (Scholten *et al.*, 2008). The amount of water is sufficiently low and anethole remains solubilised in the water/ethanol mixture (Grillo, 2003). The alcohol is miscible in all proportions with both water and anethole, whereas the anethole is miscible with ethanol in all proportions but soluble in water only up to 111 mg dm^{-3} (The Terpene Consortium, 2006). With the addition of water the *trans*-anethole spontaneously nucleates into many small droplets. These small droplets scatter light, causing the drink to appear milky white (Vitale and Katz, 2003).

Micro- or nanoemulsions are increasingly being utilised as the basis of colloidal delivery systems in the food and pharmaceutical industries to encapsulate, protect, and deliver lipophilic bioactive components (McClements, 2012). A popular approach is to incorporate poorly water soluble drugs into inert lipid vehicles, i.e. microemulsions, in order to bypass issues associated with the oral administration of poorly water soluble drugs. A self-nanoemulsifying drug delivery system (SNEDDS), for example, would be an efficient, convenient, flexible, and more patient-friendly approach (Wang *et al.*, 2009). SNEDDS are isotropic mixtures of oil, surfactants, and co-surfactants that form fine oil-in-water nanoemulsions upon mild agitation, followed by injection into aqueous

media, such as gastrointestinal fluids (Wang *et al.*, 2009).

One potential line of investigation would be to utilise FCCs as carriers of nano- and/or microemulsions in order for the improved bioavailability of the active ingredient (Chapter 6). However, depending upon the nature of the desired system, many prerequisite tests will need to be performed before experimentation is to commence.

9.2.3.1 Anethole taste tests

During the initial phases of the work outlined in this thesis, it was discussed that loading the FCC with anethole should be in the range of what people would generally describe as being pleasant, rather than overpowering or undetectable. Therefore, the diffusion of anethole from the FCC could be tailored to ensure anethole releases within this 'pleasant' range.

A series of taste-testing experiments were designed and the ethical application forms were submitted and approved; these outlined the procedure to be taken. The ethical forms and associated documents can be found in section A.2 of the appendix.

Appendix A

Chapter 9 supplementary material

THIS appendix contains supplementary material discussed in the future work sections of Chapter 9.

A.1 The unified BARGE method (UBM)

Tables A.1, A.2, A.3, and A.4 outline the reagents required for preparing saliva, gastric, duodenal and bile phases, respectively, which can be used as a starting point in the future work outlined in Chapter 9.

Table A.1: A UBM model for the saliva phase; pH 6.5 $\pm$ 0.5 (Juhasz *et al.*, 2011).

Inorganic reagents per dm^3	
KCl	896 mg
NaH_2PO_4	888 mg
KSCN	200 mg
Na_2SO_4	570 mg
NaCl	298 mg
NaOH	1.8 cm^3 of 1.0 M
Organic reagents per dm^3	
Urea	200 mg
Additional constituents per dm^3	
Amylase	145 mg
Mucin	50 mg
Uric acid	15 mg

A.2 Anethole taste-test documents

This section provides copies of the application for the ethical approval of potential research involving human participants, which is described in Chapter 9, and outlines the procedure as well as giving the sample self-consent form, sample consent form for the parent/legal guardian, and the risk assessment form.

Table A.2: A UBM model for the gastric phase; pH 0.9-1.0 (Juhasz *et al.*, 2011).

Inorganic reagents per dm^3	
NaCl	2 752 mg
NaH_2PO_4	266 mg
KCl	824 mg
$CaCl_2$	400 mg
NH_4Cl	306 mg
HCl	8.3 cm^3 of 37 %
Organic reagents per dm^3	
Glucose	650 mg
Glucuronic acid	20 mg
Urea	85 mg
Glucosaminehydrochloride	330 mg
Additional constituents per dm^3	
Bovine serum albumin	1 000 mg
Mucin	3 000 mg
Pepsin	1 000 mg

Table A.3: A UBM model for the duodenal phase; pH 7.4 $\pm$ 0.2 (Juhasz *et al.*, 2011).

Inorganic reagents per dm^3	
NaCl	7 012 mg
$NaHCO_3$	5 607 mg
KH_2PO_4	80 mg
KCl	564 mg
$MgCl_2$	50 mg
HCl	180 mm^3 of 37 %
Organic reagents per dm^3	
Urea	100 mg
Additional constituents per dm^3	
$CaCl_2$	200 mg
Bovine serum albumin	1 000 mg
Pancreatin	3 000 mg
Lipase	500 mg

Table A.4: A UBM model for the bile phase; pH 8.0 $\pm$ 0.2 (Juhasz *et al.*, 2011).

Inorganic reagents per dm^3	
NaCl	5 259 mg
$NaHCO_3$	5 785 mg
KH_2PO_4	376 mg
KCl	564 mg
$MgCl_2$	50 mg
HCl	180 $mm^3$of 37 %
Organic reagents per dm^3	
Urea	250 mg
Additional constituents per dm^3	
$CaCl_2$	222 mg
Bovine serum albumin	1 800 mg
Bile	6 000 mg

PLYMOUTH UNIVERSITY FACULTY OF SCIENCE AND TECHNOLOGY

Human Ethics Committee

APPLICATION FOR ETHICAL APPROVAL OF RESEARCH INVOLVING HUMAN PARTICIPANTS

All applicants should read the guidelines at the end of this application

This is a WORD document. Please complete in WORD and extend space where necessary.
*All applications must be word processed. Handwritten applications **will** be returned.*

Postgraduate and Staff must send one signed hard-copy to Paula Simson and send an unsigned electronic copy of your application to SciTechHumanEthics@plymouth.ac.uk

Undergraduate students should pass on the completed and signed copy of this form to their School Representative on the Science and Technology Human Ethics Committee.

---

1. TYPE OF PROJECT

1.1 What is the type of project? (Tick 1 only)

STAFF should tick one of the three options below:

Specific project ☐ ✓

Tick this box if you are seeking approval for a specific study, or set of studies, with methods that are explained fully in the following sections. This form of approval is appropriate for funded projects with a clear plan of work and limited duration.

Thematic programme of research ☐

Tick this box if you are seeking approval for a programme of work using a single paradigm. This form Of approval is appropriate for pilot work, or routine work that is ethically straightforward. Note, the maximum period of approval for thematic ethical clearance is 3 years.

Practical / Laboratory Class ☐

Tick this box if you are seeking approval for a teaching activity which involves student involvement in the role of an experimental participant.

1.2 Tick 1 only

POSTGRADUATE STUDENTS should tick one of the options below:

Taught Masters Project ☐

M.Phil / PhD by research ☐ ✓

UNDERGRADUATE STUDENTS should tick one of the two options below:

Student research project ☐

Practical / Laboratory class where you are acting as the experimenter ☐

2. APPLICATION

2.1 TITLE of Research project

Nanoporous calcium carbonate-based substrates for the controlled delivery of functional materials.

2.2 General summary of the proposed research for which ethical clearance is sought, briefly outlining the aims and objectives and providing details of interventions/procedures involving participants (no jargon)

The overall aim of this project is to study and develop modified calcium carbonates as active substrates for the slow delivery of functional materials.

A 'zero-length' cell (ZLC) is a device invented by Ruthven et al., and further developed within the Environmental and Fluid Modelling Group (EFMG) at Plymouth using organic solvents. It comprises two sinters between which a mono-layer of porous material is sandwiched. The whole device is connected to a High Performance Liquid Chromatography (HPLC) unit, and allows precise study of the diffusion characteristics from the material. Modified calcium carbonates (MCCs) are made from particles of calcium carbonate which have been acid etched to make them nanoporous.

The initial objective of the project is to understand diffusion from MCCs using a ZLC with aqueous systems. The effect of granule formulation, and tablet and granule encapsulation, will be studied, as well as the effect of the intra-granular porosity. Measurements will be made to quantify the effect of all these variables on diffusion rates of functional materials, such as drugs and flavours. In order to make these measurements, the ZLC will be extended to hold more than a monolayer of sample. The solvent will initially be milli-Q water, and will then progress to saline, and then synthesised stomach and/or oesophagus fluids and saliva in order to test the systems' ability to withstand the human body's digestive fluids. Initially the drugs and flavours will be liquid, but there is also the potential for the MCCs to slow-release solids via dissolution and/or desorption.

The research will be underpinned by new simulation software, PoreXpert. This is a much more powerful and versatile package than its predecessor Pore-Cor, and will facilitate the tailoring of MCC formulations rather than simply testing them on a trial and error basis. PoreXpert is being progressively released to market through 2012.

In the first 18 months of this project, the adsorption properties of various systems (i.e. different flavour compounds with different solvents) have been investigated.

Trans-anethole is a flavour compound found in pastis, ouzo, sambuca, etc., and creates a cloudy emulsion when mixed with appropriate ratios of ethanol and water. This is a very interesting phenomenon to study and has application in the drug delivery sector. Initially, anethole will be studied by adsorbing, absorbing and diffusing onto and through the MCCs. But to obtain a range of anethole to work with, a study involving human participants will be conducted so as to find the threshold of taste detection (i.e. the concentration of anethole that can be tasted).

2.3 Physical site(s) where research will be carried out
Davy 509
2.4 External Institutions involved in the research (e.g. other university, hospital, prison etc.)
N/A
2.5 Name, telephone number, e-mail address and position of lead person for this project (plus full details of Project Supervisor if applicable)
Charlotte Levy, charlotte.levy@plymouth.ac.uk, 01752 584797 Supervisor: Prof. Peter Matthews, p.matthews@plymouth.ac.uk, 01752 584798

2.8 Start and end date for research for which ethical clearance is sought (NB maximum period is 3 years)
Start date: 01.04.2013 **End date:** 01.04.2016
2.9 Name(s) of funding source(s) if any
Omya AG
2.10 Has funding already been received?
No ☐ **In-part** ☐ **Yes** ☐ ✓
2.11 Has this same project received ethical approval from another Ethics Committee?
No ☐ ✓ **Yes** ☐
2.12 If yes, do you want Chairman's action?
No ☐ **Yes** ☐
If yes, please include other application and approval letter and STOP HERE. If no, please continue

3. PROCEDURE

3.1 Describe procedures that participants will engage in, Please do not use jargon

Aim: to determine the level of anethole in water that can be tasted and detected orally.

Notes: The solubility of anethole in water is 111mg/L, however, in experiments conducted at Plymouth University the maximum solibility achieved has been ~70mg/L.

Participants will be mostly undergraduates on BSc (Hons) Chemistry course (ages 18 and upwards) and will be told of the nature of research and purpose of this study. We will ask them to taste several drinks; each mineral water with differing concentrations of trans-anethole. After each drink, they will be asked to mark their opinion and intensity of the flavour, and then rinse their mouth out three times with water.
The glass used will be rinsed out three times with bottled water before the next sample is poured into the glass.
There will also be a control that involves tasting the same concentration of Ribena in water before and after the anethole taste tests, however, the participants will be told that the concentration may be different. In the debriefing session, the participants will be informed that in fact, the concentration was indeed the same.

No. of participants: 45 minimum
No. of drinks to taste: 9 (+ 2 control drinks)
Concentrations of drinks to taste: 0, 1, 10, 20, 30, 40 50 60, 70 and 40mg/L anethole in water

15 of the participants will be asked to drink the anethole in water in ascending concentrations.
15 of the participants will be asked to drink the anethole in water in descending concentrations.
15 of the participants will be asked to drink the differing anethole in water concentrations randomly, as predetermined by an online random number generator (http://www.random.org/); numbers between certain limits will determine what drink the participant will drink:
1-10 = 0mg/L
11-20 = 1 mg/L
21-30 = 10 mg/L
31-40 = 20 mg/L
41-50 = 30 mg/L
51-60 = 40 mg/L
61-70 = 50 mg/L
71-80 = 60 mg/L
81-90 = 70 mg/L

Time intervals will be set between the drinks that each participant will adhere to, in order to rule out taste as a time-dependent factor.

Questionnaire after each taste
What flavour can you taste (if any) and how would you describe it?

Do you enjoy this flavour?
Yes / No

Please rate the strength of flavour you could taste for sample 1:

1 = very strong, 2 = strong, 3 = neither strong nor weak, 4 = weak, 5 = very weak
(Busch, Savage et al. 2008)

Did you find this strength of flavour to be:
Extremely unpleasant, Unpleasant, Neither pleasant nor unpleasant, Pleasant, Extremely pleasant

Was there an aftertaste? If so was it weak/strong/pleasant/unpleasant?
Yes / No
Extremely unpleasant, Unpleasant, Neither pleasant nor unpleasant, Pleasant, Extremely pleasant

Please rate the drinks in order of flavour strength preference, where 1 is the most preferred level of flavour tasted, and 9 is the least.

Questionnaire after control samples
Please rate the strength of flavour you could taste for sample 1:
1 = very strong, 2 = strong, 3 = neither strong nor weak, 4 = weak, 5 = very weak

Did you find this strength of flavour to be:
Extremely unpleasant, Unpleasant, Neither pleasant nor unpleasant, Pleasant, Extremely pleasant

3.2 How long will the procedures take? Give details

Each participant will be there for approximately 60-75 minutes.

First, they will be given a brief on the nature of my research, the purpose of the study, what they are expected to do and if they would like to continue. They will then be asked to sign a waiver (see section 5.3 and 5.4). The experiment will commence, and they will be debriefed afterwards regarding the control Ribena drinks.

3.3 Does your research involve deception?

No ☐✓ **Yes** ☐

3.4 If yes, please explain why the following conditions apply to your research:

a) Deception is completely unavoidable if the purpose of the research is to be met

The idea of the control experiments is so that we can compare their response to the Ribena drink before and after the anethole taste tests. As the drink will be the same concentration, but the participants are unaware what concentration the Ribena is, if they give the same responses both times, then their data can be deemed as more reliable than someone whose response varies for the control Ribena drinks.

b) The research objective has strong scientific merit

In order to make my doctoral research more timely and in order for me to obtain more results in a smaller time frame, I need to know the concentration range of anethole in water to work with. This will save a lot of time with regards to constructing adsorption isotherms, etc. If I know that anethole isn't tasted at more than 30mg/L, then I do not need to spend time investigating into the diffusion rates of anethole in water more than this particular concentration, for example, and can avoid upper detection threshold problems in my HPLC instrumentation, etc.

c) Any potential harm arising from the proposed deception can be effectively neutralised or reversed by the proposed debriefing procedures (see section below)

No harm (psychological or physical) will come to the participants.

3.5 Describe how you will debrief your participants

After filling in the form for the final control Ribena drink, the participant will be told immediately that in fact, it was the same concentration as before. They will then be allowed to express their sentiment (i.e. annoyance, surprise, etc.) and informed that they can contact me anytime if they wish for further information regarding the study.

3.6 Are there any ethical issues (e.g. sensitive material)?

No ☐ ✓ **Yes** ☐

3.7 If yes, please explain. You may be asked to provide ethically sensitive material. See also section 11

4. BREAKDOWN OF PARTICIPANTS

4.1 Summary of participants

Type of participant	*Number of participants*
Non-vulnerable Adults	45
Minors (< 16 years)	0
Minors (16-18 years)	0
Vulnerable Participants (other than by virtue of being a minor)	0
Other (please specify)	0
TOTAL	45

4.2 How were the sample sizes determined?

Looking at previous research regarding taste testing.

4.3 How will subjects be recruited?

I will advertise studies on the 5th floor of the Davy Building (i.e. the chemistry labs) and will also send emails around the BSc (Hons) undergraduate chemistry course to see if anyone is interested in partaking.

4.4 Will subjects be financially rewarded? If yes, please give details.

No.

5. NON-VULNERABLE ADULTS

5.1 Are some or all of the participants non-vulnerable adults?
No ☐ **Yes** ☐ ✓
5.2 How will participants be recruited? Name any other institution(s) involved
I will advertise studies on the 5th floor of the Davy Building (i.e. the chemistry labs) and will also send emails around the BSc (Hons) undergraduate chemistry course to see if anyone is interested in partaking.
5.3 Inclusion / exclusion criteria
In the emails I send out and on the posters I will put up, I will ask for adults aged over 18, who don't smoke, and have no known or suspected medical or psychological disorder.
5.4 How will participants give informed consent?
After the procedure has been explained to/presented the participants on a sheet (the only information that will not be included is the concentration of the Ribena before and after the experiments, and the order of which they'll be trying the different concentrations of anethole in water), they will be asked to sign an informed consent form saying that they agree to the experiment and understand, and will be told they can withdraw at any time
5.5 Consent form(s) attached
No ☐ **Yes** ☐ ✓
If no, why not?
5.6 Information sheet(s) attached
No ☐ **Yes** ☐ ✓
If no, why not?
5.7 How will participants be made aware of their right to withdraw at any time?
They will be told so at the beginning, before signing the informed consent form.

5.8 How will confidentiality be maintained, including archiving / destruction of primary data where appropriate, and how will the security of the data be maintained?
The data will be presented without any names.

6. MINORS <16 YEARS

6.1 Are some or all of the participants under the age of 16?
No ☐ ✓ **Yes** ☐
If yes, please consult special guidelines for working with minors. If no, please continue.

6.2 Age range(s) of minors
6.3 How will minors be recruited? (See guidelines). Name any other institution(s) involved
6.4 Inclusion / exclusion criteria
6.5 How will minors give informed consent? Please tick appropriate box and explain (See guidelines)
Opt-in ☐ **Opt-out** ☐
6.6 Consent form(s) for minor attached
No ☐ **Yes** ☐
If no, why not?
6.7 Information sheet(s) for minor attached
No ☐ **Yes** ☐
If no, why not?

6.8 Consent form(s) for parent / legal guardian attached
No ☐ **Yes** ☐
If no, why not?
6.9 Information sheet(s) for parent / legal guardian attached
No ☐ **Yes** ☐
If no, why not?
6.10 How will minors be made aware of their right to withdraw at any time?
6.11 How will confidentiality be maintained, including archiving / destruction of primary data where appropriate, and how will the security of the data be maintained?

7. MINORS 16-18 YEARS OLD

7.1 Are some or all of the participants between the ages of 16 and 18?
No ☐ ✓ **Yes** ☐
If yes, please consult special guidelines for working with minors. If no, please continue.

7.2 How will minors be recruited? (See guidelines). Name any other institution(s) involved
7.3 Inclusion / exclusion criteria
7.4 How will minors give informed consent? (See guidelines)
7.5 Consent form(s) for minor attached
No ☐ **Yes** ☐
If no, why not?
7.6 Information sheet(s) for minor attached
No ☐ **Yes** ☐
If no, why not?
7.7 Consent form(s) for parent / legal guardian attached
No ☐ **Yes** ☐

If no, why not?
7.8 Information sheet(s) for parent / legal guardian attached
No ☐ **Yes** ☐
If no, why not?
7.9 How will minors be made aware of their right to withdraw at any time?
7.10 How will confidentiality be maintained, including archiving / destruction of primary data where appropriate, and how will the security of the data be maintained?

8. VULNERABLE GROUPS

8.1 Are some or all of the participants vulnerable? (See guidelines)
No ☐ ✓ **Yes** ☐
If yes, please consult special guidelines for working with vulnerable groups. If no, please continue.

8.2 Describe vulnerability (apart from possibly being a minor)
8.3 How will vulnerable participants be recruited? Name any other institution(s) involved
8.4 Inclusion / exclusion criteria
8.5 How will participants give informed consent?
8.6 Consent form(s) for vulnerable person attached
No ☐ **Yes** ☐
If no, why not?
8.7 Information sheet(s) for vulnerable person attached
No ☐ **Yes** ☐
If no, why not?
8.8 Consent form(s) for parent / legal guardian attached
No ☐ **Yes** ☐

If no, why not?
8.9 Information sheet(s) for parent / legal guardian attached
No ☐ **Yes** ☐
If no, why not?
8.10 How will participants be made aware of their right to withdraw at any time?
8.11 How will confidentiality be maintained, including archiving / destruction of primary data where appropriate, and how will the security of the data be maintained?

9. EXTERNAL CLEARANCES

Investigators working with children and vulnerable adults legally require clearance from the Criminal Records Bureau (CRB)

9.1 Do ALL experimenters in contact with children and vulnerable adults have <u>current</u> CRB clearance? Please include photocopies.
No ☐ **Yes** ☐ **N/A** ☐ ✓
9.2 If no, explain
9.3 If your research involves external institutions (school, social service, prison, hospital etc) please provide cover letter(s) from institutional heads permitting you to carry out research on their clients, and where applicable, on their site(s). Are these included?
No ☐ **Yes** ☐ **N/A** ☐ ✓
If not, why not?

10. PHYSICAL RISK ASSESSMENT

10.1 Will participants be at risk of physical harm (e.g. from electrodes, other equipment)? (See guidelines)

No ☐ ✓ **Yes** ☐

10.2 If yes, please describe

10.3 What measures have been taken to minimise risk? Include risk assessment proformas.

Method of making the anethole solution
250ml volumetric is what our sonic bath can take
Purchase a brand new 250ml volumetric, and wash thoroughly with hot water and household soap.
Weigh out a certain amount of kosher grade anethole into the volumetric and fill almost to the mark with bottled mineral water.
Sonicate @ 60°C for a few hours.
Wait for the solution to come back up to room temperature, before using a brand new Pastuer pipette to drip the last few drops of bottled water up to the mark.
Transfer to a plastic (/glass?) bottle for storage.
This will have to be done multiple times (~4 times in total to obtain 1L) to obtain one concentration of anethole in ethanol.
Each 250ml volumetric of anethole will be tested via UV-Vis once the solution has been made, and again when the solutions have been combined. Then again, just before testing (to ensure that there has been no degradation of anethole whilst in storage).

Method of making up the Ribena solution
A brand new measuring cylinder, washed thoroughly with hot water and household soap, will be used to measure out the same amounts of Ribena and bottled mineral water for each cup.

10.4 How will you handle participants who appear to have been harmed?

A first aid qualified person will be called to the scene (Claire Williams, 5th floor of Davy Building).

11. PSYCHOLOGICAL RISK ASSESSMENT

11.1 Will participants be at risk of psychological harm (e.g. viewing explicit or emotionally sensitive material, being stressed, recounting traumatic events)? (See guidelines)
No ☐ ✓ **Yes** ☐
11.2 If yes, please describe
11.3 What measures have been taken to minimise risk?
The nature of the research is not personal in any way, and will be explained clearly that it is merely to help me with regards to choosing an appropriate concentration of anethole to work with. Any results they give will be incredibly useful.
11.4 How will you handle participants who appear to have been harmed?
I will ask them if they would like counselling, or another debriefing session with me, or if they would like their data to be destroyed. If they would like counselling, I will direct them to the university's counselling service.

12. RESEARCH OVER THE INTERNET

12.1 Will research be carried out over the internet?
No ☐ ✓ **Yes** ☐
12.2 If yes, please explain protocol in detail, explaining how informed consent will be given, right to withdraw maintained, and confidentiality maintained. Give details of how you will guard against abuse by participants or others (see guidelines)

13. CONFLICTS OF INTEREST & THIRD PARTY INTERESTS

13.1 Do any of the experimenters have a conflict of interest? (See guidelines)

No ☐ ✓ **Yes** ☐

13.2 If yes, please describe

13.3 Are there any third parties involved? (See guidelines)

No ☐ **Yes** ☐ ✓

13.4 If yes, please describe

My PhD research is sponsored by Omya AG, who stand to gain from my findings in that I will use the outcomes of this research to work with a particular concentration of anethole, and then demonstrate that their Modified Calcium Carbonates (MCCs) do, in fact, control the release of this anethole. If the findings of this research prove not to be fruitful, I can continue with my research, although it will take a lot longer than anticipated, will stop me from learning a lot of different techniques, and will also be less interesting without this experiment.

13.5 Do any of the third parties have a conflict of interest?

No ☐ ✓ **Yes** ☐

13.6 If yes, please describe

14. ADDITIONAL INFORMATION

14.1 [Optional] Give details of any professional bodies whose ethical policies apply to this research
14.2 [Optional] Please give any additional information that you wish to be considered in this application
Thank you.

15. ETHICAL PROTOCOL & DECLARATION

To the best of our knowledge and belief, this research conforms to the ethical principles laid down by the University of Plymouth and by any professional body specified in section 14 above.

This research conforms to the University's Ethical Principles for Research Involving Human Participants with regard to openness and honesty, protection from harm, right to withdraw, debriefing, confidentiality, and informed consent

Sign below where appropriate:

STAFF / RESEARCH POSTGRADUATES

	Signature	**Date**
Principal Investigator:	_____	_____
Other researchers:	_____	_____
	_____	_____
	_____	_____

Staff and Research Postgraduates should send the completed and signed copy of this form to Paula Simson, Secretary to the Science and Technology Human Research Ethics Committee, 009 Smeaton.

UG Students

	Signature	**Date**
Student:	_____	_____
Supervisor / Advisor:	_____	_____
	_____	_____
	_____	_____

Undergraduate students should pass on the completed and signed copy of this form to their School Representative on the Science and Technology Human Ethics Committee.

	Signature	**Date**
School Representative on Science and Technology Faculty Human Ethics Committee	_____	_____

SAMPLE SELF-CONSENT FORM

PLYMOUTH UNIVERSITY

FACULTY OF SCIENCE AND TECHNOLOGY

Human Ethics Committee Sample Consent Form

CONSENT TO PARICIPATE IN RESEARCH PROJECT / PRACTICAL STUDY

Name of Principal Investigator: Charlotte Levy

Title of Research: Nanoporous calcium carbonate-based substrates for the controlled release of functional materials.

Brief statement of purpose of work: Modified Calcium Carbonates (MCCs) are particles of calcium carbonate that have been acid-etched to make them porous. This work involves investigating the use of MCCs to control the release of flavours and drugs for their application in foodstuffs and pharmaceuticals. The research is currently focusing its research on the flavour compound *trans*-anethole, which is found in a number of liqueurs including pastis, ouzo and sambuca, and is responsible for the cloudy emulsion when water is added, known as the "ouzo effect." This particular study is to find a range of *trans*-anethole in water that can be tasted orally so as to have a concentration of anethole in water to work with in future experiments with MCCs.

The objectives of this research have been explained to me.

I understand that I am free to withdraw from the research at any stage, and ask for my data to be destroyed if I wish. However, I may not withdraw my data once it is submitted, as it will be anonymous.

I understand that my anonymity is guaranteed, unless I expressly state otherwise.

I understand that the Principal Investigator of this work will have attempted, as far as possible, to avoid any risks, and that safety and health risks will have been separately assessed by appropriate authorities (e.g. under COSHH regulations).

I declare that I am aged 18 or above, am a non-smoker and have no known or suspected medical or psychological disorders.

Under these circumstances, I agree to participate in the research.

Name: ……

Signature: .....…….. Date: .....…….

SAMPLE INFORMATION SHEET FOR ADULT / CHILD

PLYMOUTH UNIVERSITY
FACULTY OF SCIENCE AND TECHNOLOGY

RESEARCH INFORMATION SHEET

Name of Principal Investigator: Charlotte Levy

Title of Research: Nanoporous calcium carbonate based substrates for the controlled delivery of functional materials.

Aim of research: Modified Calcium Carbonates (MCCs) are particles of calcium carbonate that have been acid-etched to make them porous. This work involves investigating the use of MCCs to control the release of flavours and drugs for their application in foodstuffs and pharmaceuticals. The research is currently focusing its research on the flavour compound *trans*-anethole, which is found in a number of liqueurs including pastis, ouzo and sambuca, and is responsible for the cloudy emulsion when water is added, known as the “ouzo effect.” This particular study is to find a range of *trans*-anethole in water that can be tasted orally so as to have a concentration of anethole in water to work with in future experiments with MCCs.

Description of procedure
First, you will be asked to try a drink of Ribena and answer a questionnaire that asks what you thought of the flavour and its strength. Then you will try nine different samples of anethole in water, all at different concentrations. After trying each, you will fill in a questionnaire that asks you for your thoughts on the flavour and strength of the samples. Finally, you will try another drink of Ribena, at the same or a different concentration to the first Ribena drink, and will answer the same questionnaire as you did after the first Ribena drink. Please keep in mind that you will have to have to drink every 5 minutes; therefore you have 5 minutes to fill out the questionnaire and swill your mouth out three times with water before drinking the next drink.

In between each sample, you will be asked to rinse/swill your mouth out 3 times with water.

The experiment should take approximately 60-75 minutes in total.

Description of risks
No risks pertaining solely to this experiment have been identified.

Benefits of proposed research

This particular study is to find a range of *trans*-anethole in water that can be tasted orally so as to have a concentration of anethole in water to work with in future experiments with MCCs.

Right to withdraw

You are free to withdraw from the research at any stage, and ask for your data to be destroyed if you wish. However, you may not withdraw your data once it is submitted, as it will be anonymous.

If you are dissatisfied with the way the research is conducted, please contact the researcher in the first instance: telephone number: 01752 584797, email: charlotte.levy@plymouth.ac.uk . If you are still not satisfied, please contact the supervisor of the project using the following email address: p.matthews@plymouth.ac.uk . If you feel the problem has still not been resolved please contact the secretary to the Faculty of Science and Technology Human Ethics Committee: Mrs Paula Simson 01752 584503.

SAMPLE CONSENT FORM FOR PARENT/LEGAL GUARDIAN

PLYMOUTH UNIVERSITY

FACULTY OF SCIENCE AND TECHNOLOGY

Human Ethics Committee Sample Consent Form

CONSENT TO PARTICIPATE IN RESEARCH PROJECT / PRACTICAL STUDY

_____

Name of Principal Investigator

_____

Title of Research

_____

Brief statement of purpose of work

_____

I am the *parent /legal guardian of _____

The objectives of this research have been explained to me.

I understand that *she/he is free to withdraw from the research at any stage, and ask for *his/her data to be destroyed if I wish.

I understand that *his/her anonymity is guaranteed, unless I expressly state otherwise.

I understand that the Principal Investigator of this work will have attempted, as far as possible, to avoid any risks, and that safety and health risks will have been separately assessed by appropriate authorities (e.g. under COSSH regulations)

Under these circumstances, I agree for him/her to participate in the research.

** delete as appropriate*

Name: ……

Signature: .....…….. Date: .....…….

Faculty of Science and Technology Human Research Ethics Committee List of School Representatives

School of Psychology	Prof Judy Edworthy (Chair) Dr Matt Roser
School of Geography, Earth and Environmental Sciences	Dr Sanzidur Rahman
School of Biomedical & Biological Sciences	Dr David J. Price
School of Marine Science & Engineering	Dr Emily Beaumont Dr Liz Hodgkinson
School of Computing & Mathematics	Mr Martin Beck Dr Mark Dixon
External Representative	Vacant
Lay Member	Rev. David Evans

Committee Secretary: Mrs Paula Simson

email: paula.simson@plymouth.ac.uk

tel: 01752 584503

Risk Assessment Form

Project/activity/task: Taste tests of anethole in water at varying concentrations.
Persons at risk: Principally students, academic or technical staff, potentially any person in the laboratory.

Hazards	Probability	Severity	Risk Factor[2]	Controls in Place / Action to be taken[1]
Spillage of reagents.	1	1	1	Take care carrying samples. Ensure bags are packed underneath desks and chairs tucked in when no one is occupying them.
Damaged glassware/sharp edges.	1	2	1	Do not use. Give to technician for repair or disposal, or place in a glass only bin.

Assessed by	Charlotte Levy
(signed)	
(date)	27.02.13
Approved by HOS	
(signed)	
(date)	

KEY

PROBABILITY		SEVERITY		RISK FACTOR[1]	
Probable	**3**	**Critical**	**3**	**6 – 9**	**High Risk [2]**
Possible	**2**	**Serious**	**2**	**4**	**Medium Risk**
Unlikely	**1**	**Minor**	**1**	**1 – 3**	**Low Risk**

[1] The risk factor is the product of Probability and Severity. The probability is based on the situation after the controls are in place or action to be taken is allowed for.
[2] As stated in the School Safety Handbook, a high risk activity has no place in our School and will not be sanctioned.

References

Afandizadeh, S. and Foumeny, E. A. (2001), 'Design of packed bed reactors: guides to catalyst shape, size, and loading selection', *Applied Thermal Engineering* **21**(6), 669–682.

Al-Dahhan, M. H. and Dudukovi, M. P. (1996), 'Catalyst bed dilution for improving catalyst wetting in laboratory trickle-bed reactors', *AIChE Journal* **42**(9), 2594–2606.

Al-Dahhan, M. H., Wu, Y. and Dudukovic, M. P. (1995), 'Reproducible technique for packing laboratory-scale trickle-bed reactors with a mixture of catalyst and fines', *Industrial & Engineering Chemistry Research* **34**(3), 741–747.

Al-Degs, Y. S., El-Barghouthi, M. I., El-Sheikh, A. H. and Walker, G. M. (2008), 'Effect of solution pH, ionic strength, and temperature on adsorption behavior of reactive dyes on activated carbon', *Dyes and Pigments* **77**(1), 16–23.

Aligizaki, K. K. (2005), *Pore Structure of Cement-Based Materials: Testing, Interpretation and Requirements*, 1st edn, CRC Press.

Angelos, S., Liong, M., Choi, E. and Zink, J. I. (2008), 'Mesoporous silicate materials as substrates for molecular machines and drug delivery', *Chemical Engineering Journal* **137**(1), 4–13.

Arifin, D. Y., Lee, L. Y. and Wang, C.-H. (2006), 'Mathematical modeling and simulation of drug release from microspheres: implications to drug delivery systems', *Advanced Drug Delivery Reviews* **58**(12–13), 2746–1325.

Arruebo, M. (2012), 'Drug delivery from structured porous inorganic materials', *Wiley Interdisciplinary Reviews: Nanomedicine and Nanobiotechnology* **4**(1), 16–30.

Atkins, P. and de Paula, J. (2006), *Atkins' Physical Chemistry*, 8th edn, Oxford University (Clarendon) Press.

Awtry, E. H. and Loscalzo, J. (2000), 'Aspirin', *Circulation* **101**(10), 1206–1218.

Balbuena, P. B. and Gubbins, K. E. (1993), 'Theoretical interpretation of adsorption behavior of simple fluids in slit pores', *Langmuir* **79**(7), 1801–1814.

Baradari, H., Damia, C., Dutreih-Colas, M., Laborde, E., Pécout, N., Champion, E., Chulia, D. and Viana, M. (2012), 'Calcium phosphate porous pellets as drug delivery systems: effect of drug carrier composition on drug loading and *in vitro* release', *Journal of the European Ceramic Society* **32**(11), 2679–2690.

Berg, E. J. (2012), Diffusion controlled drug release from slurry formed, porous, organic and clay-derived pellets, PhD thesis, Uppsala University, Uppsala, Sweden.

Berger, R. J., Perez-Ramrez, J., Kapteijn, F. and Moulijn, J. A. (2002), 'Catalyst performance testing: the influence of catalyst bed dilution on the conversion observed', *Chemical Engineering Journal* **90**(1), 173–183.

Berthod, A., Rollet, M. and Farah, N. (1988), 'Dry adsorbed emulsions: an oral sustained drug delivery system', *Journal of Pharmaceutical Sciences* **77**(3), 216–221.

Bettelheim, F. A., Brown, W. H., Campbell, M. K. and Farrell, S. O. (2010), *Introduction to General Organic and Biochemistry*, 7th edn, Brooks/Cole Cengage Learning.

Bezdek, K. and Reid, S. (2013), 'Contact graphs of unit sphere packings revisited', *Journal of Geometry* **104**(1), 57–83.

Biradar, S., Ravichandran, P., Gopikrishnan, R., Goornavar, V., Hall, J. C., Ramesh, V., Baluchamy, S., Jeffers, R. B. and Ramesh, G. T. (2011), 'Calcium carbonate nanoparticles: synthesis, characterization and biocompatibility', *Journal of Nanoscience and Nanotechnology* **11**(8), 6868–6874.

Botet, R. (2012), 'The "ouzo effect", recent developments and application to therapeutic drug carrying', *Journal of Physics: Conference Series* **352**(1), 12–47.

Bousquet, E., Tirendi, S., Bonina, F. P., Montenegro, L., Bianchi, A. and Ciampini, N. (1992), 'Bioavailability of two formulations of acetylsalicylic acid gums', *Die Pharmazie* **47**(8), 607–609.

Brandani, F. (2002), Development and application of the zero length column (ZLC) technique for measuring Adsorption Equilibria, PhD thesis, University of Maine, Maine, USA.

Brandani, F., Ruthven, D. and Coe, C. G. (2003), 'Measurement of adsorption equilibrium by the zero length column (ZLC) technique part 1: single-component systems', *Industrial & Engineering Chemistry Research* **42**(7), 1451–1461.

Brandani, S. (1996), 'Analytical solution for ZLC desorption curves with bi-porous adsorbent particles', *Chemical Engineering Science* **51**(12), 3283–3288.

Brandani, S. (1998), 'Effects of nonlinear equilibrium on zero length column experiments', *Chemical Engineering Science* **53**(15), 2791–2798.

Brandani, S., Jama, M. A. and Ruthven, D. M. (2000), 'ZLC measurements under non-linear conditions', *Chemical Engineering Science* **55**(7), 1205–1212.

Brandani, S. and Ruthven, D. M. (1995), 'Analysis of ZLC desorption curves for liquid systems', *Chemical Engineering Science* **50**(13), 2055–2059.

Brandani, S. and Ruthven, D. M. (1996), 'Analysis of ZLC desorption curves for gaseous systems', *Adsorption* **2**(2), 133–143.

Brunson, R. J. and Chaback, J. J. (1979), 'Vaterite formation during coal liquefaction', *Chemical Geology* **25**(4), 333–338.

Burdock, G. A. (2004), *Fenaroli's Handbook of Flavor Ingredients*, 5th edn, CRC Press.

Burdock, G. A. (2007), 'Safety assessment of hydroxypropyl methylcellulose as a food ingredient', *Food and Chemical Toxicology* **45**(12), 2341–2351.

Burdukova, E., Becker, M., Bradshaw, D. and Laskowski, J. (2007), 'Presence of negative charge on the basal planes of new york talc', *Journal of Colloid and Interface Science* **315**(1), 337–342.

Calorie Control Council (2001), *Alternative Sweeteners*, 3rd edn, Marcel Dekker, Inc.

Cascarini de Torre, L. E. and Bottani, E. J. (1996), 'Adsorption energy distribution functions', *Engineering Aspects* **116**(3), 285–291.

Castro, H. T., Martínez, J. R. and Stashenko, E. (2010), 'Anethole isomerization and dimerization induced by acid sites or UV irradiation', *Molecules* **15**(7), 5012–5030.

Cavalcante, C. L. J. and Ruthven, D. M. (1995), 'Adsorption of branched and cyclic paraffins in silicalite. 2. Kinetics', *Industrial & Engineering Chemistry Research* **34**(1), 185–191.

Cavalcante Jr, C. L., Brandani, S. and Ruthven, D. M. (1997), 'Evaluation of the main diffusion path in zeolites from ZLC desorption curves', *Zeolites* **18**(4), 282–285.

Chainy, G. B. N., Manna, S. K., Chaturvedi, M. M. and Aggarwal, B. B. (2000), 'Anethole blocks both early and late cellular responses transduced by tumor necrosis factor: effect on NF-kappaB, AP-1, JNK, MAPKK and apoptosis', *Nature* **19**(25), 2943–2950.

Chang, H.-C. and Wang, L.-C. (2010), 'A simple proof of Thue's theorem on circle packing', Cornell University Library: Mathematics: Metric Geometry.

Charnay, C., Lagerge, S. and Partyka, S. (2001), 'Assessment of the surface heterogeneity of talc materials', *Journal of Colloid and Interface Science* **233**(2), 250–258.

Chatfield, C. (1978), *Statistics for Technology: A Course in Applied Statistics*, 3rd edn, Chapman & Hall.

Chen, H. and Leng, S. (2015), 'Rapid synthesis of hollow nano-structured hydroxyapatite microspheres via microwave transformation method using hollow $CaCO_3$ precursor microspheres', *Ceramics International* **41**(2, Part A), 2209–2213.

Cherntongchai, P. and Brandani, S. (2003), 'Liquid phase counter-diffusion measurements of aromatics in silicalite using the ZLC method', *Adsorption* **9**(3), 197–204.

Cherukuri, S., Friello, D., Ferroti, M., Jewell, W. and D'Amelia, R. (1982), 'Gum base, chewing gum containing same and method', Nabisco Brands Inc. Patent US4352822A.

Chevalier, E., Viana, M., Cazalbou, S., Makein, L., Dubois, J. and Chulia, D. (2010), 'Ibuprofen-loaded calcium phosphate granules: combination of innovative characterization methods to relate mechanical strength to drug location', *Acta Biomaterialia* **6**(1), 266–274.

Christophersen, P. C., Fano, M., Saaby, L., Yang, M., Nielsen, H. M. and Mu, H. (2015), 'Characterization of particulate drug delivery systems for oral delivery of peptide and protein drugs', *Current Pharmaceutical Design* **21**(19), 2611–2628.

Chung, H.-K., Kim, W.-H., Park, J., Cho, J., Jeong, T.-Y. and Park, P.-K. (2015), 'Application of Langmuir and Freundlich isotherms to predict adsorbate removal efficiency or required amount of adsorbent', *Journal of Industrial and Engineering Chemistry* **28**, 241–246.

Clausen-Schaumann, H. and Gaub, H. E. (1999), 'DNA adsorption to laterally structured charged lipid membranes', *Langmuir* **15**(23), 8246–8251.

Clissold, S. P. (1986), 'Aspirin and related derivatives of salicylic acid', *Drugs* **32**(Suppl 4), 8–26.

Cosijns, A., Vervaet, C., Luyten, J., Mullens, S., Siepmann, F., Van Hoorebeke, L., Masschaele, B., Cnudde, V. and Remon, J. P. (2007), 'Porous hydroxyapatite tablets as carriers for low-dosed drugs', *European Journal of Pharmaceutics and Biopharmaceutics* **67**(2), 498–506.

Costa, P. and José, M. S. L. (2001), 'Modeling and comparison of dissolution profiles', *European Journal of Pharmaceutical Sciences* **13**(2), 123–133.

Crank, J. (1975), *The Mathematics of Diffusion*, 2nd edn, Oxford University (Clarendon) Press.

CRC Press (1983), *CRC Handbook of Chemistry and Physics*, 63rd edn, CRC Press.

CRC Press (2006), *CRC Handbook of Chemistry and Physics*, 87rd edn, CRC Press.

Cunningham, R. S. and Geankoplis, C. J. (1968), 'Effects of different structures of porous solids on diffusion of gases in the transition region', *Industrial & Engineering Chemistry Fundamentals* **7**(4), 535–542.

Cussler, E. L. (1997), *Diffusion: Mass Transfer in Fluid Systems*, 2nd edn, Cambridge University Press.

Dąbrowski, A. (2001), 'Adsorption – from theory to practice', *Advances in Colloid and Interface Science* **93**(1–3), 135–224.

de Boer, R. (1998), 'Theory of porous media – past and present', *Journal of Applied Mathematics and Mechanics* **78**(7), 441–466.

de Leeuw, N. H. and Parker, S. C. (1998), 'Surface structure and morphology of calcium carbonate polymorphs calcite, aragonite, and vaterite: an atomistic approach', *The Journal of Physical Chemistry B* **102**(16), 2914–2922.

Di Pasqua, A. J., Sharma, K. K., Shi, Y.-L., Toms, B. B., Ouellette, W., Dabrowiak, J. C. and Asefa, T. (2008), 'Cytotoxicity of mesoporous silica nanomaterials', *Journal of Inorganic Biochemistry* **102**(7), 1416–1423.

Dickinson, S. R. and McGrath, K. M. (2004), 'Aqueous precipitation of calcium carbonate modified by hydroxyl-containing compounds', *Crystal Growth & Design* **4**(6), 1411–1418.

Dong, Y., Keil, F. J., Korup, O., Rosowski, F. and Horn, R. (2016), 'Effect of the catalyst pore structure on fixed-bed reactor performance of partial oxidation of *n*-butane: a simulation study', *Chemical Engineering Science* **142**(13), 299–309.

Dorozhkin, S. V. (2007), 'Calcium orthophosphates', *Journal of Materials Science* **42**(4), 1061–1095.

Duncan, W. L. and Möller, K. P. (2000*a*), 'On the diffusion of cyclohexane in ZSM-5 measured by zero-length-column chromatography', *Industrial & Engineering Chemistry Research* **39**(6), 2105–2113.

Duncan, W. L. and Möller, K. P. (2000*b*), 'A zero length criterion for ZLC chromatography', *Chemical Engineering Science* **55**(22), 5415–5420.

Eberle, V. A., Schoelkopf, J., Gane, P. A. C., Alles, R., Huwyler, J. and Puchkov, M. (2014), 'Floating gastroretentive drug delivery systems: comparison of experimental and simulated dissolution profiles and floatation behavior', *European Journal of Pharmaceutical Sciences* **58**, 34–43.

Eckhardt, B. (2009), 'Introduction. Turbulence transition in pipe flow: 125$^{\text{th}}$ anniversary of the publication of Reynolds' paper', *Philosophical Transactions of the Royal Society A* **367**(1888), 449–455.

Eić, M., Micke, A., Kočirík, M., Jama, M. and Zikánová, A. (2002), 'Diffusion and immobilization mechanisms in zeolites studied by ZLC chromatography', *Adsorption* **8**(1), 15–22.

Eic, M. and Ruthven, D. M. (1988), 'A new experimental technique for measurement of intracrystalline diffusivity', *Zeolites* **8**(1), 40–45.

Elabbadi, A., Jerri, H. A., Ouali, L. and Erni, P. (2000), 'Sustainable delivery systems: retention of model volatile oils trapped on hybrid calcium carbonate microparticles', *ACS Sustainable Chemistry & Engineering* **3**(9), 2178–2186.

Everett, D. H. (1988), *Basic Principles of Colloid Science*, 1$^{\text{st}}$ edn, Royal Society of Chemistry.

Fahs, A., Bistac, S. and Schmitt, M. (2010), 'Hydroxypropyl methylcellulose (HPMC) formulated films: relevance to adhesion and friction surface properties', *Carbohydrate Polymers* **80**(1), 105–114.

Freire Rosemayre, S., Moraise, S. M., Catunda-Junior, F. E. A. and Pinheiro, D. C. S. N. (2005), 'Synthesis and antioxidant, anti-inflammatory and gastroprotector activities of anethole and related compounds', *Bioorganic & Medicinal Chemistry* **13**(13), 4353–4358.

Frenning, G. (2011), 'Modelling drug release from inert matrix systems: from moving-boundary to continuous-field descriptions', *International Journal of Pharmaceutics* **418**(1), 88–99.

Frenning, G., Brohede, U. and Strømme, M. (2005), 'Finite element analysis of the release of slowly dissolving drugs from cylindrical matrix systems', *Journal of Controlled Release* **107**(2), 320–329.

Frenning, G. and Strømme, M. (2003), 'Drug release modeled by dissolution, diffusion, and immobilization', *International Journal of Pharmaceutics* **250**(1), 137–145.

Freundlich, H. (1909), *Kapilarchemie*, Vol. 2, Akademische Verlagsgesellschaft m. b. H. Leipzig.

Freundlich, H. M. F. (1906), 'Über die adsorption in lösungen', *Zeitschrift für Physikalische Chemie* **57**(A), 385–470.

Fries, E. and Zarfl, C. (2012), 'Sorption of polycyclic aromatic hydrocarbons (PAHs) to low and high density polyethylene (PE)', *Environmental Science and Pollution Research* **19**(4), 1296–1304.

Fu, Y. and Kao, W. J. (2010), 'Drug release kinetics and transport mechanisms of non-degradable and degradable polymeric delivery systems', *Expert opinion on drug delivery* **7**(4), 429–444.

Fujiwara, M., Shiokawa, K., Morigaki, K., Zhu, Y. and Nakahara, Y. (2008), 'Calcium carbonate microcapsules encapsulating biomacromolecules', *Chemical Engineering Journal* **137**(1), 14–22.

Fukshansky, L. (2011), 'Revisiting the hexagonal lattice: on optimal lattice circle packing', *Elemente der Mathematik* **66**(1), 1–9.

Gane, P. A. C. (2001), 'Mineral pigments for paper: structure, function and development potential (part I)', *Wochenblatt für Papierfabrikation* **129**(3), 110–116.

Gane, P. A. C., Matthews, G. P., Schoelkopf, J., Ridgway, C. J. and Spielmann, D. C. (2000), 'Observing fuid transport into porous coating structures: some novel findings', *TAPPI Journal* **83**(5), 1–22.

Gane, P. A. C., Ridgway, C. J. and Barceló, E. (2006), 'Analysis of pore structure enables improved tablet delivery systems', *Powder Technology* **169**(2), 77–83.

Gane, P., Buri, M., Blum, R. and Karth, B. (2004), 'Filler or pigment or processed mineral for paper, in particular a pigment containing natural $CaCO_3$, its manufacturing process, preparations containing it and their applications', Omya Development AG. Patent US20040020410A1.

Gane, P. and Schölkopf, J. (2011), 'Controlled release active agent carrier', Omya Development AG. Patent EP2591772A1.

Gane, P., Schölkopf, J. and Gantenbein, D. (2010), 'Surface-reacted calcium carbonate in combination with hydrophobic adsorbent for water treatment', Omya Development AG. Patent US20100133195A1.

Gane, P., Schölkopf, J., Gantenbein, D. and Gerard, D. (2010), 'Surface treated calcium carbonate and its use in waste water treatment', Omya Development AG. Patent EP2180944A1.

Gantenbein, D. (2012), Development of Mineral Particle Surfaces for the Adsorption of Pitch from Wood Processing and Recycling of Paper, PhD thesis, University of Plymouth, Devon, UK.

Gantenbein, D., Schoelkopf, J., Matthews, G. P. and Gane, P. A. C. (2012), 'The use of porous high surface area calcium carbonate for the adsorption of dissolved and colloidal substances from thermo mechanical pulp filtrates', *Nordic Pulp & Paper Research Journal* **27**(3), 631–638.

Gaonkar, A. G., Vasisht, N., Khare, A. R. and Sobel, R. (2014), *Microencapsulation in the Food Industry: A Practical Implementation Guide*, 1st edn, Elsevier.

Gençer, N., Demir, D., Sonmez, F. and Kucukislamoglu, M. (2012), 'New saccharin derivatives as tyrosinase inhibitors', *Bioorganic & Medicinal Chemistry* **20**(9), 2811–2821.

Good, N. E. and Izawa, S. (1972), Hydrogen ion buffers, *in* 'Photosynthesis and Nitrogen Fixation Part B', Vol. Volume 24 of *Methods in Enzymology*, Academic Press, pp. 53–68.

Good, N. E., Winget, G. D., Winter, W., Connolly, T. N., Izawa, S. and Singh, R. M. (1966), 'Hydrogen ion buffers for biological research', *Biochemistry* **5**(2), 467–77.

Grassi, M. and Grassi, G. (2005), 'Mathematical modelling and controlled drug delivery: matrix systems', *Current Drug Delivery* **2**(1), 97–116.

Grathwohl, P. (1998), *Diffusion in Natural Porous Media*, 1st edn, Springer US.

Gribble, C. M. (2010), Surface Adsorption and Pore-Level Properties of Mineral and Related Systems of Relevance to the Recycling of Paper, PhD thesis, University of Plymouth, Devon, UK.

Gribble, C. M., Matthews, G. P., Laudone, G. M., Turner, A., Ridgway, C. J., Schoelkopf, J. and Gane, P. A. C. (2011), 'Porometry, porosimetry, image analysis and void network modelling in the study of the pore-level properties of filters', *Chemical Engineering Science* **66**(16), 3701–3709.

Grillo, I. (2003), 'Small-angle neutron scattering study of a world-wide known emulsion: le pastis', *Colloids and Surfaces A* **225**(1–3), 153–160.

Gumí, T., Gascón, S., Torras, C. and Garcia-Valls, R. (2009), 'Vanillin release from macrocapsules', *Desalination* **245**(1–3), 769–775.

Güngen, A. C., Aydemir, Y., Çoban, H., Düzenli, H. and Tasdemir, C. (2016), 'Lung cancer in patients diagnosed with silicosis should be investigated', *Respiratory Medicine Case Reports* **18**, 93–95.

Gustav, M. (1908), 'Beiträge zur optik trüber medien, speziell kolloidaler metallösungen', *Annals of Physics* **330**(3), 377–445.

Hales, T. C. (2005), 'A proof of the Kepler conjecture', *Annals of Mathematics* **162**(3), 1065–1185.

Haruta, S., Hanafusa, T., Fukase, H., Miyajima, H. and Oki, T. (2003), 'An effective absorption behavior of insulin for diabetic treatment following intranasal delivery using porous spherical calcium carbonate in monkeys and healthy human volunteers', *Diabetes Technology & Therapeutics* **5**(1), 1–9.

He, J., Hong, S., Zhang, L., Gan, F. and Ho, Y. (2010), 'Equilibrium and thermodynamic parameters of adsorption of methylene blue onto rectorite', *Fresenius Environmental Bulletin* **10**(11A), 2651–2656.

Helmy, A. K., Ferreiro, E. A. and de Bussetti, S. G. (2000), 'Effect of particle association on 2,2'-bipyridyl adsorption onto kaolinite', *Journal of Colloid and Interface Science* **225**(2), 398–402.

Hessler, J. A., Budor, A., Putchakayala, K., Mecke, A., Rieger, D., Banaszak Holl, M. M., Orr, B. G., Bielinska, A., Beals, J. and Baker, J. (2005), 'Atomic force microscopy study of early morphological changes during apoptosis', *Langmuir* **21**(20), 9280–9286.

Hiemenz, P. C. and Rajagopalan, R. (1997), *Principles of Colloid and Surface Chemistry*, 3rd edn, CRC Press.

Higuchi, T. (1960), 'Physical chemical analysis of percutaneous absorption process from creams and ointments', *Journal of Cosmetic Science* **11**(2), 85–97.

Higuchi, T. (1961), 'Rate of release of medicaments from ointment bases containing drugs in suspension', *Journal of Pharmaceutical Sciences* **50**(10), 874–875.

Ho, Y.-S. (2006), 'Isotherms for the sorption of lead onto peat: comparison of linear and non-linear methods', *Polish Journal of Environmental Studies* **15**(1), 81–86.

Hombreiro-Pérez, M., Siepmann, J., Zinutti, C., Lamprecht, A., Ubrich, N., Hoffman, M., Bodmeier, R. and Maincent, P. (2003), 'Non-degradable microparticles containing a hydrophilic and/or a lipophilic drug: preparation, characterization and drug release modeling', *Journal of Controlled Release* **88**(3), 413–428.

Horikawa, D. D. D. T. and Nicholson, D. (2011), 'Capillary condensation of adsorbates in porous materials', *Advances in Colloid and Interface Science* **169**(1), 40–58.

Hu, X. and Do, D. D. (1993), 'Effect of surface energetic heterogeneity on the kinetics of adsorption of gases in microporous activated carbon', *Langmuir* **9**(10), 2530–2536.

Huang, X. and Brazel, C. S. (2001), 'On the importance and mechanisms of burst release in matrix-controlled drug delivery systems', *Journal of Controlled Release* **73**(2–3), 121–136.

Hudson, S. P., Padera, R. F., Langer, R. and Kohane, D. S. (2008), 'The biocompatibility of mesoporous silicates', *Biomaterials* **29**(30), 4045–4055.

Hufton, J. R. and Ruthven, D. M. (1993), 'Diffusion of light alkanes in silicalite studied by the zero length column method', *Industrial & Engineering Chemistry Research* **32**(10), 2379–2386.

Ilankoon, I. M. S. K. and Neethling, S. J. (2013), 'The effect of particle porosity on liquid holdup in heap leaching', *Minerals Engineering* **45**, 73–80.

Intawongse, M. and Dean, J. R. (2011), 'Use of the physiologically-based extraction test to assess the oral bioaccessibility of metals in vegetable plants grown in contaminated soil', *Environmental Pollution* **182**(1), 60–72.

Jain, K. K. (2008), *Drug Delivery System*, Vol. 437 of *Methods in Molecular Biology*, 2nd edn, Humana Press.

Jämstorp, E., Strømme, M. and Bredenberg, S. (2012), 'Influence of drug distribution and solubility on release from geopolymer pellets – a finite element method study', *Journal of Pharmaceutical Sciences* **101**(5), 1803–1810.

Johnson, A., Roy, I., Matthews, G. and Patel, D. (2003), 'An improved simulation of void structure, water retention and hydraulic conductivity in soil, using the Pore-Cor three-dimensional network', *European Journal of Soil Science* **54**(3), 477–489.

Juhasz, A. L., Weber, J. and Smith, E. (2011), 'Influence of saliva, gastric and intestinal phases on the prediction of as relative bioavailability using the unified bioaccessibility research group of europe method (UBM)', *Journal of Hazardous Materials* **197**, 161–168.

Kalies, G., Bräuer, P. and v. Szombathely, M. (2009), 'Design of liquid/solid adsorption isotherms by energy distribution functions', *Journal of Colloid and Interface Science* **331**(2), 329–334.

Kallio, T., Kekkonen, J. and Stenius, P. (2006), 'Acid/base properties and adsorption of an azo dye on coating pigments', *Journal of Dispersion Science and Technology* **27**(6), 825–834.

Kamimori, G. H., Karyekar, C. S., Otterstetter, R., Cox, D. S., Balkin, T. J., Belenky, G. L. and Eddington, N. D. (2002), 'The rate of absorption and relative bioavailability of caffeine administered in chewing gum versus capsules to normal healthy volunteers', *International Journal of Pharmaceutics* **234**(1–2), 159–167.

Kaneko, K. (1994), 'Determination of pore size and pore size distribution: 1. Adsorbents and catalysts', *Journal of Membrane Science* **96**(1–2), 59–89.

Kar, A. (2007), Hydroxyapatite Deposition Onto Nanoporous Titanium Dioxide and Assessment of Bone Cell Growth and Proliferation, PhD thesis, University of Nevada, Reno, USA.

Kärger, J. and Ruthven, D. M. (2016), 'Diffusion in nanoporous materials: fundamental principles, insights and challenges', *New Journal of Chemistry* **40**(5), 4027–4048.

Kärger, J., Ruthven Douglas, M. and Theodorou, D. N. (2012), *Diffusion in Nanoporous Materials*, 1st edn, Wiley.

Kfoury, M., Auezova, L., Greige-Gerges, H. and Fourmentin, S. (2014), 'Cyclodextrin, an efficient tool for *trans*-anethole encapsulation: chromatographic, spectroscopic, thermal and structural studies', *Food Chemistry* **164**, 655–660.

Kishore, D. and Kannan, S. (2006), 'Catalytic isomerization of estragole to anethole over hydrotalcites and HT-like compounds', *Journal of Molecular Catalysis A: Chemical* **244**(1–2), 83–92.

Kojima, C. and Watanabe, K. (2012), 'Adsorption and desorption of bioactive proteins on hydroxyapatite for protein delivery systems', *J. Drug Deliv.* **2012**(Article ID 932461), 4 pages.

Lamminmäki, T. T., Kettle, J. P. and Gane, P. A. C. (2011), 'Absorption and adsorption of dye-based inkjet inks by coating layer components and the implications for print quality', *Colloids and Surfaces A* **380**(1–3), 79–88.

Lamminmäki, T. T., Kettle, J. P., Puukko, P. J. T., Ridgway, C. J. and Gane, P. A. C. (2012), 'Short timescale inkjet ink component diffusion: an active part of the absorption mechanism into inkjet coatings', *Journal of Colloid and Interface Science* **365**(1), 222–235.

Langmuir, I. (1916), 'The constitution and fundamental properties of solids and liquids. I. Solid', *Journal of the American Chemical Society* **38**(11), 2221–2295.

Langmuir, I. (1917), 'The constitution and fundamental properties of solids and liquids. II. Liquids', *Journal of the American Chemical Society* **39**(9), 1848–1906.

Laudone, G. M. (2005), Environmentally Friendly Technology: The Behaviour of Natural and Synthetic Binder Systems within Paper Coatings, PhD thesis, University of Plymouth, Devon, UK.

Laudone, G. M., Gribble, C. M., Jones, K. L., Collier, H. and Matthews, G. P. (2015), 'Validated *a priori* calculation of tortuosity in porous materials including sandstone and limestone', *Chemical Engineering Science* **131**, 109–117.

Laudone, G. M., Matthews, G. P. and Gane, P. A. C. (2008), 'Modelling diffusion from simulated porous structures', *Chemical Engineering Science* **63**(7), 1987–1996.

Laudone, G. M., Matthews, G. P., Gane, P. A. C., Ridgway, C. J. and Schoelkopf, J. (2005), 'Estimation of the effective particle sizes within a paper coating layer using a void network model', *Chemical Engineering Science* **60**(23), 6795–6802.

Levy, C. L., Matthews, G. P., Laudone, G. M., Beckett, S., Turner, A., Schoelkopf, J. and Gane, P. A. C. (2017), 'Mechanism of adsorption of actives onto microporous functionalised calcium carbonate (FCC)', *Adsorption* **23**(4), 603–612.

Levy, C. L., Matthews, G. P., Laudone, G. M., Gribble, C. M., Turner, A., Ridgway, C. J., Gerard, D. E., Schoelkopf, J. and Gane, P. A. C. (2015), 'Diffusion and tortuosity in porous functionalized calcium carbonate', *Industrial & Engineering Chemistry Research* **54**(41), 9938–9947.

Lin, W., Huang, Y.-w., Zhou, X.-D. and Ma, Y. (2006), '*In vitro* toxicity of silica nanoparticles in human lung cancer cells', *Toxicology and Applied Pharmacology* **217**(3), 252–259.

Lobato, E. M. d. C. (2004), Determination of Surface Free Energies and Aspect Ratio of Talc, Master's thesis, Virginia Polytechnic Institute and State University, Virginia, USA.

Loos, Jan-Baptiste, W. P., Verheijen, P. J. T. and Moulijn, J. A. (2000), 'Improved estimation of zeolite diffusion coefficients from zero length column experiments', *Chemical Engineering Science* **55**(1), 51–65.

Lucas-Girot, A., Verdier, M.-C., Tribut, O., Sangleboeuf, J.-C., Allain, H. and Oudadesse, H. (2005), 'Gentamicin-loaded calcium carbonate materials: comparison of two drug-loading modes', *Journal of Biomedical Materials Research Part B* **73B**(1), 164–170.

Lv, G., Li, Z., Hoeppner, N., Wu, L. and Liao, L. (2014), 'Interactions between sulfa drug sulfadiazine and hydrophobic talc surfaces', *Colloids and Surfaces A* **446**, 172–178.

Machado, J. A. T., Zaman, S. and Baleanu, D. (2013), 'Fractional order modelling of zero length column desorption response for adsorbents with variable particle sizes', *Central European Journal of Physics* **11**(6), 881–885.

Mahato, R. I. and Narang, A. S. (2012), *Pharmaceutical Dosage Forms and Drug Delivery*, Pharmacy Education Series, 2nd edn, CRC Press, Taylor & Francis Group.

Malek, K. and Coppens, M.-O. (2003), 'Knudsen self- and Fickian diffusion in rough nanoporous media', *Journal of Chemical Physics* **119**(5), 2081–2811.

Matthews, G., Canonville, C. and Moss, A. K. (2006), 'Use of a void network model to correlate porosity, mercury porosimetry, thin section, absolute permeability and NMR relaxation time data for sandstone rocks', *Physical Review E* **73**((3 Part 1)), 031307.

Matthews, G. P. (1985), *Experimental Physical Chemistry*, 1st edn, Oxford University Press.

Mays, T. J. (2007), A new classification of pore sizes, *in* 'Characterization of Porous Solids VII Proceedings of the 7th International Symposium on the Characterization of Porous Solids (COPS-VII), Aix-en-Provence, France, 26-28 May 2005', Vol. 160 of *Studies in Surface Science and Catalysis*, Elsevier, pp. 57–62.

McClements, D. J. (2012), 'Nanoemulsions versus microemulsions: terminology, differences, and similarities', *Soft Matter* **8**(6), 1719–1729.

McCusker, L. B., Liebau, F. and Engelhardt, G. (2003), 'Nomenclature of structural and compositional characteristics of ordered microporous and mesoporous materials with inorganic hosts (IUPAC recommendations 2001)', *Microporous and Mesoporous Materials* **58**(1), 3–13.

McMinn, W. A. M., Al-Muhtaseb, A. H. and Magee, T. R. A. (2005), 'Enthalpy–entropy compensation in sorption phenomena of starch materials', *Food Research International* **38**(5), 505–510.

Mehrer, H. (2007), *Diffusion in Solids: Fundamentals, Methods, Materials, Diffusion-Controlled Processes*, Vol. 155 of *Solid-State Sciences*, Springer Berlin.

Micke, A., Kočiřik, M. and Bülow, M. (1993), 'Theory of zero length column chromatography with the condition of a well-stirred sorbing zone', *Microporous Materials* **1**(6), 373–381.

Mishra, B., Patel, B. B. and Tiwari, S. (2010), 'Colloidal nanocarriers: a review on formulation technology, types and applications toward targeted drug delivery', *Nanomedicine: Nanotechnology, Biology and Medicine* **6**(1), 9–24.

Misra, D. N. (1988), 'Adsorption on hydroxyapatite: role of hydrogen bonding and interphase coupling', *Langmuir* **4**(4), 953–958.

Misra, D. N. (1991), 'Adsorption and orientation of tetracycline on hydroxyapatite', *Calcified Tissue International* **48**(5), 362–367.

Mocchiutti, P. and Zanuttini, M. A. (2007), 'Key considerations in the determination of polyelectrolyte concentration by the colloidal titration method', *BioResources* **2**(3), 399–407.

Mochalin, V. N., Pentecost, A., Li, X.-M., Neitzel, I., Nelson, M., Wei, C., He, T., Guo, F., Gogotsi and Yury (2013), 'Adsorption of drugs on nanodiamond: Toward development of a drug delivery platform', *Mol. Pharmaceutics* **10**(10), 3728–3735.

Myers, A. L. (2004), Thermodynamics of adsorption, *in* 'Chemical Thermodynamics for Industry', Vol. 48, The Royal Society of Chemistry, pp. 243–253.

Myers, R. L. (2007), *The 100 Most Important Chemical Compounds: A Reference Guide*, 1st edn, Greenwood Press.

Neuvonen, P. J., Olkkola, K. T. and Alanen, T. (1984), 'Effect of ethanol and pH on the adsorption of drugs to activated charcoal: studies *in vitro* and in man', *Acta Pharmacol. Toxicol. (Copenh)* **236**(1–3), 91–102.

Newberne, P., Smith, R. L., Doull, J., Goodman, J. I., Munro, I. C., Portoghese, P. S., Wagner, B. M., Weil, C. S., Woods, L. A., Adams, T. B., Lucas, C. D. and Ford, R. A. (1999), 'The FEMA GRAS assessment of *trans*-anethole used as a flavouring substance', *Food and Chemical Toxicology* **37**(7), 789–811.

Ni, M. and Ratner, B. D. (2008), 'Differentiating calcium carbonate polymorphs by surface analysis techniques – an XPS and TOF-SIMS study', *Surface and Interface Analysis* **40**(10), 1356–1361.

Norris, J., Giese, R. F., Costanzo, P. M. and Oss, C. J. V. (1993), 'The surface energies of cation substituted laponite', *Clay Minerals* **28**(1), 1–11.

Oliveira, C., Silveira, N. P. d. and Rubio, J. (2010), Polymer structural and surface charge characterization on particles flocculation, *in* 'XII International Macromolecular Colloquium and 7th International Symposium on Natural Polymers and Composites', Universidade Federal do Rio Grande do Sil, Gramado, Brazil.

Öner, M., Yetiz, E., Ay, E. and Uysal, U. (2011), 'Ibuprofen release from porous hydroxyapatite tablets', *Ceramics International* **37**(7), 2117–2125.

Pan, G. and Liss, P. S. (1998*a*), 'Metastable-equilibrium adsorption theory: I. Theoretical', *Journal of Colloid and Interface Science* **201**(1), 71–76.

Pan, G. and Liss, P. S. (1998*b*), 'Metastable-equilibrium adsorption theory: II. Experimental', *Journal of Colloid and Interface Science* **201**(1), 77–85.

Pan, S. X., Davis, H. T. and Scriven, L. E. (1995), 'Modeling moisture distribution and binder migration in drying paper coatings', *TAPPI Journal* **78**(8), 127–143.

Patel, V. F., Liu, F. and Brown, M. B. (2011), 'Advances in oral transmucosal drug delivery', *Journal of Controlled Release* **153**(2), 106–116.

Pedersen, K. M. and Andersen, J. B. (2012), 'Particulate material for controlled release of active ingredients', Omya Development AG. Patent US20120321751A1.

Peng, C., Zhao, Q. and Gao, C. (2010), 'Sustained delivery of doxorubicin by porous $CaCO_3$ and chitosan/alginate multilayers-coated $CaCO_3$ microparticles', *Colloids and Surfaces A* **353**(2–3), 132–139.

Pinholt, C., Hartvig, R. A., Medlicott, N. and Jorgensen, L. (2011), 'The importance of interfaces in protein drug delivery - why is protein adsorption of interest in pharmaceutical formulations?', *Expert Opin Drug Deliv.* **8**(7), 949–964.

Pires, J., Carvalho, M. B. d., Carvalho, A. P., Guil, J. M. and Perdigón-Melón (2000), 'Heats of adsorption of *n*-hexane by thermal gravimetry with differential scanning calorimetry (TG-DSC): a tool for textural characterization of pillared clays', *Clays and Clay Minerals* **48**(3), 385–391.

Plummer, L. N. and Busenberg, E. (1982), 'The solubilities of calcite, aragonite and vaterite in CO_2-H_2O solutions between 0 and 90°C, and an evaluation of the aqueous model for the system $CaCO_3$-CO_2-H_2O', *Geochimica et Cosmochimica Acta* **46**(6), 1011–1040.

Preisig, D., Haid, D., Varum, F. J. O., Bravo, R., Alles, R., Huwyler, J. and Puchkov, M. (2014), 'Drug loading into porous calcium carbonate microparticles by solvent evaporation', *European Journal of Pharmaceutics and Biopharmaceutics* **87**(3), 548–558.

Press, W. H. and Teukolsky, S. A. (1991), 'Simulated annealing optimization over continuous spaces', *Computers in Physics* **5**(4), 426–429.

Price, J. C., Matthews, G. P., Quinlan, K., Sexton, J. and de G. Matthews, A. G. (2009), 'A depth filtration model of straining within the void networks of stainless steel filters', *AIChE Journal* **55**(12), 3134–3144.

Qiu, N., Yin, H., Ji, B., Klauke, N., Glidle, A., Zhang, Y., Song, H., Cai, L., Ma, L., Wang, G., Chen, L. and Wang, W. (2012), 'Calcium carbonate microspheres as carriers for the anticancer drug camptothecin', *Materials Science and Engineering: C* **32**(8), 2634–2640.

Rassing, M. R. (1994), 'Chewing gum as a drug delivery system', *Advanced Drug Delivery Reviews* **13**(1–2), 89–121.

Ren, J., Wang, W., Lu, S., Shen, J. and Tang, F. (2003), 'Characteristics of dispersion behavior of fine particles in different liquid media', *Powder Technology* **137**(1–2), 91–94.

Riachi, L. G. and De Maria, C. A. B. (2015), 'Peppermint antioxidants revisited', *Food Chemistry* **176**, 72–81.

Ridgway, C. J., Gane, P. A. C. and Schoelkopf, J. (2004), 'Modified calcium carbonate coatings with rapid absorption and extensive liquid uptake capacity', *Colloids and Surfaces A* **236**(1–3), 91–102.

Ridgway, C. J., Gane, P. A. C. and Schoelkopf, J. (2006), 'Achieving rapid absorption and extensive liquid uptake capacity in porous structures by decoupling capillarity and permeability: nanoporous modified calcium carbonate', *Transport in Porous Media* **63**(2), 239–259.

Rouquerol, F., Rouquerol, J. and Sing, K. (1999), *Adsorption by Powders & Porous Solids: Principles, Methodology and Applications*, 2nd edn, Academic Press.

Rouquerol, J., Avnir, D., Fairbridge, C. W., Everett, D. H., Haynes, J. M., Pernicone, N., Ramsay, J. D. F., Sing, K. S. W. and Unger, K. K. (1994), 'Recommendations for the characterization of porous solids (technical report)', *Pure and Applied Chemistry* **66**(8), 1739–1758.

Rowe, R. C., Sheskey, P. J. and Quinn, M. E. (2009), *Handbook of Pharmaceutical Excipients*, 6th edn, Pharmaceutical Press.

Ruby, M. V., Davis, A., Link, T. E., Schoof, R., Chaney, R. L., Freeman, G. B. and Paul, B. (1993), 'Development of an *in vitro* screening test to evaluate the *in vivo* bioaccessibility of ingested mine-waste lead', *Environmental Science & Technology* **27**(13), 2870–2877.

Ruby, M. V., Davis, A., Schoof, R., Eberle, S. and Sellstone, C. M. (1996), 'Estimation of lead and arsenic bioavailability using a physiologically based extraction test', *Environmental Science & Technology* **30**(2), 422–430.

Rudzinski, W. and Everett, D. H. (1992), *Adsorption of Gases on Heterogeneous Surfaces*, 1st edn, Elsevier.

Rudzinski, W., Lee, S.-L., Yan, C.-C. S. and Panczyk, T. (2001), 'A fractal approach to adsorption on heterogeneous solid surfaces. 1. The relationship between geometric and energetic surface heterogeneities', *Journal of Physical Chemistry B* **105**(44), 10847–10856.

Ruthven, D. M. (1984), *Principles of Adsorption and Adsorption Processes*, 1st edn, Wiley.

Ruthven, D. M. and Brandani, S. (2000), 'Measurement of diffusion in porous solids by zero length column (ZLC) methods', *Membrane Science and Technology* **6**, 187–212.

Ruthven, D. M., Brandani, S. and Eic, M. (2005), Measurement of diffusion in microporous solids by macroscopic methods, *in* 'Adsorption and Diffusion', Vol. 7 of *Molecular Sieves*, Springer Berlin Heidelberg, pp. 45–84.

Ruthven, D. M. and Stapleton, P. (1993), 'Measurement of liquid phase counter-diffusion in zeolite crystals by the ZLC method', *Chemical Engineering Science* **48**(1), 89–98.

Ruthven, D. M. and Vidoni, A. (2012), 'ZLC diffusion measurements: combined effect of surface resistance and internal diffusion', *Chemical Engineering Science* **71**, 1–4.

Sasikumar, S. (2013), 'Effect of particle size of calcium phosphate based bioceramic drug delivery carrier on the release kinetics of ciprofloxacin hydrochloride: an *in vitro* study', *Frontiers of Materials Science* **7**(3), 261–268.

Schatzberg, P. (1967), 'Molecular diameter of water from solubility and diffusion measurements', *The Journal of Physical Chemistry* **71**(13), 4569–4570.

Schoelkopf, J. (2002), Observation and Modelling of Fluid Transport into Porous Paper Coating Structures, PhD thesis, University of Plymouth, Devon, UK.

Schoelkopf, J. and Gane, P. (2008), 'Nano functionality of calcium carbonate', *International Paper World* **7–8**, 22–24.

Schoelkopf, J., Gane, P. A. C., Ridgway, C. J., Spielmann, D. C. and Matthews, G. P. (2003*a*), 'Imbibition behaviour of offset inks: I. Gravimetric determination of the imbibition rate of oil into pigmented coating structures', *TAPPI Journal* **2**(6), 9–13.

Schoelkopf, J., Gane, P. A. C., Ridgway, C. J., Spielmann, D. C. and Matthews, G. P. (2003*b*), 'Imbibition behaviour of offset inks: II. Gravimetric determination of vehicle separation rate into pigmented coating structures', *TAPPI Journal* **2**(7), 19–23.

Scholten, E., van der Linden, E. and This, H. (2008), 'The life of an anise-flavored alcoholic beverage: does its stability cloud or confirm theory?', *Langmuir* **24**, 1701–1706.

Sellers, E. M., Khouw, V. and Dolman, L. (1977), 'Comparative drug adsorption by activated charcoal', *J. Pharm. Sci.* **66**(11), 1640–1641.

Seri-Levy, A. and Avnir, D. (1993), 'Effects of heterogeneous surface geometry on adsorption', *Langmuir* **9**(11), 3067–3076.

Shaji, J. and Patole, V. (2008), 'Protein and peptide drug delivery: oral approaches', *Indian Journal of Pharmaceutical Sciences* **70**(3), 269–277.

Sherry, H., Jin Ching, C., Chin Wei, H. and Walter, H. C. (2009), 'Effects of nano calcium carbonate and nano calcium citrate on toxicity in ICR mice and on bone mineral density in an ovariectomized mice model', *Nanotechnology* **20**(37), 375102.

Siepmann, J. and Siepmann, F. (2008), 'Mathematical modelling of drug delivery', *International Journal of Pharmaceutics* **364**(2), 328–343.

Siepmann, J. and Siepmann, F. (2012), 'Modeling of diffusion controlled drug delivery', *Journal of Controlled Release* **161**(2), 351–362.

Silva, J. A. C. and Rodrigues, A. E. (1996), 'Analysis of ZLC technique for diffusivity measurements in bidisperse porous adsorbent pellets', *Gas Separation & Purification* **10**(4), 207–224.

Sing, K. S. W., Everett, D. H., Haul, R. A. W., Moscou, L., Pierotti, R. A., Rouquérol, J. and T., S. (1985), 'Reporting physisorption data for gas/solid systems with special reference to the determination of surface area and porosity (recommendations 1984)', *Pure and Applied Chemistry* **57**(4), 603–619.

Sips, R. (1948), 'On the structure of a catalyst surface', *The Journal of Chemical Physics* **16**(5), 490–495.

Sitnikova, N. L., Sprik, R. and Wegdam, G. (2005), 'Spontaneously formed *trans*-anethol/water/alcohol emulsions: mechanism of formation and stability', *Langmuir* **21**(16), 7083–7089.

Sloane, N. J. A. (1998), 'The sphere packing problem', *Documenta Mathematika* **3**, 387–396.

Slowing, I. I., Vivero-Escoto, J. L., Wu, C.-W. and Lin, V. S. Y. (2008), 'Mesoporous silica nanoparticles as controlled release drug delivery and gene transfection carriers', *Advanced Drug Delivery Reviews* **60**(11), 1278–1288.

Sneader, W. (2000), 'The discovery of aspirin: a reappraisal', *British Medical Journal* **321**(7276), 1591–1594.

Snoeyink, V. L. and Summers, R. S. (1999), Adsorption of organic compounds, *in* 'Water Quality and Treatment Handbook: A Handbook of Community Water Supplies (American Water Works Association)', 5th edn, McGraw-Hill.

Sokołowska, L. (1989), 'On the role of energetic and geometric heterogeneity in sorption of water vapour by soils: application of a fractal approach', *Geoderma* **45**(3–4), 251–265.

Sokołowska, M. and Bal, W. (2005), 'Cu(II) complexation by "non-coordinating" *N*-2-hydroxyethylpiperazine-*N*'-2-ethanesulfonic acid (HEPES buffer)', *Journal of Inorganic Biochemistry* **99**(8), 1653–1660.

Son, J. S., Appleford, M., Ong, J. L., Wenke, J. C., Kim, J. M., Choi, S. H. and Oh, D. S. (2011), 'Porous hydroxyapatite scaffold with three-dimensional localized drug delivery system using biodegradable microspheres', *Journal of Controlled Release* **153**(2), 133–140.

Song, X., Zhang, Y., Yan, C., Jiang, W. and Chang, C. (2013), 'The Langmuir monolayer adsorption model of organic matter into effective pores in activated carbon', *Journal of Colloid and Interface Science* **389**(1), 213–219.

Stirnimann, T., Atria, S., Schoelkopf, J., Gane, P. A. C., Alles, R., Huwyler, J. and Puchkov, M. (2014), 'Compaction of functionalized calcium carbonate, a porous and crystalline microparticulate material with a lamellar surface', *International Journal of Pharmaceutics* **466**(1–2), 266–275.

Stirnimann, T., Di Maiuta, N., Gerard, D. E., Alles, R., Huwyler, J. and Puchkov, M. (2013), 'Functionalized calcium carbonate as a novel pharmaceutical excipient for the preparation of orally dispersible tablets', *Pharmaceutical Research* **30**(7), 1915–1925.

Stockmeyer, R. (1993), 'Diffusive transport of fluids through porous solids observed by neutron transmission', *Microporous Materials* **1**(6), 383–391.

Sun, C. (2004), 'A novel method for deriving true density of pharmaceutical solids including hydrates and water-containing powders', *Journal of Pharmaceutical Sciences* **93**(3), 646–653.

Tåg, C.-M., Juuti, M., Koivunen, K. and Gane, P. A. C. (2010), 'Dynamic water transport in a pigmented porous coating medium: novel study of droplet absorption and evaporation by near-infrared spectroscopy', *Industrial & Engineering Chemistry Research* **49**(9), 4181–4189.

Tao, Z., Morrow, M. P., Asefa, T., Sharma, K. K., Duncan, C., Anan, A., Penefsky, H. S., Goodisman, J. and Souid, A.-K. (2008), 'Mesoporous silica nanoparticles inhibit cellular respiration', *Nano Letters* **8**(5), 1517–1526.

Teixeira, A. R., Chang, C.-C., Coogan, T., Kendall, R., Fan, W. and Dauenhauer, P. J. (2013), 'Dominance of surface barriers in molecular transport through silicalite-1', *The Journal of Physical Chemistry C* **117**(48), 25545–25555.

Terán, P. (2008), On convergence in necessity and its laws of large numbers, *in* 'Soft Methods for Handling Variability and Imprecision', Vol. 48 of *Advances in Soft Computing*, Springer Berlin Heidelberg, pp. 289–296.

Terán, P. (2014), 'Law of large numbers for the possibilistic mean value', *Fuzzy Sets and Systems* **245**, 116–124.

Terayama, H. (1952), 'Method of colloid titration (a new titration between polymer ions)', *Journal of Polymer Science Part A: Polymer Chemistry* **8**(2), 243–253.

The Terpene Consortium (2006), 'Test plan and robust summaries for anethole (isomer unspecified) and *trans*-anethole'. Report nr. ARZ01-14069; submitted to the EPA under the HPV Challenge Program by: The Flavor and Fragrance High Production Volume Consortia, Terpene Consortium.

Toriyama, M., Kawamoto, Y., Suzuki, T., Yokogawa, Y., Nishizawa, K. and Nagata, F. (1995), 'Wettability of calcium phosphate ceramics by water', *Journal of the Ceramic Society of Japan* **103**(1193), 46–49.

Tsuchiya, T. and Levy, G. (1972), 'Relationship between effect of activated charcoal on drug absorption in man and its drug adsorption characteristics *in vitro*', *J. Pharm. Sci.* **61**(14), 586–589.

Tyrrell, H. J. V. (1964), 'The origin and present status of Fick's diffusion law', *Journal of Chemical Education* **41**(7), 397–400.

Tzannis, S. T., Hrushesky, W. J. M., Wood, P. A. and Przybycien, T. M. (1997), 'Adsorption of a formulated protein on a drug delivery device surface', *J. Colloid Interface Sci.* **189**(2), 216–228.

Ueno, Y., Futagawa, H., Takagi, Y., Ueno, A. and Mizushima, Y. (2005), 'Drug-incorporating calcium carbonate nanoparticles for a new delivery system', *Journal of Controlled Release* **103**(1), 93–98.

Ukmar, T., Maver, U., Planinšek, O., Kaučič, V., Gaberšček, M. and Godec, A. (2011), 'Understanding controlled drug release from mesoporous silicates: theory and experiment', *Journal of Controlled Release* **155**(3), 409–417.

Umpleby, R. J., Baxter, S. C., Chen, Y., Shah, R. N. and Shimizu, K. D. (2001), 'Characterization of molecularly imprinted polymers with the Langmuir–Freundlich isotherm', *Analytical Chemistry* **73**(19), 4584–4591.

Utomo, H. D. and Hunter, K. A. (2010), 'Particle concentration effect: adsorption of divalent metal ions on coffee grounds', *Bioresource Technology* **101**(5), 1482–1486.

Van Brakel, J. and Heertjes, P. M. (1974), 'Analysis of diffusion in macroporous media in terms of a porosity, a tortuosity and a constrictivity factor', *International Journal of Heat and Mass Transferr* **17**(9), 1093–1103.

Van Den Bleek, C. M., Van Der Wiele, K. and Van Den Berg, P. J. (1969), 'The effect of dilution on the degree of conversion in fixed bed catalytic reactors', *Chemical Engineering Science* **24**(4), 681–694.

Vane, J. R. and Botting, R. M. (2003), 'The mechanism of action of aspirin', *Thrombosis Research* **110**(5–6), 255–258.

Vergnaud, J.-M. (1993), *Controlled Drug Release of Oral Dosage Forms*, 1st edn, CRC Press.

Verma, N., Salem, K. and Mewes, D. (2007), 'Simulation of micro- and macro-transport in a packed bed of porous adsorbents by lattice Boltzmann methods', *Chemical Engineering Science* **62**(14), 3685–3698.

Vitale, S. A. and Katz, J. L. (2003), 'Liquid droplet dispersions formed by homogeneous liquid-liquid nucleation: "the ouzo effect"', *Langmuir* **19**(10), 4105–4110.

Wade, J. B., Martin, G. P. and Long, D. F. (2015), 'An assessment of powder pycnometry as a means of determining granule porosity', *Pharmaceutical Development and Technology* **20**(3), 257–265.

Wallqvist, V., Claesson, P. M., Swerin, A., Schoelkopf, J. and Gane, P. A. (2009), 'Influence of wetting and dispersing agents on the interaction between talc and hydrophobic particles', *Langmuir* **25**(12), 6909–6915.

Walton, N. J., Mayer, M. J. and Narbad, A. (2003), 'Vanillin', *Phytochemistry* **63**(5), 505–515.

Wang, H., Alfredsson, V., Tropsch, J., Ettl, R. and Nylander, T. (2013), 'Formation of $CaCO_3$ deposits on hard surfaces: effect of bulk solution conditions and surface properties', *ACS Applied Materials & Interfaces* **5**(10), 4035–4045.

Wang, L., Dong, J., Chen, J., Eastoe, J. and Li, X. (2009), 'Design and optimization of a new self-nanoemulsifying drug delivery system', *Journal of Colloid and Interface Science* **330**(3), 443–448.

Wang, L. and Nancollas, G. H. (2008), 'Calcium orthophosphates: crystallization and dissolution', *Chemical Reviews* **108**(11), 4628–69.

Wang, Y., Xu, Z.-L., Xie, Y.-Y., Tian, Y.-X., Shen, Y.-D., Young, G. M., Wang, H., Lei, H.-T. and Sun, Y.-M. (2011), 'Development of polyclonal antibody-based indirect competitive enzyme-linked immunosorbent assay for sodium saccharin residue in food samples', *Food Chemistry* **126**(2), 815–820.

Washburn, E. W. (1921), 'The dynamics of capillary flow', *Phys. Rev.* **17**(3), 273–283.

Webb, P. A. and Orr, C. (1997), *Analytical Methods in Fine Particle Technology*, 1st edn, Micromeritics.

Wei, W., Ma, G.-H., Hu, G., Yu, D., McLeish, T., Su, Z.-G. and Shen, Z.-Y. (2008), 'Preparation of hierarchical hollow $CaCO_3$ particles and the application as anticancer drug carrier', *Journal of the American Chemical Society* **130**(47), 15808–15810.

Wen, H. and Park, K. (2010), *Oral Controlled Release Formulation Design and Drug Delivery: Theory to Practice*, 1st edn, John Wiley & Sons, Inc.

Whitaker, S. (1983), 'Diffusion and reaction in a micropore-macropore model of a porous medium', *Latin American Journal of Chemical Engineering and Applied Chemistry* **13**, 143–183.

Whysner, J. and Williams, G. M. (1996), 'Saccharin mechanistic data and risk assessment: urine composition, enhanced cell proliferation, and tumor promotion', *Pharmacology & Therapeutics* **71**(1–2), 225–252.

Woodford, D. W. and Lesko, L. J. (1981), 'Relative bioavailability of aspirin gum', *Journal of Pharmaceutical Sciences* **70**(12), 1341–1343.

Wragg, J., Cave, M., Basta, N., Brandon, E., Casteel, S., Denys, S., Gron, C., Oomen, A., Reimer, K., Tack, K. and Van de Wiele, T. (2011), 'An inter-laboratory trial of the unified barge bioaccessibility method for arsenic, cadmium and lead in soil', *Science of the Total Environment* **409**(19), 4016–4030.

Yildirim, I. (2001), Surface Free Energy Characterization of Powders, PhD thesis, Virginia Polytechnic Institute and State University, Virginia, US.

Zabka, M. and Rodrigues, A. E. (2007), 'Measurement of pore diffusivity of *R,S*-α-tetralol enantiomers in chiral adsorbent CHIRALPAK AD by zero length column method', *Separation and Purification Technology* **57**(1), 74–84.

Zalc, J. M., Reyes, S. C. and Iglesia, E. (2003), 'Monte-Carlo simulations of surface and gas phase diffusion in complex porous structures', *Chemical Engineering Science* **58**(20), 4605–4617.

Zhang, Y., Wang, J., Bai, X., Jiang, T., Zhang, Q. and Wang, S. (2012), 'Mesoporous silica nanoparticles for increasing the oral bioavailability and permeation of poorly water soluble drugs', *Molecular Pharmaceutics* **9**(3), 505–513.

Bound copies of published papers

Permission to reproduce these papers has been granted by the respective publisher.

I&EC research
Industrial & Engineering Chemistry Research

Article

pubs.acs.org/IECR

Diffusion and Tortuosity in Porous Functionalized Calcium Carbonate

Charlotte L. Levy,[†] G. Peter Matthews,[*,†] Giuliano M. Laudone,[†] Christopher M. Gribble,[†] Andrew Turner,[†] Cathy J. Ridgway,[‡] Daniel E. Gerard,[‡] Joachim Schoelkopf,[‡] and Patrick A. C. Gane[‡,§]

[†]Faculty of Science and Engineering, Plymouth University, Drake Circus, Plymouth PL4 8AA, United Kingdom

[‡]Omya International AG, Baslerstrasse 42, P.O. Box 335, CH-4665 Oftringen, Switzerland

[§]School of Chemical Technology, Department of Forest Products Technology, Aalto University, 00076 Aalto, Helsinki, Finland

Supporting Information

ABSTRACT: Calcium carbonate can be "functionalized" by use of etching agents such as phosphoric acid to create inter- and intraparticle porosity with a range of morphologies. Functionalized calcium carbonate has potential for use as a carrier for the delayed release of actives, such as drugs, plant protection chemicals, and food additives such as flavors. The drug or flavor is released slowly by permeation and diffusion. In order to measure the effective rate of diffusion within a range of morphologies, and hence gain insights into the optimum mode of functionalization, the diffusion of vanillin in ethanol is reported. Effective diffusion coefficients D' were measured in a flow cell connected to a high performance liquid chromatograph (HPLC). Samples were also subjected to mercury intrusion porosimetry. The resulting percolation characteristics were inverse modeled using the PoreXpert package to generate representative void structures with estimated tortuosities. It is shown that the primary particle size of a sample was a better predictor of D' calculated from the experimental diffusion curves, and also of the porosity-scaled tortuosity values, than the porosity or surface area. There was also a correlation between intraparticle tortuosity, scaled by porosity, and diffusion coefficient. The approach is validated by experimental evidence from this and related studies.

INTRODUCTION

"Functionalized" calcium carbonate (FCC) is produced by etching calcium carbonate particles and reprecipitating modified surface structure with in situ or externally supplied CO_2 in the form of carbonic acid. To facilitate the in situ production of CO_2, acids such as phosphoric acid can be used, resulting in a mixed mineral morphology. Variations in the etching process produce a range of morphologies with recrystallized surfaces, consisting of incorporated hydroxyapatite (HAP) in the case of phosphoric acid, which are dual porous (i.e., inter- and intraparticle porosity).

FCCs are proving to have a wide range of novel applications. In particular, they are being proposed as an excipient and a pharmaceutical ingredient,[1,2] because the porous nature of calcium carbonate offers a good stability of the ingredients, slow biodegradability, is easily produced, tasteless, stable, and biocompatible.[3−6] The use of HAP as a drug carrier has also been discussed in the literature.[7−12] FCC offers benefits over HAP because the current commercial methods used to produce HAP give a low yield mixed with several phases, so that the product is expensive and suitable only for small-scale and time-consuming production.[13]

Adjustments to the FCC production process can be used to produce a wide range of different morphologies, and raise the possibility of tailoring the void structures of the particles to provide controlled release delivery vehicles for actives across many fields, including drugs and flavors. (The term "active" encompasses active ingredients, active constituents, and bulk actives.) However, such tailoring can only be fully optimized by a fundamental characterization of the way in which a drug, loaded into an FCC, then flows and diffuses out over a period of time to provide the delayed release. As a main step in this characterization, we have measured the diffusion of a flavor from various morphologies of FCC. For ease of loading and analysis during this initial phase of experimentation, we have used vanillin dissolved in ethanol, because vanillin is a common and popular flavor compound, exhibits good solubility and detection sensitivity in ethanol, and is solid at room temperature. The vanillin saturates the FCC from solution, and the diffusion out of the FCC structure is then measured once the particles are surrounded in pure solvent rather than solution.

The experiments we describe are a development from those of Ruthven and co-workers.[14,15] Their "zero length" cell (ZLC) permitted the study of the intraparticle diffusivity alone of a sample or an adsorbent (i.e., decoupled from the interparticle flow) by allowing only a monolayer or zero length of sample to be held in a gas stream of the adsorbate in an inert carrier at known partial pressure.[14,16−20] They monitored the desorption when the sample was purged by the pure carrier.[21] The technique has been used to measure the diffusion rate D in porous adsorbent particles, and has been extended to study liquid-phase adsorption systems.[22−24] Previous work has suggested, as with other systems, that the interparticle diffusion of cyclohexane from between small ZSM-5 crystals is slower

Received: June 29, 2015
Revised: September 29, 2015
Accepted: September 29, 2015
Published: September 29, 2015

DOI: 10.1021/acs.iecr.5b02362
Ind. Eng. Chem. Res. 2015, 54, 9938−9947

than that between larger particles.[17,25] Ruthven measured the diffusion of mesitylene in cyclohexane through zeolites, and reported coefficients in the range of 2.8×10^{-19} to 6.0×10^{-15} $m^2\ s^{-1}$; he also attributed the low values to the small crystal size of 1−2 μm of the zeolites, with diffusion likely to be controlled by interparticle rate processes.[15]

The dead space within the HPLC flow line, detector chamber, and ZLC entry and exit ports caused the liquids to mix in a manner similar to a chromatographic line broadening effect. Because the effects being studied are so subtle as to be masked in a ZLC by this line broadening, it was necessary to lengthen the ZLC in the flow direction, converting it to what we refer to as a finite length cell (FLC). The dead space within the entry and exit ports was reduced by use of polytetrafluoroethylene (PTFE) inserts, as described below. The use of a FLC had the advantage of making the diffusional effects observable. Also, our use of a sample volume of around 1 cm^3 in the FLC is closer to that which would be found in a controlled release tablet, relative to the monolayer in a ZLC. However, the disadvantage is that the measured release rates are now dependent on diffusion and permeation effects within both the intra- and interparticle porosity, and that the system is less well described by the mathematical assumptions below. Rather than precise diffusion coefficients D, the measurements are therefore of effective diffusion coefficients D'.

Previous work helps with the elucidation of D'. It has been shown that the long-time, low-concentration region of the desorption curve in a ZLC experiment is controlled by an effectively linear adsorption isotherm.[17,26,27] Therefore, the diffusivity as loading tends to zero may still be measured, even if the system under study does not strictly conform to the assumptions of the standard ZLC model. Hufton and Duncan have shown that a long-time solution method is very robust for obtaining intraparticle diffusivities.[17,28] However, the asymptote at long times and low concentrations may be adversely affected by an erroneous baseline coupled with any inaccuracy of the measuring device. To counter this, other short-time and intermediate-time solution methods have been proposed,[22,29] whereas Duncan has suggested that these issues may be overcome by careful experimental design and operation.[17] Additionally, the deviation from the model shown by the desorption curves in the literature occurs in the initial part of the experiment.[17,22,28] Therefore, our approach has been to pack more sample into the FLC than would be used in a ZLC, to avoid erroneous baselining by amplifying the magnitude of the diffusional effects from the samples, and to calculate diffusion coefficients from the long-time region of the curve.

For comparison and validation, measurements were also made of interparticle diffusion and permeation within an equivalent packing of nonporous ground calcium carbonate (GCC) of similar size to the porous FCC particles. As FCCs have surface crystalline growths of hydroxyapatite (HAP), diffusion from pure HAP was also measured for comparison.

The basic assumption of the ZLC for liquid systems, and hence the FLC also, is that flow is laminar, and that equilibrium between fluid and adsorbed phases is maintained at all times at the outer surface of the sample, i.e., there is zero hold-up of the active passing into the mobile interparticle liquid phase. At the flow rate of 1 $cm^3\ min^{-1}$ used in this work, the Reynolds number[30] of the fluid flow was of the order of 0.01 in the HPLC capillary tubes and packed FLC, indicating laminar flow. Because we do not know the relative thickness of the hydrodynamic and mass transfer boundary layers within the current system, the Schmidt number cannot be calculated exactly. However, we assume that the Péclet number, which is the product of the Reynolds and Schmidt numbers, is made small by the smallness of the Reynolds number, and that diffusive transport is therefore significant with respect to advective transport in the system.

It is also assumed that the fluid phase is well mixed and its concentration constant throughout the sample, i.e., mathematically identical to a differential plug flow reactor or an infinitesimally small continuous stirred tank reactor. If there was fully efficient flushing, then it can be readily shown that the whole volume of the particle pack was flushed in around 20 s, in an experiment lasting around 2000 s overall. Therefore, the assumption is appropriate but not perfect.

Brandani and Ruthven[22,31] have shown that the time-dependent desorption curve obeys the equation

$$\frac{c_s}{c_0} = \sum_{n=1}^{\infty} \frac{2L\exp(-\beta_n^2(D/r^2)t)}{\beta_n^2 + (1 - L + \gamma\beta_n^2)^2 + L - 1 + \gamma\beta_n^2} \tag{1}$$

where

$$\beta_n \cot \beta_n + L - 1 - \gamma\beta_n^2 = 0 \tag{2}$$

c_s is the fluid phase sorbate/analyte concentration, and c_0 is the initial value of the fluid phase sorbate/analyte concentration at time $t = 0$. L is a dimensionless parameter defined by

$$L = \frac{Fr^2}{3VKD} \tag{3}$$

where F is the volumetric flow rate, r is the radius of the sample particles, V is the volume of sorbent in the ZLC bed, and K is the adsorption equilibrium constant. L may be interpreted as the ratio of a characteristic diffusion and washout time constant (r^2/D) to a convection/adsorption time (VK/F).[32,33] This parameter is also equal to the dimensionless adsorbed phase concentration gradient at the surface of the solid at time zero.

γ is a dimensionless parameter defined by

$$\gamma = \frac{V_f}{3VK} \tag{4}$$

where V_f is the volume of interstitial fluid in the ZLC bed. In the case of negligible interparticle fluid hold-up, $\gamma = 0$, and eq 1 simplifies to[32]

$$\frac{c_s}{c_0} = 2L \sum_{n=1}^{\infty} \frac{\exp(-\beta_n^2(D/r^2)t)}{\beta_n^2 + L(L-1)} \tag{5}$$

In the long time region, only the first term of the summation is significant, so

$$\ln \frac{c_s}{c_0} \approx \ln\left[\frac{2L}{\beta_1^2 + L(L-1)}\right] - \beta_1^2 \frac{Dt}{r^2} \tag{6}$$

which defines the logarithmic time asymptote. For large values of L, there is a further simplification because $\beta_1 \rightarrow \pi$.[20] Consequently, a semilogarithmic plot of normalized concentration versus time allows the quantities (D/r^2) and L to be obtained from the gradient and intercept, respectively, from the desorption region[32] at long time. The mathematical solution at shorter times is more complex and involves the time constant for the washout process.[22]

Another, as yet unpublished, study of this system by the present authors has established that the average adsorption of

DOI: 10.1021/acs.iecr.5b02362
Ind. Eng. Chem. Res. 2015, 54, 9938−9947

Table 1. Properties of the Mineral Particles

sample	particle size d_{50} (μm)	surface area (m^2 g^{-1})	overall porosity of sample (%)	hydroxy-apatite content (%)	calcium carbonate content (%)	morphology
GCC	7.7	1.53	22.23		97.5	
HAP	7.1	63.2	61.80	97−100		
FCC TP	7.0	55.4	61.55	51	49	roses
FCC 02	4.9	54.1	61.16	43	57	roses
FCC 03	3.1	33.5	49.33	14	86	caviar
FCC 06	5.5	141.5	67.30	85	15	brain
FCC 07	6.3	48.5	57.84	13	87	caviar
FCC 12	10.0	81.0	70.08	50	50	flaky eggs
FCC 13	23.5	66.0	53.36	50	50	golf balls

vanillin from ethanol onto all the FCC samples and HAP (Table 1) is small, 2.01 ± 0.58 mg g^{-1} when the sample is immersed in a 30 mg L^{-1} solution. The desorption process, once the surrounding liquid in the experiments is switched back to pure solvent, will contribute to D' to an extent unquantified in this work.

L gives an indication of how far removed the system is from equilibrium control, and is proportional to the flow rate. To extract a reliable time constant, it is necessary to run the experiment with at least two different flow rates.[33] However, the value of L is disregarded for the purpose of these experiments, because the D' was calculated toward the end of the experiment, when diffusion was expected to be occurring, and the initial washout of vanillin in the interparticle space would have already been achieved.

The effective diffusion coefficients can only be used for optimization of the FCC void structure if they are related to quantitative void structure parameters of the samples. As such characteristics are not measurable by direct microscopy, since that gives only two-dimensional views of the interparticle space and the particle surfaces, nor directly from any other single experimental technique, then it is necessary to gain the information with the help of a void structure model. PoreXpert is software that generates three-dimensional void structures from the inverse modeling of percolation characteristics, in this case mercury intrusion. It then allows the modeling of pore−fluid behavior, such as wetting,[34−36] and pore-level processes such as depth filtration.[37] In this work, we have employed a newly developed algorithm[38] to measure the intraparticle tortuosity of the simulated structures for comparison with the measured diffusion coefficients.

MATERIALS AND METHODS

Instrumentation. Particle sizes were measured with a Malvern Master Sizer 2000, which measured the static light scattering of particles dispersed in water, interpreted using the Mie approximation.[39] They are expressed in Table 1 as d_{50} values, namely the median particle diameters at which 50% by volume of the sample is finer than the stated value. Values of d_{98}, and the full distributions, are shown in Table S1 and Figure S1 in the Supporting Information.

Surface areas were measured with a Micromeritics Gemini V surface area analyzer.

Mercury intrusion porosimetry was carried out on the HAP sample using Thermo Fisher Pascal instruments. Each intrusion pressure was automatically held steady long enough for the intrusion volume to become constant, by means of the instruments' PASCAL (pressurization by automatic speedup and continuous adjustment logic) algorithms. The low pressure intrusion of HAP was carried out twice and the porosity was calculated from the second run; this was to exclude the agglomeration of the powder from the porosity calculations. The remaining samples in Table 1 were measured using Micromeritics Autopore mercury porosimeters, with a long (60 s) equilibration time at each pressure. The resulting intrusion curves were truncated so that no low pressure intrusion was taken into account, corresponding to void sizes greater than 10 μm.[1] This removed any variation in measured porosity due simply to changes in the initial agglomeration of the particles by the mercury. Pore and throat size distributions of each sample, generated by PoreXpert, can be viewed in Figures S2−17 of the Supporting Information.

The envelope densities of the samples were measured using a Micromeritics GeoPyc 1360 Envelope Density Analyzer equipped with a chamber of an internal diameter of 12.7 mm. The instrument measured the volume by surrounding the sample with Dry Flo powder, with a consolidation force of 28 N. The measurements were approximate, because they involved use of a powder to investigate the packing of a powder. They were therefore used simply as a cross-check to ensure that there was efficient packing into the FLC.

Micrographs were obtained with JEOL 7001F field emission and LEO 435 VPi scanning electron microscopes.

Minerals. The GCC and FCC samples, listed in Table 1, were provided by Omya AG (Oftringen, Switzerland). Their properties are listed in Table 1. The HAP was purchased from Acros Organics.

Particle Characteristics. The micrographs in Figure 1 show the morphologies of the particles. GCC is nonporous. All the particles were approximately spherical, and so for modeling purposes were assumed to be the same. All the FCC samples have clearly identifiable lamellar platelet structures protruding from their surfaces, creating the intraparticle porosity, except FCC 07 which is more akin to GCC. A subjective categorization of the particle morphologies, based on their appearance in these micrographs, is shown in Table 1. The particles are shown spread out in order to take the micrographs, but the interparticle porosity when they are more densely packed can be readily inferred. Larger versions of the images in Figure 1, together with lower magnification micrographs to aid this inference, are given in Figures S18−38 of the Supporting Information.

Flavor and Solvent. Vanillin (4-hydroxy-3-methoxybenzaldehyde) was supplied by Acros Organics, and the absolute ethanol used was HPLC grade and provided by Fisher Scientific.

Finite Length Cell (FLC) and Flow System. A cross-sectional diagram of the FLC is shown in Figure 2. It was

DOI: 10.1021/acs.iecr.5b02362
Ind. Eng. Chem. Res. 2015, 54, 9938−9947

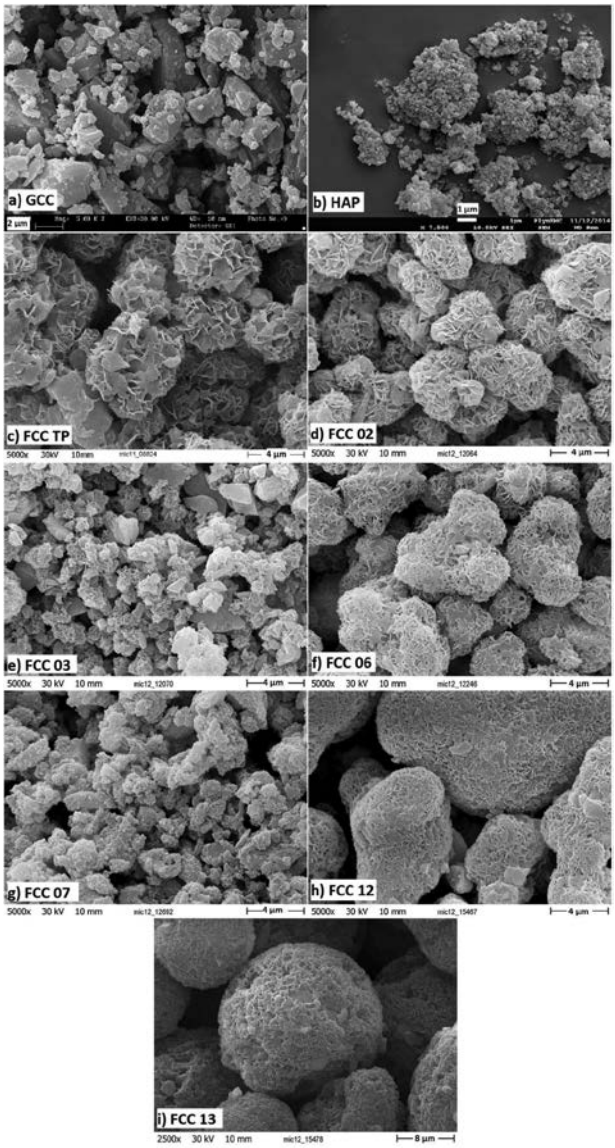

Figure 1. Scanning electron micrographs of the (a) GCC, (b) HAP, (c) FCC TP, (d) FCC 02, (e) FCC 03, (f) FCC 06, (g) FCC 07, (h) FCC 12, and (i) FCC 13 samples. Samples a, b and i have scale bars of 2, 1, and 8 μm, respectively, whereas the other samples have a scale bar of 4 μm.

constructed from 300-series grade stainless steel. To support the sample fully while maintaining sufficient liquid flow rate, a stainless steel sinter with void features in the range 0.5−1.5 μm was placed either side of the sample, and these sinters were themselves supported by coarser sinters with voids greater than 20 μm. The entry and exit channels had an internal diameter of 120 μm.[40] The flow from these channels onto the entry sinters, and out from the symmetrical exit sinters, followed the contours of PTFE inserts designed to minimize dead volume. A 10.0 mm brass lengthening column between the sinters provided the necessary volume to contain the sample. Seals for the high pressure liquid flowing through the chamber were provided by O-rings, each located in a groove, but standing proud of the surface, on one metal face and pressed against a flat opposing face.

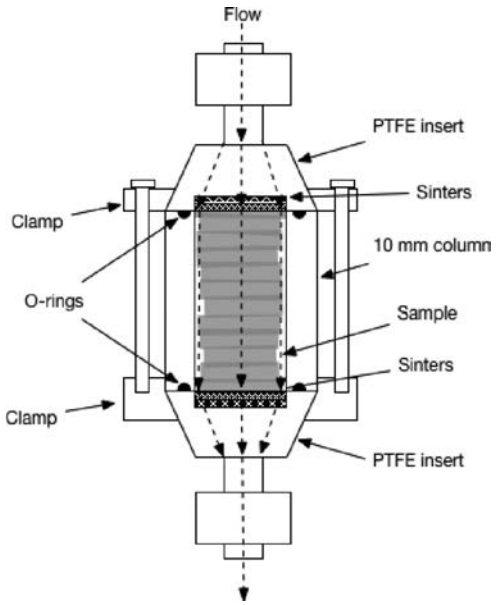

Figure 2. Vertical cross-sectional schematic of the finite length column (FLC).

To provide solvent flow through the sample, the cell was connected to a Hewlett-Packard (now Agilent) 1050 high-performance liquid chromatograph (HPLC), controlled by ChemStation software. The concentration of vanillin was measured with a diode array detector (DAD) calibrated at a wavelength of 279 nm, every 1.6 s. The response of the detector to vanillin was highly linear up to 50 mg L^{-1} (R^2 = 0.9992).

Experimental Methodology. Prior to each experiment, the FLC was loaded with the chosen powdered sample. On average, the manual packing achieved was 85% by mass of the packing achieved with the envelope pycnometer.

The overall methodology followed was that developed by Ruthven et al.[15] for the ZLC, namely to saturate the sample with a solution, then change to solvent and measure the lag caused by diffusion of the dissolved species out of the sample. The initial conditioning of the sample was carried out by flowing ethanol at 0.5 cm^3 min^{-1} through it for 30 min (pressure during this period was approximately 14.6 ± 0.2 bar). Then 50% by volume of a solution of 100 mg dm^{-3} vanillin in ethanol was added to the flow stream, and the overall flow rate increased to 4 cm^3 min^{-1} for 30 min. The pressure to maintain the required flow rate was 123.4 ± 2.7 bar. Finally, flow was switched back to pure ethanol for 45 min, at a pressure, to maintain the same flow rate, of 28.2 ± 2.2 bar, and the lag in the concentration profile of the solution emerging from the sample was measured. The time at which the flow was switched back to pure ethanol is shown as the time axis origin (t = 0) in the graphs below.

Void Network Modeling Methodology. PoreXpert represents the void structure of a porous medium as a series of identical interconnected unit cells with periodic boundary conditions. Each unit cell of side length h comprises an array of $n \times n \times n$ pores $\{n \in \mathbb{Z} | 5 \leq n \leq 30\}$, equally spaced in a Cartesian cubic-close-packed array. In this work, n = 15. Void shapes are simplified to cubic pores, positioned with their centers at each node, connected by up to six cylindrical throats in each Cartesian direction. The simplification of the void

DOI: 10.1021/acs.iecr.5b02362
Ind. Eng. Chem. Res. 2015, 54, 9938−9947

shapes does not greatly affect the percolation or diffusion properties, which depend mainly on those other properties which are quantitatively matched to experiment, namely the volume, cross-sectional size and connectivity of the voids.

The characteristics of the unit cell are adjusted using an eight-dimensional Boltzmann-annealed amoeboid simplex, which moves around parameter space searching for an optimum void network that matches closely the experimentally measured porosity and percolation characteristics of the porous media. The five parameters defining the parameter space are throat skew, throat spread, pore skew, connectivity, and correlation level.[37] There are also three Boolean parameters: namely whether the network is fully connected, whether the experimental porosity is achieved, and whether all the void features are separate in space without geometric overlap.

Throat spread and throat skew define the variance and the asymmetry of the throat size distribution. The distribution follows an Euler beta function, which encompasses Gaussian-like and Poisson-like types, as well as bimodal distributions with most void sizes at close to d_{min} and d_{max}.

The pore skew parameter bulks up the volume of pores, and compensates for the difficulty of achieving, in a regularly spaced and hence inefficiently packed matrix of void features, a value of porosity matching the value obtained experimentally. The representation of this effect in the resulting unit cells is that there are large numbers of pores at the maximum size of the distributions. These could be individual pores, but are more likely to be clusters of pores which are undifferentiated by the mercury porosimetry, because they comprise a single narrow throat allowing entry into a cluster of pores and throats all with dimensions greater than the single narrow throat. Examples are discussed below.

The tracking of weighted routes through the structure allows an estimation of tortuosity, defined as the ratio of the median of actual path lengths through a sample to the straight path across the unit cell.[38] The tortuous path length through a cluster is assumed to be the same as if the cluster was in fact a large pore of the same volume. Because all the pores and throats in the cluster are larger than the access throats to the cluster, and the access throats therefore control the overall tortuosity of the cluster, this is a reasonable approximation, which has been validated in a previous work.[38] Van Brakel[41] formulated an equation that relates the diffusion coefficient (D) with the tortuosity of the sample (τ), porosity of the sample (ϕ), and the bulk diffusion coefficient (D_{12}):

$$\frac{D}{D_{12}} = \frac{\phi}{\tau^2} \tag{7}$$

Connectivity is defined as the average of the local connectivities between neighboring voids averaged over the entire sample, or in this case over the entire representation of the sample, i.e., over a single unit cell. The average is typically found to be around 3.5, although it is recognized that in natural samples, much higher local connectivities can be observed. The short-range size autocorrelation is quantified by a correlation level parameter, which can vary between 0, for a random structure, and 1, in which throats, and hence adjoining pores, are grouped into predetermined loci according to their size. The six predetermined loci or "structure types" are completely random, vertically banded (i.e., in the $\hat{\mathbf{y}}\hat{\mathbf{z}}$ plane) (abbreviated as VB below), horizontally banded (in the $\hat{\mathbf{x}}\hat{\mathbf{y}}$ plane) with large surface features at $z = h$ leading into smaller internal features (large to small) (HLS), horizontally banded with small surface features leading into larger internal features (small to large) (HSL), horizontally banded with large surface throats, and structures with a central spherical zone of small voids (SCZ) or large voids (LCZ).

The void network resulting from this optimization procedure is not unique, so a set of several stochastic realizations may be generated which match the experimental intrusion characteristics. The most representative simulated structure for each sample is then found by choosing realizations for which none of the fitting parameters has a deviation from the mean of the set larger than the standard deviation σ of the set. If more than one sample meets that criterion, then the sample with all parameters closest to the mean was chosen. This approach is exemplified in Table 3 below.

RESULTS

Mercury Intrusion. The mercury intrusion curves are shown in Figure 3. After compensation for particle agglomeration effects, as described previously, the resulting portions of the mercury intrusion curves were all bimodal to some degree, as shown by an intermediate reduction in gradient. These points, shown as small vertical lines in Figure 3, were taken to mark the changeovers from intrusion of the interparticle space to intrusion of the intraparticle space. The intrusion volume at which this changeover occurred was used to calculate the intraparticle porosity.

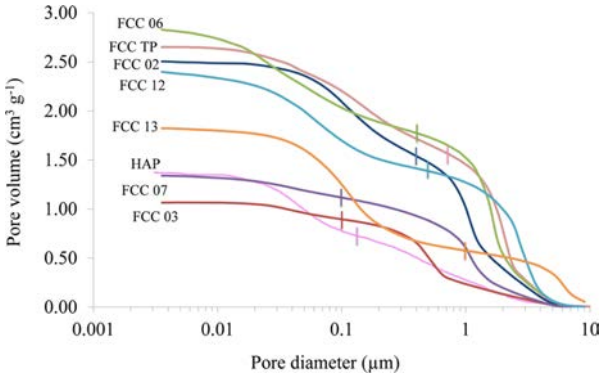

Figure 3. Mercury intrusion porosimetry curves for all FCC samples and HAP; a vertical line indicates the point at which the data were cut to model the intraparticle structure with PoreXpert.

Treatment of Diffusion Data from FLC. Figure 4 shows graphs of the natural logarithm of relative concentration plotted against time. For clarity, only a representative selection of the sample characteristics are shown; all results are shown in Figure S39 of the Supporting Information. The abscissa is labeled as "corrected time" because the experiment start times are adjusted to allow direct comparison of the curves, in the knowledge that the absolute start time of the experiment does not affect the measured slopes. The point at which the HPLC pump switches from vanillin in ethanol to pure ethanol is the point at which corrected time = 0, i.e., 60 min after the start of the entire experimental protocol as described above. The thickness of the plots represents $\pm\ \sigma$, where σ is the standard deviation of a series of at least two, and normally three, analytical replicates. It can be seen that σ does not increase with time for the blank, GCC and HAP control experiments, but does increase for most of the porous samples.

DOI: 10.1021/acs.iecr.5b02362
Ind. Eng. Chem. Res. 2015, 54, 9938−9947

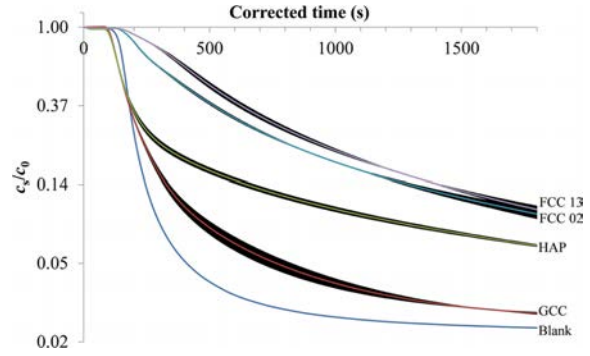

Figure 4. c_s/c_0 on a logarithmic axis versus time for the control samples and two of the FCC samples. Extents of $\pm$ σ of three replicates per packing are shown as black outlines.

In the context of the approach to data treatment described above, only the long time sections of the curves in Figure 4 were used, when the effects of packing, described below, and the line-broadening type of effects had become small. For comparison, slopes of the semilogarithmic curves were measured over two different sections of the curve, one in the range t = 1200−1400 s, and the other 1600−1800 s. All these 200 s sections were themselves linear (R^2 > 0.997), even though it can be seen that over the entire time of the experiments, the curves were nonlinear when plotted semilogarithmically, because of the mixed inter- and intraparticle effects.

Figure 5 shows the results for FCC 02 when the sample is completely demounted, and a fresh sample packed into the

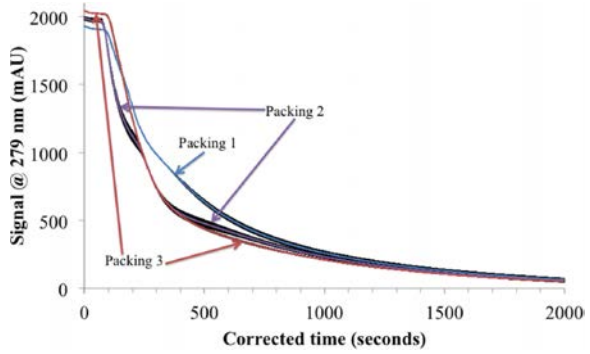

Figure 5. Reduction in detector signal with time for FCC 02 replicates, each freshly packed. The standard deviations of three analytical replicates are shown as a black thickening of the lines.

FLC; the vertical axis shows the absolute signal from the detector, to demonstrate that the normalization shown in Figure 4 does not degrade the experimental results. It confirms that different packing affects the first section of the concentration versus time curve, where interparticle effects dominate, but not the later part of the curve where the decline in concentration is rate-limited by intraparticle diffusion effects.

The slopes of these plots yield (D'/r^2), as explained above. Although, as shown in the Supporting Information, the particles cover a range of sizes, for purposes of the diffusion coefficient calculation we use the median size, $r = d_{50}$. Then applying the relation $r = d_{50}/2$, Table 1, values of (D') may be obtained, Table 2. It can be seen that the phase 1 diffusion coefficients are always greater than those of phase 2, demonstrating that during

Table 2. Effective Diffusion Coefficients D' Calculated at t = 1200−1400 s (Phase 1) and 1600−1800 s (Phase 2)

sample	intraparticle porosity	D' (phase 1) (10^{-16} m^2 s^{-1})	D' (phase 2) (10^{-16} m^2 s^{-1})
GCC	n/a	7.96	3.93
HAP	34.2	7.58	6.17
FCC TP	25.9	7.53	6.85
FCC 02	24.4	5.17	4.05
FCC 03	10.4	1.33	1.06
FCC 06	25.2	5.30	3.97
FCC 07	12.3	7.37	6.55
FCC 12	29.6	24.5	19.7
FCC 13	37.0	135	106

phase 1, and possibly phase 2, the diffusion effects have not yet converged onto a single process with a constant diffusion coefficient, as discussed below.

Figure 6 shows the dependence of the effective diffusion coefficients on particle size. It can be seen that there is a strong dependence, as shown by a coefficient of determination R^2 = 0.99 for both phase 1 and phase 2 for a second-order polynomial fit to logarithmic values of D'. Figures S40 and S41 of the Supporting Information show a possible weak dependency on porosity if FCC 13 is regarded as an outlier, and no dependence on surface area.

Modeling. The entire curves shown in Figure 3 were modeled using PoreXpert. Also modeled were the separate higher pressure (smaller diameter) and lower pressure sections. Figure S 42 of the Supporting Information gives an example of an entire mercury intrusion curve for sample FCC03, used as input for the network simulation software, with the simulated curve overlaid to show the closeness of fit. The structure type was HLST, with fitting parameters shown in Table 3, and the discrepancy of fit was 1.4%, Table 4 below. Stochastic realization 5 was chosen as the representative structure, because all of the parameter values were within $\pm$ σ of the mean. Values outside this range are underlined in Table 3.

Figure 7 shows the PoreXpert unit cell of the interparticle void space of the simulated porous structure of FCC 03 corresponding to Figure S42 of the Supporting Information and Table 3. Figure 7 also shows the unit cell of the intraparticle void space simulation. Figure S43 of the Supporting Information displays the corresponding throat and pore-size distributions; both unit cells contain large numbers of pores of maximum size that are labeled in panels c and d as undifferentiated: they could be either single pores or clusters. For the interparticle void space, with pore skew of 1.6, they are likely to be single pores. For the intraparticle space, with a pore skew of 6.1, they are more likely to be clusters, and so are shown with textured surfaces in Figure 7, just visible in the enlargement shown in Figure S45.

To reveal more of the structural characteristics of the void networks, the properties of which are governed by the sizes of the throats often obscured by pores in the figures, both unit cells are shown injected by mercury (dark gray) to 50% of their void volume from the top faces in the figures. It can be seen that percolation in the intrapore structure shown on the right of Figure 7 forms an almost planar percolation front, whereas percolation through the interpore structure is much more heterogeneous. Percolation is governed by throats, rather than pores, and this difference is in accord with the throat size distributions shown in Figure S 43 (a) and (b) of the

DOI: 10.1021/acs.iecr.5b02362
Ind. Eng. Chem. Res. 2015, 54, 9938−9947

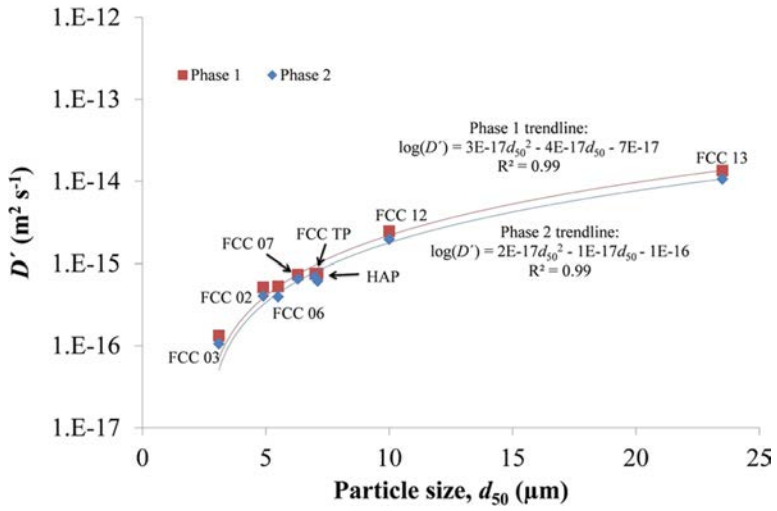

Figure 6. Dependence of D' on particle size.

Table 3. Fitting Parameters for FCC 03 When Fitting with Five Different Stochastic Realizations[a]

	stochastic realization number				
parameter	1	2	3	4	5
pore skew	6.80	9.68	5.12	1.37	1.48
throat skew	−15.16	−32.48	−27.31	46.12	0.46
throat spread	0.99	0.96	0.89	0.91	0.92
connectivity	4.35	4.26	4.03	3.99	4.12
correlation level	0.06	0.07	0.09	0.01	0.04
distance (%)	1.35	1.65	1.36	1.30	1.37
tortuosity	1.20	1.20	1.13	1.40	1.33

[a]Values greater than $\pm\ \sigma$ from the mean are underlined.

Supporting Information, which are bimodal and Poisson-like, respectively.

Table 4 provides a summary of the fits to all of the overall and intraparticle sections of the mercury intrusion curves, in terms of structure type and fit discrepancies. It also lists the corresponding simulated tortuosities.

There is no discernible trend when the quantity $(\phi/\tau_{overall}^2)$ is plotted against D'. However, a trend does emerge for $(\phi/\tau_{intraparticle}^2)$ against D', Figure 8. In terms of exponential relationships, which appear linear on the log−linear plots, R^2 = 0.63 and 0.62 for phase 1 and phase 2, respectively.

DISCUSSION

Unlike many investigations of porous materials that use highly ordered or model systems, this investigation is of real systems destined for a specific purpose: that of delayed drug or flavor release. Rather than a single sample, we have chosen to study a range of samples with different properties and morphologies. The flushing and diffusion processes are complex, and difficult to resolve. There are uncertainties introduced by the experimental approach; the HPLC system causes line broadening, and the packing of samples into the FLC, rather than ZLC, sample chamber, can never be entirely reproducible. The modeling involves a simplification of void shapes and positions, and a sometimes imperfect fit to the experimental intrusion characteristics, particularly for highly bimodal sample FCC 13, Table 4.

Therefore, one needs to ask to what extent the investigation is valid. Validation comes from several sources. The first is the difference between rate of concentration reduction for the porous samples and those of the blank and GCC, Figure 4, the latter with a similar particles size to the porous samples. The rate of reduction for all of the porous samples is much slower than either the blank or GCC. Second, the replicates showing the effect of packing of the same sample, Figure 5, confirm that the measured diffusion coefficients in this work, taken from the sections of the curve above 1200 s, are unaffected by packing and hence interparticle effects, but are rate-limited by the intraparticle effects. Third, it can be seen in Figure 5 that although the signal for packing 2 decreases monotonically, it

Table 4. PoreXpert Structure Types, Fit Discrepancies, and Calculated Tortuosities

	overall			intraparticle		
sample	structure type	discrepancy of fit (%)	overall tortuosity	structure type	discrepancy of fit (%)	overall tortuosity
HAP	HLS	1.7	1.73	HLS	1.1	1.27
FCC TP	VB	1.3	1.40	SCZ	1.4	1.13
FCC 02	VB	1.3	1.33	VB	1.2	1.20
FCC 03	HLST	1.4	1.33	HLS	1.2	1.27
FCC 06	VB	1.4	1.27	HLS	1.7	1.27
FCC 07	VB	1.2	1.27	VB	1.9	1.20
FCC 12	VB	2.3	1.27	HSL	1.8	1.13
FCC 13	HLS	3.8	1.33	HSL	1.2	1.20

DOI: 10.1021/acs.iecr.5b02362
Ind. Eng. Chem. Res. 2015, 54, 9938−9947

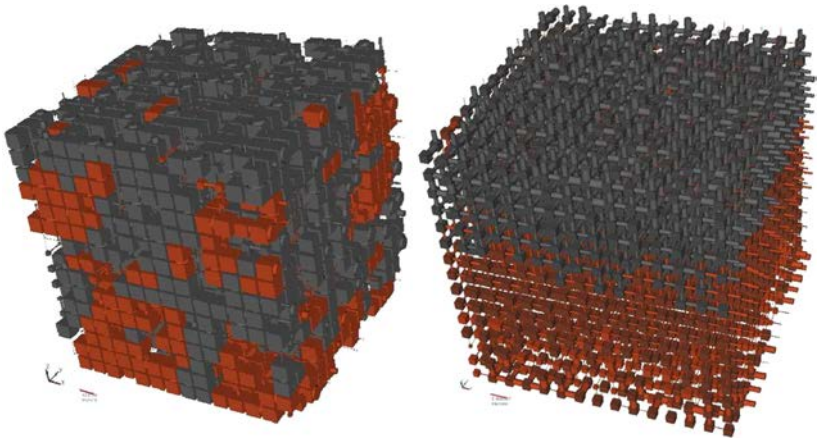

Figure 7. Simulation of the void space of the sample FCC03 filled 50% by volume of mercury from the top face. For clarity, the void space is shown solid, the solid phase is transparent, and the mercury is dark gray. The left structure is the simulated interparticle space, and the small scale bar bottom left is of length 12.6 μm. The right structure is the intraparticle space, and the small scale bar bottom left is of length 0.41 μm, i.e., twenty-eight times smaller than the left-hand structure.

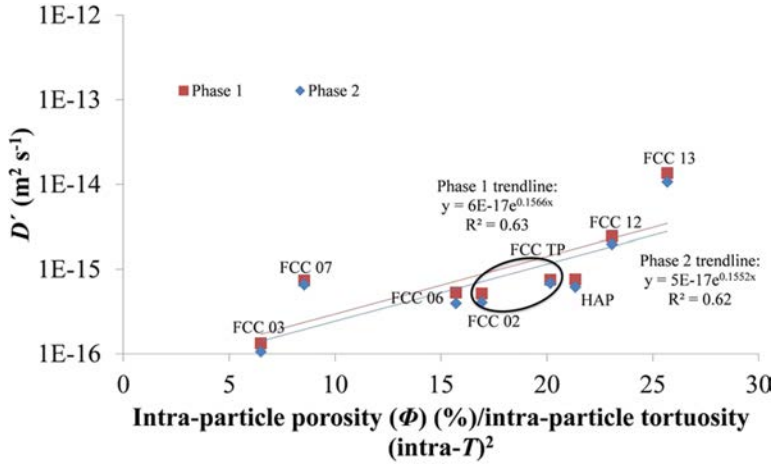

Figure 8. Plot of intraparticle tortuosity scaled with respect to intraparticle porosity versus D'.

has variations in its rate of decrease, such that its second derivative is not monotonic. However, replicate experiments with the same packing closely track along the same curve. This supports the theoretical derivation cited earlier[22] which shows that at shorter times the rate of concentration decrease is dependent on the time constant for the washout process. It can be seen that this washout process is highly reproducible, and that therefore the flow regime is behaving reproducibly under conditions of entirely stable packing and low Reynolds and Péclet numbers.

The validation of the predecessor to PoreXpert, known as Pore-Cor, has included a comparison of the void sizes when the model was mathematically microtomed, compared to image analysis of actual microtomed samples. Although the model voids were 1 or 2 orders of magnitude too small compared to experiment, use of the fallacious capillary bundle model produced voids which were some 8 orders of magnitude too small.[42] The calculation of tortuosity with the current, PoreXpert, model has recently been validated against experimental measurements on sandstone and limestone.[38]

An overall validation is the trend shown in Figure 8. Equation 7 shows that this is effectively a graph of D_{model}/D_{12} against D'. Because D_{12} is constant, then if only intraparticle effects were present, there would be a linear relationship between the two. In practice, there is an approximate logarithmic relationship as shown, due to the changeover from mixed inter- and intraprocesses to only intraparticle processes. However, we believe that the relationships shown, with R^2 values of 0.63 and 0.62, are strong enough to provide validation.

Figure 6 shows a strong dependence of D' on particle size. However, Figures S40, S41, S46, and S47 of the Supporting Information show no trends of D' with porosity, surface area, intraparticle porosity, and intraparticle tortuosity. It therefore follows that these three relationships must be dominated by morphological differences within the intraparticle voidage. A closer examination of the graphs can reveal something of the nature of this domination. Take the case of samples FCC TP and FCC 02, which can be seen in Figure 1 and Figure 5, as summarized in Table 1, to have morphologies very similar to each other. Inspection of Figures S40 and S41 of the Supporting Information show that these two samples cluster closely with respect to porosity and surface area, as highlighted by oval lines on the figures. However, they vary with respect to intraparticle tortuosity, Figure S47, which implies subsurface differences in the void space morphology of these particles not visible in electron micrographs of their surfaces, Figure 1.

DOI: 10.1021/acs.iecr.5b02362
Ind. Eng. Chem. Res. 2015, 54, 9938−9947

CONCLUSIONS

We have described a method of measuring combined diffusion effects of a dissolved liquid species loaded into the void space of a pack of interporous particles. The results are validated by comparison with blank experiments and experiments with nonporous particles of a similar size. The results show that diffusion is dependent on particle size, and that the intraparticle tortuosity, modeled by the inversion of mercury intrusion characteristics using PoreXpert, trends with diffusion when scaled by porosity.

The approach offers an important new indirect method of measuring intraparticle tortuosity, which cannot be measured directly. The validation of the experimental method and the modeling, and the demonstration of the dependence on morphology from the close tracking of two samples, opens the way for the tailoring of morphology and other properties to optimize diffusion characteristics for the optimization of functionalized calcium carbonate and other porous materials for applications such as delayed drug and flavor release. Further experiments are now being carried out with aqueous solutions and simulated digestive fluids, and with samples in which the active has been directly loaded onto the porous substrate.

ASSOCIATED CONTENT

Supporting Information

The Supporting Information is available free of charge on the ACS Publications website at DOI: 10.1021/acs.iecr.5b02362.

Particle size distributions of the samples; cumulative distributions against size; pore size distributions and throat size distributions hydroxyapatite, FCC TP, FC CTP, FCC 02, FCC 03, FCC 06, FCC 07, FCC 12, and FCC 13; scanning electron micrographs of ground calcium carbonate, hydroxyapatite, FCC TP, FCC 02, FCC 03, FCC 06, FCC 07, FCC 12, and FCC 13; vanillin concentration vs time; dependence of D' on porosity and surface area; experimental and simulated mercury intrusion characteristic for sample FCC 03; numbers of pore-throats and pores within the single unit cells of sample FCC 03; simulation of the interparticle void space of the sample FCC 03 filled 50% by volume of mercury from the top face; simulation of the intraparticle void space of the sample FCC 03 filled 50% by volume of mercury from the top face; plot of intraparticle porosity versus D'; plot of intraparticle tortuosity versus D' (PDF).

AUTHOR INFORMATION

Corresponding Author

*G. P. Matthews. E-mail: p.matthews@plymouth.ac.uk.

Notes

The authors declare no competing financial interest.

ACKNOWLEDGMENTS

The financial support of Omya International AG is gratefully acknowledged.

REFERENCES

(1) Gane, P. A. C.; Ridgway, C. J.; Barceló, E. Analysis of Pore Structure Enables Improved Tablet Delivery Systems. *Powder Technol.* **2006**, *169*, 77.

(2) Machado, J. A. T.; Zaman, S.; Baleanu, D. Fractional Order Modelling of Zero Length Column Desorption Response for Adsorbents with Variable Particle Sizes. *Cent. Eur. J. Phys.* **2013**, *11*, 881.

(3) Fujiwara, M.; Shiokawa, K.; Morigaki, K.; Zhu, Y.; Nakahara, Y. Calcium Carbonate Microcapsules Encapsulating Biomacromolecules. *Chem. Eng. J.* **2008**, *137*, 14.

(4) Pedersen, K. M.; Andersen, J. B. Particulate material for controlled release of active ingredients. U.S. Patent 20,120,321,751 A1, December 20, 2012.

(5) Ueno, Y.; Futagawa, H.; Takagi, Y.; Ueno, A.; Mizushima, Y. Drug-incorporating Calcium Carbonate Nanoparticles for a New Delivery System. *J. Controlled Release* **2005**, *103*, 93.

(6) Lucas-Girot, A.; Verdier, M.-C.; Tribut, O.; Sangleboeuf, J.-C.; Allain, H.; Oudadesse, H. Gentamicin-Loaded Calcium Carbonate Materials: Comparison of Two Drug-Loading Modes. *J. Biomed. Mater. Res., Part B* **2005**, *73B*, 164.

(7) Baradari, H.; Damia, C.; Dutreih-Colas, M.; Laborde, E.; Pécout, N.; Champion, E.; Chulia, D.; Viana, M. Calcium Phosphate Porous Pellets as Drug Delivery Systems: Effect of Drug Carrier Composition on Drug Loading and in Vitro Release. *J. Eur. Ceram. Soc.* **2012**, *32*, 2679.

(8) Chevalier, E.; Viana, M.; Cazalbou, S.; Makein, L.; Dubois, J.; Chulia, D. Ibuprofen-loaded Calcium Phosphate Granules: Combination of Innovative Characterization Methods to Relate Mechanical Strength to Drug Location. *Acta Biomater.* **2010**, *6*, 266.

(9) Cosijns, A.; Vervaet, C.; Luyten, J.; Mullens, S.; Siepmann, F.; van Hoorebeke, L.; Masschaele, B.; Cnudde, V.; Remon, J. P. Porous Hydroxyapatite Tablets as Carriers for Low-dosed Drugs. *Eur. J. Pharm. Biopharm.* **2007**, *67*, 498.

(10) Öner, M.; Yetiz, E.; Ay, E.; Uysal, U. Ibuprofen Release from Porous Hydroxyapatite Tablets. *Ceram. Int.* **2011**, *37*, 2117.

(11) Sasikumar, S. Effect of Particle Size of Calcium Phosphate Based Bioceramic Drug Delivery Carrier on the Release Kinetics of Ciprofloxacin Hydrochloride: an in Vitro Study. *Front. Mater. Sci.* **2013**, *7*, 261.

(12) Son, J. S.; Appleford, M.; Ong, J. L.; Wenke, J. C.; Kim, J. M.; Choi, S. H.; Oh, D. S. Porous Hydroxyapatite Scaffold with Three-dimensional Localized Drug Delivery System Using Biodegradable Microspheres. *J. Controlled Release* **2011**, *153*, 133.

(13) Chen, H.; Leng, S. Rapid Synthesis of Hollow Nano-structured Hydroxyapatite Microspheres via Microwave Transformation Method using Hollow CaCO3 Precursor Microspheres. *Ceram. Int.* **2015**, *41*, 2209.

(14) Eic, M.; Ruthven, D. M. A New Experimental Technique for Measurement of Intracrystalline Diffusivity. *Zeolites* **1988**, *8*, 40.

(15) Ruthven, D. M.; Stapleton, P. Measurement of Liquid Phase Counter-Diffusion in Zeolite Crystals by the ZLC Method. *Chem. Eng. Sci.* **1993**, *48*, 89.

(16) Micke, A.; Kočiřik, M.; Bülow, M. Theory of Zero Length Column Chromatography with the Condition of a Well-stirred Sorbing Zone. *Microporous Mater.* **1993**, *1*, 373.

(17) Duncan, W. L.; Möller, K. P. On the Diffusion of Cyclohexane in ZSM-5 Measured by Zero-Length-Column Chromatography. *Ind. Eng. Chem. Res.* **2000**, *39*, 2105.

(18) Loos, W. P.; Jan-Baptiste; Verheijen, P. J. T.; Moulijn, J. A. Improved Estimation of Zeolite Diffusion Coefficients from Zero-Length Column Experiments. *Chem. Eng. Sci.* **2000**, *55*, 51.

(19) Brandani, F.; Ruthven, D.; Coe, C. G. Measurement of Adsorption Equilibrium by the Zero Length Column (ZLC) Technique Part 1: Single-Component Systems. *Ind. Eng. Chem. Res.* **2003**, *42*, 1451.

(20) Ruthven, D. M.; Vidoni, A. ZLC Diffusion Measurements: Combined Effect of Surface Resistance and Internal Diffusion. *Chem. Eng. Sci.* **2012**, *71*, 1.

(21) Brandani, F. Development and Application of the Zero Length Column (ZLC) Technique for Measuring Adsorption Equilibria. Ph.D. Dissertation, The University of Maine, Orono, ME, 2002.

(22) Brandani, S.; Ruthven, D. M. Analysis of ZLC Desorption Curves for Liquid Systems. *Chem. Eng. Sci.* **1995**, *50*, 2055.

DOI: 10.1021/acs.iecr.5b02362
Ind. Eng. Chem. Res. 2015, 54, 9938−9947

(23) Cherntongchai, P.; Brandani, S. Liquid Phase Counter-Diffusion Measurements of Aromatics in Silicalite Using the ZLC Method. *Adsorption* **2003**, *9*, 197.
(24) Zabka, M.; Rodrigues, A. E. Measurement of Pore Diffusivity of R,S-a-Tetralol Enantiomers in Chiral Adsorbent CHIRALPAK AD by Zero Length Column Method. *Sep. Purif. Technol.* **2007**, *57*, 74.
(25) Cavalcante, C. L. J.; Ruthven, D. M. Adsorption of Branched and Cyclic Paraffins in Silicalite. 2. Kinetics. *Ind. Eng. Chem. Res.* **1995**, *34*, 185.
(26) Brandani, S. Effects of Nonlinear Equilibrium on Zero Length Column Experiments. *Chem. Eng. Sci.* **1998**, *53*, 2791.
(27) Brandani, S.; Jama, M. A.; Ruthven, D. M. ZLC Measurements under Non-Linear Conditions. *Chem. Eng. Sci.* **2000**, *55*, 1205.
(28) Hufton, J. R.; Ruthven, D. M. Diffusion of Light Alkanes in Silicalite Studied by the Zero Length Column Method. *Ind. Eng. Chem. Res.* **1993**, *32*, 2379.
(29) Brandani, S.; Ruthven, D. M. Analysis of ZLC Desorption Curves for Gaseous Systems. *Adsorption* **1996**, *2*, 133.
(30) Eckhardt, B. Introduction. Turbulence Transition in Pipe Flow: 125th Anniversary of the Publication of Reynolds' Paper. *Philos. Trans. R. Soc., A* **2009**, *367*, 449.
(31) Brandani, S. Analytical Solution for ZLC Desorption Curves with Bi-Porous Adsorbent Particles. *Chem. Eng. Sci.* **1996**, *51*, 3283.
(32) Duncan, W. L.; Möller, K. P. A Zero Length Criterion for ZLC Chromatography. *Chem. Eng. Sci.* **2000**, *55*, 5415.
(33) Ruthven, D. M.; Brandani, S.; Eic, M. In *Adsorption and Diffusion*; Karge, H., Weitkamp, J., Eds.; Springer: Berlin, Heidelberg, 2008.
(34) Gribble, C. M.; Matthews, G. P.; Laudone, G. M.; Turner, A.; Ridgway, C. J.; Schoelkopf, J.; Gane, P. A. C. Porometry, Porosimetry, Image Analysis and Void Network Modelling in the Study of the Pore-level Properties of Filters. *Chem. Eng. Sci.* **2011**, *66*, 3701.
(35) Laudone, G. M.; Matthews, G. P.; Gane, P. A. C. Modelling Diffusion from Simulated Porous Structures. *Chem. Eng. Sci.* **2008**, *63*, 1987.
(36) Laudone, G. M.; Matthews, G. P.; Gane, P. A. C.; Ridgway, C. J.; Schoelkopf, J. Estimation of the Effective Particle Sizes within a Paper Coating Layer Using a Void Network Model. *Chem. Eng. Sci.* **2005**, *60*, 6795.
(37) Price, J. C.; Matthews, G. P.; Quinlan, K.; Sexton, J.; Matthews, A. G. de G.; Depth, A. G. A. Filtration Model of Straining within the Void Networks of Stainless Steel Filters. *AIChE J.* **2009**, *55*, 3134.
(38) Laudone, G. M.; Gribble, C. M.; Jones, K. L.; Collier, H.; Matthews, G. P. Validated a Priori Calculation of Tortuosity in Porous Materials Including Sandstone and Limestone. *Chem. Eng. Sci.* **2015**, *131*, 109.
(39) Gustav, M. Beiträge. zur Optik trüber Medien, Speziell Kolloidaler Metallösungen. *Ann. Phys.* **1908**, *330*, 377.
(40) Gribble, C. M. Surface Adsorption and Pore-Level Properties of Mineral and Related Systems of Relevance to the Recycling of Paper. Ph.D. Dissertation, The University of Plymouth, Devon, U. K., 2010.
(41) van Brakel, J.; Heertjes, P. M. Analysis of Diffusion in Macroporous Media in Terms of a Porosity, a Tortuosity and a Constrictivity Factor. *Int. J. Heat Mass Transfer* **1974**, *17*, 1093.
(42) Matthews, G.; Canonville, C.; Moss, A. K. Use of a Void Network Model to Correlate Porosity, Mercury Porosimetry, Thin Section, Absolute Permeability and NMR Relaxation Time Data for Sandstone Rocks. *Phys. Rev. E* **2006**, *73*, 031307.

DOI: 10.1021/acs.iecr.5b02362
Ind. Eng. Chem. Res. 2015, 54, 9938−9947

Diffusion and tortuosity in porous functionalised calcium carbonate

Supporting Information

Charlotte L. Levy,[†] Giuliano M. Laudone,[†] G. Peter Matthews,[*,†] Christopher M. Gribble,[†] Andrew Turner,[†] Cathy J. Ridgway ,[‡] Daniel E. Gerard,[‡] Patrick A. C. Gane,[‡,¶] and Joachim Schölkopf[‡]

†*Faculty of Science and Engineering, Plymouth University, Drake Circus, Plymouth, PL4 8AA, UK*

‡*Omya Development AG, Baslerstrasse 42, P.O. Box 335, CH-4665, Oftringen, Switzerland*

¶*School of Chemical Technology, Department of Forest Products Technology, Aalto University, 00076 Aalto, Helsinki, Finland*

E-mail: *p.matthews@plymouth.ac.uk

Particle Size Distributions

This section provides further information regarding the particle size distributions of the samples.

Table S 1: The particle size distributions of the samples, provided by Omya AG.

Sample	d_{50} / μm	d_{98} / μm
FCC 02	4.9	9.4
FCC 03	3.1	6.9
FCC 06	5.5	10.6
FCC 07	6.3	18.5
FCC 12	10.0	25.0
FCC 13	23.5	40.4

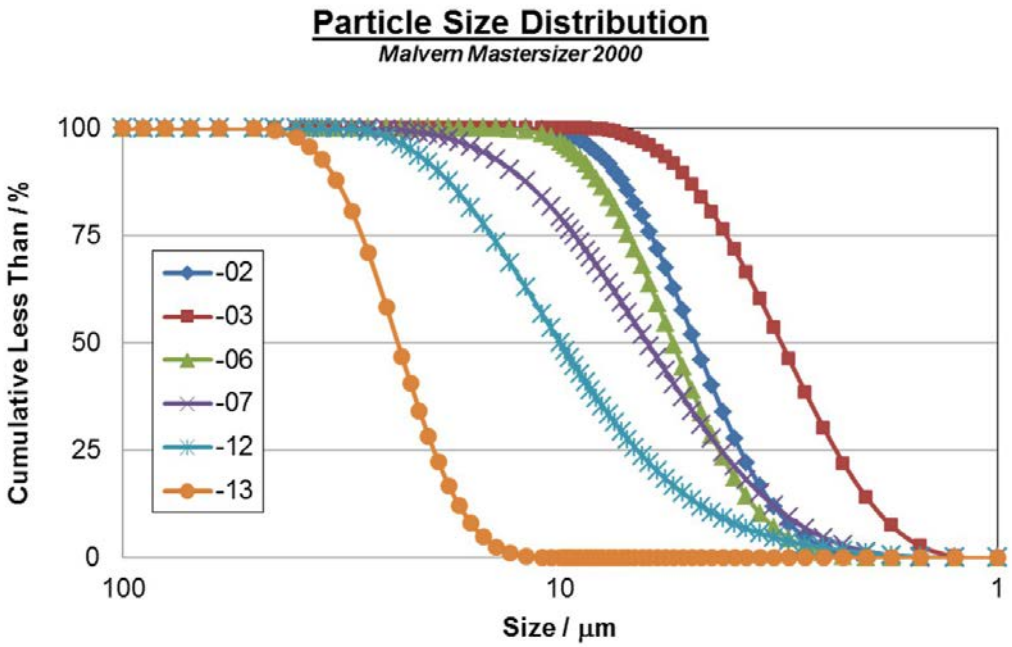

Fig. S 1: Cumulative distributions against size

PoreXpert Pore and Throat Size Distributions

This section provides further information regarding the pore and throat size distributions of the samples.

Hydroxyapatite (HAP)

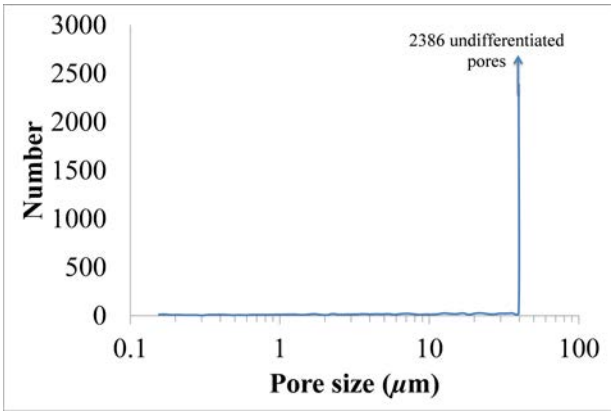

Fig. S 2: Pore size distribution, generated by PoreXpert, of hydroxyapatite (HAP).

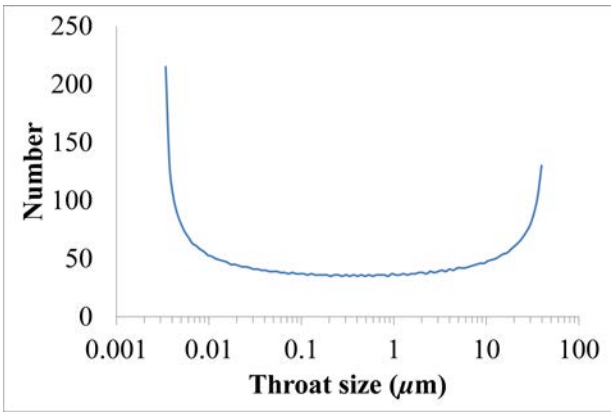

Fig. S 3: Throat size distribution, generated by PoreXpert, of hydroxyapatite (HAP).

FCC TP

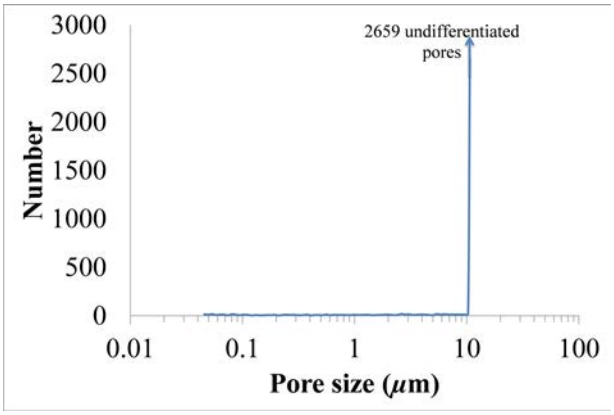

Fig. S 4: Pore size distribution, generated by PoreXpert, of FCC TP.

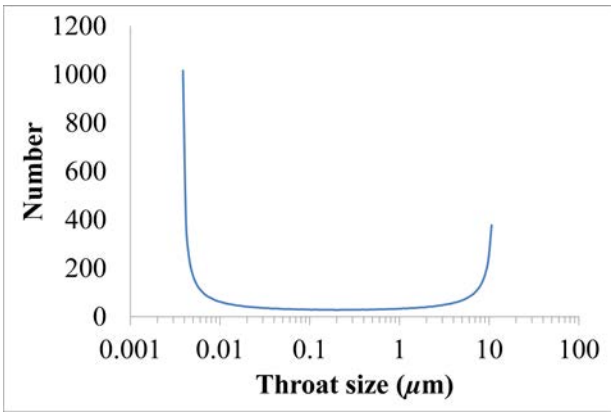

Fig. S 5: Throat size distribution, generated by PoreXpert, of FC CTP.

FCC 02

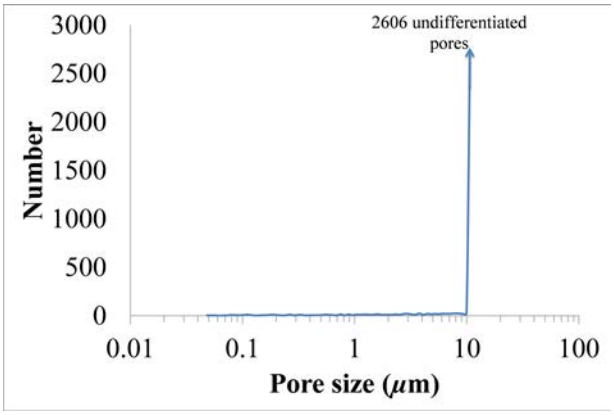

Fig. S 6: Pore size distribution, generated by PoreXpert, of FCC 02.

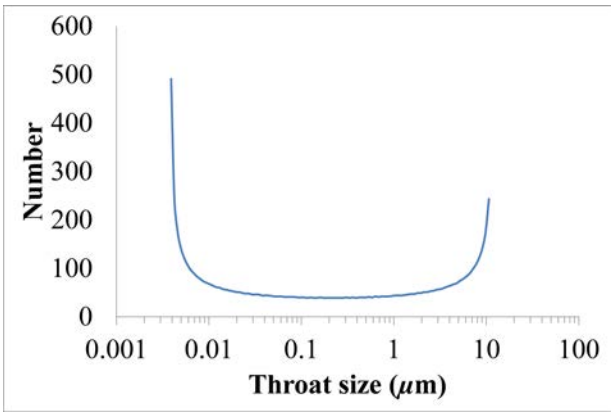

Fig. S 7: Throat size distribution, generated by PoreXpert, of FCC 02.

FCC 03

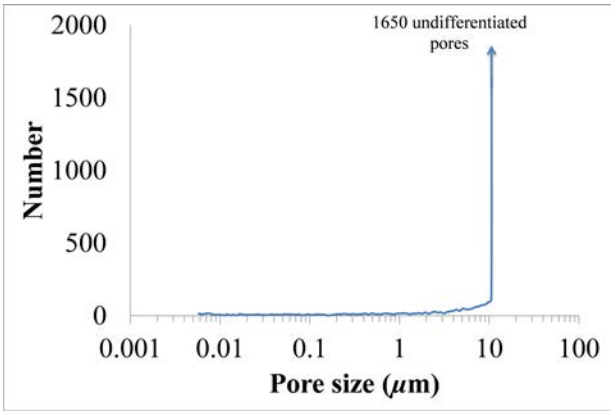

Fig. S 8: Pore size distribution, generated by PoreXpert, of FCC 03.

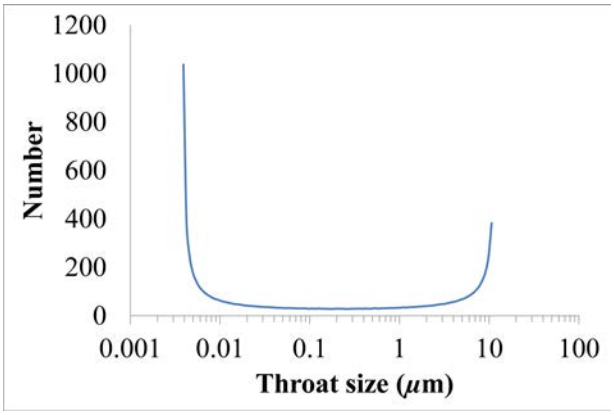

Fig. S 9: Throat size distribution, generated by PoreXpert, of FCC 03.

FCC 06

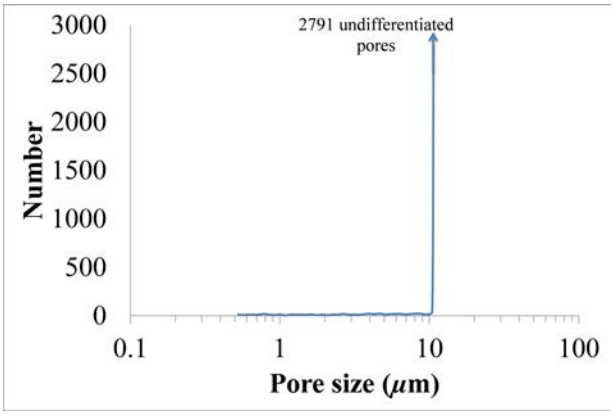

Fig. S 10: Pore size distribution, generated by PoreXpert, of FCC 06.

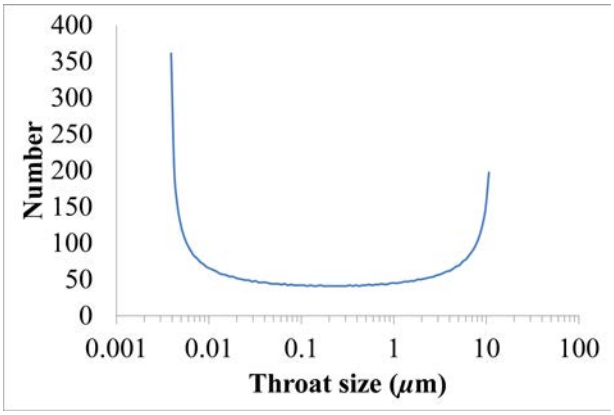

Fig. S 11: Throat size distribution, generated by PoreXpert, of FCC 06.

FCC 07

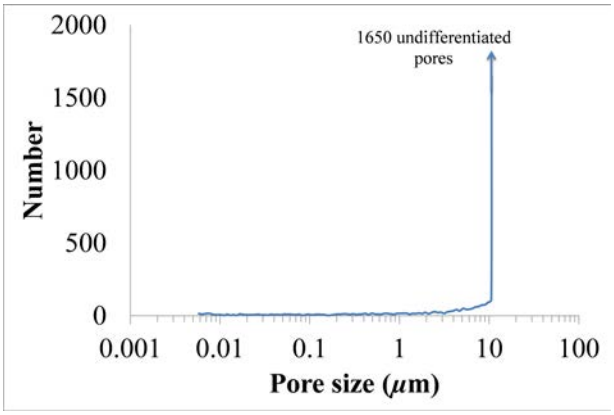

Fig. S 12: Pore size distribution, generated by PoreXpert, of FCC 07.

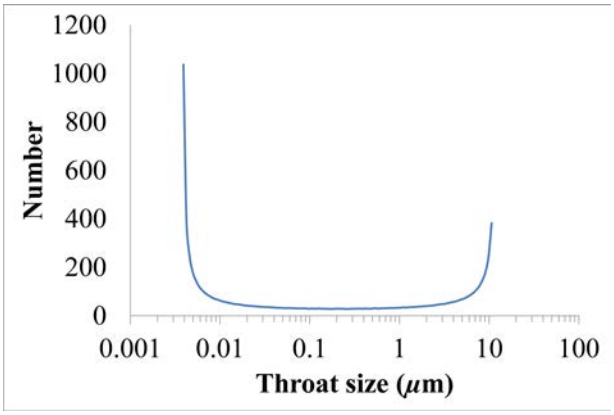

Fig. S 13: Throat size distribution, generated by PoreXpert, of FCC 07.

FCC 12

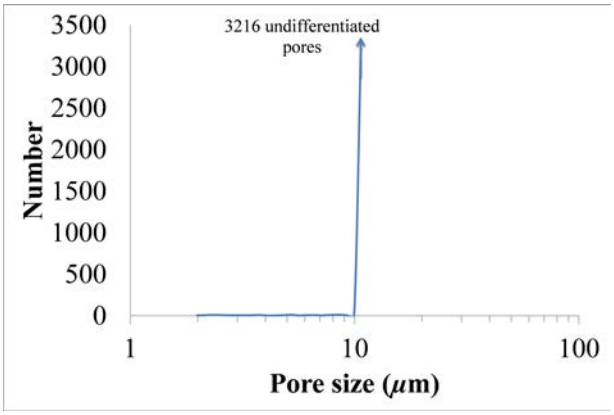

Fig. S 14: Pore size distribution, generated by PoreXpert, of FCC 12.

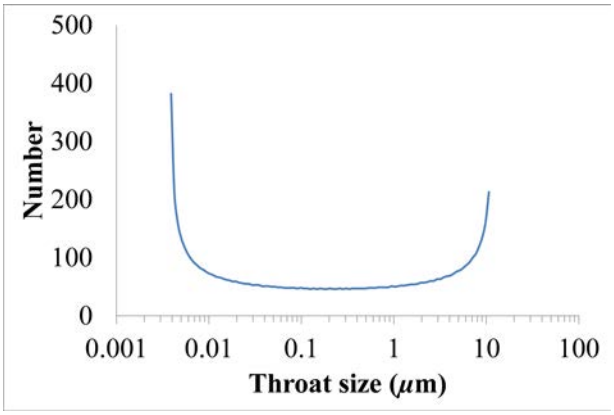

Fig. S 15: Throat size distribution, generated by PoreXpert, of FCC 12.

FCC 13

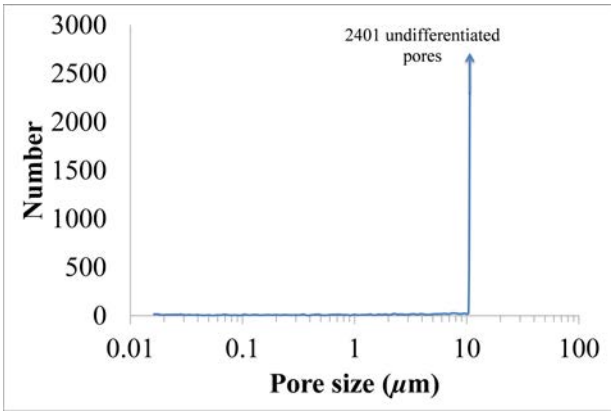

Fig. S 16: Pore size distribution, generated by PoreXpert, of FCC 13.

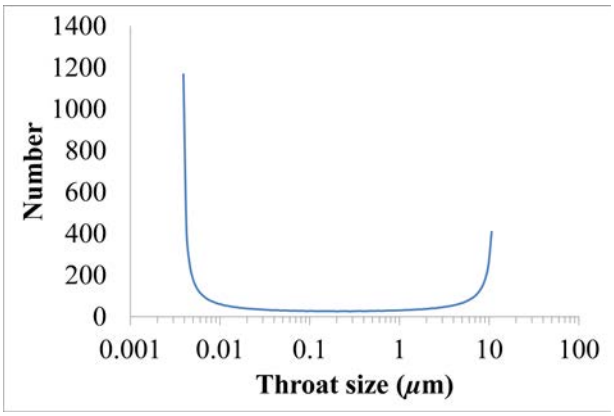

Fig. S 17: Throat size distribution, generated by PoreXpert, of FCC 13.

Scanning Electron Microscopy (SEM) images

This section provides further scanning electron micrographs (SEMs) of the samples.

Ground Calcium Carbonate (GCC)

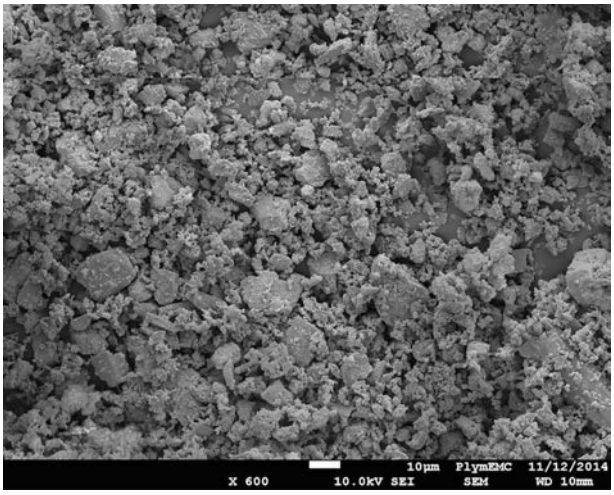

Fig. S 18: Scanning electron micrograph (SEM) of ground calcium carbonate (GCC).

Hydroxyapatite (HAP)

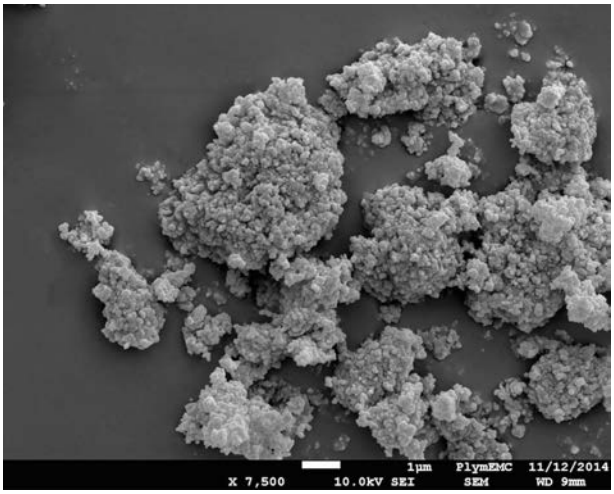

Fig. S 19: Scanning electron micrograph (SEM) of hydroxyapatite (HAP).

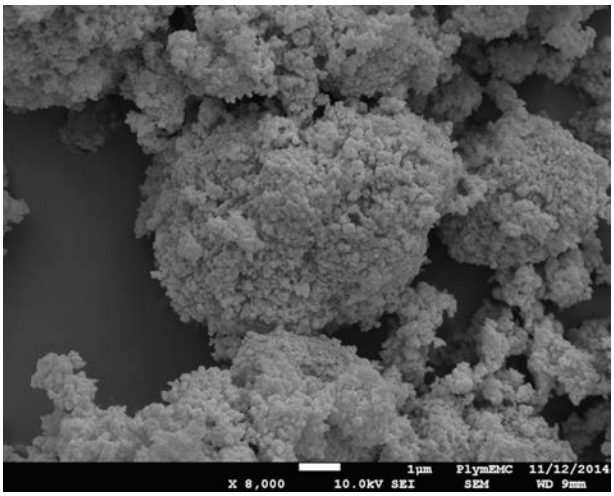

Fig. S 20: Scanning electron micrograph (SEM) of hydroxyapatite (HAP).

FCC TP

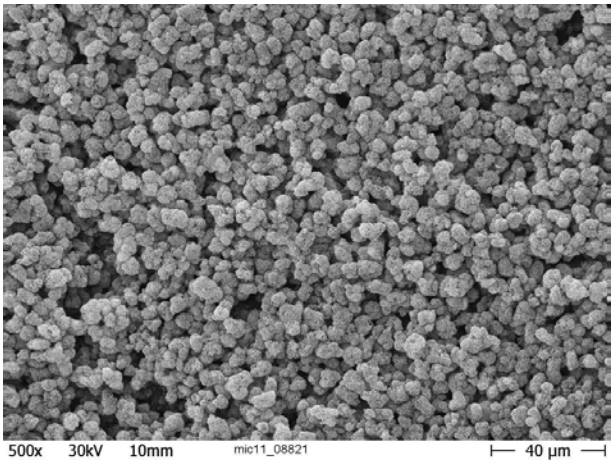

Fig. S 21: Scanning electron micrograph (SEM) of FCC TP.

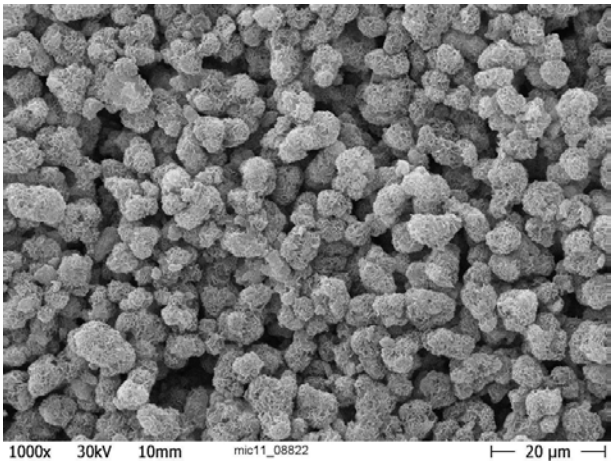

Fig. S 22: Scanning electron micrograph (SEM) of FCC TP.

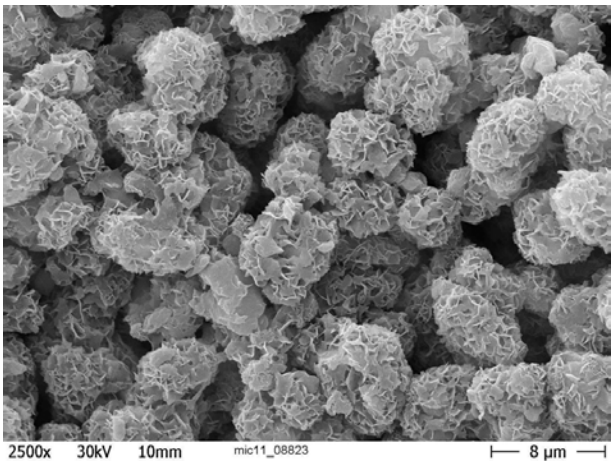

Fig. S 23: Scanning electron micrograph (SEM) of FCC TP.

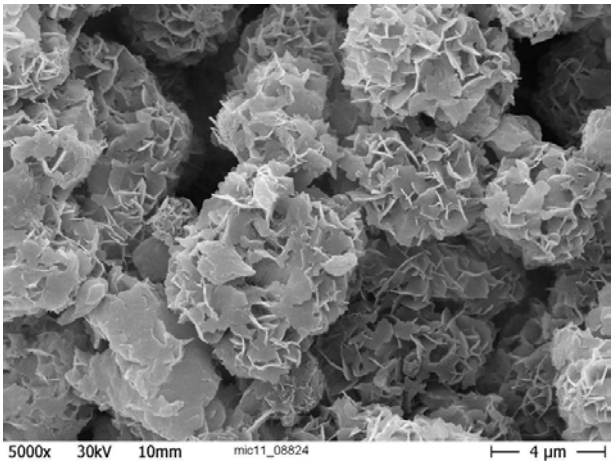

Fig. S 24: Scanning electron micrograph (SEM) of FCC TP.

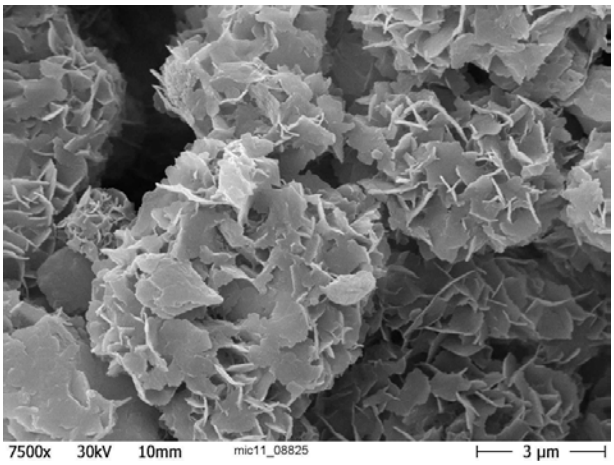

Fig. S 25: Scanning electron micrograph (SEM) of FCC TP.

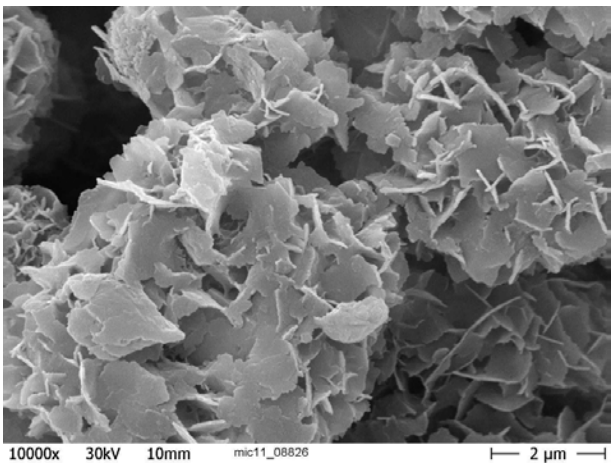

Fig. S 26: Scanning electron micrograph (SEM) of FCC TP.

FCC 02

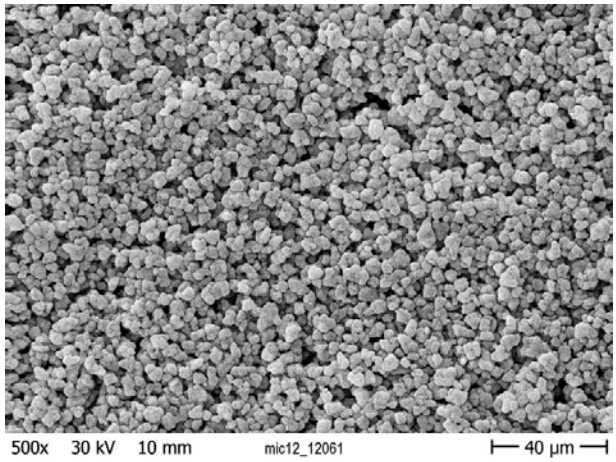

Fig. S 27: Scanning electron micrograph (SEM) of FCC 02.

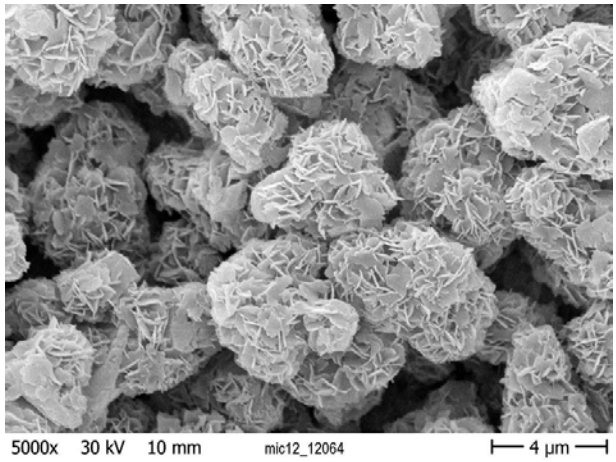

Fig. S 28: Scanning electron micrograph (SEM) of FCC 02.

FCC 03

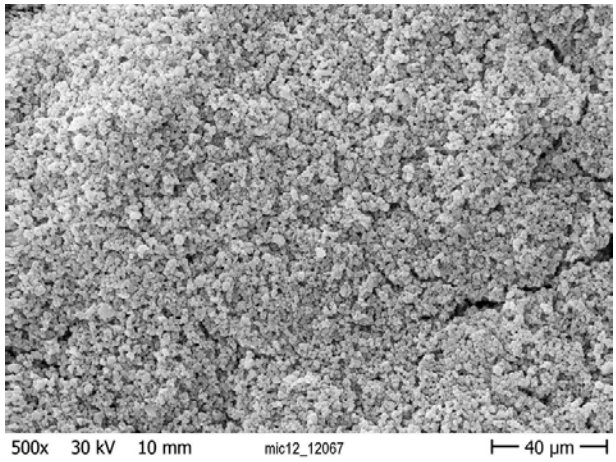

Fig. S 29: Scanning electron micrograph (SEM) of FCC 03.

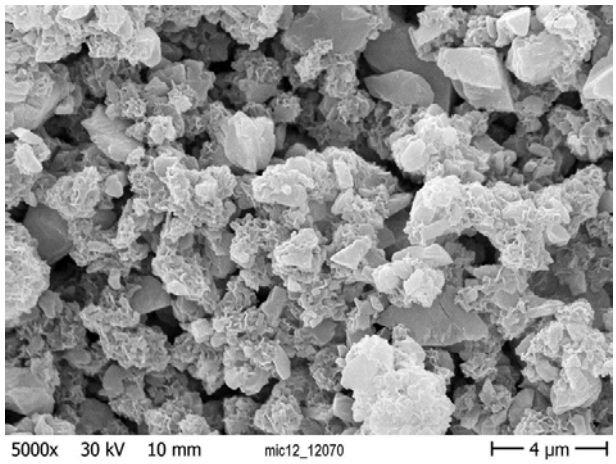

Fig. S 30: Scanning electron micrograph (SEM) of FCC 03.

FCC 06

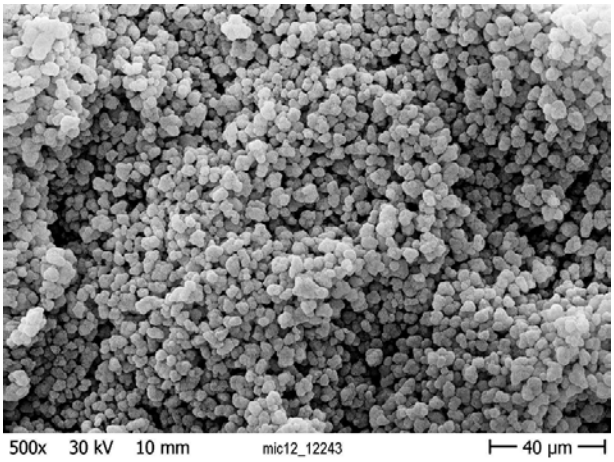

Fig. S 31: Scanning electron micrograph (SEM) of FCC 06.

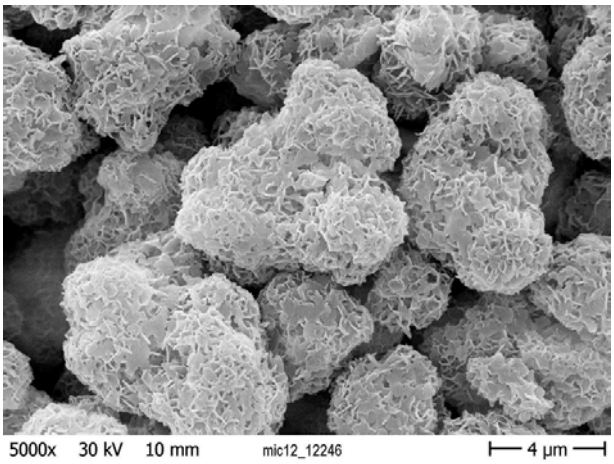

Fig. S 32: Scanning electron micrograph (SEM) of FCC 06.

FCC 07

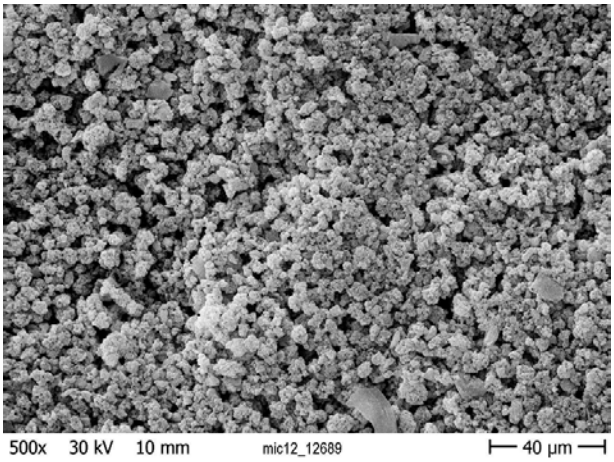

Fig. S 33: Scanning electron micrograph (SEM) of FCC 07.

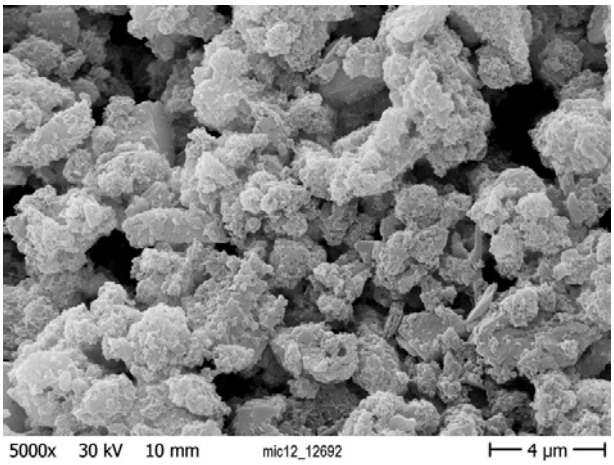

Fig. S 34: Scanning electron micrograph (SEM) of FCC 07.

FCC 12

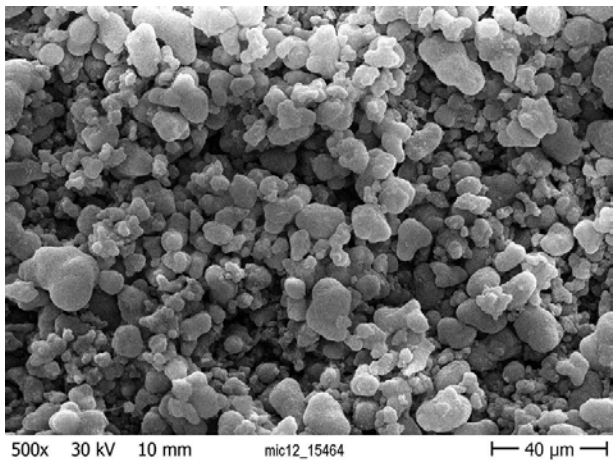

Fig. S 35: Scanning electron micrograph (SEM) of FCC 12.

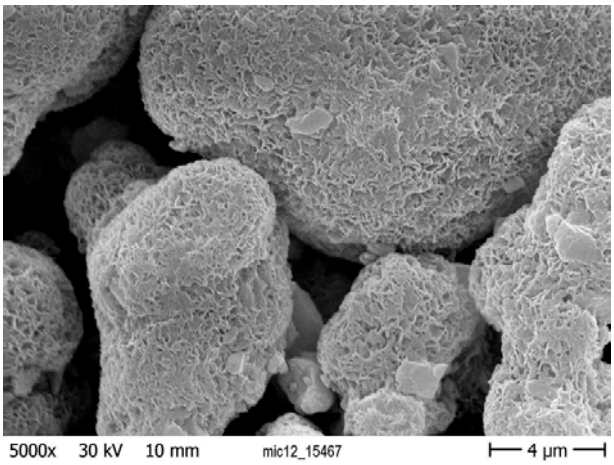

Fig. S 36: Scanning electron micrograph (SEM) of FCC 12.

FCC 13

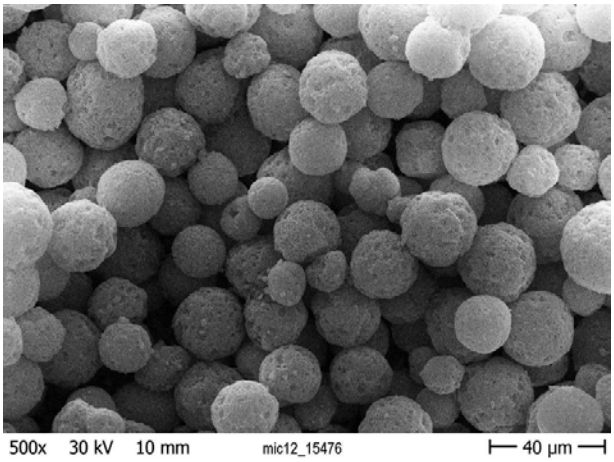

Fig. S 37: Scanning electron micrograph (SEM) of FCC 13.

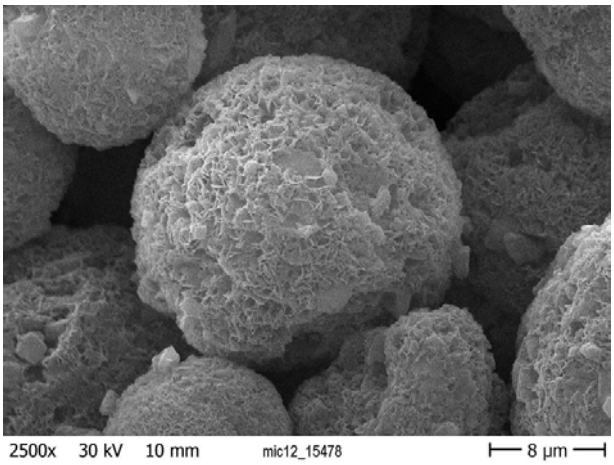

Fig. S 38: Scanning electron micrograph (SEM) of FCC 13.

Finite Length Cell (FLC) Results

This section provides additional finite length cell (FLC) data.

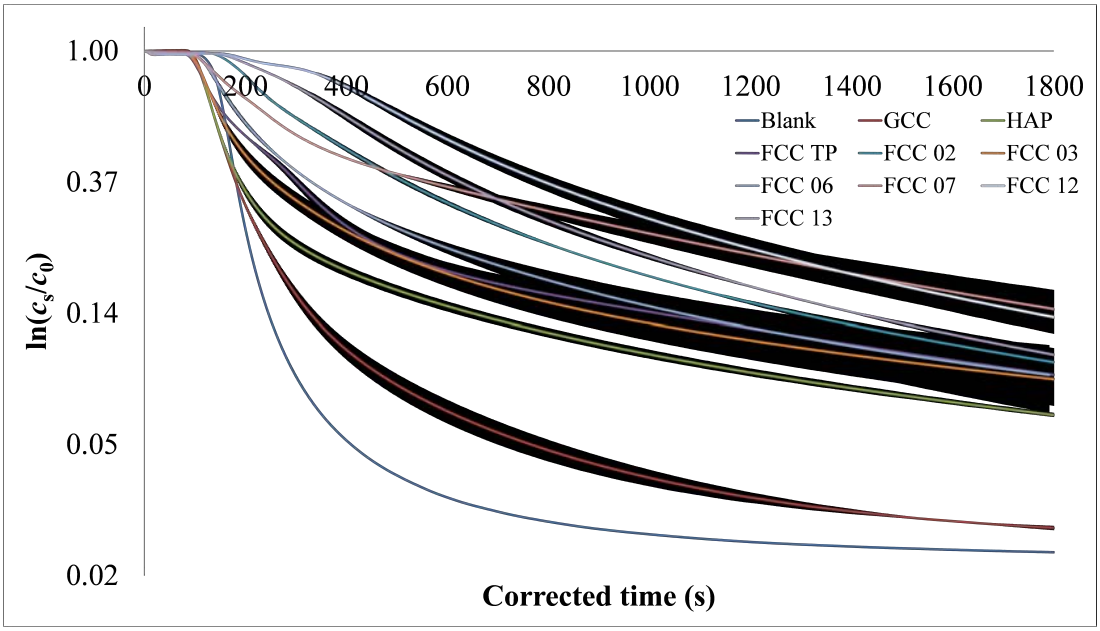

Fig. S 39: Vanillin concentration ($\ln(c_s/c_0)$) versus time. Extents of $\pm\sigma$ of three replicates per packing are shown as black outlines.

Discussion & Modelling

This section includes additional graphs that aid in the discussion of the FLC results.

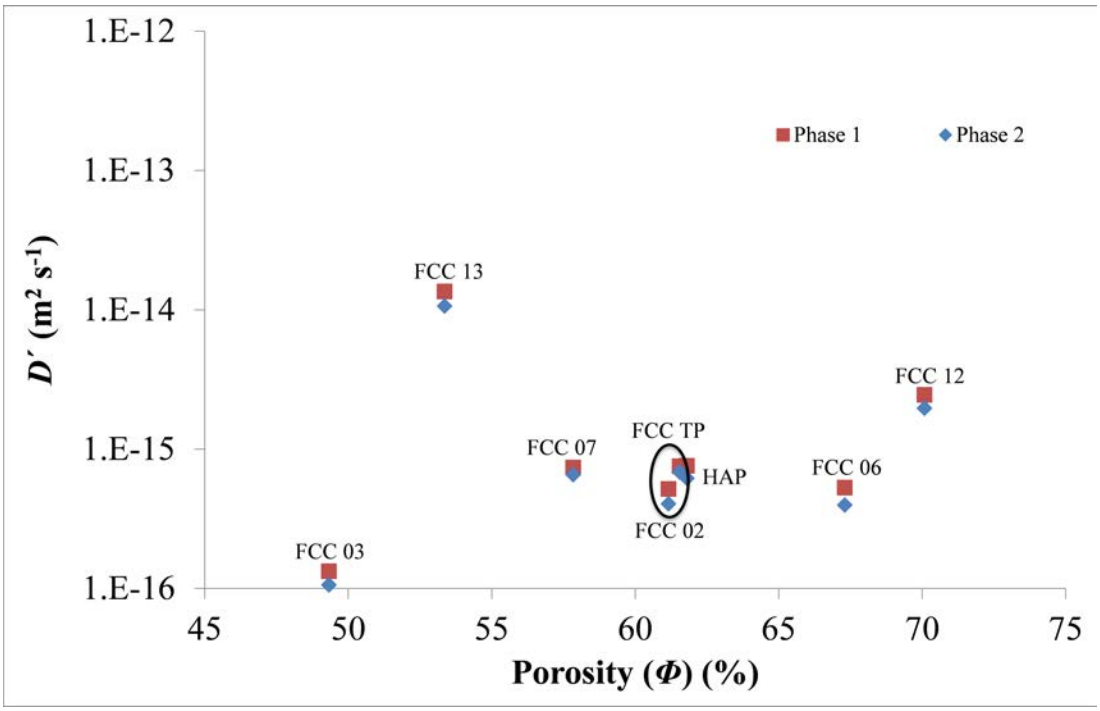

Fig. S 40: Dependence of D' on porosity. As explained in the Discussion, the properties of FCC 02 and FCC TP in this and following graphs are looped together.

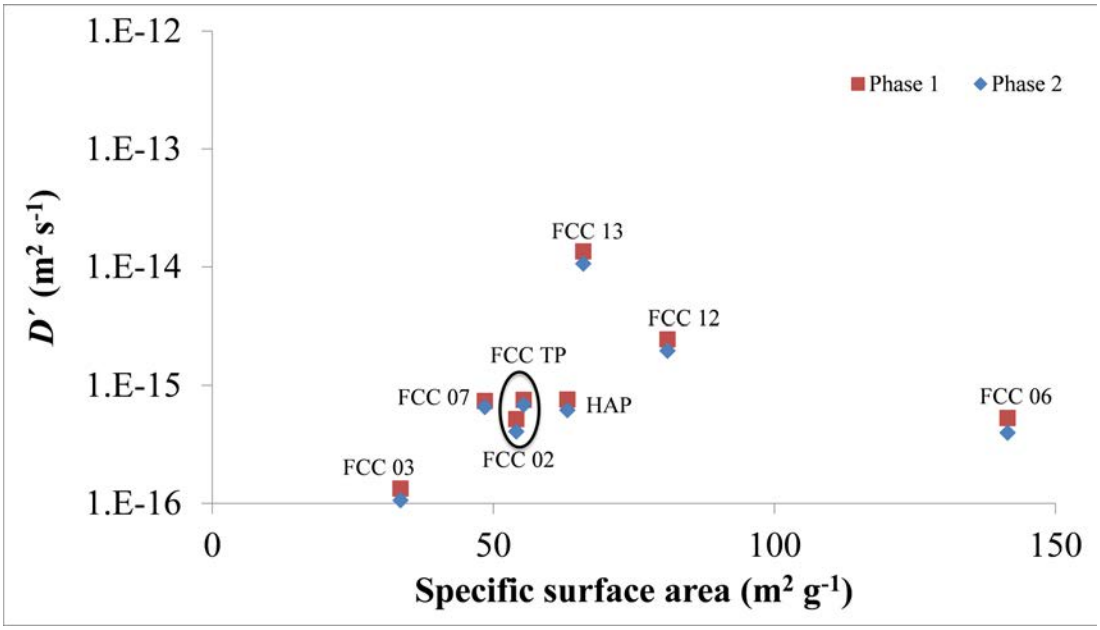

Fig. S 41: Dependence of D' on surface area.

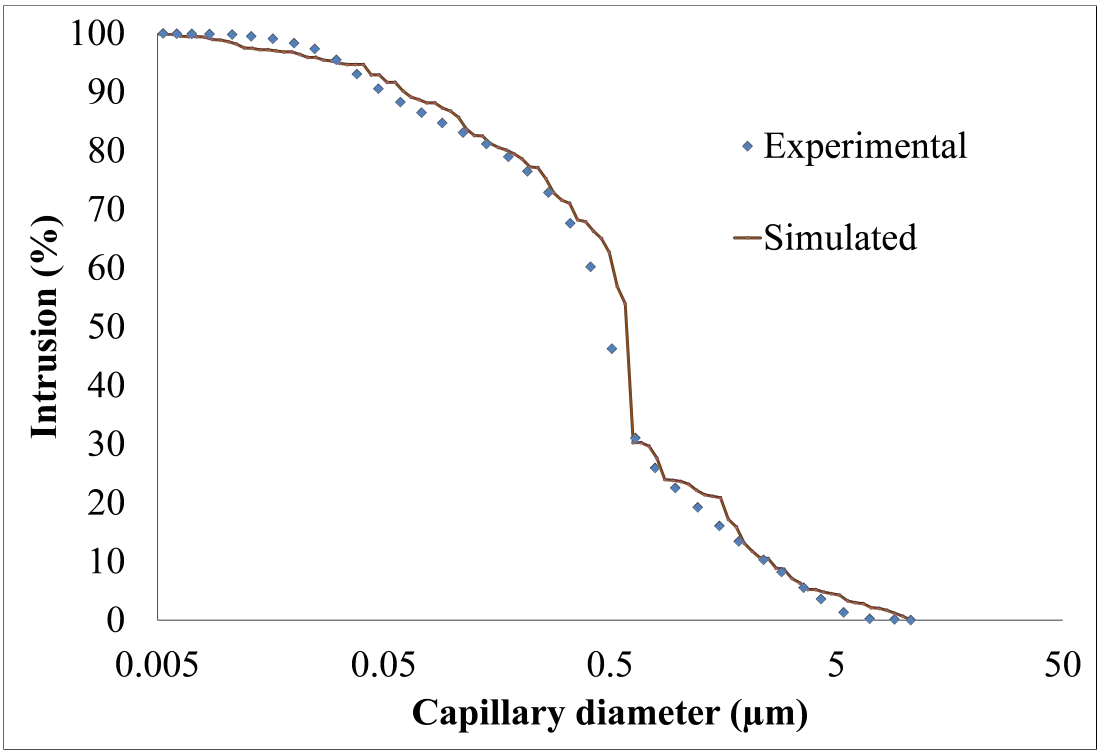

Fig. S 42: Experimental and simulated mercury intrusion characteristic for sample FCC 03.

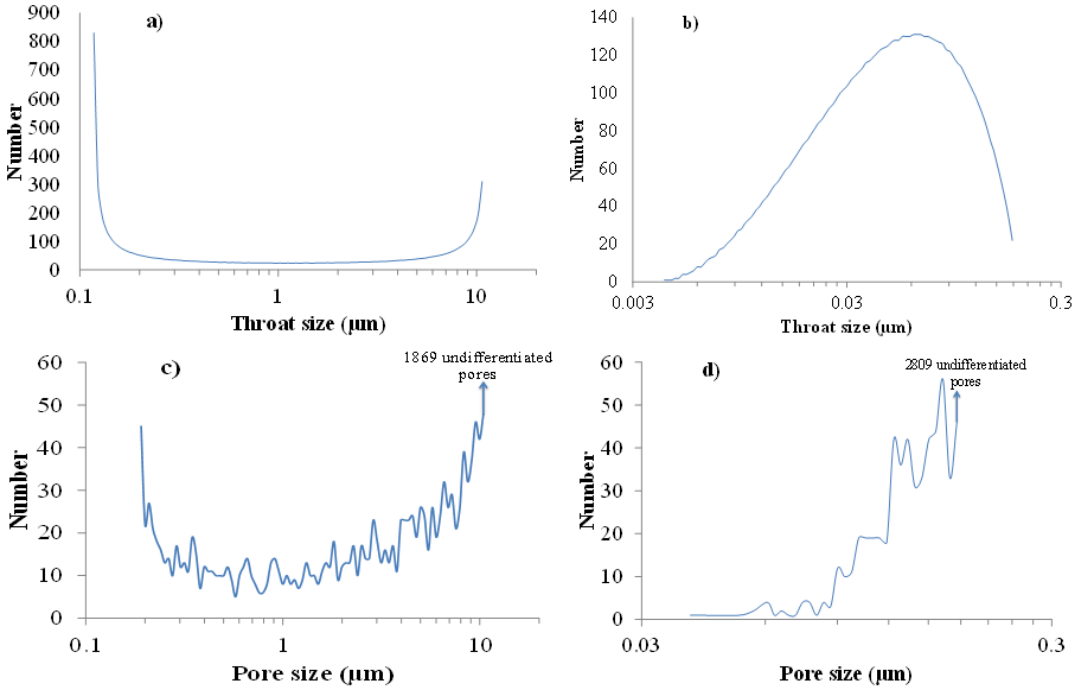

Fig. S 43: The numbers of pore-throats and pores within the single unit cells of sample FCC 03. Figures (a) and (c) displays those of inter-particle void space; Figures (b) and (d) display those of the intra-particle void space, both PoreXpert structures can be viewed in Figure 6 of the main text.

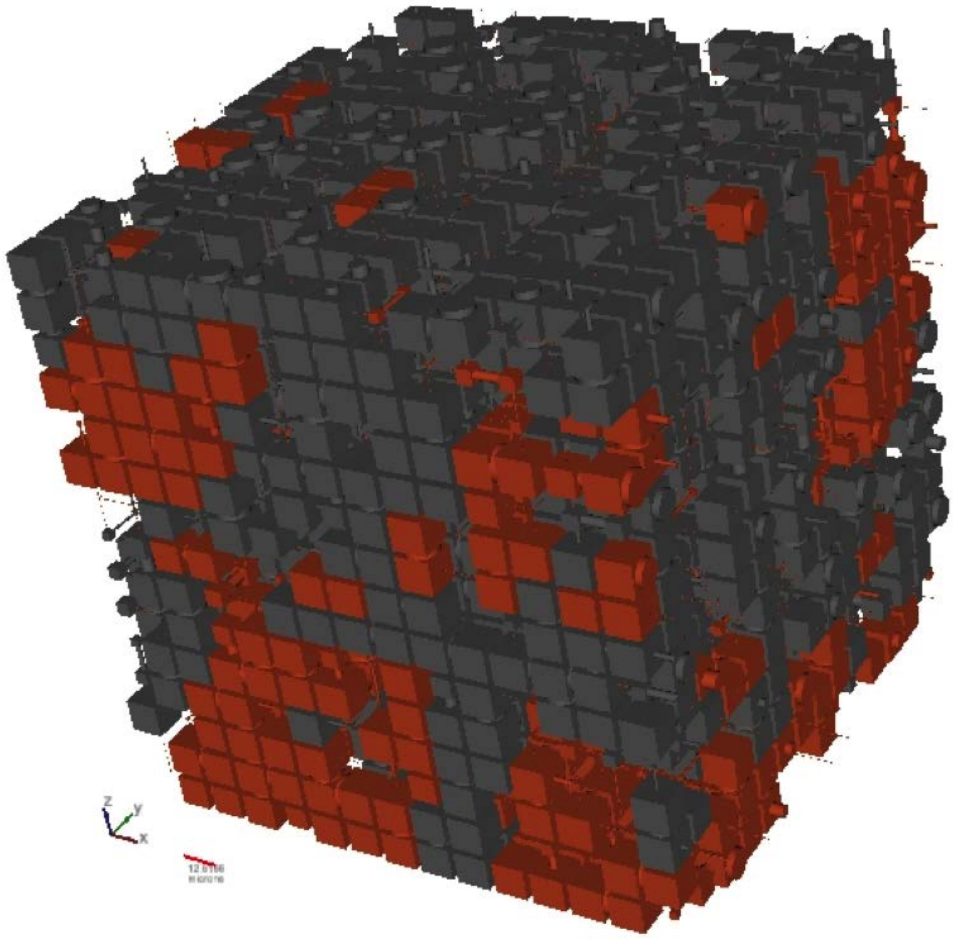

Fig. S 44: Simulation of the inter-particle void space of the sample FCC03 filled 50% by volume of mercury from the top face. For clarity, the void space is shown solid, the solid phase is transparent, and the mercury is dark grey. The left structure is the simulated inter-particle space, and the small scale bar bottom left is of length 12.6 μm. The right structure is the intra-particle space, and the small scale bar bottom left is of length 0.41 μm, i.e. 28 times smaller than the left-hand structure. Pores with textured surfaces may be pore clusters.

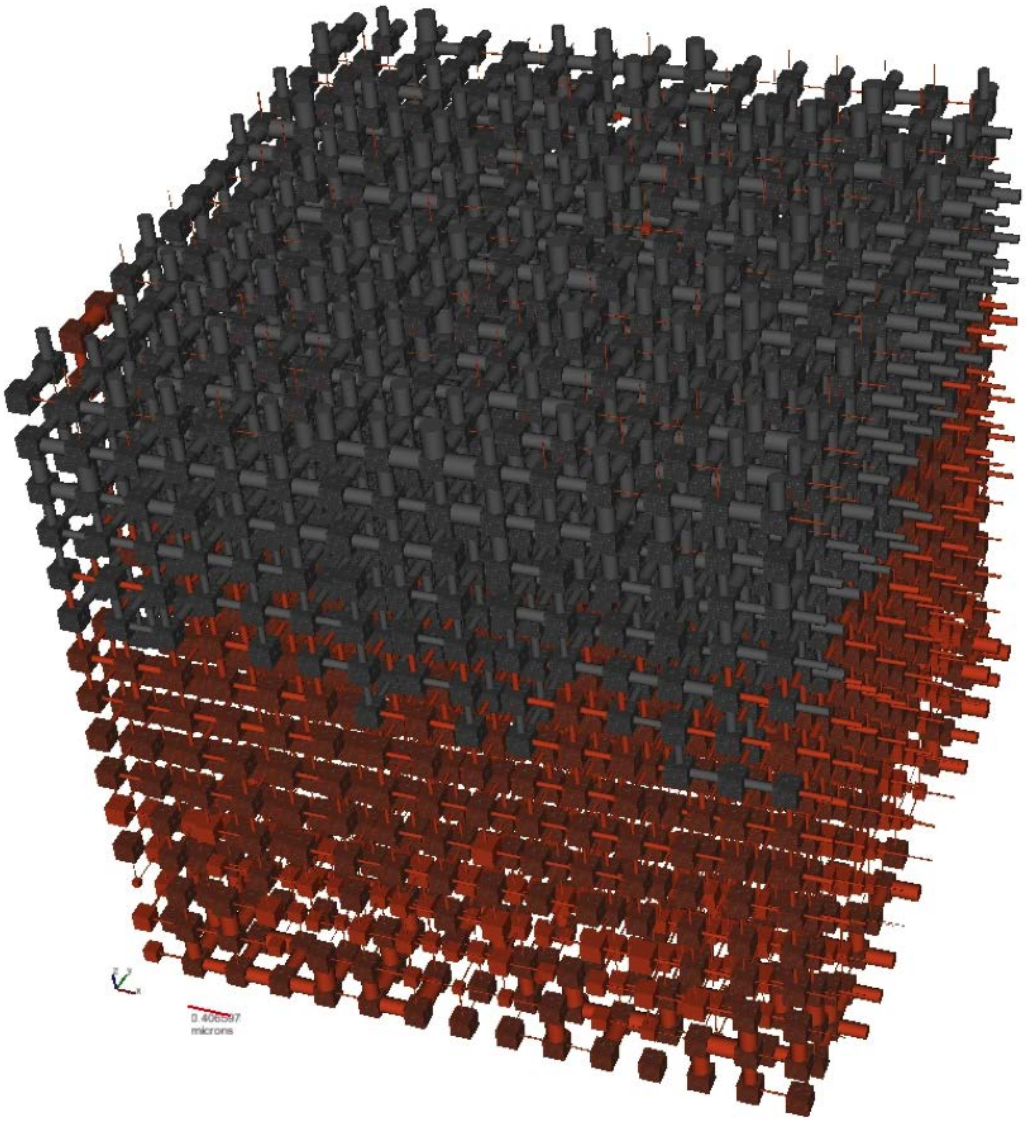

Fig. S 45: Simulation of the intra-particle void space of the sample FCC03 filled 50% by volume of mercury from the top face. For clarity, the void space is shown solid, the solid phase is transparent, and the mercury is dark grey. The left structure is the simulated inter-particle space, and the small scale bar bottom left is of length 12.6 μm. The right structure is the intra-particle space, and the small scale bar bottom left is of length 0.41 μm, i.e. 28 times smaller than the left-hand structure. Pores with textured surfaces may be pore clusters.

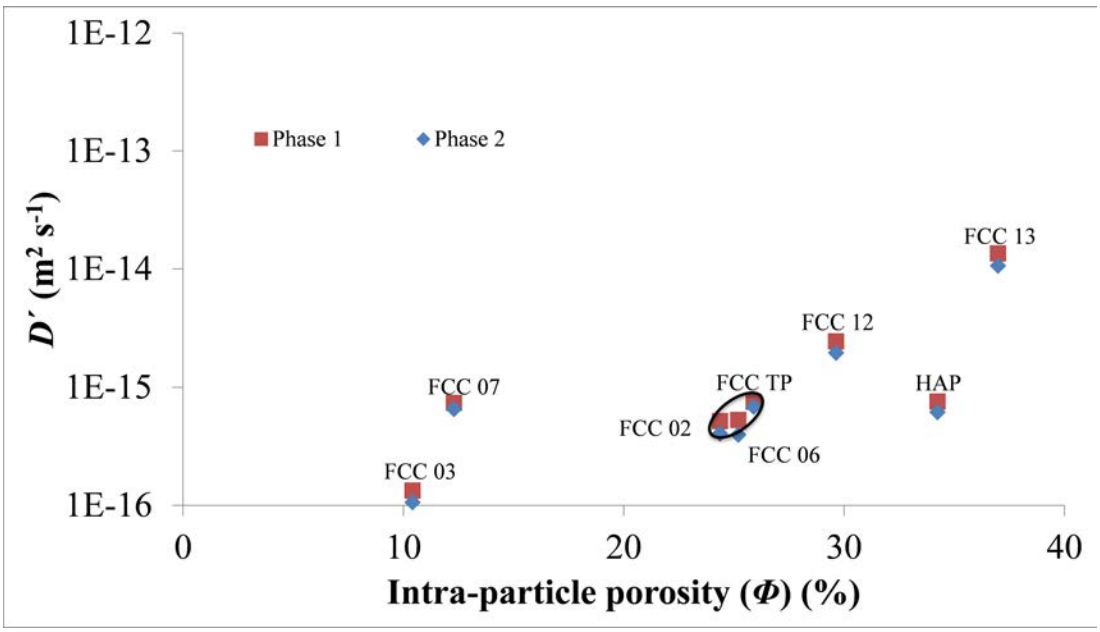

Fig. S 46: A plot of intra-particle porosity versus D'.

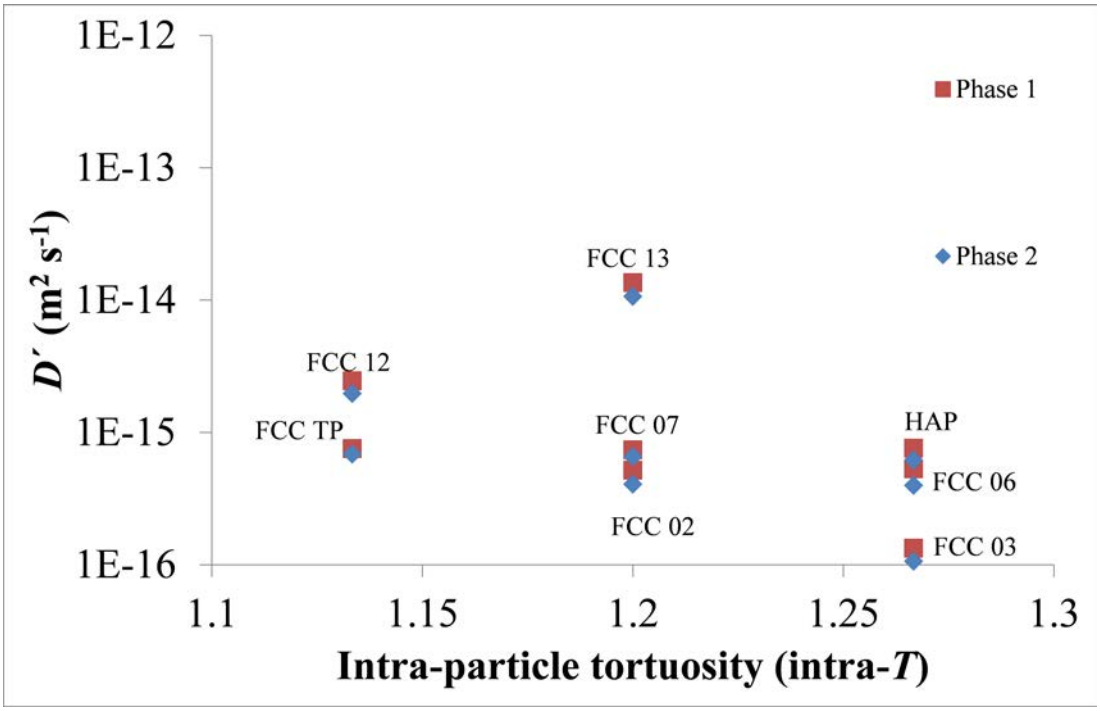

Fig. S 47: A plot of intra-particle tortuosity versus D'.

Adsorption manuscript No.
(will be inserted by the editor)

Mechanism of adsorption of actives onto microporous functionalised calcium carbonate (FCC)

Charlotte L. Levy · G. Peter Matthews · Giuliano M. Laudone · Samuel Beckett · Andrew Turner · Joachim Schoelkopf · Patrick A. C. Gane

Received: date / Accepted: date

Abstract Microporous 'functionalised' calcium carbonate (FCC) has potential for use as a carrier for the controlled release of 'actives', by permeation and diffusion. We have investigated the nature of the FCC surface and the mechanism of adsorption of two typical actives, namely the anti-inflammatory drug aspirin and the flavour compound vanillin, from chloroform and aqueous ethanolic solutions. There is indirect evidence from the quantitative perturbation of Tóth isotherms that their adsorption is hindered by a stagnant diffusion layer of water trapped in the microporosity of the FCC. To complement previous studies of the surface of FCC, it was also tested with the cationic probe benzyltrimethylammonium bromide and the anionic probe sodium 2-naphthalenesulphonate. Experimental procedures were validated by comparison with adsorption onto ground calcium carbonate and high surface area talc.

Keywords Controlled drug delivery · Controlled flavour release · Functionalised calcium carbonate (FCC) · Vanillin · Aspirin

1 Introduction

1.1 Functionalised calcium carbonate

This work is a study of the adsorption properties of dissolved organic species onto 'functionalised' calcium carbonate (FCC). FCC comprises particles with intraparticulate porosity, which is microporous according to the pore size classification of Mays (2007). The adsorbates were the anti-inflammatory drug aspirin and the flavour compound vanillin, in chloroform and aqueous ethanolic solutions. The FCC surface was also tested with the cationic probe benzyltrimethylammonium bromide (BTMAB) and the anionic probe sodium 2-naphthalenesulphonate (Na2NS). Similarly sized particles of ground calcium carbonate (GCC) were used as a (null) control adsorbent. Finnish talc with a high surface area was used as a control to check the methodology of measuring the (null) adsorption of BTMAB onto FCC.

FCCs are produced by etching calcium carbonate particles and re-precipitating a modified surface structure with in-situ or externally supplied CO_2 in the form of carbonic acid (Ridgway et al., 2004). To facilitate the in-situ production of CO_2, acids such as phosphoric acid (H_3PO_4) can be used. Variations in the etching process produce a range of morphologies with recrystallised surfaces, consisting of incorporated hydroxyapatite (HAP) in the case of phosphoric acid, which are dual porous with inter- and intraparticle porosity. FCCs have hydrophilic surfaces and exhibit both HAP and calcium carbonate crystalline structure (Gantenbein et al., 2012). FCC offers benefits over HAP because the current commercial methods used to produce HAP give a low yield mixed with several phases, so that the product is expensive and suitable only for small-scale and time-consuming production (Chen and Leng, 2015).

FCCs have a wide range of applications, particularly for the controlled release of actives such as drugs, plant protection chemicals, and food additives such as flavours. It has been proposed that the particles be utilised in various dosage forms, such as in chewing gum, a mouth or nasal spray, an inhaling device, a tablet, a lozenge, a trans-dermal patch and a powder (Pedersen and Andersen, 2012). FCCs can be tailored to suit a particular need; for example, plastically compressible FCC grades are available in the case where flavour release may require a compressive destruction of the inert carrier in the mouth combined with controlled release in order to excite the recipient's senses with flavour (Gane et al., 2006). FCCs are pharmaceutical grade analogues of

G. Peter Matthews
Room 602, Davy Building, Drake Circus, Plymouth, Devon, PL4 8AA
Tel.: +44 1752 584798
E-mail: p.matthews@plymouth.ac.uk

MCCs (modified calcium carbonates) designed for the paper industry, particularly for coatings designed for ink-jet printing (Ridgway et al., 2004). MCCs are normally treated with <1 % polyacrylate dispersant to facilitate transport and application (Alm et al., 2010; Gribble et al., 2010), whereas FCCs are free of organic chemicals.

1.2 Adsorption in the context of the controlled delivery of actives

The adsorption processes of drugs onto their delivery surfaces are important, since adsorption is the basic mechanism most commonly used for the loading of drugs onto surfaces such as nanodiamonds (Mochalin et al., 2013). Unwanted adsorption onto a surface may compromise the intended therapeutic benefit, driving up dosage levels, thus increasing treatment costs (Tzannis et al., 1997). A study by Mochalin et al. (2013) has also shown that the adsorption of poorly soluble drugs onto the surface of their nanodiamond particles may be suitable in overcoming the poor bioavailability of the drugs. They also state that the monolayer capacity for a particular drug on their surface must be determined in order to gain full advantage of the mechanism while avoiding excessive loading in order to minimise potential leakage of dangerous drugs. Pinholt et al. (2011) found that it is important to study the adsorption of peptide and protein drug products, as proteins are known to interact with interfaces of the particulate delivery system in which the effects are often irreversible adsorption and structural changes of the proteins. Kojima and Watanabe (2012) have studied HAP as a biomaterial and the adsorption and desorption of two bioactive proteins (cytochrom c and insulin) onto its surface; they concluded that HAP is a potential protein carrier with controlled release. A study by Neuvonen et al. (1984) has shown that the bioavailability of both aspirin and quinidine sulphate was significantly reduced when ingested with activated charcoal, and that a significant desorption of aspirin, but not that of quinidine, was subsequently detected. Tsuchiya and Levy's 1972 paper suggests that it may be possible to make reasonable predictions concerning the relative antidotal effectiveness of activated charcoal in humans on the basis of appropriate *in vitro* adsorption studies. Sellers et al. (1977) conducted comparative *in vitro* studies to determine the adsorption characteristics of 12 drugs onto activated charcoal in order to remediate any poorly absorbed drugs. They concluded that activated charcoal would not be helpful. Such diverse studies demonstrate that when a new drug delivery vehicle is being proposed, an investigation into the adsorptive properties of its surfaces is of paramount importance.

1.3 Adsorbates

Figure 1 shows the molecular structures of the four adsorbates used in this work. Benzyltrimethylammonium bromide (BTMAB) and sodium 2-naphthalene sulphonate (Na2NS) are charged, water soluble species, used as cationic and anionic probes, respectively.

Vanillin, a common and popular flavour compound readily soluble in ethanol, was chosen as the flavour species to adsorb onto the FCC in order to provide further insight into the mechanism of release in diffusion studies (Levy et al., 2015). It is solid at room temperature, thereby having potential to be loaded into the pores of an FCC in future work (Preisig et al., 2014). Although the use of aqueous solutions would be more applicable to biological situations, in this work adsorption from chloroform and ethanol/water solutions was studied, in order to facilitate loading of the vanillin onto the FCC, and to avoid the need for aqueous buffering which could interfere with the adsorption processes.

As an example drug, the adsorption of acetylsalicylic acid (aspirin) from aqueous ethanolic solutions is reported. Aspirin is a widely studied non-steroidal anti-inflammatory, antipyretic and analgesic drug (Vane and Botting, 2003).

1.4 Surface properties of substrates

FCC is an amphoteric material typically showing electrochemical charge values of +22 and -17 μEq g^{-1} in a polyelectrolyte titration versus the anionic polyelectrolye poly(vinyl sulfate) potassium salt (KPVS) and the cationic polyelectrolyte poly(diallyldimethylammonium chloride) (Gantenbein et al., 2012). Previous research and zeta potential measurements onto FCC surfaces have yielded complex results, suggesting that there must be both cationic and anionic surface adsorption sites (Gribble et al., 2010). The material is not suitable for measurements of its cation exchange capacity (CEC).

1.5 Previous studies of adsorption onto minerals

Gane et al. (2000) have shown that all dyes with a cationic charge show a strong adsorption onto anionically dispersed GCC. This indicates that coulombic forces contribute the strongest part of the adhesion force and is in agreement with the adsorbing mechanisms of ink jet dyes. Acidic dye molecules have a significantly weaker adhesion mechanism in which it is assumed that the COOH-groups probably interact with free surface of the calcium carbonate. Dyes with an anionic colorant revealed no adsorption onto slightly anionically dispersed calcium carbonate surfaces, suggesting the possible existence of shielded cationic sites (Lamminmäki et al., 2011). In practice, ink jet dyes are usually anionic, and

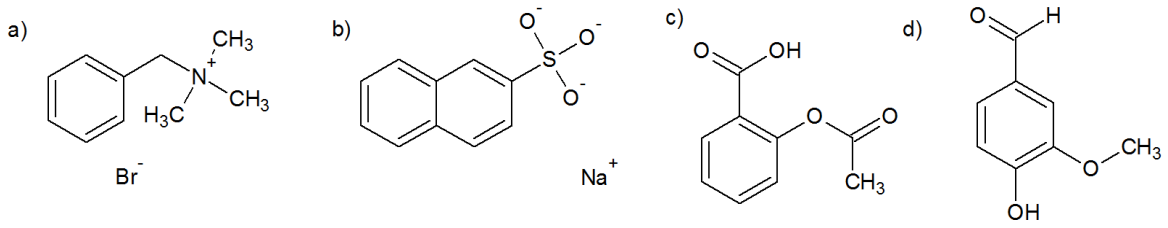

Fig. 1 Molecular structures of the four adsorbates: a) BTMAB, b) Na2NS, c) aspirin and d) vanillin.

ink jet paper coatings must therefore be cationised, at high cost.

Kallio et al. (2006) studied the adsorption of Food Black 2 (a diazo dye) onto coating pigments from polar liquids, such as water and ethanol, and from non-polar cyclohexane. They similarly concluded that electrostatic interactions are the predominating driving force for adsorption onto a variety of minerals, such as kaolin, calcium carbonate, and talc. These interactions are hydrophobic in the case of talc.

With respect to drugs, Mahato and Narang (2012) have found that adsorption generally increases as the ionization of the drug is suppressed, so that the extent of adsorption reaches a maximum when the drug is completely un-ionized. For amphoteric compounds, adsorption is at a maximum at the isoelectric point. pH and solubility effects act in concert since the un-ionized form of most drugs in aqueous solution has a low solubility. The physicochemical nature of the adsorbent affects the rate and extent of adsorption through changes in the molecular forces of attraction between the adsorbate and the adsorbent. Other work on the effect of changing the solvent showed that adsorption of actives onto calcium carbonate was irreversible from chloroform, but not from ethanol (Misra, 1991).

1.6 FCC microporosity

A recent work on diffusion from the microporosity of FCC involved intruding samples with mercury up to 400 MPa applied pressure, and deconvoluting their percolation characteristics with PoreXpert® (Levy et al., 2015). The software generated a void network of the inter- and intraparticle pore space with the same mercury percolation characteristic as the FCC sample. Figure 2 shows a 'unit cell' of the intraparticle void space, with features ranging from 4.2 to 178 nm in diameter or edge size. The solid phase is shown transparent, and the voidage shown solid. Pores with textured surfaces are void clusters with sizes undifferentiated by the mercury porosimetry. There are periodic boundary conditions at each surface of the unit cell, equivalent to each unit cell connecting to infinite replicates in each Cartesian direction. The structuring has been highlighted by intruding 50 percent mercury by volume (shown grey) from the top surface in the direction shown. It can be seen that the percolation front is relatively uniform with respect to distance from the top surface. Correspondingly diffusion of the adsorbate into the sample prior to adsorption, and out from the body of the sample, would also depend primarily on depth from the surface rather than any small-scale lateral variations.

1.7 Isotherms

We use the standard definition of adsorption density (Γ) (Pan and Liss, 1998):

$$\Gamma = \frac{(C_0 - C_{\mathrm{eq}})\, V_{\mathrm{total}}}{W_{\mathrm{solid}}} \tag{1}$$

where C_0 is the initial concentration of adsorbate in solution, C_{eq} is the supernatant concentration after adsorption has taken place, V_{total} is the volume of solution of concentration C_0 used in an adsorption experiment, and W_{solid} is the weight of the adsorbent used during the adsorption experiment.

In this work, adsorption is described by the Tóth isotherm. This isotherm has the correct functionality at both limits as $C_{\mathrm{eq}} \to 0$ and $C_{\mathrm{eq}} \to \infty$, and has previously proved useful for fitting isotherms of porous adsorbents (Rudzinski and Everett, 1992). It has the form:

$$\Gamma = \Gamma_{\max} \left(\frac{(K_{\mathrm{L}}\, C_{\mathrm{eq}})^m}{1 + (K_{\mathrm{L}} C_{\mathrm{eq}})^m} \right)^{1/m} \tag{2}$$

where $\Gamma_{\max}$ is the adsorption at maximum equilibrium concentration solution C_{eq}, and K_{L} is the Langmuir constant. The fitting parameter m, loosely associated with surface heterogeneity when $m \neq 1$, yields the Langmuir equation when $m = 1$. In the present work, the Tóth isotherm is used to describe adsorption of aspirin and vanillin from ethanol onto FCC. In the presence of up to 20 % by volume of added water it becomes:

$$\Gamma = f''(\Gamma_{\max}) \left(\frac{[K_{\mathrm{L}}\, f'(C_{\mathrm{eq}})\,]^m}{1 + [K_{\mathrm{L}}\, f'(C_{\mathrm{eq}})\,]^m} \right)^{1/m} \tag{3}$$

where the functions f' and f'' describe the effect of water on C_{eq} and $\Gamma_{\max}$ respectively.

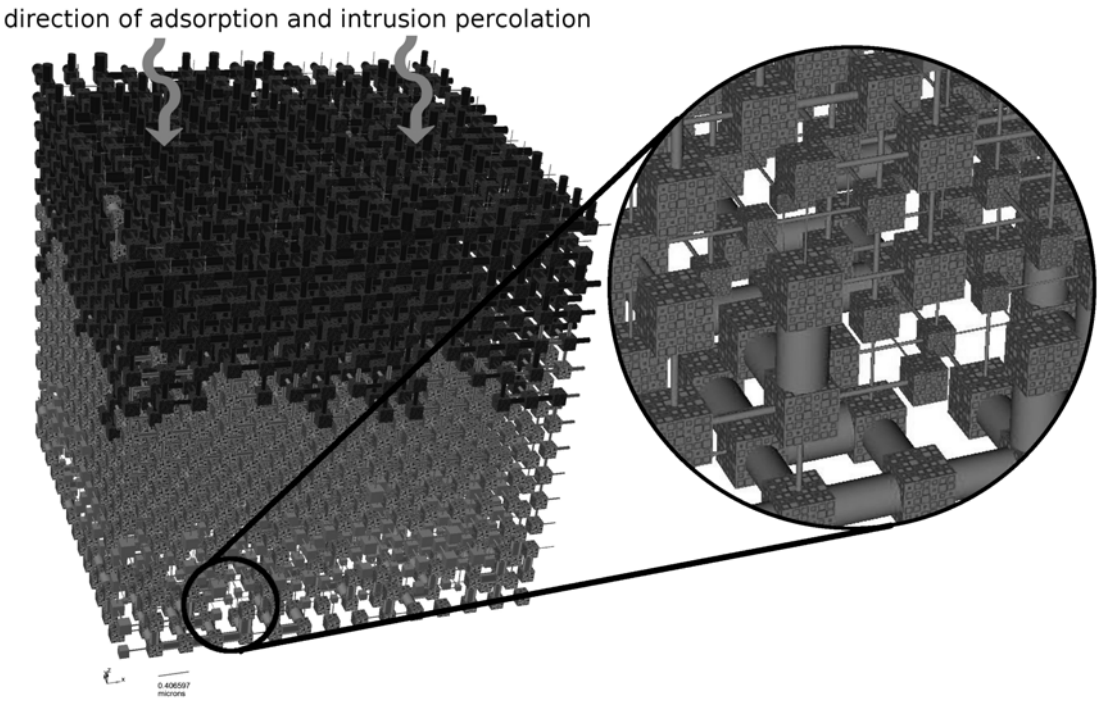

Fig. 2 PoreXpert® representation of the microporous intraparticle void space of FCC 03, as explained in the text. Scale bar bottom left: 407 nm. A colour version of the Figure is provided in the Supplementary Material.

2 Materials

2.1 Minerals

The GCC and various grades of FCC samples were provided by Omya International AG (Oftringen, Switzerland). The GCC was Italian dry ground calcium carbonate prepared with a small amount of dry grinding aid, far too little to block the surface, but sufficient to influence moisture adsorption.

The properties of the minerals are listed in Table 1. Particle sizes were measured with a Malvern Master Sizer 2000, which measured the static light scattering of particles dispersed in water, interpreted using the Mie approximation (Mie, 1908). They are expressed in Table 1 as d_{50} values, namely the median particle diameters at which 50 % by volume of the sample is finer than the stated value. The d_{50} value of 7.7 μm for GCC is somewhat higher than its stated d_{50} of 5 μm based on Stokes' Law sedimentation in aqueous suspension. Surface areas were measured with a Micromeritics Gemini V surface area analyzer. The morphologies are explained in a previous publication (Levy et al., 2015), which also details the measurement of intra-particle porosities, and are shown as scanning electron micrographs in Figure 1 of the Supplementary Material.

2.2 Adsorbates and solvents

The vanillin (4-hydroxy-3-methoxybenzaldehyde; >99 %) and chloroform (HPLC grade stabilised with amylene) were supplied by Acros Organics. The absolute ethanol (HPLC grade) was from Fisher Scientific. BTMAB (>97 %) and aspirin (acetylsalicylic acid; >99 %) were supplied by Aldrich Chemistry (Sigma-Aldrich), Na2NS (>99 %) by Fluka-Analytical (Sigma-Aldrich), and the orthophosphoric acid (85 %) by CPR Rectapur.

3 Methods

3.1 Vanillin adsorption from ethanol and chloroform

λ_{max} for vanillin in ethanol was found to be 279 nm, and 275 nm for vanillin in chloroform. The upper limit of quantification concentration was 40 mg dm^{-3}. The vanillin stock solutions were prepared via serial dilution of a 1 g dm^{-3} stock solution using borosilicate glass bulb pipettes.

An accurately known amount of approximately 0.2 g of FCC was weighed (Mettler Toledo XP504) into a 50 cm^3 polypropylene plastic centrifuge tube, after which 25 cm^3 of the desired concentration of vanillin was pipetted, using a borosilicate glass bulb pipette, into the centrifuge tube. The tube was then shaken briefly and vigorously by hand before being placed on a reciprocal shaker (Stuart SSL2) for 1 hour at 205 strokes per minute. It was then centrifuged (Centaur 2,

Table 1 Properties of the mineral particles. Particle sizes are expressed as d_{50} values, namely the median particle diameters at which 50 % by volume of the sample is finer than the stated value.

Sample	Particle size d_{50} / μm	Surface area / m^2 g^{-1}	Overall porosity / %	Intra-particle porosity / %	Hydroxy-apatite content / %	Calcium carbonate content / %	Morphology
FCC TP	7.0	55.4	61.6	25.9	51	49	Roses
FCC 02	4.9	54.1	61.2	24.4	43	57	Roses
FCC 03	3.1	33.5	49.3	10.4	14	86	Caviar
FCC 06	5.5	141.5	67.3	25.2	85	15	Brain
FCC 07	6.3	48.5	57.8	12.3	13	87	Caviar
FCC 12	10.0	81.0	70.1	29.6	50	50	Flaky eggs
FCC 13	23.5	66.0	53.4	37.0	50	50	Golf balls
GCC (control)	7.7	1.53	22.2	0	0	97.5	Heterogeneous blockey
Finnish talc (control)	5.02	45.3	-	0	0	0	High aspect ratio plate-like

Sanyo, MSE) for 15 minutes at 3 000 revolutions per minute (1 507 g). The supernatant was then decanted into a clean and stoppered conical flask. Supernatants with initial concentrations (C_0) above 40 mg dm^{-3} were diluted by a factor of 10 in 100 cm^3 volumetric flasks. The supernatants were then analysed by UV-vis spectroscopy (Hewlett Packard, now Agilent, 8452 ultraviolet-visible spectrometer).

In the case of adsorption experiments that involved a portion of the overall 25 cm^3 volume of vanillin in ethanol being replaced by water, 20 cm^3 of the desired concentration of vanillin was pipetted using a borosilicate glass bulb pipette, and the remaining 5 cm^3 of water and vanillin in ethanol solution was pipetted in using a Thermo Scientific Finnpipette (100 - 1 000 μl). The volumetric proportions of water in ethanol ranged from 1 % to 20 %.

For each concentration of adsorbate used in these adsorption experiments, another control experiment was carried out without any adsorbent sample but with the same concentration of adsorbate. The concentration of adsorbate in the supernatant with mineral sample (C_{eq} in Equation (1)) was subtracted from the concentration of adsorbate in the supernatant of the control sample (C_0) in order to take into account any experimental artefacts, such as adsorption to the walls of the plastic centrifuge tube.

As an additional control experiment, adsorption onto FCC from ethanol was measured with constant C_0 (30 mg dm^{-3}) but varying W_{solid}. The results of three experimental replicates were obtained, and showed no non-proportionate effect of substrate weight between 0.025 and 0.21 g.

3.2 BTMAB and Na2NS adsorption

The wavelength of maximum spectral absorbance (λ_{max}) for BTMAB in water was found to be 262 nm, and 274 nm for Na2NS. The upper limit for quantification of concentration by the spectrophotometer was 1 g dm^{-3} and 0.1 g dm^{-3} for BTMAB and Na2NS respectively. Electrolyte solutions, as specified below, were used to decrease the thickness of the electrical double layer and increase the probability of interactions between any surface charge on the mineral and the adsorbate.

An accurately known amount of approximately 2.0 g of FCC was weighed (Mettler Toledo Classic AB304-5 balance) into a 50 cm^3 polypropylene plastic centrifuge tube, after which 25 cm^3 of the desired concentration of adsorbate was pipetted, using a borosilicate glass bulb pipette, into the centrifuge tube. The tube was then shaken briefly and vigorously by hand. To ensure complete equilibration between adsorbate and adsorbent, the tube was then placed in a ceramic cylinder and rolled for 1 hour at around 100 revolutions per minute (Alpine Augsburg 1/25 LK). The tubes were then centrifuged (Rotina 420, Hettich Zentrifugen) for 6 minutes at 4 500 revolutions per minute (4 166 g). The supernatant was then processed through a 0.2 μm regenerated-cellulose syringe filter (Sartorius RC25) into a clean polyethylene bottle. The pH of the supernatants was recorded (Mettler Toledo SevenMulti pH meter) before being diluted for analysis. In order to carry out the spectrophotometric analysis (Perkin Elmer Lambda 2 ultraviolet-visible spectrophotometer), an aliquot of supernatant was pipetted into a quartz cuvette along with an aliquot of the solvent (using Eppendorf and Rainin pipettes) to bring the absorbance of the supernatant within the calibration range.

4 Results

4.1 Aspirin adsorption

The adsorption of aspirin onto FCC from ethanolic solutions with various relative concentrations of water (relative permittivity ϵ_r = 80.1) is shown in Figure 3. Three different

Table 2 Tóth isotherm parameters from Equations 2, 3, and 5.

Adsorbate	aspirin	vanillin	vanillin	BTMAB
Substrate	FCC	FCC	FCC	talc
Solvent	aqueous ethanol	aqueous ethanol	chloroform	water
Γ_{max} (mg g^{-1})	16.0	5.0	15.3	25.8
K_L (dm^3 mg^{-1})	0.30	0.57	0.03	11.35
m	1.00	0.58	0.50	0.26
A	0.0035	0.0020	-	-
B	0.7	1.7	-	-

stock solutions were used, and up to seven replicates were measured for each C_{eq}, with error bars as shown, which correspond to one standard deviation (σ_{devn}). Also shown are the corresponding modified Tóth isotherms (equation 3) which are discussed below. In this case, m = 1, i.e. the adsorption of aspirin from pure ethanol follows a Langmuir isotherm.

4.2 Vanillin adsorption

The adsorption of vanillin onto FCC from aqueous ethanolic solutions is shown in Figure 4, for three replicates with error bars (σ_{devn}) as shown. Also shown are the corresponding modified Tóth isotherms (Table 2).

The adsorption of vanillin from chloroform (ϵ_r = 4.8) was higher than from the more polar ethanol (ϵ_r = 24.3) (Figure 4). It was found that there was a minimal difference in the adsorption characteristics of vanillin from ethanol between different grades of FCC.

4.3 Adsorption onto GCC

GCC was used as a control substrate. No adsorption was observed of any of the species studied, from any of the solvents used.

4.4 BTMAB and Na2NS adsorption

There was a lack of adsorption of BTMAB and Na2NS onto FCC 13 in the presence of 0.1 M NaCl. Furthermore, there was no adsorption of either probe in the presence of 2 M NaCl, or in 0.005 M H_3PO_4 electrolyte solutions, or in ultrapure water. The lack of adsorption at increased concentration of electrolytes showed that adsorption did not occur even when the electric double layer at the surface of the FCC was suppressed. The null results in ultrapure water showed that the electrolyte was not itself interfering with adsorption. The use of the H_3PO_4 solution provided a check of whether the FCC surface could be re-activated, again showing a null result.

The pH of the BTMAB and Na2NS stock solutions was in the range 5.7-6.2. The pH of the supernatants involving FCC as the adsorbent was in the range 7.9-8.3, and the pH of the supernatants involving talc as the adsorbent was in the range 8.6-8.9. The supernatant pH rose after an adsorption experiment because of the very slight solubility of the calcium carbonate.

It was necessary to confirm that the null results were not due to an error in experimental procedure. Adsorption of BTMAB onto Finnish talc with a high surface area of 45.3 m^2 g^{-1} in 0.1 M NaCl solution did produce an isotherm. Error bars were calculated, based on an estimated accuracy of 1 % in determining the BTMAB concentration. A Tóth adsorption isotherm passing through all such error bars had the parameters shown in Table 2. It was found that there was no adsorption of Na2NS onto talc. The maximum observed adsorption of 9.2 mg g^{-1}, slowly asymptoting to a Γ_{max} of 25.8 mg g^{-1} (Table 2) is in accord with the maximum adsorbance of 2.14 mg g^{-1} onto talc with 33 % chlorite observed by Charnay et al. (2001).

5 Discussion

5.1 Adsorption of aqueous and ethanolic aspirin and vanillin onto FCC

The hydrophobic moieties associated with aspirin and vanillin may well play a role in the way they adsorb. Misra (1988) stated that 'a coupling agent possessing a hydrogen-bonding moiety could effectively interact with the adsorbed water on the apatite substrate. The agent will be easily displaced from the surface by water or any other hydrogen-bonding solvent if it does not possess hydrophobic moieties concomitantly with its hydrogen-bonding groups.'

In ethanolic solutions, it is possible that the -OH functional group on the ethanol orders itself around the HAP surface, leaving the -CH_3 pointing away from the surface,

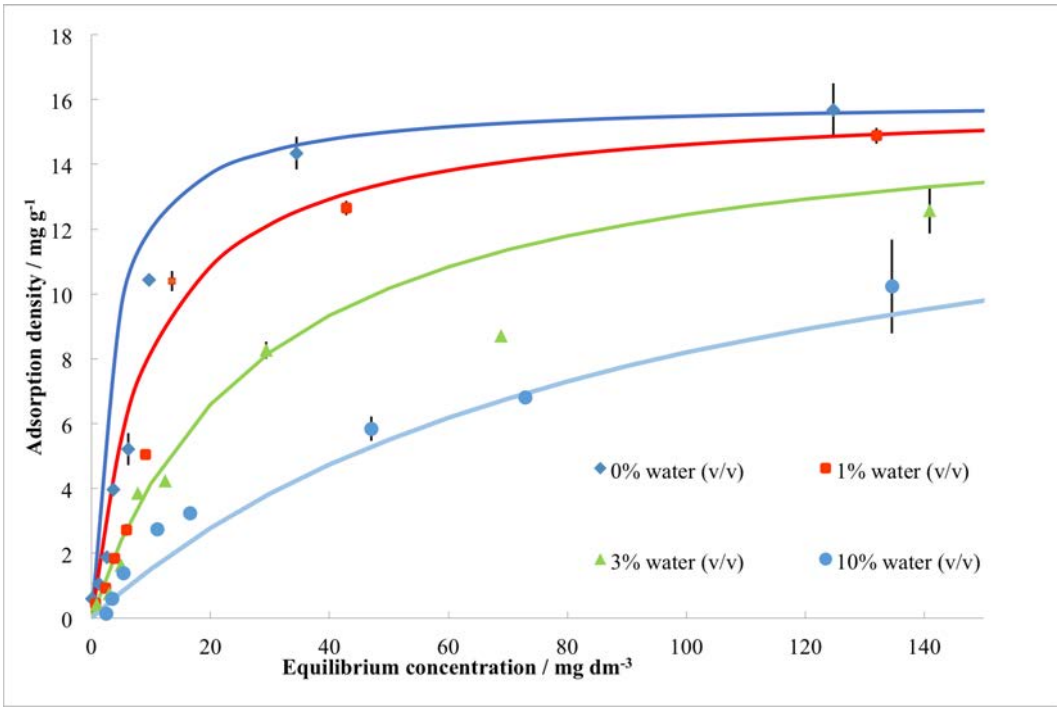

Fig. 3 Aspirin adsorption from aqueous ethanol solutions onto FCC with relative volumetric percentage of water as shown and corresponding Tóth isotherms.

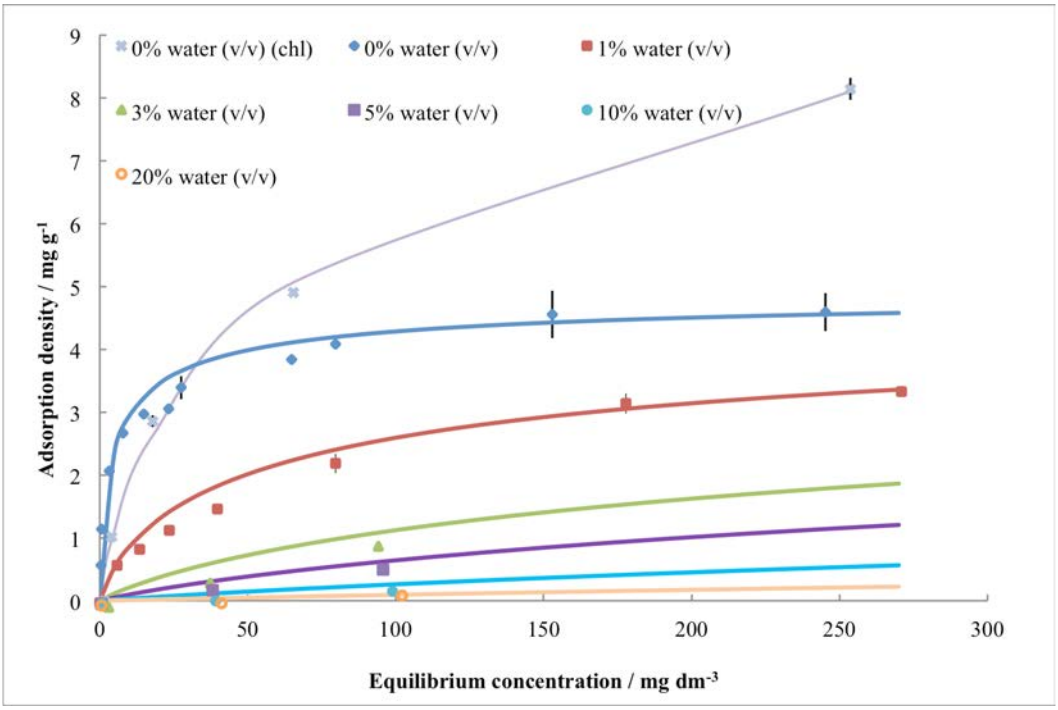

Fig. 4 Vanillin adsorption from aqueous ethanol solutions onto FCC with relative volumetric percentage of water as shown and corresponding Tóth isotherms; adsorption from chloroform is denoted with ‘chl.’

thus creating effectively hydrophobic sites. As the aspirin or vanillin approaches the FCC surface it can orientate itself so that hydrophobic interactions take place. Such speculation is supported by the observation that the use of relatively apolar chloroform ($\epsilon_r = 4.8$) as a solvent increases the amount of vanillin adsorbed (Figure 4 and Table 2).

Greater insights into the adsorption process can be made by estimating the surface coverage using the relation:

$$S_{ads} = \Gamma'_{max} \mathcal{N} \sigma \tag{4}$$

Here Γ'_{max} is the maximum adsorption (Table 2) expressed in moles per gram of substrate, $\mathcal{N}$ is the Avogadro number and σ is the effective cross-sectional area of the adsorbing cation on the surface of the substrate. Γ'_{max} is the asymptote of an imprecise extrapolation of the observed experimental data to infinite C_{eq}, and σ is also an estimate, so the equation can only give a very approximate estimate of surface coverage S_{ads}.

To calculate the surface coverage by vanillin, the volume of a known quantity of vanillin was measured by helium pycnometry (Thermo Scientific Pycnomatic ATC). From this, the volume of one vanillin molecule was deduced, and the corresponding cross-sectional area calculated as 0.44 nm^2. It follows that the calculated surface covered of FCC TP by vanillin adsorption from ethanol was 9.53 $m^2\,g^{-1}$, which is around 17 % of the overall FCC TP surface area (Table 1). For adsorption from chloroform the surface coverage was calculated to be 26.33 $m^2\,g^{-1}$, which is 48 % of the FCC's surface area.

For aspirin, the spherical-equivalent volume of a molecule was calculated from the density of aspirin of 1.404 g cm^{-3} as measured by Sun (2004) using helium pycnometry. The resulting cross-sectional area is 0.43 nm^2. It follows that the calculated surface covered of FCC TP by aspirin adsorption from ethanol was 21.64 $m^2\,g^{-1}$, which is 39 % of the overall FCC TP surface area.

On the basis of work by Schatzberg (1967), the spherical-equivalent cross-sectional area of a water molecule is 0.49 nm^2. It follows that in a solution of 1% water by volume, the water molecules in the current adsorption experiment would cover 410 m^2, relative to an available surface area of only 11 m^2 on the FCC. So there is more than enough water in the experiments to cover the entire surface of the FCC, and therefore water molecules do not simply block the adsorption sites to adsorption of vanillin.

When quantitatively explaining the effect of water on the Tóth adsorption isotherms, let us assume that the adsorption process must be analogous for both aspirin and vanillin. In the presence of water, the second derivative of the adsorption with respect to C_{eq} (i.e. curvature of the isotherm) reduces, and in the case of vanillin becomes negative as the relative water content is increased (Figures 3 and 4). As shown in these figures, it is found that to a realistic level of approximation,

$$f'(C_{eq}) = C_{eq}\left(\frac{A}{[H_2O]}\right)^B \tag{5}$$

with the parameters shown in Table 2. Furthermore, it is found that there is no effect of water on Γ_{max}, i.e. $f'' = 1$.

Therefore it is confirmed that the added water is not reducing the number of adsorption sites, in agreement with the calculation above. Instead, the results can be satisfactorily explained by assuming that there is a reduction in the effective flux of adsorbate reaching the FCC surface, caused by a stagnant layer of water trapped within the FCC microporosity, Figure 5. The orientation of the ethanol, described above, creates sites or zones which are effectively hydrophobic, shown as x in the figure.

Crank (1975) in his Figure 4.2 shows that as time increases, then for the flux Q_t at time t through a stagnant diffusion layer of thickness l, Q_t/lC_1 becomes linearly proportional to Dt/l^2, and therefore that at constant diffusion coefficient D and bulk solution concentration C_1, $Q_t \propto l^{-1}$ as $t \to \infty$. If the thickness of this diffusion layer was directly proportional to the water concentration, then $Q_t \propto [H_2O]^{-1}$. In practice, it is found that Q_t reduces approximately as $[H_2O]^{-0.7}$ for aspirin and $[H_2O]^{-1.7}$ for vanillin (Table 2). Inspection of Figure 3 shows that at higher C_{eq}, the adsorption density Γ does not follow the perturbed Tóth isotherm exactly (equation 3). These discrepancies, and the fact that the exponents are not unity, are to be expected because the aqueous diffusion layer exists within a random tortuous mesoporosity, Figure 2 (Levy et al., 2015), rather than being in the form of a stable planar layer.

Mercury porosimetry of FCC detects voids as small as 4.2 nm, subsection 1.6. The adsorption behaviour in such voids would probably differ from that shown in Figure 5, since the solvents within the voids may be partially orientationally ordered with lowered configurational entropy, and the voids would easily block. However, the PoreXpert unit cell derived from the porosimetry, Figure 2, contains very few of the smallest voids, and their contribution by volume is negligible.

5.2 Lack of adsorption of aqueous BTMAB and Na2NS onto FCC

In this work, no adsorption of BTMAB or Na2NS was observed from aqueous solution onto any grade of FCC. Lamminmäki et al. (2011) postulate that water adsorbs strongly to the surface of FCC via hydrogen bonding. Such a postulate is supported by the fact that the FCC is highly hydrophilic. The contact angle reported for 98 % pure calcium carbonate is 10° (Ren et al., 2003), and for hydroxyapatite is 31°

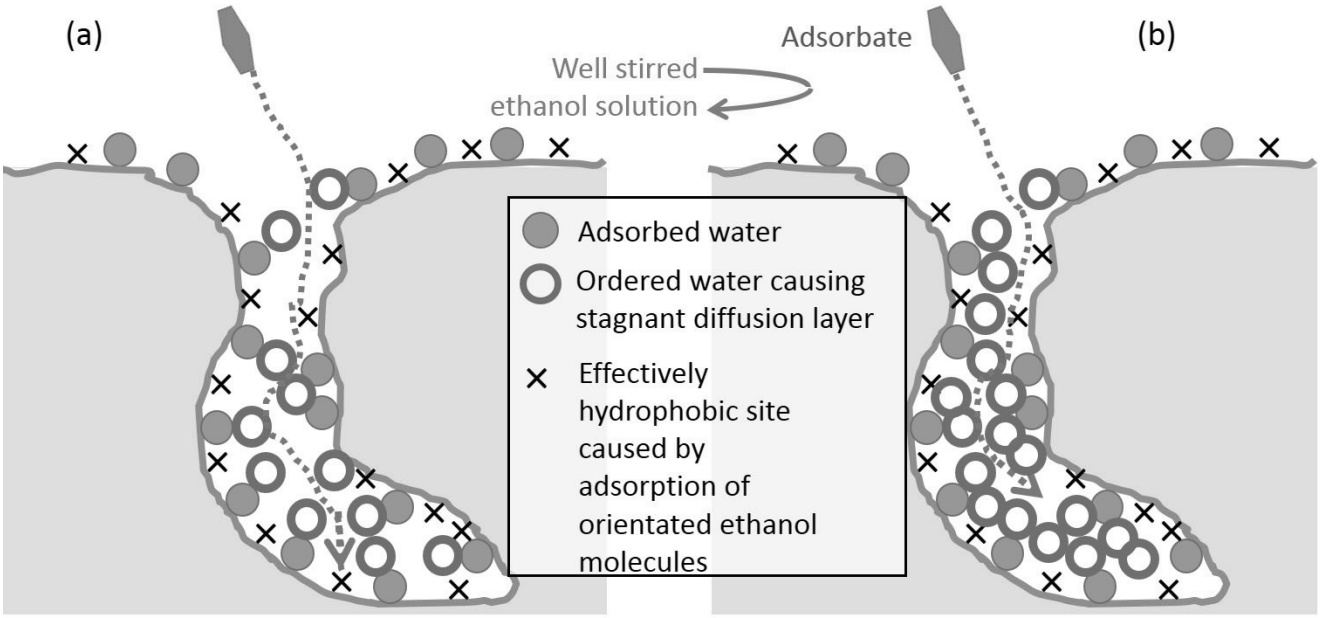

Fig. 5 Schematic diagram of the postulated mechanism for the adsorption of aspirin and vanillin onto FCC in the presence of (a) lower and (b) higher relative concentrations of water. The scale of the features is shown in Figure 2.

(Toriyama et al., 1995). As FCC is a composite of both of these materials, the FCC will also be hydrophilic. Direct observation of the contact angle of water onto FCC is not possible because water adsorbs onto the microporous surface so quickly (Tåg et al., 2010). FCC is likely to have at least a monolayer of physically adsorbed water when exposed in ambient air (Misra, 1988). However, any explanation based on surface properties does not encompass the observation that polyelectrolytes such as polyacrylate and poly(diallyldimethylammonium chloride) (PolyDADMAC) do adsorb onto FCC. An explanation could be that hydrophobic moieties are either forming hydrophobically linked micelles that are too large and wrongly oriented to adsorb, or, less likely, that tiny amounts of BTMAB and Na2NS are adsorbing and rendering the external surface hydrophobic and non-adsorbing.

6 Conclusions

We have demonstrated the adsorption properties of functionalised calcium carbonate (FCC) for aspirin and vanillin. FCC does not adsorb these species from aqueous solution. Unlike talc, which has a surface which can be characterised by the adsorption of BTMAB, the surface of FCC is amphoteric and characterisation of adsorption sites is much more elusive. However, we have demonstrated that by studying the adsorption of vanillin and aspirin from aqueous ethanolic solutions, a mechanism for the adsorption can be deduced which is quantitatively supported both by calculations of surface coverage and by the effect of water on the shapes of the adsorption isotherms.

The understanding of the mechanism of adsorption opens the way for innovative, tailored loading of actives onto FCC. It suggests that during controlled release, adsorption effects need not be taken into account. Additionally it is shown that there will be no interference with functional groups of the active, and the flavour or drug will be delivered without alteration of its efficacy or activity.

Acknowledgements The financial support of Omya International AG is gratefully acknowledged. We are grateful to Daniel Gerard and Cathy Ridgway of Omya International AG for measuring the surface areas of the substrates, and to their colleague Daniel Gantenbein for his advice. We recognise the early adsorption work onto FCC carried out by Samuel Wieck.

References

H.K. Alm, G. Ström, K. Karlström, J. Schoelkopf, P.A.C. Gane, Effect of excess dispersant on surface properties and liquid interactions on calcium carbonate containing coatings. Nord. Pulp. Pap. Res. J. **25**(1), 082–092 (2010)

C. Charnay, S. Lagerge, S. Partyka, Assessment of the surface heterogeneity of talc materials. J. Colloid Interf. Sci. **233**(2), 250–258 (2001)

H. Chen, S. Leng, Rapid synthesis of hollow nano-structured hydroxyapatite microspheres via microwave transformation method using hollow $CaCO_3$ precursor microspheres. Ceram. Int. **41**(2, Part A), 2209–2213 (2015)

J. Crank, *The Mathematics of Diffusion*, 2nd edn., (Oxford University (Clarendon) Press), 1975

P.A.C. Gane, C.J. Ridgway, E. Barceló, Analysis of pore structure enables improved tablet delivery systems. Powder Technol. **169**(2), 77–83 (2006)

P.A.C. Gane, G.P. Matthews, J. Schoelkopf, C.J. Ridgway, D.C. Spielmann, Fluid transport into porous coating structures: some novel findings. Tappi J. **83**(5), 1–22 (2000)

D. Gantenbein, J. Schoelkopf, G.P. Matthews, P.A.C. Gane, The use of porous high surface area calcium carbonate for the adsorption of dissolved and colloidal substances from thermo mechanical pulp filtrates. Nord. Pulp. Pap. Res. J. **27**(3), 631–638 (2012)

C.M. Gribble, G.P. Matthews, D. Gantenbein, A. Turner, J. Schoelkopf, P.A. Gane, Adsorption of surfactant-rich stickies onto mineral surfaces. J. Colloid Interf. Sci. **352**(2), 483–90 (2010)

T. Kallio, J. Kekkonen, P. Stenius, Acid/base properties and adsorption of an azo dye on coating pigments. J. Dispersion Sci. Technol. **27**(6), 825–834 (2006)

C. Kojima, K. Watanabe, Adsorption and desorption of bioactive proteins on hydroxyapatite for protein delivery systems. J. Drug Deliv. **2012**(Article ID 932461), 4 (2012)

T.T. Lamminmäki, J.P. Kettle, P.A.C. Gane, Absorption and adsorption of dye-based inkjet inks by coating layer components and the implications for print quality. Colloid. Surface. A **380**(1-3), 79–88 (2011)

C.L. Levy, G.P. Matthews, G.M. Laudone, C.M. Gribble, A. Turner, C.J. Ridgway, D.E. Gerard, J. Schoelkopf, P.A.C. Gane, Diffusion and tortuosity in porous functionalized calcium carbonate. Ind. Eng. Chem. Res. **54**(41), 9938–9947 (2015)

R.I. Mahato, A.S. Narang, *Pharmaceutical Dosage Forms and Drug Delivery*, 2nd edn. *Pharmacy Education Series*, (CRC Press, Taylor & Francis Group), 2012

T.J. Mays, A new classification of pore sizes, ed. by F.R.-R.J.R. P.L. Llewellyn, N. Seaton, vol. 160 (Elsevier, 2007), pp. 57–62

G. Mie, Beiträge zur optik trüber medien, speziell kolloidaler metallösungen. Ann. Phys-Berlin **330**(3), 377–445 (1908)

D.N. Misra, Adsorption on hydroxyapatite: role of hydrogen bonding and interphase coupling. Langmuir **4**(4), 953–958 (1988)

D.N. Misra, Adsorption and orientation of tetracycline on hydroxyapatite. Calcified Tissue Int. **48**(5), 362–367 (1991)

V.N. Mochalin, A. Pentecost, X.-M. Li, I. Neitzel, M. Nelson, C. Wei, T. He, F. Guo, Gogotsi, Yury, Adsorption of drugs on nanodiamond: Toward development of a drug delivery platform. Mol. Pharmaceutics **10**(10), 3728–3735 (2013)

P.J. Neuvonen, K.T. Olkkola, T. Alanen, Effect of ethanol and pH on the adsorption of drugs to activated charcoal: studies *in vitro* and in man. Acta Pharmacol. Toxicol. (Copenh) **236**(1–3), 91–102 (1984)

G. Pan, P.S. Liss, Metastable-equilibrium adsorption theory: I. Theoretical. J. Colloid Interf. Sci. **201**(1), 71–76 (1998)

K.M. Pedersen, J.B. Andersen, *Particulate material for controlled release of active ingredients*, Omya Development AG, 2012. Patent US 20120321751 A1

C. Pinholt, R.A. Hartvig, N.J. Medlicott, L. Jorgensen, The importance of interfaces in protein drug delivery - why is protein adsorption of interest in pharmaceutical formulations? Expert Opin Drug Deliv. **8**(7), 949–964 (2011)

D. Preisig, D. Haid, F.J.O. Varum, R. Bravo, R. Alles, J. Huwyler, M. Puchkov, Drug loading into porous calcium carbonate microparticles by solvent evaporation. Eur. J. Pharm. Biopharm. **87**(3), 548–558 (2014)

J. Ren, W. Wang, S. Lu, J. Shen, F. Tang, Characteristics of dispersion behavior of fine particles in different liquid media. Powder Technol. **137**(1–2), 91–94 (2003)

C.J. Ridgway, P.A.C. Gane, J. Schoelkopf, Modified calcium carbonate coatings with rapid absorption and extensive liquid uptake capacity. Colloid. Surface. A. **54**(1), 1–7 (2004)

W. Rudzinski, D.H. Everett, *Adsorption of Gases on Heterogeneous Surfaces*, 1st edn., (Elsevier Ltd.), 1992

P. Schatzberg, Molecular diameter of water from solubility and diffusion measurements. J. Phys. Chem. A **71**(13), 4569–4570 (1967)

E.M. Sellers, V. Khouw, L. Dolman, Comparative drug adsorption by activated charcoal. J. Pharm. Sci. **66**(11), 1640–1641 (1977)

C. Sun, A novel method for deriving true density of pharmaceutical solids including hydrates and water-containing powders. J. Pharm. Sci. **93**(3), 646–653 (2004)

C.-M. Tåg, M. Juuti, K. Koivunen, P.A.C. Gane, Dynamic water transport in a pigmented porous coating medium: Novel study of droplet absorption and evaporation by near-infrared spectroscopy. Ind. Eng. Chem. Res. **49**(9), 4181–4189 (2010)

M. Toriyama, Y. Kawamoto, T. Suzuki, Y. Yokogawa, K. Nishizawa, F. Nagata, Wettability of calcium phosphate ceramics by water. J. Ceram. Soc. Jpn. **103**(1193), 46–49 (1995)

T. Tsuchiya, G. Levy, Relationship between effect of activated charcoal on drug absorption in man and its drug adsorption characteristics *in vitro*. J. Pharm. Sci. **61**(14), 586–589 (1972)

S.T. Tzannis, W.J.M. Hrushesky, P.A. Wood, T.M. Przybycien, Adsorption of a formulated protein on a drug delivery device surface. J. Colloid Interface Sci. **189**(2), 216–228 (1997)

J.R. Vane, R.M. Botting, The mechanism of action of aspirin. Thromb. Res. **110**(5–6), 255–258 (2003)

Mechanism of adsorption of actives onto mesoporous functionalised calcium carbonate (FCC)

Charlotte L. Levy,[†] G. Peter Matthews,[*,†] Giuliano M. Laudone,[†] Samuel Beckett,[†] Andrew Turner,[†] Patrick A. C. Gane,[‡,¶] and Joachim Schoelkopf[‡]

[†]*Faculty of Science and Engineering, Plymouth University, Drake Circus, Plymouth, PL4 8AA, UK*

[‡]*Omya Development AG, Baslerstrasse 42, P.O. Box 335, CH-4665, Oftringen, Switzerland*

[¶]*School of Chemical Technology, Department of Forest Products Technology, Aalto University, 00076 Aalto, Helsinki, Finland*

E-mail: *p.matthews@plymouth.ac.uk

Supplementary Material for Manuscript Number ADSO-D-16-00503.1

Received: 5 October 2016 / Accepted: 7 March 2017

Scanning electron microscopy (SEM) images

Figure 1 shows scanning electron micrographs of functionalised calcium carbonate (FCC), with ground calcium carbonate (GCC), hydroxyapatite (HAP) and high surface area (HSA) talc shown for comparison.

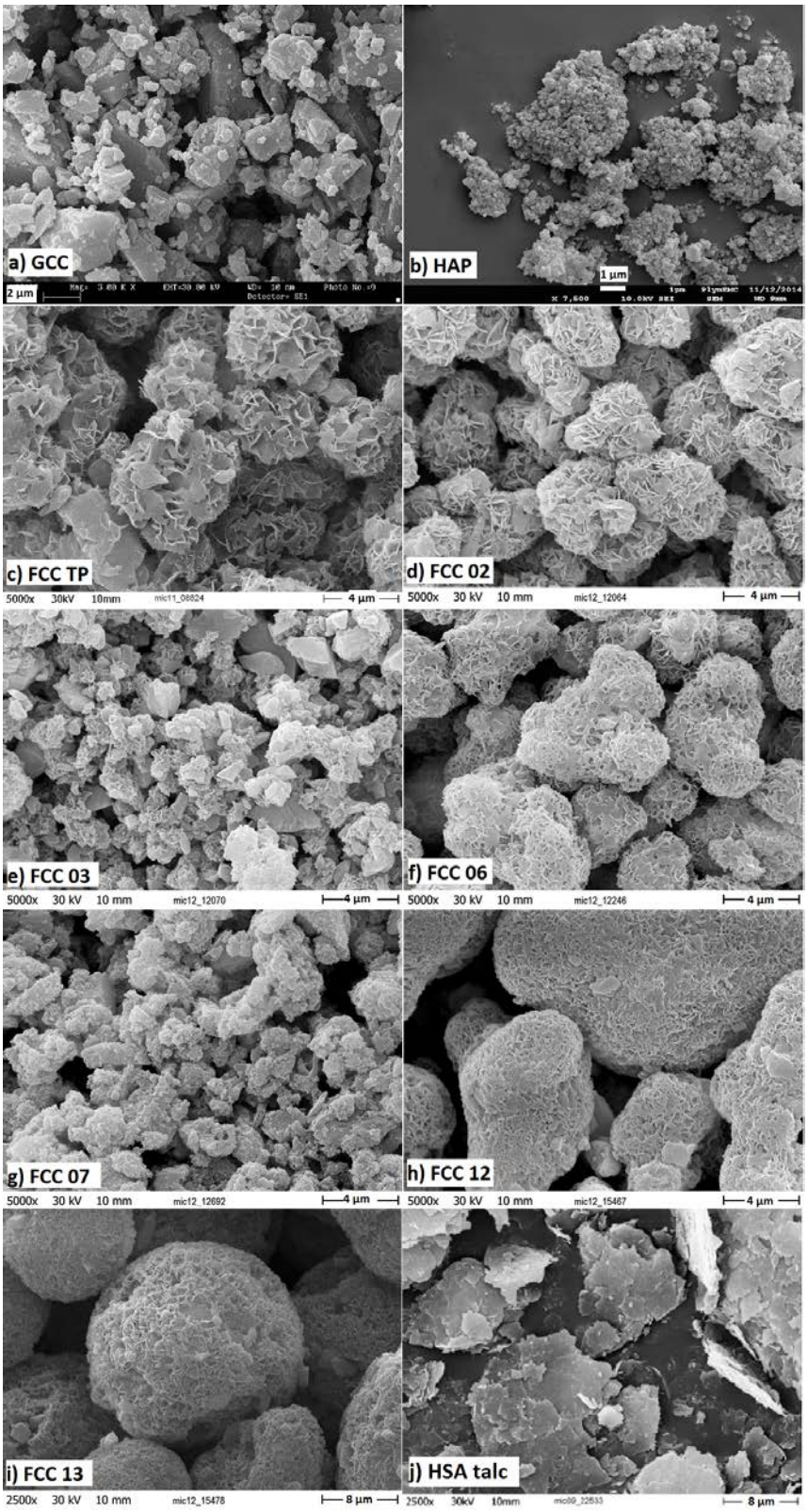

Figure 1: Scanning electron micrographs of the a) GCC, b) HAP, c) FCC TP, d) FCC 02, e) FCC 03, f) FCC 06, g) FCC 07, h) FCC 12, i) FCC 13, and j) HSA talc samples. Samples a), b), i) and j) have scale bars of 2 μm, 1 μm, 8 μm, and 8 μm, respectively, whereas the other samples have a scale bar of 4 μm.

PoreXpert® representation of microporosity

Figure 2 is a colour version of Figure 2 in the main article, and is explained there.

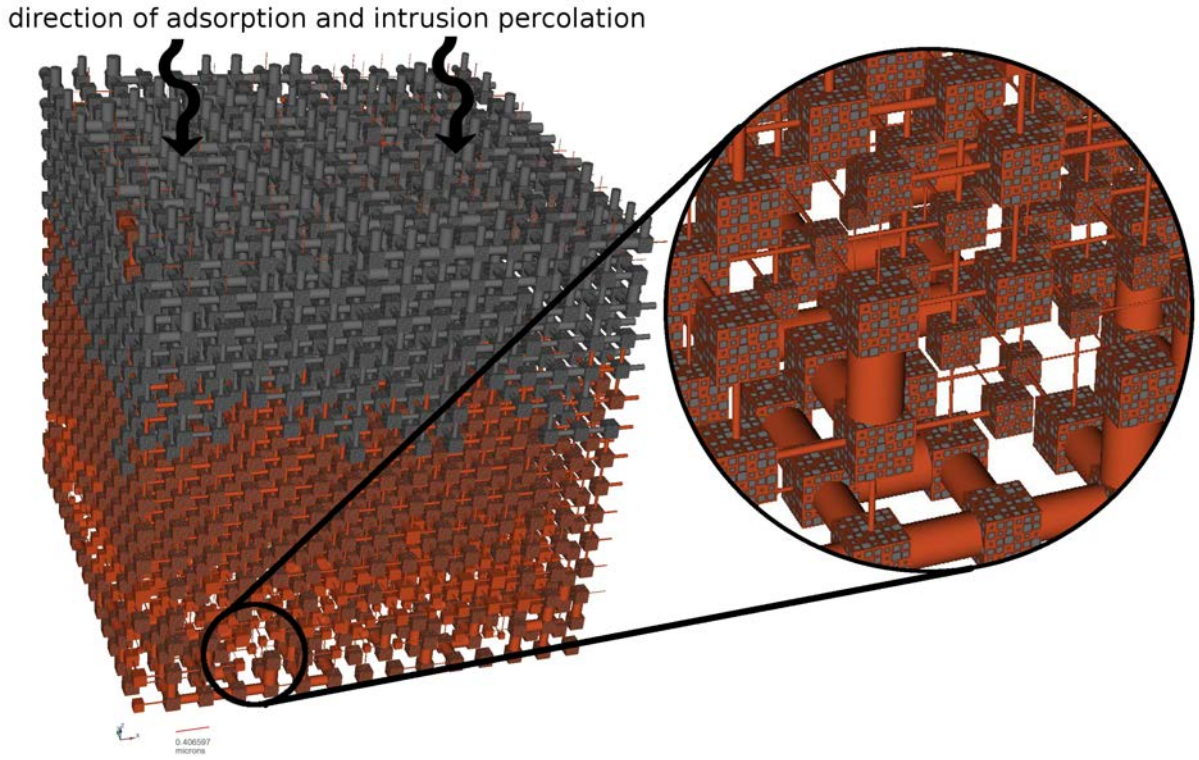

Figure 2: PoreXpert® representation of the microporous intraparticle void space of FCC 03. Scale bar bottom left: 407 nm.